

# ANNUAL REPORT

2017

and list of publications



Bayerisches Forschungsinstitut  
für Experimentelle Geochemie und Geophysik  
Universität Bayreuth

Bayerisches Geoinstitut  
Universität Bayreuth  
D-95440 Bayreuth  
Germany

Telephone: +49-(0)921-55-3700  
Telefax: +49-(0)921-55-3769  
e-mail: [bayerisches.geoinstitut@uni-bayreuth.de](mailto:bayerisches.geoinstitut@uni-bayreuth.de)  
www: <http://www.bgi.uni-bayreuth.de>

Editorial compilation by: Florian Heidelberg and Petra Buchert  
Section editors: Andreas Audétat, Tiziana Boffa Ballaran, Leonid Dubrovinsky, Dan Frost,  
Gregor Golabek, Tomoo Katsura, Hans Keppler, Hauke Marquardt,  
Katharina Marquardt, Catherine McCammon, Nobuyoshi Miyajima,  
Esther Posner, Dave Rubie, Gerd Steinle-Neumann



**Staff and guests of the Bayerisches Geoinstitut in July 2017:**

**Die Mitarbeiter und Gäste des Bayerischen Geoinstituts im Juli 2017:**

first row, from left (1. Reihe, v. links) Julia Immoor, Joana Polednia, Irina Chuvashova, Katherine Armstrong, Dariia Simonova, Stefan Keyssner, Ananya Mallik, Rong Huang, Stella Chariton, Greta Rustioni, Anna Rebaza

second row, from left (2. Reihe, v. links) Anastasiya Iskrina, Iuliia Koemets, Caterina Melai, Catherine McCammon, Laura Cialdella, Saiana Khandarkhaeva, Marija Putak Juriček, Ingrid Blanchard, Caroline Bollinger, Dorothea Wiesner, Lisa Eberhard, Eleanor Jennings, Serena Dominijanni

third row, from left (3. Reihe, v. links) Philipp Eichheimer, Vera Laurenz, Niccolò Satta, Sourav Kumar Misra, Moe Matsuoka, Petra Buchert, Sven Linhardt, Heinz Fischer, Florian Heidelbach, Hongzhan Fei, Johannes Buchen, Nobuyoshi Miyajima, Alireza Zarei, Robert Arato

back rows, from left (hintere Reihen, v. links) David Neave, Gregor Golabek, Dan Frost, Egor Zakharchenko, Anna Spivak, Marcel Thielmann, Johannes Meusbürger, Detlef Krauß, Thomas Meier, Hubert Schulze, Sylvain Petitgirard, Raphael Njul, Takaaki Kawazoe, Stefan Übelhack, Lydia Kison-Herzing, Andreas Audétat, Razvan Caracas, Gerd Steinle-Neumann, Hans Keppler, Tommaso Mandolini, Filipe Ferreira, Dmitry Druzhbin, Matteo Urgese, Sergey Ovsyannikov, Sumith Abeykoon, Jia Chang, Lin Wang, Steffen Klumbach, Haihao Guo, Jie Yao, Luca Ziberna, Takahiro Yoshioka

Absent (Es fehlten) Tiziana Boffa Ballaran, Pierre Condamine, Leonid Dubrovinsky, Nicole Fischer, Takayuki Ishii, Tomoo Katsura, Egor Koemets, Holger Kriegl, Alexander Kurnosov, Zhaodong Liu, Hauke Marquardt, Katharina Marquardt, Anke Potzel, Gerd Ramming, Oliver Rausch, Dave Rubie, Romina Scharfenberg, Kirsten Schulze, Svyatoslav Sheheka, Nicki Siersch, Ulrike Trenz, Fabian Wagle



## Contents

Foreword/Vorwort .....	11/I
1. Advisory Board and Directorship .....	13
1.1 Advisory Board .....	13
1.2 Leadership .....	13
2. Staff, Funding and Facilities .....	15
2.1 Staff .....	15
2.2 Funding .....	15
2.3 Laboratory and office facilities .....	21
2.4 Experimental and analytical equipment .....	21
3. Forschungsprojekte – Zusammenfassung in deutscher Sprache .....	III
3. Research Projects .....	23
3.1 <i>Earth and Planetary Structure and Dynamics</i> .....	23
a. Impact splash chondrule formation during planetesimal recycling (G.J. Golabek, T. Lichtenberg/Zurich, C.P. Dullemond/Heidelberg, M. Schönbächler/Zurich, T.V. Gerya/Zurich, M.R. Meyer/Ann Arbor) .....	24
b. Coupling collision and geodynamical models (G.J. Golabek, A. Emsenhuber and M. Jutzi/Bern, E.I. Asphaug/Tucson and T.V. Gerya/Zurich) .....	26
c. Understanding evolution of interior of the Moon by <i>in situ</i> density determination of deep lunar melts (A. Mallik, T. Ejaz/Kharagpur, S. Petitgirard, S. Shcheka, W. Malfait/Zurich, M. Wilke/Potsdam and G. Garapic/New Paltz) .....	27
d. Constraints on Lunar structure from combined geochemical, mineralogical, and geophysical modeling (A. Mallik, in collaboration with H. Fuqua/ Berkeley, P. Bremner/Gainesville, M.R. Diamond/Berkeley, S.J. Lock/ Cambridge, S. Panovska/Potsdam, Y. Nishikawa and H.J. Perez/Paris, A. Shahar/Washington DC, W.R. Panero/Columbus, P.H. Lognonne/Paris and U. Faul/Cambridge) .....	28
e. The post-spinel transition in the system $Mg_2SiO_4$ - $Fe_2SiO_4$ : Complete agreement with the 660-km discontinuity depth and the zero-pressure interval explaining the sharp discontinuity (T. Ishii, R. Huang, H. Fei, I. Koemets, Z. Liu, F. Maeda and L. Yuan/Sendai, L. Wang, D. Druzhbin, T. Takafumi/ Hiroshima, S. Bhat, R. Farla/Hamburg, T. Kawazoe, N. Tsujino/Misasa, E. Kulik/Hamburg, Y. Higo/Kouto, Y. Tange/Kouto and T. Katsura) .....	29
f. Numerical modelling of water in Earth's mantle (P. Eichheimer, M. Thielmann, G.J. Golabek) .....	31
g. The effect of an interconnected weak layer network on lower mantle dynamics (M. Urgese, G.J. Golabek, H. Marquardt, M. Thielmann and J. Hernlund/Tokyo) .....	32

h.	3D numerical permeability determination (P. Eichheimer, M. Thielmann, G.J. Golabek, in collaboration with W. Fujita, M. Nakamura and S. Okumura/Sendai) .....	34
i.	Mineral scale modelling of two-phase deformation with application to the lower mantle (M. Thielmann, G.J. Golabek and H. Marquardt) .....	34
3.2	<i>Geochemistry</i> .....	36
a.	Mantle composition constraints on different planet formation scenarios (S.A. Jacobson and D.C. Rubie, in collaboration with A. Morbidelli/Nice) ....	39
b.	Accretionary core formation is insufficient to explain the depletion of Mo and W in the Earth's mantle (E.S. Jennings, D.C. Rubie, S.A. Jacobson, A. Morbidelli/Nice, Y. Nakajima/Washington D.C., A.K. Vogel/Mendig, L.A. Rose-Weston/Thunder Bay, D.J. Frost) .....	40
c.	Sulfide-silicate partitioning of moderately siderophile elements at high pressure and high temperature (S. Abeykoon, V. Laurenz, D.J. Frost, D.C. Rubie and A.K. Vogel) .....	42
d.	The behaviour of Re and Os during sulfide segregation to the Earth's core (V. Laurenz, D.C. Rubie and D.J. Frost; in collaboration with M. Lagos/Bonn) .....	44
e.	The evolution of highly-siderophile elements in the lunar mantle (D.C. Rubie, V. Laurenz, A. Morbidelli/Nice, M. Wiczorek/Nice and L. Elkins-Tanton/Tempe) .....	45
f.	The fate of carbon during the differentiation of the Earth (I. Blanchard, E.S. Jennings, S. Petitgirard and D.C. Rubie) .....	47
g.	Mass transport and structural properties of oxygen in liquid iron at high pressure: Kinetic implications for metal-silicate chemical equilibration during core formation (E.S. Posner, D.C. Rubie, G. Steinle-Neumann, D.J. Frost and V. Vlček/Los Angeles) .....	49
h.	A model for the effect of pressure on the oxidation state of iron in a deep magma ocean (K. Armstrong, D.J. Frost, D.C. Rubie, C.A. McCammon and T. Boffa Ballaran) .....	52
i.	Partitioning of ferric iron between majorite and melt under conditions of Earth's transition zone (C. Beyer/Bochum, R. Myhill/Bristol, K. Marquardt and C.A. McCammon) .....	53
j.	The oxidation state of iron in highly refractory peridotites (L. Ziberna, V. Cerantola/Grenoble, G. Bulanova/Bristol, C. Smith/Bristol, L. Faccincani/Padova, C. Melai, C.A. McCammon and D.J. Frost) .....	55
k.	FeTiMM – A new oxybarometer for mafic to felsic magmas (R. Arató and A. Audétat) .....	56
l.	Diamond formation in the Earth's transition zone investigated by melting relations in the system MgO-FeO-SiO <sub>2</sub> -(Na,Ca,K-CO <sub>3</sub> ) (A. Spivak, Y. Litvin and E. Zakharchenko/Chernogolovka; D. Simonova and L.S. Dubrovinsky) .....	58

m.	Solubility of thermodynamically stable diamond in MgCO <sub>3</sub> –FeCO <sub>3</sub> –Na <sub>2</sub> CO <sub>3</sub> carbonate melts at 6 GPa (A. Spivak and Y. Litvin/Chernogolovka; G. Khachtryan/Moscow, I. Chuvashova, D. Simonova, N.A. Dubrovinskaia/Bayreuth and L.S. Dubrovinsky) .....	60
n.	Experimental investigation of the origin of ferropericlase inclusions in super-deep diamonds and the oxidation state of the lower mantle (V. Stagno and S. Dominijanni/Rome, L. Ziberna, T. Boffa Ballaran and D.J. Frost, in collaboration with T. Arimoto and T. Irifune/Matsuyama) .....	61
o.	The partitioning of water at the onset of melting in the mantle transition zone (P. Condamine and D.J. Frost) .....	62
p.	The effect of chlorine on the transport of trace elements in subduction zones (G. Rustioni, A. Audétat and H. Keppler) .....	63
q.	The fate of ophicarbonates during subduction (L. Eberhard and D.J. Frost) ...	65
r.	Internally consistent geobarometers for igneous cumulates (L. Ziberna, E.C.R. Green/Zurich and J. Blundy/Bristol) .....	67
s.	Clinopyroxene- and hornblende-rich xenoliths provide insights into the metal budget of two arc-related magma systems: Santa Rita and Cerrillos, New Mexico, USA (J. Chang and A. Audétat) .....	69
t.	Gold diffusion into and out of quartz-hosted fluid inclusions during re-equilibration experiments at 600-800 °C and 2 kbar (H. Guo and A. Audétat) .....	72
u.	Magmatic-hydrothermal evolution of the barren Huangshan pluton, Anhui province, China: A melt- and fluid inclusion study (D. Zhang and A. Audétat) .....	74
3.3	<i>Mineralogy, Crystal Chemistry and Phase Transformations</i> .....	77
a.	Synthesis of large single-crystals of MgSiO <sub>3</sub> akimotoite (G. Criniti, T. Ishii, N.C. Siersch and T. Boffa Ballaran) .....	78
b.	Phase relations in the ternary system MgO–AlO <sub>1.5</sub> –SiO <sub>2</sub> at lower mantle conditions and the Al substitution mechanisms in bridgmanite (Z. Liu, H. Grüniger/Bayreuth, R. Huang, T. Boffa Ballaran, D.J. Frost, T. Katsura and J. Senker/Bayreuth) .....	79
c.	The speciation of Fe and Al in bridgmanite (R. Huang, T. Boffa Ballaran, C.A. McCammon, N. Miyajima and D.J. Frost) .....	82
d.	Phase relations and crystal chemistry of FeAlO <sub>3</sub> -bearing bridgmanite (Z. Liu, L.S. Dubrovinsky, C.A. McCammon and T. Katsura) .....	84
e.	Iron behaviour in Fe,Al-bearing bridgmanite between 35-80 Gpa (D.M. Vasiukov/Bayreuth, J. van Driel/London, C.A. McCammon, E. Bykova/Hamburg, M. Bykov, G. Aprilis, V. Cerantola/Grenoble, I. Kuppenko/Münster, T. Kawazoe, R. Myhill, V. Prakapenka/Argonne, H.-P. Liermann/Hamburg, M. Hanfland and A.I. Chumakov/Grenoble, L.S. Dubrovinsky and N.A. Dubrovinskaia/Bayreuth) .....	85

f.	Coordination and local structure of silica to core-mantle boundary pressure (S. Petitgirard, C. Sahle/Grenoble, C. Weis/Dortmund, K. Gilmore/Grenoble, G. Spiekermann/Potsdam, M. Wilke/Potsdam and C. Sternemann/Dortmund) .....	87
g.	Squeezed silica with pentacoordinate silicon and face-sharing octahedra (E. Bykova/Hamburg, M. Bykov, A. Černok/London, N.A. Dubrovinskaia/Bayreuth, L.S. Dubrovinsky, J. Tidholm and S.I. Simak/Linköping, O. Hellman/Pasadena, M. Belov and I.A. Abrikosov/Moscow, H.-P. Liermann/Hamburg, M. Hanfland/Grenoble, C. Prescher and V.B. Prakapenka/Argonne) .....	88
h.	Pentacoordinated silicon in the high-pressure polymorph of danburite (A. Pakhomova and E. Bykova/Hamburg, M. Bykov, K. Glazyrin/Hamburg, B. Gasharova/Karlsruhe, H.-P. Liermann/Hamburg, M. Mezouar/Grenoble, L. Gorelova and S. Krivovichev/Saint-Petersburg, in collaboration with L.S. Dubrovinsky) .....	90
i.	Reaction of MgCO <sub>3</sub> and Fe observed by transmission electron microscopy (F. Maeda/Sendai, N. Miyajima; S. Kamada, T. Sakamaki and A. Suzuki/Sendai) .....	92
j.	Crystal structure of Fe-bearing MgCO <sub>3</sub> tetracarbonate at 95 GPa from single-crystal X-ray diffraction (S. Chariton, E. Bykova/Hamburg, M. Bykov, V. Cerantola/Grenoble, E. Koemets, G. Aprilis, M. Hanfland/Grenoble, C.A. McCammon and L.S. Dubrovinsky) .....	93
k.	High-pressure behaviour of $\delta$ -AlOOH and magnesium silicate Phase D (D. Simonova, E. Bykova/Hamburg, M. Bykov, T. Kawazoe and L.S. Dubrovinsky) .....	95
l.	Time-resolved X-ray diffraction and dynamic compression on the ice VI-VII phase transition (A.S.J. Méndez, H. Marquardt and H-P. Liermann/Hamburg) .....	97
m.	Time resolved X-ray diffraction of Mg <sub>0.8</sub> Fe <sub>0.2</sub> O across its spin transition under dynamic compression (A.S.J. Mendez, H. Marquardt and H-P. Liermann/Hamburg) .....	98
n.	B1-B2 transition in MgO at multi Mbar pressure from ab initio simulations (F. Trybel and G. Steinle-Neumann) .....	99
o.	High-pressure behaviour of magnetite-magnesioferrite solid solution (C. Melai, A. Kurnosov and T. Boffa Ballaran, in collaboration with L. Uenver-Thiele and A.B. Woodland/Frankfurt) .....	102
p.	Reaction of mackinawite (FeS) in aqueous solutions (C.A. McCammon, in collaboration with M. Wan and S. Peiffer/Bayreuth and C. Schröder/Stirling) .....	103
3.4	<i>Physical Properties of Minerals</i> .....	106
a.	High-pressure single-crystal elasticity of iron-bearing wadsleyite and the reflectivity of the 410-km discontinuity (J. Buchen, H. Marquardt, S. Speziale/Potsdam, T. Kawazoe/Hiroshima, T. Boffa Ballaran and A. Kurnosov) .....	107

b.	The effect of hydration on the elastic wave velocities of ringwoodite at pressures of Earth's transition zone (K. Schulze, H. Marquardt, A. Kurnosov, T. Boffa Ballaran, C.A. McCammon, K. Marquardt, in collaboration with T. Kawazoe/Hiroshima and M. Koch-Müller/Potsdam) .....	108
c.	Elasticity of phase E single crystals (N. Satta, H. Marquardt, A. Kurnosov, T. Kawazoe and T. Boffa Ballaran) .....	110
d.	Single-crystal X-ray diffraction on AlSiO <sub>3</sub> OH "phase egg" to high pressure (K. Schulze, T. Boffa Ballaran, M.G. Pamato/London and A. Pakomova/Hamburg) .....	111
e.	Single-crystal sound velocity measurements on natural majoritic garnets from Jagersfontein kimberlite (I. Koemets, H. Marquardt, A. Kurnosov and L.S. Dubrovinsky) .....	112
f.	Influence of aluminium on the elasticity of majorite-pyropite garnet (Z. Liu, N. Siersch, T. Boffa Ballaran, D.J. Frost, N. Cai/Stony Brook, S. Gréaux and T. Irifune/Matsuyama) .....	113
g.	The effect of the iron spin crossover on ferropericlase compressional velocities measured at seismic frequencies (H. Marquardt, A.S.J. Mendéz, H.-P. Liermann/Hamburg and J. Buchen) .....	115
h.	Elastic properties of Fe- and Al-bearing akimotoite (N.C. Siersch, T. Boffa Ballaran, Z. Liu, T. Ishii, D.J. Frost and T. Katsura, in collaboration with Y. Wang and T. Yu/Argonne) .....	117
i.	Quasi-hydrostatic compression and sound wave velocities of polycrystalline stishovite: Evaluating the seismic signature of silica in the lower mantle (J. Buchen, H. Marquardt, K. Schulze, A. Kurnosov, A. Chaudhari, S. Speziale/Potsdam and N. Nishiyama/Hamburg) .....	118
j.	Ionic conductivity of natural olivine (H. Fei, D. Druzhbin and T. Katsura) ....	120
k.	Electronic transport properties of liquid Fe-S alloys from ab initio computations (F. Wagle and G. Steinle-Neumann) .....	122
3.5	<i>Fluids, Melts and their Interaction with Minerals</i> .....	126
a.	Carbon monoxide solubility in silicate melts (T. Yoshioka, T. Nakamura/Sendai, D. Nakashima/Sendai, S. Shcheka and H. Keppler) .....	127
b.	<i>In situ</i> observation of bubble nucleation in silicate melts at precisely controlled pressure and temperature (M. Masotta/Pisa and H. Keppler) .....	128
c.	Electrical conductivity of HCl-H <sub>2</sub> O fluids at high pressure and high temperature (S. Klumbach and H. Keppler) .....	130
d.	Experimental determination of the nitrogen-carrying capacity of subducted slab-derived melt (A. Mallik, M. Wiedenbeck/Potsdam and Y. Li/Guangzhou) .....	132
e.	Phlogopite-peridotite melting and the role of fluorine in volatile storage in the upper mantle (P. Condamine, D.J. Frost and E. Médard/Clermont-Ferrand) .....	132

f.	Fluorine partitioning between hydrous minerals and incipient melt in the lithospheric mantle (P. Condamine, E. Médard/Clermont-Ferrand, J. Francomme/Milan and D. Laporte/Clermont-Ferrand) .....	134
g.	The effect of pressure on Cr redox systematics in reduced basaltic liquids (A.S. Bell/Albuquerque, K. Armstrong, D.J. Frost and M. Newville/Chicago) .....	136
h.	Influence of cooling rate on Mg <sub>2</sub> SiO <sub>4</sub> and MgSiO <sub>3</sub> glass structure from MD simulations (J. Yao, G. Steinle-Neumann and F. Wagle) .....	138
i.	On the feasibility of measuring stable isotope fractionation between melts and fluids by in situ Raman spectroscopy (A. Zarei, S. Klumbach and H. Keppler) .....	140
3.6	<i>Rheology</i> .....	142
a.	Experimental deformation of garnet single crystals at high temperature and pressure (T. Mandolini and F. Heidelbach) .....	143
b.	Interference of olivine A and B type textures during deformation under progressively increasing pressure (N. Walte/Garching, F. Heidelbach and D.J. Frost) .....	146
c.	Experimental study of pinch-and-swell structures in viscously contrasting materials (R. Farla/Hamburg, F. Heidelbach, M. Urgese, P. Bons/Tübingen, E. Gomez-Rivas/Tübingen and A. Griera/Barcelona) .....	148
d.	Experimental deformation of natural magnetite at high pressure and temperature (D. Silva-Souza/Ouro Preto, C. Bollinger and F. Heidelbach) ....	150
e.	High-temperature/-pressure deformation experiments of (Mg,Fe)O indicate {100}<011> slip in Earth's lower mantle (J. Immoor, H. Marquardt, H.-P. Liermann/Hamburg, L. Miyagi/Salt Lake City, F. Lin/Salt Lake City, S. Speziale/Potsdam, S. Merkel/Lille, J. Buchen and A. Kurnosov) .....	153
f.	Rheology of forsterite: Crystal slip plasticity vs. grain boundary sliding (C. Bollinger, K. Marquardt, F. Ferreira, M. Thielmann and P. Knödler/Bayreuth) .....	155
g.	Transmission of dislocations across olivine grain boundaries (F. Ferreira and K. Marquardt) .....	157
h.	Chemical signature of migrating grain boundaries in polycrystalline olivine (Y. Boneh/Providence and K. Marquardt) .....	159
i.	Small water dependence of the dislocation mobility in the olivine [001](100) slip system (L. Wang, T. Kawazoe, N. Miyajima and T. Katsura) .....	162
j.	Activation of the [100](001) slip system by water incorporation in olivine (L. Wang, T. Kawazoe, N. Miyajima and T. Katsura) .....	164
k.	Diffusion controlled motion of [001](010) screw dislocation in natural olivine (L. Wang and T. Katsura) .....	165
l.	Measurement of the silicon self-diffusion coefficient in single-crystal wadsleyite (D. Druzhbin, H. Fei, R. Dohmen/Bochum, Y. Lin/Beijing, C. Zhang/Beijing, M. Wiedenbeck/Potsdam and T. Katsura) .....	168

m.	Interplay between shear heating and grain size evolution in ductile shear zones (M. Thielmann and T. Duretz/Rennes) .....	169
3.7	<i>Materials Science</i> .....	171
a.	Boron allotrope with $\alpha$ -Ga structure synthesized at high pressure and high temperature (I. Chuvashova, E. Bykova/Hamburg, M. Bykov, L.S. Dubrovinsky, N.A. Dubrovinskaia/Bayreuth, V. Prakapenka/Chicago, M. Mezouar/Grenoble and K. Glazyrin/Hamburg) .....	172
b.	Novel compounds in the iron-nitrogen system synthesized in laser-heated diamond anvil cells (M. Bykov, E. Bykova/Hamburg, G. Aprilis, K. Glazyrin/Hamburg, E. Koemets, I. Chuvashova, M. Mezouar/Grenoble, V. Prakapenka/Chicago, H.-P. Liermann/Hamburg, F. Tasnádi/Linköping, A.V. Ponomareva/Moscow, I.A. Abrikosov/Linköping, N.A. Dubrovinskaia/Bayreuth and L.S. Dubrovinsky) .....	173
c.	Investigation of chemical reactions between Fe and oxygen at pressures up to 70 GPa and high temperature (E. Koemets, E. Bykova/Hamburg, M. Bykov, G. Aprilis, S. Chariton; J. Haines, S. Clement and J. Rouquette/Montpellier; V. Prakapenka/Chicago, M. Hanfland/Grenoble and L.S. Dubrovinsky) .....	175
d.	Equation of state of TaC to 39 GPa and 1073 K (S. Speziale/Potsdam, J. Immoor, H.-P. Liermann/Hamburg, S. Merkel/Lille and H. Marquardt) .....	176
e.	Inversion of conduction type of germanium under pressure (S.V. Ovsyannikov, in collaboration with N.V. Morozova and I.V. Korobeinikov/Yekaterinburg) .....	178
f.	Unusual phase transition in $\text{CaCo}_3\text{V}_4\text{O}_{12}$ perovskite under high pressure (S.V. Ovsyannikov; E. Bykova and A. Pakhomova/Hamburg; D.P. Kozlenko/Dubna, M. Bykov, S.E. Kichanov/Dubna; N.V. Morozova and I.V. Korobeinikov/Yekaterinburg; F. Wilhelm and A. Rogalev/Grenoble; A.A. Tsirlin/Augsburg, A. Kurnosov; Y.G. Zainulin, N.I. Kadyrova and A.P. Tyutyunnik/Yekaterinburg and L.S. Dubrovinsky) .....	180
g.	Phase relations and activity-composition relations in the system ZnO-MgO-SiO <sub>2</sub> (N. Farmer/Acton, in collaboration with P. Condamine and D.J. Frost) .....	182
h.	Grain boundary diffusion and grain boundary segregation of multiple elements in Yttrium Aluminium Garnet (YAG) – experimentally determined using the bicrystal setup (J. Polednia, K. Marquardt and R. Dohmen/Bochum) .....	184
3.8	<i>Methodological Developments</i> .....	186
a.	Diamond anvils with a round table (DART-anvils) designed for high-pressure experiments in DAC (L.S. Dubrovinsky, N.A. Dubrovinskaia/Bayreuth, E. Koemets, M. Bykov, G. Aprilis/Bayreuth; E. Bykova, A. Pakhomova and K. Glazyrin/Hamburg; V. Prakapenka and E. Greenberg/Argonne) .....	187

b.	Single crystal X-ray diffraction experiments above 200 Gpa (S. Khandarkhaeva, L.S. Dubrovinsky, N.A. Dubrovinskaia/Bayreuth; P. Sedmak and J. Wright/Grenoble) .....	188
c.	Fully time resolved synchrotron Mössbauer spectroscopy for pulsed laser heating experiments in diamond anvil cells (C. Strohm/Hamburg, G. Aprilis/ Bayreuth, I. Kuppenko/Münster and D. Vasiukov/Bayreuth; V. Cerantola, A.I. Chumakov and R. Rüffer/Grenoble; C.A. McCammon and L.S. Dubrovinsky) .....	190
d.	Development of novel techniques for high-pressure NMR in diamond anvil cells (T. Meier, S. Petitgirard and L.S. Dubrovinsky) .....	192
e.	Development and calibration of a waveguide-based flexible CO <sub>2</sub> laser heating system: High-temperature Brillouin spectroscopy measurement of single crystal MgO (A. Kurnosov, H. Marquardt and L.S. Dubrovinsky) .....	194
f.	A portable system for the measurement of optical losses of visible light in DACs (T. Fedotenko/Bayreuth, S. Khandarkhaeva, E. Koemets, N.A. Dubrovinskaia/Bayreuth and L.S. Dubrovinsky) .....	196
g.	LH-DAC experiments with metal-encapsulated samples: Preliminary results and numerical modelling (M.A. Baron/Paris, O.T. Lord/Bristol, M.J. Walter/Bristol, M. Thielmann, N. Miyajima; S. Petitgirard and R.G. Trønnes/Oslo) .....	197
h.	Diamond anvil cell partitioning experiments for core formation studies: Testing the limitations of electron microprobe analysis (E.S. Jennings, V. Laurenz, J. Wade/Oxford, S. Petitgirard and D.C. Rubie) .....	200
i.	An Atom Probe Tomography (ATP) investigation of exsolution textures in quenched metal from DAC partitioning experiments (E.S. Jennings, J. Wade and J. Douglas/Oxford and D.C. Rubie) .....	202
j.	Quantitative determination of iron oxidation states in minerals using Fe L <sub>2,3</sub> -edge electron energy-loss near-edge structure spectroscopy: A geochemical application of EELS revisited (N. Miyajima, R. Huang, F. Sorbadere/Issoire, T. Boffa Ballaran, C.A. McCammon and D.J. Frost) .....	204
k.	The single-crystal diamond trap (SCDT) method: A new way to determine mineral solubilities in fluids at high pressure and high temperature (S. Abeykoon and A. Audétat) .....	206
4.	International Research and Training Group – "Deep Earth Volatile Cycles" .....	209
5.	Publications, Conference Presentations, Seminars .....	213
5.1	Publications (published) .....	213
a)	Refereed international journals .....	213
b)	Popular scientific magazines .....	220
5.2	Publications (submitted, in press) .....	221
5.3	Presentations at scientific institutions and at congresses .....	225
5.4	Lectures and seminars at Bayerisches Geoinstitut .....	242
5.5	Conference organization .....	244

6.	Visiting scientists .....	245
6.1	Visiting scientists funded by the Bayerisches Geoinstitut .....	245
6.2	Visiting scientists supported by other externally funded BGI projects .....	246
6.3	Visiting scientists supported by the DFG Core Facility programme .....	247
6.4	Visitors (externally funded) .....	247
7.	Additional scientific activities .....	251
7.1	Habilitation/Theses .....	251
7.2	Honours and awards .....	251
7.3	Editorship of scientific journals .....	252
7.4	Membership of scientific advisory bodies .....	252
8.	Scientific and Technical Personnel .....	255
	Index .....	259
	Obituary/Nachruf Kurt Klasinski .....	265



IRTG students at the tertiary basalt cone of the Parkstein volcano during the field trip of the IRTG doctoral seminar held at Bayreuth in September 2017; the field trip was guided by Dr. Andreas Peterek from the Bavarian-Bohemian Geopark.

IRTG-Studenten am tertiären Basaltkegel des Parkstein Vulkans während der Exkursions des IRTG-Doktorandenseminars in Bayreuth im September 2017; die Exkursion wurde von Dr. Andreas Peterek vom Bayerisch-Böhmischen Geopark geleitet.

## Foreword

2017 was the first full year of our DFG funded International Research and Training Group (IRTG) "Deep Earth Volatile Cycles", which is run in collaboration with our partners at Tohoku University in Japan. This programme provides training for doctoral students who perform research at both partner institutes. This year has seen a significant ramping-up of cooperative research efforts and we have been very pleased to welcome numerous researchers from Japan to the BGI. In this yearbook you will already find a number of reports that have resulted from joint research projects. Students and supervisors from Japan also attended a joint doctoral student symposium held at the BGI in September where the weather was still sufficiently clement to also allow a field trip to the nearby Oligocene volcanic pipe at Parkstein (photo left) and the KTB deep continental bore-hole at Windischeschenbach. More details of IRTG activities for 2017 are reported in section 4 of the yearbook. We were particularly pleased to hear that Professor Eiji Ohtani of Tohoku University will receive the Alexander von Humboldt Research Award in 2018 and will therefore perform a research sabbatical at the institute for a period of one year. This will further strengthen research ties between our two institutions.

In 2017 interviews were held for a brand new professorship at the Bayerisches Geoinstitut in Experimental Planetology. We expect to announce the successful candidate for this position in early 2018. For many years, researchers at the institute have applied experimental methods to understand the formation and properties of other planets in the solar system and several examples of such research can be found in the current yearbook. I anticipate that the new professor will bring further depth and breadth to this field of research at the institute in the coming years.

There are a number of research highlights in section 3 of this year's yearbook. The top of the lower mantle is marked globally by a sharp change in mineral properties at 660 km depth, which causes the reflection of seismic waves. Since its discovery scientists have debated whether this seismic discontinuity marks a change in the chemical composition of the mantle or if it results from a pressure-induced mineral phase transformation. This debate appeared to be settled after high-pressure experiments demonstrated that the mineral ringwoodite transforms to an assemblage of bridgmanite and ferropericlase at approximately these conditions. However, a series of studies that used *in situ* X-ray diffraction to accurately measure experimental pressures found that this transition would occur at a depth that was far too shallow to cause the 660 km discontinuity. A report in section 3.1 now resolves this issue by implementing a series of innovative procedures in the large volume press and finds indeed that the bridgmanite-forming transformation can cause the 660 km discontinuity. Best of all, however, the report allows the first reliable estimate to be made for the global average temperature of the mantle at this depth, which is approximately 1650 °C.

As reported in previous yearbooks, developments in diamond anvil cell (DAC) technology continue to increase the frontier of attainable pressure. This has inevitably led to samples becoming smaller, which makes their characterization at extreme conditions challenging, particularly when they contain light elements that interact weakly with X-rays. In section 3.7 a remarkable breakthrough is reported in the application of nuclear magnetic resonance (NMR) measurements in the DAC. Through the use of a miniaturized magnetic lens, approximately ½ mm in diameter, that sits between the tips of the diamond anvils and raises the sensitivity of the NMR signal, BGI scientists have been able to perform NMR measurements up to a pressure of 70 GPa, more than an order of magnitude higher in pressure than previous measurements. NMR reveals information on the bonding environment of specific elements in minerals and fluids and is particularly suitable for studying light elements such as hydrogen. It can also be used to detect magnetic transitions and metallization. Even higher pressures are potentially possible, which will allow structural changes in materials to be investigated even under extreme pressures where sample sizes inhibit the use of other techniques.

The year was punctuated by the very sad loss of our long-serving electronics engineer Kurt Klasinski. Mr Klasinski was responsible for designing the control systems for many pieces of equipment at the institute and his remarkable efforts helped large numbers of institute staff and visitors to perform their research. An obituary for Mr Klasinski can be found at the end of the yearbook. Two long-serving members of the institute's vital support staff, Stefan Keyssner and Hubert Schulze, retired in the middle of the year. They are surely both familiar faces to many people who have visited the institute over the last decades and I take this opportunity to thank them for their many years of committed service.

On the behalf of my colleagues, I would like to thank the *Free State of Bavaria* as represented by the *Bavarian State Ministry of Science, Research and Art*, as well as the *Commission for High-Pressure Research in Geoscience* for their continuing support and strong commitment to the Bayerisches Geoinstitut. I would further like to thank the *President and Leadership of the University of Bayreuth* for their high regard of the profile field "High Pressure and High Temperature Research". We also gratefully acknowledge generous support from external funding agencies, in particular the *Alexander von Humboldt Foundation*, the *European Union*, the *German Science Foundation*, and the *Federal Ministry of Education and Research*, which continue to contribute greatly to the further development and success of the Geoinstitut.

Bayreuth, March 2018

Dan Frost

## Vorwort

2017 war das erste vollständige Jahr unserer von der DFG geförderten Internationalen Forschungs- und Trainingsgruppe (IRTG) "Deep Earth Volatile Cycles", die in Zusammenarbeit mit unseren Partnern an der Tohoku Universität in Japan durchgeführt wird. In diesem Programm werden Doktoranden ausgebildet, die an beiden Partnerinstituten forschen. Im letzten Jahr konnten wir die Forschungsk Kooperationen deutlich intensivieren und haben uns sehr darüber gefreut, zahlreiche Forscher aus Japan am BGI begrüßen zu können. In diesem Jahrbuch finden Sie bereits eine Reihe von Berichten, die sich aus gemeinsamen Forschungsprojekten ergeben haben. Studenten und Betreuer aus Japan nahmen auch an einem gemeinsamen Doktorandensymposium teil, das im September am BGI stattfand. Das Wetter war ausreichend gut, um auch eine Exkursion zum tertiären Vulkan bei Parkstein (Foto auf Seite 10) sowie zur kontinentalen Tiefbohrung (KTB) nahe Windischeschenbach zu unternehmen. Weitere Einzelheiten zu den IRTG-Aktivitäten in 2017 sind im Abschnitt 4 des Jahrbuchs zu finden. Besonders freuen wir uns auch, dass Professor Eiji Ohtani von der Tohoku Universität im Jahr 2018 den Alexander von Humboldt-Forschungspreis erhält und daher ein Forschungsjahr am Bayerischen Geoinstitut verbringen wird. Dies wird die Forschungsbeziehungen zwischen unseren beiden Institutionen weiter stärken.

Im Jahr 2017 wurden am BGI Interviews für eine zusätzliche Professur für Experimentelle Planetologie geführt. Wir erwarten, die erfolgreiche Kandidatin/den erfolgreichen Kandidaten für diese Position Anfang 2018 bekannt geben zu können. Forscher des Instituts haben seit vielen Jahren experimentelle Methoden angewandt, um die Entstehung und Eigenschaften anderer Planeten im Sonnensystem zu verstehen, und mehrere Beispiele solcher Forschungsergebnisse finden sich im vorliegenden Jahrbuch. Ich gehe davon aus, dass die neue Professur dieses Forschungsfeld in den kommenden Jahren noch weiter vertiefen wird.

In Kapitel 3 des vorliegenden Jahrbuchs finden sich eine Reihe von Forschungshöhepunkten. Die Obergrenze des unteren Erdmantels ist weltweit durch eine starke Veränderung der Mineraleigenschaften in 660 km Tiefe gekennzeichnet, was die Reflexion seismischer Wellen verursacht. Seit ihrer Entdeckung haben Wissenschaftler darüber diskutiert, ob diese seismische Diskontinuität eine Veränderung der chemischen Zusammensetzung des Mantels oder eine druckinduzierte Mineralphasenumwandlung darstellt. Nachdem Hochdruckexperimente gezeigt hatten, dass sich das Mineral Ringwoodit unter diesen Bedingungen in eine Paragenese von Bridgmanit und Ferroperiklas umwandelt, schien diese Debatte beigelegt zu sein. Eine Reihe von Studien, die mittels *in situ*-Röntgenbeugung den Druck in den Experimenten genau messen konnten, ergaben jedoch, dass dieser Übergang in einer Tiefe stattfindet, die viel zu niedrig ist, um die Diskontinuität in 660 km Tiefe zu verursachen. Ein Bericht in Abschnitt 3.1 klärt nun diese offene Frage. Mithilfe einer Reihe innovativer Verfahren in der Vielstempelpresse wurde herausgefunden, dass die Bridgmanit-bildende Umwandlung die Diskontinuität in 660 km Tiefe tatsächlich verursachen kann. Vor allem aber erlaubt diese Arbeit die erste verlässliche Schätzung der globalen Durchschnittstemperatur des Mantels in dieser Tiefe von etwa 1650 °C.

Wie in früheren Jahrbüchern berichtet, haben Entwicklungen in der Technologie der Diamantstempelzellen den Bereich des experimentell erreichbaren Drucks deutlich erweitert. Dies hat zwangsläufig dazu geführt, dass die Proben kleiner geworden sind, was ihre Charakterisierung unter extremen Bedingungen schwierig macht, insbesondere wenn sie leichte Elemente enthalten, die schwach mit Röntgenstrahlen wechselwirken. In Abschnitt 3.7 wird ein bemerkenswerter Durchbruch in der Anwendung von Kernspinresonanz (NMR)-Messungen in der Diamantstempelzelle beschrieben. Durch die Verwendung einer miniaturisierten magnetischen Linse von etwa  $\frac{1}{2}$  mm Durchmesser, die zwischen den Spitzen der Diamantstempel sitzt und die Empfindlichkeit der Messung des NMR-Signals erhöht, konnten BGI-Wissenschaftler NMR-Messungen bis zu einem Druck von 70 GPa durchführen, mehr als eine Größenordnung höher im Druck als vorherige Studien. Die NMR liefert Informationen über die Bindungsumgebung bestimmter Elemente in Mineralen und Flüssigkeiten und eignet sich daher besonders für die Untersuchung von leichten Elementen wie Wasserstoff. Sie kann auch verwendet werden, um magnetische Übergänge und die Metallisierung zu erkennen. Auch noch höhere Drücke sind potentiell möglich, was die Untersuchung struktureller Veränderungen unter extremen Drücken ermöglichen wird, wenn die Probengröße den Einsatz anderer Techniken unmöglich macht.

Das Jahr 2017 wurde durch den sehr traurigen Verlust unseres langjährigen Elektronikingenieurs Kurt Klasinski überschattet. Herr Klasinski war verantwortlich für die Gestaltung der Kontrollsysteme für viele Ausrüstungsgegenstände am Institut und seine bemerkenswerten Bemühungen halfen zahlreichen Mitarbeitern und Besuchern des Instituts, ihre Forschungen durchzuführen. Ein Nachruf auf Herrn Klasinski ist am Ende des Jahrbuches zu finden. Zwei weitere langjährige Mitarbeiter des Instituts, Stefan Keyssner und Hubert Schulze, sind im Laufe des Jahres in den Ruhestand getreten. Sie sind für viele Menschen, die das Institut in den letzten Jahrzehnten besucht haben, sicherlich vertraute Gesichter, und ich nutze die Gelegenheit, um ihnen für ihre langjährige, engagierte Arbeit zu danken.

Meine Kollegen und ich möchten dem *Freistaat Bayern*, vertreten durch das *Bayerische Staatsministerium für Wissenschaft, Forschung und Kunst*, und der *Kommission für Geowissenschaftliche Hochdruckforschung der Bayerischen Akademie der Wissenschaften* unseren Dank für ihre fortwährende Unterstützung des Bayerischen Geoinstituts aussprechen. Darüber hinaus möchten wir dem Präsidenten und der Hochschulleitung der Universität Bayreuth ausdrücklich für ihre zuverlässige und kontinuierliche Unterstützung des Profilsfeldes 'Hochdruck- und Hochtemperaturforschung' danken. Wir sind auch für die großzügige Förderung durch externe Geldgeber dankbar, insbesondere der *Alexander-von-Humboldt-Stiftung*, der *Europäischen Union* und der *Deutschen Forschungsgemeinschaft*, die ebenfalls wesentlich zur Entwicklung und zum Erfolg des Bayerischen Geoinstituts beigetragen haben.

Bayreuth, im März 2018

Dan Frost

## 1. Advisory Board and Directorship

### 1.1 Advisory Board

The *Beirat für Geowissenschaftliche Hochdruckforschung der Bayerischen Akademie der Wissenschaften* advises on the organisation and scientific activities of the institute. Members of this board are:

Prof. Dr. Gerhard BREY	Institut für Geowissenschaften der Johann Wolfgang Goethe-Universität, Frankfurt am Main
Prof. Dr. Ulrich CHRISTENSEN	Max-Planck-Institut für Sonnensystemforschung, Katlenburg-Lindau
Prof. Dr. Rudolf GROSS (Vice Chairman)	Walther-Meißner-Institut für Tieftemperaturforschung (WMI), Garching
Prof. Dr. Rüdiger KNIEP	Emeritus, Max-Planck-Institut für Chemische Physik fester Stoffe, Dresden
Prof. Dr. Herbert PALME	Emeritus, Institut für Mineralogie und Geochemie der Universität zu Köln – Senckenberg Forschungsinstitut und Naturmuseum Frankfurt/M.
Prof. Dr. Markus RIEDERER (Chairman)	Julius-von-Sachs-Institut für Biowissenschaften, Würzburg
Prof. Dr. Ekhard SALJE, FRS, FRSA	Department of Earth Sciences, University of Cambridge
Prof. Dr. Heinrich SOFFEL <i>until 10.11.2017</i>	Emeritus, Institut für Allgemeine und Angewandte Geophysik der Universität München
Prof. Dr. Christine THOMAS <i>from 10.11.2017</i>	Institut für Geophysik der Westfälischen Wilhelms-Universität Münster

The Advisory Board held a meeting in Bayreuth (05.05.2017).

### 1.2 Leadership

Prof. Dr. Dan FROST (Director)  
Prof. Dr. Tomoo KATSURA (Deputy Director)  
Prof. Dr. Hans KEPPLER



## 2. Staff, Funding and Facilities

### 2.1 Staff

At the end of 2017 the following staff positions existed in the Institute:

- Scientific staff: **13**
- Technical staff: **13**
- Administrative staff: **2**
- Administrative officer: **1**

During 2017, 47 scientific positions (450 months) were funded by grants raised externally by staff members of the institute. In addition 4 long-term scientific positions (37.5 months) were funded by the resources of the BGI Visiting Scientists' Programme (see Sect. 8) which also supported short-term visits for discussing future projects or presenting research results (see Sect. 5). 12 student assistants (98.5 months) were funded by externally raised grants. 8 scientists (77 months) were supported by personal grants (stipends).

### 2.2 Funding

In 2017, the following financial resources were available from the Free State of Bavaria:

- Visiting Scientists' Programme: 251.000 €
- Consumables: 458.000 €
- Investment funding: 60.000 €

The total amount of national/international external funding ("*Drittmittel*") used for ongoing research projects in 2017 was 3.385.000 € (Positions: 2.185.000 €; equipment, consumables and travel grants: 1.200.000 €).

	positions	equipment, consum- ables, travel grants	total
• AvH	95.000 €	40.000 €	135.000 €
• BMBF	144.000 €	221.000 €	365.000 €
• DFG	1.669.000 €	895.000 €	2.564.000 €
• EU	241.000 €	38.000 €	279.000 €
• Others	36.000 €	6.000 €	<u>42.000 €</u>
			<b>3.385.000 €</b>

(AvH = Alexander von Humboldt Foundation; BMBF = Federal Ministry of Education and Research; DFG = German Science Foundation; EU = European Union; Others: DAAD, Chinese Science Council, Japanese Society for the Promotion of Science, German-Israeli Foundation for Scientific Research and Development)

In the following list only the BGI components of the funding is listed in cases where joint projects involved other research institutions. Principal investigators and the duration of the grants are listed in brackets. Total project funding refers to the funding over the entire duration of this project.

<b>Funding institution</b>	<b>Project, Funding</b>	<b>Total Project Funding</b>
BAdW	Bavarian Academy of Sciences research project (H. Marquardt)	36.000 €
BMBF	05K16WCA (H. Keppeler – 7/16-6/19) "Aufbau einer Hochdruckpresse vom Multi-Anvil-Typ an der Forschungs-Neutronenquelle FRM II in Garching" Total funding:	410.278 €
BMBF	05K16WC2 (T. Katsura – 7/16-6/19) "Erweiterung der Druckbereiche der In-Situ-Röntgen- beobachtung mit der Großvolumen-Hochdruckapparatur an der PETRA-III-Extension des Deutschen Elektronen- Synchrotrons DESY" Total funding:	543.478 €
DFG	AU 314/5-1 (A. Audétat – 10/14-9/17) "Development of new oxybarometers for silicic magmas" Position: E13/2, 36 months 90.900 € student assistant 5.000 € Consumables: 35.000 € Overhead: 26.100 €	157.000 €
DFG	BO 2550/7-1 (T. Boffa Ballaran, A. Woodland – 8/13-3/17) "Crystal chemistry of ferric iron in the deep upper mantle and transition zone" Position: student assistant 5.000 € Consumables and travel funding: 9.500 € Overhead: 2.900 €	17.400 €
DFG	BO 2550/7-2 (T. Boffa Ballaran, A. Woodland – 10/17-9/19) "Stabilities and properties of Mg, Al and Cr-bearing solid solutions of newly discovered Fe <sup>3+</sup> -Fe <sup>2+</sup> oxides at transition zone conditions: approaching geologically relevant compositions" Position: student assistant 7.500 € Consumables and travel funding: 7.000 € Overhead: 3.200 €	17.700 €
DFG	BO 2550/8-1 (T. Boffa Ballaran – 9/14-7/17) DFG SPP 1385 'The first 10 Million Years of the Solar System – a Planetary Materials Approach' "Der Einfluss von Mantel Rheologie auf die frühe Differenzierung eisiger Satelliten" Positions: E 13, 24 months 127.200 € student assistant 10.000 € Consumables: 12.285 € Equipment: 27.216 € Overhead: 35.300 €	212.001 €

DFG	DU 393/9-1 (L.S. Dubrovinsky – 1/15-12/17) DFG TP 7 'Chemische Reaktionen zwischen Karbonaten und pyrolitischem Erdmantel und Entstehung ultratiefer Diamanten' "Structures, properties and reactions of carbonates at high temperatures and pressures" Position: E 13 (66 %), 36 months 120.600 € Consumables: 32.250 € Overhead: 30.600 €	183.450 €
DFG	DU 393/10-1 (L.S. Dubrovinsky, C.A. McCammon – 8/15-7/17) DFG SPP 1833 'Building a Habitable Earth' "Leichte Elemente im Kern einer bewohnbaren Erde" Position: E 13, 36 months 206.700 € Consumables: 20.250 € Overhead: 45.400 €	272.350 €
DFG	DU 393/13-1 (L.S. Dubrovinsky – 4/17-3/20) "Mantel formende Materialien von Super Erden bei Statischen Drücken von über 500 GPa und hohen Temperaturen" Position: E 13, 36 months 209.400 € student assistant 8.000 € Consumables: 27.750 € Overhead: 53.900 €	299.050 €
DFG	FR 1555/10-1 (D.J. Frost – 8/15-7/18) DFG SPP 1833 'Building a Habitable Earth' "Die Ermittlung des Mechanismus der frühzeitigen Oxidation des Erdinneren" Position: E 13 (75 %), 36 months 143.600 € Consumables: 22.250 € Overhead: 33.200 €	199.050 €
DFG	FR 1555/11-1 (D.J. Frost – 3/16-2/23) Gottfried Wilhelm Leibniz-Preis 2016	2.500.000 €
DFG	GRK 2156/1 (D.J. Frost, et al. – 4/16-10/20) Internationales Graduiertenkolleg "Deep Earth Volatile Cycles"	3.257.358 €
DFG	KA 3434/7-1 (T. Katsura – 6/14-12/17) "Messung der Si-Korngrenzendiffusion von Forsterit in Abhängigkeit des Wassergehalts: Bestimmung der Steigerung der Kriechrate in verschiedenen Regionen des oberen Erdmantels" 1 position: E 13 75%, 36 months 133.300 € student assistant 5.000 € Consumables and travel funding: 20.388 € Overhead: 31.700 €	190.388 €

DFG	KA 3434/8-1 (T. Katsura – 4/15-3/18) "Messung von Si-Selbstdiffusionskoeffizienten in Wadsleyit als Funktion des Wassergehaltes" 1 position: E 13, 36 months 195.300 € student assistant 5.000 € Consumables and travel funding: 16.000 € Overhead: 43.300 €	259.600 €
DFG	KA 3434/9-1 (T. Katsura – 9/15-8/18) "Bestimmung des Drei-Phasen-Stabilitätsfelds des Postspinell-Übergangs in (Mg,Fe) <sub>2</sub> SiO <sub>4</sub> : Erörterung der extremen Schärfe der 660-km-Diskontinuität und deren Bedeutung für die chemische Struktur und die Dynamik des tiefen Erdmantels" 1 position: E 13, 36 months 196.600 € student assistant 5.000 € Consumables and travel funding: 45.750 € Overhead: 49.500 €	296.850 €
DFG	KE 501/8-2 (H. Keppler – 2014-2017) "In-situ observation of the crystallization kinetics and texture evolution of basalts" Total funding:	174.000 €
DFG	KE 501/11-1 (H. Keppler – 2013-2018) "Electrical conductivity and dissociation of fluids in crust and mantle" Total funding:	267.800 €
DFG	KE 501/13-1 (H. Keppler – 2016-2018) "Nitrogen in the deep mantle" Total funding:	214.669 €
DFG	KE 501/15-1 (H. Keppler – 2017-2019) "Hochdrucklabore des Bayerischen Geoinstituts" Total funding:	371.878 €
DFG	MA 4534/4-1 (H. Marquardt – 9/15-8/18) "Deformationsexperimente an (Mg,Fe)O Ferroperiklas bei hohen Drücken und gleichzeitig hohen Temperaturen" Positions: E13 2/3, 36 months: 123.000 € Consumables: 33.850 € Overhead: 31.400 €	188.250 €
DFG	MA 4534/5-1 (H. Marquardt – 6/17-5/20) "Experimentelle Untersuchung von planetaren Eis-Verbindungen bei hohen Drücken mittels dynamisch-betriebener Diamantstempelzellen" Positions: E13 75 %, 36 months: 145.700 € Consumables: 27.750 € Overhead: 38.200 €	211.650 €
DFG	MA 6287/3-1 (K. Marquardt, R. Dohmen – 9/15-8/18) "Elementverteilung in Geomaterial-Korngrenzen unter Berücksichtigung ihrer Geometrie" Positions: E13 2/3, 36 months: 123.000 € student assistant 2.500 € Consumables: 26.445 € Overhead: 30.400 €	182.345 €

DFG	MA 6287/5-1 (S. Chakraborty, K. Marquardt, T. Fockenberg – 10/16-9/19) "Experimentelle Kalibrierung von Granat-Pyroxen Diffusionschronometrie für Anwendungen in terrestrische und planetare Proben" Positions: student assistant 5.000 € Consumables: 5.000 € Overhead: 2.200 €	12.200 €
DFG	MA 6287/6-1 (K. Marquardt – 11/16-10/19) "Änderungen der Korngrenzcharakterverteilung in Olivin-dominierten Gesteinen als Funktion des Chemismus" Positions: E13 75 %, 36 months: 147.000 € student assistant 5.000 € Consumables, global funding: 45.030 € Overhead: 43.300 €	240.330 €
DFG	MC 3/18-1 (C.A. McCammon, L.S. Dubrovinsky, D.J. Frost – 7/13-2/17) "The effect of pressure, temperature and oxygen fugacity on the stability of subducted carbonates and implications for the deep carbon cycle" Positions: E 13/2, 36 months 88.000 € student assistant 5.000 € Equipment, consumables and travel funding: 31.650 € Overhead: 24.900 €	149.550 €
DFG	MC 3/19-2 (C.A. McCammon, S. Gilder – 9/13-9/17) DFG SPP 1488 (PlanetMag) "How pressure influences the magnetic properties of titanomagnetite and iron with implications for magnetic anomalies and core fields" Equipment, consumables and travel funding: 6.400 € Overhead: 1.300 €	7.700 €
DFG	MC 3/20-1 (C.A. McCammon – 10/15-9/18) DFG FOR 2125 (CarboPaT) "Elastic properties of carbonates at high pressure and high temperature" Positions: E13 2/3, 36 months: 123.000 € Equipment, consumables and travel funding: 32.250 € Overhead: 30.600 €	185.850 €
DFG	MC 3/21-1 (C.A. McCammon – 6/17-5/20) "Fe Spinübergang im Erdmantel: Einblicke durch Röntgen-Raman-Streuung und Röntgenabsorptionsspektroskopie" Positions: student assistant (Bachelor) 9.482 € Equipment, consumables and travel funding: 6.000 € Overhead: 3.400 €	18.882 €

DFG	OV 110/1-3 (S.V. Ovsyannikov – 4/16-2/18) "Structural and electronic properties of sesquioxides at high pressures and temperatures: new forms, new insights and new possible applications" Positions: E 13, 24 months 136.600 € Consumables and travel funding: 20.000 € Overhead: 31.300 €	187.900 €
DFG	PE 2334/1-1 (S. Petitgirard – 10/15-9/17) DFG SPP 1833 'Building a Habitable Earth' "Dichte und Verbleib von Silikatschmelzen im frühen Erdmantel" Positions: E 13, 24 months 136.600 € Consumables and travel fundings: 20.000 € Overhead: 31.300 €	187.900 €
DFG	RU 1323/10-1 (D.C. Rubie – 01/17-12/19) DFG SPP 1833 'Building a Habitable Earth' "Entstehung und Entwicklung des Magmaozeans und Differentiation von Kern und Mantel während der Akkretion der Erde" Positions: E 13, 36 months 206.700 € Consumables: 7.250 € Overhead: 42.800 €	256.750 €
DFG	STE 1105/10-1 (G. Steinle-Neumann – 4/14-3/17) DFG SPP 1488 (PlanetMag) "Structure and electronic transport properties of metallic liquids at conditions of planetary cores" Positions: E 13 2/3, 36 months 125.500 € student assistant 18.798 € Consumables: 9.820 € Overhead: 30.800 €	184.918 €
DFG	STE 1105/12-1 (G. Steinle-Neumann, D.J. Frost, N. Tosi – 11/16-10/19) DFG SPP 1833 'Building a Habitable Earth' "Kristallisation des irdischen Magmaozeans: Thermo- und Geodynamik" Positions: E13 (75%), 36 months 143.600 € student assistant 5.000 € Consumables: 8.250 € Overhead: 31.400 €	188.250 €
DFG	STE 1105/13-1 (G. Steinle-Neumann – 8/17-7/20) DFG through FOR 2440 (Matter Under Planetary Interior Conditions) "Thermodynamic properties of silicate solids and liquids and iron to the TPa range from <i>ab initio</i> calculations" Positions: E13 (75%), 36 months 145.700 € student assistant 15.000 € Consumables: 7.750 € Overhead: 37.100 €	205.550 €

DFG	Emmy Noether-Programm (H. Marquardt – 2014-2019) "Structure and Elasticity of GeoMaterials at Extreme Conditions (GeoMaX)" Positions: group leader, E14/E15, 60 months: 375.400 € post doc, E13, 60 months: 317.200 € 2 PhD students, 2/3 E13, 36 months: 264.400 € student assistant: 11.904 € Consumables, travel funding: 222.550 € Investments: 127.714 € Overhead: 184.400 €	1.503.568 €
EU	European Research Council (ERC) Advanced Grant No. 290568 (D.C. Rubie – 5/12-4/17) "Accretion and Early Differentiation of the Earth and Terrestrial Planets" ("ACCRETE") Positions, consumables and travel funding:	1.826.200 €

### 2.3 Laboratory and office facilities

The institute occupies an area of

ca. 1350 m<sup>2</sup> laboratory space

ca. 480 m<sup>2</sup> infrastructural areas (machine shops, computer facilities, seminar room, library)

ca. 460 m<sup>2</sup> office space

in a building which was completed in 1994.

### 2.4 Experimental and analytical equipment

The following major equipment is available at the Bayerisches Geoinstitut:

#### I. High-pressure apparatus

15 MN/1500 tonne Kawai-type multianvil high-pressure apparatus (40 GPa, 2000 K)

6 x 8 MN/6x800 tonne independently acting-anvil press (25 GPa, 3000 K)

50 MN/5000 tonne multianvil press (25 GPa, 3000 K)

12 MN/1200 tonne multianvil press (25 GPa, 3000 K)

10 MN/1000 tonne multianvil press (25 GPa, 3000 K)

5 MN/500 tonne multianvil press (20 GPa, 3000 K)

5 MN/500 tonne press with a deformation DIA apparatus

4 piston-cylinder presses (4 GPa, 2100 K)

Cold-seal vessels (700 MPa, 1100 K, H<sub>2</sub>O), TZM vessels (300 MPa, 1400 K, gas), rapid-quench device

Internally-heated autoclave (1 GPa, 1600 K)

High-pressure gas loading apparatus for DAC

## II. Structural and chemical analysis

1 X-ray powder micro-diffractometer

1 X-ray powder diffractometer with furnace and cryostat

2 automated single-crystal X-ray diffractometers

High-brilliance X-ray system

Single crystal X-ray diffraction with super-bright source

1 Mössbauer spectrometer (1.5 - 1300 K)

3 Mössbauer microspectrometers

2 FTIR spectrometers with IR microscope

FEG transmission electron microscope (TEM), 200 kV analytical, with EDS and PEELS

FEG scanning TEM, 80-200 kV analytical, with 4-SDDs EDS and post-column energy filter (EFTEM/EELS)

FEG scanning electron microscope (SEM) with BSE detector, EDS, EBSD and CL

Dual beam device, focused ion beam (FIB) and FEG SEM. In situ easy-lift manipulator, STEM and EDS detector, and beam deceleration option

3 Micro-Raman spectrometers with ultraviolet and visible lasers

Tandem-multipass Fabry-Perot interferometer for Brillouin scattering spectroscopy

JEOL JXA-8200 electron microprobe; fully-automated with 14 crystals, 5 spectrometer configuration, EDX, capability for light elements

193 nm Excimer Laser-Ablation ICP-MS

Water content determination by Karl-Fischer titration

GC/MS-MS for organic analyses

Confocal 3D surface measurement system

## III. *In situ* determination of properties

Diamond anvil cells for powder and single crystal X-ray diffraction, Mössbauer, IR, Raman, optical spectroscopy, electrical resistivity measurements up to at least 100 GPa

Facility for in situ hydrothermal studies in DAC

Externally heated DACs for in situ studies at pressures to 100 GPa and 1200 K

1-atm furnaces to 1950 K, gas mixing to 1600 K, zirconia fO<sub>2</sub> probes

1-atm high-temperature creep apparatus

Gigahertz ultrasonic interferometer with interface to resistance-heated diamond-anvil cells

Freezing-heating stage for fluid inclusion studies

Impedance/gain-phase analyser for electrical conductivity studies

Apparatus for in situ measurements of thermal diffusivity at high P and T

Laser-heating facility for DAC

Portable laser heating system for DAC

*The Geoinstitut is provided with well equipped machine shops, an electronic workshop and sample preparation laboratories. It has also access to the university computer centre.*

### 3. Forschungsprojekte

#### 3.1 Struktur und Dynamik der Erde und Planeten

Die terrestrischen Planeten im Sonnensystem entstanden über einen Zeitraum von etwa 100 Millionen Jahren. Moderne astrophysikalische Modelle deuten darauf hin, dass Planetesimale, die ersten Bausteine der Planeten, wenige Dutzend bis hundert Kilometer große Körper waren. In der frühen Phase kollidierten diese Planetesimale untereinander und in späteren Stadien der Akkretion kam es zu Zusammenstößen von mehrere tausend Kilometer messenden planetaren Embryos mit den verbleibenden Planetesimalen und untereinander. Die Freisetzung kinetischer Energie und der Zerfall kurzlebiger radioaktiver Isotope führte zumindest teilweise zum Aufschmelzen der wachsenden Körper und mündete in die Bildung eines Magmaozeans. Die letzte große Kollision der Proto-Erde mit einem etwa Mars-großen Körper führte dabei zur Bildung einer heißen Scheibe aus welcher der anfangs aufgeschmolzene Erdmond hervorging.

Die erste Studie in diesem Kapitel untersucht die Entstehung von sogenannten Chondrulen, millimetergroßen Kügelchen, die in den meisten primitiven Meteoriten gefunden werden. Mittels zweidimensionaler Modelle wurde untersucht, wann und unter welchen Bedingungen Chondrulen durch Kollisionen zwischen teilweise aufgeschmolzenen Planetesimalen aus Schmelztröpfchen, die sowohl Silikate als auch Eisen enthalten, entstehen können. Die numerischen Resultate bestätigen, dass sich Chondrulen in den ersten Millionen Jahren nach Entstehung des Sonnensystems bilden und später in neu entstehende Planetesimale inkorporiert werden können.

Die zweite Studie widmet sich der Phase der Planetenentstehung, in der planetare Embryos miteinander kollidierten, um größere Körper zu bilden. Hierfür wurden dreidimensionale SPH-Modelle (SPH = *smoothed particle hydrodynamics*) mit geodynamischen Modellen kombiniert, um sowohl die Kollision als auch die längerfristige Entwicklung des Zielkörpers zu modellieren. Diese Kombination bietet die Möglichkeit, die Limitierung sowohl der SPH-Modelle, dass nur wenige Tage nach der Kollision modelliert werden, als auch die der geodynamischen Modelle, dass nur vertikale Einschläge mittels Parametrisierung simuliert werden, zu beseitigen. Zu diesem Zweck wird das Endresultat einer spezifischen SPH-Simulation als Anfangsbedingung für das geodynamische Modell genutzt. In ausführlichen Berechnungen wurde ermittelt, wann nach der Kollision der Datentransfer durchgeführt werden kann, ohne dass mit der Zeit weiterhin zurückfallendes Auswurfmaterial die längerfristige thermomechanische Entwicklung des Körpers beeinflusst.

Kurz nach seiner Entstehung vor mehr als 4,4 Milliarden Jahren war das Innere des Mondes aufgeschmolzen. Die dritte Studie beschäftigt sich mit der möglichen Existenz einer bis heute geschmolzenen Schicht im untersten Mondmantel, deren Existenz vor einigen Jahren aufgrund der Neuauswertung von seismischen Daten vorgeschlagen wurde. Basierend auf Kristallisationsmodellen für den lunaren Magmaozean wurde Eisen- und Titan-reiches Material vorgeschlagen, das nach seiner späten Kristallisation zur Kern-Mantel-Grenze

absank und dort wieder aufgeschmolzen wurde. In dieser Studie soll geklärt werden, ob unter den heutigen Druck- und Temperaturbedingungen im untersten Mondmantel dieses Material sowohl geschmolzen als auch dichter sein kann als der umgebende Mantel, um damit seine Stabilität an der Kern-Mantel-Grenze zu erklären.

Die vierte Studie des Kapitels beschäftigt sich mit der inneren Struktur des Erdmondes. Hierfür wurde ein eindimensionales Modell des Mondinneren entwickelt, das geophysikalische, geochemische und mineralogische Daten kombiniert. Unter Annahme verschiedener Temperaturprofile und wahlweise eines homogenen oder geschichteten Mondmantels, wurde mittels der Modelle ein großer Parameterraum abgedeckt, indem verschiedene Parameter wie zum Beispiel die Schichtdicken variiert wurden. Es zeigte sich, dass dieses kombinierte Modell es ermöglicht, den Radius des Mondkerns, der bislang nur ungenau bekannt war, deutlich einzugrenzen.

Nach dem Ende der Akkretion kühlten die terrestrischen Planeten ab und der anfängliche Magmaozean kristallisierte aus. Dies führte zur Entstehung von Phasenübergängen im nun festen Erdmantel, welche mittels seismologischer Methoden nachgewiesen wurden. Die folgende fünfte Studie stellt Laborexperimente vor, die sich dem Phasenübergang von Ringwoodit zu Bridgmanit und Ferroperiklas widmen. Diese Experimente zeigen, dass dieser Phasenübergang sehr scharf ist, und bestätigen, dass dieser die seismische Diskontinuität bei 660 km sehr gut erklären kann.

Geochemische Studien zeigten in den letzten Jahren, dass bereits während der Entstehung der Erde Wasser auf diese gelangt ist. In der nächsten Studie wird mittels hochauflösender numerischer zweidimensionaler Modelle des oberen Mantels untersucht, wie das Wasser während der weiteren Entwicklung der Erde von der Oberfläche mittels subduzierender Platten ins Erdinnere transportiert wird und wie sich das Wasser im Erdmantel verteilt.

Der untere Mantel setzt sich größtenteils aus dem bereits erwähnten Mineral Bridgmanit und einer deutlich kleineren Menge an Ferroperiklas zusammen. Die globalen Mantelkonvektionsmodelle der folgenden Studie zeigen, dass der rheologisch deutlich schwächere Ferroperiklas in stark deformierten Regionen des unteren Mantels ein verbundenes Gefüge bilden kann, während in weniger deformierten Mantelregionen der festere Bridgmanit die Rheologie kontrolliert. Dies könnte die Resultate seismischer Tomographie erklären, die eine Stagnation von subduziertem Material in einer Tiefe von ca. 1000 km anzeigen, während in anderen Mantelregionen offenbar Material ohne Stagnation in größere Tiefe transportiert werden kann.

Selbst hochauflösende numerische Modelle des Erdmantels können Prozesse auf der Mikroskala nicht auflösen. Die zwei folgenden Beiträge zeigen, dass numerische Modelle von Prozessen auf der Mikroskala zusätzlich zu Laborexperimenten zum Verständnis dieser Vorgänge beitragen können. Diese Resultate können entsprechend genutzt werden, um bessere Parametrisierungen von so unterschiedlichen Prozessen wie Wassertransport in Mantel und Lithosphäre als auch Deformation von Zwei-Phasen-Gemischen herzuleiten, um damit zukünftige globale numerische Modelle realistischer zu gestalten.

### 3.2 Geochemie

Die Beiträge in diesem Kapitel untersuchen die Prozesse, die zum Transport und der Umverteilung der chemischen Elemente in Kruste, Mantel und Kern der Erde geführt haben. Beginnend mit der Abtrennung des metallischen Erdkerns und weitergehend durch die geochemischen Kreisläufe, die den Erdmantel mit der Oberfläche verbinden, listet dieses Kapitel vielfältige Mechanismen auf, die die Diversität der Zusammensetzung innerhalb der Erde geschaffen haben und zu Elementanreicherungen führen, die für die Entwicklung ökonomischer Erzlagerstätten notwendig sind.

Die ersten sieben Beiträge beschäftigen sich mit der Trennung von Kern und Mantel in der Erde, aber auch im Mond, mit der Zielsetzung, die Bedingungen einzugrenzen, unter denen sich Planeten bilden und differenzieren. Der erste nutzt astrophysikalische Modelle, um die Planetenbildung zu simulieren und die chemische Zusammensetzung der anwachsenden Planeten nachzuvollziehen. Es ergibt sich, dass das am besten passende Modell für die Bildung terrestrischer Planeten mit einer protoplanetaren Gasscheibe beginnt, die einen Gradienten im Oxidationszustand aufweist, der nahe der Sonne am stärksten reduzierend ist. Im nächsten Beitrag werden experimentelle Daten zur Partitionierung von Molybdän und Wolfram zwischen dem silikatischen Mantel und dem metallischen Kern vorgestellt. Ein physikalisches Modell für die Kernbildung wird getestet, in dem große Kollisionen gegen Ende der Akkretion Material zum Kern beitragen, der aufgrund seiner Größe nicht vollständig mit dem Erdmantel equilibriert wird. Solch ein Modell ist aber offenbar inkonsistent mit den niedrigen Konzentrationen dieser Elemente im gegenwärtigen Erdmantel, was bedeutet, dass das Modell entweder nicht korrekt ist oder ein weiteres Detail der Akkretion übersehen wurde. Der folgende Beitrag untersucht dieses Problem weiter, indem er die Rolle von Sulfidschmelzen während der Kernbildung einbezieht. Eine Sulfidschmelze würde sich gegen Ende der Akkretion unausweichlich vom silikatischen Mantel getrennt und mit dem Erdkern vereinigt haben. Die Experimente dazu zeigen jedoch, dass diese Trennung keinen Einfluss auf die Wolframkonzentration des Erdmantels gehabt hätte und so die gegenwärtige Konzentration dieses Elements im Mantel nicht erklären kann. Der nächste Bericht untersucht die Konsequenzen derselben späten Abtrennung einer Sulfidschmelze auf die Konzentrationen von Rhenium und Osmium im Erdmantel. Die Experimente zeigen, dass die Affinität dieser Elemente für die Sulfidschmelze mit dem Druck ansteigt, was zu Folgerungen führt, die die Sulfidseparation als späte Phase der Kernbildung unterstützen oder zumindest nicht ausschließen. Im folgenden Beitrag wird eine Reihe von sehr siderophilen Elementen, die Metalle gegenüber Silikaten stark bevorzugen, dazu benutzt, die Kernbildung des Mondes zu untersuchen. Die Konzentration dieser Elemente in lunaren Gesteinen ist deutlich geringer als in vergleichbaren Gesteinen in der Erde, wohingegen eine Hinzufügung von spätem Material in beiden eine ähnliche Konzentration erzeugt haben sollte. Dieser Unterschied wird durch eine viel spätere Abtrennung der Sulfidschmelze auf dem Mond im Vergleich zur Erde erklärt, wobei in beiden Fällen eine Anreicherung dieser Elemente im Kern erfolgt wäre. Die relativ hohen Drücke in der Erde hätten zu einer niedrigen Löslichkeit der Sulfide in der Silikatschmelze geführt, so dass die Abtrennungsphase vor dem Ende der Planetenbildung

abgeschlossen gewesen wäre. Unter den niedrigeren Druckbedingungen des Mondes dagegen wurde die Sulfidsättigung in der Silikatschmelze erst erreicht, als der Mantel fast komplett kristallisiert war, wodurch das Sulfid in der Restschmelze konzentriert wurde. Diese trennte sich erst dann vom Mantel, als die Akkretionsphase schon beendet war. In der folgenden Studie wurden Experimente mit Laser-beheizten Diamantstempelzellen dazu benutzt, das Ausmaß des Eintrags von Kohlenstoff in den Erdkern während der Akkretion zu ermitteln. Es ist sehr wahrscheinlich, dass der Kern eines der größten Kohlenstoffreservoirs der Erde beherbergt, aber es ist auch möglich, dass Löslichkeit von Kohlenstoff in Metall mit hohem Druck aufgrund des Einflusses von Silizium stark abnimmt. Im letzten Beitrag zum Erdkern wurde die Löslichkeitsrate von Sauerstoff in metallischem Eisen mithilfe von Experimenten bestimmt und mit molekulardynamischen Modellen berechnet. Die Schlussfolgerungen sind für dasselbe Modell relevant, das im ersten Beitrag dieses Kapitels untersucht wurde, in dem die Rolle von großen Impaktorkernen untersucht wurde, die relativ intakt bleiben, während sie in der späten Akkretionsphase absinken und sich mit dem Erdkern vereinigen. Die Resultate zeigen, dass – unter der Annahme von Sauerstoff als leichtem Element im Kern – dann die Kerne der großen Impaktoren zerbrechen mussten, um Partikel zu liefern, die klein genug waren, um sich im passenden Zeitraum durch Diffusion mit dem Silikatmantel im Gleichgewicht zu sein.

Die folgenden vier Beiträge beschäftigen sich mit dem Oxidationszustand des Erdmantels und der Erdkruste. Der erste davon beschreibt den Oxidationszustand des tiefen Magmaozeans, der während der Akkretion und Kernbildung existierte. In Experimenten, die bei konstanter relativer Sauerstoff fugazität durchgeführt wurden, wurde ein Anteil an oxidiertem Eisen ( $\text{Fe}^{3+}$ ) in der Silikatschmelze gefunden, der mit steigendem Druck erst abfällt und dann wieder ansteigt. Dieses Verhalten kann durch eine Umkehr der Volumenänderung des  $\text{Fe}^{2+}/\text{Fe}^{3+}$ -Gleichgewichtsverhältnisses in der Schmelze erklärt werden. Das bedeutet, dass ein tiefer Magmaocean im Gleichgewicht mit metallischem Eisen an seiner Basis nach dem Abschluss der Kernbildung noch signifikante Anteile an oxidiertem  $\text{Fe}^{3+}$  enthalten haben könnte, was im Gegensatz zur konventionellen Annahme steht, dass er praktisch  $\text{Fe}^{3+}$ -frei war. In der nächsten Studie wurden experimentelle Kalibrierungen des Gehaltes von  $\text{Fe}^{3+}$  in Granaten als Funktion des Druckes, der Zusammensetzung und des Oxidationszustandes durchgeführt, um die Bildungsbedingungen von Diamanten zu interpretieren, die solche Minerale als Einschluss enthalten. Es konnte jedoch nur eine sehr geringe Abhängigkeit von Druck oder Sauerstoff fugazität festgestellt werden, insbesondere für solche Granat-Zusammensetzungen, die am häufigsten in diesen Typen von Diamanten gefunden werden. Im folgenden Projekt wurden Experimente durchgeführt, um die Sauerstoff fugazität in refraktischen Mantelgesteinen zu bestimmen. Kratonische Mantelgesteine sind in der Vergangenheit intensiv aufgeschmolzen worden und Gesteine aus diesen Regionen zeigen eine starke Anreicherung an Chrom, das sich während der Teilaufschmelzung konzentriert. Die Bestimmung des Effekts von Aufschmelzung auf den Redox-Zustand erfordert, dass der Einfluss von Chrom auf die Phasengleichgewichte, die zur Messung der Sauerstoff fugazität dienen, bekannt ist. Im letzten Beitrag über Redoxprozesse wird eine neue Methode zur Bestimmung der Sauerstoff fugazität vorgestellt, d. h. ein Oxybarometer, das auf Eisen-Titan-

Austausch (FeTiMM) zwischen Magnetit und Silikatschmelzen basiert. Dieses Oxybarometer ist geeignet für den Einsatz in der kompletten Reihe von mafischen zu felsischen Magmen, und wurde unabhängig mit einer weiteren Oxybarometer-Technik getestet, wobei es seine hohe Genauigkeit und Flexibilität unter Beweis stellte.

Die folgenden drei Beiträge beschäftigen sich mit der Bildung und Erhaltung von Diamanten. Im ersten werden die Schmelzphasenbeziehungen in einem Karbonatsystem mit mehreren Komponenten untersucht, um die Bildung von Diamanten in der Übergangszone des Erdmantels zu verstehen. Die Komponenten dieses Systems wurden nach der chemischen Zusammensetzung von typischen Mineraleinschlüssen in natürlichen Diamanten ausgewählt. Die Untersuchung hat tatsächlich existierende, charakteristische Reihen von Mineraleinschlüssen in Diamanten erfolgreich reproduziert. Im darauffolgenden Beitrag wurde die Rate der Diamantenauflösung in Karbonatschmelze im Stabilitätsfeld von Diamant gemessen. Aufgrund dieser Messungen wird postuliert, dass während des Aufstiegs von Diamantführenden Schmelzen vom oberen Erdmantel zur Oberfläche Diamantkörner von 1 mm Größe ca. 7 % ihrer Masse in die umgebende Schmelze verlieren würden. Der letzte Beitrag zu Diamanten untersucht ihre Bildung in einem Szenario, bei dem karbonatische Schmelzen in stärker reduzierende Bereiche des unteren Erdmantels wandern, wo Eisen- und Nickel-reiche metallische Legierungen existieren können. Diamanten können tatsächlich durch die Reduktion von Karbonatphasen gebildet werden, während die koexistierenden Metalllegierungen oxidiert werden. Als Resultat bilden sich Eisen-Nickeloxide und es ist daher wohl kein Zufall, dass solche Oxide charakteristische Einschlüsse in Diamanten des tiefen Erdmantels sind.

Die folgenden drei Beiträge beschäftigen sich mit den Folgen von volatilen Komponenten auf die Geochemie des Erdmantels, wobei sich die ersten beiden auf den Bereich der Subduktionszonen konzentrieren. In der ersten Studie werden Experimente mit sogenannten Diamant-Fallen beschrieben, die die Wirkung der Fluid-Salinität auf die Verteilungskoeffizienten von Spurenelementen zwischen Fluiden und subduziertem Krustenmaterial untersuchen. Es wurde herausgefunden, dass der Chlorgehalt die Partitionierung vieler Spurenelemente in die Fluidphase stark erhöht, wohingegen Elemente mit hoher Feldstärke wie Titan, Niob und Tantal relativ wenig beeinflusst werden. Die charakteristische Spurenelementsignatur von Inselbogen-Magmen kann so durch Mantelmetasomatismus mit Chlor-haltigen Fluiden erklärt werden und erfordert nicht die früher postulierte Reaktion mit wasserhaltigen Schmelzen. Der darauffolgende Beitrag untersucht den Werdegang von sogenannten Ophikarbonaten in Subduktionszonen. Diese Gesteine bilden sich durch Alterierung von ozeanischer Lithosphäre durch Meerwasser und bestehen aus wasserhaltigen Serpentinmineralen und Kalziumkarbonat. Ihr Schicksal während der Subduktion ist wichtig für den Transport von Kohlenstoff in den Mantel und frühere thermodynamische Berechnungen haben die Möglichkeit aufgezeigt, dass die Dehydrierung des Serpentin zur Auflösung des Karbonats in diesen Gesteinen führt und so die tiefe Subduktion von Kohlenstoff begrenzt. Obwohl dieser Ansatz experimentell noch nicht ausreichend geprüft wurde, zeigen erste Resultate, dass die thermodynamischen

Berechnungen die experimentellen Ergebnisse nicht zufriedenstellend darstellen. Im letzten Beitrag zu volatilen Elementen im Mantel werden Experimente beschrieben, die die Zusammensetzung von geringen, wasserhaltigen Teilschmelzen bei Bedingungen der Mantelübergangszone bestimmen sollen. Eine Reihe von Studien haben vorgeschlagen, dass geringe seismische Geschwindigkeiten nahe der Übergangszone durch partielle wasserhaltige Schmelzen verursacht sein könnten. Die Bestimmung der ursprünglichen Schmelzzusammensetzungen ist jedoch extrem herausfordernd, da die meisten plausiblen Schmelzanteile zu klein sind, um sie zu analysieren. Stattdessen muss eine Serie iterativer Experimente durchgeführt werden, um einen größeren Schmelzanteil mit derselben Mineralassoziation zu equilibrieren, wie sie für einen sehr kleinen Schmelzanteil zu erwarten wäre.

Der folgende Beitrag ist der letzte, der sich mit dem Erdmantel befasst, und er beschreibt Versuche, die Bildungstiefe von magmatischen Kumulatgesteinen zu bestimmen. Insbesondere Magmen, die im Bereich von Inselbögen aufsteigen, differenzieren sich durch fraktionierte Kristallisation zum oberen Mantel und der unteren Kruste hin, und lassen dabei Kumulatgesteine zurück. Xenolithe dieser Gesteine sind sehr selten, aber extrem wertvoll für das Verständnis, wie Schmelzzusammensetzungen des Mantels sich in die Magmaserien entwickeln, die an der Erdoberfläche gefunden werden. In den vorgestellten Experimenten wird ein Polyreaktions-Ansatz verwendet, um die Drücke von Spinell-, Klinopyroxen-, Olivin- und Plagioklas-haltigen Kumulat-Xenolithen zu bestimmen, wobei sehr kleine Unsicherheiten von ca. 1 kbar erreicht werden.

Die letzten drei Beiträge konzentrieren sich auf Themen der Lagerstättengeologie. In der ersten Studie werden Sulfid- und Schmelzeinschlüsse in Hornblende-reichen Xenolithen von zwei magmatischen Systemen im Südwesten der USA dazu verwendet, das Potential von Kupfer-Mineralisationen in Inselbogen-Magmen zu bewerten. Die vorgelegten Ergebnisse deuten darauf hin, dass die Bildung von Hornblende-reichen Kumulaten in der tiefen Erdkruste zwar einen negativen Einfluss auf das Mineralisationspotential der residuellen Schmelzen und Fluide hat, aber die Kumulate selbst ergiebige Ausgangsgesteine für spätere partielle Aufschmelzungsprozesse darstellen. Im folgenden Beitrag zeigen Experimente mit dem Hydrothermal-Autoklaven, dass synthetische Fluideinschlüsse in Quarz signifikante Mengen an Gold durch Diffusion bei 600-800 °C innerhalb von wenigen Tagen hinzugewinnen oder verlieren können. Diese Ergebnisse bedeuten, dass Goldkonzentrationen, die in natürlichen Fluideinschlüssen gemessen werden, mit Vorsicht bewertet werden müssen. Im letzten Beitrag dieses Kapitels wird eine detaillierte Untersuchung von Schmelz- und Fluideinschlüssen in dem ökonomisch unergiebigem Huangshan Granit in China beschrieben, um die Faktoren einzugrenzen, die das Mineralisationspotential von granitischen Magmasystemen kontrollieren. Es wurde herausgefunden, dass der Molybdängehalt von Fluiden und Schmelzen in ähnlicher Höhe vorliegt wie in porphyrischen Magmasystemen mit Molybdänmineralisationen, was darauf hindeutet, dass zusätzlich zum Fehlen fokussierten Fluidflusses weitere Faktoren für den Mangel von Mineralisationen im Huangshan Granit verantwortlich sind.

### 3.3 Mineralogie, Kristallchemie und Phasenübergänge

Die physikalischen und chemischen Eigenschaften im Inneren der Planeten hängen vom Verhalten der sie aufbauenden Minerale ab, welches wiederum vom genauen atomaren Aufbau bestimmt wird. Mineralogische und kristallchemische Untersuchungen bei den Druck- und Temperaturbedingungen, wie sie im Inneren von Planeten vorherrschen, sind daher unabdingbar für die Interpretation von geophysikalischen Beobachtungen, für das Verständnis von geochemischen Randbedingungen und für Modelle der inneren Dynamik von Planeten. Druck- und temperaturbedingte Phasenübergänge, die in planetaren Materialien vorkommen, erschweren das Erstellen von mineralogischen Modellen und müssen mit experimentellen und theoretischen Methoden erforscht werden. In diesem Kapitel werden verschiedene experimentelle und computergerechnete Resultate präsentiert, die unser Verständnis der Mantel-Mineralogie von Planeten und der Kristallchemie von wichtigen Geomaterialien erweitern, sowie neue Ergebnisse zu Phasenübergängen im Inneren von Planeten liefern.

Der erste Beitrag in diesem Kapitel beschreibt die Synthese und strukturelle Charakterisierung von großen Akimotoit-Einkristallen, einem  $\text{MgSiO}_3$  Hochdruckpolymorph, welches eine Erklärung für die in der Übergangszone beobachtete seismische Anisotropie in subduzierten Erdplatten liefern könnte. Die folgenden vier Kapitel untersuchen die Kristallchemie von  $(\text{Mg,Fe,Al})(\text{Al,Fe,Si})\text{O}_3$  Bridgmanit, dem Hauptbestandteil des unteren Erdmantels (660-2900 km Tiefe). Die Arbeiten zielen darauf ab, den Einbaumechanismus von Fe und Al in die Bridgmanit-Struktur sowie die Abhängigkeit des  $\text{Fe}^{3+}/\text{Fe}^{2+}$  Verhältnisses von der Sauerstoffugazität und den Synthesebedingungen besser zu verstehen. Hierzu wurden zahlreiche analytische Methodiken angewandt, insbesondere  $^{27}\text{Al}$  Festkörper-NMR Spektroskopie, Mikrosondenanalyse, Einkristall- und Pulver-Röntgendiffraktometrie, Mössbauer-Spektroskopie, Transmissionselektronenmikroskopie sowie lasergeheizte Diamantstempelzellen zur Synthese.

Die folgenden drei Beiträge beschreiben experimentelle Arbeiten, die zum Ziel haben, die Koordination von Silizium in Gläsern und Kristallen bei hohen Drücken besser zu verstehen. In der ersten Arbeit wird gezeigt, dass die Koordinationszahl von Silizium in  $\text{SiO}_2$  Glas mit dem Druck ansteigt, bis es oberhalb von 60 GPa in einer 6-fach Koordination vorliegt. Der zweite Beitrag berichtet über eine neues  $\text{SiO}_2$ -Polymorph, welches 5-fach koordiniertes Silizium und Oktaeder mit gemeinsamen Flächen enthält und oberhalb von 30 GPa entsteht. Die dritte Arbeit diskutiert Hochdruck-Phasenübergänge in  $\text{CaB}_2\text{Si}_2\text{O}_8$  Danburit, die mit einer Änderung der Koordinationszahl von Silizium verbunden sind. Das Ergebnis legt nahe, dass  $\text{SiO}_5$  Gruppen nicht so selten sind wie bisher angenommen und sich während Phasenübergängen in Silikaten bilden könnten.

Experimentelle Arbeiten zur Kristallstruktur und -chemie werden in den nächsten drei Beiträgen im Hinblick auf den Kreislauf von flüchtigen Bestandteilen durch das tiefe

Erdinnere diskutiert. Karbonate sind wichtige kohlenstoffhaltige Minerale in subduzierten Erdplatten und die erste Arbeit untersucht Reaktionen zwischen  $\text{MgCO}_3$  Magnesit und metallischem Eisen im unteren Erdmantel. Die Ergebnisse deuten darauf hin, dass Magnesit im unteren Mantel unter reduzierenden Bedingungen stabil sein könnte, auch beim Vorhandensein von metallischem Eisen. Diesem Beitrag folgt eine Arbeit in welcher eisenhaltiger Magnesit bei hohen Drücken mit einem Laser geheizt wurde, wobei sich eine neue monokline Phase gebildet hat. Diese Beobachtung legt nahe, dass das Stabilitätsfeld spezieller Karbonate von ihrer Kristallchemie abhängt. Im dritten Beitrag werden Messungen vorgestellt, in denen Einkristalle von  $\delta\text{-AlOOH}$ , einer möglichen wasserhaltigen Phase im tiefen Mantel, mittels Synchrotron-Röntgenbeugung bis zu einem Druck von 30 GPa bei Raumtemperatur untersucht wurden.

Phasenübergänge, welche bei Bedingungen stattfinden, die im Inneren von Planeten zu erwarten sind, werden in den folgenden drei Beiträgen diskutiert. Die ersten zwei experimentellen Arbeiten präsentieren Ergebnisse aus zeitaufgelösten Röntgenbeugungsexperimenten, welche für den Phasenübergang von Eis VI nach Eis VII und den Spinübergang in  $(\text{Mg,Fe})\text{O}$  Ferropertiklas durchgeführt wurden. Kompressionsraten von bis zu 1 TPa/s wurden in einer neuartigen dynamischen Diamantstempelzelle erreicht, welche es unter anderem erlaubt, die Kinetik von Phasenübergängen zu bestimmen. Der dritte Beitrag zeigt computergerechnete Resultate des B1-B2 Phasenübergangs in MgO von dem angenommen wird, dass er im Mantel von Super-Erden stattfindet, bei Bedingungen die in Experimenten schwer zu erreichen sind.

Im vorletzten Beitrag werden Strukturverfeinerungen von Einkristall-Intensitätsdaten präsentiert, die an eisenreichem Magnesioferrit ( $\text{Mg}_{0.6}\text{Fe}_{2.4}\text{O}_4$ ) gemessen wurden. Weiterhin wurde die Zustandsgleichung bis 16 GPa gemessen und es wird gezeigt, dass die Kompressibilität von Magnesioferrit der von Magnetit ähnelt.

Oxidationsprozesse in Mackinawit, einem Eisensulfid welches in anoxischen Umgebungen vorkommt, werden im letzten Beitrag untersucht. Die Datenauswertung soll die wahrscheinlichsten Reaktionswege, sowie die Reaktionskinetik bestimmen und damit Einblicke in Prozesse erlauben, die in der frühen Erde abgelaufen sind.

### **3.4 Physikalische Eigenschaften von Mineralen**

Seismologie ist der Schlüssel für das Verständnis des unzugänglichen Erdinneren. Durch Erdbeben angeregte elastische Wellen werden in der Erde gebrochen und reflektiert, und können so zur Untersuchung des tiefen Erdinneren genutzt werden, um Informationen über die elastische Struktur und letztendlich die Physik und Chemie der unzugänglichen Bereiche bis hin zum Erdmittelpunkt zu sammeln. Die Geschwindigkeiten seismischer Wellen hängen von den elastischen Moduli und der spezifischen Dichte des Materials ab, durch das sich die

Wellen fortpflanzen. Beide Eigenschaften werden wiederum durch die Kristallstruktur und die chemische Zusammensetzung der enthaltenen Minerale sowie durch Druck und Temperatur bestimmt. Die elastischen Moduli sind darüberhinaus abhängig von der Wellenfrequenz und Kristallorientierung. Die Messung der elektrischen Leitfähigkeit ist eine komplementäre physikalische Methode zur Untersuchung des ausgedehnten unzugänglichen Erdinneren. Die Fortpflanzung von elektromagnetischen Signalen im Erdmantel hängt von der elektrischen Leitfähigkeit der Mineralvergesellschaftungen ab, die nur durch Experimente unter extremen Bedingungen oder theoretische Berechnungen verstanden werden können. Dieses Kapitel beschreibt einige der neuesten Resultate, die sich auf die folgenden Schlüsselfragen beziehen:

- Was bedeuten Änderungen in den seismischen Wellengeschwindigkeiten für die Zusammensetzung und die Temperaturprofile im Erdmantel? Können wir auf diese Art wasserreiche Regionen im Mantel erkennen?
- Was ist die Wirkung von Druck, Temperatur und Zusammensetzung auf die elektrische Leitfähigkeit in der Erde?

Die ersten Beiträge untersuchen die Abhängigkeit der seismischen Wellengeschwindigkeit vom Wasser-/Wasserstoffgehalt in Wadsleyit und Ringwoodit, von der Kationen-Substitution in Granat-Mischkristallen der Majorit-Pyrop-Reihe bzw. verschieden zusammengesetzten Akimotoiten, vom Fe-Spin Übergang in Ferropiriklas und von der quasi-hydrostatischen Kompression von nanokristallinem Stishovit. Experimente, die die Wellengeschwindigkeiten direkt bestimmen, wurden entweder mit Laserlicht (Brillouinstreuung im Terahertzbereich) oder mit Ultraschallwellen (oft im Megahertzbereich) bei gleichzeitiger Bestimmung der spezifischen Dichte als Funktion von Druck (und Temperatur) durchgeführt. Die Kombination von Geschwindigkeiten mit präzisen Dichtedaten aus Einkristall-Röntgenbeugung (z. B. für dichte, wasserreiche Silikate wie Phase E und Phase EGG) ergibt elastische Moduli, die mit seismischen Messungen verglichen werden können. Untersuchungen von wasserhaltigem Wadsleyit und Ringwoodit liefern wichtige Anhaltspunkte für die Erkennung von Wasser in der Übergangszone des Erdmantels. Erdbebenwellen haben typischerweise Frequenzen von ca. 1 Hz und Wellenlängen im km-Bereich und sind daher zu groß für die Dimensionen von experimentellen Hochdruckproben. Dynamische (piezo-getriebene) Diamantstempelzellen-Experimente zum Spinübergang des Eisens in Ferropiriklas zeigen eine starke Erniedrigung des Kompressionsmoduls über diesen Übergang hinweg, und stellen die ersten direkten Messungen des elastischen Verhaltens einer Probe bei Drücken des unteren Erdmantels und realen seismischen Frequenzen in der Diamantstempelzelle dar.

Die letzten Beiträge des Kapitels betonen die Transporteigenschaften von natürlichem Olivin im oberen Erdmantel sowie von flüssigen Fe-S Legierungen im inneren Erdkern. Die erstere experimentelle Arbeit zeigt, dass Leitfähigkeitsanomalien bei 70-120 km Tiefe unter jungen ozeanischen Platten gut durch ionische Leitfähigkeitsmechanismen in Olivin erklärt werden

können, während im letzteren Beitrag *ab initio*-Berechnungen demonstrieren, dass das Vorhandensein von leichten Elementen die elektronischen Transporteigenschaften im flüssigen Erdkern substantiell verändert und damit einen Einblick in die thermische Entwicklung von terrestrischen Planeten und die Stabilität von potentiellen Geodynamos liefert.

### **3.5 Fluide, Schmelzen und ihre Wechselwirkung mit Mineralen**

Die Gesamtmenge an flüchtigen Elementen auf unserem Planeten wurde wahrscheinlich in der frühesten Erdgeschichte durch das Gleichgewicht zwischen einem Magmaozean und der Atmosphäre mitbestimmt. Leider existieren kaum Daten über die Löslichkeit von flüchtigen Elementen in Silikatschmelzen unter reduzierenden Bedingungen. Unter anderem wurde spekuliert, dass Kohlenmonoxid (CO) in Silikatschmelzen möglicherweise sehr viel weniger löslich ist als Kohlendioxid (CO<sub>2</sub>). Der erste Beitrag in diesem Kapitel beschreibt die ersten direkten Messungen der Löslichkeit von CO in Silikatschmelzen mit rhyolitischer bis basaltischer Zusammensetzung. Die Daten zeigen, dass CO nicht sehr viel weniger löslich ist als CO<sub>2</sub>. Eine große Menge von Kohlenstoff muss daher ursprünglich im Magmaozean gelöst worden sein. Die Entgasung von Magmen transportiert flüchtige Bestandteile aus der Erdkruste und dem Mantel in die Atmosphäre. Dieser Prozess erfordert die Bildung von Gasblasen in einem Magma. Mit Hilfe einer technischen Neuentwicklung am Bayerischen Geoinstitut ist es jetzt möglich, diesen Prozess in einer Druckzelle unter dem Mikroskop bei genau definierten Druck- und Temperaturbedingungen direkt zu beobachten. Die Experimente, die im zweiten Beitrag dieses Kapitels beschrieben werden, deuten darauf hin, dass für die Bildung von Wasserdampf-Blasen in einem Magma nur eine sehr geringe Übersättigung benötigt wird. Ein wichtiges Problem bei der Vorhersage von Vulkaneruptionen ist es, Magmenkammern unterhalb von Vulkanen von hydrothermalen Systemen zu unterscheiden. Beide Objekte können Bodenbewegungen verursachen und führen zu verringerten seismischen Geschwindigkeiten und erhöhten elektrischen Leitfähigkeiten im Untergrund. Neue Leitfähigkeitsdaten für das System HCl-H<sub>2</sub>O, das besonders relevant ist für subvulkanische Systeme, werden im nächsten Beitrag beschrieben. Die neuen Daten werden dabei helfen, magnetotellurische Messungen an aktiven Vulkanen korrekt zu interpretieren und saure hydrothermale Fluide von Silikatschmelzen zu unterscheiden.

Der Erdmantel ist ein wichtiges Reservoir flüchtiger Elemente. Ein Beitrag in diesem Jahresbericht untersucht die Effizienz, mit der Stickstoff in den tiefen Mantel subduziert wird. Eine wichtige Schlussfolgerung dieser Studie ist, dass der Atmosphärendruck im Archaikum wahrscheinlich höher war als heute. Die folgenden beiden Beiträge untersuchen die Speicherung von Fluor im Mantel und seinen Einfluss auf die Schmelzbildung. Unter anderem vergrößert Fluor das Stabilitätsfeld von Phlogopit und beeinflusst dadurch indirekt auch die Speicherung von Wasser. Die Sauerstofffugazität im Mantel kontrolliert den Oxidationszustand von Übergangsmetallen wie Eisen oder Chrom. Eine Studie in diesem

Kapitel zeigt, dass  $\text{Cr}^{2+}$  in basaltischen Schmelzen unter hohem Druck relativ zu  $\text{Cr}^{3+}$  stabilisiert wird.

Die letzten beiden Beiträge in diesem Kapitel des Jahresberichts beschäftigen sich mit einigen technischen Problemen bei der Untersuchung von Silikatschmelzen und Fluiden bei hohen Drücken und Temperaturen. Gläser werden oft untersucht als Modelle für Silikatschmelzen. Eine molekular-dynamische Studie zeigt jedoch, dass selbst bei extrem schnellen Abschreckgeschwindigkeiten die Struktur des Glases von der Silikatschmelze signifikant verschieden ist. Experimentelle Messungen der Fraktionierung von Wasserstoff-Isotopen zwischen koexistierenden Silikatschmelzen und wässrigen Fluiden sind extrem schwierig. *In situ*-Untersuchungen mit Raman-Spektroskopie wurden vorgeschlagen, jedoch zeigt der letzte Beitrag in diesem Kapitel, dass einige der hierbei gemachten Annahmen grundsätzlich falsch sind. Die in der Literatur angegebenen Fraktionierungsfaktoren aus *in situ*-Raman-Messungen sind daher wohl fehlerhaft.

### 3.6 Rheologie

Eine Vielzahl von Prozessen, die die Geschichte der Erde und ihren gegenwärtigen Zustand geformt haben, haben ihren Ursprung in dynamischen Massenbewegungen wie den Fließbewegungen des Erdmantels und der Plattentektonik. Solche Bewegungen sind die Konsequenzen der rheologischen Reaktion der Mantel- und Krustengesteine auf deviatorische Spannungen. Die Verformungseigenschaften der Gesteine müssen daher unter den Bedingungen dieser Regionen der Erde bestimmt werden. Das rheologische Verhalten von Gesteinen ist jedoch komplex. Obwohl es im Grunde hauptsächlich durch die Fließgesetze der konstituierenden Minerale bestimmt wird, sind diese wiederum durch eine Vielzahl von Parametern wie Temperatur, Druck, chemische Zusammensetzung, Spannungszustände und ihre jeweiligen zeitlichen Verläufe beeinflusst. Darüber hinaus ist die Gesteinsrheologie stark durch texturale Charakteristika wie Korngröße, kristallographische Vorzugsorientierungen und Korngrenzenkonfigurationen bestimmt. Aus diesen Gründen verfolgt das Geoinstitut folgende verschiedene Ansätze, um die Fließgesetze der Hauptminerale und Texturereffekte auf die Gesteinsrheologie zu untersuchen.

In den ersten fünf Beiträgen wurden direkte Deformationsversuche durchgeführt. Das Geoinstitut verfügt über eine neuartige Vielstempelpresse mit sechs unabhängig voneinander verfahrbaren Stempeln, die es erlauben, Proben unter den Druck- und Temperaturbedingungen des gesamten oberen Erdmantels zu deformieren. Zwei Pressen mit demselben Konzept wurden von Wissenschaftlern des Geoinstituts auch an der Neutronenquelle in Garching bzw. der Röntgenquelle DESY in Hamburg installiert. Diese sind die Hauptwerkzeuge in den ersten vier Beiträgen. In der ersten Untersuchung wurden reine Scherungsexperimente an Pyrop-reichen Granat-Einkristallen durchgeführt, um die Bedingungen einzuengen, die zur Aktivierung von intrakristallinen Gleitsystemen in Granat

führen. Die Resultate zeigen, dass die Verformungsraten sowie der absolute Verformungsbetrag dabei einen stärkeren Einfluss zu haben scheinen als die Temperatur. In der zweiten Studie wurden polykristalline Olivinaggregate unter den Bedingungen des tiefen oberen Erdmantels plastisch deformiert, um einen vorhergesagten Wechsel im dominierenden intrakristallinen Gleitsystem mit ansteigendem Umschließungsdruck zu untersuchen. Jedoch selbst bei den geringsten Verformungsraten (und entsprechend niedrigsten Fließspannungen) zeigen die Texturen eine Einregelung beider in Frage kommenden Gleitsysteme [100](010) and [001](010), so dass beide offenbar ähnlich stark während der Deformation aktiviert wurden. Im dritten Beitrag wurden sog. Boudinage-Strukturen in lagigen zweiphasen-Gesteinen untersucht. Die Forscher konnten nachweisen, dass ein Viskositätskontrast zwischen zwei Lagen nicht ausreichend ist, um Boudinage-Strukturen zu generieren, sondern dass dafür weitere Kontraste, z. B. in der Kornstruktur, vorhanden sein müssen. In der vierten Studie wurden polykristalline Magnetitproben unter oxidierenden Bedingungen deformiert, um die Wechselwirkungen zwischen Verformung und dem Magnetit-Hämatit Phasenübergang zu verstehen, die in Bändereisenerz-Lagerstätten oft beobachtet werden. Es konnte gezeigt werden, dass deviatorische Spannungen die Bildung von Hämatit sehr stark fördern und dabei möglicherweise sogar den Effekt der Sauerstoffugazität übersteigen. In der fünften Studie wurde versucht, das dominante Gleitsystem von Ferroperiklas unter den Bedingungen des unteren Erdmantels zu bestimmen, um mögliche seismische Anisotropien im unteren Erdmantel quantifizieren zu können. Im Unterschied zu den vorherigen Beiträgen wurde hier die Diamantstempelpresse als Deformationsapparat benutzt, um einen ausreichend hohen Druck zu erreichen. Die Forscher fanden heraus, dass bei niedrigen Druck-Temperatur-Bedingungen Gleitung hauptsächlich auf der {110} Gitterebene stattfindet, bei hohen Drücken und Temperaturen jedoch Gleitung auf {100} in ungefähr gleichem Maße wichtig wird.

In jüngerer Zeit ist die Korngrenzgleitung in zunehmendem Maße als wichtiger Deformationsmechanismus identifiziert worden. Die drei folgenden Beiträge beschäftigen sich daher mit der Rolle der Korngrenzen während der Deformation von Olivinaggregaten. Die erste Studie über dieses Thema versuchte, die Korngrenzgleitung in Olivinproben zu identifizieren, die hauptsächlich durch Versetzungskriechen deformiert wurden. In der zweiten Untersuchung wurde die geometrische Kompatibilität zwischen Nachbarkörnern als Funktion der Gesamtverformung analysiert, wobei sich vor allem Korngrenzen mit einer gemeinsamen (010) Gitterebene während der Scherdeformation bildeten. Dieses Ergebnis deutet darauf hin, dass die kristallographische Einregelung und der intergranulare Transfer von Gleitung intrinsisch auf dieser Gitterebene korreliert sind. Die letzte Studie zu diesem Thema konzentriert sich auf die Charakterisierung der Korngrenzen von Porphyroblasten, die durch abnormes Kornwachstum in die umgebende Matrix entstehen.

Die nächsten vier Beiträge untersuchen die Wirkungen verschiedener physikalischer und chemischer Konditionen auf die Fließgesetze von Olivin und seinen Hochdruckpolymorphen durch indirekte Methoden. Im ersten Beitrag mit dieser Strategie wird die Abhängigkeit der Versetzungsmobilität im [001](010) Gleitsystem vom Wassergehalt mithilfe der

Versetzungserholungstechnik bestimmt. Die Forscher fanden heraus, dass die Abhängigkeit der Mobilität vom Wassergehalt nur sehr gering ist. Die folgende Untersuchung zeigt, dass Versetzungsgleitung im System [100](010) im trockenen Zustand nicht aktiviert werden kann, und nur durch Beigabe von Wasser ermöglicht wird. In der dritten Studie wird berichtet, dass die Gleitung von Schraubenversetzungen im [001](010) Gleitsystem die identische Aktivierungsenergie wie die Selbstdiffusion von Si hat, und es wird daraus geschlossen, dass die Bewegung dieses Typs von Versetzungen Diffusions-kontrolliert ist. Im letzten Beitrag mit diesem Ansatz wurde der Selbstdiffusionskoeffizient von Si in Wadsleyit-Einkristallen gemessen, um die Rheologie in der Übergangszone des oberen Erdmantels abzuschätzen. Die gefundenen Diffusionskoeffizienten sind eine Größenordnung höher als solche in vorhergehenden Untersuchungen, was bedeuten würde, dass die Festigkeit von Wadsleyit signifikant geringer wäre als bisher angenommen.

Während alle bisherigen Beiträge die rheologischen Eigenschaften von (Mantel-)mineralen mit verschiedenen experimentellen und analytischen Methoden untersucht haben, werden im letzten Beitrag numerische Simulationen angewendet. Dabei wurden die Wechselwirkungen von Korngrößenreduktion und Scheraufheizung analysiert, die zu einer Lokalisierung von duktiler Deformation führen.

### **3.7 Materialwissenschaften**

Forschungsarbeiten in Physik, Chemie sowie Materialwissenschaften unter hohem Druck haben am Bayerischen Geoinstitut immer eine wichtige Rolle gespielt, wenn sie auch weniger Raum einnehmen als Arbeiten in den Geowissenschaften. Häufig sind sie mit Fragen verbunden, die sich bei der Untersuchung von Geomaterialien ergeben, und die dann an Modell-Materialien untersucht werden, bei denen sich bestimmte Phänomene isoliert darstellen lassen. Wichtige Beispiele sind hierbei die Übergänge in elektrischer Leitfähigkeit, zum Beispiel von isolierendem zu metallischem Verhalten, sowie Untersuchungen von Materialien, die im gleichen Strukturtyp auftreten, zum Beispiel Perowskite. Am Bayerischen Geoinstitut steht die wissenschaftliche Expertise sowie die Ausrüstung in Hochdruck-technologie und Analytik zur Verfügung, die die Lösung schwieriger Fragen zu physikalischen und chemischen Eigenschaften von Materialien möglich macht. In diesem Jahresbericht stellen wir Forschungsergebnisse zu verschiedenen Typen von Festkörpern vor: Elemente, binäre sowie komplexe Oxide, Nitride und Carbide. Die Hälfte der Beiträge befasst sich mit Einkristall-Röntgenbeugung unter hohem Druck, ein Gebiet in dem das Bayerische Geoinstitut weltweit führend ist.

Die Struktur aller bekannten Formen von Boron ( $\alpha$ -B bis  $\epsilon$ -B) basiert auf  $B_{12}$  Icosaedern, die verschieden zusammengesetzt werden, wobei vor 30 Jahren ein nicht-ikosaedrisches Allotrop auf der Basis von  $\alpha$ -Ga vorhergesagt wurde. Diese Struktur ( $\zeta$ -B) wurde jetzt mit Hilfe von Einkristall-Röntgenbeugung bei einem Druck von 115 GPa bestätigt. Zwei weitere

Untersuchungen im vorliegenden Jahresbericht befassen sich mit Einkristall-Röntgenbeugung bei einem Druck von mehr als 100 GPa bei denen neue Phasen beobachtet wurden, zum einen im System Fe-N, zum anderen für Fe-O. Im Fe-N System sind dies  $\text{Fe}_3\text{N}_2$ , FeN,  $\text{FeN}_2$  und  $\text{FeN}_4$ , wobei besonders die  $\text{FeN}_4$  Phase (bei 115 GPa) von Interesse ist, in der Fe mit vier N in einem gestörten Oktaeder koordiniert ist. In  $\text{FeN}_4$  treten sowohl N=N Doppelbindungen als auch N-N Einzelbindungen auf. Im System Fe-O wird die Struktur der bereits länger bekannten  $\text{FeO}_2$  Phase beschrieben, in der Eisen mit dem ungewöhnlichen  $\text{Fe}^{4+}$  Oxidationszustand auftritt.

Karbidre repräsentieren eine wichtige Klasse von keramischen Werkstoffen, die sich durch eine hohe thermische Stabilität und mechanische Stärke auszeichnen. Ihr Verhalten und ihre Stabilität bei hohem Druck sind jedoch nicht in einem notwendigen Maß charakterisiert. Im vorliegenden Beitrag zum Jahresbericht wird ein wichtiges Karbid, TaC, bei hohem Druck und hoher Temperatur untersucht und die mechanische Stärke durch einen hohen Kompressionsmodul bestätigt.

Mit Hilfe einer Kombination von Methoden, die wiederum Röntgenbeugung beinhaltet, untersuchen die zwei folgenden Beiträge Germanium und  $\text{CaCo}_3\text{V}_4\text{O}_{12}$  in der Perowskit-Struktur. Die Arbeit an Germanium zeigt einen Übergang des Halbleiter-Mechanismus von einem *n*-Typ zu einem *p*-Typ unter Druck (sowohl unter Kompression als auch bei einem Eindruck), der unter Entlastung nicht reversibel ist. Dies erlaubt die Einstellung eines traditionellen Halbleiters, bei dem zum Beispiel eine *p*-Zone auf eine *n*-Typ Matrix eingepreßt werden kann. Diese Art Halbleiter-Druck ermöglicht neue Anwendungen des altbekannten Halbleiters Ge. Die Untersuchungen an  $\text{CaCo}_3\text{V}_4\text{O}_{12}$  zeigen ein interessantes Verhalten von fundamentalem Interesse auf: In diesem Kristall nehmen die  $\text{Co}^{2+}$ -Ionen Freiräume innerhalb der Perowskit-Struktur ein, die von  $\text{V}^{4+}$  auf der oktaedrisch koordinierten B-Stelle und  $\text{Ca}^{2+}$  auf der A-Stelle gebildet wird. Damit sind die  $\text{Co}^{2+}$ -Ionen von vier  $\text{O}^{2-}$  umgeben, mit denen sie eine Ebene bilden. Unter Druck wird  $\text{Co}^{2+}$  aus den Ebenen gedrückt, was zu einer Polarisation des Kristalls führen sollte, die mit Hilfe eines externen Feldes eingestellt werden könnte.

In einer Reihe von Experimenten in der Stempel-Zylinder sowie der Vielstempel Presse wird der Austausch von  $\text{Zn}^{2+}$  und  $\text{Mg}^{2+}$  zwischen  $\text{Zn}_2\text{SiO}_4$  Willemit und  $\text{Mg}_2\text{SiO}_4$  Olivin in Abhängigkeit vom Druck untersucht, mit dem Ziel, dieses System als zuverlässiges Geobarometer zu kalibrieren. Im Druckbereich bis 4 GPa vergrößert sich die Löslichkeit von  $\text{Zn}^{2+}$  in Olivin, die von  $\text{Mg}^{2+}$  verkleinert sich in Willemit, was die Anwendbarkeit dieses Systems als Geobarometer bestätigt. Bei ca. 4 GPa, tritt für Willemit ein Phasenübergang auf und die Trends in der Löslichkeit kehren sich um, womit Willemit in diesem Druckbereich als Geobarometer nicht mehr hilfreich ist.

Der letzte Beitrag in diesem Abschnitt des Jahresberichts kommt ohne Anwendung von Druck aus. Stattdessen wird hier die Diffusion von Spurenelementen in Yttrium Aluminium

Granat (YAG) untersucht, einem Material, das als Laserquelle Anwendung findet. Die Diffusion solcher Elemente entlang der Korngrenzen können sich negativ auf die Eigenschaften von YAG auswirken, zum Beispiel auf seine Lebensdauer. In der Untersuchung wird aufgezeigt, dass die Diffusion von Elementen, die nicht in YAG löslich sind, entlang von Korngrenzen im Vergleich zu Diffusion durch das Material ein sehr schneller Prozess ist, der die Stabilität von YAG negativ beeinflusst.

### **3.8 Methodische Entwicklungen**

Ein wichtiges Ziel in experimentellen Studien in den Geo- und planetaren Wissenschaften sowie den Materialwissenschaften ist sowohl die Entwicklung neuer Techniken als auch die Verbesserung schon vorhandener Ansätze. Solche Entwicklungen umfassen die Ausweitung des experimentell realisierbaren Druck-Temperatur-Bereiches, Verbesserungen in der Kontrolle und Charakterisierung der Probenumgebung in solchen Hochdruckexperimenten und neue Methoden zur chemischen Analyse von Mineralen und Fluidphasen, die experimentell hergestellt werden. Die elf Beiträge dieses Kapitels decken viele wichtige Aspekte solcher methodologischen Entwicklungen ab.

Die ersten neun Studien in diesem methodologischen Kapitel beschäftigen sich mit Experimenten in der Laser-beheizten Diamantstempelzelle. Die Laser-beheizte Diamantstempelzelle ist die wichtigste experimentelle Apparatur, mit der Materialien bei Drücken untersucht werden können, die deutlich höher sind als die erreichbaren Drücke in der Vielstempelpresse. Sie wird daher genutzt, um Experimente im Megabar-Druckbereich und bei Temperaturen von bis zu ca. 5000 K durchzuführen, und ist so das experimentelle Hauptwerkzeug, um den tiefen Erdmantel und metallischen Kern, sowie frühe Prozesse der planetaren Differentiation zu verstehen. Aufgrund der Transparenz der Diamantstempel ist mit dieser Technik ein weites Spektrum von *in situ*-Messungen an Proben unter hohem Druck und hoher Temperatur möglich. Der erste Beitrag beschreibt ein neues Stempeldesign, das eine Reihe von wichtigen Vorteilen bietet. Insbesondere vereinfacht und verbessert der neue Entwurf *in situ*-Beugungsexperimente an Einkristallen unter hohem Druck. Die zweite Studie präsentiert Entwicklungen von Röntgenbeugungsexperimenten an Einkristallen bis zu bislang unerreicht hohen Drücken von 200 GPa. Um solch hohe Drücke zu erreichen, wurde in dieser Studie die kürzlich entwickelte zweistufige Diamantstempelzelle mit einer extrem kleinen Probengröße von 1  $\mu\text{m}$  genutzt.

Mössbauerspektroskopie ist eine wichtige Analysenmethode für die Charakterisierung des Oxidationszustandes und der strukturellen, dynamischen und magnetischen Eigenschaften von Materialien. Diese Methode wurde jetzt so weiterentwickelt, dass man Proben simultan bei hohem Druck und hoher Temperatur in der Diamantstempelpresse messen kann, wobei die hohen Temperaturen durch beidseitig gepulste Laserstrahlen erreicht werden können, wenn die Beheizung mit einem kontinuierlichen Laser nicht möglich ist. Diese Entwicklung

wird es möglich machen, in der Zukunft auch Eigenschaften wie die thermische Leitfähigkeit unter extremen Bedingungen zu untersuchen. Nukleare Magnetresonanz (NMR) ist eine vielfältig anwendbare Methode, die zur Charakterisierung der atomaren Struktur von Materialien (z. B. bei hohem Druck abgeschreckten Silikatgläsern) unter Raumbedingungen angewendet wird. Der vierte Beitrag beschreibt technisch sehr anspruchsvolle Entwicklungen, die *in situ*-NMR Messungen an Proben unter hohem Druck in Diamantstempelzellen ermöglichen werden. Diesem Beitrag folgt eine Beschreibung der Entwicklung eines mobilen Heizsystems mit CO<sub>2</sub>-Laser für die Diamantstempel-Experimente. Die Nutzung von CO<sub>2</sub>-Lasern für Diamantstempel-Experimente war in der Vergangenheit wegen technischer Schwierigkeiten begrenzt, aber ein großer Vorteil dieser Technik ist es, dass auch optisch transparente Proben auf hohe Temperaturen aufgeheizt werden können. Der Erfolg der jüngsten Entwicklungen wird durch die Messung von Schallwellengeschwindigkeiten in MgO-Einkristallen bei Temperaturen von 2300 K mithilfe von Brillouinspektroskopie bestätigt. Der sechste Beitrag beschreibt Entwicklungen, die es ermöglichen, Änderungen in der optischen Transparenz von Proben bei hohen Drücken zu messen, die durch druckinduzierte Strukturübergänge erzeugt werden. Die folgende Studie präsentiert die Nutzung von Metallkapseln als Probenbehälter in Laser-beheizten Diamantstempel-Experimenten. Das ist aufgrund der sehr kleinen Probenvolumen äußerst herausfordernd, hat aber die Vorteile, insbesondere für petrologische Experimente, dass chemische Kontamination vermieden und der normalerweise sehr hohe Temperaturgradient innerhalb der Probe stark reduziert wird. Die letzten beiden Beiträge zur Laser-beheizten Diamantstempelzelle befassen sich mit der Partitionierung von Elementen zwischen flüssigen Silikat- und Metallschmelzen, um die Geochemie der planetaren Kernbildung zu verstehen. Die erste Studie untersucht die Probleme bei der chemischen Analyse von extrem kleinen und dünnen Proben mit der Elektronenmikrosonde und quantifiziert die Fehler und Messgrenzen mithilfe von sorgfältig präparierten Proben sowie theoretischen Modellberechnungen. Der letzte Beitrag dieses Blocks beschreibt die Mikrostruktur und Chemie von abgeschrecktem flüssigen Eisen mithilfe der tomographischen Atomsonde mit einer Auflösung im Nanometerbereich.

Die letzten beiden Beiträge dieses Kapitels beschreiben methodologische Fortschritte in den Bereichen der Spektroskopie, bzw. der Minerallöslichkeit in Fluiden. Im ersten Beitrag wird die Nutzung von Elektronenenergieverlust-Spektroskopie (EELS, ELNES) im Transmissionselektronenmikroskop weiter entwickelt, um den Oxidationszustand in Hochdruckmineralparagenesen zu untersuchen, die in der Vielstempel-Experimente synthetisiert wurden und für den unteren Erdmantel relevant sind. Schließlich wird eine neue Methode zur Fixierung von Fluiden in Diamant-Einkristallen vorgestellt, die zur Untersuchung der Zusammensetzung von Fluideinschlüssen verwendet wurde, die sich im chemischen Gleichgewicht mit neu gebildeten Mineralen befanden.

### 3. Research Projects

#### 3.1 Earth and Planetary Structure and Dynamics

The terrestrial planets formed within roughly 100 million years after the start of the solar system. Modern astrophysical theories indicate that planetesimals had sizes ranging from a few dozen to hundreds of kilometers. In the beginning collisions involved planetesimals, during the later stages of accretion planetary embryos collided with remaining planetesimals and with other embryos. Due to the release of kinetic energy and decay of short-lived radioactive isotopes, magma oceans formed on the growing planetary bodies. The last giant impact involving proto-Earth and a Mars-sized impactor body led to the formation of a hot disk from which the initially molten Moon accreted.

The first contribution in this section deals with chondrules, millimeter-sized quenched droplets that can be found in most primitive meteorites. The study uses two-dimensional numerical models to determine under which conditions chondrules containing both iron and silicates can form due to collisions among partially molten planetesimals. The results confirm that chondrule formation can occur during the first few million years after the formation of the solar system and that chondrules can be incorporated into later-formed planetesimals.

The second contribution discusses the phase of planet formation when planetary embryos collided among each other and formed larger terrestrial objects. For this purpose a three-dimensional SPH (*=smoothed particle hydrodynamics*) model was serially coupled with a three-dimensional geodynamical model to study both the impact process and longer-term evolution of the target body. This method allows the limitations of both SPH models and geodynamical models to be overcome. Namely, SPH models describe a short time after the impact process. On the other hand, impact processes can be only prescribed in a simplified way in geodynamical models. Therefore the final state of each SPH simulation serves as input data for a geodynamical model. Since ejecta material falling back onto the target body can affect the thermomechanical evolution, detailed tests were performed to assess the sensitivity of the handoff time between both models.

Shortly after its formation more than 4.4 billion years ago, the lunar interior was molten. The third study discusses the potential existence of a present-day molten layer in the lowermost lunar mantle as suggested by a reanalysis of seismic data obtained a few years ago. Based on crystallization models it has been suggested that iron and titanium-rich material solidified late and sank down to the core-mantle boundary, where the material experienced remelting. The experiments aim at determining whether this material could be molten at the present-day pressure and temperature conditions in the lowermost lunar mantle and whether this material would also be negatively buoyant compared to ambient mantle material, thus explaining its stability at the core-mantle boundary.

The fourth study deals with the lunar interior structure. For this purpose a one-dimensional model was developed that utilizes geophysical, geochemical and mineralogical data to improve our understanding of the lunar interior. Using different temperature profiles and

either a homogeneous or differentiated lunar mantle, a large parameter space was covered by varying various parameters such as layer thicknesses. The results show that this combined model allows for an improved determination of the lunar core radius that was previously not well known.

After the end of accretion the terrestrial planets started to cool down and the magma ocean crystallized. This led to the formation of phase boundaries in the solid mantle that can be detected using seismological methods. The next contribution presents laboratory experiments on the phase transition from ringwoodite to bridgmanite and ferropericlase. The results show that this phase transition is very sharp and that its depth fits very well with the detected 660 km discontinuity.

Geochemical studies showed in recent years that water was already delivered during the Earth's formation. The next study employs high resolution numerical models of the upper mantle to study how water was transported during Earth's evolution by subducting slabs into the Earth's interior and how water is distributed in the mantle.

The Earth's lower mantle is mostly made of bridgmanite and smaller quantities of ferropericlase. The global-scale mantle convection models of the next study show that the weaker ferropericlase can interconnect in high strain regions of the lower mantle while the rheology of less deformed mantle regions is controlled by the more viscous bridgmanite. This could explain seismic tomography data showing that certain slabs stagnate around 1000 km depth, while slabs passing other mantle regions can sink deeper into the mantle without any stagnation.

Even high-resolution models of the Earth's mantle are unable to resolve processes occurring on the micro-scale. The next two contributions demonstrate that numerical models of micro-scale processes can support laboratory experiments to improve our understanding of these processes. These results can be used to develop better parametrizations of various processes like water transport in the Earth's mantle or the deformation of two-phase mixtures, thus enabling more realistic global-scale numerical models to be performed in the future.

**a.** *Impact splash chondrule formation during planetesimal recycling (G.J. Golabek, T. Lichtenberg/Zurich, C.P. Dullemond/Heidelberg, M. Schönbachler/Zurich, T.V. Gerya/Zurich, M.R. Meyer/Ann Arbor)*

Chondrules, mm-sized igneous-textured spherules, are the dominant bulk silicate constituent of chondritic meteorites and originate from highly energetic, local processes during the first million years after the birth of the Sun. So far, an astrophysically consistent chondrule formation scenario explaining major chemical, isotopic and textural features, in particular Fe,Ni metal abundances, bulk Fe/Mg ratios and intra-chondrite chemical and isotopic diversity, remains elusive. We examine the prospect of forming chondrules from impact splashes among planetesimals heated by radioactive decay of short-lived radionuclides using thermomechanical models of their interior evolution. Intensely melted planetesimals with

interior magma oceans became rapidly chemically equilibrated and physically differentiated. Therefore, collisional interactions among such bodies would have resulted in chondrule-like but basaltic spherules, which are not observed in the meteoritic record. This inconsistency with the expected dynamical interactions hints at an incomplete understanding of the planetary growth regime during the lifetime of the solar protoplanetary disk. To resolve this conundrum, we examine how the observed chemical and isotopic features of chondrules constrain the dynamical environment of accreting chondrite parent bodies by interpreting the meteoritic record as an impact-generated proxy of early solar system planetesimals that underwent repeated collision and reaccretion cycles. Using a coupled evolution-collision model we demonstrate that the vast majority of collisional debris feeding the asteroid main belt must be derived from planetesimals which were partially molten at maximum (Fig. 3.1-1).

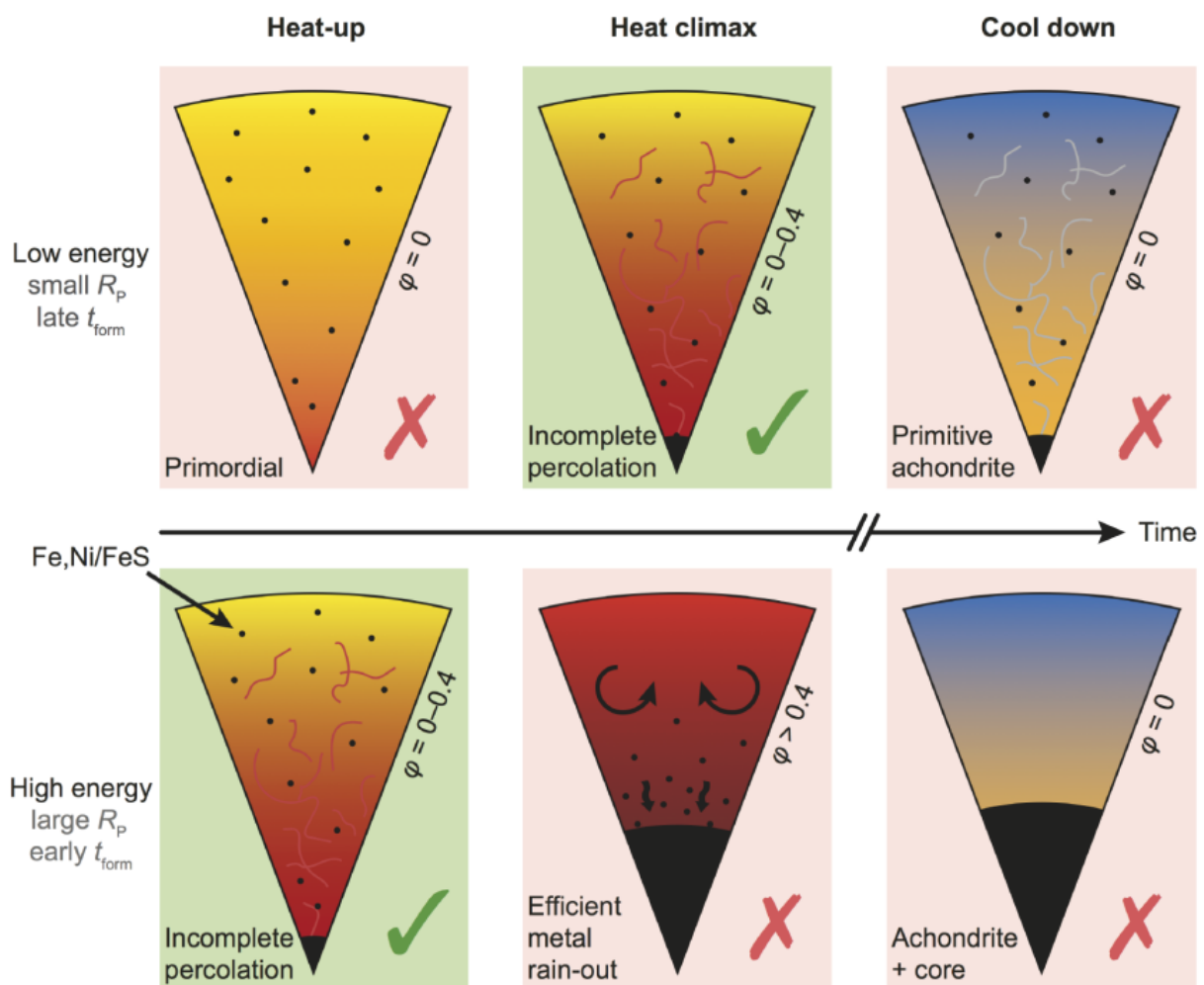


Fig. 3.1-1: Schematic illustration of the qualitative thermomechanical planetesimal evolution regimes. (Top) Low-energy bodies with relatively small radii or late formation times, which were eligible chondrule precursor bodies (in green) around their heat climax. (Bottom) High-energy bodies with either large radii or early formation times, which were eligible precursor bodies only during their brief initial heat-up phase. Models highlighted in red either do not feature sufficient radiogenic pre-heating or have lost their primordial metal abundances due to efficient metal-silicate segregation processes.

Therefore, the precursors of chondrite parent bodies either formed primarily small, from sub-canonical aluminium-26 reservoirs, or collisional destruction mechanisms were efficient enough to shatter planetesimals before they reached the magma ocean phase.

**b. Coupling collision and geodynamical models** (G.J. Golabek, A. Emsenhuber and M. Jutzi/Bern, E.I. Asphaug/Tucson and T.V. Gerya/Zurich)

Giant impacts have been suggested to explain various characteristics of terrestrial planets and their moons. However, so far in most models only the immediate effects of the collisions have been considered, while the long-term interior evolution of the impacted planets was not studied. Here we present a new approach, combining 3-D shock physics collision calculations (Fig. 3.1-2) with 3-D thermochemical interior evolution models.

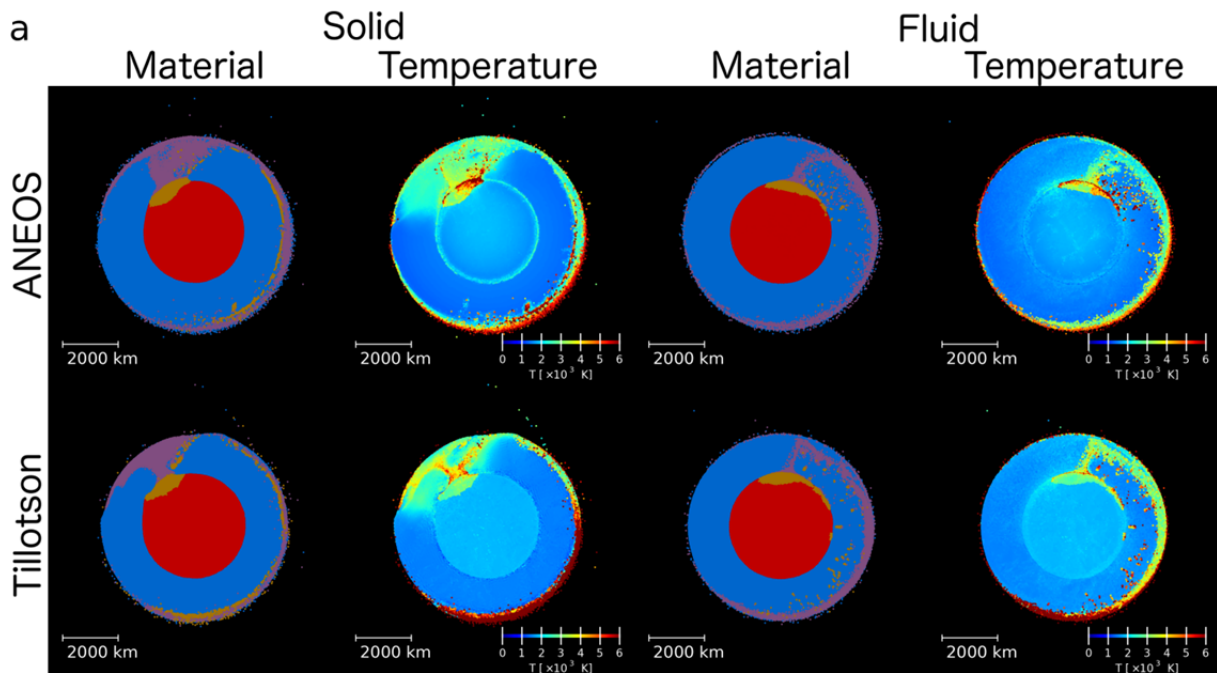


Fig. 3.1-2: Material and temperature distributions resulting from grazing collision simulations and at  $t = 18$  h after the impact. Colors for material distribution are as follows: blue for target mantle, purple for impactor mantle, red for target core and orange for impactor core.

We apply the combined methods to a demonstration example of a giant impact on a Mars-sized body, using typical collisional parameters from previous studies. While the material parameters (equation of state, rheology model) used in the impact simulations can have some effect on the long-term evolution, we find that the impact angle is the most crucial parameter

for the resulting spatial distribution of the newly formed crust. The results indicate that a dichotomous crustal pattern can form after a head-on collision, while this is not the case when considering a more likely grazing collision. Our results underline that end-to-end 3-D calculations of the entire process are required to study in the future the effects of large-scale impacts on the evolution of planetary interiors.

*c. Understanding evolution of interior of the Moon by in situ density determination of deep lunar melts (A. Mallik, T. Ejaz/Kharagpur, S. Petitgirard, S. Shcheka, W. Malfait/Zurich, M. Wilke/Potsdam and G. Garapic/New Paltz)*

Eleven of the 25 varieties of pristine, near-primary lunar glasses from Apollo missions 11 to 17, have FeO concentrations > 6 wt. % and TiO<sub>2</sub> concentrations > 16 wt. %. Experiments on these pristine lunar glasses source their depths in the lunar mantle between 275-690 km from the surface. How are Fe-Ti-rich sources formed in the lunar mantle at such depths, when the crystallization of the lunar magma ocean should prevent this? Perhaps the most appealing way to do so is by overturn of the lunar mantle. The last 95 % of the lunar magma ocean during crystallization produced a dense, radioactive element-rich (KREEP), ilmenite (Fe-Ti)-rich layer below the floatation crust of plagioclase, which could sink through the mantle due to its density. If the Moon does have a Fe-rich core, this layer could sink until the CMB where it can undergo heating by radioactive decay and rise as an upwelling once it achieves thermal buoyancy. The upwelling could provide heat for partial melting to produce mare basalts in the lunar interior. Inefficient overturn, convective mixing and/or upwelling could have created Fe-Ti-rich zones in the lunar mantle that may have been sources for Fe-Ti-rich mare basalts. On the other hand, a partially molten layer near the CMB of the present-day Moon has been proposed based on the absence of observed deep far-side quakes, reflected phases from deep moonquakes as well as tidal energy dissipation in the lunar interior. The most likely source for the partial melt would be the Fe-Ti-rich layer that is the product of the overturn episode and the melt will be stable at the CMB only if it is denser than the overlying mantle. So far, based on published estimates, lunar basalts that likely contain contributions from this overturned Fe-Ti-rich layer are less dense than the overlying mantle at *P-T* conditions of their generation, hence, they will rise and not sink. The phase equilibria and melt compositions will be highly dependent on the proportion of mixing between this Fe-Ti-rich layer and the surrounding ambient mantle.

We have undertaken an experimental study to investigate the phase equilibria of the Fe-Ti-rich layer and the ambient mantle (mixed in different proportions) at pressures ranging from 2 to 4.8 GPa, covering the depths from sources of Fe-Ti-rich basalts (obtained from previous studies) to the lunar CMB. Preliminary results show that the overturned Fe-Ti rich layer will undergo complete melting at *P-T* conditions relevant for generation of Fe-Ti rich mare basalts. This implies that a melt of the same composition as the Fe-Ti rich layer will sink to the CMB and remain stable until the present day, only if it is denser than the surrounding mantle.

Density estimates of the molten Fe-Ti layer obtained using the current range of published values of isothermal bulk moduli and their pressure-temperature derivatives do not help conclude the fate of such melt because the densities encompass values that are both higher and lower than that of the lunar mantle (Fig. 3.1-3). Hence, we have proposed to measure the density of Fe-Ti enriched lunar melts *in situ* at the relevant *P-T* conditions using the X-ray absorption technique in a Paris-Edinburgh press at ESRF. The depth of density crossover between these melts and the ambient lunar mantle will determine whether: (a) the melts will sink and settle at the lunar core-mantle boundary (CMB), forming the partial melt layer suspected at the present CMB based on seismic studies; or, (b) the melts will rise, undergo reactive flow with the surrounding lunar mantle, and likely erupt as mare basalts that have been sampled by Apollo and Luna missions.

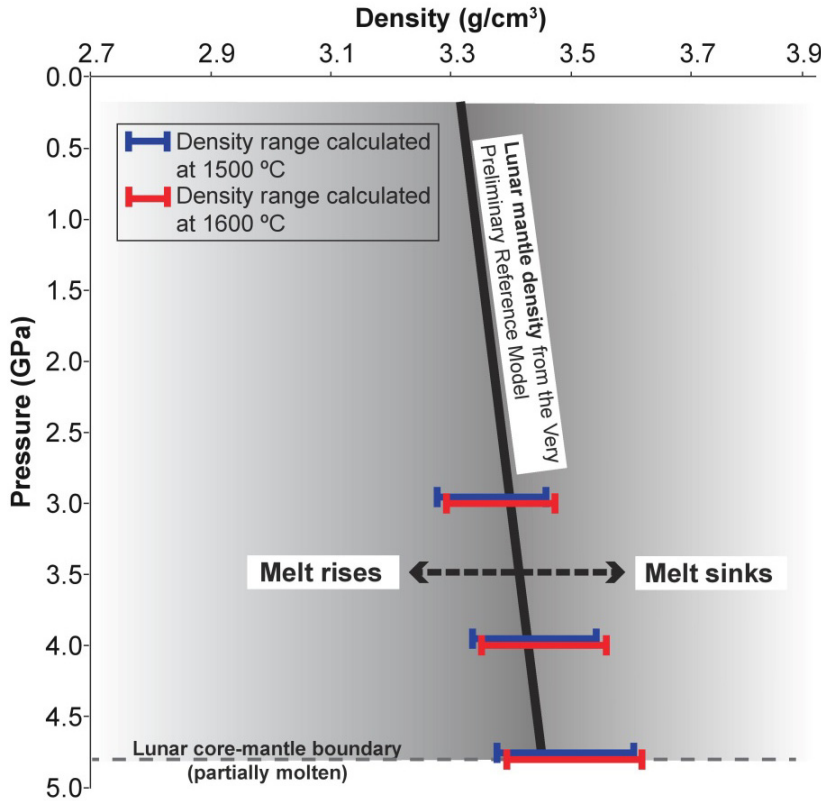


Fig. 3.1-3: Calculated density ranges of Fe-Ti-rich lunar melt using published values of isothermal bulk moduli and their pressure-temperature derivatives from previous studies.

**d.** *Constraints on Lunar structure from combined geochemical, mineralogical, and geophysical modeling (A. Mallik, in collaboration with H. Fuqua/Berkeley, P. Bremner/Gainesville, M.R. Diamond/Berkeley, S.J. Lock/Cambridge, S. Panovska/Potsdam, Y. Nishikawa and H.J. Perez/Paris, A. Shahar/Washington DC, W.R. Panero/Columbus, P.H. Lognonne/Paris and U. Faul/Cambridge)*

The internal structure of the Moon is poorly constrained. In this study, we use a multidisciplinary approach to attempt to constrain key parameters of the lunar structure. We use 1-D lunar compositional models with chemically and mineralogically distinct layers, and

forward calculated physical parameters, in order to constrain the internal structure. We consider both a chemically well-mixed model with uniform bulk composition, and a chemically stratified model that includes a mantle with preserved mineralogical stratigraphy from magma ocean crystallization. Additionally, we use four different lunar temperature profiles that span the range of proposed selenotherms, giving eight separate sets of lunar models. In each set, we employed a grid search and a differential evolution genetic search algorithm to extensively explore model space, where the thickness of individual compositional layers was varied. In total, we forward calculated over one hundred thousand lunar models.

It has been proposed that a dense, partially molten layer exists at the CMB to explain the lack of observed far-side deep moonquakes, the observation of reflected seismic phases from deep moonquakes, and enhanced tidal dissipation. However, subsequent models have proposed that these observables can be explained in other ways. In this study, using a variety of modeling techniques, we find that such a layer may have been formed by overturn of an ilmenite-rich layer, formed after the crystallization of a magma ocean. We therefore include a denser layer (modeled as an ilmenite-rich layer) at both the top and bottom of the lunar mantle in our models.

From our preliminary results, we find models that explain the observed lunar mass and moment of inertia and estimated bulk silicate lunar composition from previous studies. We find that only a narrow range of core radii are consistent with these constraints. Furthermore, in the chemically well-mixed models, we find that a dense layer is required in the upper mantle to meet the moment of inertia requirement. In no set of models is the mass of the lower dense layer well constrained. For the models that fit the observed mass and moment of inertia, we calculated 1-D seismic velocity profiles, most of which compare well with those determined by inverting the Apollo seismic data from previous studies.

*e. The post-spinel transition in the system  $Mg_2SiO_4$ - $Fe_2SiO_4$ : Complete agreement with the 660-km discontinuity depth and the zero-pressure interval explaining the sharp discontinuity (T. Ishii, R. Huang, H. Fei, I. Koemets, Z. Liu, F. Maeda and L. Yuan/Sendai, L. Wang, D. Druzhbin, T. Takafumi/Hiroshima, S. Bhat, R. Farla/Hamburg, T. Kawazoe, N. Tsujino/Misasa, E. Kulik/Hamburg, Y. Higo/Kouto, Y. Tange/Kouto and T. Katsura)*

The 660-km seismic discontinuity (D660) is key to understanding the structure and dynamics of the Earth's mantle. Seismological studies showed that the discontinuity depth corresponds to 23.4 GPa and the thickness is extremely sharp (less than 2 km = 0.1 GPa). It is believed that the post-spinel (Psp) transition, the decomposition of ringwoodite (Rw) to bridgmanite (Brg) + ferropericlae (*f*Pc), is the cause of the D660. These seismological features of D660 therefore have to be explained by the Psp transition. Nevertheless, all *in situ* X-ray diffraction studies with Kawai-type multianvil presses (KMAP) give transition pressures at 1900-2000 K

that are 0.5-2 GPa lower than at the D660. Experimental uncertainty in pressure ( $> 0.2$  GPa) also hampers a definitive conclusion to the transition interval. In this study, we carefully examined the pressure and sharpness of the Psp transition in the system  $\text{Mg}_2\text{SiO}_4\text{-Fe}_2\text{SiO}_4$  using our advanced KMAP techniques.

Energy dispersive X-ray diffraction experiments under high pressure and temperature were conducted using the KMAP, SPEED-*Mk.II*, combined with a cell assembly (Fig. 3.1-4) at the synchrotron radiation facility, SPring-8, in Japan. We took the following special strategies. (1) The starting materials were mixtures of olivine, orthopyroxene and (*f*)Pc with bulk compositions of  $\text{Mg}_2\text{SiO}_4$  ( $\text{Fo}_{100}$ ) and  $(\text{Mg}_{0.7}\text{Fe}_{0.3})_2\text{SiO}_4$  ( $\text{Fo}_{70}$ ), respectively, allowing both normal and reversal transitions. (2) We loaded both samples in the same sample chamber to determine these phase transitions simultaneously (Fig. 3.1-4c). (3) Based on the transition pressure difference between  $\text{Fo}_{100}$  (Rw to Brg + Pc) and  $\text{Fo}_{70}$  (Rw + *f*Pc + stishovite (St) to Brg + *f*Pc + St), we constrained the upper limit of the Psp transition binary loop thickness (Rw + Brg + *f*Pc). (4) Pressure drop during heating was suppressed by increasing press load (forced pumping technique). (5) Sample pressures with a precision of  $\sim 0.05$  GPa were determined using high-count and clean multiple peaks (mainly eight) of a MgO pressure marker obtained by wide opening for the X-ray (Fig. 3.1-4d). (6) The width of the binary loop at  $\text{Fo}_{70}$  was estimated based on available thermodynamic data obtained from the literature's partitioning experiments.

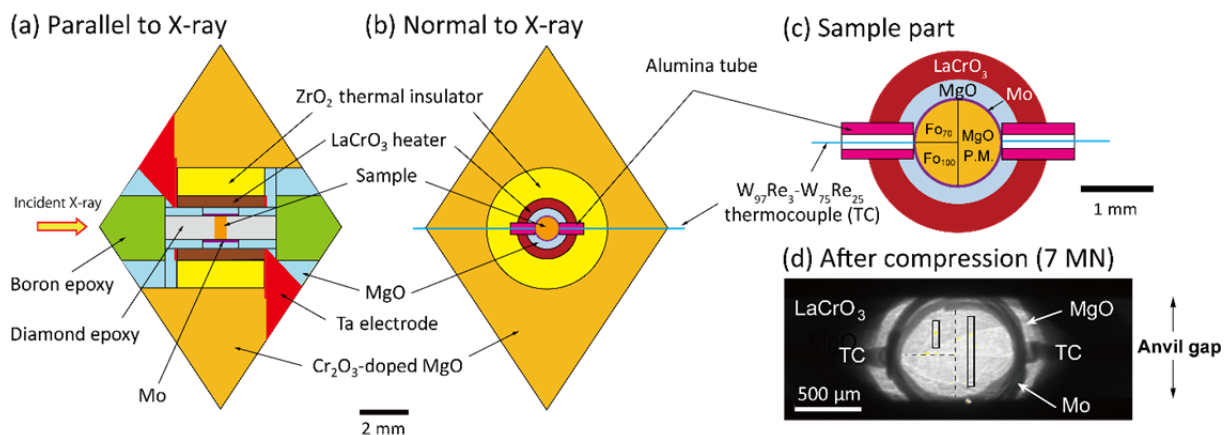


Fig. 3.1-4: (a-c) Cross sections of a cell assembly for *in situ* X-ray diffraction experiments. (d) A radiography image of the sample part after compression. Small and large boxes are typical incident X-ray slit sizes for samples and the MgO pressure marker (P.M.), respectively.

Our findings are as below. (1) The transition pressure in  $\text{Fo}_{100}$  completely agrees with the D660 depth at an expected mantle temperature of 1900-2000 K (Fig. 3.1-5a), indicating that the apparently lower pressures reported by previous studies are probably experimental artefacts due to the pressure drop upon heating. (2) The effect of Fe component on the

transition pressure is almost zero (Fig. 3.1-5b). (3) The hypothetical transition pressure in  $\text{Fe}_2\text{SiO}_4$  is higher than in  $\text{Fo}_{100}$ , contrary to the previous understanding (Fig. 3.1-5b). (4) The pressure difference of 0.14 GPa between  $\text{Fo}_{100}$  and  $\text{Fo}_{70}$  and the Fe/Mg partition coefficients among Brg, Rw and  $f\text{Pc}$  suggest that the pressure interval is almost zero at  $\text{Fo}_{90}$  ( $\sim 0.01$  GPa at 1700 K and even smaller at 2000 K) (Fig. 3.1-5b), explaining the sharp D660. Thus, we conclude that the Psp transition undoubtedly corresponds to the D660.

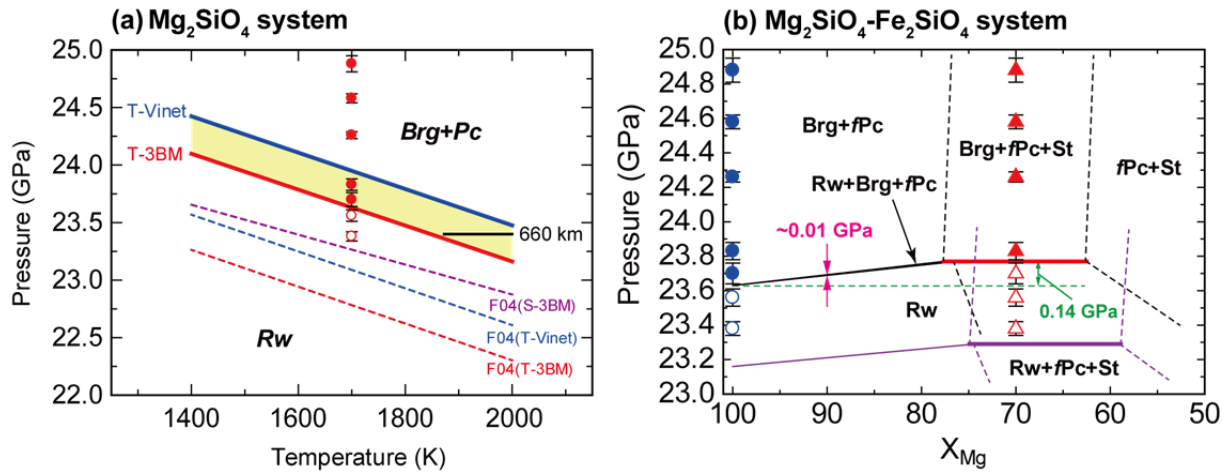


Fig. 3.1-5: (a) Phase boundaries of the Psp transition in  $\text{Mg}_2\text{SiO}_4$ . Plots are the present data determined based on the Tange MgO scale [Tange *et al.* J. Geophys. Res., 114, B3, 2009]. Solid lines (T-3BM and T-Vinet) were drawn based on the Clapeyron slope [Fei *et al.* J. Geophys. Res.109, B2, 2004] recalculated based on the Tange MgO scale. Dashed lines were the phase boundary reported (F04 (S-3BM)) by Fei *et al.* [2004] and those recalculated (F04 (T-3BM and Vinet)) based on the Tange MgO scale. Bold black line is an expected P-T range of D660. (b) Phase diagram in the system  $\text{Mg}_2\text{SiO}_4\text{-Fe}_2\text{SiO}_4$  at 1700 (black). Phase diagram at 2000 K (purple) were drawn with the Clapeyron slope by Fei *et al.* [2004]. Bold red and purple lines were calculated using literature's thermodynamic data.

**f. Numerical modelling of water in Earth's mantle (P. Eichheimer, M. Thielmann, G.J. Golabek)**

The transport and storage of water in the mantle significantly affects several material properties of mantle rocks and thus water plays a key role in a variety of geodynamical processes (tectonics, magmatism etc.). The processes driving transport and circulation of  $\text{H}_2\text{O}$  in subduction zones remain a debated topic. Geological and seismological observations suggest different inflow mechanisms of water *e.g.*, slab bending, thermal cracking and serpentinization, followed by dehydration of the slab. Employing 2D simulations (Fig. 3.1-6) of subduction over time we can estimate the loss of water from the slab into the mantle wedge caused by dehydration processes. Using this first-order approximation we are able to make first-order estimations on how much water can be delivered into the deeper mantle.

Furthermore both shallow and steep subduction can be observed on Earth. Most previous numerical models did not take different dip angles and subduction velocities of slabs into account. To which extent these parameters and processes influence the inflow of water still remains unclear. In the next steps we want to study the effect of those parameters systematically.

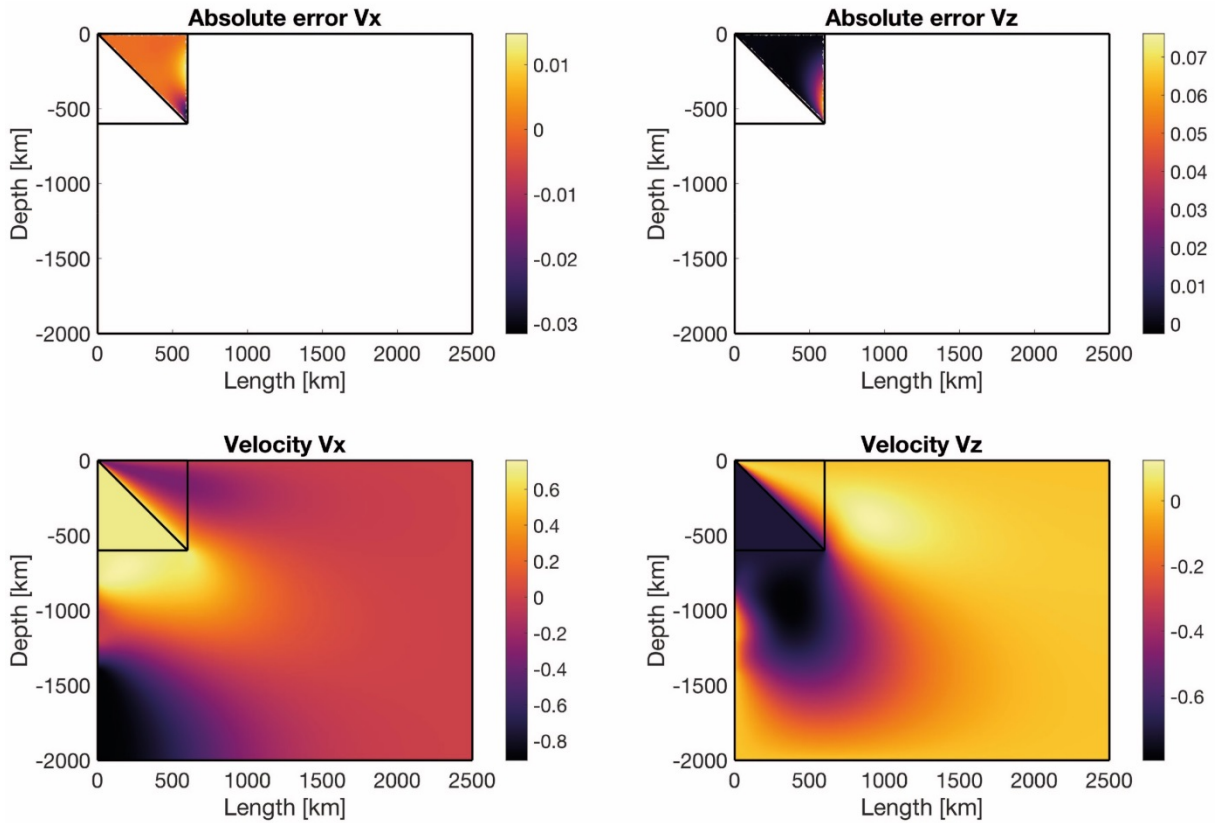


Fig. 3.1-6: (Top panel) Computed errors of the velocities in x and z direction in comparison to the velocities computed using the analytical solution for the cornerflow assuming a fixed plate. (Bottom panel) Velocities in x and z direction within the whole model domain.

**g.** *The effect of an interconnected weak layer network on lower mantle dynamics (M. Urgese, G.J. Golabek, H. Marquardt, M. Thielmann and J. Hernlund/Tokyo)*

The Earth's lower mantle, ranging from 660 km to 2890 km depth, plays a key role for global dynamics. This region of the Earth, which links the hot liquid outer core to the Earth's upper mantle and surface, constitutes more than 50 % of Earth's volume and is the largest geochemical reservoir for most elements. The Earth's lower mantle is dominated by the mineral phases (Mg,Fe)O ferropericlase and (Mg,Fe,Al)(Al,Si)O<sub>3</sub> bridgmanite. Experiments suggest that these two minerals have markedly different rheological properties, with ferropericlase likely being the weaker phase. This implies that two endmember scenarios can describe the rheology of the two-phase mixture: (i) The weak ferropericlase exists as an

isolated phase within the bridgmanite matrix that controls the bulk deformation behaviour and (ii) ferropericlase develops an interconnected weak layer network and dominates the bulk deformation. Theoretical considerations suggest that the effective viscosity between these endmember cases varies by 2-3 orders of magnitude. It has been suggested by recent studies that the mantle regions where rheology is controlled by the stiffer bridgmanite might explain the stagnation of subducting slabs at around 1000 km depth as detected by various seismic tomography studies.

In this project, we quantitatively test the effects of possible crossovers between the two endmember scenarios within Earth's lower mantle. For this purpose we perform global-scale 2D spherical annulus simulations using the state-of-the-art finite volume code StagYY. For this study we implement various strain-weakening approaches (Fig. 3.1-7) to test whether distinct regions characterized by unconnected ferropericlase can persist throughout Earth's long-term evolution.

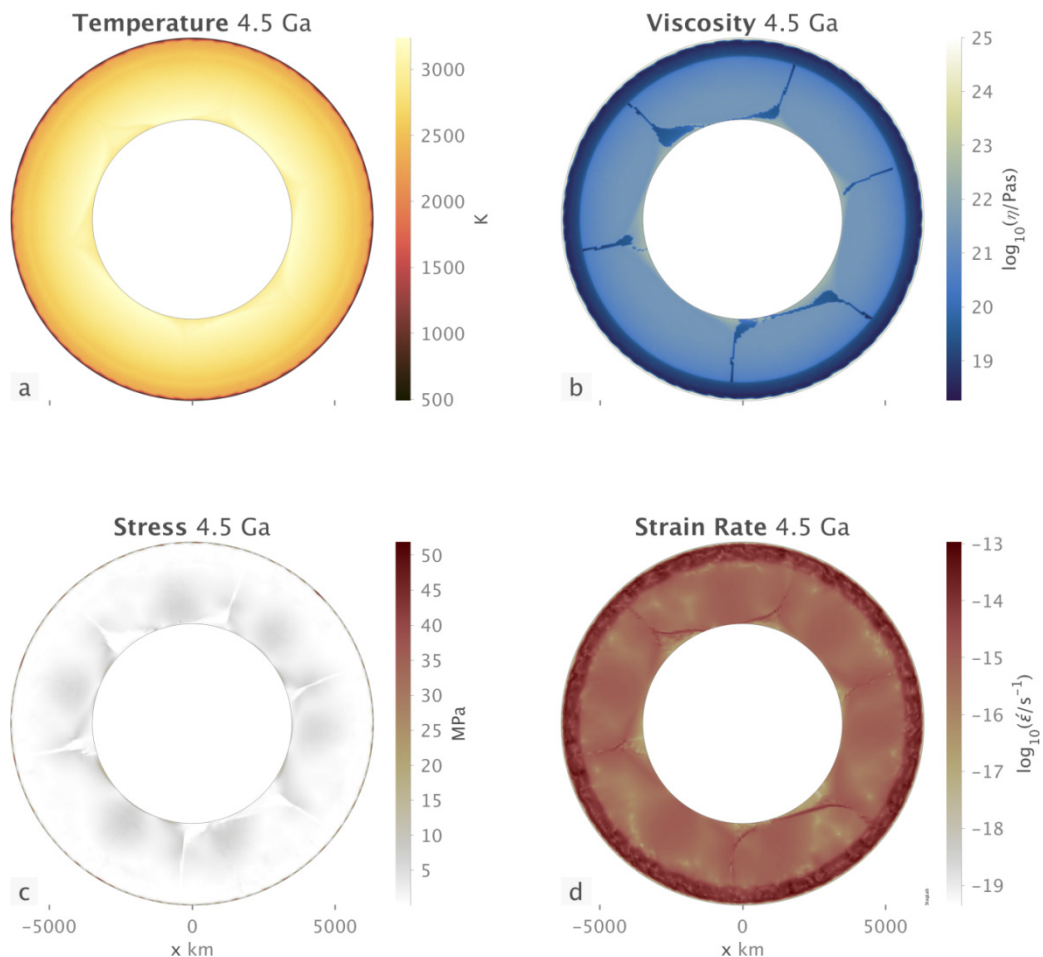


Fig. 3.1-7: Results of a 2D spherical annulus calculation after 4.5 Gyr of evolution assuming a viscosity contrast of 100 between bridgmanite and ferropericlase. The viscosity subplot shows several weak high strain regions separating more viscous weakly deformed blocks that remain stable on the long-term.

**h.** *3D numerical permeability determination (P. Eichheimer, M. Thielmann, G.J. Golabek, in collaboration with W. Fujita, M. Nakamura and S. Okumura/Sendai)*

Fluids are released by mineral dehydration reactions within subduction zones and move upwards due to their positive buoyancy. Therefore permeability is a key factor for fluid migration, thus it is necessary to determine this parameter on the microscale using state-of-the-art methods. For this purpose we use a numerical approach to determine the permeability of rock samples recovered from subduction zones. To calculate the permeability the 3D thermomechanical code LaMEM (Lithospheric and Mantle Evolution Model) developed by Anton Popov and Boris Kaus is used. In several preprocessing steps the given computed tomography (CT) data from literature are converted into a regular three-dimensional cartesian grid. The effective permeability is then computed using the solution of the Stokes equations plugged into Darcy's law. With these technical implementations we are able to obtain permeabilities in three dimensions at high resolutions.

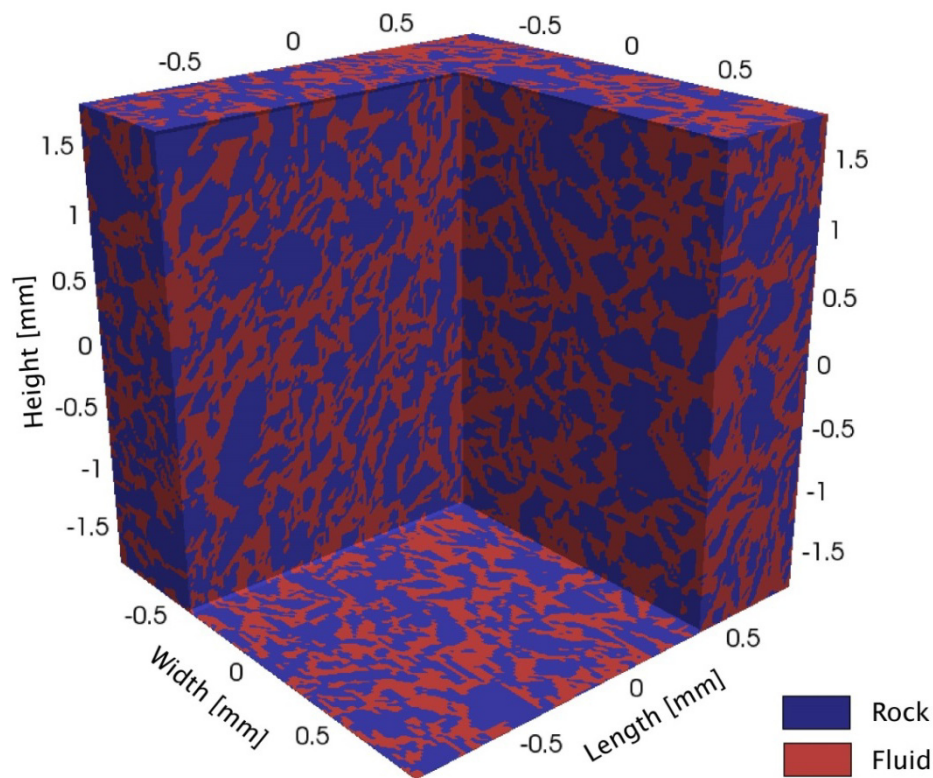


Fig. 3.1-8: Processed granular CT data displaying an interconnected fluid network.

**i.** *Mineral scale modelling of two-phase deformation with application to the lower mantle (M. Thielmann, G.J. Golabek and H. Marquardt)*

Rocks in the lower mantle are not homogeneous, but consist of different mineralogical phases, with the two most abundant phases being bridgmanite and ferropericlase. Recent experiments

have highlighted the importance of ferropericlasite in the deformation of the lower mantle, since linkage of the weak phase might induce a switch from a load-bearing framework (controlled by bridgmanite rheology) to a interconnected weak layer state (controlled by ferropericlasite rheology). As the rheology of both phases at mantle temperatures and pressures is not well known, we use numerical models (Fig. 3.1-9) to systematically study the effect of phase distribution and rheology on effective rheological properties.

The distribution of weak phases is prescribed using random fields, thus making a statistical approach indispensable. The usage of random fields also allows us to prescribe a certain topology of the weak phase and to investigate its effect on bulk properties.

Adding a weak phase has several effects: First, the internal strain rate, stress and pressure fields become strongly heterogeneous, thus resulting in at times unexpected behaviour and localization of deformation. Second, the bulk rock is weakened. The amount of weakening strongly depends on the topology of the weak phase as well as on its rheology. The results obtained in this project can be used to (i) develop upscaling methods that can then be used in large scale simulations and (ii) to help determine the rheologies of bridgmanite and ferropericlasite in laboratory experiments. They also highlight the need of more deformation experiments at high temperatures and pressures to better determine the rheology of the two constituents at these conditions.

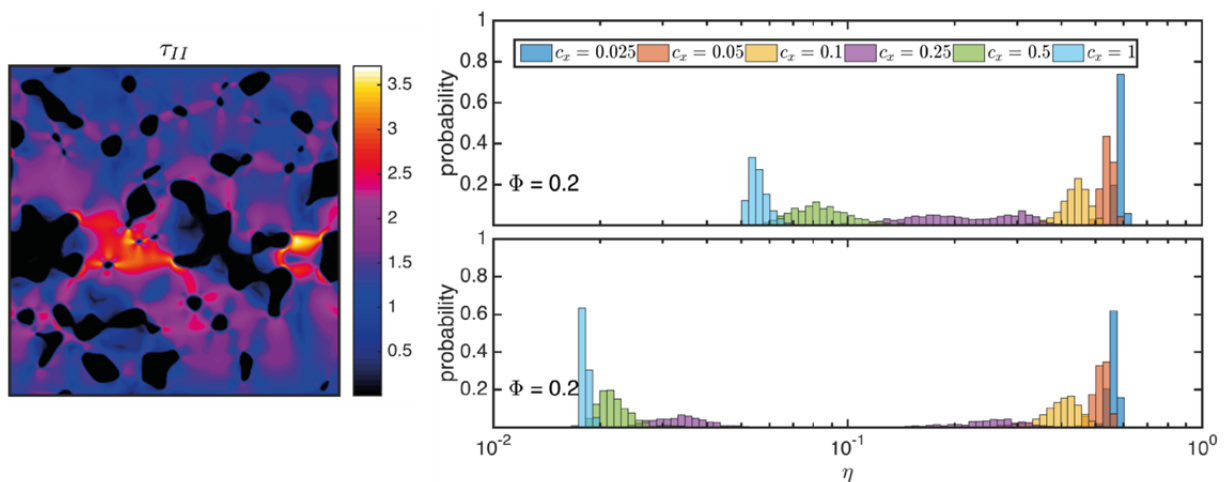


Fig. 3.1-9: (left) Stress distribution in one model with 20 % of a weak phase (100 times weaker than the more abundant phase) Here, both phases have a nonlinear rheology with a stress exponent of  $n = 3$ . (right) Probability distributions for obtaining a certain bulk viscosity depending on the topology of the weak phase. The topology is determined by the correlation length  $c_x$  (see legend), where small values indicate isolated blobs and larger values indicate elongated (and possibly connected) structures in the shear direction.

### 3.2 Geochemistry

The contributions in this section examine the processes that have led to the transport and redistribution of chemical elements within the Earth's crust, mantle and core. Starting with the separation of the Earth's metallic core and continuing through the geochemical cycling that has linked Earth's mantle to the surface, this chapter charts numerous mechanisms that have created compositional diversity within the Earth, which might be considered to culminate in the element enrichments required for the development of economic ore deposits.

The first seven contributions in this section examine the process of core-mantle separation on both the Earth, and also the Moon, with the principal aim of constraining the conditions under which planets form and differentiate. The first uses astrophysical models to simulate planet formation and track the chemical composition of the growing planets. It finds the best fitting model for terrestrial planet formation starts with an initial disc with a gradient in oxidation state that was more reduced near the sun. In the next contribution experimental data on the partitioning of molybdenum and tungsten between silicate mantle and core materials are examined. A physical model for core formation is tested where large collisions towards the end of accretion contribute core material which, due to its size, does not fully equilibrate with the Earth's mantle. Such a model is found to be inconsistent with the much lower levels of these elements in the current mantle, implying either that the model is incorrect or that some further detail in the accretion process has been overlooked. The following contribution tries to further investigate this problem by examining the role of sulphide melts during core formation. Sulphide melt would have inevitably separated from the silicate mantle towards the end of accretion and entered the core. However, the experiments show that this separation would not have influenced the tungsten concentration of the mantle and thus cannot explain the current mantle concentration of this element. The next report examines the consequences of the same late stage separation of sulphide melt for the concentrations of rhenium and osmium in the mantle. The experiments show that there is an increase in the affinity of both elements for sulphide melts with pressure, which leads to model conclusions that support, or at least do not contradict, sulphide separation as a stage of core formation. In the following contribution a set of similar co-called highly siderophile elements, which strongly prefer metals to silicates, are used to examine core formation on the Moon. The concentration of these elements in lunar rocks is much lower than on the Earth, whereas the addition of late material to both bodies should have led to more similar concentrations. This difference is explained by much later separation of a sulphide melt on the Moon, compared to the Earth, which in both cases striped these elements into the core. On Earth, pressure inside the liquid interior would have led to a low solubility of sulphides in the silicate melt leading to a phase of separation that finished before the end of accretion. On the moon the pressure in the interior was lower and sulphide saturation was not reached until the interior magma ocean had almost completely crystallised, concentrating sulphide in the final melt, which only then separated, long after accretion had finished. In the following study laser heated diamond anvil

cell experiments are being used to study the extent to which carbon may have entered the core during accretion. It is quite likely that the core hosts one of the largest reservoirs of carbon on Earth but it is also possible that carbon solubility in metal decreases at high pressures due to the influence of silicon. In the last contribution on the core the rate at which oxygen can dissolve in iron metal has been measured using experiments and first-principles molecular dynamics calculation. The conclusions are relevant to the same model that was examined in the first study of this section, where the role of large impactor cores was examined that remain relatively intact as they plunge and merge with the Earth's core during the later stages of accretion. The results show that if oxygen is a light element in the core, then the cores of large impactors would have had to break up to render particles that were small enough to equilibrate diffusively with the silicate mantle in suitable time scales.

The following four contributions deal with the oxidation state of the Earth's mantle and crust. The first of these examines the oxidation state of a deep silicate magma ocean that would have existed during accretion and core formation. In experiments performed at a constant relative oxygen fugacity the ferric iron content of a silicate melt is found to first decrease and then increase with pressure. This behaviour is explained through a reversal in the volume change of the melt ferrous-ferric iron equilibrium. This means that a deep magma ocean in equilibrium with metallic iron at its base, after the conclusion of core formation, could still have contained a significant proportion of ferric iron, in contrast to the conventional view, which would have assumed it was essentially ferric iron free. In the next study experimental calibrations of the ferric iron contents of garnet minerals as a function of pressure, composition and oxygen fugacity are performed in order to interpret the conditions under which diamonds containing inclusions of such minerals formed. Very little pressure or oxygen fugacity dependence is found, however, particularly for the mineral compositions that are most commonly found in these types of diamonds. In the following study experiments are being performed to enable the oxygen fugacity of refractory mantle rocks to be determined. Cratonic mantle has undergone intense melting in the past and rocks from these regions are enriched in chromium, which becomes concentrated within the rocks during melting. To determine the effects of melting on the redox state requires constraints on the effect of chrome on the equilibria used to measure the oxygen fugacity. In the last contribution on redox processes a new method for determining the oxygen fugacity, *i.e.*, an oxybarometer, has been calibrated based on iron-titanium exchange between magnetite and silicate melt. This oxybarometer, which is given the name FeTiMM, is suitable for use over the entire range of mafic to felsic magmas and has been independently tested using another oxybarometer technique, demonstrating its high accuracy and flexibility.

The next three contributions deal with the formation and preservation of diamonds. The first examines melting phase relations of multicomponent carbonate systems to understand the formation of diamonds in the transition zone. The components of this system were chosen according to the composition of mineral inclusions found in natural diamonds. The study has

been successful in reproducing several distinct suits of minerals found in diamond inclusions. In the next study the rate of diamond dissolution in carbonate melt is measured in the diamond stability field. It is proposed that during the ascent of magmas carrying diamonds from the upper mantle to the surface, diamond grains of 1 mm size would be expected to lose approximately 7 % of their mass to the surrounding melt. The last contribution on diamonds examines their formation in a scenario where carbonate melts might migrate into more reducing regions of the lower mantle, where iron and nickel rich metallic alloys may exist. Diamonds are indeed found to form by reduction of carbonate phases as the metal alloys are oxidised. As a result iron-nickel oxides form and it is probably no coincidence that such oxides are a characteristic inclusion found in deep mantle diamonds.

The next three contributions deal with the consequences of volatile components for mantle geochemistry, the first two of which focus on subduction zone settings. In the first study diamond trap experiments are described that examine the effect of fluid salinity on the partitioning of trace elements between fluids and subducting crustal material. It is found that chlorine greatly enhances the partitioning of many trace elements into the fluid phase, whereas so called high field strength elements such as titanium, niobium and tantalum are comparatively little affected. The characteristic trace element signature of arc magmas can thus be explained by mantle metasomatism by chlorine-bearing fluids and does not require the previously proposed involvement of hydrous melts. The following contribution deals with the fate of ophiicarbonates in subduction zones. These rocks form through the alteration of the oceanic lithosphere by seawater and contain hydrous serpentine minerals and calcium carbonate. Their fate is important for the subduction of carbon into the mantle and previous thermodynamic calculations have raised the possibility that serpentine dehydration may dissolve most of the carbonate from these rocks, thus limiting the deep subduction of carbon. Although this idea has not yet been fully tested early results show that thermodynamic calculations do not faithfully reproduce the experimental assemblages. In the final contribution on volatiles in the mantle experiments are described to determine the composition of small degree hydrous partial melts at transition zone conditions. A number of studies have proposed that slow seismic velocities near the transition zone may be caused by hydrous partial melting. Determining the causal melt compositions is extremely challenging, however, because the most plausible melt fractions are too small to analyse. Instead a series of iteration experiments has to be performed to equilibrate a larger melt pool with the same mineral assemblage expected for very small melt degrees.

The next contribution is the last that deals with the Earth's mantle and describes attempts to calibrate the formation depth of igneous cumulate rocks. Particularly within island arc settings rising magmas differentiate through fractional crystallisation towards the top of the mantle and in the lower crust, leaving behind cumulate rocks. Xenoliths of these rocks are quite rare but vital for understanding how melt compositions from the mantle evolve into the magma suits found at the surface. Here a multiple-reaction approach is being used to determine

pressures of spinel, clinopyroxene, olivine and plagioclase bearing cumulate xenoliths, which is achieved with relatively small uncertainties of approximately 1 kbar.

The last three contributions focus on topics in economic geology. In the first study sulphide and melt inclusions in hornblende-rich xenoliths are investigated from two magmatic systems in the southwestern USA to gain insights into the copper mineralization potential of arc magmas. The results suggest that the formation of hornblende-rich cumulates in the deep crust has a negative influence on the mineralization potential of the residual liquids, but that the cumulates themselves may constitute fertile sources for later partial melting events. In the following contribution experiments in cold-seal pressure vessels demonstrate that quartz-hosted, synthetic fluid inclusions can diffusively gain or lose significant quantities of gold within a matter of only a few days at temperatures of 600-800°C. These results suggest that gold concentrations measured in natural fluid inclusions have to be treated with caution. In the final contribution in this section a detailed melt- and fluid inclusion study is described performed on the economically barren Huangshan granite in China to constrain the factors that control the mineralization potential of granitic magma systems. It is found that the molybdenum contents of fluids and melts were similar to those present in porphyry molybdenum-mineralized magma systems, suggesting that other factors such as a lack of focused fluid flow were responsible for the lack of mineralization in the Huangshan granite.

**a. Mantle composition constraints on different planet formation scenarios (S.A. Jacobson and D.C. Rubie, in collaboration with A. Morbidelli/Nice)**

Terrestrial planet formation has been focused on creating scenarios that match the orbits and masses of the inner planets and the distribution of masses and orbits in the asteroid belt. However, differences between planet formation scenarios also has a consequence for the composition of the final terrestrial planets.

In order to track the mantle compositions of each simulated planet, we follow the process described in Rubie *et al.* (2015) *Icarus* 248: 89. A number of different numerical N-body simulations for each planet formation scenario were chosen based on their ability to match the orbits and masses of the terrestrial planets. Then in each of these simulations, initial compositions were assigned to each of the starting planetesimals and planetary embryos according to heliocentric gradients in the disk. The oxidation gradient is the most significant volatility gradient in the disk and responsible for driving significant changes in the differentiation state of the initial bodies as a function of semi-major axis as well as the final planets. As these bodies grow from accretion of one another, the projectile cores from each collision equilibrate with portions of the target mantle. The fraction of each body participates in equilibration is determined by laboratory and numerical fluid experiments. Furthermore, the equilibrated mantle composition is set by partitioning coefficients determined by high-pressure laboratory experiments.

We experimented with three different planet formation scenarios: the Grand Tack scenario, the eccentric Jupiter and Saturn scenario and the Truncated Disk scenario. In each of these scenarios, we vary the oxidation gradient in the terrestrial disk so as to find a best fit disk that best reproduces the final mantle composition of the Earth-like planet. We measure the quality of the fits using a chi square statistic focused on 11 different species of varying siderophility. Early results indicate that the best fit Earth-like planets require an oxidation gradient in the disk so that the growing Earth-like planet's accretion chemistry transitions from reducing to oxidizing conditions throughout planet formation.

**b.** *Accretionary core formation is insufficient to explain the depletion of Mo and W in the Earth's mantle (E.S. Jennings, D.C. Rubie, S.A. Jacobson, A. Morbidelli/Nice, Y. Nakajima/Washington D.C., A.K. Vogel/Mendig, L.A. Rose-Weston/Thunder Bay, D.J. Frost)*

The metal-silicate liquid-liquid partitioning of Mo and W during core formation must be well constrained in order to understand the evolution of the Earth and other planetary bodies, because the Hf-W isotopic system is used to date early planetary evolution. Previous experimental studies produced varying and inconsistent models, making it difficult to extrapolate the partitioning behaviour of W and Mo to core-segregation conditions. The partition coefficients of W and Mo have variously been suggested to depend on pressure, temperature, silicate and metal compositions, and the high cationic charges of W and Mo in silicate melts make their partition coefficients particularly sensitive to oxygen fugacity.

We combined 48 new high-*PT* experiments with a comprehensive database of previous partitioning experiments to re-examine the systematics of Mo and W partitioning, and produced revised partitioning models from the large combined dataset. Expressed as the equilibrium coefficient (the activity-corrected distribution coefficient):

$$K^{\text{W}} = 0.61(0.28) - 4091(670)/T \quad \text{RMS error} = 0.31$$

$$K^{\text{Mo}} = 1.47(0.44) - 1448(851)/T - 67.1(20.9)P/T \quad \text{RMS error} = 0.28$$

W has a 6+ oxidation state in silicate melts: it is particularly sensitive to silicate and metallic melt compositions, and becomes more siderophile with increasing temperature (Fig. 3.2-1a). Mo has a 4+ oxidation state in silicate melts (Fig. 3.2-1b). Its partitioning is less sensitive to silicate melt composition, but also depends on metallic melt composition.  $D_{\text{Mo}}$  stays approximately equally siderophile with increasing depth in the Earth. Partitioning of W was sensitive to silicate melt composition, in particular the CaO content, and the dataset was thus restricted to ultramafic compositions relevant to magma ocean conditions. In addition, both W and Mo are known to become more siderophile with increasing C content of the iron liquid. We performed new experiments with varying C concentrations and developed an analytical method and standard for C analysis by EPMA, and quantify this behaviour with the interaction parameters  $\varepsilon_{\text{C}}^{\text{Mo}} = -7.0 \pm 0.3$  and  $\varepsilon_{\text{C}}^{\text{W}} = -7.4 \pm 0.6$ .

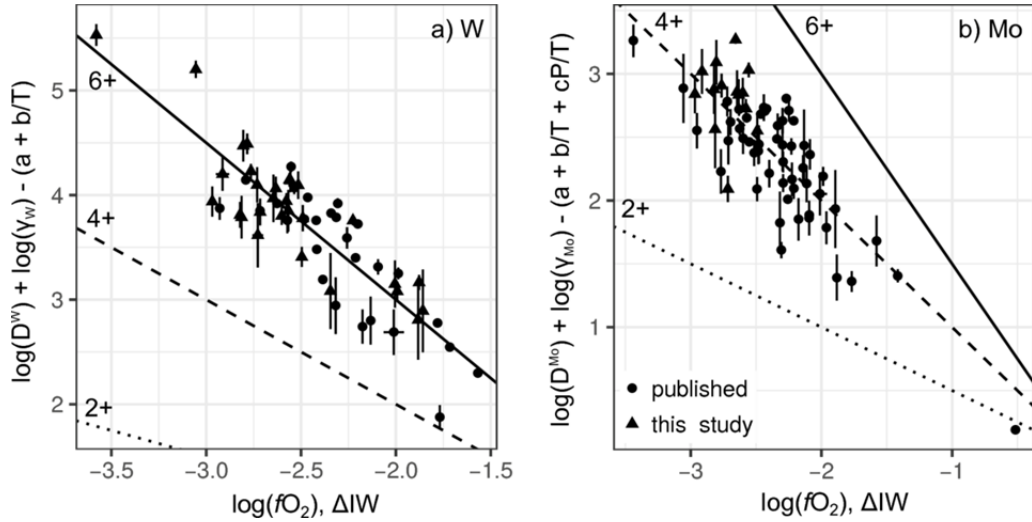


Fig. 3.2-1:  $\log(D)$  adjusted with trace metal activity terms and P and T terms plotted as a function of  $\log(fO_2)$ ,  $\Delta IW$  (see text), for a) W and b) Mo. Data expressed in this way shows the relationship between valence state  $n$ ,  $D$ , and  $fO_2$ , where the slope is equal to  $1/4$  of the valence  $n$ . Lines are theoretical, not fitted. Only carbon-free data are shown.

The revised partition coefficients are incorporated into a combined N-body accretion and differentiation model, which is refined by least squares optimisation to use the Bulk Silicate Earth concentrations to constrain the heterogeneous accretion process. We find that, when all other compositional and physical parameters are Earth-like, the predicted silicate Earth Mo and W concentrations are consistently two and four times overabundant, respectively (Fig. 3.2-2). This is attributed to the incomplete equilibration of late oxidised impactors with the resultant magma ocean and the silicate portion of the Earth. If the model outcome is correct, fractionation processes in late magma ocean(s) must be responsible for ultimately reducing Mo and W concentrations to present-day levels. For example, a high-pressure crystallisation-driven saturation of dispersed metal could strip excess siderophile elements and sequester them to the core, and carbon in those metals would increase the efficiency of this process. This means that the BSE is not a good proxy for the silicate Earth's initial Hf/W, which has implications for the interpretation of  $^{182}\text{Hf}$ - $^{182}\text{W}$  systematics.

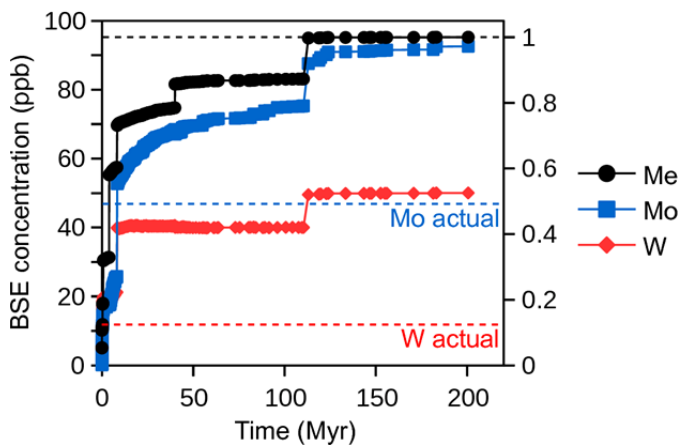


Fig. 3.2-2: The evolution of the mass of the Earth ( $M_e$ ) relative to today's value, BSE Mo and BSE W, as a function of time from the onset of accretion, according to the N-body accretion and differentiation simulation. Present-day values are marked with dashed lines.

*c. Sulfide-silicate partitioning of moderately siderophile elements at high pressure and high temperature (S. Abeykoon, V. Laurenz, D.J. Frost, D.C. Rubie and A.K. Vogel)*

Partition coefficients of siderophile elements between liquid iron and mantle material provide fundamental information on the conditions prevailing during core formation. For example, the abundances of moderately siderophile elements (MSEs) in the Earth's mantle can be reconciled with metal-silicate equilibration at high pressures and temperatures. We have recently proposed, that in addition to Fe-rich metal an immiscible sulfide melt stabilized and segregated to the core during some phases of accretion. Removal of such sulfide liquid to the core would have also had an effect on those MSEs that are also chalcophile, for example Ni or Co. Partitioning of MSEs between the core and mantle depended largely on P-T- $fO_2$  conditions, but also on the composition of the phases involved.

We have experimentally investigated the effect of sulfur on metal-silicate partitioning behaviour of four MSEs (W, Mo, Ni and Co) at constant P and T (2573 K, 11 GPa). The sulfur concentration in the metal was varied by mixing pure Fe metal and pure FeS in different proportions. Also, we conducted a series of experiments at pressures between 7 and 16 GPa and temperatures from 2273 to 2623 K to investigate sulfide-silicate partitioning of W, Mo, Ni and Co. In both series of experiments, a molten peridotitic silicate was equilibrated with liquid metal or sulfide doped with the elements of interest (~ 1 wt. % each) at high P and T. Prior to the experiments, the starting silicate powder was reduced at FMQ-2 for 24 hours in a 1-atm gas-mixing furnace. Single crystal MgO capsules were used for all multianvil experiments. Quenched peridotite, sulfide, metal and ferropericlase phases were analyzed for major element compositions by electron microprobe and for trace element concentrations using LA-ICPMS. We calculated the molar metal-silicate exchange coefficients ( $K_D^{metal-silicate}$ ) using partition coefficients ( $D^{metal-silicate}$ ) of individual elements by normalizing them to  $D_{Fe}^{metal-silicate}$ . The sulfide-silicate exchange coefficients ( $K_D^{sulfide-silicate}$ ) were calculated accordingly.

Our results indicate that at constant  $P$ - $T$  conditions (11 GPa and 2300 °C)  $K_D^{metal-silicate}$  for Ni remains constant with increasing sulfur content of the metal, whereas those of Co, W and Mo decrease. A continuous trend can be observed for Ni and Co up to about 36 wt. % of sulfur ( $X_S \approx 0.5$  - stoichiometric FeS). In contrast, the linear trends of  $K_D^{sulfide-silicate}$  for Mo and W with increasing sulfur concentration only continue until the eutectic composition ( $X_S \approx 0.3$  at 11 GPa). An abrupt decrease in  $K_D$  of both W and Mo is observed for sulfide compositions ( $X_S > 0.3$ , Fig. 3.2-3).

Our experimental sulfide-silicate partitioning results are plotted in Fig. 3.2-4.  $K_D^{sulfide-silicate}$  for Co and Ni are fairly constant with increasing temperature and decrease with increasing pressure. The  $K_D^{sulfide-silicate}$  for both Mo and W decrease with increasing T and only Mo shows a decreasing trend with increasing P (Fig. 3.2-4). Comparing our results with previous studies shows, that  $K_D^{metal-silicate}$  and  $K_D^{sulfide-silicate}$  are comparable for both Ni and Co. In contrast for

W and Mo  $K_D^{sulfide-silicate}$  are orders of magnitude lower than  $K_D^{metal-silicate}$ , and also show the opposite slope with increasing T. These results underline the importance of verifying whether linear trends can be used for the complete range of compositions along the Fe-FeS binary, or if FeS sulfide-silicate partitioning needs to be determined individually. Overall, results confirm that Co, Ni and Mo behave as chalcophile elements under the conditions investigated, while W does not partition into sulfide liquids. Tungsten shows the strongest S-avoidance among the elements studied. Therefore, segregation of a sulfide melt to the core is expected to influence mantle abundances of Ni, Co and to a lesser extent Mo, whereas W will remain largely unaffected during sulfide segregation.

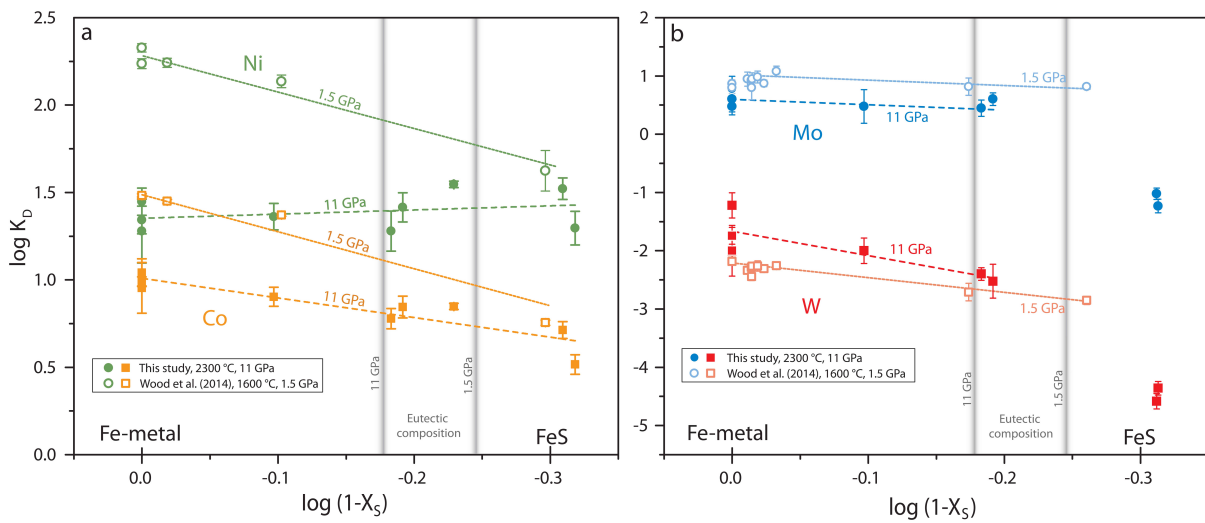


Fig. 3.2-3: The exchange coefficients of a) Ni and Co and b) W and Mo as a function of  $(1-X_S)$ , where  $X_S$  is the mole fraction of sulfur. Eutectic compositions in the Fe-FeS system at 1.5 GPa and 11 GPa are shown as grey vertical lines for comparison.

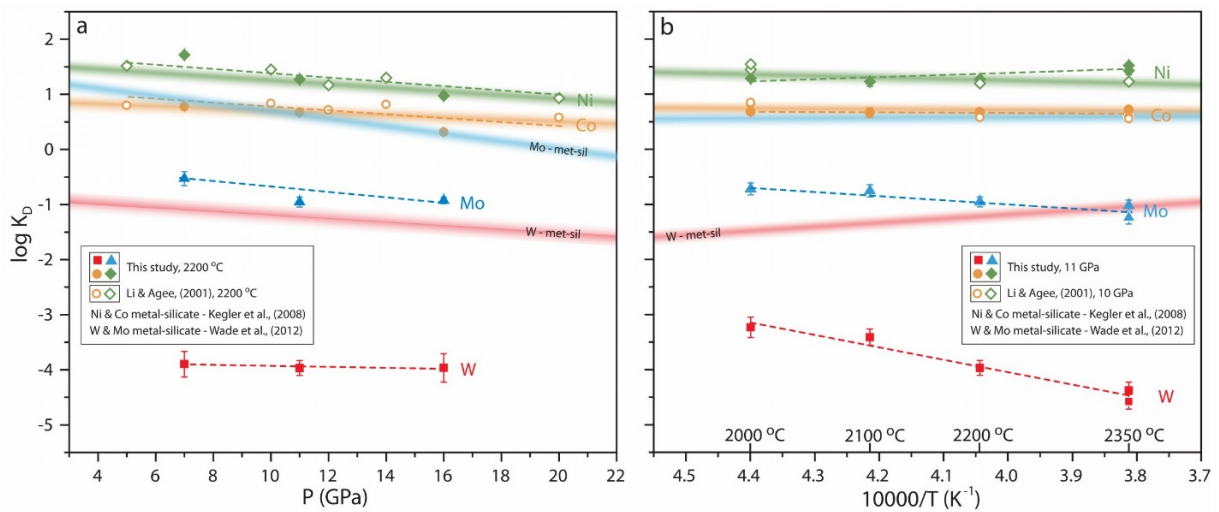


Fig. 3.2-4: The exchange coefficients of Ni, Co, W and Mo between sulfide and silicate as a function of a) pressure and b) inverse temperature.

**d.** *The behaviour of Re and Os during sulfide segregation to the Earth's core (V. Laurenz, D.C. Rubie and D.J. Frost; in collaboration with M. Lagos/Bonn)*

The classical model to explain the near-chondritic proportions of the highly siderophile elements (HSEs - Re, Os, Ir, Ru, Pt, Pd, Rh, Au) in the Earth's mantle involves segregation of Fe-rich metal to form the Earth's core. This process would leave the mantle strongly depleted in HSEs with highly fractionated relative abundances. After core formation ceased, the addition of chondritic material ("Late-Veneer") to the mantle then increased the HSE abundances to their current values, also establishing their chondritic ratios. In detail, the behaviour of the HSEs during core formation will be affected by the presence of light elements. One of the potential light elements in the core is S. Sulfur may not only partition into core-forming metal, but also exsolves as FeS sulfide during magma ocean crystallization and sequesters to the core. Our recent experimental results show that the latter is key to explaining suprachondritic Pd/Ir and Ru/Ir observed for the Earth's mantle.

Two of the HSEs, Re and Os, have not been included in our recent sulfide-segregation model due to the lack of high  $P$ - $T$  sulfide-silicate partitioning data. Their importance, however, stems from the  $\beta^-$ -decay of  $^{187}\text{Re}$  to  $^{187}\text{Os}$  with a half-life of 41.6 Ga.  $^{187}\text{Os}/^{188}\text{Os}$  ratios of the mantle can therefore be utilized as a monitor of its time-integrated Re/Os ratio. The Earth's mantle shows an overall enstatite chondrite-like Os-isotope composition indicating that the Earth's mantle evolved with a long-term chondritic Re/Os ratio. The question arises as to whether our sulfide segregation model is consistent with this overall chondritic Re/Os ratio of the mantle. At low  $P$ - $T$  conditions (1200-1400°C and 1 bar) Os is much more chalcophile than Re. This would lead to a fractionation of Re from Os during sulfide segregation, which is inconsistent with the observed chondritic Re/Os of the mantle. However, Re appears to become more chalcophile with decreasing  $f\text{O}_2$ , indicating that reducing conditions during core formation (IW-2) could promote partitioning of Re into sulfides.

To assess whether sulfide segregation is consistent with the chondritic Re/Os signature of the mantle, we performed three sets of experiments to study 1) the sulfide-silicate partitioning of Re and Os at high pressures and temperatures; 2) the metal-silicate partitioning of Os at high  $P$ - $T$  conditions; 3) the effect of S on the metal-silicate partitioning of Re and Os. All experiments were run in a multianvil-apparatus using single crystal MgO capsules and a synthetic peridotite as the silicate starting composition. In the first set of experiments the peridotite liquid was equilibrated with a FeS sulfide melt doped with Re and Os (~ 10 wt. % each). Temperature and pressure were varied from 2100 to 2400 °C and from 7 to 21 GPa, respectively. For the second set we used the same  $P$ - $T$  conditions as for set 1) and equilibrated the peridotite melt with Fe-rich metal containing up to 10 wt. % Re and 50 wt. % Os. In the third set 3 we equilibrated the peridotite with a range of compositions along the Fe-FeS binary at constant  $P$  (11GPa) and  $T$  (2200°C). Major element compositions of quenched silicate and metal or sulfide melts were determined by electron microprobe, whereas Re and Os concentrations in the silicate were analysed using LA-ICPMS.

Sulfide-silicate exchange coefficients calculated from our experiments reveal that  $K_D^{\text{sulfide-silicate}}$  (Os) is  $\sim 1.5$ -2 orders of magnitude higher than  $K_D^{\text{sulfide-silicate}}$  (Re). Nevertheless, Re and Os are both chalcophile at high pressures and temperatures, and become more chalcophile with increasing pressure and temperature (Fig. 3.2-5). Results from metal-silicate partitioning experiments show that Re and Os become less siderophile with increasing S-concentrations in the metal. This effect is similar to the other HSEs and also the moderately siderophile elements W and Mo.

We used our newly determined metal-silicate and sulfide-silicate exchange coefficients to model the behaviour of Re and Os in a simple core-formation model. Our model includes the segregation of Fe-rich metal to form the Earth's core, followed by the exsolution and segregation of FeS sulfide melt to the core. Finally, 0.5 %  $M_E$  of chondritic material was added during the Late-Veneer. The HSE mantle abundances calculated in our model agree well with their abundances reported in the literature. More importantly, the model also reproduces the chondritic Re/Os ratios. Therefore, sulfide segregation is consistent with the chondritic Os-isotope composition of Earth's mantle and its long-term chondritic Re/Os ratio.

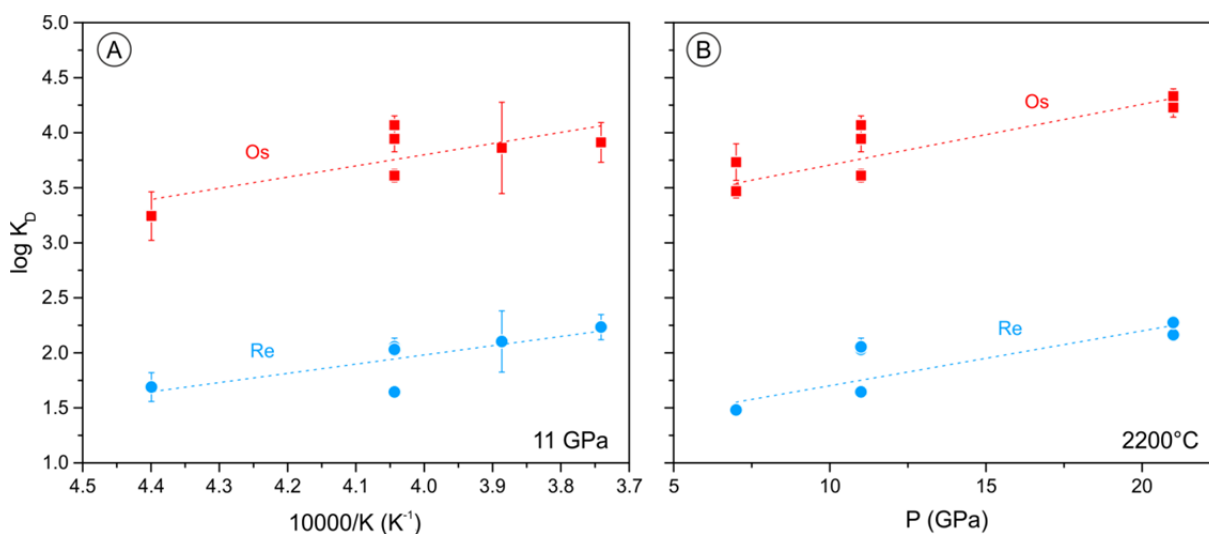


Fig. 3.2-5: Partitioning of Re and Os between FeS sulfide melt and peridotite liquid. Logarithmic values of the exchange coefficient  $K_D^{\text{sulfide-silicate}}$  of Re and Os are plotted as a function of inverse temperature (A) and pressure (B). Generally,  $K_D^{\text{sulfide-silicate}}$  (Os) is about 2 orders of magnitude higher than that of Re.

**e.** *The evolution of highly-siderophile elements in the lunar mantle (D.C. Rubie, V. Laurenz, A. Morbidelli/Nice, M. Wiczorek/Nice and L. Elkins-Tanton/Tempe)*

Compared with concentrations in the chondritic building blocks of the terrestrial planets, the highly siderophile elements (HSEs: Re, Os, Ir, Ru, Pt, Pd and Au) in Earth's mantle are depleted by more than two orders of magnitude but are present in near-chondritic relative

abundances. The concentrations of these elements in the mantle are considered to have resulted from two processes: (1) the almost complete extraction of the HSEs into Earth's core by metal-silicate and sulfide-silicate partitioning, followed by (2) the late accretion of chondritic material after the end of core formation and crystallization of the Earth's final magma ocean. We have shown previously that a key process was the late exsolution and segregation of FeS liquid (the "Hadean Matte") during magma ocean crystallization which transported HSEs to the core because of their strongly chalcophile (sulfide-loving) behaviour. According to this combination of events, the HSE concentrations in Earth's mantle provide a measure of the mass of late accreted material, which is estimated to be on the order of 0.5 % of Earth's total mass ( $\sim 5 \times 10^{-3} M_E$ , where  $M_E$  is Earth's mass).

HSE concentrations in the lunar mantle are extremely low and suggest that late accretion on the Moon added a mass of only  $\sim 2.5 \times 10^{-6} M_E$ . This indicates that the mass of late accreted material on Earth is about 2000 times greater than on the Moon. Conventionally, it is assumed that late accretion started on the Moon immediately following core-mantle differentiation (*i.e.*, shortly after the Moon's formation), in which case this ratio is surprisingly large because the ratio of accretional cross sections (taking gravitational focusing into account) is only  $\sim 20$ . An alternative possibility is that the HSEs were stripped from the lunar mantle by FeS exsolution and segregation much later than the time of core formation such that late accretion started much later on the Moon than on Earth. This could be the case if FeS liquid exsolved during magma ocean crystallisation and removed the HSEs from at least the upper mantle (as suggested for the Earth) provided crystallisation of the lunar magma ocean was slow and occurred very late (as has been proposed in the literature).

The conditions under which FeS liquid exsolves from a magma ocean depends on the *sulfur concentration at sulfide saturation* (SCSS) of the silicate magma. SCSS decreases with increasing pressure and with decreasing temperature. Thus, in Earth's deep magma ocean, the average value decreased to become very low during cooling and crystallization, causing FeS liquid to exsolve and segregate with the HSEs to the core. Because pressures in the lunar magma ocean were much lower than for the Earth, SCSS values were, in contrast, very high. In addition, the compositions of lunar basalts do not indicate sulfide saturation. Thus the situation on the Moon was different from the Earth.

The lunar magma ocean most likely crystallized from the bottom up with the silicate minerals (mainly olivine, pyroxene and plagioclase) that formed during magma ocean crystallization forming a growing cumulative zone at the base of the magma ocean. These minerals accommodate essentially neither sulfur nor HSEs in their structures because these elements are highly incompatible. Thus in the Moon, sulfur and the HSEs became increasingly concentrated in the residual silicate magma that resided above the cumulative zone of crystallization and below the growing anorthositic crust. As magma ocean crystallization approached completion, the FeS concentration inevitably became high in the remaining low fraction of magma and eventually must have exceeded SCSS, even when the latter had a high value (Fig. 3.2-6). When crystallization of the LMO reached completion, all sulfur would

have exsolved as FeS liquid, irrespective of SCSS values, and the entire budget of HSEs would have partitioned into the FeS because of their high sulfide-silicate partition coefficients ( $10^5$ - $10^6$ ). This resulted in FeS and the HSEs being trapped near the top of the lunar mantle, together with oxides such as ilmenite and Fe-rich silicate phases. The presence of the latter phases caused the upper regions of the cumulate zone to have a high density. Large-scale overturn of the lunar mantle is predicted to have occurred as a consequence of the inverted density profile. Such overturn transported FeS and the HSEs at least to the deep mantle and possibly to the core, leaving the upper lunar mantle highly depleted in S and the HSEs. Thus, if magma ocean crystallization was slow on the Moon, taking as long as 100-200 My as has been predicted, the current low HSE concentrations in the lunar mantle reflect the accretion of late veneer that started very late, only after the occurrence of mantle overturn event.

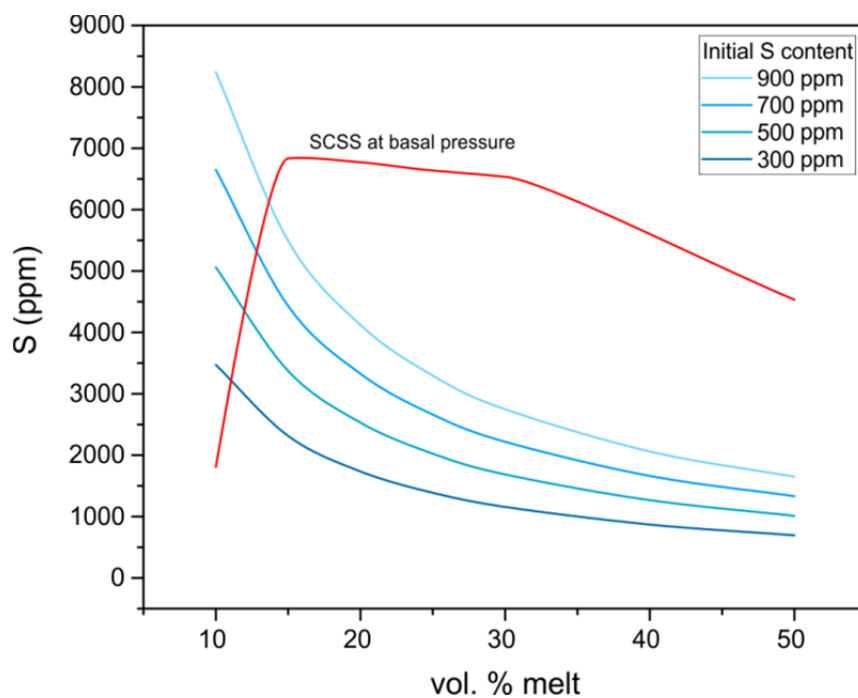


Fig. 3.2-6: Sulfur concentration at sulfide saturation (SCSS) calculated as a function of the residual melt volume during crystallization of the lunar magma ocean (red curve). SCSS is calculated at the base of residual melt layers using a model from the literature; The sharp decrease in its value at < 15-20 % melt is caused by the evolution of melt composition. The blue curves show the concentration of S in the residual melt layer for different bulk S contents of the Moon. FeS exsolution commences where the SCSS curve intersects the appropriate blue curve.

**f. The fate of carbon during the differentiation of the Earth (I. Blanchard, E.S. Jennings, S. Petitgirard and D.C. Rubie)**

The element carbon can be both volatile and siderophile. Thus, understanding its behaviour during Earth's accretion and differentiation is crucial, as it can provide essential insights into

the composition of Earth's early atmosphere, the timing of volatile delivery, and core composition. We want to better constrain the fate of carbon during the formation of the core by conducting high-pressure (P) – high-temperature (T) metal–silicate partitioning experiments to investigate the behaviour of carbon during Earth's differentiation. Experiments are carried out using the laser-heated diamond anvil cell apparatus (LH-DAC) in order to cover a wide range of P-T conditions.

The Earth's core consists mostly of iron, alloyed with ~ 5 % Ni and ~ 10 % light elements (Si, O, S and/or C) in order to explain the density that is inferred from seismology. The nature of this alloy is intimately linked to the conditions that occurred during the formation of the core in terms of P, T, and chemistry. While Si and O have been studied over a wide range of P–T conditions, little is known about the behaviour of carbon during Earth's differentiation, *i.e.*, in a deep magma ocean environment where core forming metal equilibrated and separated. Previous studies in large volume presses highlighted the importance of chemistry (especially  $fO_2$  and S content), but the P–T control has not been investigated above 8 GPa. Thus, there is, as yet, no successful model that can explain the amount of carbon present in the bulk silicate Earth (BSE). The aim of this study is to extend this database to core-mantle differentiation conditions (40-70 GPa and 3000-4500 K). Extending the study of carbon solubility in molten iron to such conditions is fundamental to better constrain the thermodynamics of its partitioning during core formation processes. Knowing the relative contribution of core formation processes in the concentration of carbon on BSE will help to address the amount that has been subsequently added by the late veneer.

The silicate component of the starting material was synthesized using aerodynamic levitation, whereas a piston-cylinder was used to produce a C-rich Fe alloy.  $Fe_3C$  was also synthesized with the piston cylinder to use as a standard for the analysis of C. The LH-DAC experiments were performed by loading two silicate discs of the same composition into the gasket chamber with a smaller disk of metal encapsulated between them such that the silicate material provides thermal insulation during heating. Laser heating was maintained for tens of seconds, which was sufficient to achieve thermodynamic equilibrium given the small sample size and the high temperatures of the experiments. Run products are recovered using a Focused Ion Beam instrument (FIB) to obtain a 3 microns thick sample made of two distinct phases (metal and silicate) that are each < 5-10  $\mu m$  across. The sample is then welded to a TEM grid in order to perform analyses of major elements (see Fig. 3.2-7 for a typical run product). To determine the quantity of carbon that is dissolved in the silicate in each of our runs, nanoSIMS analyses will be performed.

These will be the first measurements of carbon partitioning at conditions relevant to Earth's differentiation. The ratio of carbon concentration in the metal phase to that in the silicate phase is defined as the partition coefficient: we will model how this ratio varies as a function of P and T whilst keeping other variables (*e.g.*, composition) approximately constant. The resultant thermodynamic parameterization of these effects will allow us to interpolate to core-formation conditions, thus allowing us to predict feasible core compositions. Given that

carbon can affect the partitioning behaviour of other siderophile elements, results will be further constrained by a requirement for self-consistency with other siderophile element partitioning, which will be examined through comprehensive accretionary modelling. The obtained partitioning data will be modelled with a thermodynamically-based parameterization, which will ultimately be integrated into sophisticated state of the art accretion/differentiation models of planetary bodies, where the effect of carbon on the distribution of other species and vice-versa will be rigorously accounted for.

Because carbon is both siderophile and volatile, this study will be a milestone in the comprehension of volatile behaviour during the first million years of Earth's formation. The timing of the delivery of volatile elements to the Earth is an important unresolved issue in Earth sciences with the main arguments being either for the addition of volatiles throughout accretion or mainly focused towards the end. Knowledge of the behaviour of carbon during core formation is essential for deciphering between these two scenarios.

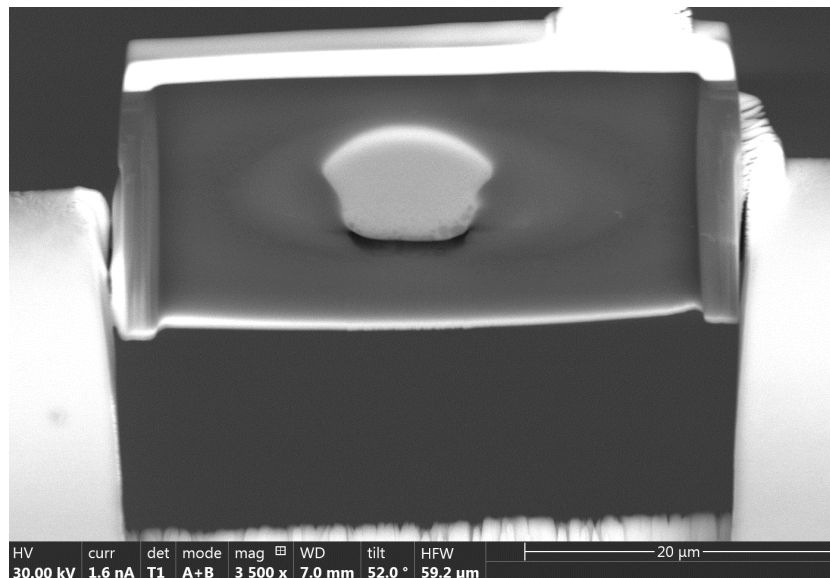


Fig. 3.2-7: Backscattered image of a C-rich sample synthesised at 50 GPa and 3700 K and removed from the laser heated diamond cell gasket using a focused ion beam. The quenched iron metal melt (bright white area just above the centre of the image) has segregated from the surrounding molten silicate.

**g.** *Mass transport and structural properties of oxygen in liquid iron at high pressure: Kinetic implications for metal-silicate chemical equilibration during core formation (E.S. Posner, D.C. Rubie, G. Steinle-Neumann, D.J. Frost and V. Vlček/Los Angeles)*

Oxygen is a potential light element in the Earth's core although its concentration is unknown. The amount of oxygen sequestered into the core during the Earth's accretion and core formation can be estimated by understanding the effects of pressure, temperature, and oxygen fugacity on (i) oxygen solubility in liquid iron and its metal-silicate partition coefficient, in

addition to (ii) transport properties of oxygen in both liquid iron and silicate melt, which dictate the kinetics of metal-silicate chemical equilibration. Pressure-induced structural changes in silicate melt and/or liquid iron alloy have been used to explain changes in the metal-silicate partitioning behaviour of transition metals (*e.g.*, Ni, Co, W), and are also expected to affect light alloying elements. Because transport properties (diffusion, viscosity) are sensitive to structural properties of liquid metals, they can be used as 'indicators' of the liquid structure, which is challenging to measure directly. Therefore, in order to (i) estimate the length and timescales of metal-silicate chemical equilibrium of oxygen in a magma ocean, (ii) investigate potential structural changes in oxygen-bearing liquid iron alloy, and (iii) extend experimental data to conditions of the Earth's outer core, we have performed a combination of high-pressure experiments and first-principles molecular dynamics (FP-MD) simulations. Oxygen diffusion experiments were performed at 3-18 GPa and 1975-2643 K using a multianvil apparatus. FP-MD simulations of liquid  $\text{Fe}_{0.96}\text{O}_{0.04}$  were conducted at 0-330 GPa and 2200-5500 K, and structural properties were investigated by analyzing the partial radial distribution functions (RDFs).

Results obtained from the experiments and calculations are in good agreement and indicate a negligible pressure effect of oxygen diffusion in liquid Fe (activation volume,  $\Delta V \sim 0$ ) up to approximately 18-25 GPa, or a liquid density of  $\sim 8 \text{ g cm}^{-3}$  (Fig. 3.2-8a). In contrast, the pressure dependence of Fe self-diffusion is positive ( $\Delta V > 0$ ) (Fig. 3.2-8a). Structural analysis indicates a change in the dominant compression mechanism operating in liquid  $\text{Fe}_{0.96}\text{O}_{0.04}$  at a density of  $\sim 8 \text{ g cm}^{-3}$ , corresponding to a structural change from body centered cubic (bcc)-like to a combination of bcc-like + face centered cubic (fcc)-like, in agreement with previous experimental studies of liquid Fe (Sanloup *et al.*, 2000) and liquid Fe-3.5 wt. % C (Shibazaki *et al.*, 2015). For densities  $\lesssim 8 \text{ g cm}^{-3}$ , compression is accommodated by a closer packing of both Fe and O with coordination numbers increasing from  $\sim 10$  to  $\sim 13$  and  $\sim 3$  to  $\sim 6$ , respectively (Fig. 3.2-8b). For larger densities, the liquid is essentially close-packed and compression is accommodated by reduction in the atomic volumes of Fe and O, and an increased effect of pressure on the oxygen self-diffusion coefficient is observed. The pressure-induced structural transformation of oxygen-bearing liquid iron alloy provides an explanation for the change in pressure dependence of oxygen solubility in liquid iron previously reported in the literature.

We use oxygen diffusion parameters obtained in this study to constrain the maximum size of descending liquid metal droplets in a magma ocean required for chemical equilibrium between molten silicate and liquid iron alloy (Fig. 3.2-9). Oxygen diffusion in liquid iron is sufficiently rapid such that chemical equilibration in small liquid droplets (radius,  $r \sim 1 \text{ mm}$ ) would require less than 1 min even at very low magma ocean temperatures ( $\sim 2500 \text{ K}$ ), but larger droplets ( $r \gtrsim 20 \text{ cm}$ ) would remain in chemical disequilibrium upon sinking to primordial CMB depths (Fig. 3.2-9). Our results indicate that if the composition of Earth's core is representative of equilibrium chemical exchange with a silicate magma ocean, then it could only have been accomplished by large-scale break-up of impactor cores to liquid metal droplet sizes significantly smaller than a few tens of centimeters. If large metallic bodies remained intact upon impact, then it is not kinetically feasible to achieve chemical

equilibrium during core formation. Further study is underway to investigate the transport behaviour and structural properties of other light elements in liquid iron, including carbon, sulfur, and nitrogen.

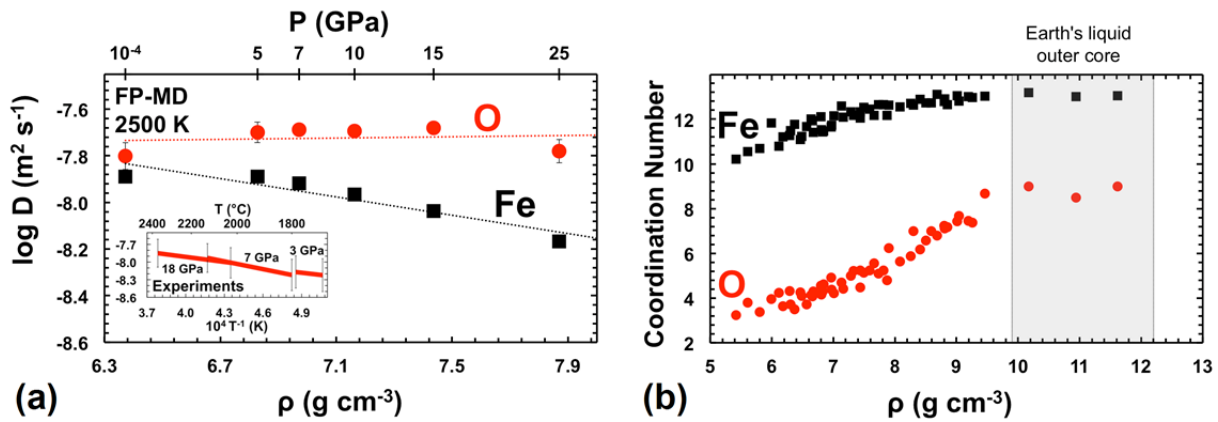


Fig. 3.2-8: (a) Self-diffusion coefficients calculated from FP-MD simulations of liquid  $\text{Fe}_{0.96}\text{O}_{0.04}$  at 2500 K and pressures of approximately 1 bar to 25 GPa. The inset shows Arrhenius curves fitted to experimental oxygen diffusion data. In both experiments and calculations, the effect of  $P$  on the oxygen diffusion coefficient is found to be negligible. In contrast, Fe self-diffusion coefficients decrease monotonically with pressure. (b) Average coordination numbers of Fe and O determined from partial radial distribution functions obtained from FP-MD simulations of liquid  $\text{Fe}_{0.96}\text{O}_{0.04}$  over a wide density range.

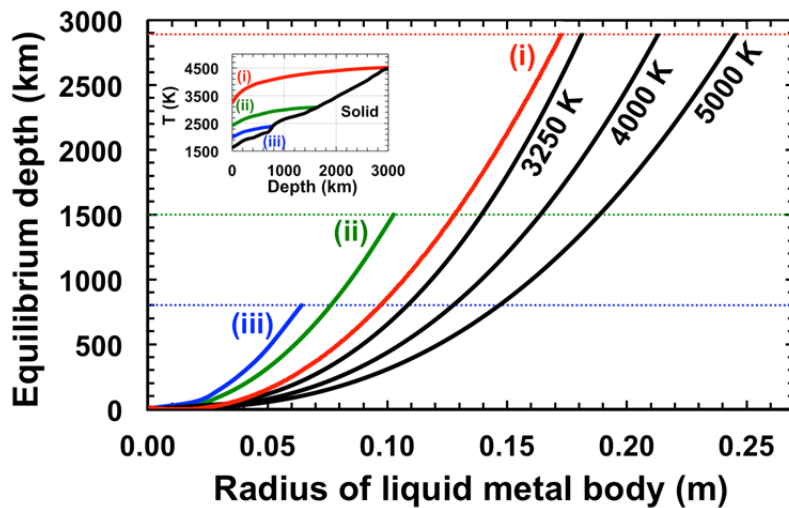


Fig. 3.2-9: Equilibrium depths as a function of liquid metal droplet radius along isentropes for a magma ocean of (i) 2891 km, (ii) 1500 km, and (iii) 800 km depth. Primordial CMB depths are shown as horizontal lines of the corresponding color. Also shown are equilibrium depths for droplets along fixed isotherms (black curves). The maximum droplet radius for chemical equilibrium of oxygen between liquid metal and liquid silicate in a deep magma ocean is therefore constrained to a few tens of centimeters.

**h.** *A model for the effect of pressure on the oxidation state of iron in a deep magma ocean (K. Armstrong, D.J. Frost, D.C. Rubie, C.A. McCammon and T. Boffa Ballaran)*

We have conducted experiments at variable pressures and at a constant relative oxygen fugacity to explore the possibility that pressure stabilises the ferric iron component in silicate melts. Andesite powder, plus approximately 20 wt. % Ru/RuO<sub>2</sub>, was sealed in welded Pt capsules and equilibrated at high pressure and superliquidus temperatures in a multianvil press. Ferric/ferrous iron ratios of the recovered quenched liquids were determined with transmission Mössbauer spectroscopy. Previous studies show that, to 7 GPa, the ferric iron content of such the melts decreases with pressure at the Ru-RuO<sub>2</sub> oxygen buffer. Our results extend the available data to 23 GPa, and show that the melt Fe<sup>3+</sup>/ΣFe ratio reaches a minimum at approximately 10 GPa, but above 17 GPa clearly begins to increase again with pressure.

The Fe<sup>3+</sup>/ΣFe ratio of the silicate melt can be described by the equilibrium, FeO + ¼ O<sub>2</sub> = FeO<sub>1.5</sub>, leading to an oxygen fugacity  $fO_2$  dependence that can be described by,

$$\frac{1}{4} \ln fO_2 = \ln(X_{FeO_{1.5}} / X_{FeO}) + \ln(\gamma_{FeO_{1.5}} / \gamma_{FeO}) + \Delta G^0_{(P,T)} / RT \quad [1]$$

where  $\Delta G^0_{(P,T)}$  is the free energy change of the pure end member equilibrium at the temperature and pressure of interest,  $R$  is the gas constant, and  $X$ s and  $\gamma$ s are, respectively, the mole fractions and activity coefficients of the Fe-oxide components. Pressure affects the  $fO_2$  - Fe<sup>3+</sup>/ΣFe relationship through the volume change ( $\Delta V$ ) of the equilibrium, which is accounted for through:

$$\Delta G^0_{(P,T)} = \Delta G^0_{(P_0,T)} + \int_0^P \Delta V dP \quad [2]$$

Equations for the  $fO_2$  of the Ru-RuO<sub>2</sub> buffer and  $\Delta G^0_{(P_0,T)}$  in addition to activity-composition relations for the iron oxides can be taken from the literature, although it should be noted that current  $fO_2$  equations assumes a constant  $\Delta V$  for the Ru-RuO<sub>2</sub> buffer, which is unrealistic and currently being investigated. The experimental melt Fe<sup>3+</sup>/ΣFe ratios can then be described as a function of pressure by fitting equation of state terms that describe  $\int_0^P \Delta V dP$ . We found the Murnaghan and Birch-Murnaghan equations of state to be insufficiently flexible for this purpose, and we therefore employed the modified Tait equation of state,

$$V / V_0 = 1 - a (1 - (1 + bP)^{-c}) \quad [3]$$

where the terms  $a$ ,  $b$  and  $c$  are functions of  $\kappa_0$ ,  $\kappa_0'$  and  $\kappa_0''$ , the bulk modulus at ambient conditions and the first and second pressure derivatives respectively. Estimates for the room pressure partial molar volumes of FeO<sub>1.5</sub> and FeO as a function of temperature are also available in the literature so that the experimental data could be fit by refining values of  $\kappa_0$  and  $\kappa_0'$  for each iron oxide. Trade-offs allow a range of values of  $\kappa_0'$  of FeO and FeO<sub>1.5</sub> to sufficiently reproduce the shape of the data set (Fig. 3.2-10), but it is clear that  $\kappa_0'$  of FeO must be  $> 4$ , and  $\kappa_0'$  of FeO<sub>1.5</sub> must be  $< 4$ . At this stage the quality of the data does not justify refinement of  $\kappa_0''$ .

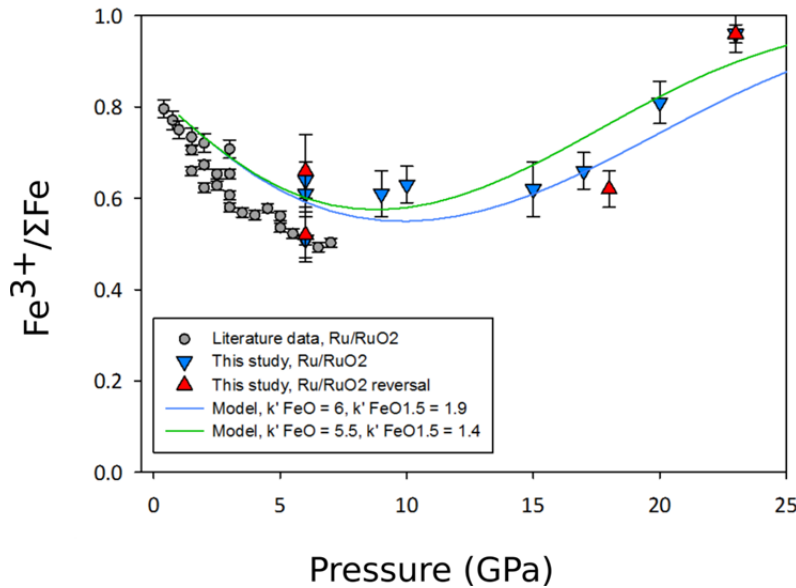


Fig. 3.2-10: Equation of state models for silicate melt iron oxide components using the modified Tait equation are refined by fitting experimental data on the  $\text{Fe}^{3+}/\Sigma\text{Fe}$  ratio of andesitic melt buffered by a Ru-RuO<sub>2</sub> assemblage.

If core-forming metal were to collect at the base of a magma ocean then the ferric iron content of the convecting magma is likely to be constrained by metal-silicate equilibration at these high-pressure and -temperature conditions. At upper mantle pressures, the  $\text{Fe}^{3+}/\Sigma\text{Fe}$  ratio of silicate liquids is near zero in equilibrium with iron metal. Our results indicate, however, that a deep magma ocean extending to lower mantle conditions would contain significant levels of ferric iron due to a reversal in the  $\Delta V$  of the iron oxidation equilibrium. Convective mixing would homogenise the magma ocean, and a gradient of decreasing  $f\text{O}_2$  with depth would result. The melt would be at a much greater oxygen fugacity at the surface, in equilibrium with more oxidised volatile species (H<sub>2</sub>O, CO<sub>2</sub>, etc.), and would degas an oxidised, rather than reduced, atmosphere. Crystallisation of this magma ocean would render a mantle oxygen fugacity gradient similar to that in the Earth today.

**i. Partitioning of ferric iron between majorite and melt under conditions of Earth's transition zone (C. Beyer/Bochum, R. Myhill/Bristol, K. Marquardt and C.A. McCammon)**

Knowledge on the oxidation state of iron in major constituents of the Earth's mantle is crucial for deciphering the capacity of mantle derived rocks to transport oxidized material to greater depths, where it has a strong impact on the partitioning of iron, the stability of mantle phases and the speciation of carbon and other volatile species. Ferric iron resides almost exclusively on the octahedral site "Y" in garnets (with general formula unit X<sub>3</sub>Y<sub>2</sub>Si<sub>3</sub>O<sub>12</sub>), with the garnet  $\text{Fe}^{3+}/\Sigma\text{Fe}$  ratio increasing at a given oxygen fugacities with increasing pressure, leading potentially to autoredox reactions such as:



Ferric iron competes for the "Y" site with several other cations such as Al<sup>3+</sup>, Cr<sup>3+</sup>, Mg<sup>2+</sup>Si<sup>4+</sup> (local charge balance), and Si<sub>2</sub><sup>4+</sup> (charge balanced by Na on the dodecahedral "X" site). Bulk composition may, therefore, have an important influence over the activity of Fe<sup>3+</sup> on the "Y" site.

We have experimentally investigated the effect of bulk composition on redox reactions involving ferric iron in majoritic garnet at pressures between 14 to 20 GPa and temperatures of 1600 and 1800 °C using a multianvil apparatus. Synthetic basalt and peridotite bulk starting materials were enclosed in Fe- and Re-foil capsules, the latter also containing  $\text{ReO}_2$ , to buffer the  $f\text{O}_2$  of the samples.  $\text{Fe}^{3+}/\Sigma\text{Fe}$  in the recovered majorites has been measured using TEM-EELS on individual grains and Mössbauer spectroscopy on the bulk sample. We found that both methods are in very good agreement and can be applied to majorites with total iron as little as 4 wt. %.

For Mg-Si majoritic garnet ( $\text{Mg}_4\text{Si}_4\text{O}_{12}$ ) we found that  $\text{Fe}^{3+}/\Sigma\text{Fe}$  increases with pressure/majorite fraction (Fig. 3.2-11). From Fe-saturated to Re- $\text{ReO}_2$  buffered conditions,  $\text{Fe}^{3+}/\Sigma\text{Fe}$  rises by a factor of 3-4. In contrast, the incorporation of  $\text{Fe}^{3+}$  in eclogitic majorites (Na-majorite) is broadly independent of pressure and imposed  $f\text{O}_2$ . This clearly shows that the substitution mechanism in majorite must be taken into account when modeling iron partitioning and the redox-buffering potential of majorite-bearing lithologies. After some further experiments the ultimate goal will be to develop a model to predict garnet iron speciation at conditions of the Earth's transition zone as a function of composition, pressure, temperature and oxygen fugacity.

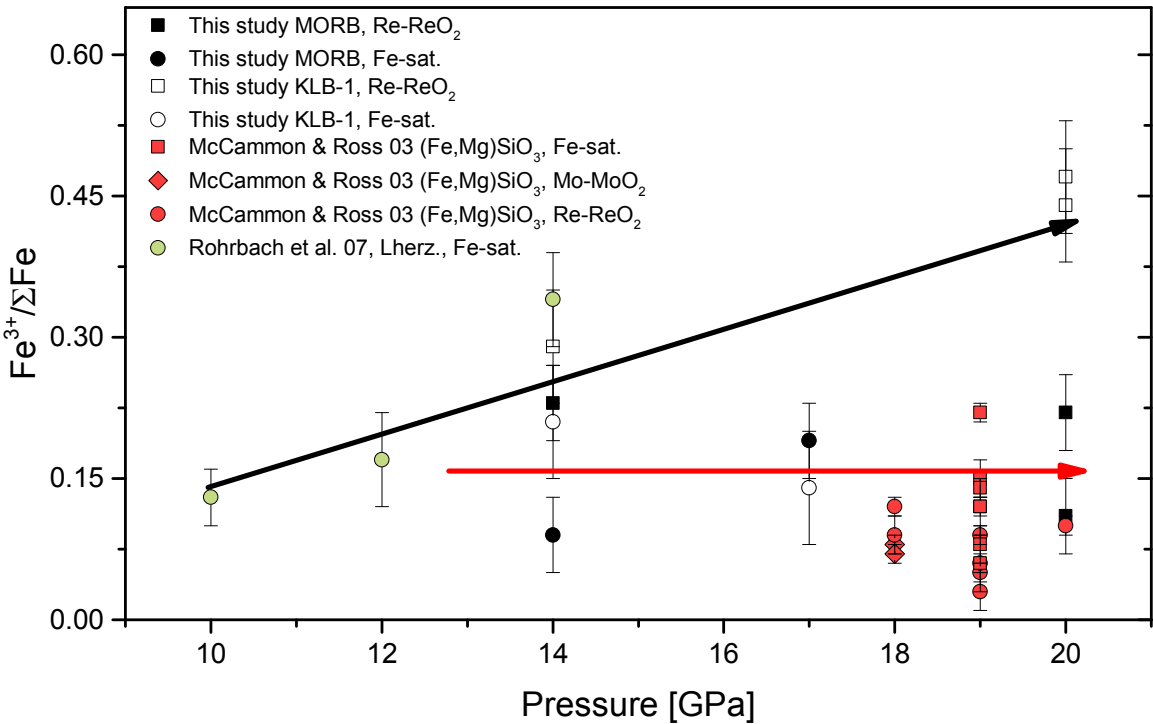


Fig. 3.2-11: Garnet  $\text{Fe}^{3+}/\Sigma\text{Fe}$  ratio as a function of experimental pressure at various oxygen fugacities compared to previous studies. The black arrow indicates the trend for garnets produced in a peridotitic bulk composition at  $\text{Re-ReO}_2$ , whereas, the red arrow indicates the trend for garnets from a basaltic bulk composition over a range of redox conditions. Rohrbach *et al.* (2007, *Nature*, 449, 456-458); McCammon and Ross (2003, *Phys. Chem. Mineral.*, 30, 206-216).

**j.** *The oxidation state of iron in highly refractory peridotites (L. Ziberna, V. Cerantola/Grenoble, G. Bulanova/Bristol, C. Smith/Bristol, L. Faccincani/Padova, C. Melai, C.A. McCammon and D.J. Frost)*

Most of the available information on the Archean history of the Earth's interior is preserved in cratonic mantle xenoliths and inclusion-bearing diamonds hosted in kimberlites. It is well accepted that the cratonic mantle formed by extensive melting during Archean, which left highly refractory residua and was followed by percolation of fluids and melts that metasomatized most of the lithospheric mantle. Evidence of such highly refractory residua come from geochemical signatures in mantle xenoliths and the high proportions of harzburgitic mineral assemblages preserved as inclusions in diamonds. However, due to the paucity of mantle xenoliths representing the pristine highly refractory mantle and the difficulties in performing high-pressure (P) and high-temperature (T) experiments in highly refractory compositions, phase relations, redox state and geochemical process in these mantle domains are still poorly understood. For example, the effects of high degree melting on the redox state of the cratonic lithosphere have been masked by later phases of metasomatism in mantle xenoliths, although these effects may have influenced samples trapped in diamonds to a different extent. To tackle these issues, we have investigated xenoliths and diamond-hosted inclusions from the Murowa kimberlite, Zimbabwe Craton, which are rare examples of highly refractory mantle fragments. The project involves both a Mössbauer study aimed at quantifying the oxidation state of Fe in the xenoliths and diamond inclusions, and high-P and high-T experiments to investigate phase relations and ferric-ferrous iron partitioning in highly refractory peridotitic assemblages.

The mantle xenoliths are dunites and harzburgites with textures from coarse granular to porphyroclastic. Orthopyroxene modes are usually < 10 %, clinopyroxene is either absent or < 2 % and the aluminous phase is almost exclusively Cr-spinel. Diamonds are mostly octahedral in shape and have been polished down to expose some of the inclusions. These inclusions are mostly Cr-spinel, with some minor garnet and orthopyroxene. Olivines and orthopyroxenes in xenoliths and diamonds have similar mg# [ $\text{Mg}/(\text{Mg}+\text{Fe}^{2+})$ ], in the range 0.90-0.95.  $\text{Cr}_2\text{O}_3$  in spinel covers a range of 20-65 wt. % in the xenolith samples and 61-66 wt. % in the diamond-hosted inclusions.  $^{57}\text{Fe}$  Mössbauer analyses of Cr-spinel, garnet, clinopyroxene and orthopyroxene, have been performed using the synchrotron Mössbauer source (SMS) available at the Nuclear Resonance beamline ID18, ESRF, Grenoble. For the xenoliths, 100-150  $\mu\text{m}$ -thick sections were cut and glued with crystalbond<sup>TM</sup> resin on glass slides with  $\varnothing$  1 mm holes drilled in the center, which corresponded with the analyzed area.

Mössbauer spectra for Cr-spinel, ortho- and clinopyroxene were fitted using the program MossA with the full transmission integral and a Lorentzian-squared source line shape. Preliminary fitting results were obtained using Lorentzian shape doublets, one for  $\text{Fe}^{2+}$  and one for  $\text{Fe}^{3+}$ . Values of  $\text{Fe}^{3+}/\Sigma\text{Fe}$  were calculated based on relative area ratios of the doublets. Estimated uncertainties in  $\text{Fe}^{3+}/\Sigma\text{Fe}$  vary between 0.02 and 0.04 ( $2\sigma$ ).  $\text{Fe}^{3+}/\Sigma\text{Fe}$  in Cr-spinels in mantle xenoliths vary in the range 0.04-0.09, while in diamonds the range is 0.09-0.14. Orthopyroxenes in both xenoliths and diamond inclusions show no resolvable  $\text{Fe}^{3+}$

components, suggesting  $\text{Fe}^{3+}/\Sigma\text{Fe} < 0.03$ .  $\text{Fe}^{3+}/\Sigma\text{Fe}$  is low also in clinopyroxenes (occurring only in mantle xenoliths), ranging between 0.05 and 0.07.

The first set of high-P and high-T experiments have been performed using a 500 tonne multianvil press. A starting material resembling the composition of a harzburgitic xenolith from the Murowa kimberlite was prepared and reduced in a 1-atm furnace, at 1200 °C, and oxygen fugacity ( $f\text{O}_2$ ) of 2 log units below the quartz-fayalite-magnetite oxygen buffer. Approximately 5 wt. % Ir powder was then added to act as a redox sensor. A double capsule arrangement was employed with an inner Pt capsule containing the harzburgitic compositions included in a graphite sleeve and an outer capsule containing the inner Pt capsule and a mixture of graphite and  $\text{Mg}(\text{OH})_2$  to act as a fluid redox buffer. Experiments were performed at 5 GPa and 1200-1300 °C for 24 h. These first experiments successfully produced an assemblage of olivine + orthopyroxene + garnet + Cr-spinel in the inner capsule (Fig. 3.2-12). The outer capsule consists of periclase coexisting with a fluid and a quench crystal assemblage. Further multianvil experiments at different P and T conditions and electron microprobe and  $^{57}\text{Fe}$  Mössbauer analyses of the existing and future experimental products will be performed. The obtained data will be used in combination with the petrological information obtained on the xenoliths and diamond inclusions from the Murowa kimberlite to allow the redox processes affecting this cratonic mantle section to be assessed both during initial high degree melting and subsequent metasomatism. Using these results models for craton and diamond formation will be tested.

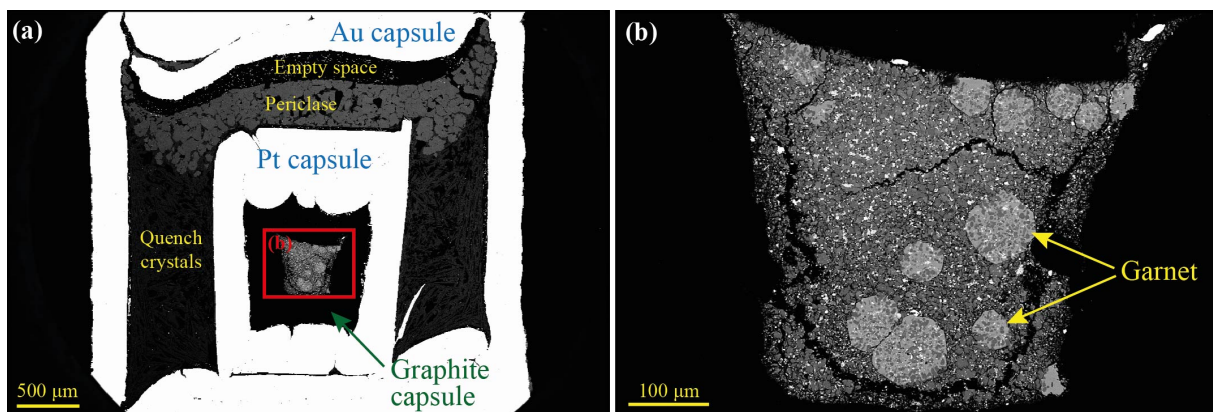


Fig. 3.2-12: Back-scattered electron images of a run product showing (a) the double capsule setup and (b) a close-up of the inner capsule. Phases identified in the inner capsule are olivine, orthopyroxene, Mg-chromite and inclusion-rich garnet.

**k. *FeTiMM* – A new oxybarometer for mafic to felsic magmas (R. Arató and A. Audétat)**

Oxygen fugacity is an important thermodynamic parameter in magmatic systems because it exerts a first order control on phase equilibria as well as on mineral–melt and fluid–melt partition coefficients. The most commonly used and most reliable way to reconstruct magmatic  $f\text{O}_2$  is via magnetite–ilmenite oxybarometry. However, reconstruction of magmatic

$fO_2$  in igneous rocks remains difficult, particularly in the case of intrusives, because during slow cooling Fe-Ti-oxide minerals usually get either reset or altered. Furthermore, many magmas do not contain ilmenite, precluding the application of magnetite–ilmenite oxybarometry.

The aim of this study was to develop an oxybarometer that is based on element partitioning between magnetite and silicate melt, such that it can be applied to samples in which these phases occur as inclusions within phenocrysts and thus were protected from re-equilibration and alteration during slow cooling. Magnetite solubility in silicic melts has been shown previously to depend on  $fO_2$ , however, it also depends strongly on temperature (T) and melt composition. We noticed that the effect of melt composition on magnetite solubility is similar to that on  $TiO_2$  solubility, with the latter being independent of  $fO_2$ . Hence, the effect of melt composition can be diminished by dividing the mgt–melt partition coefficient of Fe ( $D_{Fe}^{mgt/melt}$ ) by that of Ti ( $D_{Ti}^{mgt/melt}$ ). We tested this idea first on a set of 50 of own (ilmenite-undersaturated) experiments conducted in the system magnetite–H<sub>2</sub>O–rhyolite melt, then extended the calibration dataset with a series of (ilmenite-saturated) experimental literature data. The whole dataset comprises experiments run at 750-1100 °C, 0.1-700 MPa, oxygen fugacities of -1.3 to +5.5 log units relative to the fayalite-magnetite-quartz buffer ( $\Delta FMQ$ -1.3 to  $\Delta FMQ$ +5.5), with melt compositions of 48-79 wt. % SiO<sub>2</sub> and ASI = 0.3-1.3, and magnetite compositions of 0.01-28 wt. % TiO<sub>2</sub>. Based on the extended dataset of 109 experiments we developed a model (which we hereinafter call FeTiMM) that allows  $fO_2$  to be calculated as a function of  $D_{Fe-Ti}^{mgt/melt}$  (with FeO<sub>tot</sub> and TiO<sub>2</sub> measured in weight percent, and the melt composition reported dry) and the melt compositional parameter  $AMCNK = \text{molar } Al_2O_3 / (CaO + Na_2O + K_2O + MgO)$ :

$$\Delta FMQ = (\log(D_{FeO_{tot}}^{mgt/melt} / D_{TiO_2}^{mgt/melt}) + 0.137 * AMCNK + 0.102) / (0.288 * AMCNK + 0.054)$$

The overall uncertainty of the FeTiMM model, calculated from the errors of the fits increases from  $\pm 0.2$ - $0.3$  log units  $fO_2$  at  $\leq \Delta FMQ + 1.5$ , to  $\pm 0.3$ - $0.5$  log units  $fO_2$  at  $\Delta FMQ + 4.5$ . The performance of FeTiMM on the 59 ilmenite-saturated experiments is shown in Fig. 3.2-13. For this test, we relied on  $fO_2$  values calculated *via* magnetite–ilmenite oxybarometry (Ghiorso & Evans, Am. J. Sci. 308, 957, 2008). The uncertainty of the latter model was not explicitly stated, but it can be estimated at *ca.*  $\pm 0.3$ - $0.5$  log units, *i.e.*, similar to the uncertainty associated with our model. Within these errors, 63 out of the 109 experiments show perfect agreement between the two methods, and all but five experiments return  $fO_2$  values that agree within  $\leq 0.5$  log units. No correlations are evident between the degree of correspondence and  $fO_2$ , temperature, melt SiO<sub>2</sub> content, ASI, or magnetite composition, suggesting that FeTiMM works equally well over the entire range of the investigated P-T-X conditions. The results of a first application of FeTiMM to 19 natural samples of rhyolitic to dacitic composition are also promising. All samples are ilmenite-saturated, such that  $fO_2$  could be independently constrained *via* magnetite–ilmenite oxybarometry. In all but one

sample, FeTiMM returned  $f_{O_2}$  values that agree within 0.5 log units with those obtained *via* magnetite–ilmenite oxybarometry. One of the main advantages of FeTiMM is that it can be applied to magmas that do not contain ilmenite, which is true for many igneous rocks of mafic to felsic composition, particularly for alkali-rich ones. Another major advantage of the method is that it can be applied to slowly-cooled and/or altered rocks if magnetite and silicate melt are present as inclusions within phenocrysts (preferably quartz) and are analyzed as entities by LA-ICP-MS, thereby effectively reversing compositional heterogeneities that developed within the inclusions during slow cooling.

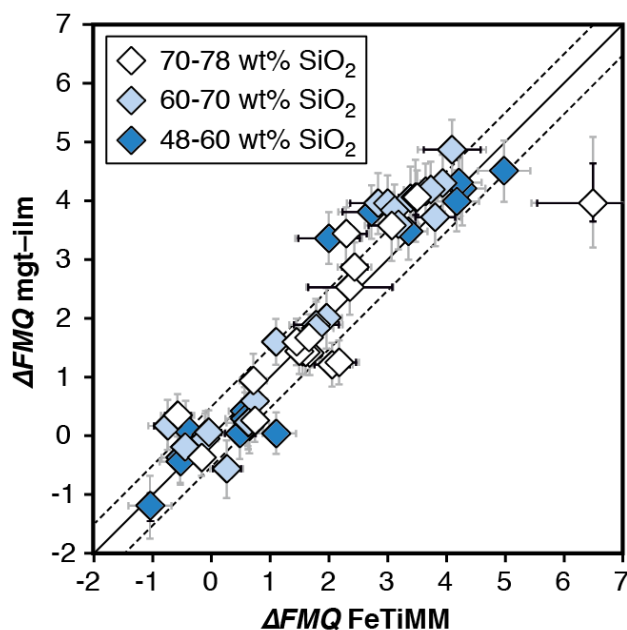


Fig. 3.2-13: Performance of FeTiMM in ilmenite-saturated magmas. Oxygen fugacities (expressed in log units relative to the FMQ buffer) obtained *via* FeTiMM are compared with ones obtained *via* magnetite–ilmenite oxybarometry using the model of (Ghiorso & Evans, Am. J. Sci. 308, 957, 2008). Black error bars (in most cases smaller than symbol size) denote the analytical error, whereas the grey error bars denote the overall error that includes both the analytical scatter and the error inherent to the model.

**I. Diamond formation in the Earth's transition zone investigated by melting relations in the system  $MgO-FeO-SiO_2-(Na,Ca,K-CO_3)$  (A. Spivak, Y. Litvin and E. Zakharchenko/Chernogolovka; D. Simonova and L.S. Dubrovinsky)**

Mineral inclusions in natural diamonds that formed at depths corresponding to the transition zone comprise mostly wadsleyite and ringwoodite (polymorphs of olivine composition  $(Mg,Fe)_2SiO_4$ ), majorite garnet, magnesiowustite  $(Fe,Mg)O$ , stishovite  $SiO_2$ , and Na, Mg, Fe, Ca, K-carbonates. Therefore, melting phase relations in the system  $MgO-FeO-SiO_2 - (Na,Mg,Fe,Ca,K)CO_3$  are essential to understand the genesis of diamonds and associated minerals in the transition zone.

Experimental studies of the melting relations in this system were carried out at 20 GPa, *i.e.*, within the stability field of ringwoodite (18-24 GPa at depths of 520-660 km), in a large volume press. For the carbonate component we used either Na<sub>2</sub>CO<sub>3</sub> alone or a Na<sub>2</sub>CO<sub>3</sub>-CaCO<sub>3</sub>-K<sub>2</sub>CO<sub>3</sub> mixture. It was found that Mg-Fe solid solutions of ringwoodite (Mg,Fe)<sub>2</sub>SiO<sub>4</sub> become unstable with increasing iron content of the melts. As a result of reaction with melts, ringwoodite disproportionates to stishovite and wustite. This is a sign of the invariant peritectic reaction ringwoodite + melt = magnesiowustite + stishovite. As a result of this reaction, ringwoodite disappears, and a univariant association of magnesiowustite + stishovite + melt is formed. With decreasing temperature two stishovite-containing subsolidus assemblages formed: (1) ringwoodite (Mg,Fe)<sub>2</sub>SiO<sub>4</sub> + stishovite SiO<sub>2</sub> + ferropericlasemagnesiowustite solid solutions phases (Mg,Fe)O ↔ (Fe,Mg)O, and (2) magnesiowustite (Fe,Mg)O + stishovite SiO<sub>2</sub> (Fig. 3.2-14).

According to our preliminary data, partial reaction of the Ca-carbonate with the silicate components of the investigated system led to the formation of CaSiO<sub>3</sub> perovskite. In general, these experimental results are consistent with the nature of primary mineral inclusions present in diamonds that formed at transition zone depths. The appearance of stishovite is symptomatic for our experimental diamond-forming system. This fact, combined with the presence of stishovite inclusions in natural diamonds, suggest that the diamond-forming melts of the transition zone experience an evolution from ultrabasic ringwoodite-containing rocks to basic stishovite-containing rocks.

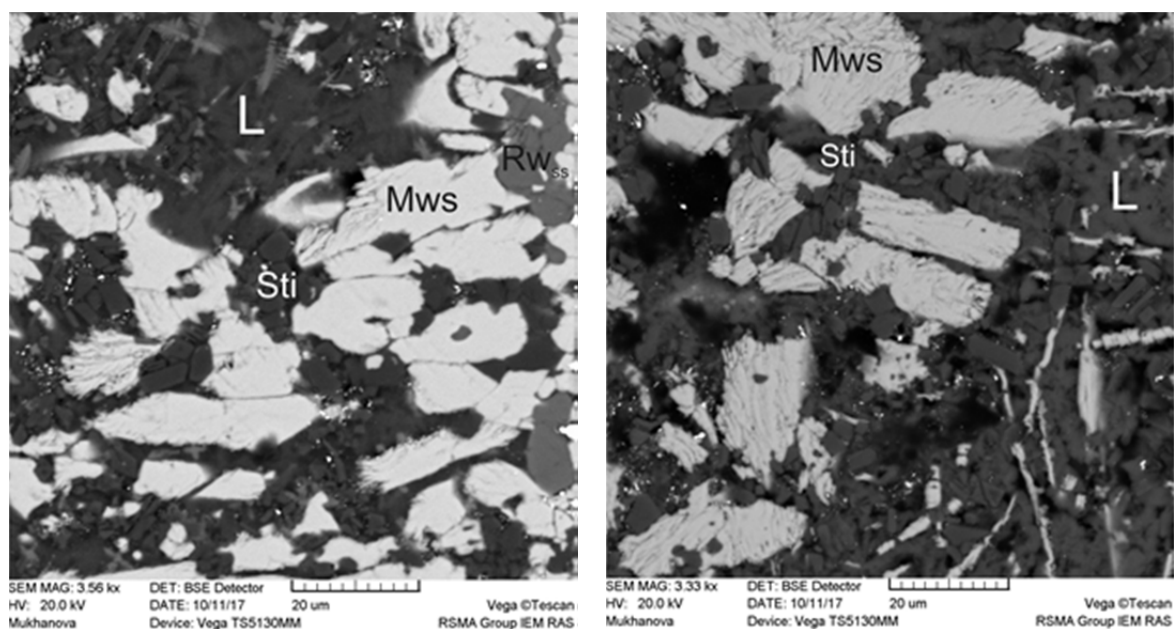


Fig. 3.2-14: SEM images of experimental samples, indicating a peritectic decomposition of ringwoodite with the formation of magnesiowustite and stishovite in the diamond-forming system of the transitional zone of the Earth's mantle: (left) smp. # S6875b 20 GPa, 1400 °C, (right) smp. # S6875a 20 GPa, 1400 °C.

**m. Solubility of thermodynamically stable diamond in  $MgCO_3$ – $FeCO_3$ – $Na_2CO_3$  carbonate melts at 6 GPa (A. Spivak and Y. Litvin/Chernogolovka; G. Khachtryan/Moscow, I. Chuvashova, D. Simonova, N.A. Dubrovinskaia/Bayreuth and L.S. Dubrovinsky)**

The diamond content of kimberlite bodies depends in part on the amount of diamonds formed in the parental silicate-carbonate-carbon melts at depths of 150-250 km, and in part on their survival during the transport to shallow levels. Diamonds lose part of their mass via dissolution into the transporting carbonate-containing kimberlite melts during the short ascent time and the solidification of the melts within the continental crust. The interaction of transporting kimberlite melts and diamonds is indicated by shape and crystal face changes due to natural dissolution. The scale of the loss of diamond mass during dissolution can be determined experimentally.

An experimental study of diamond solubility was carried out in the multicomponent carbonate system  $MgCO_3$  (30 wt. %) –  $FeCO_3$  (35 wt. %) –  $Na_2CO_3$  (35 wt. %) at 6 GPa and 1400 °C with durations of 1, 2, 3 and 4 hours using the large-volume toroidal anvil press MavoPress LPRU 1200 -555/50.

In the 3 hour experiment (approximate time of kimberlite magma ascent from the upper mantle to the surface), the diamond crystals lost 6-7.5 wt. % of their mass by dissolution into the surrounding carbonate melt (Fig. 3.2-15). After quenching, the bulk material is composed of dendritic carbonate microphases. The diamond faces are entirely covered with a thin, black graphite film, which seems to have formed during quenching after partial dissolution of the diamond. Thus, the experimental results reveal the processes of dissolution of thermodynamically stable diamonds by a carbonate melt.

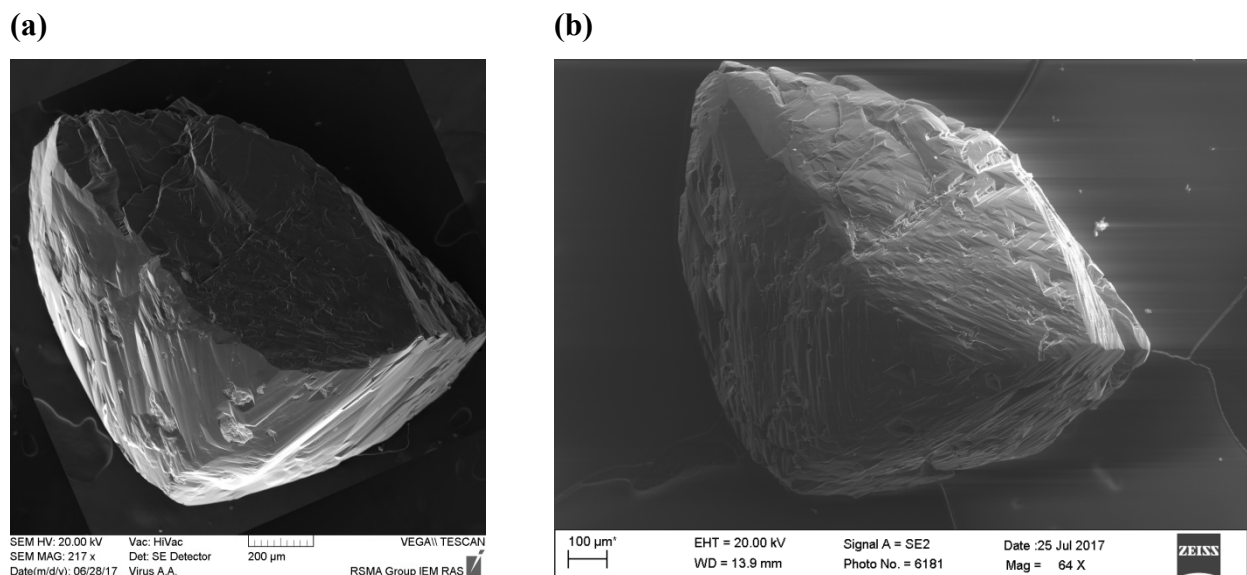


Fig. 3.2-15: SEM images of natural single crystal diamond before (a) and after (b) interaction with carbonate melt at 6 GPa and 1400 °C with a duration time of 3 hours (mass loss was 7.3 wt. %).

n. *Experimental investigation of the origin of ferropericlase inclusions in super-deep diamonds and the oxidation state of the lower mantle (V. Stagno and S. Dominijanni/Rome, L. Ziberna, T. Boffa Ballaran and D.J. Frost, in collaboration with T. Arimoto and T. Irifune/Matsuyama)*

Super-deep (SD) diamonds represent a unique opportunity to investigate geochemical processes occurring in the Earth's asthenospheric mantle through the analyses of their trapped minerals. More than 55 % of all the natural inclusions in SD diamonds collected worldwide show the presence of (Mg,Fe)O phases with FeO contents varying between 5 % and almost pure wustite (Fig. 3.2-16). In addition, these inclusions show variable NiO contents up to 1.5 wt. %, which is higher than expected for (Mg,Fe)O phases equilibrated with FeNi alloy at, for example, lower mantle conditions.

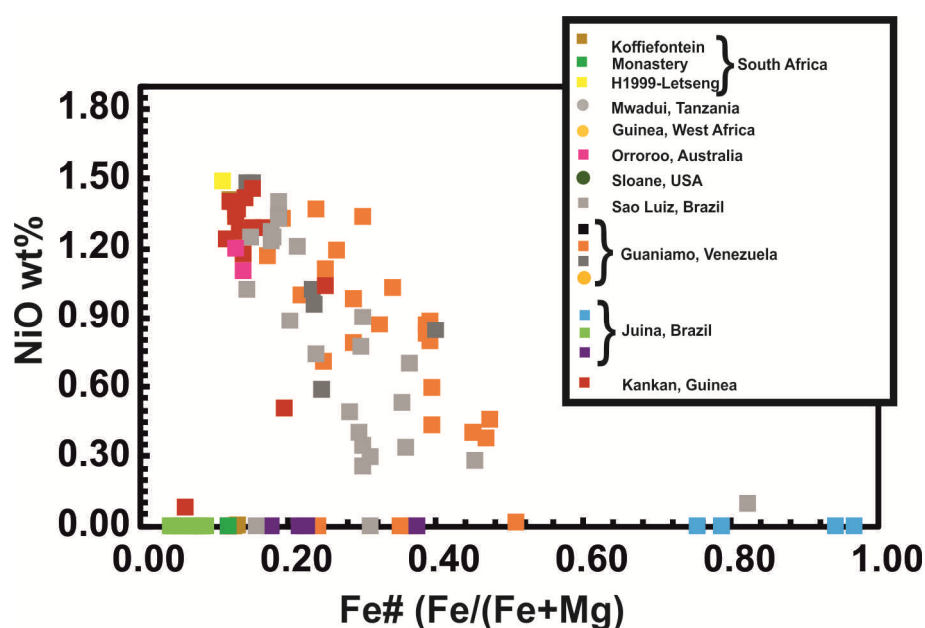


Fig. 3.2-16: Chemical composition of natural (Mg,Fe)O inclusions trapped in super-deep diamonds from worldwide localities reported as wt. % NiO vs. Fe# [Fe/(Fe+Mg)].

In this study, we have investigated the role of oxygen fugacity on the FeO and NiO content of ferropericlase at conditions at which diamonds might form by reduction of carbonate. Experiments were performed at pressures of 24-50 GPa and temperatures of 1400-1700 °C with the multianvil apparatus using a mixture of natural magnesite, graphite, synthetic ferropericlase and FeNi alloy as representative of a simplified lower mantle mineral assemblage with and without bridgmanite. The recovered run products were polished and analyzed by X-ray microdiffraction for phase identification, and scanning electron microscopy and electron microprobe for textural and chemical analyses, respectively. Preliminary results show the formation of Ni-rich ferropericlase and tiny diamonds at the rim of almost pure magnesite (Fig. 3.2-17). No textural evidence for redox reactions were found near bridgmanite. The chemical composition of ferropericlase formed by reduction of

magnesite revealed variable FeO and NiO contents related to the composition of the starting material.

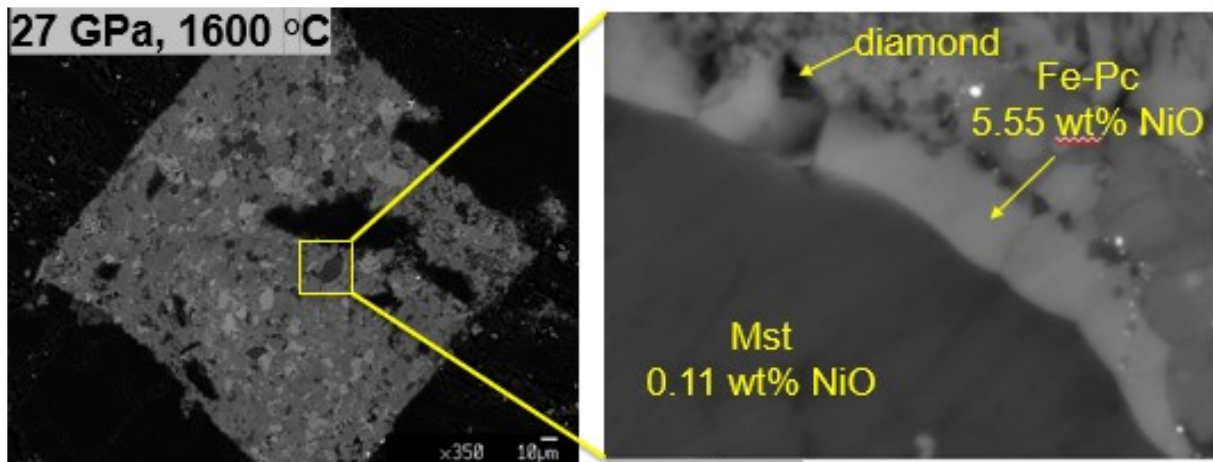


Fig. 3.2-17: a) BSE image showing a typical run product consisting of ferro-periclase (Fe-Pc), bridgmanite, magnesite (Mst), diamond, and bright phases of Ir(-Fe) used as a redox sensor. The right panel shows a rim of Fe-periclase enriched in NiO formed around a grain of almost pure magnesite, along with tiny crystals of diamonds.

Our data indicate that up to pressures of 50 GPa the  $fO_2$  of diamond formation from carbonate, magnesite in this case, remains approximately 2 log units above the level where FeNi alloy is stable. If the bulk of the lower mantle has the same oxygen content reflected by typical upper mantle  $Fe^{3+}/\Sigma Fe$  ratios, then the  $fO_2$  will tend to approach values close to the iron-wüstite buffer where Fe-Ni metal will be stable. An influx of carbonate into the lower mantle, potentially from subducting slabs, would result in diamond formation but would also raise the  $fO_2$  to levels near to carbonate stability. This would oxidise FeNi alloy to form (Mg,Fe)O that could become trapped as inclusions in the forming diamond.

**o. The partitioning of water at the onset of melting in the mantle transition zone (P. Condamine and D.J. Frost)**

The Earth's mantle plays a crucial role in the global geochemical cycle of volatile elements. This deep cycle involves processes such as subduction, convection, partial melting and metasomatism, which influence the availability and mobility of volatile elements in the interior. A key parameter in the mobilization of H<sub>2</sub>O in the mantle is its partition coefficient between minerals and melts. In the deeper mantle such melts are likely to be of very small degree given the probably small concentration of H<sub>2</sub>O and the significant capacity of nominally anhydrous minerals to incorporate H<sub>2</sub>O at these conditions. Never the less, some geophysical observations of slow shear wave velocities at near transition zone depths have been interpreted as resulting from the presence of volatile induced partial melts and it has been proposed that some kimberlite melts may originate from these depths.

In this study, the incipient melt composition for a peridotite assemblage in the mantle transition zone is being determined. A further goal of the project is to then determine H<sub>2</sub>O mineral-melt partition coefficients to understand and parameterize the onset of melting in the transition zone, which in turn can potentially influence the storage of volatiles in the deep Earth. Experiments are performed in a multianvil apparatus at 15 GPa and 1500 °C, *i.e.*, at near adiabatic conditions, using a natural KLB-1 peridotite. Because the bulk H<sub>2</sub>O content of the mantle is very low, incipient melting of peridotite will not modify mineral compositions, except for the most incompatible elements. Thus, it is necessary to determine such partition coefficients at very low degrees of melting. Iterative sandwich experiments are conducted in order to obtain the incipient melt composition in equilibrium with near solidus peridotite. A high proportion of hydrous glass (~ 70 wt. %) is added to the capsule to ensure quench melt recognition and enhance mineral growth processes to further facilitate both major and volatile element analyses. During the experiment the melt equilibrates with the peridotite assemblage and the melt composition is modified. Mass balance is employed to determine the melt H<sub>2</sub>O content. The resulting melt is then used as the starting glass in the next experiment.

Provisional melt compositions exhibit affinities with group I-type kimberlite rocks, with a strong silica-undersaturation (27 wt. % SiO<sub>2</sub>) and high MgO (25 wt. %) and CaO (15 wt. %) contents. However, recrystallization effects observed on the first iterations (Fig. 3.2-18) demonstrate that the melt composition is not yet in equilibrium with a near solidus model peridotite and to approach incipient melt degrees will require further iterative experiments.

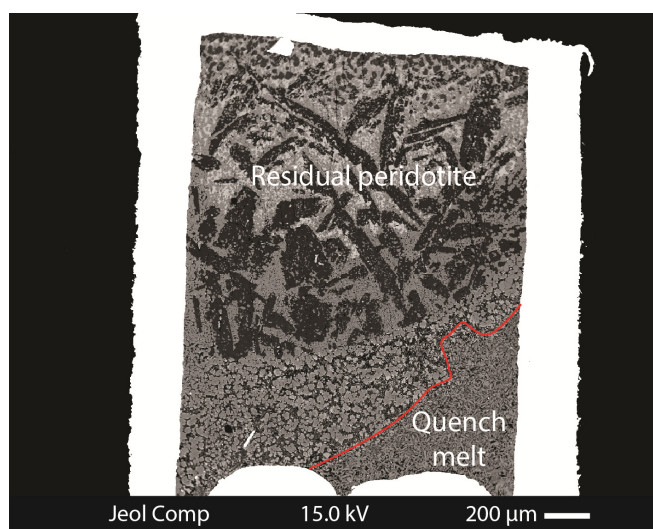


Fig. 3.2-18: Backscattered electron image showing an experimental product, from 15 GPa, of an iterative sandwich experiment. Most of the initial glass composition added (70 wt. %) has crystallized during equilibration with the residual peridotite.

**p.** *The effect of chlorine on the transport of trace elements in subduction zones (G. Rustioni, A. Audétat and H. Keppler)*

Arc volcanism in subduction zones is the main source of calc-alkaline magmas that formed the continental crust. It is generally accepted that these magmas are produced by partial

melting of the metasomatized mantle wedge overlying the subducting slab, but the exact nature of the slab-derived mobile phase that triggers mantle melting is still under debate. The standard model assumes that the mobile phase is an aqueous fluid released by the breakdown of hydrous minerals contained in the subducting oceanic lithosphere. On the other hand, some recent studies suggested that fluid transport of trace elements is inefficient and cannot explain the enrichment pattern observed in arc magmas. Hydrous melts produced by direct melting of the subducting sediments and the slab itself have, therefore, sometimes been proposed as the main agents of mantle metasomatism.

However, although the ability of water to dissolve ions is reduced along the pressure and temperature path of subduction, the presence of ligands may enhance the solubility of trace elements as neutral complexes. In subduction zone fluids, chlorine is probably the most relevant complexing agent due to its chemical affinity and elevated abundance, which typically ranges from 1 to 15 wt. % of NaCl.

To evaluate how chlorine affects trace element partitioning between fluid and eclogitic minerals at subduction zone conditions, a series of experiments was conducted in a piston cylinder apparatus. Different fluid compositions ranging from pure water to a salinity of 10 wt. % of NaCl were investigated at 4 GPa and 800 °C using the diamond trap method. In this technique, a diamond powder layer, placed between glass with average MORB composition (see Fig. 3.2-19), provides empty pores in which only the fluid may circulate during experiments. Ideally, the solid material found inside the diamond trap portion of the capsule corresponds to dissolved fluid component that precipitated during quenching. This allows one of the main challenges in the experimental determination of fluid/mineral partition coefficients to be overcome, since the precipitates can often not be easily distinguished from minerals crystallized in equilibrium with the fluid.



Fig. 3.2-19: A capsule with a diamond trap layer between eclogite recovered from a piston cylinder experiment at 4 GPa and 800 °C. The capsule width is approximately 5 mm.

In all experiments, eclogitic mineral assemblages consisting of garnet and omphacite with accessory kyanite, rutile and coesite were produced. After each experiment, the diamond trap was analyzed in the frozen state with laser ablation inductively coupled plasma mass spectrometry (LA-ICP-MS). This allows the solid precipitates to be measured together with the frozen aqueous fluid and, therefore, to directly obtain the entire composition of the fluid in equilibrium with the minerals. LA-ICP-MS analyses were also carried out on garnets and the resulting fluid/garnet partition coefficients are shown in Fig. 3.2-20.

The results indicate that the fluid transport of Rare Earth Elements (REE) is strongly enhanced for salinities typically occurring in natural subduction zone fluids. On the other hand, the partitioning behaviour of High-Field Strength Elements (HFSE) is less affected by the addition of Cl. This result is also in good agreement with natural observations in volcanic arc magmas, such as the characteristic Nb-Ta negative anomaly. The preliminary data obtained in this study, therefore, suggest that in most cases, Cl-bearing aqueous fluids are likely the mobile phase responsible for metasomatism and melting in the mantle wedge.

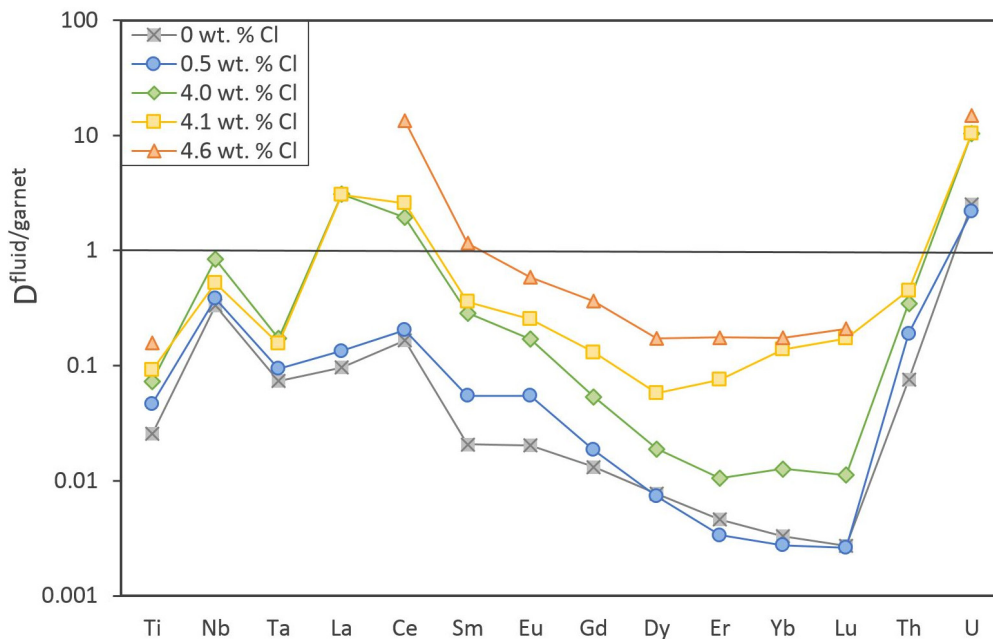


Fig. 3.2-20: Fluid/garnet partition coefficients of various trace elements from five diamond trap experiments conducted at 4 GPa and 800 °C with different initial fluid salinity.

**q. The fate of ophicarbonates during subduction (L. Eberhard and D.J. Frost)**

Ophicarbonates are carbonated ultramafic rocks formed by alteration of the oceanic lithosphere. They can in general be described as assemblages of serpentine minerals and calcium carbonate and are found in slices of altered mantle rocks that have been tectonically emplaced into the ocean floor and within ophiolite complexes. Ophicarbonates likely

transport both water and carbon into the mantle at subduction zones and although many of them were likely altered near the ocean floor, they provide evidence for how the oceanic mantle may incorporate volatiles. Due to their relative simplicity, however, they also provide an excellent bulk composition through which to investigate the effects of dehydration on the mobility of carbon, something which has formed the basis of many theoretical studies but few experimental ones. In addition, however, serpentine minerals often contain significant quantities of ferric iron, the creation of which during serpentinisation is in fact associated with the development of very reducing conditions. Neither the effects of ferric iron on serpentine stability nor the relationship between the serpentine  $Fe^{3+}/\Sigma Fe$  ratio and oxygen fugacity has been investigated. Thus although serpentine has been the focus of intense interest, one of its most important components in terms of the oxidation state of the mantle and carbon speciation in subduction zones is poorly understood.

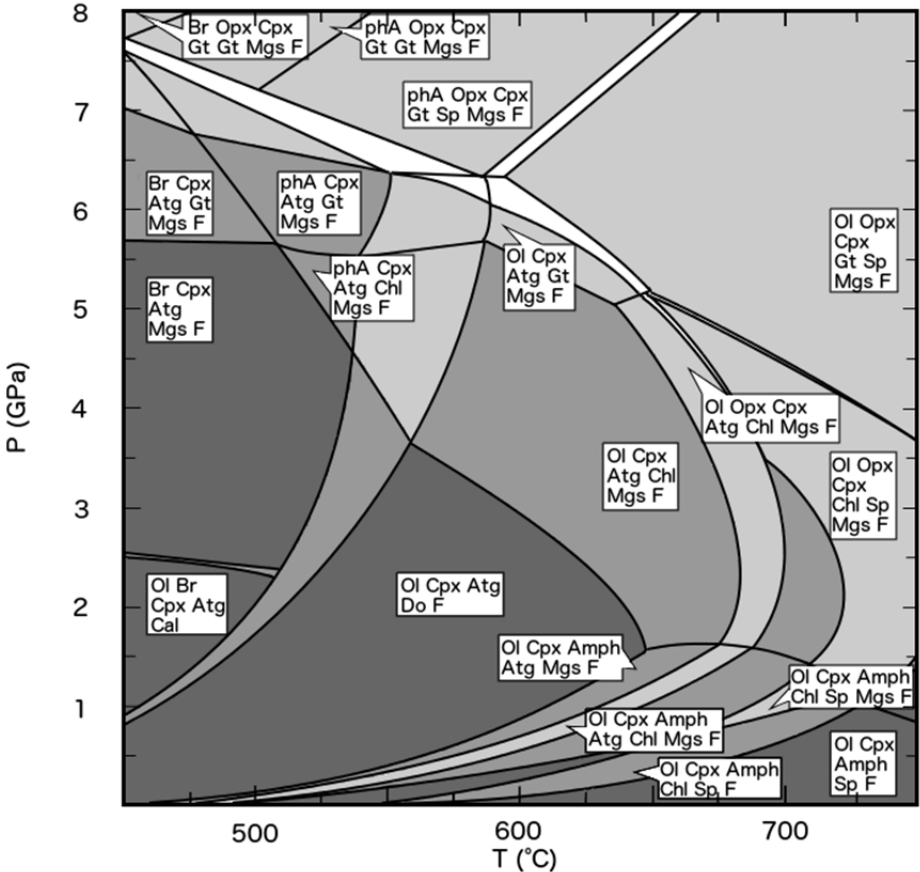


Fig. 3.2-21: PT- diagram for ophicarbonates (serpentinite +  $CaCO_3$ ) in the FMASHC system calculated with Perple\_X. The abbreviations are antigorite (Atg), olivine (Ol), Fluid (F), magnesite (Mgs), calcite (Cal), dolomite (Do), garnet (Gt), spinel (Sp), amphibole (Amph), chlorite (Chl), brucite (Br) and phase A (phA).

Here we are examining the fate of ophicarbonates assemblages at subduction zone conditions to determine the mutual influences of devolatilisation on hydrous minerals and carbonates. Thermodynamic models such as that shown in Fig. 3.2-21 act as a guide for these

experiments, but due to uncertainties, extrapolations and simplifications in the thermodynamic data employed inconsistencies with the predicted phase relations likely exist. Experiments are conducted with a multianvil apparatus, currently at 3 GPa and temperatures between 600 and 900 °C. The starting material is a natural serpentinite from the Zermatt-Saas zone (CH). This serpentinite is mainly composed of antigorite but contains 5 % magnetite and < 1 % sulphides. Electron microprobe analyses and Mössbauer spectroscopy have been employed to determine the composition and the ferric/ferrous ratio in addition to providing information on the coordination of the iron fraction. The starting serpentinite material is hence comprised of 95 %  $\text{Mg}_{45.7}\text{Fe}^{2+}_2\text{Cr}_{0.1}\text{Fe}^{3+}\text{Al}_{0.9}(\text{Si}_{32.6}\text{Al}_{1.4})\text{O}_{85}(\text{OH})_{61.5}$  antigorite + 5 %  $\text{Fe}_3\text{O}_4$  magnetite. This material is then mixed with 20 wt. %  $\text{CaCO}_3$  and 5 wt. % of Ir metal, the latter in order to determine the oxygen fugacity. Experiments are performed for periods of approximately one week. Recovered products are analysed using the electron microprobe, such that mineral proportions can be determined through mass balance, in addition to x ray diffraction. A recovered run product from 3 GPa and 780°C is show in Fig. 3.2-22. At these conditions both antigorite and chlorite are unstable. The phase relations, however, already deviate from those predicted in the thermodynamic calculations shown in Fig. 3.2-21 because dolomite and garnet are stable rather than magnesite and spinel.

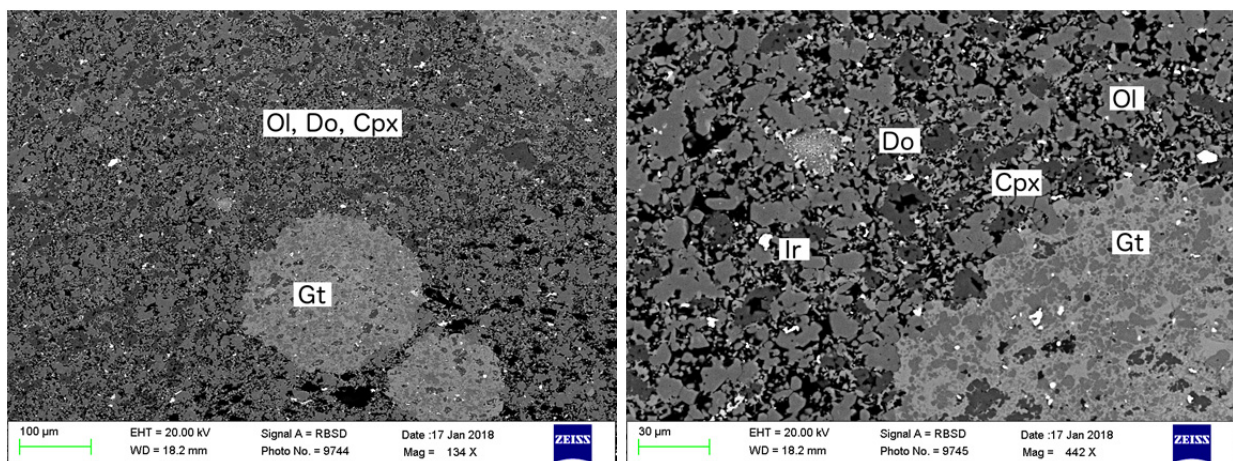


Fig. 3.2-22: Recovered products from an experiment performed at 3 GPa and 780°C containing serpentinite plus 20 wt. % calcite showing poikilitic garnet grains growing within a ground mass of olivine, dolomite and cpx. The proportion of Fe in the Ir-Fe alloy grains is used to estimate the oxygen fugacity. The image right is an enlargement from the centre of that shown left. Abbreviations are the same as in Fig. 3.2-21.

**r.** *Internally consistent geobarometers for igneous cumulates (L. Ziberna, E.C.R. Green/Zurich and J. Blundy/Bristol)*

Mafic and ultramafic igneous cumulates are the solid residua left after differentiation of basaltic magmas in the crust and crust-mantle boundary zone. On the surface, such rocks are recovered either as xenoliths hosted in the erupted magmas or as portions of crustal segments

exposed by tectonic events. Estimating their conditions of formation is one of the key steps to understanding both magmatic differentiation and the structure of the crust and crust-mantle boundary zone. Conventional geobarometers for these cumulate rocks are affected by several problems. For example, only one or two phases are used in the geobarometer formulations, despite often the assemblages contain more phases that potentially record valuable P-T information. Then, calibrations are based on experimental data covering limited ranges of composition. In addition, the accuracy and precision of thermobarometric results for natural samples are rarely reported and not easily quantifiable, and when evaluated against experimental data not used for the calibration, existing geobarometers show high uncertainties in the predicted pressure ( $\sigma_P > 3\text{-}4$  kbar, which translates to  $> 10$  km in the depth of formation).

In this project, we aim to tackle the above issues by testing and refining a multiple-reaction approach in combination with the average pressure (P) method (Powell & Holland, 1994, *Am. Mineral.* 79, 120-133). Initial attempts using the assemblage spinel + clinopyroxene + olivine + plagioclase have already shown that this method successfully predicts the pressures of the available phase equilibrium experiments in basaltic to andesitic systems and that the application to natural rocks should therefore produces precise estimates ( $\sigma_P = 0.8\text{-}1.5$  kbar). An example is shown in Fig. 3.2-23 where the pressure of a cumulate xenolith is calculated

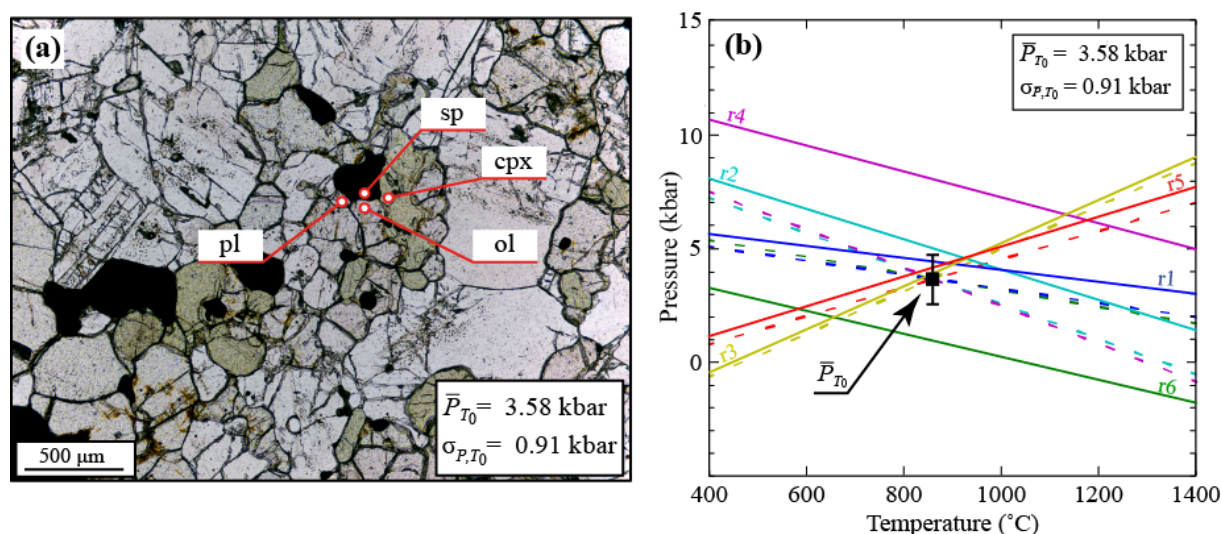


Fig. 3.2-23: An example of a multiple-reaction approach and average pressure (avP) methodology applied to a cumulate xenolith. (a) Photomicrograph (plain polarized light) of a cumulate xenoliths with locations of the microprobe analyses used for the pressure calculations shown in (b). Temperature  $T_0 = 870$  °C. The assemblage used for the calculations is spinel (sp) + clinopyroxene (cpx) + olivine (ol) + plagioclase (pl). In the minimization procedure, avP makes minimal adjustments to the enthalpies and activities of end-members in order for the reactions to coincide at  $\bar{P}$ . Reactions derived from the initial input data, *i.e.*, enthalpies and activities at the measured compositions, are shown as solid curves. Reactions after minimization are shown as dashed curves.

using a minimisation of 6 different reactions involving the cumulate phases. We are additionally calibrating and refining average P calculations and mixing models for amphibole and orthopyroxene bearing assemblages, which also frequently occur in mafic/ultramafic cumulate rocks. In addition, it is known that slow cooling after magma crystallization causes complex intra- and inter-crystalline cation redistribution, which is different for each cation and depends on temperature, cooling rate and phase properties. We are therefore also investigating the effect of such redistribution on multiple-reaction thermobarometry. Overall, the project aims to provide the first internally consistent method for estimating the pressure of formation of igneous rocks across entire suites that can include samples with different mineralogical assemblages.

*s. Clinopyroxene- and hornblende-rich xenoliths provide insights into the metal budget of two arc-related magma systems: Santa Rita and Cerrillos, New Mexico, USA (J. Chang and A. Audétat)*

Porphyry Cu mineralization is commonly associated with arc magmas that are characterized by relatively high oxidation state and high H<sub>2</sub>O contents. However, the influence of the metal content of magmas on their mineralization potential is still debated: many researchers infer that mineralizing magmas were unusually metal-rich; others concluded that this is not necessarily the case but that they were unusually sulfur-rich or that unusually large magma chambers are required. The metal budget of arc magmas is difficult to constrain because most of them became saturated in sulfides at some stage in their evolution and because volatiles and metals are usually lost during rock solidification. We have performed petrographic studies and quantitative analyses of minerals, melt- and sulfide inclusions on clinopyroxene- and hornblende-rich xenoliths from two Laramide-age, porphyry Cu ore-related magma systems at Santa Rita and Cerrillos in order to constrain the pressure, temperature, melt composition and metal budget of the magmas that formed the xenoliths. These results are used to gain insights into the behaviour of ore-forming metals during the evolution of arc magmas.

The investigated xenoliths were divided into three groups based on their mineralogical and textural characteristics: primary cumulate, reaction-replacement hornblendite, and hornblende gabbro. The thermobarometry results suggest that the clinopyroxene- and hornblende-rich xenoliths formed at a pressure of  $\sim 4 \pm 1$  kbar, with temperature decreasing from clinopyroxene cumulates (1000-1100 °C), to reaction-replacement hornblendites (900-1000 °C), to hornblende gabbro ( $\sim 880$  °C) at Santa Rita. Magnetite-ilmenite oxybarometry suggests that the oxygen fugacity at Santa Rita ( $\Delta\text{NNO} + 1.2$ ) was lower than that at Cerrillos ( $\Delta\text{NNO} + 1.3-1.9$ ), which fits with the presence of anhydrite inclusions in the samples from Cerrillos but the absence of anhydrite in the samples from Santa Rita. Clinopyroxene and hornblende  $\pm$  plagioclase cumulates were produced by nucleation, growth and settling of various mineral assemblages from silicate melts. Most of the reaction-replacement

hornblendites seem to have formed by the reaction of residual melts with precursory clinopyroxene ± phlogopite ± olivine assemblages in a crystal-rich melt environment, whereas the matrix-bearing hornblende gabbros likely crystallized *in situ* from the residual melts.

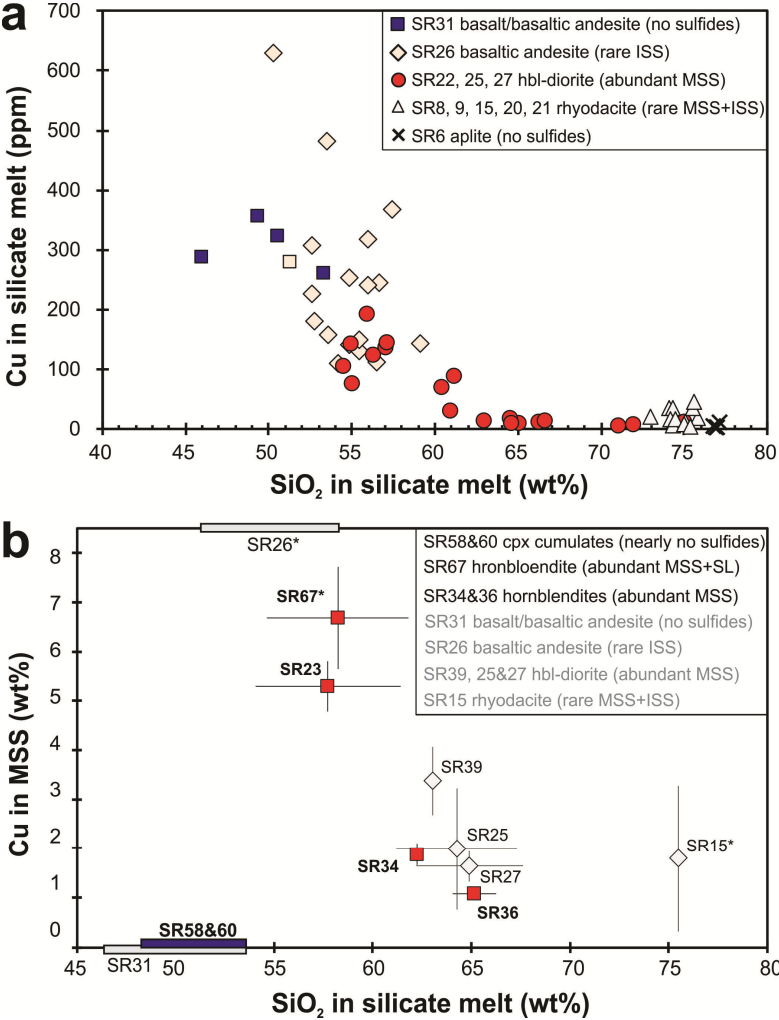


Fig. 3.2-24: (a) Cu content vs. SiO<sub>2</sub> content of melt inclusions in various phenocrysts from porphyry rocks at Santa Rita; (b) Cu content in MSS vs. SiO<sub>2</sub> content in melt inclusions of clinopyroxene cumulates, hornblende cumulates, and porphyry rocks at Santa Rita.

The evolution of copper in the magma system at Santa Rita is well constrained by melt inclusions analyzed from variously evolved dikes (Fig. 3.2-24a): Cu contents in the most primitive (45-52 wt. % SiO<sub>2</sub>), sulfide-undersaturated melts were relatively constant at 250-350 ppm, but quickly dropped to < 100 ppm Cu between 52 and 60 wt. % SiO<sub>2</sub> once sulfide saturation was reached. In contrast, Cu contents in melt inclusions from clinopyroxene cumulates and hornblendites at Santa Rita are highly variable (8-1800 ppm) and do not show any systematic trends with mineralogy or melt SiO<sub>2</sub> contents, which indicates that the Cu content of melt inclusions was modified by post-entrapment diffusion. The absence of sulfides in clinopyroxene cumulates indicates that the mafic silicate melts (47-53 wt. % SiO<sub>2</sub>) were sulfide-undersaturated; the occurrence of abundant sulfides (up to ~ 0.7 wt. %) and the decreasing Cu contents in MSS in hornblendites also imply rapidly decreasing Cu

concentrations in the melts as they evolved from ~ 53 to 62 wt. % SiO<sub>2</sub> (Fig. 3.2-24b). The Cu evolution in the melts that formed the clinopyroxene cumulates and the hornblendites was quantitatively modeled by closed-system fractional crystallization (Fig. 3.2-25). The modeling results suggest that Cu contents in the melts decrease dramatically after sulfide-saturation at ~ 55 wt. % SiO<sub>2</sub>. The modeled Cu evolution matches the observed evolution in the melt inclusions of variously evolved dikes at Santa Rita. The evolution of Cu in the magmas at Cerrillos is poorly constrained, but the absence of sulfides in clinopyroxene cumulates and their common occurrence in hornblende ± plagioclase cumulates indicates a similar evolution as at Santa Rita.

The formation of clinopyroxene cumulates probably does not have any negative influence on the mineralization potential, whereas hornblendites that form at depth do. However, the hornblendites that form in the final, upper crustal magma chamber should not have a negative influence because any contained sulfides likely get destroyed at late-magmatic stages. Consequently, fertile upper crustal magma chambers are favoured by relatively rapid ascent of little-evolved magmas through the crust (*i.e.*, without extensive production of hornblendites on the way), and/or by conditions that suppress sulfide formation altogether, *i.e.*, very high *f*O<sub>2</sub> and/or high alkalinity. In addition, as hornblendite lithologies tend to more commonly form in the lower arc crust and are easily re-melted, they may represent a fertile source for ore-forming magmas in post-subduction or collisional tectonic settings.

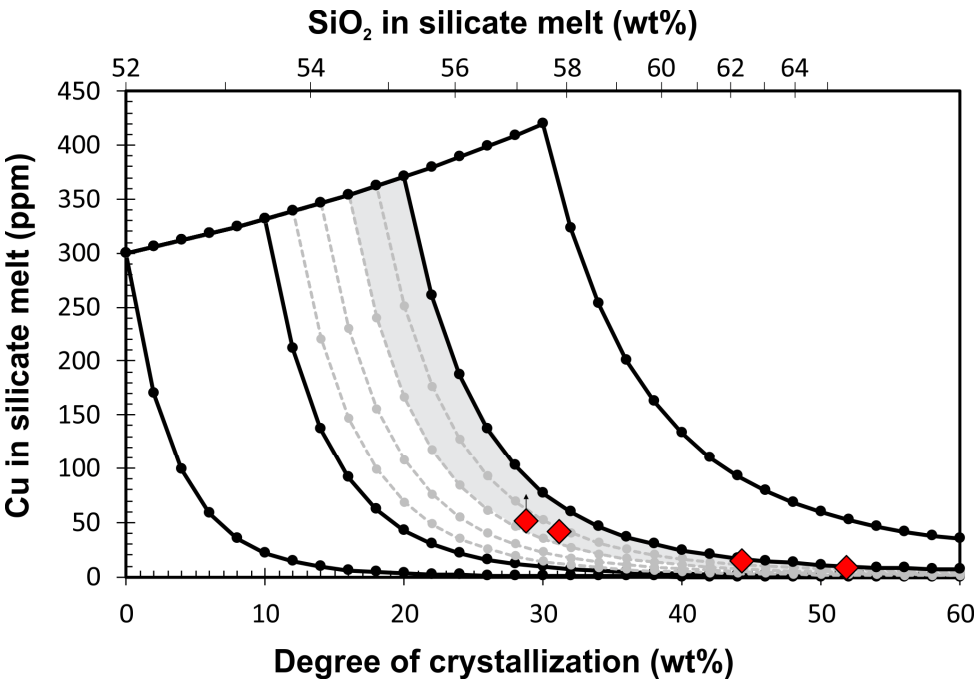


Fig. 3.2-25: Fractional crystallization models for the evolution of Cu content in silicate melts that formed the hornblende cumulates at Santa Rita. The grey area represents the most likely Cu evolution trend in silicate melt when sulfide-saturation was reached at 55 wt. % SiO<sub>2</sub>.

**t. Gold diffusion into and out of quartz-hosted fluid inclusions during re-equilibration experiments at 600-800 °C and 2 kbar (H. Guo and A. Audétat)**

Fluid inclusions record crucial information about the physical and chemical nature of fluids in various geological settings and have been particularly well-studied in the context of magmatic-hydrothermal ore deposits. Quartz is the most commonly studied host mineral because of its transparency, weathering-resistance and simple chemical composition. However, several studies have shown that quartz-hosted fluid inclusions can diffusively gain or lose H<sub>2</sub>, molecular H<sub>2</sub>O, and small, single-charged ions such as of Na<sup>+</sup>, Cu<sup>+</sup>, Ag<sup>+</sup> and Li<sup>+</sup> after their formation. The present study demonstrates that also Au can be diffusively gained or lost at P-T conditions typical of high-temperature magmatic-hydrothermal fluids.

In the pre-runs, fluid inclusions were synthesized by growing new quartz on pieces of etched quartz in single Au or Pt capsules at 800 °C and 600 °C, 2 kbar. Aqueous solutions were prepared with analytical grade NaCl, HCl, KCl, RbCl, CsCl, KOH and deionized H<sub>2</sub>O (in same case, elemental sulfur was added as solids). In the re-equilibration experiments, the quartz pieces recovered from pre-runs were loaded together with a new piece of etched quartz and fluid into new gold, platinum capsules, or into Au<sub>95</sub>Cu<sub>05</sub> alloy capsules. The composition of individual fluid inclusions before and after re-equilibration experiments was measured by LA-ICP-MS.

Fluid inclusions synthesized in pre-runs display a large variety of shapes and measure up to ~ 50 µm in length (Figs. 3.2-26a,c). After re-equilibration, some fluid inclusions show notable changes in morphology, *i.e.*, originally irregular and elongated fluid inclusions attained more isometric and regular shapes (Figs. 3.2-26b,d). In the sulfur-bearing re-equilibration experiment conducted in a Au<sub>95</sub>Cu<sub>05</sub> alloy capsule, the fluid inclusions contained large Cu sulfide daughter crystals after re-equilibration (Fig. 3.2-26d). Fluid inclusions containing 5 wt. % KCl synthesized in platinum capsules at 800 °C and 600 °C, 2 kbar were re-equilibrated in new gold capsules filled with Cs-spiked, HCl- and NaCl-bearing solutions at the same P-T conditions for 4-14 days. Both Na and Au were significantly gained during the re-equilibration process, with Na increasing up to 0.23 wt. % and Au increasing up to 570 ppm at 800 °C (Fig. 3.2-27a). Similar observations were made in an experiment conducted at 600 °C, 2 kbar (Fig. 3.2-27b). The high K-content and absence of Cs in re-equilibrated fluid inclusions proves that they did not crack open during the experiment, implying that Na and Au were gained by diffusion through the quartz lattice. Reverse experiments were conducted by synthesizing Au-bearing fluid inclusions in gold capsules and then re-equilibrating them in a platinum capsule, which resulted in loss of up to ~ 900 ppm Au (Fig. 3.2-27c). Two experiments were also performed to test whether Au could be gained solely due to decreasing acidity in the external fluid. However, no corresponding evidence was found. To test whether the formation of Cu-rich sulfide phases within fluid inclusions has any influence on Au uptake, fluid inclusions synthesized from a solution containing 9.8 wt. % NaCl, 2.3 wt. % S, 393±22 ppm Rb, 370±70 ppm Au and a pH of < 1 were re-equilibrated in a solution containing 9.9 wt. % NaCl, 1.5 wt. % KOH, 1.5 wt. % sulfur, 72±7 ppm Cs, 48±13 ppm Au,

and a pH of 2 in a  $\text{Au}_{95}\text{Cu}_{05}$  alloy capsule. This re-equilibration caused the fluid inclusions to gain  $6.8 \pm 2.1$  wt. % Cu and  $\sim 0.7$  wt. % Na, but no gain of Au was detected (Fig. 3.2-27d).

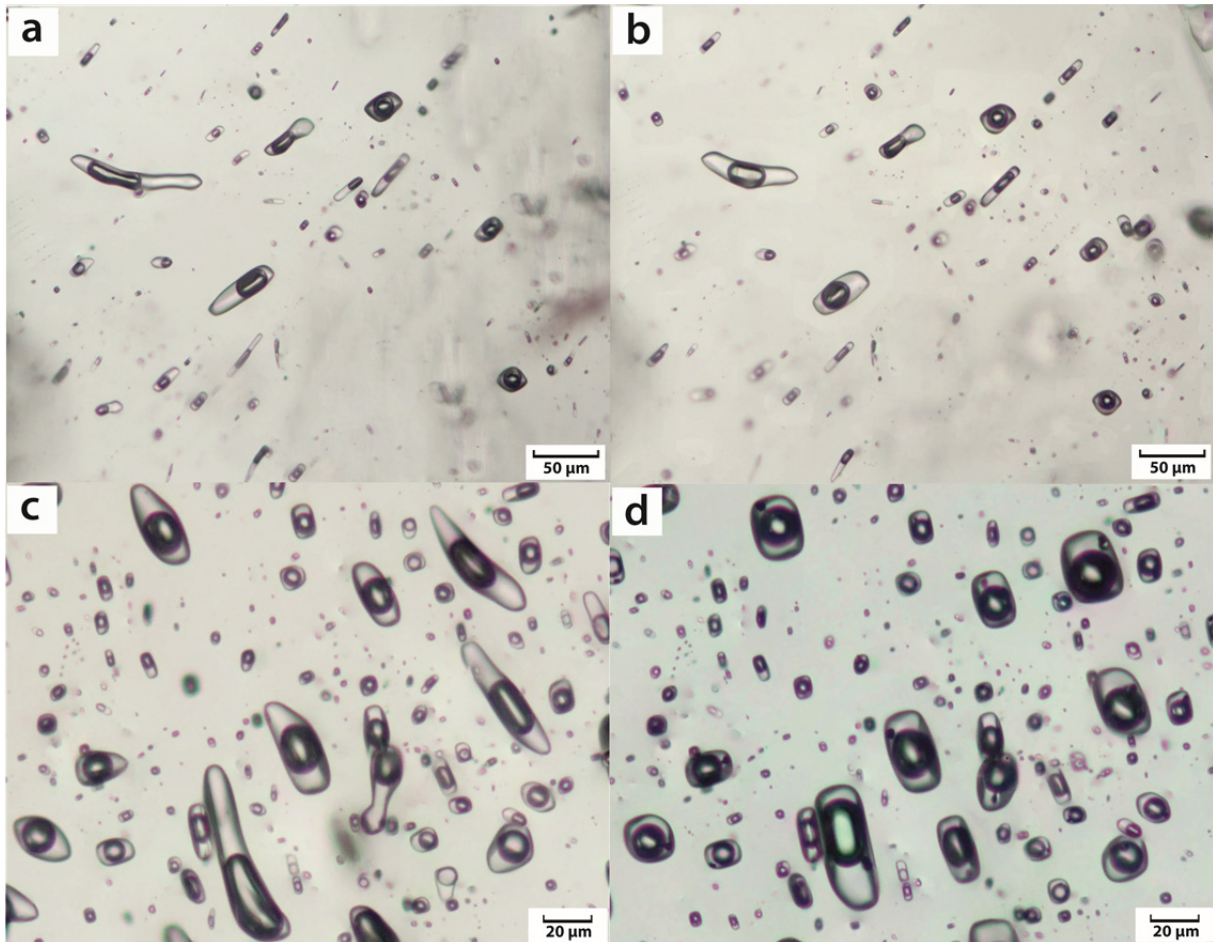


Fig. 3.2-26: Transmitted-light photomicrographs of fluid inclusions obtained in this study: (a) fluid inclusions synthesized at 800 °C and 2 kbar before re-equilibration, (b) the same fluid inclusions after re-equilibration at 800 °C and 2 kbar for 4 days, (c) sulfur bearing fluid inclusions synthesized at 800 °C and 2 kbar before re-equilibration, (d) the same fluid inclusions after re-equilibration in a  $\text{Au}_{95}\text{Cu}_{05}$  capsule at 800 °C and 2 kbar for 7 days. Notice the appearance of opaque sulfide daughter crystals in the fluid inclusions in (d).

To sum up, Au diffusion appears to be driven by chemical potential gradients of Au. In contrast to the behaviour of  $\text{Na}^+$  and  $\text{Cu}^+$ , no evidence for diffusive exchange of  $\text{Au}^+$  with  $\text{H}^+$  was found, nor that Au uptake could be promoted by the formation of Cu-bearing sulfide daughter crystals. If Au concentrations in natural, quartz-hosted fluid inclusions from magmatic-hydrothermal ore deposits have been affected, then they likely lost Au rather than gained it. At temperatures below 400 °C diffusional loss or gain of Au is considered unlikely in magmatic-hydrothermal systems, but potentially was significant in samples from orogenic Au gold deposits.

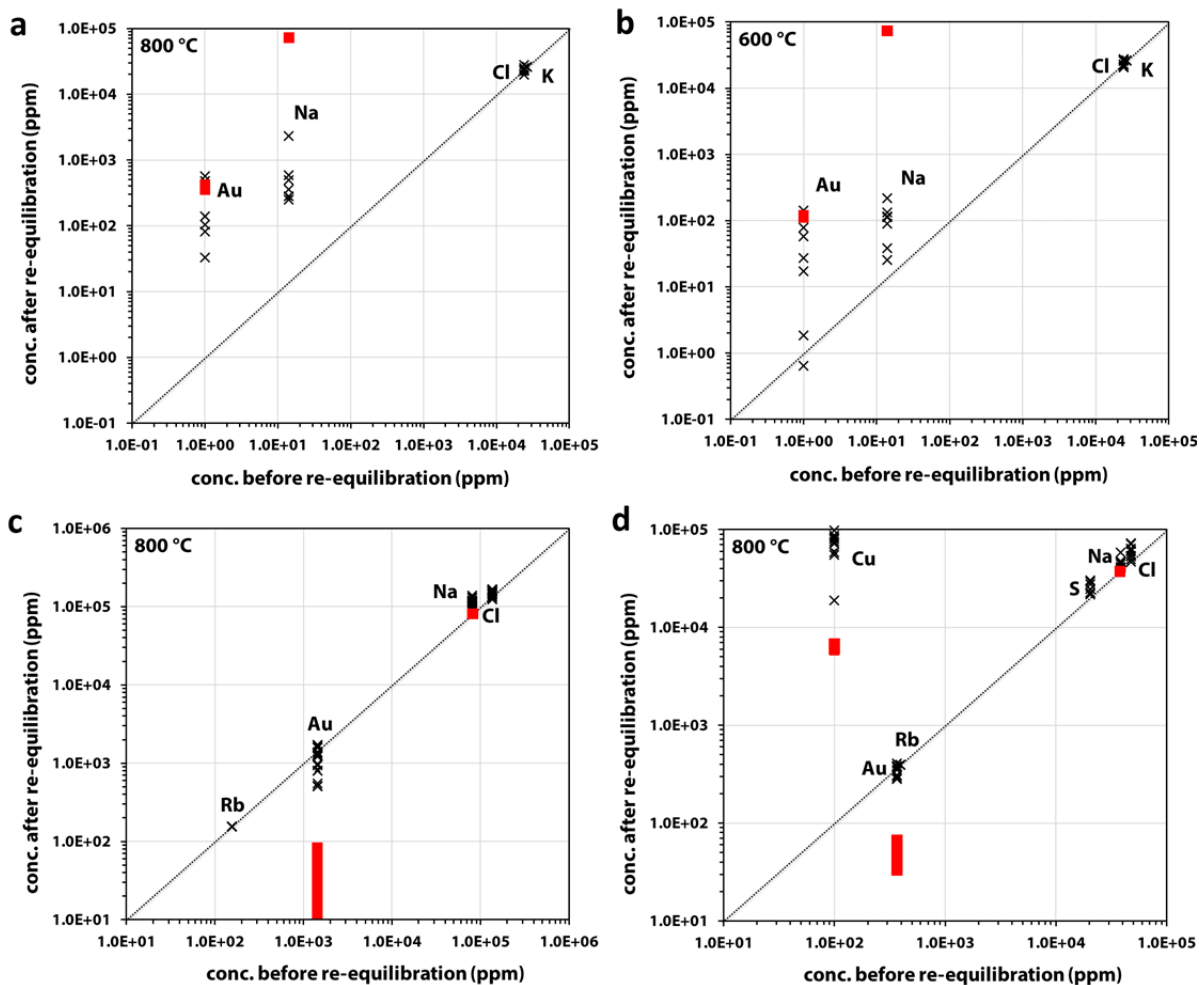


Fig. 3.2-27: Composition of fluid inclusions before versus after re-equilibration (crosses), plus the composition of the external fluid present during the re-equilibration experiment (red bars): (a) fluid inclusions containing 5.0 wt. % KCl, re-equilibrated in an external fluid containing 3.5 wt. % HCl + 20.1 wt. % NaCl + 115±9 ppm Cs at 800 °C, 2 kbar for 4 days. (b) the same as in (a) but re-equilibrated at 600 °C, 2 kbar for 14 days. (c) fluid inclusions which originally contained 20.6 wt. % NaCl, 1440±250 ppm Au, and 156±11 ppm Rb, re-equilibrated in an external fluid containing 20.3 wt. % NaCl + 14.9 wt. % KCl + 0.2 wt. % KOH within a Pt capsule at 800 °C, 2 kbar for 4 days. (d) fluid inclusions which originally contained 9.8 wt. % NaCl + 2.3 wt. % S + 393±22 ppm Rb + 370±70 ppm Au, re-equilibrated in an external fluid containing 9.9 wt. % NaCl + 72±7 ppm Cs + 1.5 wt. % KOH within a Au<sub>95</sub>Cu<sub>5</sub> capsule at 800 °C, 2 kbar for 7 days. The Cu content of the fluid inclusions after the pre-run was below the detection limit of 30-100 ppm.

**u.** *Magmatic-hydrothermal evolution of the barren Huangshan pluton, Anhui province, China: A melt- and fluid inclusion study (D. Zhang and A. Audétat)*

Intermediate to felsic magmas emplaced in the upper crust represent the source of various types of magmatic-hydrothermal ore deposits such as porphyry Cu deposits, porphyry Mo

deposits, intrusion-related Au deposits, Sn-W deposits, and various skarn deposits (Fe, Cu, Mo, Pb, Zn, Ag, Au). However, only a few intrusions are economically mineralized, whereas most intrusions remained barren or are only weakly mineralized. The fundamental differences between barren and mineralized systems can only be identified if data are available from both types of system. To increase our knowledge of the factors that control the mineralization potential of silicic magma systems the magmatic-hydrothermal evolution of the ~ 125 Ma old Huangshan granite in Eastern China was reconstructed. This granite shows geochemical similarities to Climax-type porphyry Mo mineralizing magmas but is evidently barren.

Melt inclusions analyzed from the Huangshan granite have rhyolitic compositions (72.6-77.7 wt. % SiO<sub>2</sub>) and show an extremely wide range of Cs contents from 10 ppm to up to 2000 ppm, implying melt entrapment at crystallinities up to > 99 %. The compositions of the least-evolved melt inclusions (< 30 ppm Cs) overlap with those of whole-rocks, whereas highly evolved melts (> 100 ppm Cs) followed an unusual evolution trend (Fig. 3.2-28) that appears to be related to high F contents (1.0-2.5 wt. % F). The Mo content of the bulk magma is estimated at 3-6 ppm.

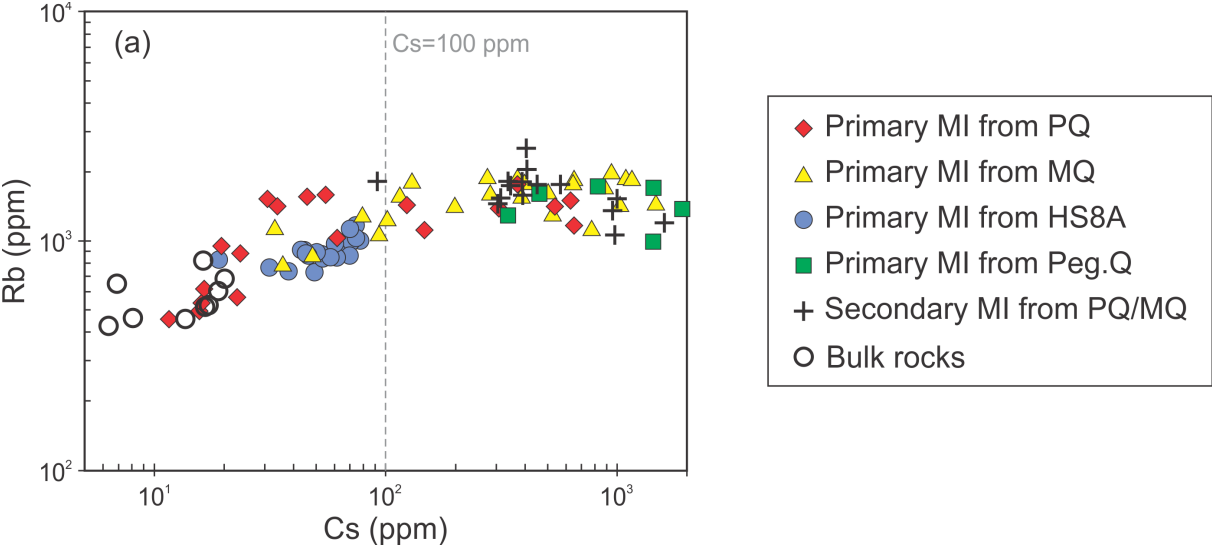


Fig. 3.2-28: Cs versus Rb diagram of melt inclusions (MI) from different types of quartz crystals in the Huangshan pluton, showing a distinct evolutionary trend from least- to highly evolved melts. Quartz types include quartz phenocryst (PQ), matrix quartz (MQ), pegmatitic quartz (Peg. Q) and euhedral quartz crystals in a miarolitic cavity (as represented by sample HS8A).

The fluid evolution of the Huangshan granite was dominated by intermediate-density fluids with salinities of 4.5-5.0 wt. %. No evidence for fluid immiscibility was found, which is indicative of relatively high confining pressures. This conclusion is supported by reconstructed near-solidus crystallization conditions of ~ 700 °C and ~ 1.8 kbar based on coexisting fluid- and melt inclusions in miarolitic cavities. Due to the enrichment of fluorine

during fractional crystallization some very late-stage, residual silicate melts remained liquid down to 600 °C. The intermediate-density, magmatic fluids contained 60-95 ppm Mo.

The results imply that both the fluids and the melts of the barren Huangshan pluton contained similar amounts of Mo as those present in porphyry Mo-mineralized systems. The barren nature of the Huangshan granite is thus not a consequence of low Mo abundances. Also the reconstructed melt viscosity (Fig. 3.2-29;  $\log \eta = 3.8-5.2$  Pa s), the magma volume (230 km<sup>3</sup>), and the emplacement depth (~ 7 km) are within the ranges displayed by mineralized systems. The only parameter that seems to have been different at Huangshan is a lack of focused fluid flow, as indicated by the common presence of miarolitic cavities. Most likely, the lack of focused fluid flow resulted from its flat roof geometry.

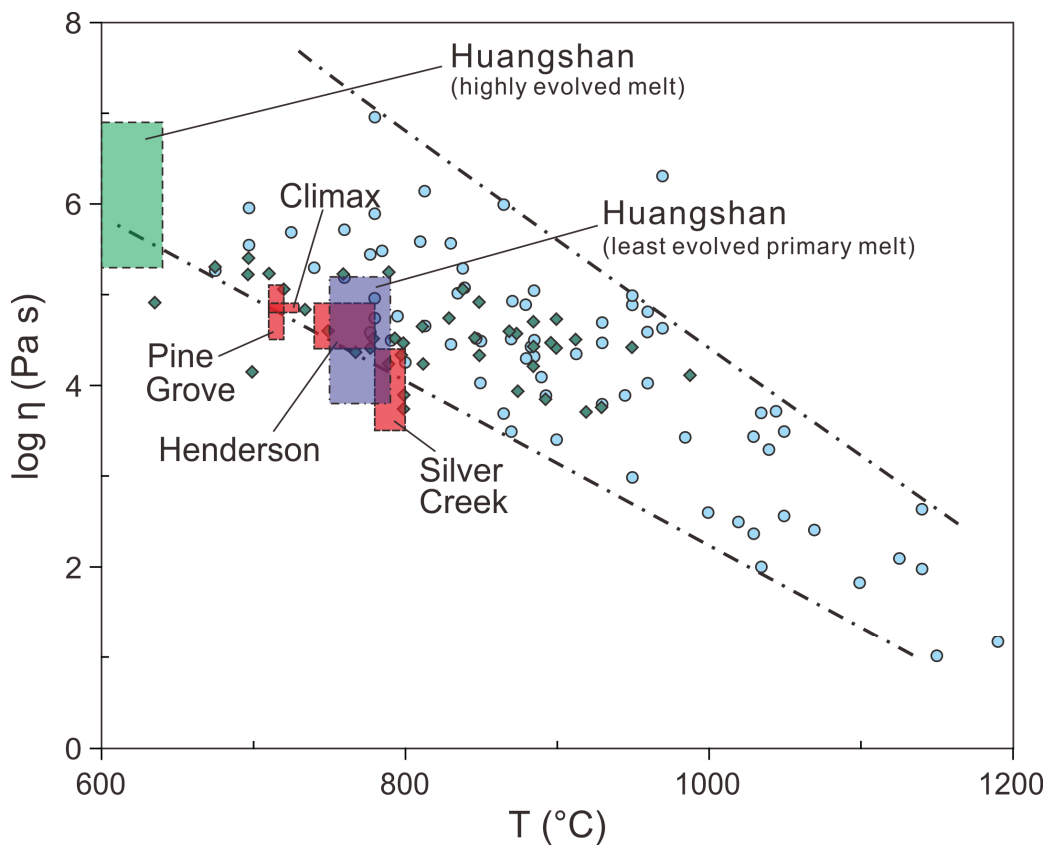


Fig. 3.2-29: Temperature versus melt viscosity ( $\log \eta$ ) diagram, showing estimated melt viscosities in the Huangshan pluton and four Climax-type porphyry Mo-mineralizing magmas (Climax, Henderson, Silver Creek and Pine Grove) compared to estimates for normal granitic to basaltic melts (diamonds and circles).

### 3.3 Mineralogy, Crystal Chemistry and Phase Transformations

The physical and chemical properties of planetary interiors are dictated by the behaviour of the constituent minerals that, in turn, are sensitive to details of their atomic structure. Mineralogical and crystal chemical investigations at pressure and temperature conditions representing deep planetary interiors are thus fundamental to interpret geophysical observations, understand geochemical constraints and construct models of interior dynamics. Pressure- or temperature-induced phase transitions occurring in planetary materials complicate the mineralogical models and need to be studied by experiments and theory. Within this chapter, a variety of new experimental and computational results are presented advancing our understanding of the mineralogy of planetary mantles and of the crystal chemistry of major Earth materials as well as providing new constraints on phase transitions occurring in planetary bodies.

The first contribution of this section reports on the synthesis and structural characterisation of large single crystals of akimotoite, a  $\text{MgSiO}_3$  high-pressure polymorph that might cause the observed seismic anisotropy in slabs stagnating in the Earth's transition zone. The following four contributions focus on the crystal chemistry of  $(\text{Mg,Fe,Al})(\text{Al,Fe,Si})\text{O}_3$  bridgmanite, the major mineral in the Earth's lower mantle (660-2900 km depth). These studies aim to constrain the incorporation mechanism of Al and Fe into the bridgmanite structure, as well as to determine the dependence of the  $\text{Fe}^{3+}/\text{Fe}^{2+}$  ratio on oxygen fugacity and synthesis conditions. To this end several analytical techniques have been used, in particular  $^{27}\text{Al}$  solid-state NMR spectroscopy, microprobe analysis, single-crystal and powder X-ray diffraction, Mössbauer spectroscopy, Transmission Electron Microscopy and the laser-heating diamond anvil cell.

The following three contributions report experimental work aimed at understanding the coordination of silicon in glasses and crystals at high pressures. The first work shows that the coordination of silicon in  $\text{SiO}_2$  glass increases with pressure until it becomes dominantly six-fold coordinated at pressures above 60 GPa. The second reports on new  $\text{SiO}_2$  polymorphs occurring at pressures above 30 GPa that possess penta-coordinated silicon and contain face-sharing octahedra. The third reports on the high-pressure phase transitions occurring in  $\text{CaB}_2\text{Si}_2\text{O}_8$  danburite associated with the change in coordination of silicon. The results suggest that  $\text{SiO}_5$  groups could be not as rare as previously thought and might form as intermediate configurations upon transformation of silicate minerals.

Experimental works on crystal structures and chemistry related to deep Earth volatile cycles are presented in the following three contributions. Carbonate minerals are the main carbon-bearing components in subducting slabs and the first work investigates reactions between  $\text{MgCO}_3$ , magnesite and metallic Fe at lower mantle conditions. The results suggest that magnesite might be stable under reduced lower mantle conditions even in the presence of metallic iron. This is followed by a contribution where Fe-bearing magnesite has been laser-heated at high pressures and a new monoclinic phase was observed. Thus, specific carbonate stability fields appear to depend on their crystal chemistry. The third of these contribution presents results obtained from synchrotron X-ray diffraction up to 30 GPa at room

temperature performed on single-crystals of  $\delta$ -AlOOH, a potential water-bearing phase in the deep mantle.

Phase transitions occurring under conditions expected in deep planetary interiors are discussed in the next three contributions. The first two experimental works present results from time-resolved X-ray diffraction measurements across the H<sub>2</sub>O ice VI-VII transition as well as the iron spin crossover in (Mg,Fe)O ferropericlase. Compression rates of up to 1 TPa/s have been achieved using a novel dynamic diamond anvil cell, allowing the quantification of phase transition kinetics. The third contribution reports computational results on the B1-B2 phase transition expected to occur in MgO in the mantles of super-Earth planets at pressure and temperature conditions that are still challenging to reach in experimental studies.

In the second to last contribution, structural refinements of single crystal X-ray diffraction intensity data are reported for Fe-rich magnesioferrite (Mg<sub>0.6</sub>Fe<sub>2.4</sub>O<sub>4</sub>) and the equation of state was obtained up to 16 GPa revealing a compressibility that closely resembles that of magnetite.

Oxidation processes in mackinawite, an iron sulphide that occurs in many anoxic environments, are investigated in the final contribution. Data analysis is ongoing to determine likely reaction pathways as well as reaction kinetics in an attempt to gain insight into processes occurring in the early Earth.

**a. Synthesis of large single-crystals of MgSiO<sub>3</sub> akimotoite (G. Criniti, T. Ishii, N.C. Siersch and T. Boffa Ballaran)**

Akimotoite, the ilmenite-structured polymorph of MgSiO<sub>3</sub>, is thought to be one of the constituents of harzburgitic and peridotitic subducting layers in the mantle transition zone. Due to its strong elastic anisotropy, it might also be responsible for the compressional seismic wave anisotropy observed in several stagnating slabs at depth of Earth's mantle transition zone. The aim of this study was to synthesise large single crystals (> 50-60  $\mu$ m) of akimotoite, that are required to perform elasticity measurements (*e.g.*, Brillouin spectroscopy) for better constraining the elastic behaviour of this mineral at mantle conditions.

Single crystals of MgSiO<sub>3</sub> akimotoite with grain sizes up to  $\sim$  0.4 mm were synthesized at 22 GPa and 1600 °C for 4 h in a multianvil apparatus. A fine mixture of MgSiO<sub>3</sub> enstatite and Mg<sub>2</sub>SiO<sub>4</sub> forsterite together with H<sub>2</sub>O was used as starting material. The run product was examined with a microfocused X-ray diffraction system and consisted of akimotoite and stishovite. Several single crystals (Fig. 3.3-1) were selected and tested with a single crystal X-ray diffractometer, indicating nearly 100 % akimotoite. For the best crystal a complete intensity data collection was performed. The resulting unit-cell parameters for this crystal are  $a = 4.7273(5)$  Å,  $c = 13.5560(4)$  Å, with a cell volume of 262.35(5) Å<sup>3</sup>. Structural refinements were performed using space group  $R\bar{3}$  and the akimotoite structure obtained (Fig. 3.3-2) is consistent with data reported in the literature.

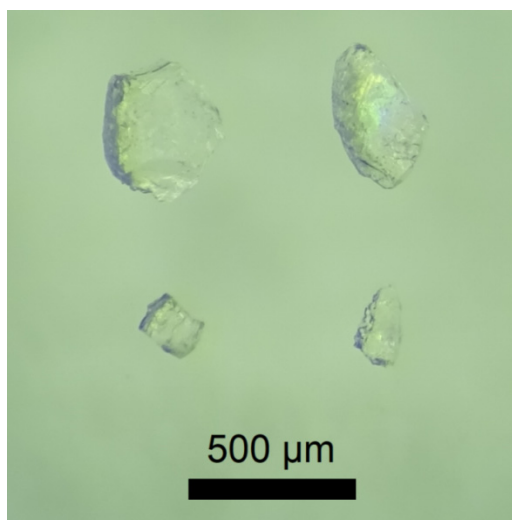


Fig. 3.3-1: Photograph of single crystals of akimotoite selected and analysed in this study.

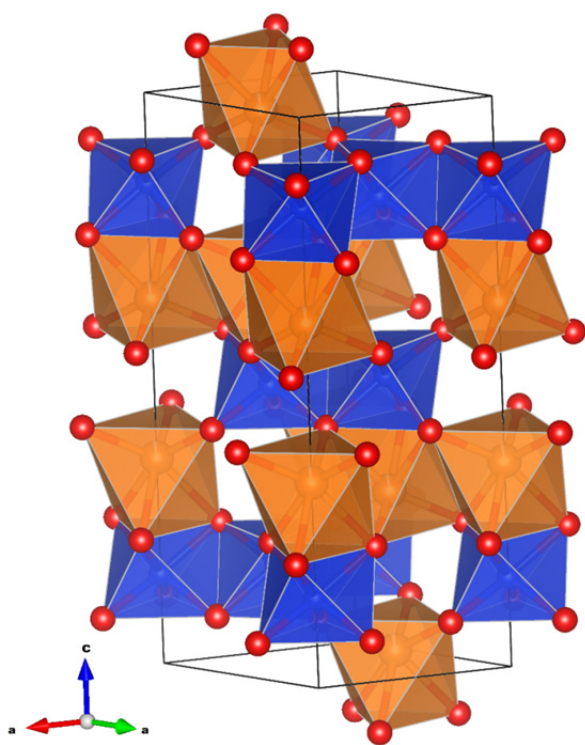


Fig. 3.3-2: Crystal structure of  $\text{MgSiO}_3$  akimotoite obtained from the single-crystal intensity data collected in this study. Blue octahedra: Si atoms; orange octahedra: Mg atoms; and red spheres: oxygen atoms.

**b.** *Phase relations in the ternary system  $\text{MgO}-\text{AlO}_{1.5}-\text{SiO}_2$  at lower mantle conditions and the Al substitution mechanisms in bridgmanite (Z. Liu, H. Grüninger/Bayreuth, R. Huang, T. Boffa Ballaran, D.J. Frost, T. Katsura and J. Senker/Bayreuth)*

Petrological studies indicate that the Earth's lower mantle (660-2900 km depth), which comprises more than 50 % of the Earth by volume is composed of the mineral bridgmanite, with general formula  $(\text{Mg,Fe, Al})(\text{Al,Fe,Si})\text{O}_3$ .  $\text{Al}^{3+}$  can be incorporated into bridgmanite through the components  $\text{Al}_2\text{O}_3$  and  $\text{MgAlO}_{2.5}$ , as a result of substitution mechanisms that can be considered as a charge-coupled mechanism (CCM) and an oxygen vacancy mechanism

(OVM), respectively. In the case of CCM,  $\text{Al}^{3+}$  occupies the A ( $\text{Mg}^{2+}$ ) and B ( $\text{Si}^{4+}$ ) sites in the orthorhombic perovskite-type bridgmanite structure, whereas it occupies only the B site with formation of oxygen vacancies for charge balance in the case of OVM. The OVM substitution may be particularly important for the incorporation of  $\text{H}_2\text{O}$  and noble gases in bridgmanite and may also have important effects on transport properties. The ability to quantify the proportions of  $\text{MgAlO}_{2.5}$  and  $\text{Al}_2\text{O}_3$  components is, therefore, very important for determining the variation of physical and chemical properties in the lower mantle.

Here, we have determined phase relations in the ternary system  $\text{MgO}-\text{AlO}_{1.5}-\text{SiO}_2$  and systematically investigated  $\text{MgAlO}_{2.5}$  and  $\text{Al}_2\text{O}_3$  solubility in bridgmanite in the MgO-saturated systems  $\text{MgSiO}_3-\text{MgAlO}_{2.5}$  and  $\text{MgSiO}_3-\text{MgAl}_2\text{O}_4$ , in the charge-coupled system  $\text{MgSiO}_3-\text{Al}_2\text{O}_3$ , and in the  $\text{SiO}_2$ -saturated system  $\text{MgSiO}_3-\text{Al}_2\text{SiO}_5$  at a pressure of 27 GPa and a temperature of 2000 K (Fig. 3.3-3).

In the MgO-saturated system  $\text{MgSiO}_3-\text{MgAlO}_{2.5}$  the Al substitution mechanisms were initially assessed using site assignments determined from electron microprobe analyses. These show that the OVM mechanism dominates in Al-poor bridgmanite and increases with increasing Al content up to approximately 0.1 cations per formula unit (pfu) based on 3 oxygens. At this Al content approximately 0.06 cations pfu of Al occupying the Si site are charge balanced by oxygen vacancy formation. Above 0.1 Al cations pfu, however, the OVM rapidly decreases and at an Al content of approximately 0.15 cations pfu the CCM starts to dominate. Above approximately 0.2 Al cations pfu the OVM drops to a negligible level.

In order to constrain the Al coordination environment in bridgmanite and to validate the microprobe results, two samples with 0.05 and 0.1 cations pfu of Al were measured using  $^{27}\text{Al}$  solid-state NMR spectroscopy. The NMR spectra from the two bridgmanite samples are shown in Fig. 3.3-4 and provide clear evidence for both the CCM and OVM substitutions. The 0.1 Al pfu sample shows peaks that correspond to symmetric octahedral  $\text{AlO}_6$ , as well as distorted  $\text{AlO}_8$  species, which are expected for the CCM where Al enters both the 6 fold oxygen coordinated Si site and 8 fold coordinated Mg site. Additionally, however, peaks for  $\text{AlO}_5$  and  $\text{AlO}_4$  species are also observed in both samples, implying short range ordering of oxygen vacancies around Al substituted Si sites. Furthermore, the spectra show that the OVM is clearly the preferred mechanism in Al-poor bridgmanite (blue), while in bridgmanite with higher Al contents (red) the CCM is proportionately larger, in excellent agreement with site assignments based on electron microprobe analyses.

The OVM reaches its maximum in MgO saturated systems along the  $\text{MgSiO}_3-\text{MgAlO}_{2.5}$  and  $\text{MgSiO}_3-\text{MgAl}_2\text{O}_4$  joins, whereas bridgmanites formed in  $\text{Al}_2\text{O}_3$  and  $\text{SiO}_2$  saturated assemblages are dominated by the CCM substitution with minimal OVM component, regardless of the Al content. As the lower mantle is MgO saturated and the Al contents over which the OVM substitution dominates cover an important range of plausible bridgmanite compositions, quantifying the variation of the OVM component is an important step in determining the physical and chemical properties of the lower mantle.

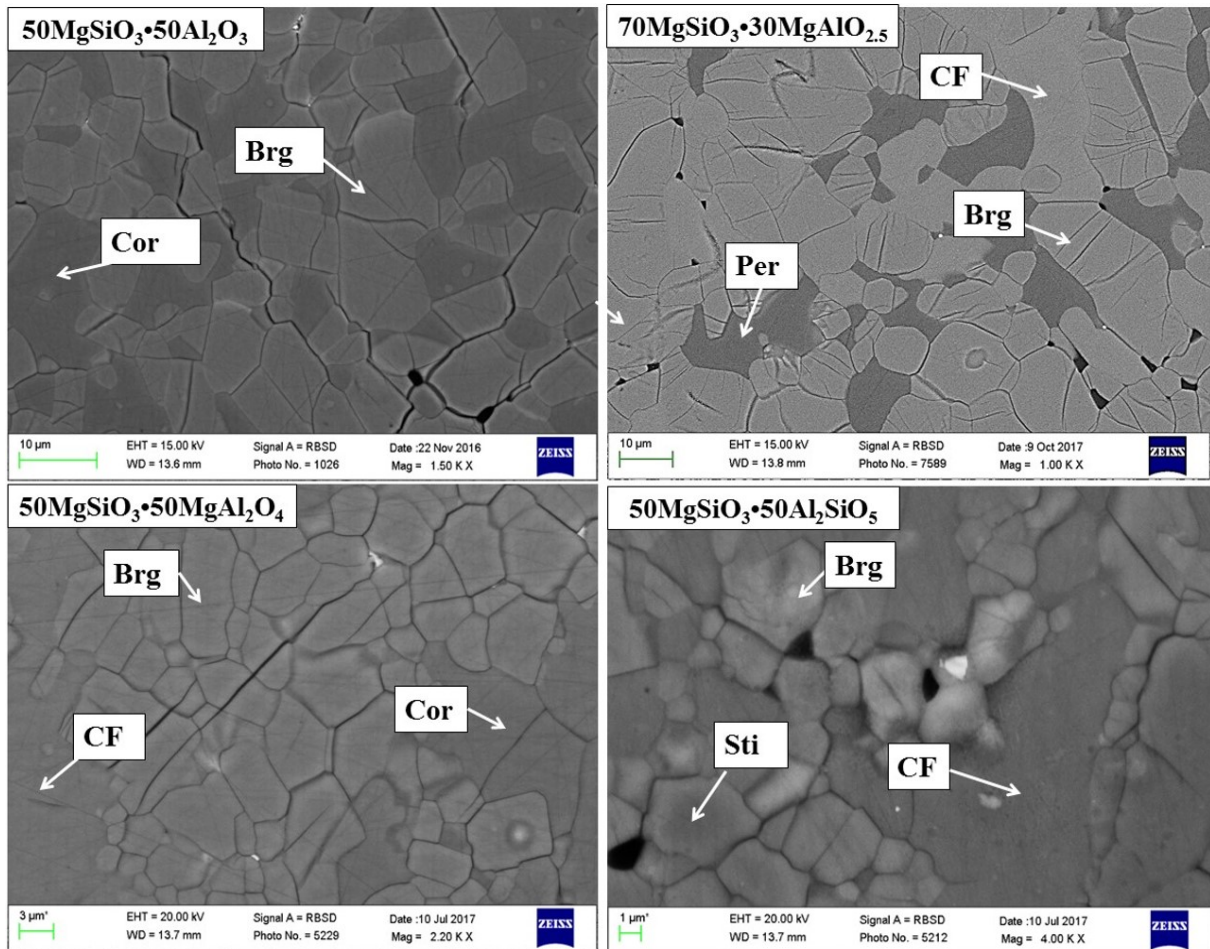


Fig. 3.3-3: Representative back-scattered electron images of run products in the ternary system MgO–AlO<sub>1.5</sub>–SiO<sub>2</sub>. Abbreviations: Brg: bridgmanite; CF: calcium ferrite-type structure of MgAl<sub>2</sub>O<sub>4</sub>; Per: periclase; Cor: corundum; Sti: stishovite.

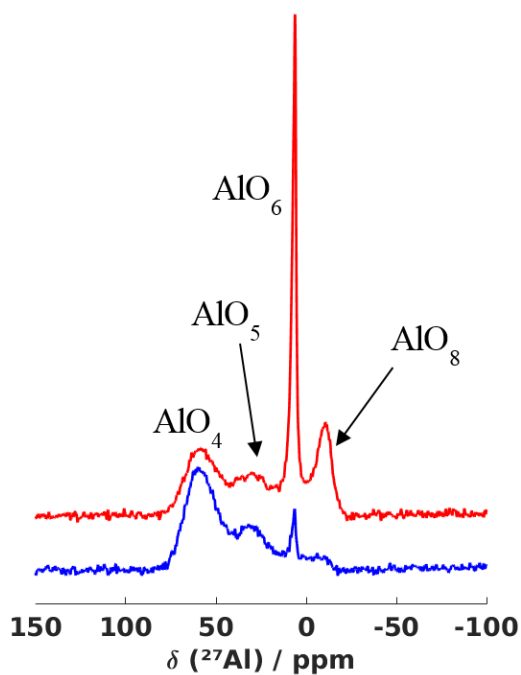


Fig. 3.3-4: <sup>27</sup>Al solid-state NMR MAS spectra of bridgmanite containing 0.05 (blue) and 0.1 (red) Al cations pfu showing the presence of AlO<sub>4</sub> ( $\delta = 70$  ppm), AlO<sub>5</sub> ( $\delta = 40$  ppm), AlO<sub>6</sub> ( $\delta = 6.8$  ppm) and AlO<sub>8</sub> ( $\delta = -2$  ppm) species.

c. *The speciation of Fe and Al in bridgmanite (R. Huang, T. Boffa Ballaran, C.A. McCammon, N. Miyajima and D.J. Frost)*

Understanding the  $\text{Fe}^{3+}$  concentration in perovskite-structured  $(\text{Mg,Fe,Al})(\text{Si,Al,Fe})\text{O}_3$  bridgmanite as a function of composition and oxygen fugacity is important for determining the redox state of the Earth's lower mantle, which in turn influences C-O-H fluid speciation and may have influenced the redox state of the mantle as a whole during core formation. Furthermore, knowledge of the relationship between Al and  $\text{Fe}^{3+}$  in bridgmanite is important for constructing compositional models for the lower mantle that are required to derive and compare seismic velocity-depth profiles for specific lower mantle compositions. Moreover, Fe and Al incorporation mechanisms in bridgmanite also will likely affect lower mantle geochemical and transport properties.

In this study, we are investigating the relationship between  $\text{Fe}^{3+}/\sum\text{Fe}$  in bridgmanite and oxygen fugacity; we synthesized large bridgmanite single crystals of various compositions to constrain the partial molar volumes of the important bridgmanite components and we are exploring their influence on bridgmanite elasticity.

Bridgmanite samples with varying Fe and Al concentrations up to a total of 40 mol. % were synthesized in multianvil runs at 25 GPa and between 1700 ~ 2000 °C. To make large single crystals, we started most experiments water saturated. By adding Fe metal, water or hematite we could access relatively low, intermediate and high oxygen fugacities, which we measured using oxy-thermobarometry methods involving accessory phases. Chemical analyses were conducted using an electron microprobe and  $\text{Fe}^{3+}/\sum\text{Fe}$  ratios were determined using Mössbauer spectroscopy or energy-loss near-edge structure (ELNES) spectroscopy. The unit-cell parameters of single crystals were determined using the eight-position centering method on a HUBER four-circle diffractometer. The reflection intensity data were collected using an Xcalibur diffractometer with  $\text{MoK}\alpha$  radiation and a CCD detector.

An SEM image of a recovered sample which contained excess  $\text{Fe}_2\text{O}_3$  in the starting material is shown in Fig. 3.3-5. In the recovered run products bridgmanite coexists with ferropericlase and the newly discovered multivalent iron oxide  $(\text{Mg,Fe})_4\text{O}_5$ , which has a *Cmcm* structure.

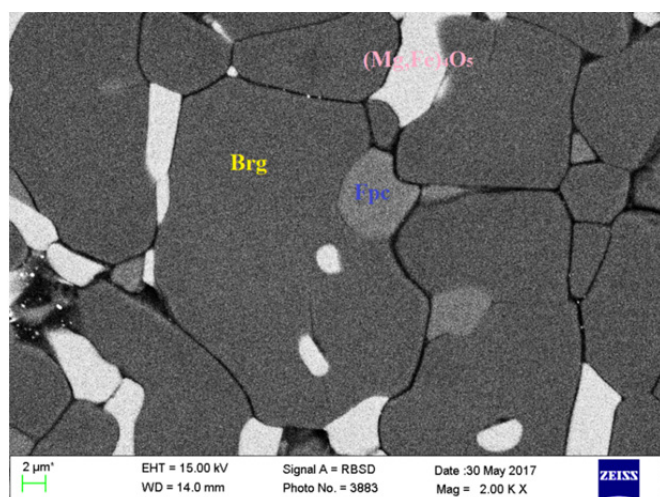


Fig. 3.3-5: Scanning electron microscope image of Fe–Al bridgmanite crystals recovered from a multianvil experiment. The starting material contained excess hematite and the recovered bridgmanite coexisted with ferropericlase and  $(\text{Mg,Fe})_4\text{O}_5$ .

Using microprobe and  $\text{Fe}^{3+}/\Sigma\text{Fe}$  ratio determinations for all samples, the site occupancies of  $\text{Fe}^{3+}$  can be determined as a function of the Al content, as shown in Fig. 3.3-6. For the bridgmanite syntheses we attempted to keep the bulk Fe concentration constant, while changing only the  $\text{Fe}^{3+}/\Sigma\text{Fe}$  ratio, although this becomes difficult as Fe and  $\text{Fe}_2\text{O}_3$  saturation often lead to increases in the bridgmanite bulk Fe content. Our experiments, combined with previous data, show three broad regimes of differing  $\text{Fe}^{3+}$  incorporation as a function of Al content. At low Al contents,  $\text{Fe}^{3+}$  appears to occupy predominantly the Si, *i.e.*, B, site of the bridgmanite structure and the charge balance is likely maintained through the formation of oxygen vacancies. At Al cation contents between 0.03 and 0.08,  $\text{Fe}^{3+}$  appears to substitute sub-equally between both A and B sites forming a charge balanced coupled substitution component  $\text{FeFeO}_3$ . When Al contents exceed  $\sim 0.08$  cations per formula unit, which also corresponds approximately to the  $\text{Fe}^{3+}$  content of the synthesized bridgmanites,  $\text{Fe}^{3+}$  appears to strongly prefer the Mg site, *i.e.*, A site, producing a charge coupled  $\text{FeAlO}_3$  component. Samples from this study, which were mainly produced with Al contents of  $\sim 0.07$  cations per formula unit, show an almost linear relationship between  $\text{Fe}^{3+}/\Sigma\text{Fe}$  and  $\log f\text{O}_2$ . Using unit cell parameters of the different bridgmanite samples we estimate the partial molar volumes for  $\text{Fe}^{3+}$  and Al substitution components. These results indicate that the  $\text{FeAlO}_3$  component should be the most favoured substitution mechanism at high pressures.

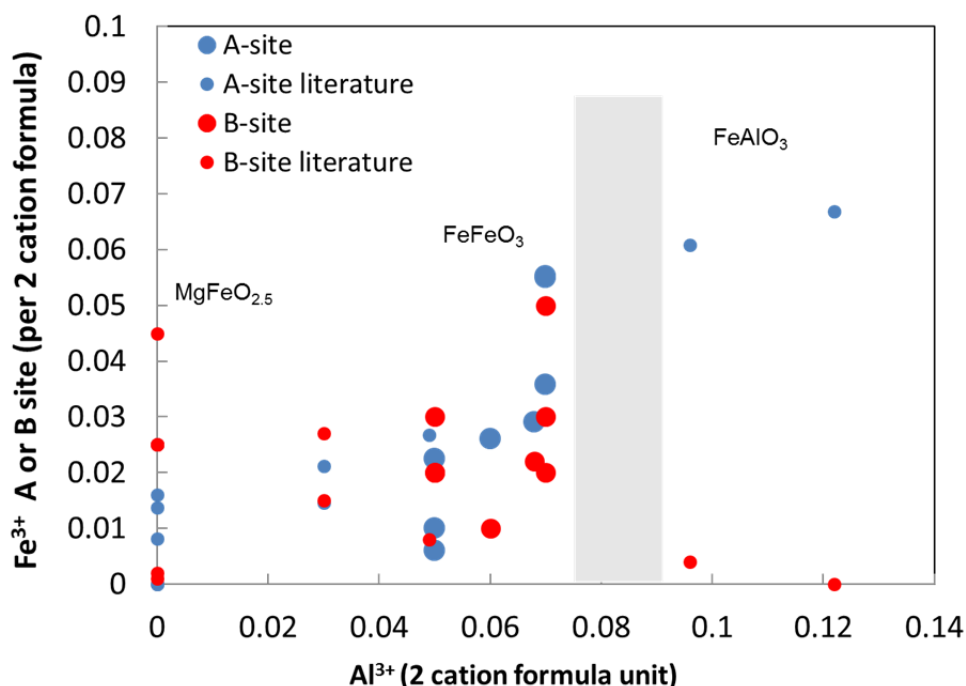


Fig. 3.3-6: The  $\text{Fe}^{3+}$  distribution between bridgmanite A and B crystallographic sites as a function of  $\text{Al}^{3+}$  content per 2 cations formula unit. As the Al content increases, the dominant substitution mechanism changes from  $\text{MgFeO}_{2.5}$  to  $\text{FeFeO}_3$  and finally to  $\text{FeAlO}_3$ . The shaded region marks a seemingly dramatic change in substitution mechanism to  $\text{FeAlO}_3$ . This region is also consistent with the bridgmanite Al content expected for an ultrabasic lower mantle, at pressures above those of garnet stability.

**d. Phase relations and crystal chemistry of FeAlO<sub>3</sub>-bearing bridgmanite** (Z. Liu, L.S. Dubrovinsky, C.A. McCammon and T. Katsura)

MgSiO<sub>3</sub> bridgmanite, the most abundant phase in the lower mantle (about 80 % by volume), can contain a significant amount of aluminium and iron. Iron in bridgmanite preferably forms the Fe<sup>3+</sup>AlO<sub>3</sub> component in the presence of aluminium through the reaction of Al<sub>2</sub>O<sub>3</sub> + 3Fe<sup>2+</sup>O = 2Fe<sup>3+</sup>AlO<sub>3</sub> + Fe<sup>0</sup> even under low oxygen fugacity conditions. The incorporation of Fe<sup>3+</sup>AlO<sub>3</sub> can significantly affect the physical and chemical properties of bridgmanite, such as

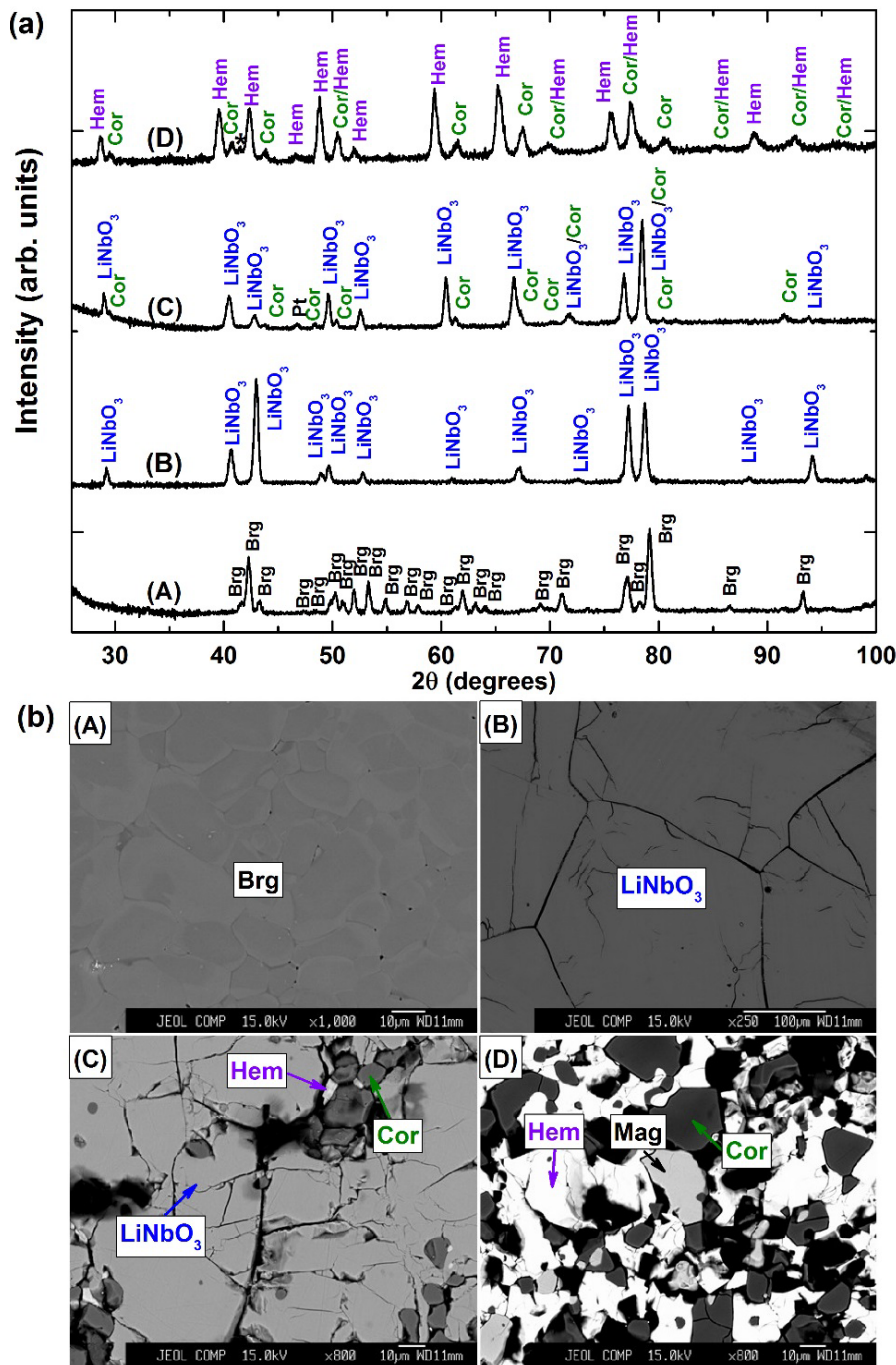


Fig. 3-3.7: (a) Representative X-ray diffraction profiles and (b) back-scattered electron images of run products in the system MgSiO<sub>3</sub>-FeAlO<sub>3</sub>. A) 15 mol. % FeAlO<sub>3</sub>; B) 50 mol. % FeAlO<sub>3</sub>; C) 75 mol. % FeAlO<sub>3</sub> and D) 100 mol. % FeAlO<sub>3</sub>.

Abbreviations:  
 Brg, bridgmanite;  
 Cor, corundum;  
 Hem, hematite;  
 Mag, magnetite  
 (star symbol).

compressibility, elasticity, electrical conductivity and Mg-Fe partitioning in lower mantle phases. Hence, the existence of FeAlO<sub>3</sub> component in bridgmanite must be evaluated to elucidate the complex crystal chemistry of bridgmanite and thereby to constrain the mineralogy of the lower mantle.

Here, we investigated the phase relations and crystal chemistry of bridgmanite in the system MgSiO<sub>3</sub> - FeAlO<sub>3</sub> at a constant pressure of 27 GPa and a constant temperature of 2000 K in a multianvil apparatus with tungsten carbide anvils. We found that starting materials with FeAlO<sub>3</sub> content below 40 mol. % would crystallize into a single phase of bridgmanite. The run product recovered from the synthesis with the starting material containing 50 mol. % FeAlO<sub>3</sub> contain a LiNbO<sub>3</sub>-type structured phase with a rhombohedral symmetry (afterwards defined as LiNbO<sub>3</sub>-type phase) rather than the bridgmanite phase with an orthorhombic structure (Fig. 3.3-7), whereas that recovered from the starting composition containing 75 mol. % FeAlO<sub>3</sub> consisted of LiNbO<sub>3</sub>-type phase together with corundum and some trace of hematite and pure FeAlO<sub>3</sub> decomposed into corundum, hematite and trace amount of magnetite. This result further confirms that pure FeAlO<sub>3</sub> bridgmanite does not exist at lower mantle conditions, and therefore, a maximum of the FeAlO<sub>3</sub> solubility in the bridgmanite exists. Our electron microprobe analysis suggests that bridgmanite can incorporate a maximum of 63 mol. % FeAlO<sub>3</sub> content through the charge coupled substitution in the uppermost region of the lower mantle. Although bridgmanite has been put forward as a potential host for water and argon in the lower mantle by trapping them in oxygen vacancies, such capabilities will rapidly decrease with the enrichment of FeAlO<sub>3</sub> component in the bridgmanite because the enrichment of FeAlO<sub>3</sub> component would significantly suppress of the existence of oxygen vacancies.

*e. Iron behaviour in Fe,Al-bearing bridgmanite between 35-80 GPa (D.M. Vasiukov/Bayreuth, J. van Driel/London, C.A. McCammon, E. Bykova/Hamburg, M. Bykov, G. Aprilis, V. Cerantola/Grenoble, I. Kuppenko/Münster, T. Kawazoe, R. Myhill, V. Prakapenka/Argonne, H.-P. Liermann/Hamburg, M. Hanfland and A.I. Chumakov/Grenoble, L.S. Dubrovinsky and N.A. Dubrovinskaia/Bayreuth)*

Bridgmanite is the most abundant mineral in the Earth's interior and volumetrically dominates the lower mantle. The behaviour of iron (namely, its oxidation and spin state, cation site preference, etc.) in bridgmanite at lower mantle conditions has been highly debated and remains controversial. While iron in Fe,Al-bearing bridgmanite synthesised in a multianvil press (~ 26 GPa) has a high proportion of ferric iron independent of oxygen fugacity ( $\text{Fe}^{3+}/\text{Fe}_{\text{tot}} \sim 60\%$ ), a recent study in the literature reported that  $\text{Fe}^{3+}/\text{Fe}_{\text{tot}}$  of bridgmanite in a laser-heated diamond anvil cell varies with synthesis pressure. To investigate the reason for this difference, we carried out a series of experiments on bridgmanite using a laser-heated diamond anvil cell.

We used two glasses as precursors for bridgmanite, both with the same approximate composition ( $\text{Mg}_{0.88}\text{Fe}_{0.09}\text{Al}_{0.06}\text{Si}_{0.97}\text{O}_3$ ) but different  $\text{Fe}^{3+}/\text{Fe}_{\text{tot}}$  ratios. Part of the first glass ( $\text{Fe}^{3+}/\text{Fe}_{\text{tot}} \sim 50\%$ ) was annealed in a CO-CO<sub>2</sub> gas mixing furnace to make the second glass ( $\text{Fe}^{3+}/\text{Fe}_{\text{tot}} \sim 0\%$ ). After laser heating the two glasses in a diamond anvil cell at pressures of 35-80 GPa, the obtained bridgmanite samples were investigated by X-ray diffraction (XRD) at different synchrotron facilities (APS, PETRA III, ESRF) to determine the crystal structure, and by Mössbauer Spectroscopy using the Synchrotron Mössbauer Source at the Nuclear Resonance Beamline ID18 (ESRF) to determine the iron electronic state.

Data analysis is still ongoing, but already our results have shown that  $\text{Fe}^{3+}/\text{Fe}_{\text{tot}}$  in bridgmanite depends on the oxidation state of the precursor glass, where the oxidised glass gave bridgmanite with a higher  $\text{Fe}^{3+}/\text{Fe}_{\text{tot}}$  ratio. We observed evidence for the disproportionation reaction  $3\text{Fe}^{2+} \leftrightarrow 2\text{Fe}^{3+} + \text{Fe}^0$  in bridgmanite made from reduced glass. While it is challenging to detect hcp- or bcc-iron phases using XRD due to their small abundance and the overlap of diffraction peaks, we confirmed the presence of bcc-iron in Mössbauer spectra of decompressed samples (Fig. 3.3-8) synthesised from reduced glass at pressures up to 50 GPa.

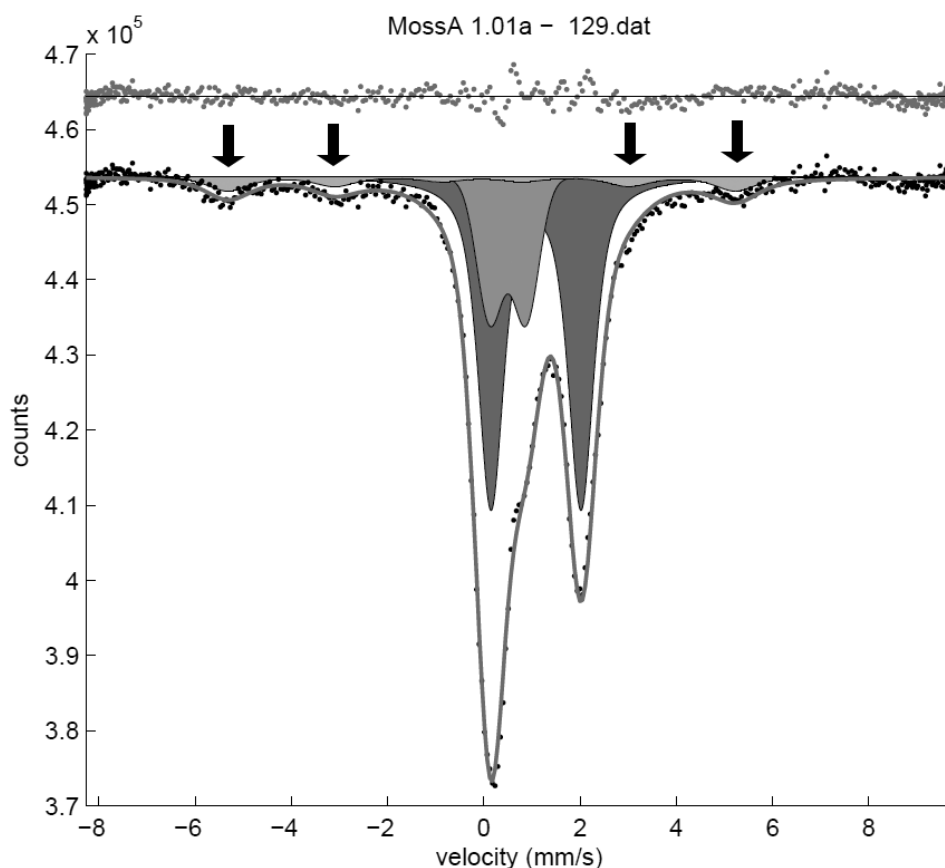


Fig. 3.3-8: Mössbauer spectrum of bridgmanite after decompression. The sample was synthesised by laser heating the reduced glass at 35 GPa. Doublets with large and small quadrupole splitting are assigned to  $\text{Fe}^{2+}$  and  $\text{Fe}^{3+}$ , respectively. Arrows indicate the outer lines of the magnetic sextet assigned to bcc-iron.

**f. Coordination and local structure of silica to core-mantle boundary pressure** (S. Petitgirard, C. Sahle/Grenoble, C. Weis/Dortmund, K. Gilmore/Grenoble, G. Spiekermann/Potsdam, M. Wilke/Potsdam and C. Sternemann/Dortmund)

SiO<sub>2</sub> is the main constituent of the deep silicate Earth controlling the silicate-network structure of melts, thus their physical properties at depth. We have measured the structural changes in SiO<sub>2</sub> glass under pressure up to 110 GPa using X-ray Raman Scattering spectroscopy, simultaneously at the O K-edge and for the first time the Si L<sub>2,3</sub> edge (Fig. 3.3-9). We have combined our measurement with molecular dynamic calculations (Fig. 3.3-9) and we found a striking match between the two experimental techniques. This allows the

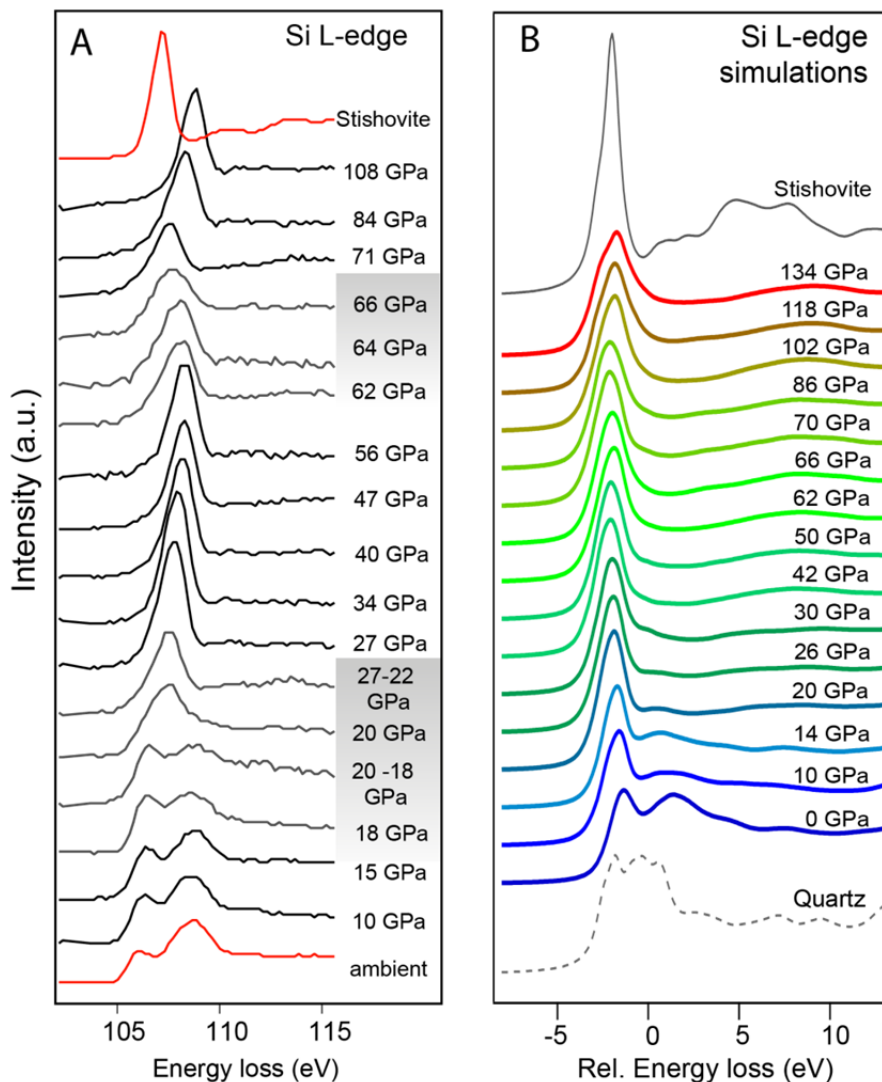


Fig. 3.3-9: A) Measurements of the Si L<sub>2,3</sub> edge in eV as a function of pressure. The shaded areas represent the two largest changes in the spectra from 20 to 27 GPa and from 60 to 70 GPa, respectively. The spectra in red are reference spectra collected at ambient conditions for a SiO<sub>2</sub> glass and for stishovite; B) Calculated spectra of the Si L<sub>2,3</sub> edge from 0 to 134 GPa and references samples (stishovite and quartz) obtained from first principle MD calculations.

short-range and electronic structure of silicon and oxygen as well as the coordination evolution of silicon to core-mantle boundary (CMB) pressures to be determined. The four-fold silicon species are preserved up to about 18 GPa and disappear in the pressure range between 20 to 27 GPa (Fig. 3.3-9). At such pressures, the four-fold Si species are replaced by five-fold coordinated species, mixed with six-fold Si species. The latter increase gradually over 35-40 GPa up to 60 GPa. At this pressure, a further transition is observed in both edges corresponding to a drop of the five-fold Si species (Fig. 3.3-9). The six-fold Si becomes dominant at  $P > 60$  GPa in the deep lower mantle while the remaining five-fold Si vanishes gradually. From our MD results, the average coordination number of six is achieved for pressures corresponding to the deep mantle close to CMB pressure. Higher coordination will take place only for pressures equivalent or higher than 130 GPa. This may explain the further densification observed by means of Brillouin spectroscopy. The addition of cation-network modifiers in melts may shift this densification to lower pressure making magmas neutrally buoyant in the deep mantle on top of the CMB.

**g.** *Squeezed silica with pentacoordinate silicon and face-sharing octahedra* (E. Bykova/Hamburg, M. Bykov, A. Černok/London, N.A. Dubrovinskaia/Bayreuth, L.S. Dubrovinsky, J. Tidholm and S.I. Simak/Linköping, O. Hellman/Pasadena, M. Belov and I.A. Abrikosov/Moscow, H.-P. Liermann/Hamburg, M. Hanfland/Grenoble, C. Prescher and V.B. Prakapenka/Argonne)

Silica ( $\text{SiO}_2$ ) is known for having often an enigmatic behaviour at high pressures as well as rich polymorphism, which has been extensively studied to understand the behaviour of materials in deep planetary interiors. So far, the identified high-pressure and high-temperature polymorphs of  $\text{SiO}_2$  possess structures built of four- or six- coordinated silicon, whereas the existence of penta-coordinate silicon in silica phases was only theoretically predicted. Moreover the transformation path to the different polymorphs depends on the starting  $\text{SiO}_2$  phase.

Coesite is hitherto the densest known stable silica polymorph with tetrahedrally coordinated silicon and, as such, it plays an important role as a model material for a large class of technologically and scientifically important framework silicates. Coesite also is especially interesting because theory predicts its possible direct transformation to seifertite (the  $\alpha$ - $\text{PbO}_2$ -structured post-stishovite  $\text{SiO}_2$  phase) at the relatively low pressures of about 22 GPa, whereas seifertite is known to be thermodynamically stable only above 100 GPa.

Here we apply single-crystal X-ray diffraction coupled with diamond anvil cells in order to both characterize the  $\text{SiO}_2$  phases which appear on compression of coesite and to describe their high-pressure behaviour. Several independent experiments were performed at different synchrotron radiation facilities to pressures over 70 GPa. In agreement with previous data, in all experiments we observed the transformation of coesite-I to coesite-II (at pressures exceeding 20 GPa). Upon further compression (above 25 GPa) coesite-II transformed to another phase with triclinic unit cell, which we called coesite-III. Similar to coesite-I and

coesite-II, the major building blocks of the structure are four-member rings of SiO<sub>4</sub> tetrahedra (Fig. 3.3-10). Phase transitions to coesite-II and coesite-III have a minor effect on the molar volume, so that the compressional behaviour of all coesite phases with tetra-coordinated silicon may be described by the same 3<sup>rd</sup> order Birch-Murnaghan equation of state (EOS) with  $V_0/Z=34.20(1) \text{ \AA}^3$ ,  $K_0=103(2) \text{ GPa}$  and  $K'=3.02(15)$ .

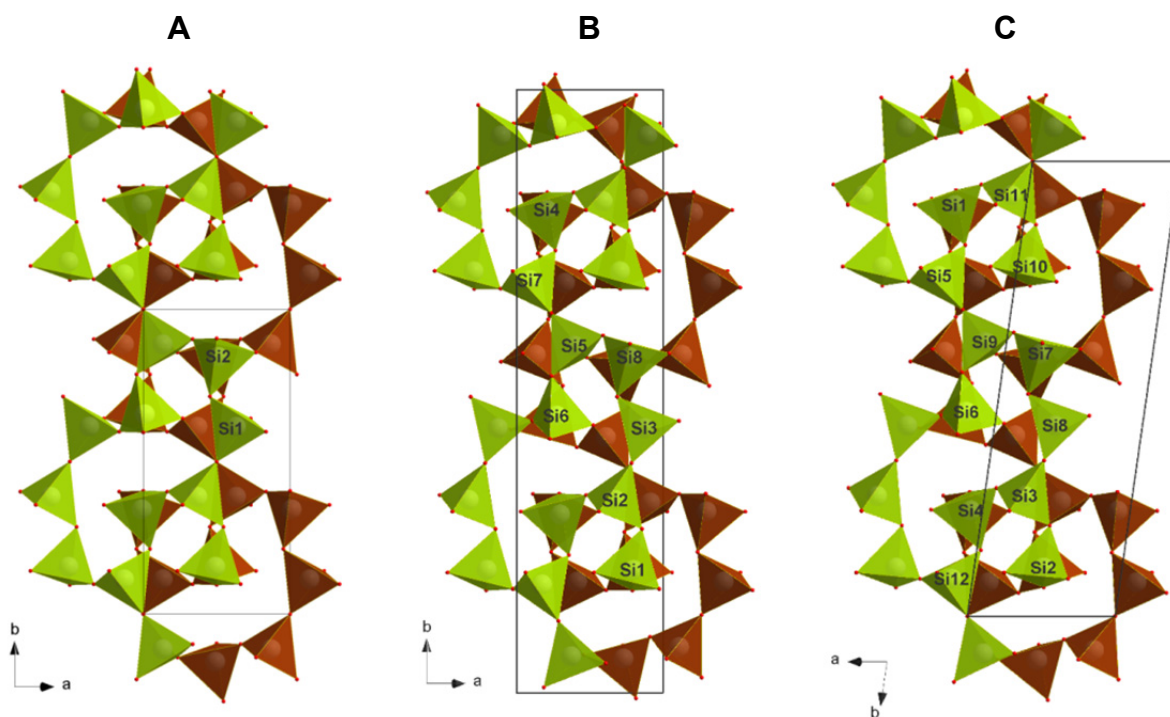


Fig. 3.3-10: Crystal structures of A) coesite-I (20 GPa); B) coesite-II (27 GPa); and C) coesite-III (28 GPa).

On compression beyond ca. 30 GPa, a new set of reflections suggest that a new triclinic (space group  $P-1$ ) phase, which we called coesite-IV, appears with lattice parameters distinctly different from any of those known for other coesite-derived polymorphs. Upon further compression, the reflections of coesite-IV split giving rise to another new triclinic (space group  $P-1$ ) phase, coesite-V. Above  $\sim 50$  GPa, only coesite-V is present. The structure of coesite-IV possesses *tetra*-, *penta*- and *hexa*-coordinated silicon; the structure of coesite-V maintains only *penta*- and *hexa*-coordinated silicon (Fig. 3.3-11). The structures of coesite-IV and coesite-V may be considered as a three-dimensional framework of face- and edge-sharing octahedra with the empty space filled by SiO<sub>5</sub> and SiO<sub>4</sub> (in coesite-IV), or only SiO<sub>5</sub> (in coesite-V) polyhedra (Fig. 3.3-11). The presence of face-sharing octahedra has so far never been observed or even expected in silica, silicates or glasses. Our results suggest that possible silicate liquids in the Earth's lower mantle may have complex structures making them more compressible compared to previously considered models.

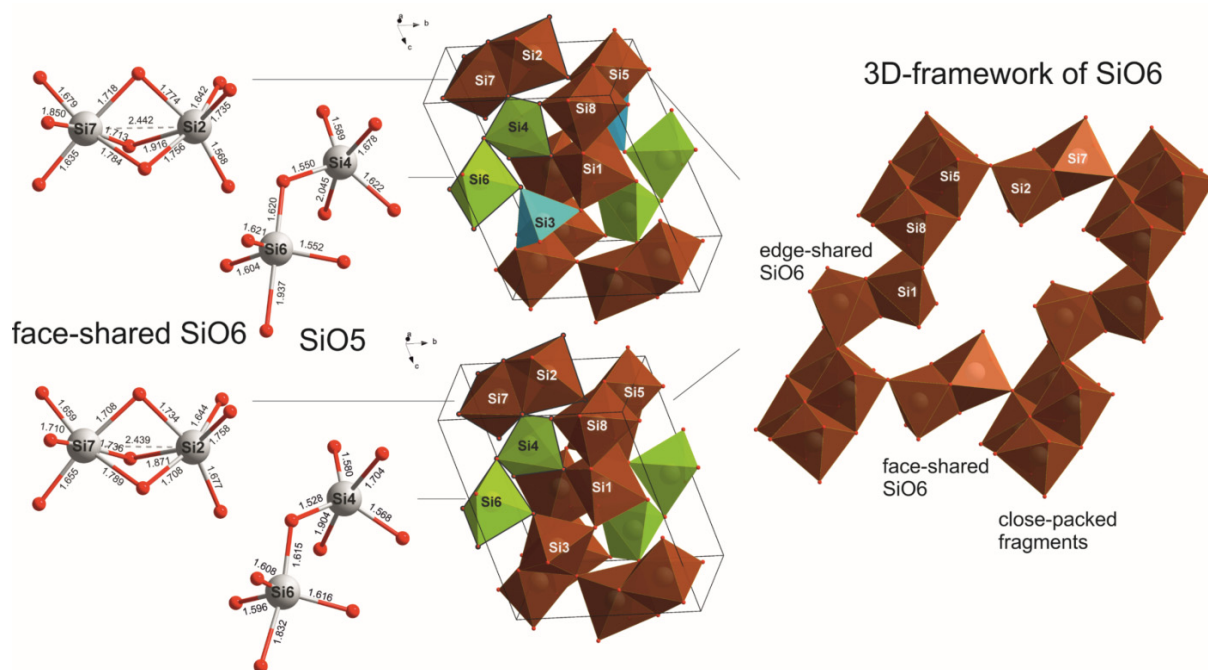


Fig. 3.3-11: Crystal structures of coesite-IV and coesite-V. Polyhedral models of the structures of coesite-IV (top) and coesite-V (bottom) (SiO<sub>6</sub> octahedra are brown, SiO<sub>5</sub> polyhedra are green; SiO<sub>4</sub> tetrahedra are blue); ball and stick models of polyhedra representing building blocks of the structures of coesite-IV and coesite-V (two SiO<sub>6</sub> octahedra sharing a face; two SiO<sub>5</sub> polyhedra sharing a corner) (left); a fragment of the structures, similar for both coesite-IV and coesite V, showing a 3D framework of SiO<sub>6</sub> octahedra (right).

**h.** *Pentacoordinated silicon in the high-pressure polymorph of danburite (A. Pakhomova and E. Bykova/Hamburg, M. Bykov, K. Glazyrin/Hamburg, B. Gasharova/Karsruhe, H.-P. Liermann/Hamburg, M. Mezouar/Grenoble, L. Gorelova and S. Krivovichev/Saint-Petersburg, in collaboration with L.S. Dubrovinsky)*

Due to their high technological and geological relevance, silicates are one of the most studied inorganic compounds. At ambient conditions, silicon in silicates is almost exclusively coordinated by four oxygen atoms, while at high pressure its coordination increases from four- to six-fold. Only very few examples of structures with five-fold coordinated Si are known and these examples are limited to the cases where SiO<sub>5</sub> groups coexist with SiO<sub>4</sub> tetrahedra and/or SiO<sub>6</sub> octahedra.

Here we report a high-pressure single-crystal X-ray diffraction study of danburite, CaB<sub>2</sub>Si<sub>2</sub>O<sub>8</sub>, for which we have discovered that it is the first compound showing a step-wise transition of Si coordination from tetrahedral to octahedral through a trigonal bipyramid. Along the compression, Si<sub>2</sub>O<sub>7</sub> groups of danburite first transform into chains of corner-sharing SiO<sub>5</sub> trigonal bipyramids (danburite-II) and later into chains of edge-sharing SiO<sub>6</sub> octahedra (danburite-III) (Fig. 3.3-12).

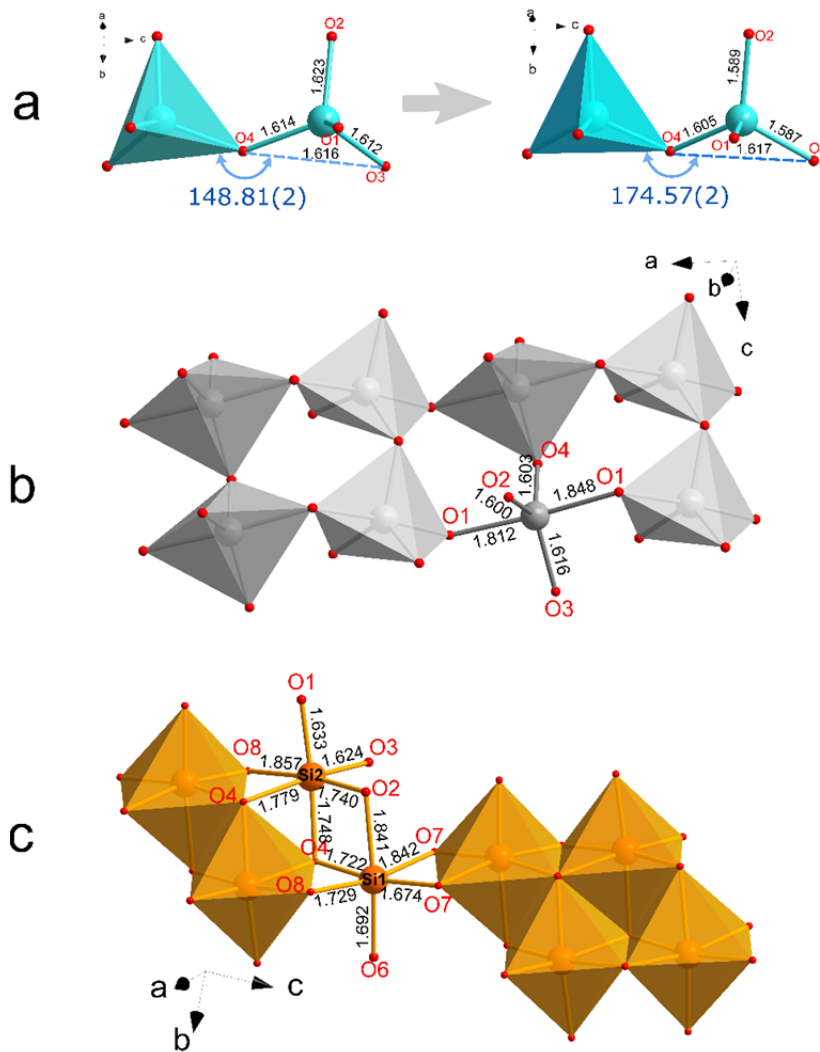


Fig. 3.3-12: Evolution with pressure of silicon-based structural units in danburite. a) Distortion of  $\text{Si}_2\text{O}_7$  ditetrahedral group from 1.1(1) to 22.6(1) GPa. Note the respective increase of  $\text{O}_3\text{-O}_4\text{-O}_3$  angle from  $148.81(2)$  to  $174.57(2)^\circ$  that causes the anomalous enlargement of the  $c$ -axis during compression; b) a chain built on  $\text{SiO}_5$  trigonal bipyramids in the structure of danburite-II ( $Pnam$ ) at 25.4(1) GPa; c) the chain built on edge-sharing  $\text{SiO}_6$  octahedra in danburite-III ( $P-1$ ) at 25.4(1) GPa. The Si-O bond distances are given in angstroms.

The mechanism of such pressure-induced transformation is based on the evolution of the crystal structure towards the close packing architecture. At ambient conditions danburite possesses a relatively open structure, which has no direct relation to a close-packed arrangement of oxygen atoms. In contrast, danburite-III is dense and its structure is based upon a cubic close-packed (CCP) arrangement formed by both Ca and O atoms. The structure of danburite-II can be described as having elements of distorted CCP and hexagonal close-packed (HCP) arrangement. The observed unusual  $\text{SiO}_5$  configuration was found to be a consequence of filling up the pentacoordinated voids in the distorted hexagonal close packing of danburite-II.

Our results on the phase transitions of danburite and comparisons with other known examples of silicates with pentacoordinated silicon suggest that  $\text{SiO}_5$  groups may be not as rare as previously thought and may form as intermediate configurations upon: (a) transformation of silicates with relatively open structures into phases based upon close packing of oxygen (or oxygen and large cations) and (b) transformations of close-packed structures that involves transition between tetrahedral and octahedral voids due to the shifts of close-packed layers.

*i. Reaction of  $\text{MgCO}_3$  and Fe observed by transmission electron microscopy (F. Maeda/Sendai, N. Miyajima; S. Kamada, T. Sakamaki and A. Suzuki/Sendai)*

Carbonate minerals are major carbon-bearing components in subducting slabs and play a role in the deep carbon cycle in the Earth's interior. Magnesite,  $\text{MgCO}_3$ , especially has been considered to be the most stable carbonate in a wide P–T range down to the lowermost mantle. The stability of magnesite depends on redox conditions, characterized by oxygen fugacity ( $f\text{O}_2$ ). The lower mantle can be reduced enough for metallic iron to exist and hence magnesite is expected to transform into diamond or iron-carbide through deep subduction. However, there is a lack of experimental data to properly constrain the behaviour of  $\text{MgCO}_3$  at the pressures, temperatures and  $f\text{O}_2$  of the deep lower mantle.

We investigated a possible reaction between  $\text{MgCO}_3$  and metallic Fe at lower mantle conditions by observing textures of a recovered sample from a laser-heated diamond anvil cell (LHDAC) experiment. A natural single crystal of magnesite ( $\text{Mg}_{0.994}\text{Ca}_{0.003}\text{Fe}_{0.003}\text{CO}_3$ ) from Bahia in Brazil and reagent metallic iron (Mitsuwa Chemical Co., purity 99.5 %) were used as starting materials. The single crystal of magnesite was sandwiched by two iron foils. The samples were surrounded by KCl pressure mediums in the DAC chamber. The high P–T experiment was conducted at 79 GPa and 2500 K for 30 minutes. The sample was recovered from LHDAC to ambient conditions and prepared using a focused ion beam (FIB) system (Fig. 3.3-13a) for the analysis with transmission electron microscopy (TEM). A qualitative chemical analysis was conducted using energy dispersive X-ray spectroscopy (EDXS).

The scanning TEM image of the recovered sample shows that magnesite and iron foils have reacted along the contact area (Fig. 3.3-13b). The reaction area is less than 1  $\mu\text{m}$  in width and shows an Fe-rich and Mg-poor nature based on the EDXS mapping (Fig. 3.3-14). The chemical feature of the reaction area suggests that the reaction products may be iron-carbide and/or magnesiowustite. The narrow width of the reaction area can be caused by a large temperature gradient during laser heating: the reaction between magnesite and iron proceeded at a higher temperature near the iron foils than the temperature present inside the magnesite crystal. However, if the temperature gradient is small, magnesite, iron, and their reaction products might coexist as a stable phase assemblage. The width of the reaction area can be then related to the diffusion of elements during laser heating. If this assumption is correct, magnesite is stable under reduced lower mantle conditions even in the presence of metallic iron.

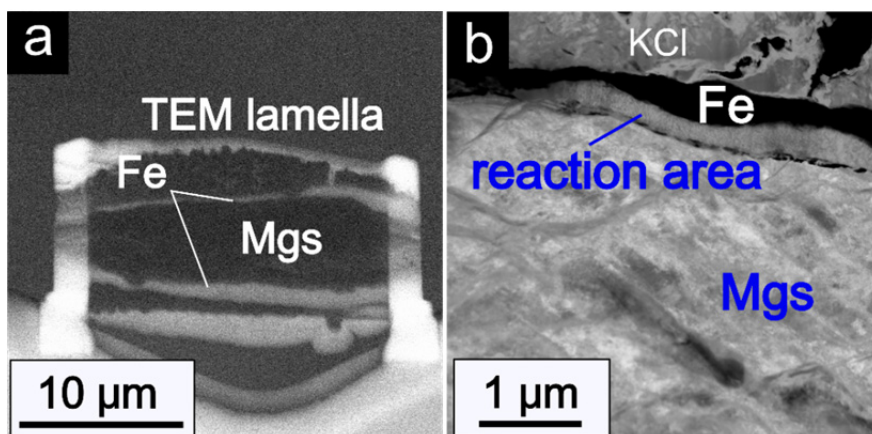


Fig. 3.3-13: (a) Backscattered electron image of a lamella from the recovered LHDAC sample made by FIB. (b) Dark-field STEM image of the reaction rim between magnesite (Mgs) and iron (Fe).

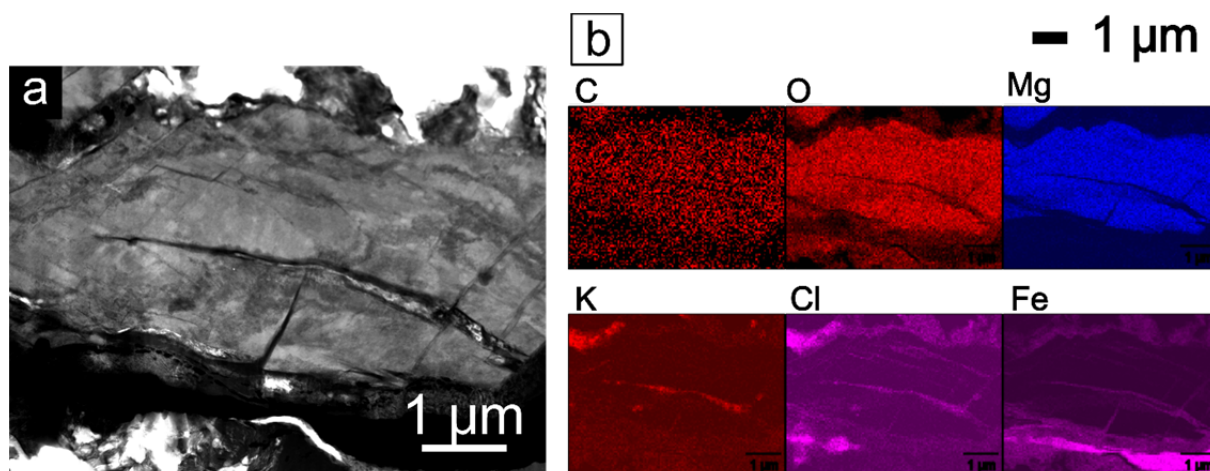


Fig. 3.3-14: (a) Bright-field STEM image of the analysed lamella. (b) Elemental mapping acquired using STEM-EDXS.

**j.** *Crystal structure of Fe-bearing  $\text{MgCO}_3$  tetracarbonate at 95 GPa from single-crystal X-ray diffraction (S. Chariton, E. Bykova/Hamburg, M. Bykov, V. Cerantola/Grenoble, E. Koemets, G. Aprilis, M. Hanfland/Grenoble, C.A. McCammon and L.S. Dubrovinsky)*

Much interest has been focused recently on the high-pressure behaviour of carbonates due to recent discoveries of novel compounds with tetrahedral  $\text{CO}_4^{4-}$  units. According to theoretical predictions, the existence of  $\text{CO}_4$ -bearing carbonates stimulates further discussion concerning their role as potential analogues for silicates, their potential existence in the complex mineralogy of the D'' region as well as their involvement in crystal-chemical reactions between silicates and carbonates at depths greater than 1600 km within the Earth.

In spite of the potential importance of these tetrahedrally-coordinated carbonates, they still are poorly explored because their accurate structure characterization is very challenging. Here, we

describe the high-pressure crystal structure of a Fe-bearing  $\text{MgCO}_3$  tetracarbonate determined using single-crystal X-ray diffraction coupled with synchrotron radiation.

The synthesis of  $\text{Fe}_{0.1}\text{Mg}_{0.9}\text{CO}_3$  single crystals was performed using a multianvil apparatus. Subsequently, a crystal of less than  $10\ \mu\text{m}$  in size with high quality X-ray diffraction profiles was loaded in a diamond anvil cell with Ne as a pressure-transmitting medium. Using diamonds of  $120\ \mu\text{m}$  culet size, the sample was compressed to 94 GPa. A double-sided laser heating system was then used to heat the sample at  $\sim 2700(150)$  K. Single-crystal X-ray Diffraction (SCXRD) measurements were performed at the ID15b beamline of the European Synchrotron Radiation Facility (Grenoble, France).

Before heating, the structure was indexed in the  $R\bar{3}c$  space group, which is typical for calcite-type structured carbonates. The structure is built up from  $(\text{Mg,Fe})\text{O}_6$  octahedra (with  $\text{Fe}^{2+}$  in the low spin state) and  $\text{CO}_3$  planar equilateral triangular groups arranged in a manner characteristic for distorted NaCl-type structures. After heating, a complete structure rearrangement took place. The new phase observed ( $\text{Fe}_{0.4}\text{Mg}_{2.6}\text{C}_3\text{O}_9$ ) belongs to the family of tetrahedrally coordinated carbonates. The structure has a monoclinic symmetry ( $C2/m$ ) and consists of 3-membered rings of  $\text{CO}_4$  tetrahedra alternated with  $(\text{Fe,Mg})$  polyhedra perpendicular to the b-axis (Fig. 3.3-15). We can distinguish three crystallographic cation positions: 1) Me1 site which is occupied by 0.6 atoms of Mg and 0.4 atoms of Fe surrounded by 8 oxygens forming bicapped prisms; 2) Me2 occupied preferentially by Mg (0.9) and only with minor amount of Fe (0.1) also 8-coordinated by oxygen, forming square antiprisms; and 3) Me3 which is fully occupied by Mg in  $\text{MgO}_6$  octahedra (Fig. 3.3-15).

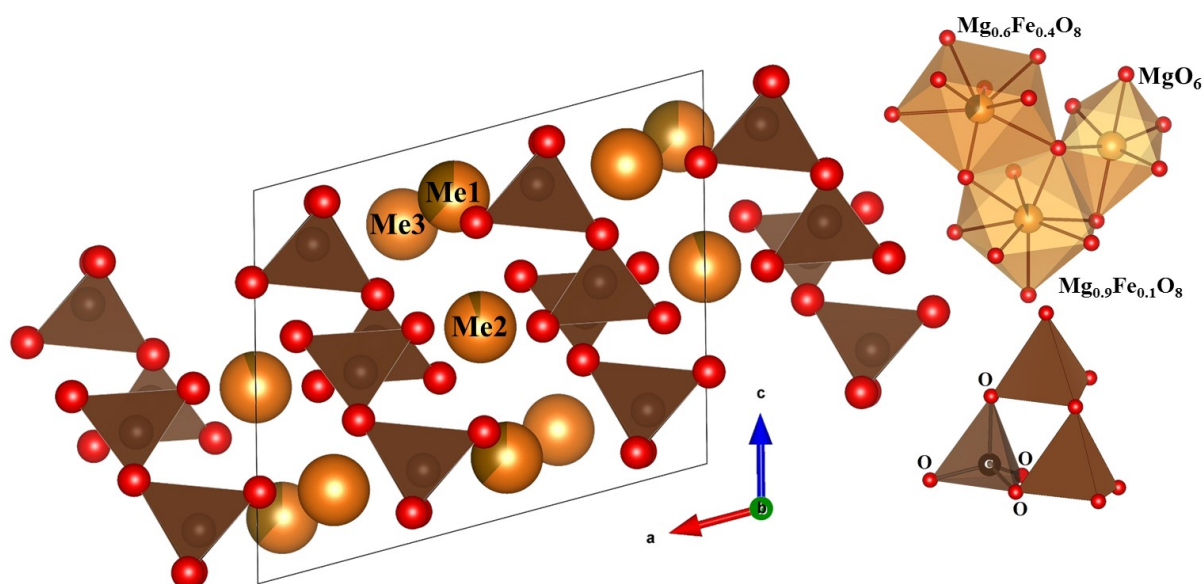


Fig. 3.3-15: The crystal structure of  $\text{Fe}_{0.4}\text{Mg}_{2.6}\text{C}_3\text{O}_9$  tetracarbonate with characteristic  $\text{CO}_4$  tetrahedra units.

Single-crystal X-ray diffraction is a powerful and unique tool to reveal the complex structure of carbonates and their high-pressure tetracarbonate polymorphs. We have previously described other forms of tetracarbonate structures. For example,  $\text{MnC}_2\text{O}_5$  forms after decomposition of  $\text{MnCO}_3$  at  $\sim 65$  GPa, while  $\text{Fe}_4\text{C}_3\text{O}_{12}$  and  $\text{Fe}_4\text{C}_4\text{O}_{13}$  form after decomposition of  $\text{FeCO}_3$  at 74 and 94 GPa, respectively. Formation of  $\text{Mg}_2\text{Fe}_2\text{C}_4\text{O}_{13}$  after heating a 70 % Fe-bearing magnesite at 135 GPa has been reported in the literature. These results lead to two conclusions. Firstly, it is clear that specific carbonate stability fields depend strongly on stoichiometry and on the type of metal cation present. Secondly,  $\text{CO}_4$  units have the ability to form polymerisable networks and thus can be more flexible than previously thought and more similar to silicates. Such important observations have significant implications for carbon reservoirs and offer new insights into the global geodynamic carbon cycle.

**k.** *High-pressure behaviour of  $\delta$ -AlOOH and magnesium silicate Phase D (D. Simonova, E. Bykova/Hamburg, M. Bykov, T. Kawazoe and L.S. Dubrovinsky)*

Water takes part in many aspects of the dynamics of the Earth. If water is transported into the deep mantle the viscosity, melting temperature and atomic diffusion properties of the mantle rocks are considerably affected. The properties of high-pressure hydrous minerals, thus, play an important role for the understanding of the petrology and geochemical evolution of the Earth's mantle. In this context water bearing dense phases like  $\delta$ -AlOOH are interesting object to be investigated at elevated pressures and temperatures. So far high-pressure studies of  $\delta$ -AlOOH were performed on single crystals (in case of  $\delta$ -AlOOH) at relatively low pressures (below 12 GPa) resulting in a limited structural information and accuracy of the equation of state of this material.

Here we present results obtained from synchrotron X-ray diffraction of high-quality single-crystals of  $\delta$ -AlOOH collected up to 30 GPa at room temperature. Single crystals of  $\delta$ -AlOOH were synthesised at high-pressure and high-temperature conditions at the Bayerisches Geoinstitut by decomposition of  $\text{Al}(\text{OH})_3$  at 21 GPa and 1050 °C upon heating during 4 hours in a 1000 ton multianvil Haymag press. High-quality single-crystals were selected by X-ray diffraction employing a three-circle Bruker diffractometer equipped with a SMART APEX CCD detector and a high-brilliance Rigaku rotating anode (Mo- $K\alpha$  radiation) with Osmic focusing X-ray optics. The  $\delta$ -AlOOH selected crystals are orthorhombic with unit-cell parameters  $a = 2.827(2)$  Å,  $b = 4.2022(4)$  Å,  $c = 4.709(1)$  Å, and  $V = 56.39(3)$  Å<sup>3</sup>/unit cell. High-pressure single crystal X-ray diffraction measurements were performed at the extreme condition beamline P02.2 at PETRA III (Hamburg) using a wavelength of 0.28995 Å. A less than 30 µm small crystal of  $\delta$ -AlOOH was insert in a diamond cell (250 µm diameter culets) together with a ruby for pressure calibration. Neon was used as pressure-transmitting medium. Diffraction data were collected at room temperature up to 30 GPa every 2 to 4 GPa. The volume compressibility obtained is presented in Fig. 3.3-16 and compared with data present in the literature. Between 7.55 and 9.7 GPa we observed a phase transition. This is evident by the appearance of new systematic absences in the  $hk0$  plane, although no volume

discontinuity is observable. At 7.55 the only observed systematic absences indicate the presence of the 21 screw axis ( $hk0: h=2n$ ), while at 9.7 GPa only the reflections following the  $h+l=2n$  rule remain visible (Fig. 3.3-17). This corresponds to the appearance of a new  $n$  glide plane in the system and overall increase of the symmetry from  $P2_1nm$  to  $Pnmm$ .

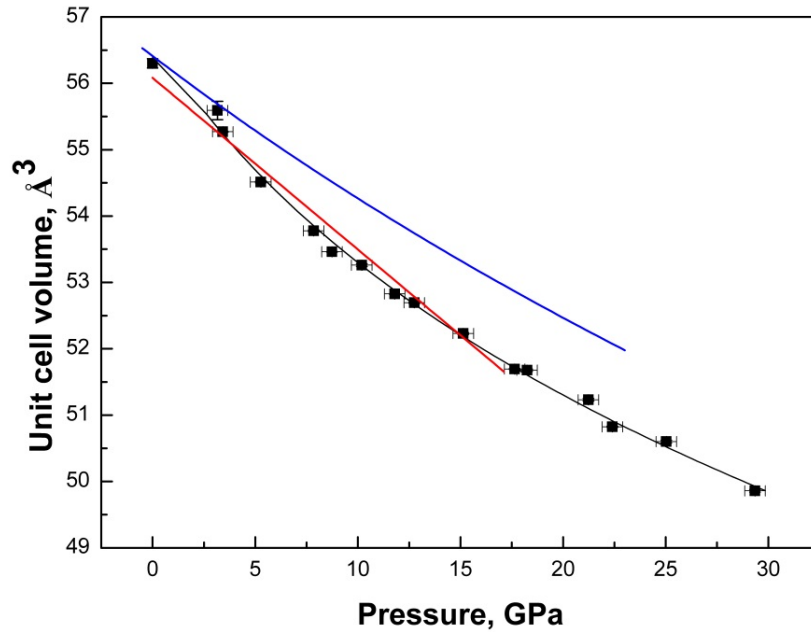


Fig. 3.3-16: Bulk compressibility of  $\delta$ -AlOOH investigated in this study (black) compared with data present in the literature (blue: Vanpeteghem *et al.* 2002, *Geophys. Res Letters*, 29:1119; red: Suzuki 2009, *Mineral. Mag.*, 73:479).

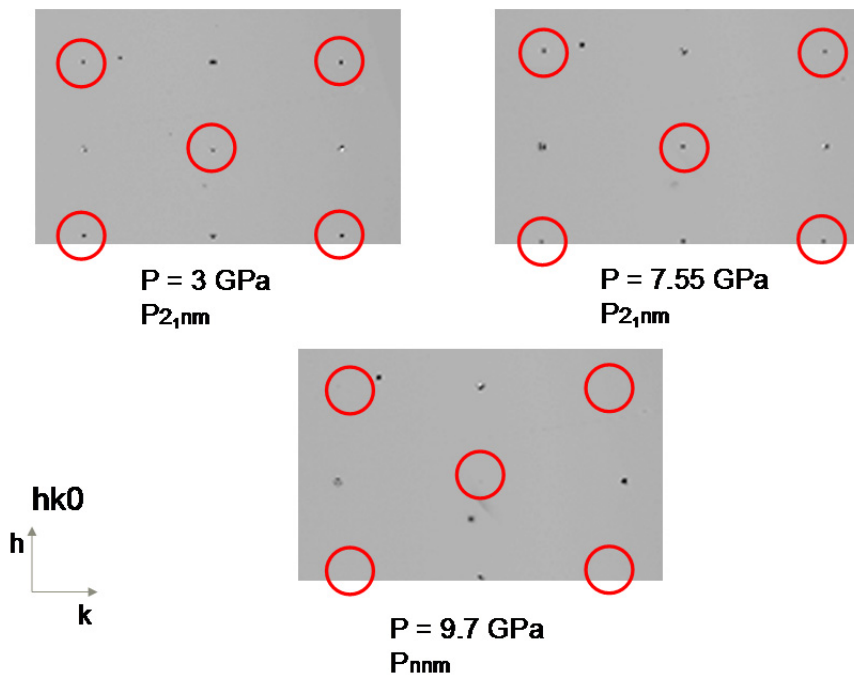


Fig. 3.3-17: Precession images of single-crystal diffraction data for  $\delta$ -AlOOH in the  $a$ - $b$  plane at different pressures.

1. *Time-resolved X-ray diffraction and dynamic compression on the ice VI-VII phase transition (A.S.J. Méndez, H. Marquardt and H-P. Liermann/Hamburg)*

Planetary ice compounds comprise a substantial fraction of the interior structure of Giant Planets as Uranus and Neptune that, for example, contain a thick intermediate layer of hot ices made up of about 56 % H<sub>2</sub>O, 36 % CH<sub>4</sub> and 8 % NH<sub>3</sub> on top of a rocky core. In planetary bodies, these ices are subject to a wide range of conditions of pressure and temperature, ranging in pressure from 20 to 600 GPa at temperatures of up to 7000 K. These conditions may lead to unique physical chemical properties, such as superionicity, which may have a decisive role on the formation of magnetic fields in these planetary bodies.

In the present study, we aim to characterize the behaviour of high-pressure ices using a novel resistive-heated Dynamically Driven Diamond Anvil Cell (RHdDAC). Time-resolved XRD measurements at the Extreme Conditions Beamline, PETRA III, DESY are facilitated through the use of two very fast and sensitive GaAs Lambda detectors which provide an extraordinary time resolution. An example of our preliminary work is shown in Fig. 3.3-18, where we collected XRD data across the H<sub>2</sub>O ice VI-VII transition at room temperature in the dDAC.

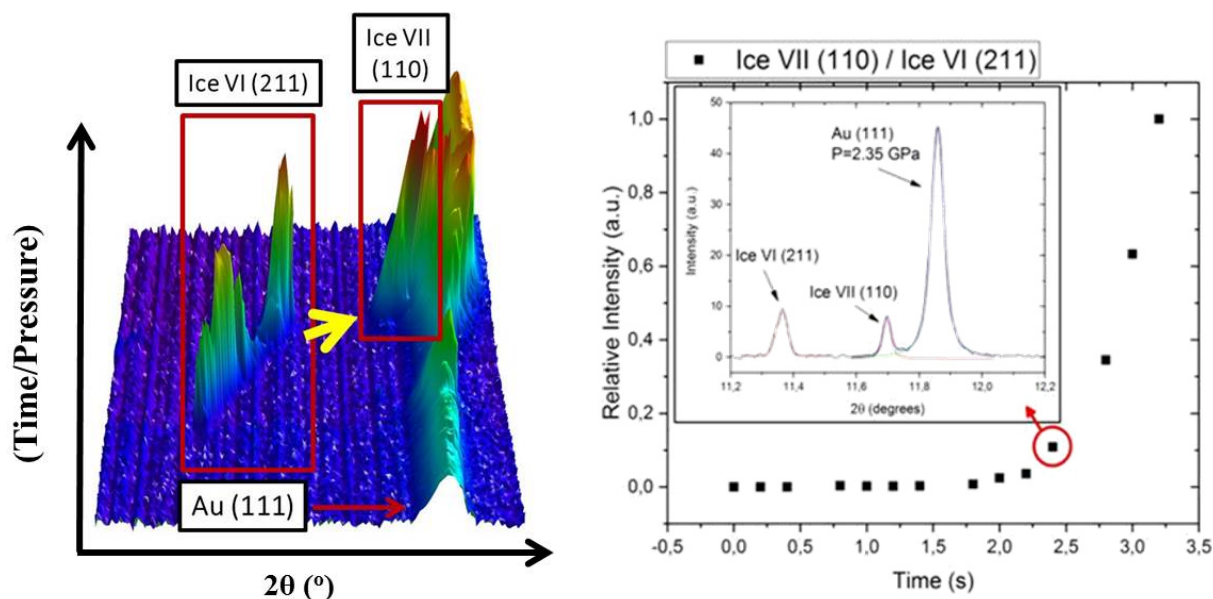


Fig. 3.3-18: (left) 3D-plot of an experiment with a compression rate of 0.01 GPa/s. (right) Relative intensities of the reflections (211) and (110) of ice VI and VII, respectively, as function of time. The inset in the graph corresponds to an integrated diffraction pattern acquired at 2.35 GPa.

Liquid water was loaded together with gold as pressure standard. The phase transition from ice VI to VII is clearly visible on the 3D-plot shown in Fig. 3.3-18a. Ice VI crystallizes from liquid at around 1 GPa and its (211) reflection shifts to higher  $2\theta$  angles with increasing pressure. At 1.9 GPa, first signs of a phase transition are visible with a new reflection arising

at around 11.7 degrees  $2\theta$ . This can be indexed as the (110) reflections of ice VII which gets more intense as the (211) reflections of ice VI progressively disappears with increasing pressure. Evolution of relative intensities as a function of time is plotted in Fig. 3.3-18b. Data analysis is in process in order to characterize the phase transition kinetics.

**m. Time resolved X-ray diffraction of  $Mg_{0.8}Fe_{0.2}O$  across its spin transition under dynamic compression (A.S.J. Mendez, H. Marquardt and H-P. Liermann/Hamburg)**

(Mg,Fe)O ferropericlyase is the second most abundant phase in the Earth's lower mantle. At pressures from 40 to 60 GPa,  $Fe^{2+}$  in ferropericlyase changes its electronic configuration from high spin (HS) to low spin (LS) by pairing 3d-electrons. Across the spin transition, there is a remarkable volume collapse with possible implications for mantle dynamic processes.

Here we present a time resolved X-ray diffraction study across the (Mg,Fe)O spin transition under dynamic compression at room temperature employing different compression rates ranging from 0.01, 10 GPa/s to 1 TPa/s to detect a possible compression rate dependence of the spin transition. Dynamically Driven Diamond Anvil Cell (dDAC) experiments have been carried out at the Extreme Conditions Beamline, PETRA III, DESY (Fig. 3.3-19). A powdered sample of  $Mg_{0.8}Fe_{0.2}O$  was loaded together with gold as pressure standard. Superfast collection of X-ray diffraction images is facilitated through the use of two very sensitive GaAs Lambda detectors. These detectors enable a sampling frequency of up to 2 kHz each. By triggering the detectors 0.25 ms apart we are able to reach an effective repetition rate of 4 kHz, making it possible to follow the spin crossover at very fast compression rates.

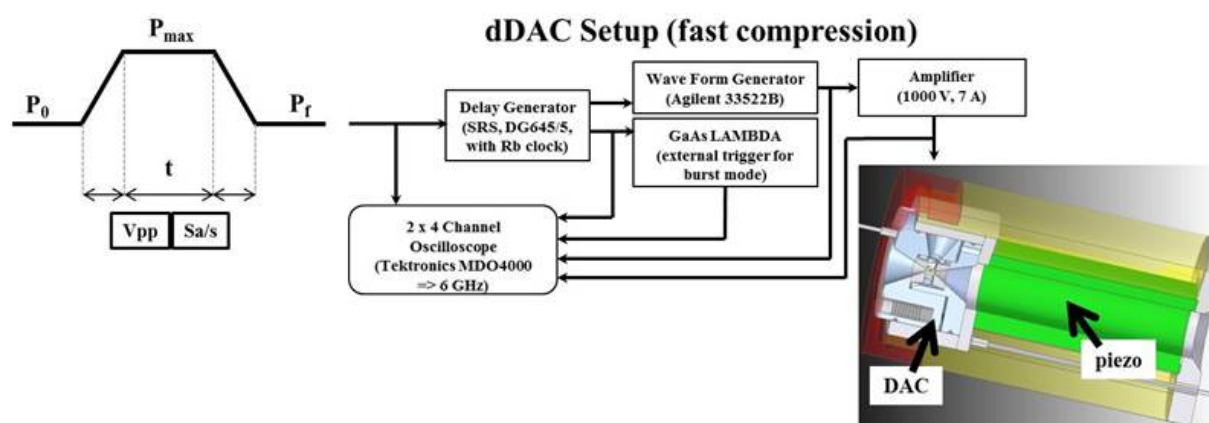


Fig. 3.3-19: Scheme of the dDAC setup employed in this work. (From left to right) Profile of the linear ramps that have been applied to the piezo-drive. The signal is triggered using a waveform generator and an oscilloscope. Lambda detectors are connected to the system to automatically start the image acquisition. The dDAC consists of a standard DAC coupled to a piezoelectric actuator.

The equation of state of the high spin ferropericlase calculated from static compression experiments reported in the literature is plotted in Fig. 3.3-20, along with our experimental data collected at different compression rates. Our data reveal a clear volume collapse when iron undergoes the spin transition. Initial data analysis indicates that there are no major effects of compression rate since the transition pressure remains constant and the trend of our experimental data matches that from static experiments. Some deviations from the EOS provided by previous static-pressure experiments are, however, observed at pressures above 60 GPa for low-spin (MgFe)O. Data analysis is ongoing to understand the cause of the observed deviations.

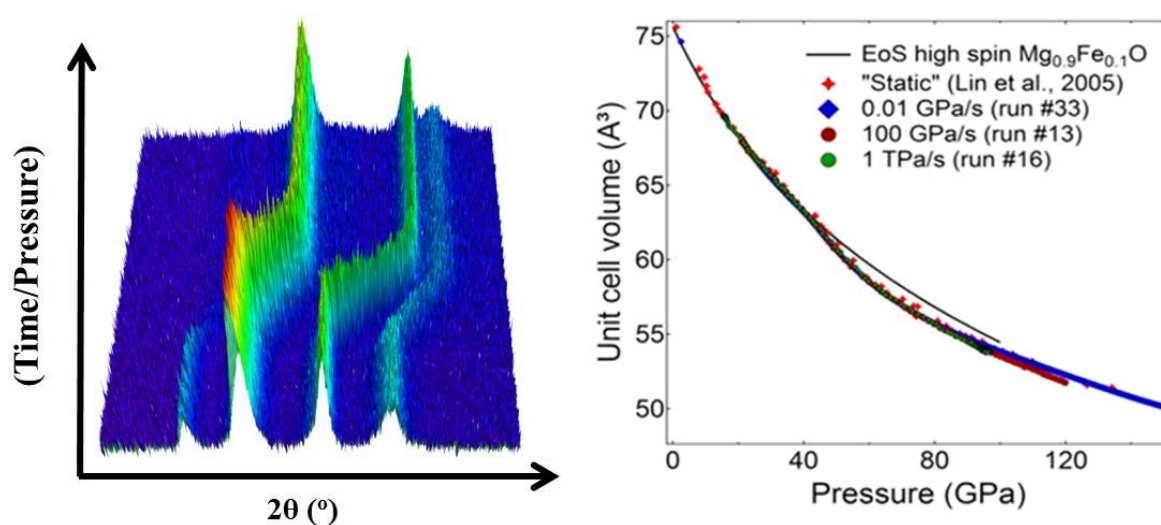


Fig. 3.3-20: (left) 3D-plot made of diffraction images collected during a dynamic compression run on ferropericlase. From low to high  $2\theta$  angles: (Mg,Fe)O (111), Au (111), (Mg,Fe)O (200) and Au (200). (right) Comparison of compression curves across the spin transition between static (Lin *et al.* 2005, Nature 436: 377) and dynamic experiments.

**n. B1-B2 transition in MgO at multi Mbar pressure from ab initio simulations (F. Trybel and G. Steinle-Neumann)**

Currently, observational constraints on the structure of exosolar planets are limited to mass and radius, which makes a description of their internal structure ambiguous. Nevertheless, by using equations of state for silicate and iron, some are found to fall between pure iron and silicate planets, suggesting that their interior structure resembles that of the terrestrial planets in our solar system and leading them to be characterized as super-Earths. In order to better constrain this characterisation, material properties at pressures ( $P$ ) and temperatures ( $T$ ) that significantly exceed those in the Earth's interior are required, beyond 1 TPa and 10,000 K. One of the most important minerals in the Earth's mantle and likely to be also found in the interior of rocky super-Earths is ferropericlase (MgO-FeO). Experiments, including the newly

feasible ramp-compression and reverberating shock techniques, and computations show that while the B1 phase (NaCl structure) is very stable, a phase transition to B2 (CsCl structure) occurs at  $P$  higher than 350 GPa, conditions easily reached in the mantle of large super-Earths. However, while the transition pressure at static conditions is now well established, the Clausius-Clapyron slope is not.

From computations, a phase transition can be predicted through the comparison of the Gibbs energy of the involved phases, and it is possible to calculate the thermodynamic potential with density functional theory (DFT) based methods, including vibrational contributions either based on molecular or lattice dynamics. In lattice dynamics (LD), there are different approaches capable of calculating the vibrational free energy. The most intuitive one is the small displacement method, used for example within the program PHON. A sufficient number of atoms, determined through the symmetry of the lattice, are displaced and the corresponding restoring forces are calculated within a DFT framework, *e.g.*, Quantum Espresso, through the Hellmann-Feynman theorem. From the forces, one can determine the dynamical matrix of the lattice and through diagonalization the phonon frequencies,  $\omega$ . Sampling the frequencies in the Brillouin-Zone, the phonon density of states or frequency distribution function  $g(\omega)$  is computed. The vibrational contribution to the Helmholtz energy is given as:

$$F_{vib} = k_B T \int_0^\infty d\omega g(\omega) \ln(2 \sinh(\frac{\hbar\omega}{2k_B T})) \quad (1)$$

in the quasi-harmonic (qha) model, where all inter-atomic forces are assumed to be purely harmonic, but volume dependent. In equation (1),  $k_B$  is the Boltzmann constant and  $\hbar$  the reduced Planck constant. It is important to note that within the framework of the small displacement method, the LO-TO mode splitting of the optical modes is not considered. This is in fact only significant when looking at the phonon dispersion relation, but has negligible impact on the results for the thermodynamic properties. A second approach to calculate  $F_{vib}$  is the linear response method or density functional perturbation theory (DFPT), in which the second derivative of the energy surface is calculated with respect to a given perturbation. Calculation of the derivative with respect to atomic displacements leads to the dynamical matrix and therefore to phonon frequencies. The major benefit of this method is the natural incorporation of the LO-TO splitting and the fact that it is integrated in the DFT-code in a seamless way, *e.g.*, in Quantum Espresso itself.

Using a series of different volumes to compute the total energy of the system ( $E$ ),  $F_{vib}$  and therefore the total Helmholtz energy  $F = E + F_{vib}$ , a number of isothermal Birch-Murnaghan equations of state (EOS) are fitted to our results. The corresponding pressure is calculated using the fit parameters, and through a Legendre transformation, the Gibbs energy is determined. The phase transition is then obtained from the intersection of the isothermal Gibbs energy curves for the B1 and B2 phase of MgO. In Figure 3.3-21, the black dashed line represents our results for the transition  $P$  from the qha linear response calculation with Quantum Espresso using the generalized gradient approximation. At 0 K, but considering the zero point vibrational energy, we predict a slightly lower transition  $P$  than prior

computational work, a trend that continues to high  $T$ , where decaying shock experiments observe the transition also at higher pressure than the ones we predict here.

From our simulations in the qha approximation, the Clausius-Clapeyron slope is  $dP/dT = -14$  MPa/K, lower by a factor of two than estimates from prior simulations ( $-33$  MPa/K). The volume collapse across the B1-B2 transition is predicted approximately constant for the  $T$ -range considered, and within 4-5 % range as prior computational and experimental works.

As we have stated above, in the qha approximation the phonon frequencies are independent of  $T$ , while the inter-atomic forces within a lattice are not harmonic, in general, and further contributions to the vibrational energy need to be taken into account. This is possible through extensions of the LD approaches presented above and through other methods, *e.g.*, *ab initio* molecular dynamics. Unstable modes in the B2-phase can be dynamically stabilized through thermal and anharmonic contributions, which will also allow for better constraints on the high- $T$  equations-of-state. It is necessary to include these in order to obtain sufficiently good predictions for the B1 to B2 phase transition.

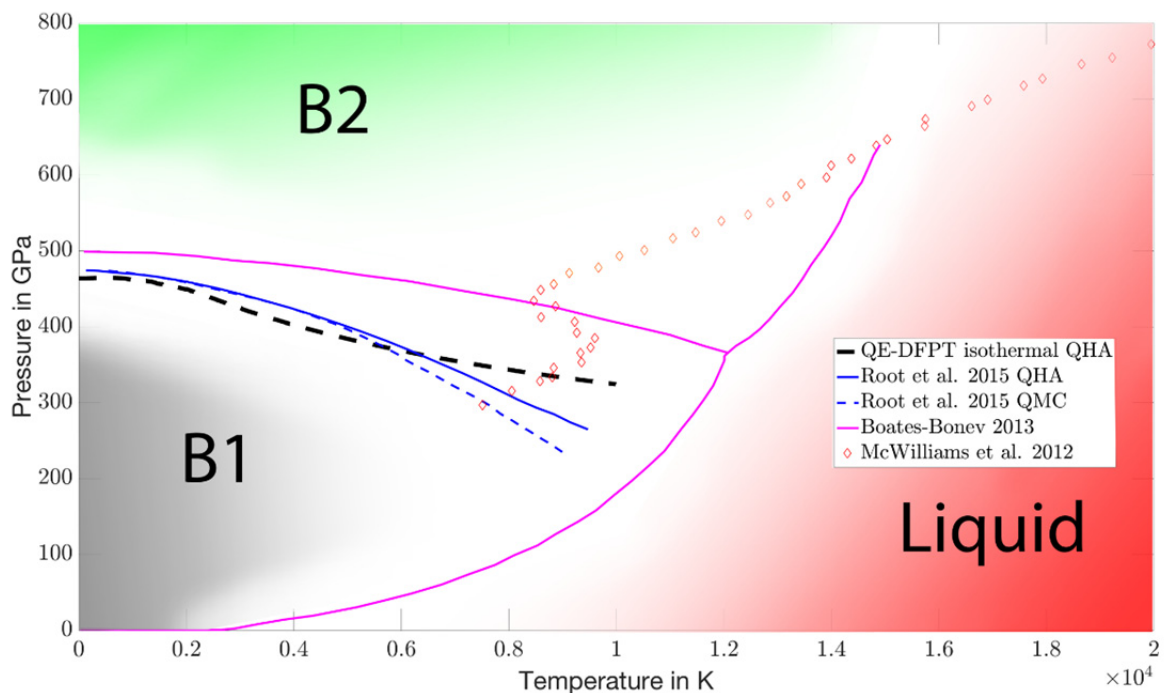


Fig. 3.3-21:  $P$ - $T$  phase diagram of MgO. The stability fields of the B1, B2 and liquid phases are indicated in color. The B1-B2 phase transition from our quasi-harmonic lattice dynamics simulations is shown by the black dashed line. For comparison, the corresponding transition from Root *et al.* 2015, Phys. Rev. Lett., 115:198501 (blue lines, solid for quasi-harmonic simulations and dashed for a quantum Monte Carlo inversion of experimental data), a phase diagram by Boates & Bonev 2013, Phys. Rev. Lett., 110:135504 (magenta lines) from simulations and data points from a decaying shock wave experiment (diamonds) by McWilliams *et al.* 2012, Science, 338:6112 are included.

o. *High-pressure behaviour of magnetite-magnesioferrite solid solution (C. Melai, A. Kurnosov and T. Boffa Ballaran, in collaboration with L. Uenver-Thiele and A.B. Woodland/Frankfurt)*

AB<sub>2</sub>O<sub>4</sub> oxides form a variety of aluminates, ferrites and chromites; they are associated with different geological environments in metamorphic, sedimentary, and igneous rocks of the Earth's crust, and they transform to high-pressure phases of nesosilicates in the Earth's mantle. Among these oxides, spinel-group minerals are important petrological indicators and their widespread occurrence is a result of the very large number of cations of different valences that can be incorporated in the two non-equivalent sites of their structure. In fact, the spinel structure (*Fd $\bar{3}m$* ) is based on a nearly ideal cubic close-packed array of oxygen atoms with two non-equivalent cation sites, a tetrahedrally coordinated T site and an octahedrally coordinated M site. In simple spinels, A and B represent ions of either 2+ and 3+ or 4+ and 2+ charges, defining the so called "2-3 type spinels" or the "4-2 type spinels". Most natural spinel, with exception of Cr-rich ones, can be represented to good approximation by the system: spinel (*s.s.*) (MgAl<sub>2</sub>O<sub>4</sub>) – hercynite (*hrc*) (FeAl<sub>2</sub>O<sub>4</sub>) – magnesioferrite (*mf*) (MgFe<sub>2</sub>O<sub>4</sub>) – magnetite (*mgt*) (FeFe<sub>2</sub>O<sub>4</sub>).

Spinel group minerals have been reported to transform into denser orthorhombic structures of CaFe<sub>2</sub>O<sub>4</sub> (*Pnma*), CaTiO<sub>2</sub>O<sub>4</sub> (*Cmcm*) or CaMn<sub>2</sub>O<sub>4</sub> (*Pbcm*) type at high pressure or disproportionate to their constituent oxides as well as to novel oxides. In particular magnesioferrite has been shown to break down to its constituent Fe<sub>2</sub>O<sub>3</sub>+MgO at 8-10 GPa and 900-1200°C, whereas at higher temperatures it disproportionates into hematite and unquenchable magnesium-iron oxides (Mg<sub>4</sub>Fe<sub>2</sub>O<sub>7</sub>, Mg<sub>5</sub>Fe<sub>2</sub>O<sub>8</sub>) with complex stoichiometry. The proper characterization of these phases, however, is made difficult by their unquenchable nature, which requires *in situ* measurements for a more accurate structural identification. Also magnetite breaks down into Fe<sub>4</sub>O<sub>5</sub>+ Fe<sub>2</sub>O<sub>3</sub> at 10 GPa and 700-1400 °C. These oxides assemblage remains then stable up to higher pressure and temperature conditions. Very little is known about the behaviour of sample with compositions belonging to the mf-mgt solid solution, which represent compositions closer to those found in inclusion in diamond and therefore represent a better proxy for natural spinel.

Here, we have performed structural refinements of intensity data of Fe-rich magnesioferrite (Mg<sub>0.6</sub>Fe<sub>2.4</sub>O<sub>4</sub>) collected by means of single crystal X-ray diffraction both at ambient and non-ambient conditions. Furthermore, the equation of state for Mg<sub>0.6</sub>Fe<sub>2.4</sub>O<sub>4</sub> was obtained up to 16 GPa. The bulk compressibility can be described using a second-order Birch-Murnaghan equation of state. The compressibility data have been compared with data of the mf and mgt end-members reported in the literature (Fig. 3.3-22). The behaviour of the Fe-rich magnesioferrite investigated in this study appears to be very close to that of magnetite, whereas any comparison with mf is made difficult due to the contradictory results reported in the literature.

Fe-rich magnesioferrite crystals also were heated at 16 GPa and 1500 K by means of a double-side laser heating system both *in house* and at the ESRF Synchrotron Facility. After laser heating the sample was analysed by X-ray diffraction. No reflections belonging to the

Fe-rich magnesioferrite structure were observed, however new reflections appeared which could be indexed as hematite + complex Fe-Mg oxides in agreement with previous observations made on recovered run products from syntheses performed at similar conditions by means of multianvil experiments. This explorative study shows that *in situ* laser heating of single crystals may be a useful technique for the characterization of unquenchable phases.

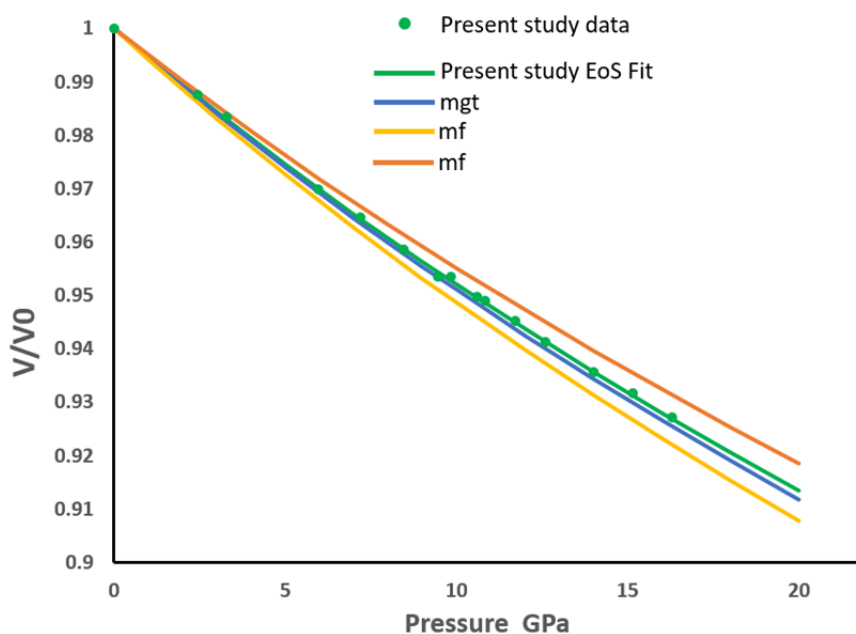


Fig. 3.3-22: Variation with pressure of the unit-cell volume of the Fe-rich magnesioferrite sample investigated in this study (green) compared with data for mf (orange: Levy *et al.* 2004, Phys. Chem. Minerals, 31:122; yellow: Greenberg *et al.* 2009, High Press. Res., 29:764) and mgt (blue: Gatta *et al.* 2007, Phys. Chem. Minerals, 34:627). The reported values are normalized with respect to their respective volumes measured at room pressure.

**p.** Reaction of mackinawite (FeS) in aqueous solutions (C.A. McCammon, in collaboration with M. Wan and S. Peiffer/Bayreuth and C. Schröder/Stirling)

Mackinawite, FeS, is an important iron sulphide that occurs in many anoxic environments. It has likely existed since the Hadean eon and plays a pivotal role in both biotic and abiotic cycling of iron and sulphur in aqueous systems through its reactivity and the numerous pathways to stable species. Mackinawite can be preserved over extended periods in reduced sulphur solutions, but it rapidly oxidises at ambient atmospheric conditions. To investigate abiotic pathways of mackinawite reaction under controlled oxidation to gain insight into early Earth processes, we undertook a Mössbauer study of mackinawite ageing in different aqueous solutions.

We conducted all reactions in a glove box under anoxic conditions ( $O_2 < 1$  ppm). A solution containing freshly precipitated mackinawite was prepared by adding aqueous  $^{57}\text{Fe}$ -enriched

Fe(II) to a Na<sub>2</sub>S solution and then the result was split into four portions and exposed to different oxidants: (1) 10 ml of air (oxygen) was added to 50 ml; (2) 40 mg of synthetic lepidocrocite,  $\gamma$ -FeOOH, was added to 50 ml; (3) 2 ml of polysulphide solution was added to 50 ml; and (4) no oxidants were added to 30 ml (control). The entire experiment ran over slightly more than five months. Samples for Mössbauer spectroscopy were harvested periodically from the solutions in the glove box and transported in an inert atmosphere to a continuous flow liquid helium cryostat operating at 4 K.

The Mössbauer spectrum of fresh mackinawite is a singlet (Fig. 3.3-23, top row), and changes to mackinawite can be easily monitored by observing changes in the Mössbauer spectrum. The spectra of the control sample, for example, did not change during the entire experiment (Fig. 3.3-23, right column), indicating that no reaction occurred in the absence of oxidants. After exposure to a small amount of oxygen, mackinawite reacted slowly, showing development of a weak magnetic component only after 154 days (Fig. 3.3-23, left column). Reaction with lepidocrocite (not shown) proceeded slightly more rapidly, with a more pronounced magnetic component after 154 days. In contrast, there was rapid reaction after adding polysulphide, with development of strong magnetic splitting during the subsequent sampling and complete loss of mackinawite after 154 days (Fig. 3.3-23, middle column). In

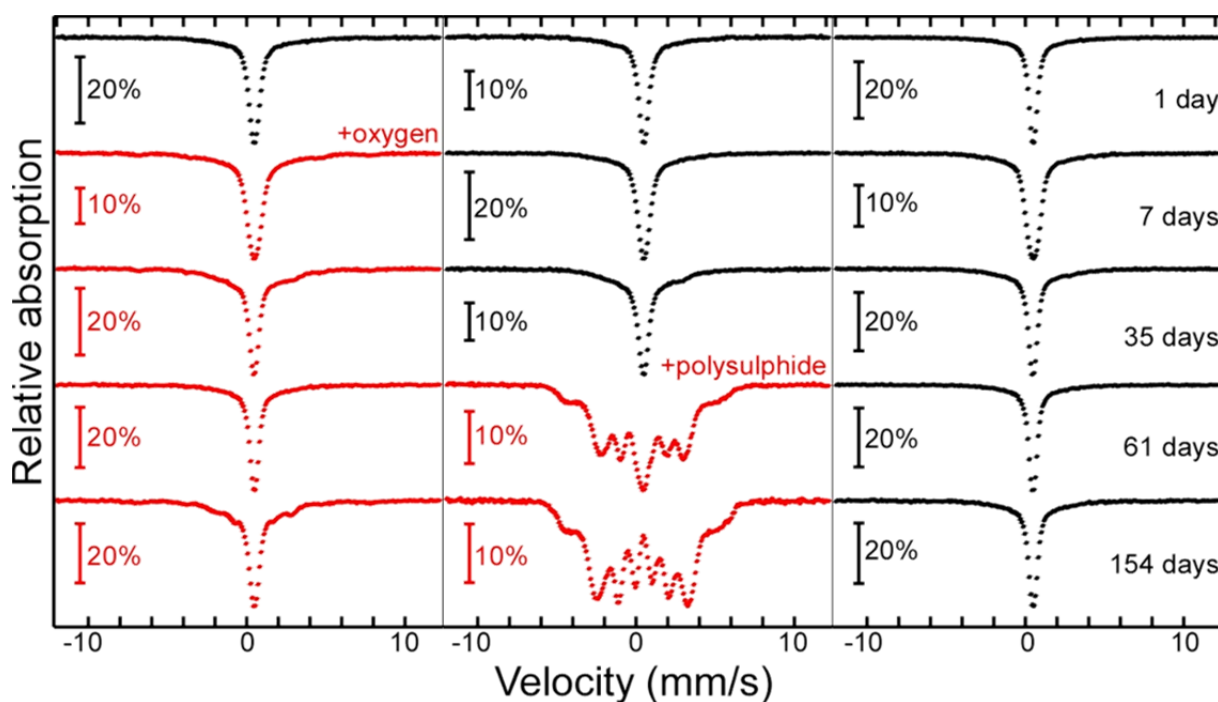


Fig. 3.3-23: Mössbauer spectra of mackinawite before (black) and after (red) addition of oxidants. Samples were reacted in aqueous solutions in a glove box and extracted anoxically for measurement after the indicated times. The left column spectra are from a solution where oxygen was added after one day, the middle column spectra are from a solution where polysulphide was added after 41 days, and the right column spectra are from a solution where nothing was added (control). All spectra were collected at 4 K.

preliminary trials, all spectra were fit with a simple model involving a singlet and several magnetic components. For oxidation by oxygen and/or lepidocrocite, a single magnetic component dominated with centre shift similar to the value for mackinawite and a hyperfine field of approximately 16 T. Comparison with previous results suggests that it corresponds to a metastable phase with  $\text{FeS}_x$  stoichiometry. This phase also appeared after adding polysulphide, but was joined by other magnetic phases yet to be identified as well as a small amount of  $\text{Fe}_3\text{S}_4$ . None of the reactions reached a stable endpoint by the end of the experiment, but all samples could be oxidised completely to pyrite by exposure to air after measurement in the cryostat. Wet chemistry was performed at the same intervals as Mössbauer spectroscopy to determine concentrations of aqueous S(-II) as well as total and dissolved Fe(II), and analysis is ongoing to determine likely reaction pathways as well as kinetics.

### 3.4 Physical Properties of Minerals

Seismology is the key to understanding the Earth's inaccessible interior. Elastic waves excited by earthquakes are refracted and reflected within the Earth and can be used to probe its depth and gather information on the elastic structure and ultimately the physics and chemistry of inaccessible regions down to the Earth's centre. Seismic wave velocities depend on the elastic moduli and density of the material in which the waves propagate. Both properties depend in turn on the crystal structure and chemical composition of the constituent minerals as well as on pressure and temperature. Elastic moduli further depend on the frequency of the measurement and crystal orientation. Electrical conductivity is a complementary probe for investigating the vast yet inaccessible interior of our planet. The propagation of electromagnetic signals in the mantle and core depends on the electrical conductivity of the constituent assemblages, which can only be understood through experiments at extreme conditions or computational studies. This chapter describes some of the most recent results that address the following key questions:

- What are the implications of seismic wave velocity variation for the composition and temperature profiles in the mantle? Can we detect regions of water enrichment?
- What is the effect of pressure, temperature and composition on the electrical conductivity within the Earth?

The first contributions investigate the dependence of seismic wave velocity on water/hydrogen content in wadsleyite and ringwoodite, cation substitution in solid solutions of majorite-pyrope garnet and akimotoite, iron spin crossover in ferropericlase and quasi-hydrostatic compression of nanopolycrystalline stishovite. Experiments that directly constrain wave velocities were conducted using either laser light (Brillouin scattering, in the gigahertz range) or ultrasonic sound waves (often in the megahertz range) with simultaneous density measurements as a function of pressure (and temperature). A combination of velocities with precise density data by single-crystal X-ray diffraction (*e.g.*, dense hydrous silicates, phase E and phase egg) yields elastic moduli that can be compared with seismic measurements or the results of high-frequency experiments. Studies of hydrous wadsleyite and hydrous ringwoodite provide important constraints on the detection of water in the mantle transition zone. Seismic waves typically have frequencies of about 1 Hz and wavelengths on the order of kilometres, far exceeding the dimensions of high-pressure samples. Dynamic (piezo-driven) diamond anvil cell (DAC) experiments on iron spin crossover in ferropericlase show a marked depression of bulk modulus across the spin crossover, and represent the first direct measurements of the elastic response of a sample at lower mantle pressures and seismic frequencies in the DAC.

The final contributions highlight the electronic transport properties of natural olivine in the upper mantle and liquid Fe-S alloys in the inner core. The former experimental work

demonstrates that conductivity anomalies at 70-120 km depth beneath young oceanic plates can be well explained by ionic conduction mechanisms in olivine, while the latter *ab initio* computations show that the presence of light elements substantially changes the electronic transport properties in a liquid iron core, providing insight into the thermal evolution of terrestrial planets and the stability of a potential dynamo.

**a.** *High-pressure single-crystal elasticity of iron-bearing wadsleyite and the reflectivity of the 410-km discontinuity* (J. Buchen, H. Marquardt, S. Speziale/Potsdam, T. Kawazoe/Hiroshima, T. Boffa Ballaran and A. Kurnosov)

The transition zone in the Earth's mantle may act as a deep reservoir for hydrogen and regulate deep cycling of H<sub>2</sub>O or "water" through Earth's history with important consequences for the dynamic evolution of Earth's mantle and hydrosphere. In their crystal structures, the transition zone minerals wadsleyite,  $\beta$ -(Mg,Fe)<sub>2</sub>SiO<sub>4</sub>, and ringwoodite,  $\gamma$ -(Mg,Fe)<sub>2</sub>SiO<sub>4</sub>, can incorporate water in the form of hydroxyl groups and, given their high abundance, allow the retention of considerable amounts of hydrogen in the transition zone. However, attempts to constrain the present-day hydration state of the transition zone by geophysical remote sensing have led to inconsistent results. Based on new experimental data on the high-pressure elasticity of iron-bearing wadsleyite, we evaluate the effect of hydration on sound wave velocities both within the shallow transition zone and across the 410-km discontinuity.

The complete elasticity tensors of iron-bearing wadsleyite single crystals were determined at eight pressures between 0 and 20 GPa. We performed single-crystal X-ray diffraction and Brillouin spectroscopy on wadsleyite crystals with complementary orientations that were loaded together into the same diamond anvil cell (DAC). Specimens of suitable size were cut from double-sided polished, oriented thin sections using a focused ion beam. Unit-cell volumes and single-crystal sound wave velocities at all experimental pressures were inverted simultaneously to obtain an internally consistent high-pressure elasticity model for iron-bearing wadsleyite. The direct comparison of aggregate sound wave velocities for the composition in this study (Fe/(Mg+Fe) = 0.112(2), 0.24(2) wt. % H<sub>2</sub>O) with those reported in the literature for strongly hydrous iron-bearing wadsleyite but identical Fe/(Mg+Fe) ratio reveals a velocity cross-over between less hydrous and strongly hydrous compositions for both P-waves and S-waves (Fig. 3.4-1a). As a result, aggregate sound wave velocities of anhydrous and hydrous iron-bearing wadsleyite are virtually indistinguishable at pressures of the shallow transition zone. We estimated the effect of temperature on the velocity cross-over points using tabulated thermoelastic parameters, the validity of which we confirmed by first experiments at combined high pressures and high temperatures. With increasing temperature, the cross-over points shift to higher pressures but the differences in P-wave and S-wave velocities between anhydrous and hydrous wadsleyite remain too small to be detected by seismic tomography.

We combined our experimental results with literature data on wadsleyite and olivine with different compositions to model velocity, density and impedance contrasts across the 410-km discontinuity, which is thought to arise from the olivine-wadsleyite phase transition. While hydration appears to have a small effect on velocity contrasts, impedance contrasts depend strongly on the water content of wadsleyite, irrespective of the assumed partition coefficient of H<sub>2</sub>O between olivine and wadsleyite (Fig. 3.4-1b). Therefore, we propose the impedance contrast, or reflectivity, of the 410-km discontinuity as a sensitive geophysical observable to detect and quantify hydration in the deep upper mantle.

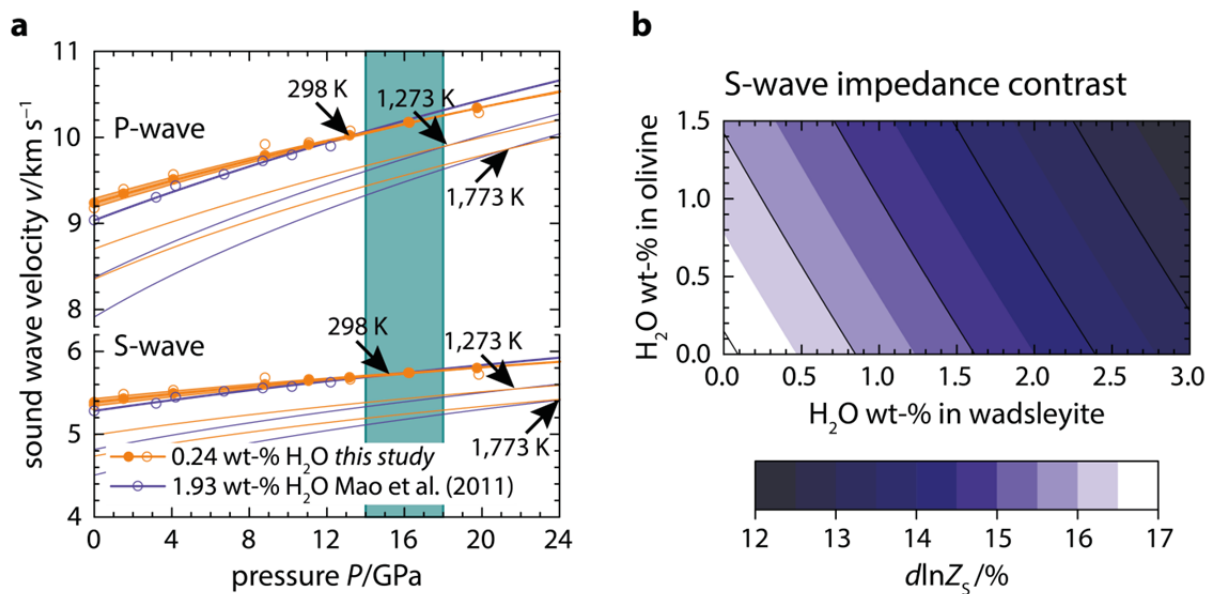


Fig. 3.4-1: (a) Aggregate sound wave velocities of iron-bearing wadsleyite ( $\text{Mg}_{0.89}\text{Fe}_{0.11}$ )<sub>2</sub>SiO<sub>4</sub> with 0.24 wt. % H<sub>2</sub>O (this study) and 1.93 wt. % H<sub>2</sub>O (Mao *et al.* 2011, *Am. Mineral.* 96: 1606); solid symbols: global inversion; open symbols: individual inversions; note how the velocity cross-over points (black arrows) shift with temperature. Green shading marks the pressure range of the wadsleyite stability field. (b) S-wave impedance contrast  $d\ln Z_s$  at 14 GPa and 298 K between olivine and wadsleyite as a function of H<sub>2</sub>O content.

**b.** *The effect of hydration on the elastic wave velocities of ringwoodite at pressures of Earth's transition zone (K. Schulze, H. Marquardt, A. Kurnosov, T. Boffa Ballaran, C.A. McCammon, K. Marquardt, in collaboration with T. Kawazoe/Hiroshima and M. Koch-Müller/Potsdam)*

The idea of a hydrated transition zone is based on mineral physics experiments that have shown that wadsleyite and ringwoodite can incorporate up to 2-3 wt. % H<sub>2</sub>O into their crystal structure. The hypothesis of at least partial hydration is supported by the characterisation of a ringwoodite diamond inclusion which is reported to contain about 1.4 wt. % H<sub>2</sub>O.

Geophysicists have tried to quantify the amount of water in the transition zone using remote sensing techniques, particularly seismology. These studies have led to quite a wide range of results, sometimes contradicting one another, which may partly be related to uncertainties in mineral physics reference data.

Using the novel method of FIB-tailored single crystal samples suitable for comparative Brillouin spectroscopy and X-ray diffraction measurements (see BGI Annual Reports 2015 and 2016), we determined a high-pressure elasticity dataset for three Fo89 ringwoodite samples with different hydration states. Eight Brillouin spectroscopy runs were performed to a maximum pressure of 22 GPa.

Our results (Fig. 3.4-2) reveal a reduction of the effect of hydration on elastic wave velocity with increasing pressure. Our results were obtained from experiments on three samples in one diamond anvil cell and are interpolated in terms of pressure, leading to a robust dataset. Using our measurements, we modelled the relative change of the aggregate velocities with pressure and hydration state. Figure 3.4-3 shows our results at 300 K for both longitudinal and shear velocities for a Fo89 ringwoodite aggregate. For ringwoodite containing 1 wt. %  $\text{H}_2\text{O}$ , both aggregate velocities would decrease by less than 1 % compared to the anhydrous case at transition zone pressures. The here-inferred reduction of seismic wave velocities caused by hydration is less than one third of that reported by previous work. When we additionally take into account the fact that a pyrolitic mantle is made up of only 60 vol. % ringwoodite at depths between 520 and 660 km, the effect of hydrated ringwoodite is further reduced. We conclude that the effect of water in ringwoodite in the transition zone might not be resolvable by seismology.

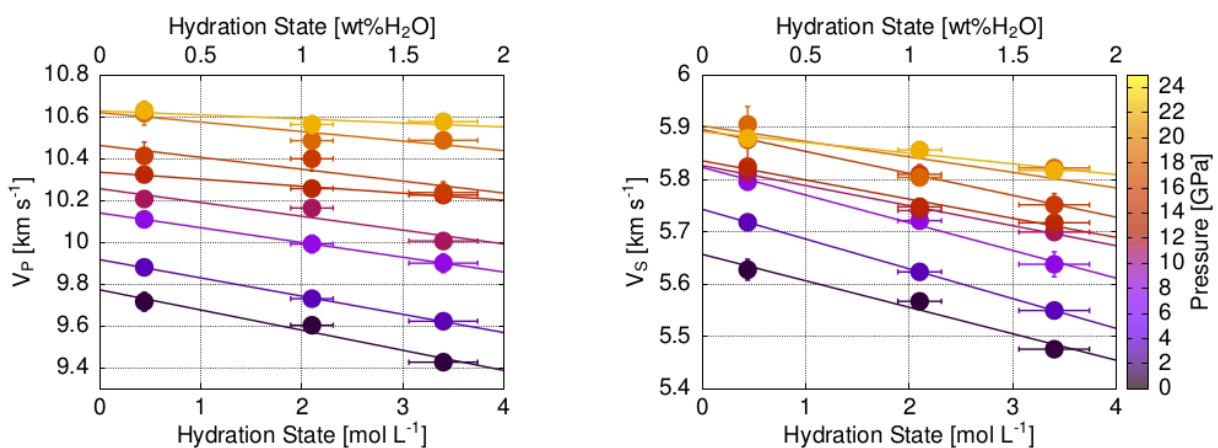


Fig. 3.4-2: Longitudinal (left) and shear (right) aggregate velocities as a function of hydration state and pressure for three Fo89 ringwoodite samples.

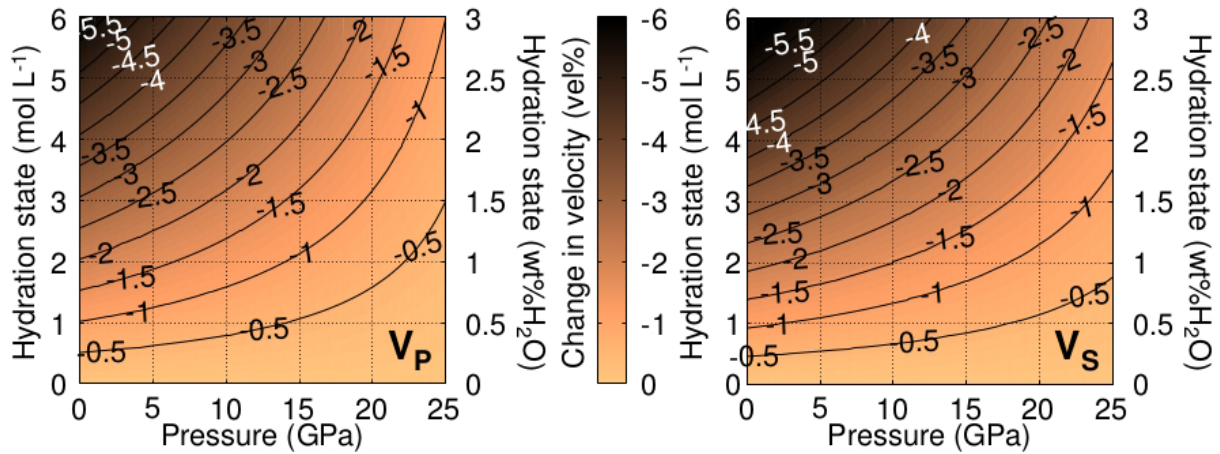


Fig. 3.4-3: Model for pure Fo89 ringwoodite longitudinal (left) and shear (right) aggregate velocities for different pressure and hydration conditions at 300 K. The change in velocities is referenced to the anhydrous case.

**c. Elasticity of phase E single crystals** (N. Satta, H. Marquardt, A. Kurnosov, T. Kawazoe and T. Boffa Ballaran)

Slab subduction is the main mechanism to recycle water deep into the Earth's interior. Water is mainly incorporated as hydroxyl groups in serpentine, minerals which form as a result of alteration of olivine and pyroxene on the sea floor. During subduction, dehydration of serpentine is expected to take place at 180-200 km depth. In a cold subduction scenario, however, a fraction of the initially subducted water can continue its journey towards the deeper mantle after serpentine breakdown. This is possible because water can be stored in Dense Hydrous Magnesium Silicate (DHMS) phases, a group of phases that have been so far only found experimentally. Phase E is one of the DHMS that is stable at high temperature; therefore it can plausibly play a role in the deep water cycle. Investigation of the elastic properties of the phases that might transport water into the deep mantle is needed to map water recycling into the mantle using seismological observations. In particular, the predicted low bulk modulus for phase E from previous studies potentially allows the detection of this hydrous phase by seismology.

In this project, we are investigating the elasticity of phase E single crystals using Brillouin spectroscopy and X-ray diffraction. Dark blue phase E crystals with a size of about 200  $\mu\text{m}$  were synthesized at 14 GPa and 1100  $^{\circ}\text{C}$  for 3 hours in a multianvil apparatus. The starting material was a mixture of San Carlos olivine powder and water. High-quality crystals were selected based on X-ray diffraction measurements. Due to the trigonal symmetry of phase E, acoustic wave velocities in at least two different crystallographic planes have to be measured to constrain the full elastic tensor. For this reason, two crystals were oriented in (100) and (001) directions and then double-sided polished to a final thickness of about 20  $\mu\text{m}$ . At the present time, we have completed investigating the platelet with (100) orientation using Brillouin spectroscopy and we are planning to start measuring the second platelet. On the first sample, experimentally measured frequency shifts associated with the fast transverse and the

longitudinal acoustic modes have been collected in 18 different propagation directions and then converted to acoustic velocities (Fig. 3.4-4). To facilitate room pressure measurements, the platelets have been loaded without a pressure-transmitting medium in a diamond anvil cell (DAC). Chemical and structural analyses are being performed to provide reliable density values of our selected samples. By combining all of the data, we will be able to solve the Christoffel equation using a least-square fitting procedure and the full tensor of phase E will be determined.

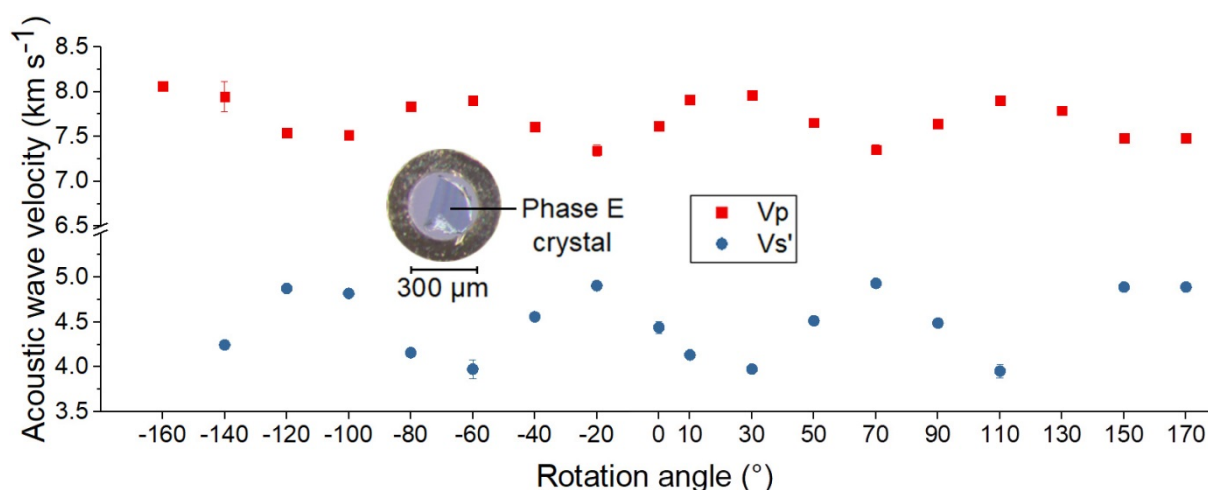


Fig. 3.4-4: Experimentally measured dispersion of fast transverse ( $V_{s'}$ ) and longitudinal ( $V_p$ ) acoustic velocities as a function of the rotation angle for the phase E platelet with (100) orientation at ambient conditions. The inset shows the phase E crystal loaded into the DAC without pressure-transmitting medium.

**d. Single-crystal X-ray diffraction on  $AlSiO_3OH$  "phase egg" to high pressure (K. Schulze, T. Boffa Ballaran, M.G. Pamato/London and A. Pakomova/Hamburg)**

Subducted oceanic crust transports water into the Earth's mantle that can be incorporated into high-pressure hydrous aluminosilicate phases. The physical properties of these hydrous phases may therefore be crucial to understanding the deep Earth's water cycle. One of these phases,  $AlSiO_3OH$  phase egg, may crystallise in the siliceous sedimentary component of subducting slabs above 11 GPa and is stable up to 20 GPa and 1600 °C. It has a monoclinic structure with Si entirely present in octahedral coordination. In this study, we performed a single-crystal synchrotron X-ray diffraction study on  $AlSiO_3OH$  phase egg at room temperature up to a pressure of 23.3 GPa.

The pressure-volume data were fitted using a third-order Eulerian finite-strain equation of state (Fig. 3.4-5). The derived bulk modulus at ambient conditions is similar to the value that was obtained in a powder diffraction study reported in the literature, within uncertainties. In contrast, the bulk modulus pressure derivative calculated in this study is more than 50 % larger than the one obtained in the powder diffraction study. The  $\beta$  angle decreases with pressure up to 14 GPa and then remains constant at a value of  $\sim 97.8^\circ$  up to the maximum

pressure reached. The largest lattice strain is found to be along the  $b$ -axis, which is the most compressible direction. Structure refinement on high-pressure measurements will be performed to identify the mechanisms that control the anisotropic compressibility of this material.

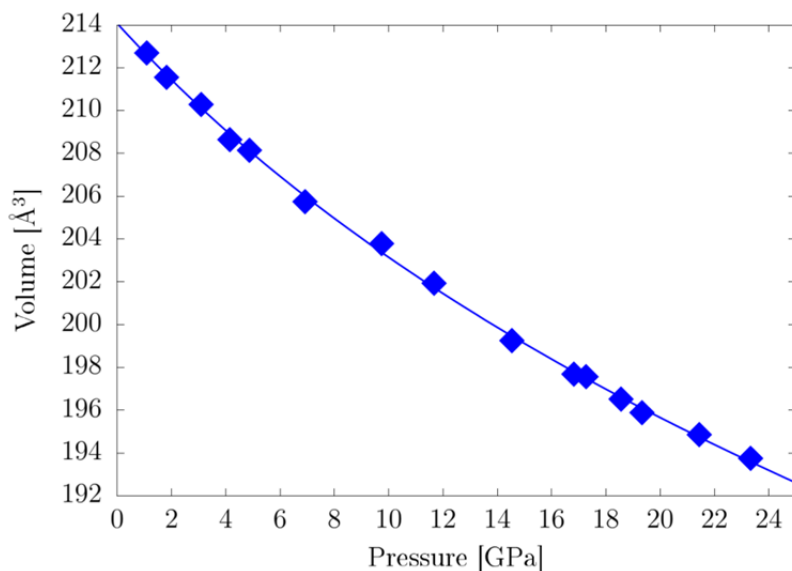


Fig. 3.4-5: Pressure evolution of the unit cell volume of  $\text{AlSiO}_3\text{OH}$  phase egg to 23.3 GPa at room temperature, fitted to a third-order Eulerian strain equation of state.

*e. Single-crystal sound velocity measurements on natural majoritic garnets from Jagersfontein kimberlite (I. Koemets, H. Marquardt, A. Kurnosov and L.S. Dubrovinsky)*

Garnet is an abundant mineral in the Earth's upper mantle. With increasing depth, the fraction of Mg-majoritic garnet  $\text{Mg}_3(\text{MgSi})(\text{SiO}_4)_3$  in upper mantle rocks is thought to increase. Natural majoritic garnets are rare; hence previous sound velocity measurements on natural samples used polycrystalline specimens. In this project, we conducted room pressure Brillouin spectroscopy measurements on inclusions of natural single-crystal majoritic garnet extracted from diamonds originating from Jagersfontein kimberlite in South Africa.

The majorite fraction in the studied garnet inclusions ranges from 7 to 42 %. The inclusions were polished to 20-40  $\mu\text{m}$  thickness and loaded into a diamond anvil cell without applying pressure. Brillouin scattering measurements were performed at BGI. The power of the incident beam at the sample was 100-200 mW and 30 % of the initial laser power passed through the sample. Measurements were performed in several directions within the single crystals, and the collection time for a single Brillouin spectrum was between 0.5 and 2 h.

The dependence of sound velocity on crystallisation pressure is shown in Fig. 3.4-6a, where the crystallisation pressure was estimated from composition based on a geobarometer reported recently in the literature. There is no obvious correlation of velocity with the pressure at which the inclusions last equilibrated. We also estimated the sound velocity of majorite with compositions close to those of our natural samples using literature data for endmembers of the

corresponding garnet solid solutions and Voigt averaging. There is good agreement between estimated and observed values (Fig. 3.4-6b). We calculate the bulk and shear modulus of the majorite end-member component from the sample with the highest majorite fraction (42 %) to be 164.5(24) and 85.0(12) GPa, respectively.

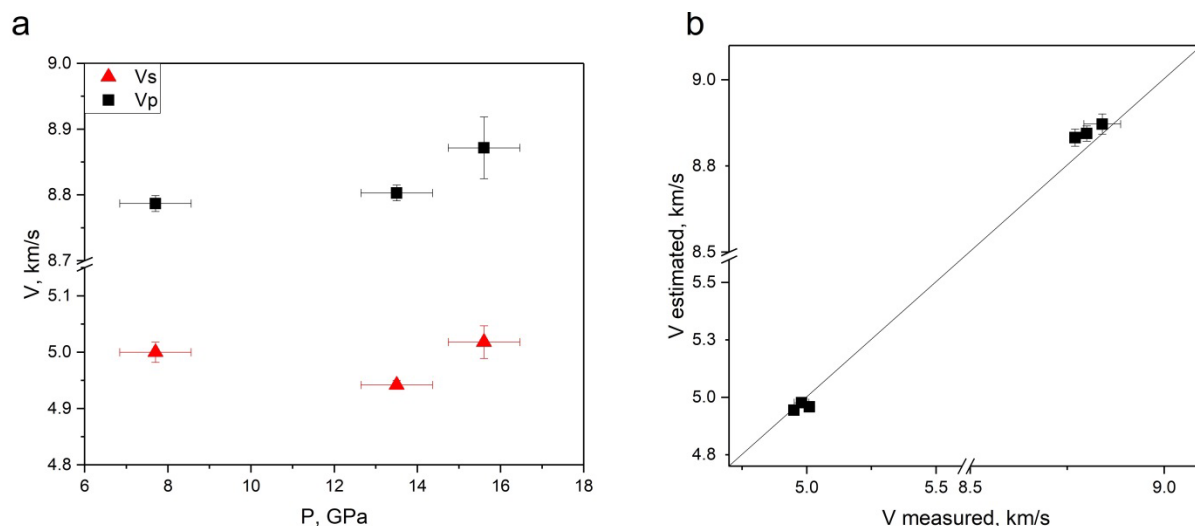


Fig. 3.4-6: (a) Sound velocities of natural single-crystal majorite inclusions from diamonds as a function of pressure calculated using a recently reported geobarometer. (b) Sound velocities measured in this work compared to literature data with values estimated using Voigt averaging.

**f. Influence of aluminium on the elasticity of majorite-pyrope garnet (Z. Liu, N. Siersch, T. Boffa Ballaran, D.J. Frost, N. Cai/Stony Brook, S. Gréaux and T. Irifune/Matsuyama)**

Garnet,  $X_3Y_2Z_3O_{12}$  (where  $X^{2+} = \text{Mg, Fe, Ca, Mn}$ ;  $Y^{3+} = \text{Al, Fe, Cr}$ ;  $Z^{4+} = \text{Si, Ge}$ ), is one of the most abundant rock-forming minerals in the Earth's crust and mantle. With increasing depth from the upper mantle to the transition zone, an aluminium-deficient garnet called majorite forms from the gradual dissolution of clinopyroxene into garnet. The majorite-pyrope system is thus the most dominant and hence relevant garnet solid solution in the upper mantle and transition zone. Petrological studies demonstrate that majoritic garnet comprises approximately 40 % and 60 % by volume of pyrolite and mid-ocean ridge basalt compositions in the mantle transition zone, respectively. Accordingly, the elasticity of majorite-pyrope garnet is crucial for interpreting the mineralogy of the mantle from seismic velocity profiles.

Here, polycrystalline gem-quality majorite-pyrope garnets were prepared by hot-pressing the glass starting material at high pressure and high temperature using a Kawai-type multianvil apparatus combined with tungsten carbide anvils (see Fig. 3.4-7a). The synthetic polycrystalline garnets are well-sintered, nearly cylindrical in shape, free of micro-cracks and transparent or translucent in colour. In these samples the phase transition from the cubic to tetragonal structure was found to occur at a pyrope content of 26 mol. % along the  $\text{Mg}_3\text{Al}_2\text{Si}_3\text{O}_{12}$  (pyrope) -  $\text{Mg}_4\text{Si}_4\text{O}_{12}$  (majorite) join.

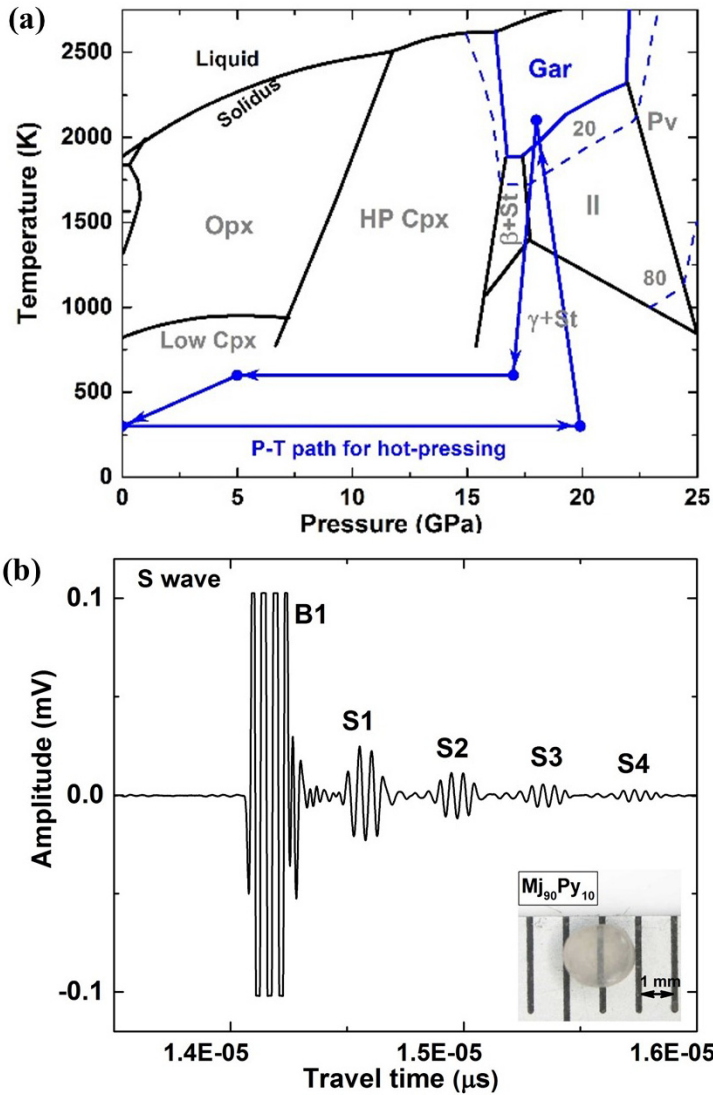


Fig. 3.4-7: (a)  $P$ - $T$  paths for hot-pressing polycrystalline aggregates in the phase diagram of  $\text{MgSiO}_3$ . (b) An example of waveform data for  $S$ -waves at 40 MHz for garnet sample  $\text{Mj}_{90}\text{Py}_{10}$  (shown in the inset) at ambient conditions. B1 is the wave echo from the interface of the buffer rod, while S1-S4 represent the echo trains from the interface at the back of the sample.

Travel times of  $P$ - and  $S$ -waves were measured by the pulse echo overlap method at the resonant frequencies of 60 and 40 MHz, respectively.  $P$ - and  $S$ -wave acoustic signals were generated by a 10° Y-cut  $\text{LiNbO}_3$  piezoelectric transducer attached at one end of a  $\text{SiO}_2$  glass rod that served as a delay line buffer of the signal into the garnet specimen. The samples were attached to the other end of the glass buffer rod using a low-viscosity epoxy bond. Figure 3.4-7b shows a typical acoustic signal obtained at 40 MHz ( $S$ -wave) for the  $\text{Mj}_{90}\text{Py}_{10}$  garnet, in which the echo at the interface between buffer and sample (B1) is followed by four successive echoes from the other end of the garnet sample (S1, S2, S3 and S4 for  $S$ -wave). As shown in Fig. 3.4-8, both  $V_P$  and  $V_S$  have a linear compositional dependence with pyrope content. Our results are generally consistent with earlier studies using both ultrasonic interferometry and Brillouin scattering methods. From the measured densities and acoustic wave velocities, we can derive the elastic bulk ( $K_S$ ) and shear ( $G$ ) moduli using the equations  $K_S = \rho \cdot (V_P^2 - 4V_S^2/3)$  and  $G = \rho \cdot V_S^2$ . Our study implies that the elastic moduli, *i.e.*, bulk ( $K_S$ ) and shear ( $G$ ) modulus, of garnets increase almost linearly with increasing pyrope content. The aluminium component plays a dominant role in the variation of elasticity for majorite-pyrope garnet, while the phase transition from the cubic to the tetragonal phase is apparently invisible in the elasticity variation of these garnets.

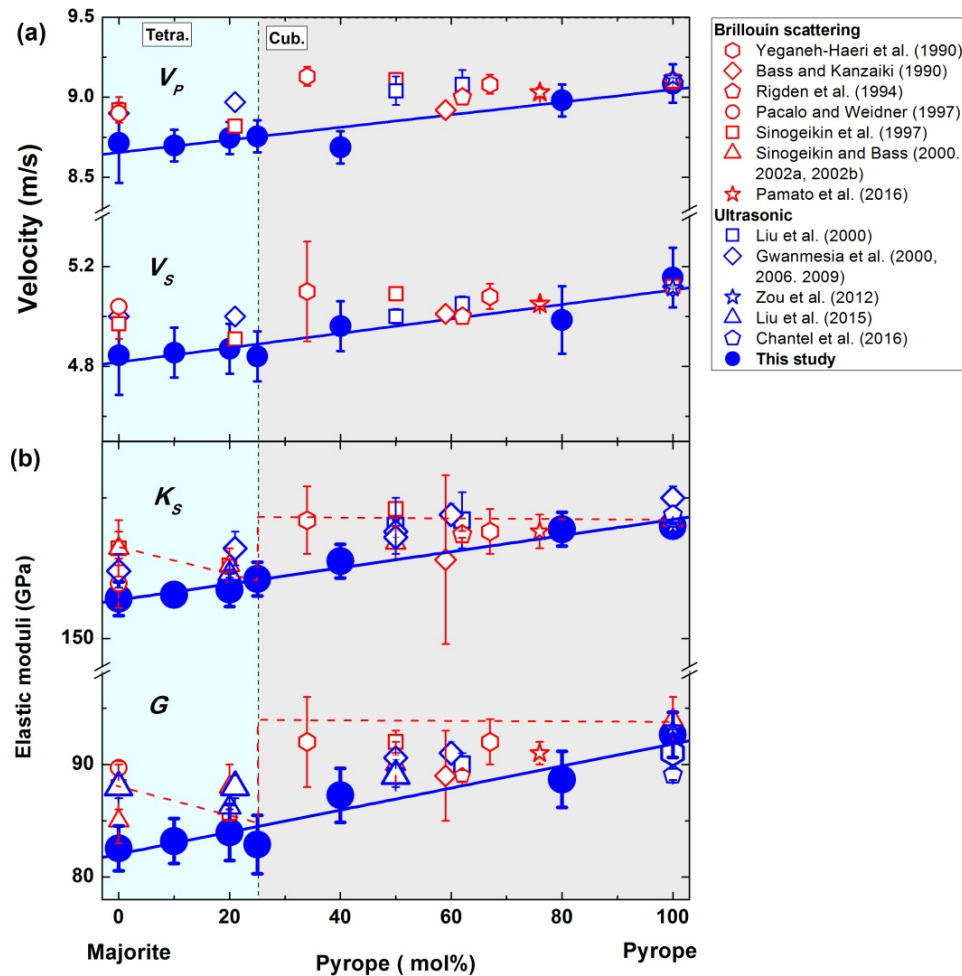


Fig. 3.4-8: (a) Effect of pyrope content along the majorite-pyrope join at ambient conditions on (a) elastic wave velocities for compression ( $V_P$ ) and shear ( $V_S$ ) waves; and (b) bulk ( $K_S$ ) and shear ( $G$ ) moduli. Blue shading indicates the region where garnets are tetragonal, while cubic garnets form in the grey region. The blue solid lines are linear fits of the present data, while the red dashed line is a previously proposed fit based on Brillouin scattering results. Brillouin scattering studies: Yeganeh-Haeri *et al.* (1990; GRL 17: 2453); Bass & Kanzaiki (1990; GRL 17: 1989); Rigden *et al.* (1994; PEPI 86: 35); Pacalo & Weidner (1997; PEPI 99: 145); Sinogeikin *et al.* (1997; PCM 24: 115); Sinogeikin & Bass (2002a; GRL 9: 2453); Sinogeikin & Bass (2002b, EPSL 203: 549); Pamato *et al.* (2016; EPSL 451: 114). Ultrasonic measurement studies: Liu *et al.* (2000; PEPI 120: 153); Gwanmesia *et al.* (2000; PCM 27: 445); Gwanmesia *et al.* (2006; PEPI 155: 179); Gwanmesia *et al.* (2009; PEPI 174: 105); Zou *et al.* (2012; JAP 112: 014910); Liu *et al.* (2015; PCM 42: 213); Chantel *et al.* (2016; Am. Mineral. 101: 991).

**g.** *The effect of the iron spin crossover on ferropericlase compressional velocities measured at seismic frequencies (H. Marquardt, A.S.J. Mendéz, H.-P. Liermann/Hamburg and J. Buchen)*

(Mg,Fe)O ferropericlase, the second most abundant mineral in Earth's lower mantle, undergoes a change of electronic spin state at pressures of about 50 GPa. Experimental

measurements of elastic wave speeds show that this iron spin crossover leads to a marked decrease of compressional wave velocities in ferropericlase with wide-ranging implications for the interpretation of seismic observations in the lower mantle. This reduction of wave velocities is a consequence of the enhanced compressibility, or decreased bulk modulus, of the ferropericlase structure in the pressure region where it changes its electronic spin state. However, previous measurements of the spin crossover effect on elastic wave velocities were performed at very high frequencies (GHz) and no direct measurements at seismic frequencies ( $\sim 1$  Hz) have been conducted. Here we use a dynamic (piezo-driven) diamond anvil cell (dDAC) in conjunction with time-resolved synchrotron X-ray diffraction to directly quantify the bulk modulus of ferropericlase in the high-spin and low-spin states as well as across the iron spin crossover. In our experiments, we loaded powder of ferropericlase along with platinum as an internal pressure standard. Customized compression paths, including sinusoidal oscillations, were applied to the diamond anvil cell by the piezo-electric actuator at a given pressure in order to simulate a propagating compressional wave (Fig. 3.4-9). X-ray diffraction images were collected on two GaAs Lambda detectors available at the Extreme Conditions Beamline P02.2 at PETRA III, DESY. Images were continuously taken with a single image collection time of 10 ms, *i.e.*, 100 images were collected within one oscillation.

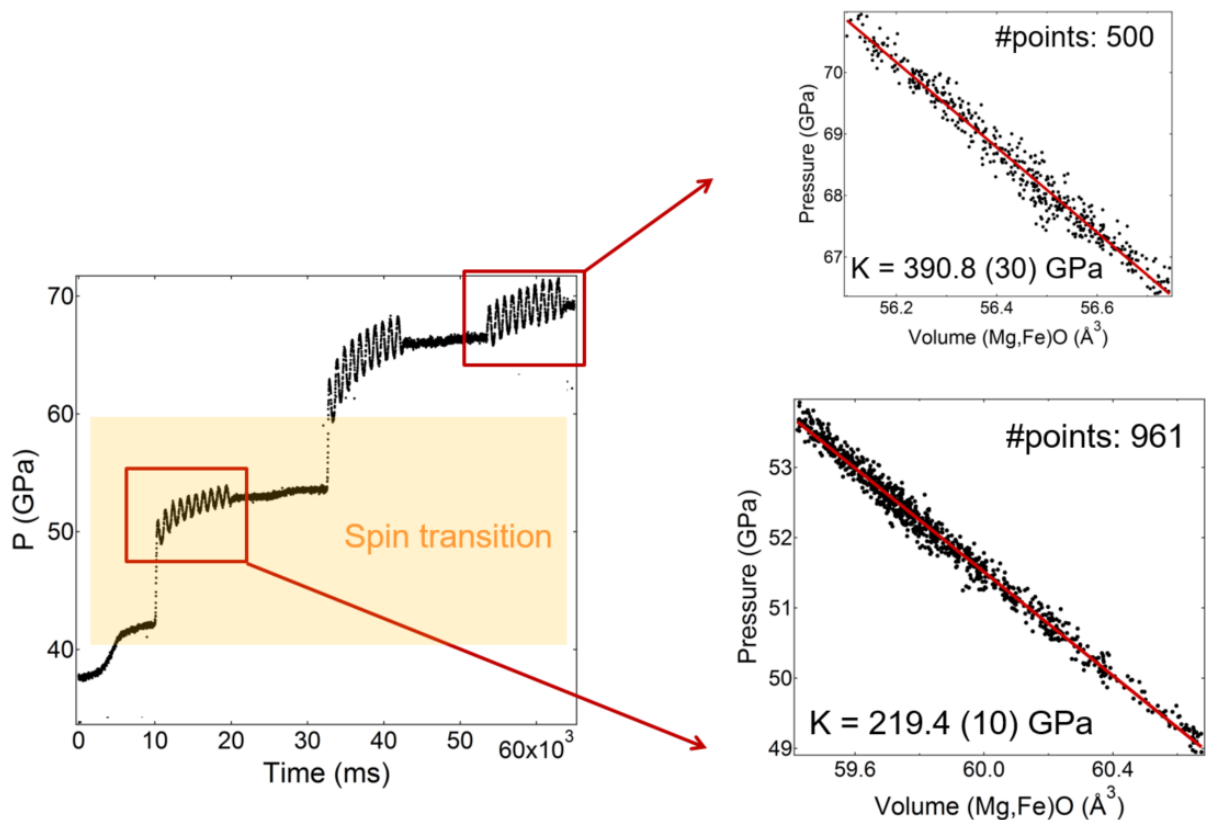


Fig. 3.4-9: (left) Compression path of the sample with time as determined from the gold pressure standard. The approximate pressure range of the iron spin crossover is highlighted. (right) Gold pressure plotted against the unit-cell volume of ferropericlase. The linear slopes in the diagrams correspond to the isothermal bulk modulus  $K_T$ . The isothermal bulk modulus is markedly reduced in the spin transition region.

From the measured change of ferropericlasite unit-cell volume as a function of applied stress, the bulk modulus is calculated (Fig. 3.4-9). A preliminary analysis of our data shows a marked depression of bulk modulus across the iron spin crossover, qualitatively consistent with measurements at high frequencies. We consider our experiments to be the first direct measurements of the elastic response of a sample at lower mantle pressures at seismic frequencies in the diamond anvil cell.

**h.** *Elastic properties of Fe- and Al-bearing akimotoite (N.C. Siersch, T. Boffa Ballaran, Z. Liu, T. Ishii, D.J. Frost and T. Katsura, in collaboration with Y. Wang and T. Yu/Argonne)*

The Earth's transition zone between 410 and 660 km depth is most likely dominated by the minerals ringwoodite and majoritic garnet assuming a peridotitic mantle bulk composition. However, seismic wave velocities calculated using the elastic properties of these two minerals are slower than those actually observed globally for this region. These faster wave velocities could indicate that temperatures are lower than normally assumed at the base of the transition zone, possibly due to the presence of stagnating cold slab material. However, lower temperatures would also favour the formation of akimotoite, a  $\text{MgSiO}_3$  polymorph stable between 22 and 24 GPa and 1100 to 1700 °C, which in turn would influence the seismic velocities. Although the elastic properties of the  $\text{MgSiO}_3$  akimotoite endmember have been studied, no data are available for compositions relevant for the Earth's transition zone, *i.e.*, containing some Fe and Al substitution. If it can be demonstrated that mineral assemblages containing akimotoite reproduce the transition zone velocity structure, then this would have important implications for the thermal structure and consequently for the dynamics of the Earth's mantle.

Three well-sintered polycrystalline akimotoite samples containing 8 mol. % of FeO, 2.5 mol. %  $\text{Al}_2\text{O}_3$  and 20 mol. % of  $\text{Al}_2\text{O}_3$  were synthesized in the IRIS-15 (1500 ton) multianvil apparatus at 25 to 27 GPa and 800 to 850 °C for 1 hour from glassy starting materials. After recovering, the samples were carefully investigated using an X-ray micro-diffractometer equipped with a Co tube ( $\lambda=1.79026 \text{ \AA}$ ) to ensure that the samples were monomineralic. Scanning electron microscopy was performed to determine that the grain size was approximately 1  $\mu\text{m}$  and to ensure chemical homogeneity of all grains. Furthermore, electron microprobe analyses were conducted in order to determine the exact compositions. All samples were double-sided polished and inserted into a modified 10/4 multianvil cell assembly equipped with a Re heater and a D-type thermocouple suitable to perform ultrasonic measurements. A  $\text{LiNbO}_3$  transducer, dual cut for the production and detection of P- and S-waves, was glued with epoxy on one truncation of an anvil polished to mirror quality. High pressure and temperature experiments were performed at the 13 ID-D beam line of the Advanced Photon Source using an ultrasonic system to collect compressional and shear wave velocities of the different akimotoite compositions at different pressure and temperature points up to 26 GPa and 800 °C. Synchrotron radiation was used to measure the sample length *in situ* by employing X-ray radiography and to determine the density of the akimotoite samples through diffraction.

The incorporation of Fe and Al into the akimotoite structure has a major effect on both the compressional and shear wave velocities (Fig. 3.4-10). All samples in fact have slower wave velocities than the  $\text{MgSiO}_3$  akimotoite endmember. These newly obtained elastic properties will be used to model seismic wave velocities for different lithologies possibly stable at the base of the transition zone that will then be compared to the seismic reference model.

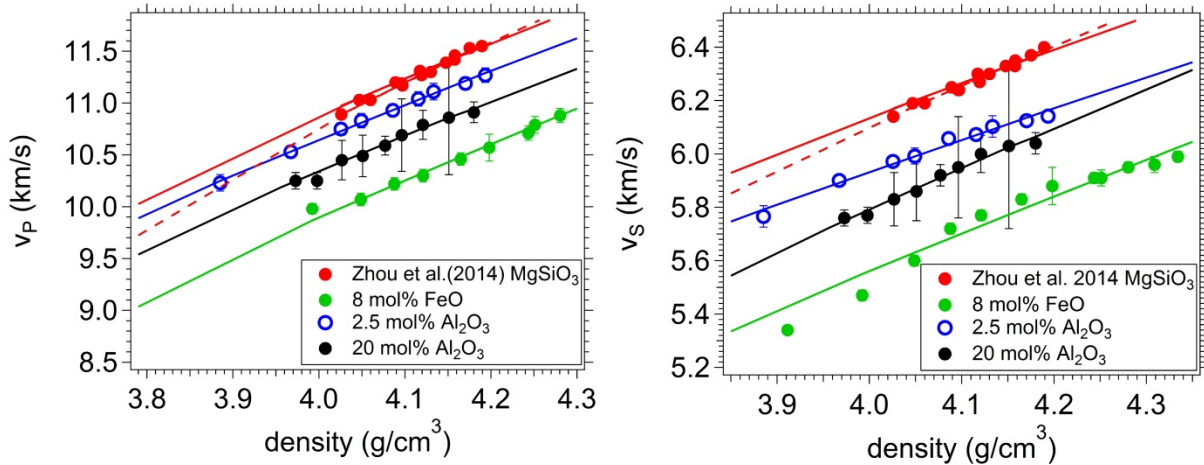


Fig. 3.4-10: Compressional and shear wave velocities of four different akimotoite compositions versus density. The incorporation of Fe (green) and Al (blue and black) clearly slows down the seismic wave velocities relative to the  $\text{MgSiO}_3$  endmember (red) (Zhou *et al.* 2014, PEPI 228: 97).

*i. Quasi-hydrostatic compression and sound wave velocities of polycrystalline stishovite: Evaluating the seismic signature of silica in the lower mantle (J. Buchen, H. Marquardt, K. Schulze, A. Kurnosov, A. Chaudhari, S. Speziale/Potsdam and N. Nishiyama/Hamburg)*

At conditions of the Earth's lower mantle, free crystalline silica  $\text{SiO}_2$  contributes to the mineralogical composition of basaltic rocks with up to 20 vol. %. Basaltic oceanic crust can be carried into the lower mantle by subduction. To detect deep remnants of subducted basaltic crust by seismological methods, we need to know the elastic properties of the constituent minerals at relevant pressures and temperatures. Stishovite, rutile-structured  $\text{SiO}_2$ , was shown to undergo a ferroelastic phase transition at pressures of the lower mantle entailing changes in the elastic behaviour. We performed X-ray diffraction and Brillouin scattering experiments on sintered stishovite polycrystals at pressures relevant to the lower mantle and found that quasi-hydrostatically compressed polycrystals show a peculiar elastic response to compression with potential implications for the detection of silica-rich material in the lower mantle.

Sintered nanocrystalline stishovite was synthesized at 15.6 GPa and 1300 °C in a multianvil press with a grain size of 150-200 nm. A 13  $\mu\text{m}$  thin, double-sided polished disk was prepared from the stishovite polycrystal. Circular specimens with diameters of 40  $\mu\text{m}$  were cut from

this disk using a focused ion beam and loaded into diamond anvil cells together with ruby spheres for pressure determination. In contrast to previous studies on polycrystalline stishovite compressed non-hydrostatically, we used neon as a pressure-transmitting medium to ensure quasi-hydrostatic stress conditions. High-pressure X-ray diffraction was carried out at beamline ID15 at the European Synchrotron Radiation Facility (ESRF, Grenoble) up to 73 GPa. Brillouin spectra were recorded up to 60 GPa using Brillouin spectroscopy facilities installed at Deutsches Elektronen-Synchrotron (DESY, Hamburg) and Bayerisches Geoinstitut (BGI, Bayreuth). Unit-cell volumes obtained from the refinement of X-ray diffraction patterns were combined with literature data on stishovite single crystals compressed in neon to derive an equation of state (EOS) for both tetragonal stishovite and the orthorhombic high-pressure phase (Fig. 3.4-11a). Based on this EOS and shear wave velocities extracted from Brillouin spectra, we constructed a high-pressure elasticity model for both phases (Fig. 3.4-11b).

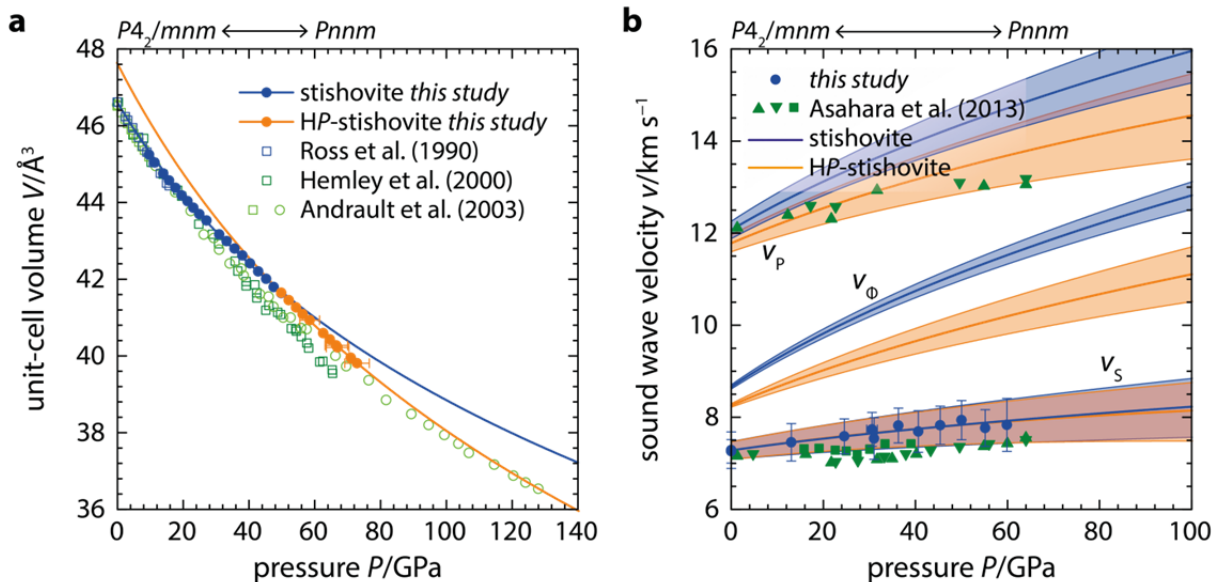


Fig. 3.4-11: (a) Compression curves of stishovite polycrystal and HP-stishovite (orthorhombic phase): solid circles (this study), open squares (single crystal data of Ross *et al.* 1990, *Am. Mineral.* 75: 739 and Hemley *et al.* 2000, *Solid State Comm.* 114: 527), and open circles (powder data of Andraut *et al.* 2003, *Am. Mineral.* 88: 301). (b) Sound wave velocities for polycrystalline stishovite under quasi-hydrostatic (this study) and non-hydrostatic (Ashara *et al.* 2013, *Am. Mineral.* 98: 2053) stress conditions:  $v_P$  (compressional wave),  $v_S$  (shear wave),  $v_\Phi$  (bulk sound). Lines were calculated from a high-pressure elasticity model based on the experimental quasi-hydrostatic EOS and shear wave velocities. Shaded regions represent combined uncertainties ( $\pm 1\sigma$ ) in the EOS and elasticity parameters. Note the coincidence of shear wave velocities for the tetragonal and orthorhombic phases as opposed to the diverging bulk sound velocities. The reported pressure range for the tetragonal-orthorhombic phase transition is marked at the top of each panel.

We found that the ferroelastic phase transition does not lead to shear wave softening in a sintered stishovite polycrystal. Instead, the lower bulk modulus and higher density of the orthorhombic high-pressure phase result in a reduction of bulk and compressional sound wave velocities (Fig. 3.4-11b). This behaviour differs from observations on stishovite single crystals and powders, and we tentatively attribute these differences to the complex elastic response of sintered polycrystals, which closely resemble rocks. Our preliminary results suggest that the presence of a free crystalline silica phase in the lower mantle might be detected by a drop in bulk and compressional wave speeds caused by the ferroelastic phase transition in stishovite.

**j. Ionic conductivity of natural olivine (H. Fei, D. Druzhbin and T. Katsura)**

The electrical conductivity of olivine has three major mechanisms: proton conduction ( $\sigma_p$ ) due to the migration of free protons ( $H^+$ ) incorporated within the crystal structure, small polaron conduction ( $\sigma_h$ ) through the hopping of electron holes ( $h^+$ ) between ferric and ferrous iron, and ionic conduction ( $\sigma_i$ ) by the migration of Mg vacancies ( $V_{Mg}$ ). These mechanisms dominate olivine conductivity at relatively low ( $< \sim 1300$  K), moderate ( $\sim 1300$ - $1700$  K), and high ( $> 1800$  K) temperatures, respectively. Both  $\sigma_p$  and  $\sigma_h$  have been well studied in previous studies whereas  $\sigma_i$  is poorly constrained because the contribution of  $\sigma_i$  to mantle conduction was considered to be negligible. However, recent studies in the literature pointed out that  $\sigma_i$  might be an important conduction mechanism in the upper mantle based on self-diffusion experiments and  $\sigma_i$  measurements in iron-free forsterite.

In order to evaluate the contribution of  $\sigma_i$  to the conduction of iron-bearing mantle, we systematically measured  $\sigma_i$  in natural olivine single crystals as a function of pressure from 2 to 8 GPa at temperatures from 1750 to 2200 K, and oxygen fugacity buffered by MMO (Mo-MoO<sub>2</sub>), RRO (Re-ReO<sub>2</sub>), and MH (Fe<sub>3</sub>O<sub>4</sub>-Fe<sub>2</sub>O<sub>3</sub>) in multianvil experiments using the Solartron 1260 Impedance/Gain-Phase Analyzer. The conductivity ( $\sigma_i$ ) along both [100] and [001] directions ( $\sigma_{i[100]}$  and  $\sigma_{i[001]}$ , respectively) systematically increases with increasing temperature and oxygen fugacity, and decreases with increasing pressure (Fig. 3.4-12a). The conductivity  $\sigma_{i[001]}$  is about 0.6 orders of magnitude higher than  $\sigma_{i[100]}$  (Fig. 3.4-12b). The activation energy for  $\sigma_{i[100]}$  is 220-240 kJ/mol; whereas that for  $\sigma_{i[001]}$  is about 280 kJ/mol. The activation volume is found to be 2.6 cm<sup>3</sup>/mol.

A comparison of  $\sigma_h$ ,  $\sigma_p$ , and  $\sigma_i$  under upper mantle conditions is shown in Fig. 3.4-13. By assuming a bulk water content of 100 wt. ppm (corresponding to  $\sim 30$  wt. ppm in olivine) and oxygen fugacity near FMQ buffer, we have  $\sigma_{i[001]} \gg \sigma_{i[100]}$  and  $\sigma_i \gg \sigma_h \gg \sigma_p$  in the asthenosphere beneath both young and old plates. Namely,  $\sigma_i$  dominates olivine conduction almost in the entire asthenosphere. In addition, the conductivity anomaly at 70-120 km depth beneath young oceanic plates interpreted from magnetotelluric data can be well explained by  $\sigma_i$  in olivine.

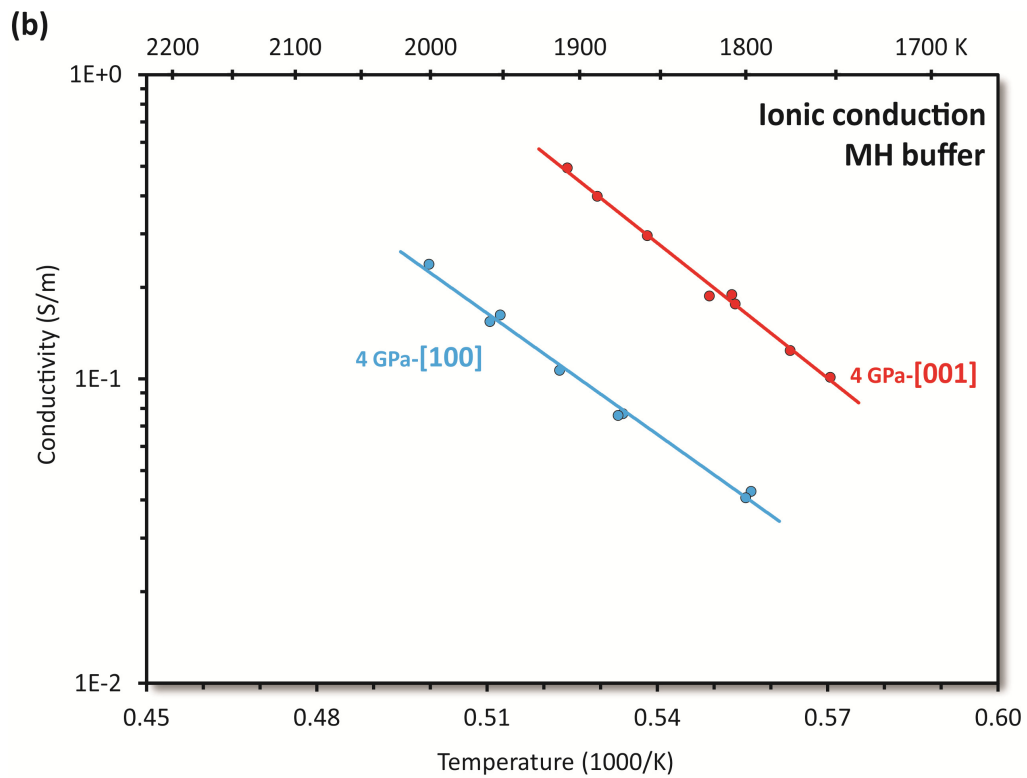
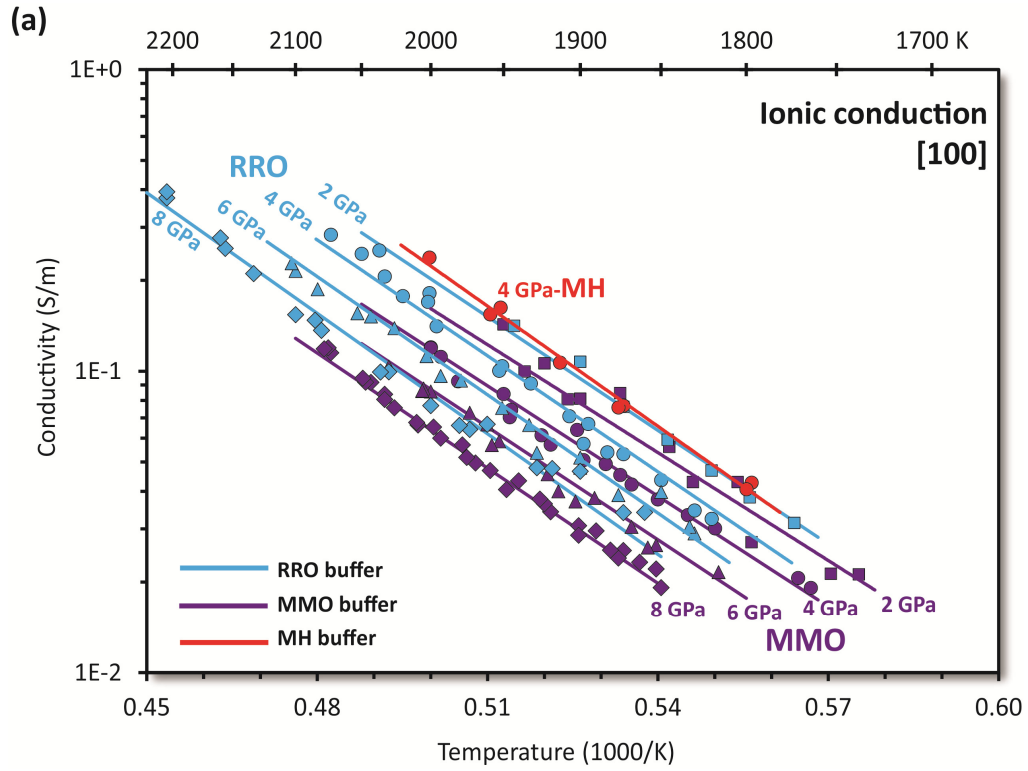


Fig. 3.4-12: Ionic conductivity of natural olivine single crystal at (a) 1750-2200 K, 2-8 GPa along the [100] direction buffered by MH ( $\text{Fe}_3\text{O}_4\text{-Fe}_2\text{O}_3$ ), RRO ( $\text{Re-ReO}_2$ ), and MMO ( $\text{Mo-MoO}_2$ ); and (b) along the [100] and [001] directions buffered by MH.

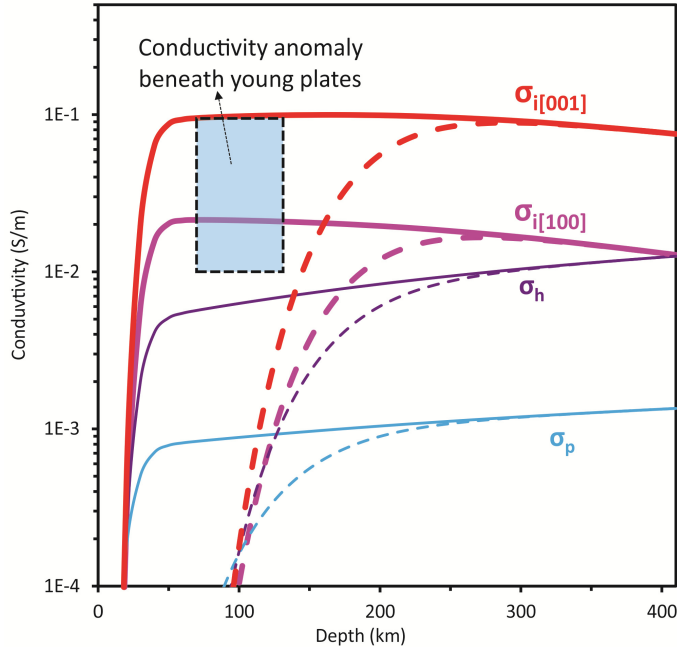


Fig. 3.4-13: Comparison of  $\sigma_h$ ,  $\sigma_p$ , and  $\sigma_i$  in the upper mantle beneath 5 Ma (solid line) and 150 Ma (dashed line) plates. The  $\sigma_h$  and  $\sigma_p$  data are taken from Yoshino *et al.* (2009; EPSL 288: 291). The 5 and 150 Ma geotherms are from Katsura *et al.* (2017; Tectonophysics 717: 162). The conductivity anomaly at 70-120 km depth beneath young plates is interpreted from magnetotelluric data reported by Evan *et al.* (2005; Nature 437: 249) and Baba *et al.* (2006; JGR 111: B02101).

**k. Electronic transport properties of liquid Fe-S alloys from *ab initio* computations (F. Wagle and G. Steinle-Neumann)**

Sulphur is a likely light element candidate in iron-rich cores of terrestrial planets, since it is cosmically abundant and incorporates well into the structure of liquid iron, due to compatibility in both chemistry and size. The presence of light elements substantially changes electronic transport properties, such as electrical resistivity  $\rho_{el}$  and thermal conductivity  $\lambda_{th}$ , compared to pure iron. These properties are key to understanding the thermal evolution of terrestrial planets and the stability of a potential dynamo, but are currently challenging to determine experimentally under extreme pressure ( $P$ ) and temperature ( $T$ ) conditions.

We performed density functional theory-based molecular dynamics simulations (DFT-MD) with 128 atoms in the  $NVT$  ensemble, *i.e.*, involving the number of particles, volume and temperature. Cubic cells of different volume and sulphur content were set up by randomly replacing Fe atoms in molten configurations from previous studies. Atomic coordinates were updated using a time step of one femtosecond, while  $T$  was controlled by the Nosé thermostat. At each time step, the electron density is computed using the projector-augmented wave-method (PAW) with the PBE exchange-correlation functional at a single  $k$ -point. We extract uncorrelated snapshots from the MD simulations and compute Kohn-Sham wavefunctions  $\psi_k$ , their energy eigenvalues  $\epsilon_k$  and the gradients of the Hamiltonian with respect to a shift in wave-vector  $\partial\mathcal{H}/\partial\mathbf{k}$ . From those,  $\rho_{el}$  and  $\lambda_{th}$  are computed using the Kubo-Greenwood equation.

As a consequence of increasing impurity disorder, we find that  $\rho_{el}$  increases substantially with increasing sulphur concentration. Figure 3.4-14 shows that the  $T$ -coefficient of resistivity (TCR) (*i.e.*, the slope) changes not only with sulphur concentration ( $c$ ), but also with

compression. We observe that it decreases gradually with decreasing cell volume for both Fe<sub>7</sub>S (Fig. 3.4-14a) and Fe<sub>3</sub>S (Fig. 3.4-14b), up to the extreme case where the slope changes sign and becomes negative for high sulphur concentration and compression.

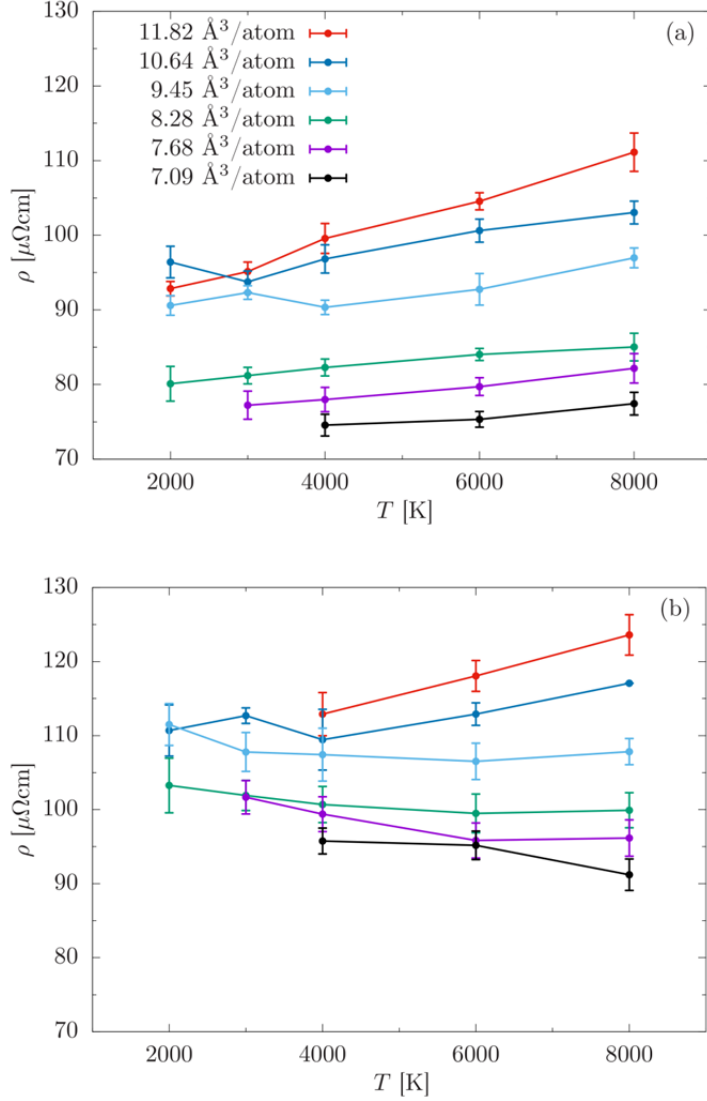


Fig. 3.4-14: Electrical resistivity as a function of temperature along isochores for two different sulphur concentrations: (a) Fe<sub>7</sub>S; (b) Fe<sub>3</sub>S.

At high  $T$  and a high degree of disorder, resistivity saturation due to various mechanisms has been reported to be a dominant effect in liquid metal alloys. This gives rise to the presumption that for our system, the onset of resistivity saturation is triggered by both compression and impurities simultaneously and, in the saturation limit, a previously hidden  $T$ -effect is revealed, which is strong enough for the TCR to change its sign. We see evidence for  $P$ ,  $T$ , and  $c$ -induced saturation, satisfying the Ioffe-Regel-condition (*i.e.*, the electron mean free path becomes equal to the mean interatomic distance) in the most extreme case.

The negative TCR can be understood in terms of an  $s$ - $d$  electron scattering model: transition metals are characterized by localized  $d$ -electrons in the vicinity of the Fermi level (Fig. 3.4-

15), with a high electronic density of states (DOS) and low Fermi velocity. The  $s$ -electrons therefore carry most of the electric current, but can be scattered into  $d$ -states by interaction with phonons, which is the reason for the high resistivity of transition metals.

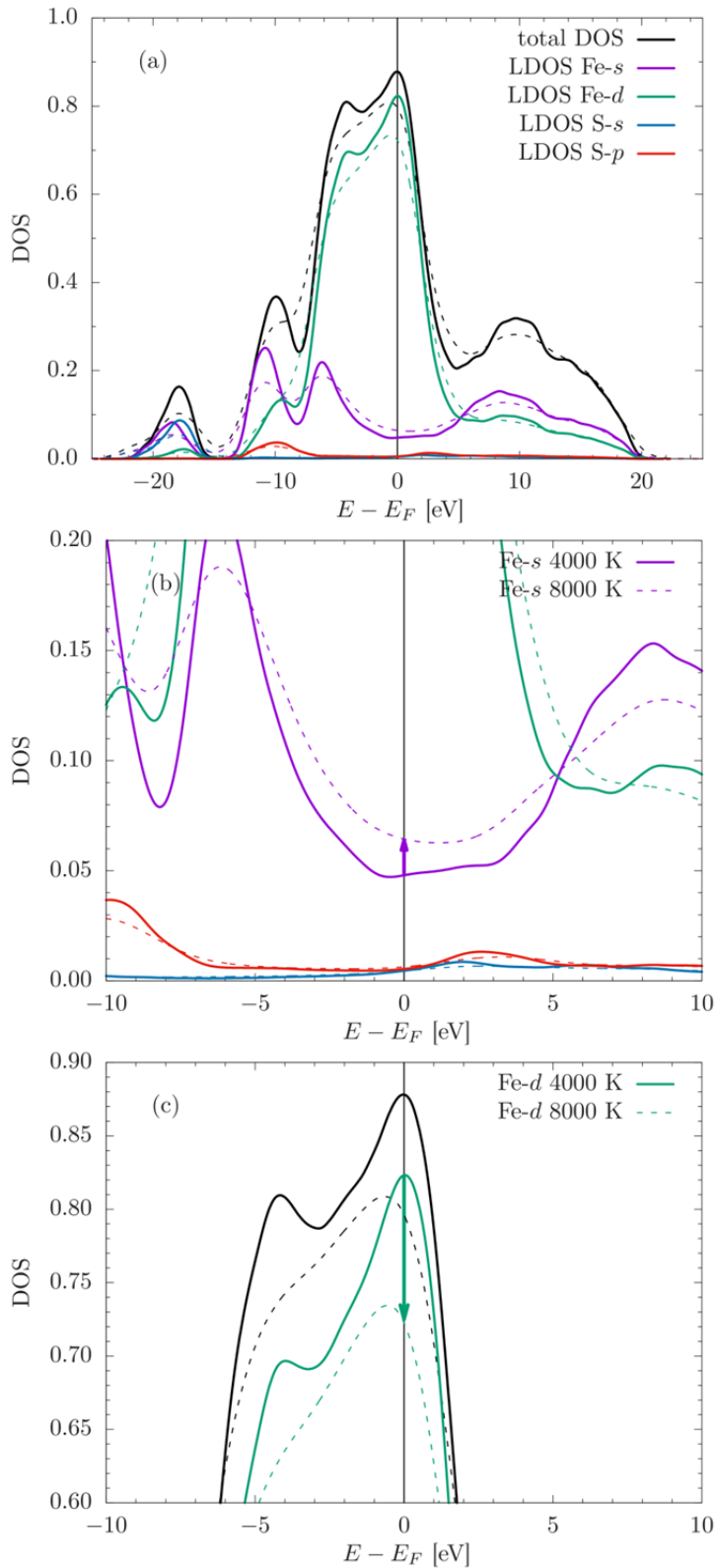


Fig. 3.4-15: (a) Electronic density of states of Fe<sub>3</sub>S at different temperatures at the smallest volume, corresponding to pressures in the Earth's core. The change of the  $s$ - and  $d$ -DOS with temperature is shown in detail in panels (b) and (c), respectively.

With increasing  $T$ , we observe a broadening of peaks in the DOS (Fig. 3.4-15a) as eigenvalues shift when the minimal atomic distances decrease due to the thermal energy introduced into the system. This has two effects: (i) The broadening of the double peak in the  $s$ -DOS around  $-8$  eV and the single peak around  $8$  eV leads to an increase at the Fermi level (Fig. 3.4-15b), thus reducing resistivity, and (ii) the  $d$ -DOS at the Fermi level becomes smaller (Fig. 3.4-15c) and fewer states are available for  $s$ - $d$  scattering processes around the Fermi level.

Concentration dependent values for  $\lambda_{th}$  are very similar to those from previous studies of Fe-Si alloys and range from  $\approx 85 - 125 \text{ Wm}^{-1}\text{K}^{-1}$  at  $P$  and  $T$  corresponding to the Earth's uppermost outer core. In contrast to  $\rho_{el}$ , no anomalous  $T$ -dependence has been observed.

### 3.5 Fluids, melts and their interaction with minerals

The volatile budget of our planet was probably strongly affected by the equilibrium between a reduced magma ocean and a primordial atmosphere very early in Earth's history. Unfortunately, the solubility of volatiles in silicate melts is poorly studied under reducing conditions. This has led to suggestions that carbon may hardly dissolve in silicate melts, if carbon monoxide (CO), rather than CO<sub>2</sub> is the dominant species in the gas phase. The contribution at the beginning of this chapter shows the first direct measurements of CO solubility in silicate melts ranging from rhyolitic to basaltic composition. The data show that CO solubility, although lower than that of CO<sub>2</sub>, is surprisingly high, implying that a large amount of carbon may have been initially sequestered into a magma ocean. Degassing of magmas transports volatiles from the mantle and crust into the atmosphere. This process requires the formation of gas bubbles in a magma. Through a major technical advance recently made at Bayerisches Geoinstitut, it is now possible to directly observe this process *in situ* under a microscope under precisely controlled conditions of pressure and temperature. The experiments described in the second contribution of this chapter suggest that only little supersaturation is necessary to nucleate bubbles of water vapour in a silicate melt. A major problem in forecasting volcanic eruptions is to distinguish magma chambers from hydrothermal systems below active volcanoes. Both objects may cause ground movements and may show up in geophysical data as regions of reduced seismic velocities and enhanced electrical conductivity. New electrical conductivity data for the HCl-H<sub>2</sub>O system that is quite relevant for subvolcanic systems are reported in the next section of this chapter. They will help to distinguish the signature of acidic fluids and of silicate melts in magnetotelluric surveys of active volcanoes.

Earth's mantle is a very important reservoir of volatiles. One contribution in this report looks at the efficiency of nitrogen recycling into the deep mantle by subduction. An important conclusion from this study is that bulk atmospheric pressure in the Archean may have been higher than today. The two following contributions investigate the storage of fluorine in the mantle and its effect on melting. Among other things, the presence of fluorine enlarges the stability limit of phlogopite and thereby indirectly also influences water storage in the mantle. Variations of oxygen fugacity in the mantle affect the valence of some transition metal, most notably iron, but also chromium. An experimental study in this chapter suggests that in basaltic melts, Cr<sup>2+</sup> becomes stabilized relative to Cr<sup>3+</sup> with increasing pressure.

The last two contributions in this chapter of the annual report consider some technical difficulties in studying silicate melts and fluids at high pressures and temperatures. Glasses are often used as models of silicate melt, but a quantum mechanical study shows that even at extremely high quench rates, significant differences exist between the structure of a melt and that of a quenched glass. Measuring hydrogen isotope fractionations between coexisting aqueous fluids and silicate melts has proved to be extremely difficult. *In situ* studies of isotope fractionation by Raman spectroscopy have been proposed, but the last contribution in this chapter shows that some assumptions in these studies are fundamentally in error and the corresponding fractionation factors reported in the literature are unlikely to reflect reality.

**a.** *Carbon monoxide solubility in silicate melts (T. Yoshioka, T. Nakamura/Sendai, D. Nakashima/Sendai, S. Shcheka and H. Keppler)*

In the modern Earth, carbon dissolves in magmas mostly as carbon dioxide (CO<sub>2</sub>), which plays an important role in melting process and volcanic eruptions. The behaviour of carbon monoxide (CO) is not well studied, because it is a trace component in volcanic gases. However, under more reduced conditions that likely prevailed in the early history of Earth and Moon, CO may have been an important volatile component. Therefore, in order to understand the behaviour of carbon under reducing conditions, we investigated the solubility of carbon monoxide in basaltic melts.

Two series of solubility experiments were conducted in an internally heated pressure vessel (IHPV) and in a piston cylinder apparatus. In order to avoid complications due to redox exchange reactions with Fe<sup>2+</sup> and Fe<sup>3+</sup>, a synthetic, Fe-free MORB glass was used as starting material. For IHPV experiments, the glass and CO gas were directly sealed into a Pt capsule. These experiments were conducted at 1250-1400 °C and 2-5 kbar for 3-6 hours. For piston cylinder experiments, the Fe-free MORB glass, Ag<sub>2</sub>C<sub>2</sub>O<sub>4</sub> (as a CO<sub>2</sub> source) and graphite were sealed in Pt<sub>95</sub>Rh<sub>5</sub>-Pt capsules. Those experiments were conducted at 1400-1600 °C and 10-20 kbar for 6 hours. In both types of experiments, the equilibrium  $2 \text{CO} = \text{CO}_2 + \text{C}$  (graphite) was reached upon heating, as indicated for example by the precipitation of graphite in the IHPV experiments. Therefore, the gas phase coexisting with the melt was a mixture of CO with some CO<sub>2</sub> and the redox conditions were controlled by the graphite-CO (GCO) buffer. Carbon contents in the quenched glasses were quantified by the CAMECA IMS 7f secondary ion mass spectrometer at Tohoku University. Standards were CO<sub>2</sub>-bearing glasses synthesized in a piston cylinder apparatus under oxidizing conditions. The carbon content of the standards was quantified by FTIR.

Figure 3.5-1 shows the bulk carbon (CO + CO<sub>2</sub>) solubility in Fe-free MORB glasses at various pressures and temperatures. Carbon solubility at low pressure (2-5 kbar) and high pressure (10-20 kbar) is in the range of 100-600 ppm and 1000-3000 ppm by weight, respectively. Pressure clearly enhances carbon solubility at both low and high pressure, with the data from the IHPV and piston cylinder experiments falling on one single trend following Henry's law. In contrast to this, the effect of temperature is minor. Carbon solubility slightly increases with temperature at high pressure whereas it decreases with temperature. A similar effect is known for water solubility in silicate melts.

Overall, the carbon solubility in equilibrium with a reduced, CO-rich fluid phase is about half of that expected for pure CO<sub>2</sub>. This implies that CO is not orders of magnitude less soluble than CO<sub>2</sub> in silicate melts and the contribution of CO to bulk carbon solubility cannot be neglected. This has two important consequences: (1) For a magma ocean coexisting with a reduced, CO-rich gas phase, the amount of carbon dissolved in the silicate melt is not much lower than for oxidizing conditions; (2) on the other hand, the relatively high solubility of CO in silicate melts makes it rather unlikely that dissolved carbon was driving the fire-fountain-type eruptions on the early Moon. This is because according to our data, the low carbon contents in lunar magmas would not be sufficient to produce high overpressures, even if the carbon were dissolved as CO.

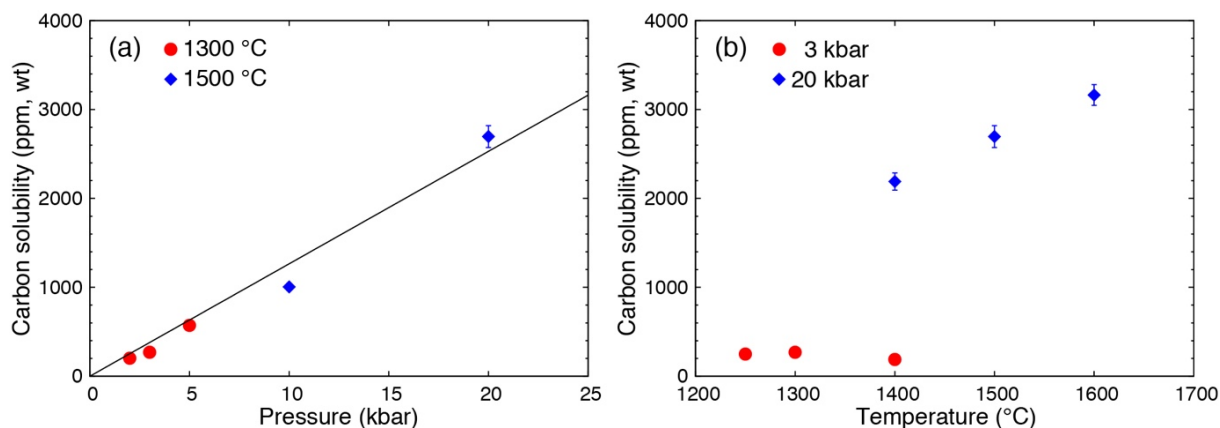


Fig. 3.5-1: Carbon solubility in Fe-free basalt in equilibrium with a CO-rich fluid versus (a) pressure and (b) temperature. Red and blue symbols are data obtained with an internally heated pressure vessel and a piston cylinder apparatus, respectively. Carbon solubility is nearly proportional to pressure whereas the temperature effect is small and depends on pressure.

**b. In situ observation of bubble nucleation in silicate melts at precisely controlled pressure and temperature (M. Masotta/Pisa and H. Keppler)**

Magmatic degassing controls the intensity and the style of volcanic eruptions. Understanding the mechanisms and rates at which volatiles are exsolved and released from the magma is fundamental for forecasting volcanic activity and the hazards associated with explosive eruptions. Natural samples and products from quench experiments provide only a snapshot of the final state of volatile exsolution, leaving the processes occurring during its early stages unconstrained. In order to fill this gap, we developed a new hydrothermal moissanite cell for *in situ* experiments at pressures up to 1000 bar and temperature to 850 °C. The central part of this cell is a sample holder with a cylindrical sample chamber connected to a capillary that can be attached to a pressure line (Fig. 3.5-2). Sample holder and capillary were made out of one single piece of the Nimonic 105 super alloy by spark erosion. In the cell, the sample chamber is sandwiched between the two moissanite anvils and sealed against the anvils with gold foil. The new technique allows the direct observation of various phenomena, such as bubble nucleation, growth and dissolution in silicate melts, at accurately controlled rates of heating, cooling and compression or decompression.

Several pilot experiments were performed on a haplogranitic melt at 715 °C and under variable pressure regimes (pressure oscillations between 500 and 1000 bar and decompression from 800 to 200 bar at variable decompression rates). Bubble nucleation occurs in a short single event upon heating of the melt above the glass transformation temperature and upon decompression, but only during the first 100 bar of decompression. New bubbles nucleate only at a distance from existing bubbles larger than the mean diffusive path of water in the melt (Fig. 3.5-3). Bubbles expand and shrink instantaneously in response to any pressure change. The bubble-bubble contact induced during pressure cycling and decompression does not favour bubble coalescence, which is never observed at contact times shorter than 60 s.

However, repeated pressure changes favour the diffusive coarsening of larger bubbles at the expense of the smaller ones (Ostwald ripening). Experiments with the haplogranite show that, under the most favourable conditions of volatile supersaturation (as imposed by the experiment), highly viscous melts are likely to maintain the packing of bubbles for longer time before fragmentation. *In situ* observation with the new hydrothermal moissanite cell allow to carefully assess the conditions of bubble nucleation, eliminating the uncertainty involved in the post-mortem observation of natural and experimental samples.

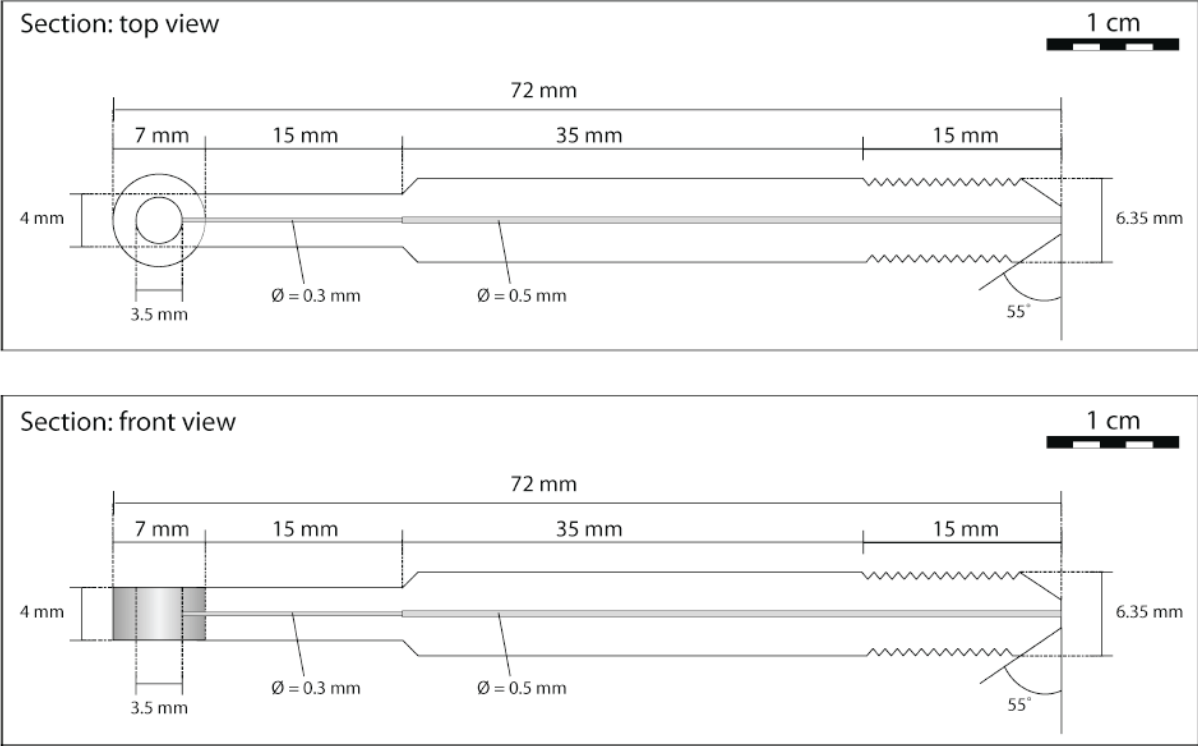


Fig. 3.5-2: Sample holder for the new hydrothermal moissanite cell. The sample chamber on the left of the piece will be sandwiched between two moissanite anvils; rings of gold foil on top of the anvils provide tight sealing.

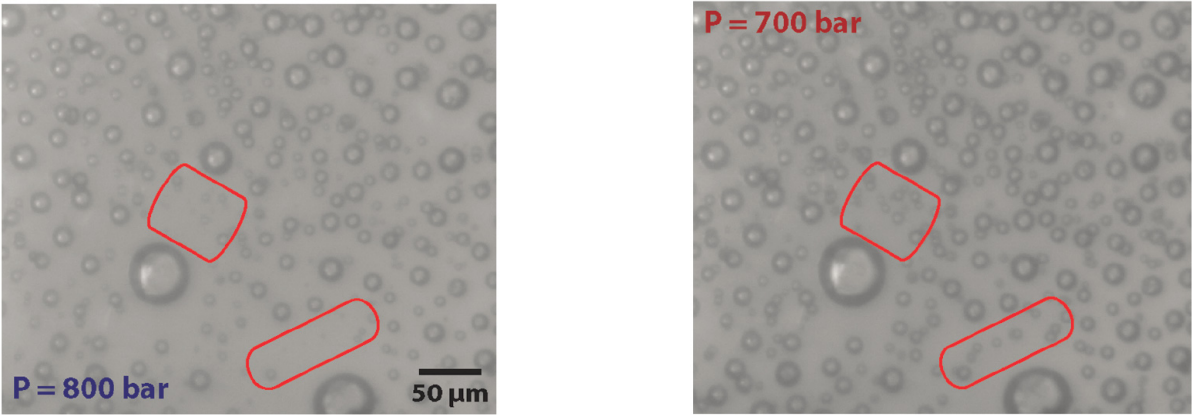


Fig. 3.5-3: Nucleation of new gas bubbles in a hydrous haplogranitic melt at 715 °C during decompression with 50 bar/min.

c. *Electrical conductivity of HCl-H<sub>2</sub>O fluids at high pressure and high temperature (S. Klumbach and H. Keppler)*

Magnetotelluric surveys often show regions of elevated electrical conductivity below active volcanoes. These anomalies may be caused by magma bodies or by circulating hydrothermal systems. Distinguishing these two possibilities is essential for the assessment of volcanic hazards and for predicting eruptions. Until recently, there was a lack of electrical conductivity data for aqueous fluids under elevated pressures and temperatures, which hampered the quantitative interpretation of magnetotelluric data. Recently, studies at Bayerisches Geoinstitut yielded conductivity data for the NaCl-H<sub>2</sub>O system. In this contribution, additional measurements were carried out in the HCl-H<sub>2</sub>O system, since HCl is often a significant fluid component in acidic hydrothermal systems below active volcanoes.

Electrical conductivities were measured in a modified Bassett-type diamond anvil cell. A diamond platelet with a cylindrical borehole in the center is placed between two gold-covered rhenium gaskets, which serve as electrodes for impedance measurements. Preliminary results up to 0.6 GPa and 500 °C are shown here (Fig. 3.5-4). The most recent experiments were performed up to 0.9 GPa and 800 °C, but they have not yet been evaluated completely.

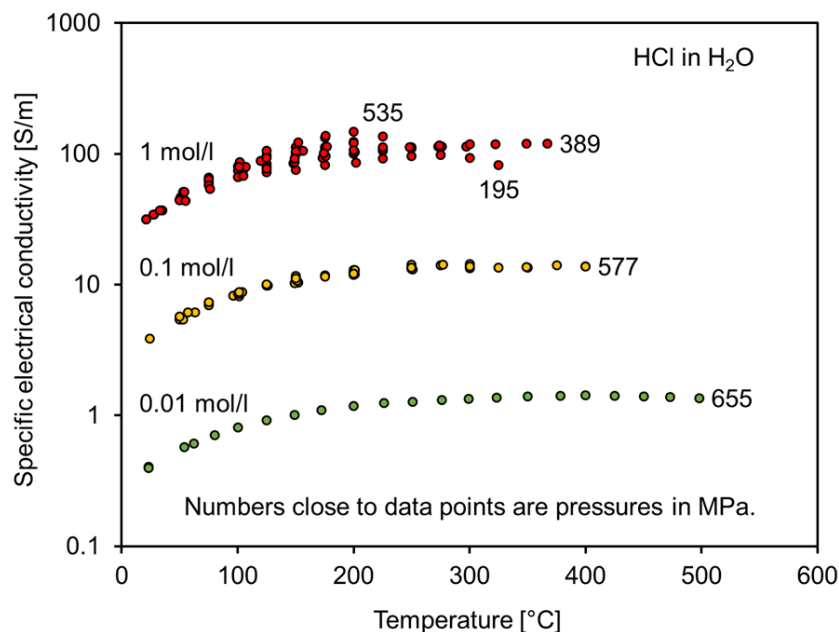


Fig. 3.5-4: Electrical conductivity of HCl-bearing aqueous fluids with different concentrations as measured in diamond anvil cell experiments. Note that these are isochoric experiments, such that pressure increases with temperature. HCl concentrations refer to mol/l at standard conditions.

Figure 3.5-4 clearly shows that higher HCl concentrations lead to higher electrical conductivities due to a higher number of charge carriers. Moreover, conductivity increases

with temperature up to about 300 °C due to a higher mobility of the charge carriers. Further increasing temperature leads to ion association and decreasing conductivity. Pressure generally increases the conductivity, since it enhances dissociation.

Based on the data presented in Fig. 3.5-4 the specific electrical conductance  $\sigma$  (in S/m) of HCl-bearing aqueous solutions preliminary can be described by

$$\log \sigma = - 1.49 - 25.7 T^{-1} + 0.96 \log c + 2.33 \log \rho + \log \Lambda_0$$

where  $T$  is the temperature in K,  $c$  is HCl concentration in wt. %,  $\rho$  is the density of pure water at given pressure and temperature, and  $\Lambda_0$  is the limiting molar conductance of the fluid (in  $\text{S cm}^2 \text{ mol}^{-1}$ ), which is given by the equation

$$\Lambda_0 = 1190 - 257 \rho + 708\,977 T^{-1} - 277\,461\,050 T^{-2}$$

Figure 3.5-5 shows that this numerical model reproduces the experimental data very well; it should also allow moderate extrapolations in temperature, fluid density, and composition.

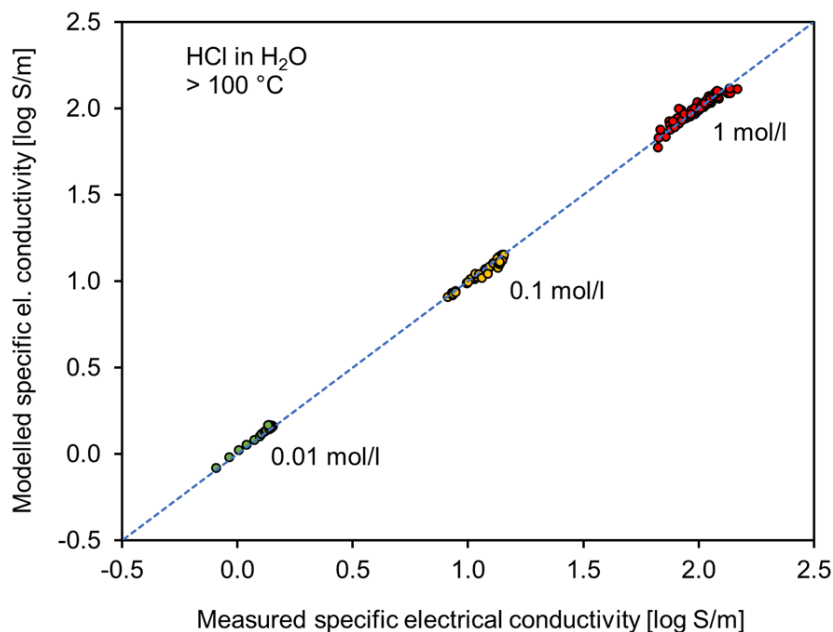


Fig. 3.5-5: Comparison of measured electrical conductivities of HCl-bearing aqueous fluids with those predicted by the numerical model.

In general, conductivities in the HCl-H<sub>2</sub>O system are up to one order of magnitude higher than in the NaCl-H<sub>2</sub>O system under otherwise comparable conditions. This means that even small concentrations of HCl in hydrothermal fluids need to be considered for an appropriate modeling of the electrical conductivity in subvolcanic hydrothermal systems.

**d. *Experimental determination of the nitrogen-carrying capacity of subducted slab-derived melt (A. Mallik, M. Wiedenbeck/Potsdam and Y. Li/Guangzhou)***

Nitrogen (N) is the most abundant element in the present day terrestrial atmosphere (78 % by volume). It is one of the key elements present in bio-macromolecules (*e.g.*, nucleic acids and proteins) and therefore plays a major role in the evolution of life on Earth. The presence of nitrogen in the atmosphere may enhance the potency of greenhouse gases and may help to retain H<sub>2</sub>O on the Earth. Thus, studying N cycling from the atmosphere to the deep Earth and back is important for understanding the evolution of the atmosphere and of climate of the Earth. Subduction zones are the principal tectonic setting relevant for the recycling of N from the atmosphere into the mantle, mostly through subduction of sediments. We are investigating the mechanism and efficiency of N transfer from the subducted slab to the arc source by an experimental approach. This includes estimating the N carrying capacity of fluids and slab-derived melts, N-isotopic fractionation during transfer from the slab to the arc source and partitioning of N between slab-derived fluids/melts, the subducted slab and mantle minerals. Preliminary results from this study show that 45-74 % of the nitrogen introduced into the mantle by subduction survive the filter of arc magmatism and enter the deep mantle. Extrapolating this rate of efficiency of sequestering N from the surficial reservoirs to the deep mantle through time, the Archean atmosphere appears to have been more N-rich than the present one, enough to warm the Archean climate above freezing. Also, using the rate of N recycling through the deep mantle and the isotopic composition of the recycled N, the N isotopic composition of the primitive mantle has been estimated, which will be used in future studies to constrain the nature of parent bodies that accreted to form the Earth. The long-term goal of this study is to correlate deep N cycling to that of noble gases, H<sub>2</sub>O and C to constrain the composition and dynamics of terrestrial reservoirs that host these volatiles, as well as, to investigate how these deep volatile cycles can give us an insight into the accretionary history of the Earth, especially the nature of parent bodies that formed the Earth.

**e. *Phlogopite-peridotite melting and the role of fluorine in volatile storage in the upper mantle (P. Condamine, D.J. Frost and E. Médard/Clermont-Ferrand)***

Phlogopite is a common accessory mantle phase, particularly in the subcontinental mantle, as observed in xenoliths from kimberlites and alkali basalts. Its presence significantly affects the H and K cycle within the Earth's mantle and in subduction zones. Whereas phlogopite-bearing basaltic, slab-like assemblages have been intensively studied to understand the recycling processes in subduction zones, very little is known about the capacity of such hydrous phases to store volatile elements in the peridotitic mantle.

The main purpose of this study is to better constrain the recycling of fluorine and hydrogen and their storage in the upper mantle within hydrous phases. This involves two main

problems: 1) Studying the effect of fluorine on the stability of phlogopite and amphibole, which in turn will affect the recycling of water into the deep mantle. 2) Determining the incipient melt compositions from such assemblages in the mantle and their ability to produce K-rich magmas.

Experiments were carried out in a multianvil apparatus between 6 and 8 GPa at 1200-1400 °C, from sub-solidus conditions to high degrees of melting, using a KLB-1 peridotite starting material containing 10 wt. % of natural, fluorine-bearing (0.7 wt. %) phlogopite. Iterative sandwich experiments were used to study the very first melts in equilibrium with the peridotite.

At 6 GPa, phlogopite is stable in the residual peridotite above the water-undersaturated solidus (located at 1200-1250 °C) up to 1350 °C (Fig. 3.5-6). At 8 GPa, provisional results show that phlogopite is stable to more than 1400 °C, above the mantle adiabat temperature. Thus, natural fluorine-bearing phlogopite is stable to temperatures 100-150 °C higher than expected from previous studies.

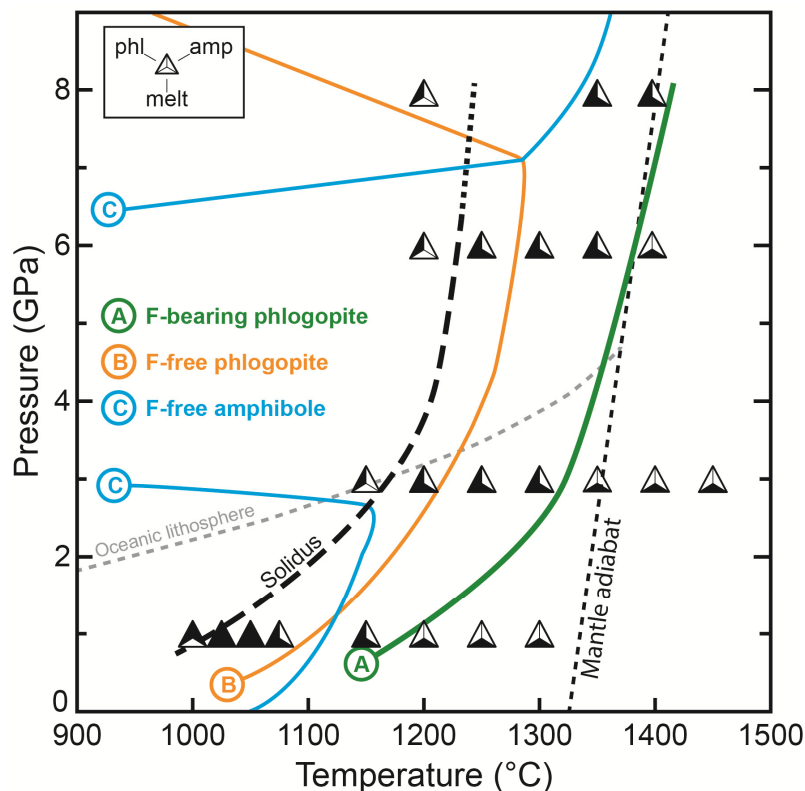


Fig. 3.5-6: Stability of K-rich, hydrous phases in a peridotitic assemblage. The phlogopite stability limit at fluorine-bearing conditions determined in this study is given as curve A and crosses the mantle adiabat at a pressure > 6 GPa. Curves B and C are for a fluorine-free system.

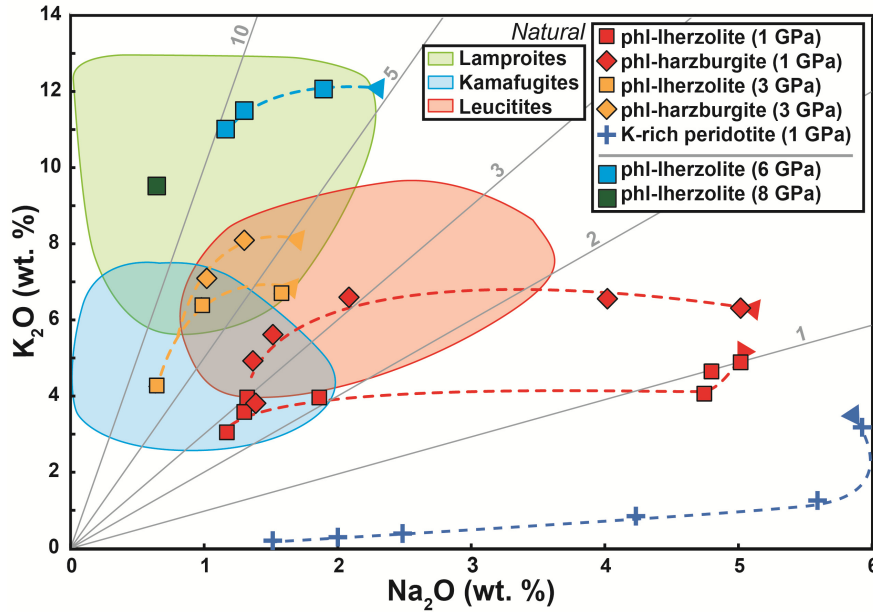


Fig. 3.5-7:  $K_2O$  vs  $Na_2O$  content of experimental melts derived from K-rich or phlogopite-peridotite assemblages compared with the three main groups of ultrapotassic natural rocks. Experiments at 6 and 8 GPa from this study exhibit  $K_2O/Na_2O$  ratio similar to lamproites. Grey lines give  $K_2O/Na_2O$  ratios.

Preliminary melt compositions obtained from sandwich experiments are silica-undersaturated and exhibit very high  $K_2O$  contents, ranging between 11-12 wt. % at low to moderate degrees of melting (10-25 wt. %). In contrast to this,  $Na_2O$  contents are very low (1-2 wt. %), leading to high  $K_2O/Na_2O$  ratios (6-14), thus sharing strong affinities with natural lamproitic compositions (Fig. 3.5-7).

Due to the presence of small amounts of fluorine within the mantle, phlogopite may remain stable in the deep mantle at adiabatic temperatures. This is of importance for the storage of volatile elements and their mobility during magmatic processes. During melting, the presence of phlogopite will produce extreme  $K_2O/Na_2O$  ratios and peculiar trace element signatures in low-degree partial melts, owing to the affinity of phlogopite to large ion lithophile elements.

**f.** *Fluorine partitioning between hydrous minerals and incipient melt in the lithospheric mantle (P. Condamine, E. Médard/Clermont-Ferrand, J. Francomme/Milan and D. Laporte/Clermont-Ferrand)*

The aim of this study is, principally, to first to better understand the distribution of fluorine in mantle phases. Previous studies have emphasized its role in the genesis of K-rich, Al-poor magmas such as group I ultrapotassic melts (lamproites). Because pressure has a strong effect on phlogopite chemistry in the mantle, which in turn influences incipient melt compositions, the partitioning of fluorine between minerals and melts was studied for a wide range of compositions.

The fluorine contents of both hydrous phases and silicate melts were analyzed in experimental charges representing incipient melting of phlogopite ± amphibole-bearing peridotite within both the spinel and the garnet stability fields (1-3 GPa). An electron microprobe was used with 15 kV voltage, 80 nA beam current and a counting time of 180 s, leading to a detection limit of about 250 ppm.

Fluorine substitution for OH significantly affects the phlogopite composition, especially its alumina content (Fig. 3.5-8). At very high fluorine contents, phlogopite becomes perpotassic in composition. The fluorine partition coefficient between hydrous phases and silicate melts is strongly affected by the melt composition, ranging from 2.2 to 4.3 in our trachytic to trachyandesite compositions (Fig. 3.5-9). For highly depolymerized melts (NBO/T > 2), corresponding mainly to melts formed at pressure above 5 GPa, fluorine becomes incompatible in phlogopite, limiting its retention in the mantle during partial melting events.

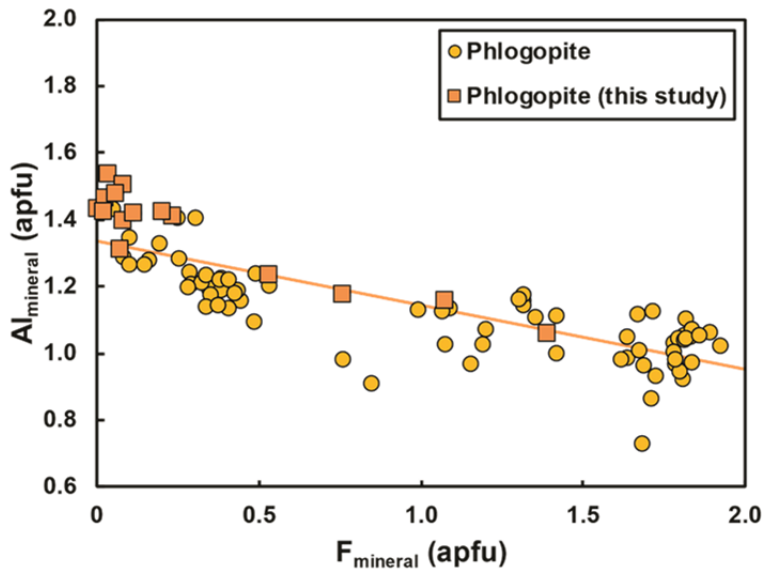


Fig. 3.5-8: Alumina content (atom per formula unit) in phlogopite as a function of fluorine content. At very high fluorine contents, phlogopite becomes perpotassic in composition. Circles are data compiled from the literature.

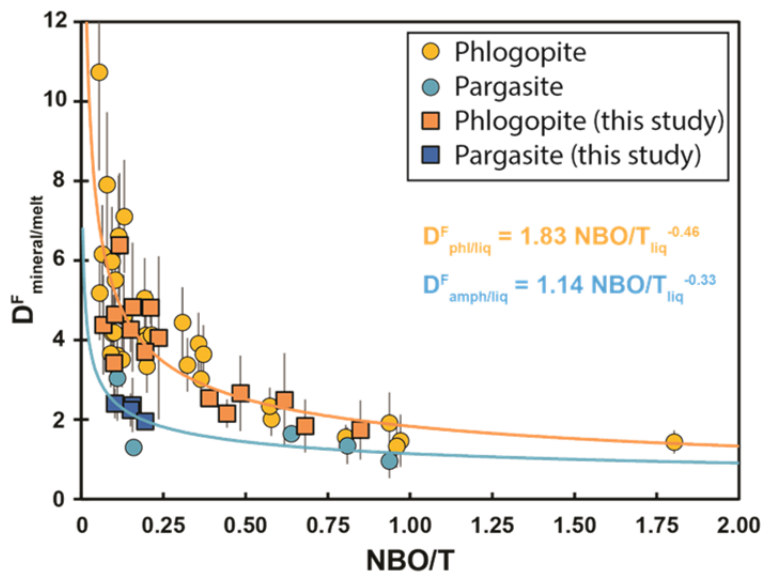


Fig. 3.5-9: Fluorine partition coefficients between minerals and melts as a function of melt composition and polymerization, represented by the NBO/T parameter. Circles are data compiled from the literature.

*g. The effect of pressure on Cr redox systematics in reduced basaltic liquids (A.S. Bell/Albuquerque, K. Armstrong, D.J. Frost and M. Newville/Chicago)*

Chromium is a minor, yet important multi-valent element in basaltic magmas. Understanding the redox systematics of Cr in mafic magmas has important implications for 1) contextualizing  $\mu$ -XANES measurements of Cr valence in olivine and pyroxene, 2) predicting Cr-spinel stability and, 3) deepening our current understanding of the silicate-metal partitioning of Cr during core formation. Like all other homogenous redox reactions in silicate liquids, the equilibrium  $\text{Cr}^{2+}/\Sigma\text{Cr}$  is controlled by temperature, pressure, and liquid composition.

We have performed a series of multianvil experiments to investigate how pressure influences the equilibrium Cr valence in basaltic liquids. MORB liquids were equilibrated with liquid Fe-C alloys at 1750 °C and pressures of 2, 4, and 6 GPa. The experiments were conducted at reduced conditions to effectively eliminate the presence of  $\text{Fe}^{3+}$  in the liquid, as the Cr valence ratio is not preserved when ferric iron-bearing liquids are quenched. The  $\text{Cr}^{2+}/\Sigma\text{Cr}$  of the quenched silicate glass produced in these experiments were measured via Cr K-edge XANES at the Advanced Photon Source GSECARS Beamline 13 IDE. The oxygen fugacity of the experiments was controlled by the equilibrium between the silicate liquid and the liquid Fe-C alloy. The  $f\text{O}_2$  values of the experiments were calculated from the standard state free energy of the FeO-Fe reaction at 1750 °C and the calculated activities of FeO and Fe in the silicate liquid and metallic liquid, respectively. The relatively large density contrast between FeO in the silicate liquid and Fe in the metallic alloy shifts the equilibrium  $f\text{O}_2$  values to higher values with increasing pressure (*i.e.*,  $\Delta_r V_{\text{FeO-Fe}} < 0$ ). To account for this pressure effect, the molar volumes of  $\text{FeO}^{\text{sil}}$  and  $\text{Fe}^{\text{alloy}}$  were calculated with a Murnaghan EOS; the molar volumes were then used to correct the  $\Delta_r G^\circ_{(1750\text{ °C-1bar})}$  of the FeO-Fe reaction to its value at the pressure of interest. The calculated  $f\text{O}_2$  values for the experiments are shown in Fig. 3.5-10. They are approximately 2 log units below the iron-wustite buffer.

The effects of pressure on the measured  $\text{Cr}^{2+}/\Sigma\text{Cr}$  of the experimental liquids and calculated  $\ln K'$  values of the  $\text{CrO} + \frac{1}{4}\text{O}_2 = \text{CrO}_{1.5}$  equilibrium are shown in Figs. 3.5-11 (top) and 3.5-11 (bottom). On the surface, the measured  $\text{Cr}^{2+}/\Sigma\text{Cr}$  of the liquids seems to have no apparent correlation with pressure, which would suggest that the molar volumes of CrO and  $\text{CrO}_{1.5}$  in the liquid are nearly identical. However, the  $f\text{O}_2$  at which the experiments equilibrated also increases by  $\sim 1.5$  log unit from 2 GPa to 6 GPa, and this increase in  $f\text{O}_2$  masks the true effect of pressure on the Cr valence state in the liquid. To account for this, we have plotted the calculated  $\ln K'$  values as function of pressure. The decrease in  $\ln K'$  with increasing pressure suggests a negative  $\Delta_r V$  for the  $\text{CrO-CrO}_{1.5}$  valence reaction in the liquid. With this data we estimate  $\Delta_r V = -3.1 \text{ cm}^3 \text{ mol}^{-1}$ , which translates to a  $d(\Delta_r G^\circ)/dP = -3.2 \text{ kJ GPa}^{-1}$  for the Cr valence reaction. This analysis suggests that pressure increases  $\text{Cr}^{2+}/\Sigma\text{Cr}$ . The negative sign of the apparent  $\Delta_r V$  is somewhat curious as  $\text{Cr}^{2+}$  should have the larger ionic radius and thus larger molar volume. However, this systematics may be rationalized if one considers that  $\text{Cr}^{2+}$

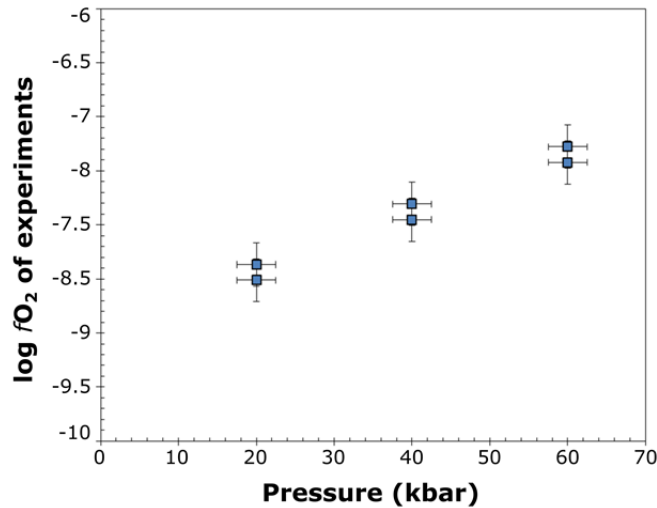


Fig. 3.5-10: Calculated oxygen fugacities of the experiments based on the equilibrium between Fe-C alloy and FeO in the silicate melt.

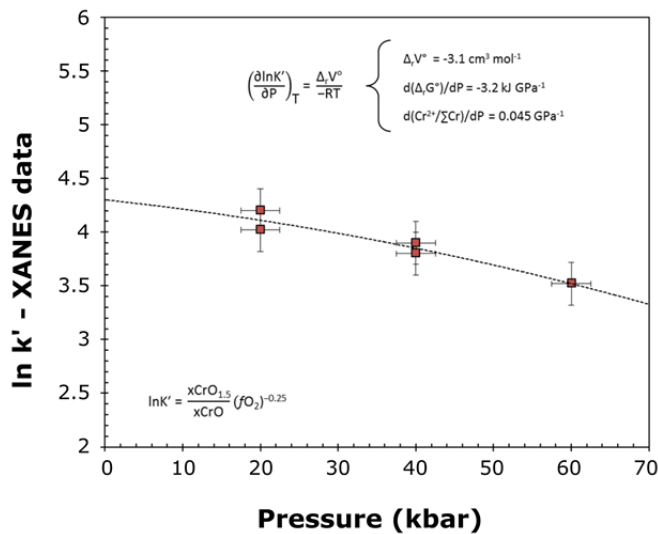
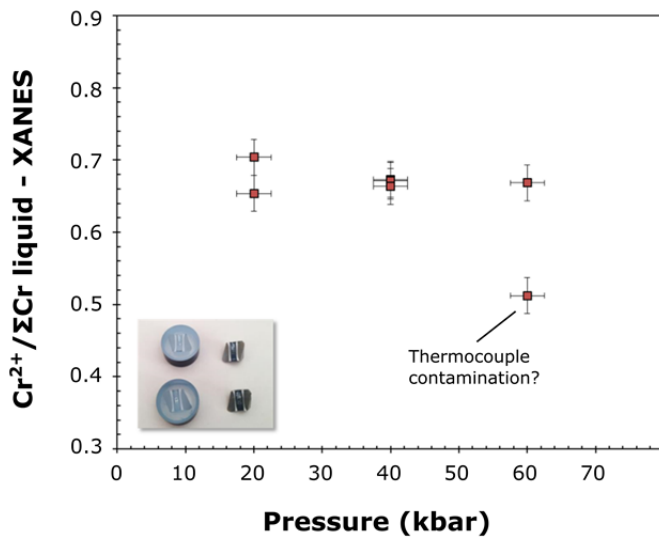


Fig. 3.5-11: Results of XANES analyses of the Cr valence state in silicate glasses reported as Cr<sup>2+</sup>/ΣCr (top) and as the calculated lnK' (bottom) of the equilibrium CrO + 1/4O<sub>2</sub> = CrO<sub>1.5</sub> as a function of pressure. Pressure appears to have no effect on Cr valence, however once the effects of the increasing fO<sub>2</sub> are accounted for, the decrease in lnK' with pressure equates to an increase in Cr<sup>2+</sup> as a result of pressure alone.

in silicate liquids is a Jahn-Teller active cation that may adopt a tetragonally (axially) compressed, octahedral coordination state. In contrast,  $\text{Cr}^{3+}$  is known to occupy highly symmetrical regular octahedral coordination polyhedra. The apparent molar volume data derived in this study is consistent with the interpretation that  $\text{Cr}^{2+}$  occupies compressed octahedral sites in the liquid.

**h.** *Influence of cooling rate on  $\text{Mg}_2\text{SiO}_4$  and  $\text{MgSiO}_3$  glass structure from MD simulations (J. Yao, G. Steinle-Neumann and F. Wagle)*

Direct measurements of the physical properties and the structure of silicate liquids are challenging due to their high melting point. Many measurements therefore rely on silicate glass, quenched from the melt. The extent to which they represent liquid structure, however, cannot always be unambiguously evaluated. We have therefore performed first-principles molecular dynamics simulations on  $\text{Mg}_2\text{SiO}_4$  and  $\text{MgSiO}_3$  melt (2000 K) and glass at 300 K, cooled from the liquid at different rates: cooling varies between direct quench, 1K/fs and 0.1 K/fs, still many orders of magnitudes faster than experimentally obtainable rates. With phonon energies of  $\sim 30$  meV (periods of  $\sim 100$  fs) for  $\text{Mg}_2\text{SiO}_4$ , even the slow cooling rate corresponds to a change in temperature of 10 K during the relaxation time of an individual phonon vibration. Therefore, it is not clear whether in the MD simulations a specific configuration is cooled slowly enough for a complete relaxation within the glass. However, slower cooling rates are currently not technically feasible with available computer resources. The MD simulations are performed for cells with 210 atoms each and at a cell volume of  $13.55 \text{ \AA}^3/\text{atom}$  in order to directly compare structural features between them.

While experiments using neutrons or X-rays provide information on the structure in reciprocal space and only for integrated properties, partial radial distribution functions (RDF,  $g_{\alpha\beta}(r)$  for species  $\alpha$  and  $\beta$ ) can be computed from the configurations of the MD trajectory as the probability of finding an atom of type  $\beta$  at distance  $r$  from atom  $\alpha$ . From the partial RDF, partial structure factors are determined by a Fourier transform, with proper weighting by the X-ray form factor and coherent neutron scattering length, respectively. They can be summed to the total structure factor as measured in experiments.

For  $\text{Mg}_2\text{SiO}_4$  and  $\text{MgSiO}_3$ , partial RDFs are virtually indistinguishable for all atom pairs, independent of whether they are for the melt or for the glass, with the exception of subtle, but significant changes in O-O distances for the forsterite composition. The O-O RDF is dominated in all cases by the nearest neighbor peak at  $2.72 \text{ \AA}$  (Fig. 3.5-12), which corresponds to the O-O distances within a  $\text{SiO}_4$  tetrahedron. With slow cooling, for  $\text{Mg}_2\text{SiO}_4$  a satellite peak emerges at slightly larger distance ( $\sim 3.15 \text{ \AA}$ ), which is reminiscent of the distances between oxygen atoms of different isolated tetrahedra in the olivine structure. For crystalline  $\text{MgSiO}_3$  at ambient condition (proto- or ortho-enstatite) the distribution of O-O distances is more continuous than for  $\text{Mg}_2\text{SiO}_4$ , and a secondary peak does not develop in the glass. In order to investigate the signature of the two distinct peaks in the O-O partial RDF, we have fitted these with two Gaussian functions (Fig. 3.5-12) and consider their signature in

the partial O-O structure factor, and consequently the total neutron structure factor that is dominated by the oxygen signal (Fig. 3.5-13). The Fourier transforms of the two Gaussian functions account for the general behaviour of the O-O and total neutron structure factor of the  $\text{Mg}_2\text{SiO}_4$  glass (Fig. 3.5-13), but no distinct features in the O-O structure factor can be attributed to either Gaussians individually. For  $\text{MgSiO}_3$ , the single Gaussian fit cannot account for the location of the main peak in the O-O structure factor.

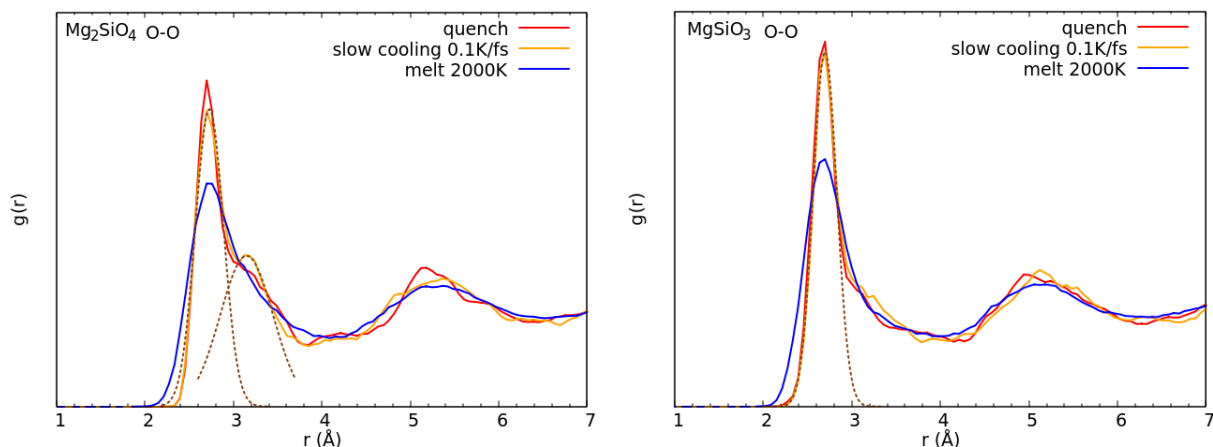


Fig. 3.5-12: Partial oxygen-oxygen radial distribution function for  $\text{Mg}_2\text{SiO}_4$  and  $\text{MgSiO}_3$  melt and glass. The O-O RDF of both  $\text{MgSiO}_3$  and  $\text{Mg}_2\text{SiO}_4$  has a maximum peak at  $\sim 2.7 \text{ \AA}$  fitted with a Gaussian (dashed lines). For the slowly cooled  $\text{Mg}_2\text{SiO}_4$  glass the partial RDF shows a distinct satellite peak emerging at  $\sim 3.15 \text{ \AA}$ , also fitted with a Gaussian (dashed line).

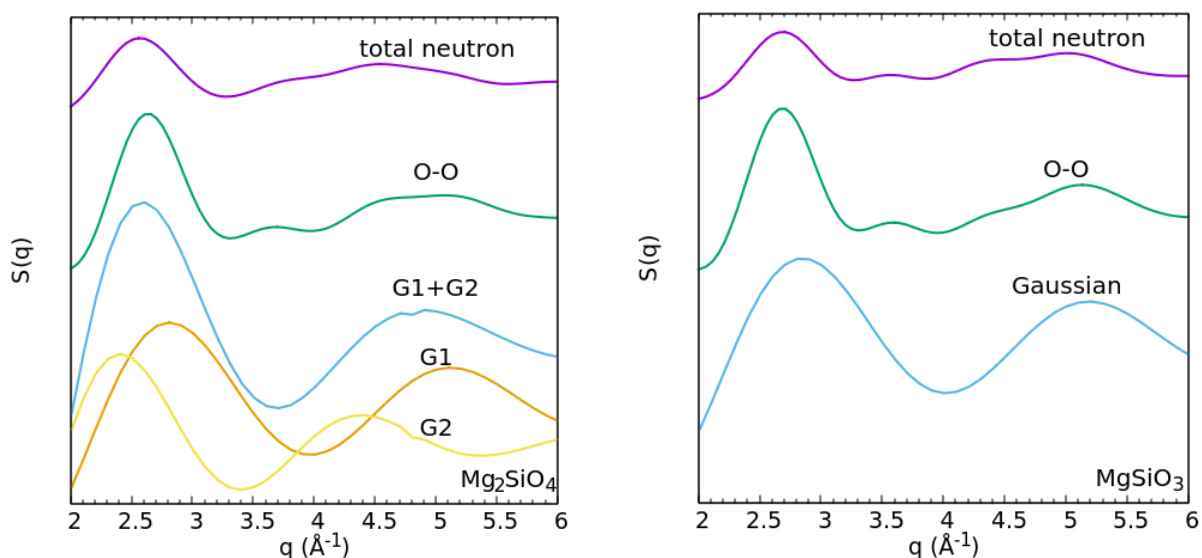


Fig. 3.5-13: Total neutron and O-O structure factors for slowly cooled (0.1 K/fs)  $\text{Mg}_2\text{SiO}_4$  and  $\text{MgSiO}_3$  glasses. For the  $\text{Mg}_2\text{SiO}_4$  glass, the structure factor contributions from the Gaussian fits to the peaks and the satellite peak (as well as their sum,  $G_1 + G_2$ ) are included for comparison.

A satellite peak in the RDF of Mg<sub>2</sub>SiO<sub>4</sub> glass at slightly larger distances than 3 Å has previously been observed in the total RDF derived from diffraction experiments. However, there it was assigned to Mg-O bond distances, an inference that is not supported by the computed Mg-O RDF. Moreover, in crystalline forsterite there are no Mg-O bond lengths in that distance region either.

**i. On the feasibility of measuring stable isotope fractionation between melts and fluids by *in situ* Raman spectroscopy (A. Zarei, S. Klumbach and H. Keppler)**

Stable isotope fractionation factors at elevated pressures and temperatures are usually determined by equilibrating some phases under the desired conditions, followed by quenching and mass-spectrometric analysis of the quenched samples. A number of recent studies have suggested that *in situ* Raman spectroscopy in a hydrothermal diamond anvil cell could be an attractive alternative for measuring stable isotope fractionation factors. This method is based on the fact that vibrational frequencies depend on the masses of the atoms involved and therefore, different isotopes often produce well-separated bands in the Raman spectrum. While this method appears very attractive in principle, it has sometimes yielded rather surprising results, such as very large fractionation factors between aqueous fluids and silicate melts even at magmatic temperatures. The purpose of the present contribution is therefore to evaluate some of the basic assumptions involved in studying stable isotope fractionation by *in situ* Raman spectroscopy. Provided that two different isotopic species can be distinguished by different vibrational frequencies in the Raman spectrum, their concentrations in any phase may be determined using the equation

$$I_a = \sigma_a c_a I_0$$

where  $I_a$  is the Raman intensity of species a,  $\sigma_a$  is the Raman scattering cross section of this species,  $c_a$  is the concentration of a in a given phase, and  $I_0$  is the intensity of incident laser radiation. In the previous *in situ* studies of isotope fractionation, it was always assumed that the scattering cross sections of two different isotope species a and b of the same molecule are equal,  $\sigma_a = \sigma_b$ . This assumption, however, requires experimental verification.

In order to verify whether isotopic substitutions may lead to changes in Raman scattering cross sections, we studied the system H<sub>2</sub>O-D<sub>2</sub>O. In this system, large isotopic shifts occur due to the large mass difference between normal hydrogen and deuterium. In the present study, four series of measurements were carried out: (1) The Raman scattering of H<sub>2</sub>O and of D<sub>2</sub>O was measured at ambient conditions, using Na<sub>2</sub>SO<sub>4</sub> as internal standard; (2) similar measurements were carried out in an externally heated diamond cell at elevated pressures and temperatures; (3) the Raman scattering of a mixture of H<sub>2</sub>O and D<sub>2</sub>O (1:1 molar ratio) was measured at ambient conditions (Fig. 3.5-14); and finally, (4) a series of haplogranitic glasses containing variable amounts of H<sub>2</sub>O or D<sub>2</sub>O was investigated.

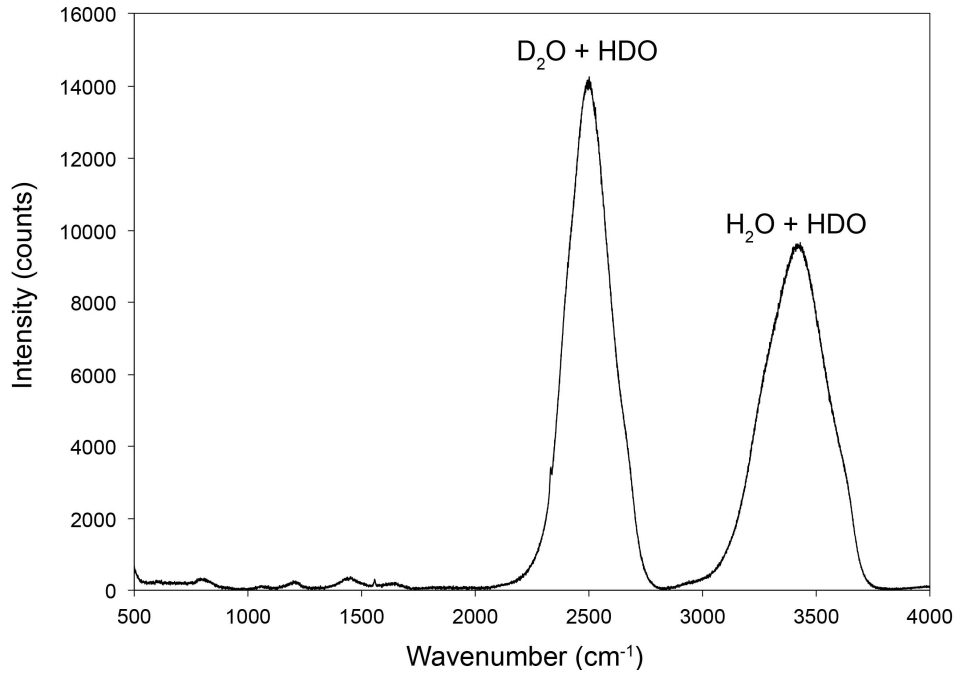


Fig. 3.5-14: Raman spectrum of a 1:1 (molar) mixture of H<sub>2</sub>O and D<sub>2</sub>O at ambient conditions. The antisymmetric stretching vibration of HDO overlaps with the H<sub>2</sub>O peak, the symmetric stretching vibration with the D<sub>2</sub>O peak.

The experiments showed that in aqueous fluids, the integral intensity of the H<sub>2</sub>O band is always higher than for the D<sub>2</sub>O band, both at ambient conditions (Fig. 3.5-14) and at elevated pressures and temperatures. However, in the haplogranitic glasses, the OD bands are stronger than the OH bands for equal concentrations of H<sub>2</sub>O and D<sub>2</sub>O in the glass. The latter observation can be explained by the expected increase of scattering intensities with the fourth power of absolute frequency, while the higher scattering efficiency of H<sub>2</sub>O in fluids may be related to Fermi resonance. *In situ* measurements of H/D isotope fractionation between coexisting fluids and silicate melt would therefore require extremely careful calibrations of scattering cross sections. Data reported in the literature that were obtained without such a calibration are very likely unreliable.

### 3.6 Rheology

A large number of processes that have shaped the Earth's history and present state originate from dynamic motions such as mantle flow and plate movements. Such motions are the consequences of rheological responses of constituent materials to deviatoric stresses. Rheological properties of rocks composing the Earth's crust and mantle therefore have to be determined under conditions corresponding to these regions. Rheological behaviors of rocks are, however, very complicated. Although they should be primarily controlled by flow laws of constituent minerals, mineral flow laws are already complex, and are functions of various parameters such as temperature, pressure, chemical compositions, stress conditions and their histories. Furthermore, rock rheology is largely affected by textures such as grain size, crystallographic preferred orientation and grain-boundary configurations. For these reasons, the Bayerisches Geoinstitut has adopted the following various approaches to investigate flow laws of constituent minerals and textural effects on rock rheology.

In the first five contributions rock deformation experiments were conducted. The Bayerisches Geoinstitut possesses a novel multi-anvil apparatus equipped with 6 independent rams, which allows sample deformation under the entire upper-mantle conditions. Two similar machines have been also installed in neutron and synchrotron radiation facilities by BGI scientists. These are the main tools for the four contributions. The first study conducted pure-shear deformation experiments on pyrope-rich garnet to clarify a mechanism to enhance its plasticity. The current results show that strain rates and experienced total strains enhance plasticity more dramatically than temperature. In the second study olivine aggregates were plastically deformed under conditions of the bottom of the upper mantle, to investigate a previously proposed change in dominating slip system with increasing confining pressure. However, even at the slowest strain rates (lowest flow stresses) a preferred alignment of both [100](010) and [001](010) slip systems suggests that both are active under the experimental conditions. The third study investigated boudinage (pinch-and-swell) structures in layered two-phase rocks. The researchers demonstrated that viscosity contrast between two layers is not sufficient for boudinage development, and some additional conditions such as the presence of large grains are necessary. In the fourth study magnetite aggregates were deformed in order to understand the interplay between deformation and the magnetite-hematite transition such as it is found frequently in ore-forming banded iron formations. It was found that deviatoric stresses enhance strongly the formation of hematite from magnetite, possibly even superseding the effect of oxygen fugacity. The fifth study attempted to determine dominant slip systems of ferropericlase under lower-mantle conditions to investigate seismic anisotropy in the lower mantle. Unlike the above studies, the DAC was adopted as a deformation apparatus due to the high-pressure conditions. The researchers suggested that, although slip on {110} is dominant at low pressure-temperature conditions, slip on {100} becomes equally important at higher pressure-temperature conditions.

Recently, the significance of grain-boundary sliding in rock deformation has been increasingly recognized. The next three contributions have investigated the role of grain boundaries in deformation of olivine aggregates. The first contribution with this topic

attempted to detect grain boundary sliding under conditions where dislocation creep has been considered a dominant deformation mechanism. The second contribution studied geometrical compatibility among neighboring grains as a function of total bulk strain and finds that (010) grain boundaries are developed during shear. It is suggested that crystal alignment and slip transfer are intrinsically correlated on this lattice plane. The last study with this topic focuses on porphyroblasts formed by abnormal grain growth to characterize grain boundaries between porphyroblasts and matrix grains.

The next four contributions have attempted to evaluate effects of physical and chemical conditions on flow laws of olivine and its high-pressure polymorph by indirect methods. The first contribution with this strategy aims to determine the water-content dependence of dislocation mobility activated by the [001](010) slip by means of the dislocation recovery technique. The researchers concluded that the effect of water-incorporation on this dislocation motion is rather small. The next contribution reports that the [100](001) slip does not work under dry conditions, but is activated by water incorporation. The third contribution reports that motion of screw dislocations activated by the [001](010) slip has identical activation energy with Si diffusion to conclude that this dislocation motion is diffusion-controlled. The last contribution with this strategy measured the Si self-diffusion coefficient of single-crystal wadsleyite to evaluate transition-zone rheology. They report Si self-diffusion coefficients of wadsleyite that are one order of magnitude larger than previously reported values, indicating a much softer rheology of wadsleyite than previously thought.

Although the above studies investigated rheology of mantle constituents by experimental and analytical methods, the last contribution in this section adopted numerical simulations. The workers investigated the interplay of grain size reduction and shear heating which results in ductile strain localization.

**a. *Experimental deformation of garnet single crystals at high temperature and pressure (T. Mandolini and F. Heidelbach)***

Garnet is one of the major constituents of the subducting oceanic crust and the mantle transition zone. Constraints upon its rheological behaviour are poor. Studies on natural samples have shown garnet being ductile deformed by grain boundary processes or dislocation creep at high temperature. TEM studies on experimental garnet single crystals have revealed crystal plasticity enhanced by activation glide systems at high T and high P – high T conditions. Discrepancies still exist considering the extrapolation to natural deformation conditions and the related general assumption that garnet would remain rigid. We attempted to understand at which conditions garnet would undergo plastic deformation and by which mechanism.

We conducted pure-shear experiments on pyrope-rich garnet single crystals using the six-ram multianvil deformation apparatus-in house at temperatures 900-1100 °C and confining pressure 3.5 GPa, varying either  $\epsilon$  or  $\dot{\epsilon}$  values. The SEM-EBSD technique was employed to

analyze the microfabrics of experimental samples on the surface parallel to the experimental extension and compression directions. EBSD results interpretation were made possible by acquisition of texture component maps (TC, Fig. 3.6-1) quantifying the amount of internal lattice rotation due to dislocation density, inverse pole figures (IPFs) and pole figures (PFs) analysis. Schmid factor determination component from EBSD analysis was employed to qualitatively detect the potential slip systems activation.

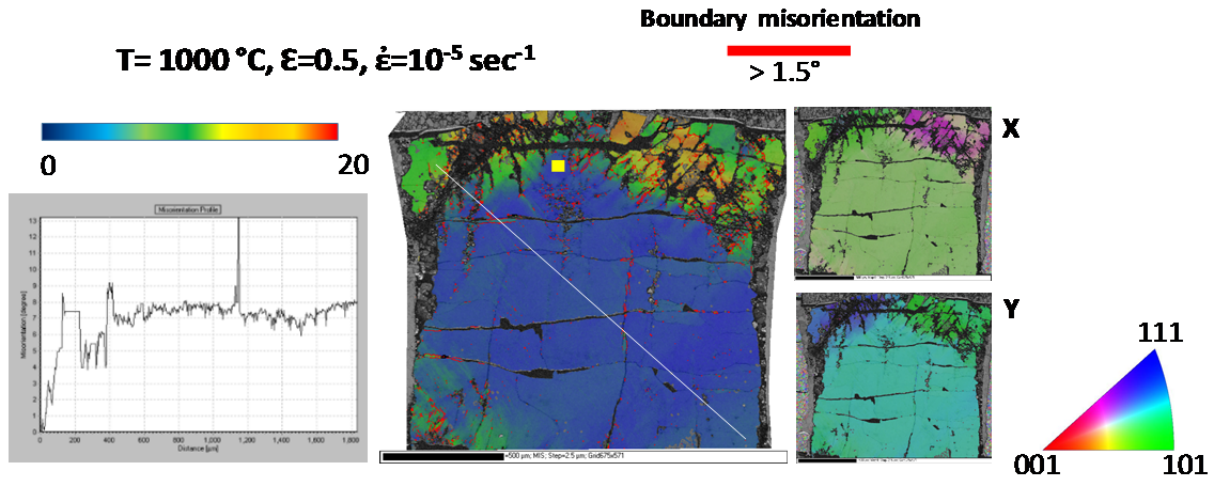


Fig. 3.6-1: Representative colour-coded TC map with overlapped grain-boundary map (sample M643) showing overall sample misorientation from a single reference point (yellow square), which was assumed to be close to the original orientation of the garnet crystal before the experiment. Misorientation profile measured along the white line relative to an initial point of reference is given. IPF colour-coded maps as a function of X and Y are also given. Note the evident orientation change in the upper corners of the sample. Lamellae structure evident; presence of melt and new solid phase was also detected. Only garnet is colour-coded mapped. T=temperature.  $\epsilon$ =strain.  $\dot{\epsilon}$ =strain rate.

The extent of intracrystalline deformation was found to be more evident with increasing  $\epsilon$  and  $\dot{\epsilon}$  at constant temperature. LPO describe circle dispersion of poles to  $\{100\}, \{110\}, \{111\}$  around the intermediate sample axis (Z) on PFs and increasing deviation from initial lattice orientation on IPFs (Fig. 3.6-2). Schmid factors are in agreement with these observed features described above.

Pyrope-rich garnet undergoing plastic deformation with potential slip system activation was observed. Maximum misorientation angles  $\omega$  describe positive trend as a function of  $\epsilon$  transferred to the samples, showing correlation with potential and easier slip system activation with increasing  $\epsilon$  (Fig. 3.6-3). Pyrope garnets experience greater plastic deformation by dislocation glide as a function of increasing  $\epsilon$  and  $\dot{\epsilon}$ , whereas the influence of temperature could not be clearly demonstrated. We recognized the following potential slip systems were possibly activated:  $\langle 111 \rangle \{110\}$ ,  $\langle 111 \rangle \{112\}$ ,  $\langle 111 \rangle \{123\}$  and  $\langle 100 \rangle \{001\}$ ,  $\langle 100 \rangle \{010\}$ ,  $\langle 100 \rangle \{011\}$ . Further TEM investigation is required to prove and quantify garnet single crystal glide systems inferred from Schmid factor determination in this EBSD work, as well as the overall garnet single crystal rheological behaviour.

Deformation-induced melting in garnet was recognized as an unexpected finding in three samples even though deformation experiments were performed far from the melting temperature of pyrope at 3.5 GPa. A tentative explanation based on microstructural observations as well as considerations of P,T and stress conditions is that local partial melting can be induced by deviatoric stress states where the lowest stress is near the pressure at which melting may occur. We observed the melting extent increasing with increasing temperature (at constant  $\epsilon$  and  $\dot{\epsilon}$ ) and decreasing  $\dot{\epsilon}$ /increasing run duration (at the same  $\epsilon$  conditions and constant temperature).

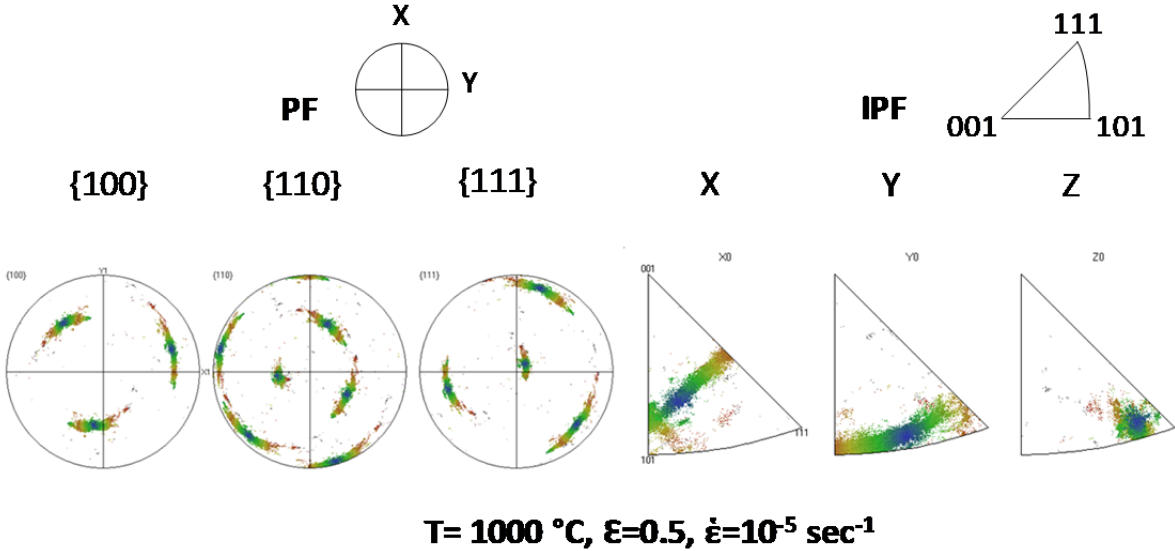


Fig. 3.6-2: Representative PFs and IPFs (sample M643) showing poles circle dispersion around the intermediate sample axis (Z) and increasing deviation from initial lattice orientation (blue colour-coded), respectively. T=temperature.  $\epsilon$ =strain.  $\dot{\epsilon}$ =strain rate.

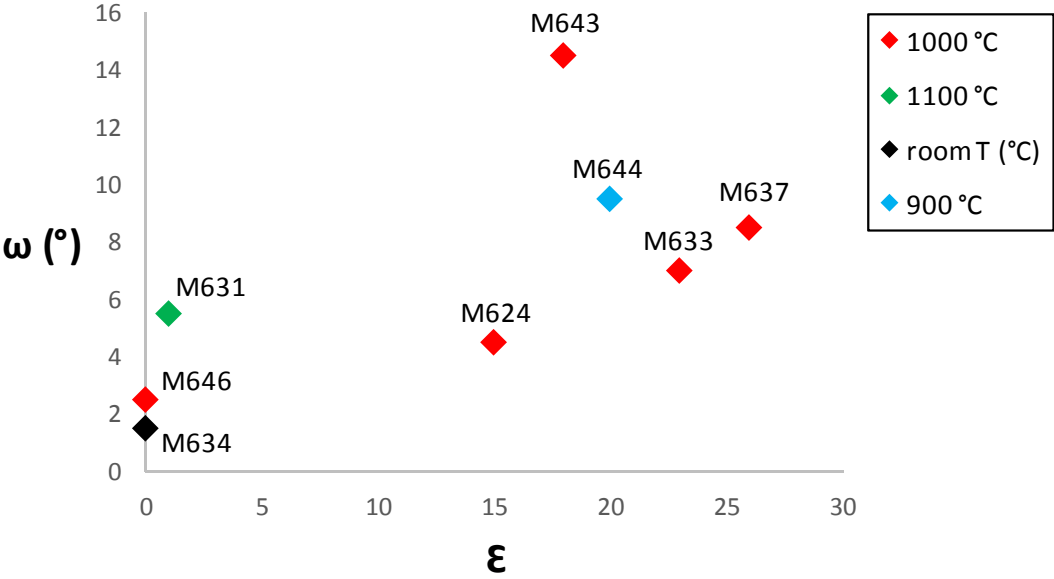


Fig. 3.6-3: Diagram showing maximum misorientation angle  $\omega$  as a function of measured  $\epsilon$  for different temperature conditions.

**b. Interference of olivine A and B type textures during deformation under progressively increasing pressure (N. Walte/Garching, F. Heidelbach and D.J. Frost)**

A deformation-induced crystallographic preferred orientation (CPO) in olivine is commonly considered the explanation for the widespread seismic anisotropy of the top part of the upper mantle. The connection between mantle flow and seismic anisotropy is, however, complicated by the fact that a given strain geometry may result in a host of different CPOs. This variation is interpreted to reflect a switch in the dominant glide system that occurs as a response to changing parameters such as flow stress, water content, and lithostatic pressure. Especially the latter has been suggested to cause a switch from [100](010) to [001](010) as the dominant glide system over a pressure range of about 5-8 GPa. It is however controversial, and has alternatively been explained as caused by high (laboratory) flow stress and/or an increased water incorporation in olivine. For this study we investigated the CPO development of deformed San Carlos olivine at surrounding pressures of 2-14 GPa to reassess the role of pressure and to follow the CPO development for aggregates that experience increasing surrounding pressure during deformation as a simplified model for upper mantle material that is transported into larger depths, *e.g.* close to subducting slabs.

Experiments were performed in the SAPHiR three-axis press at FRM II in Garching (see previous annual reports). Ground and oven dried San Carlos olivine powder was filled in 1.6 x 1.5 mm Re capsules and inserted in 8 mm assemblies of fired pyrophyllite that contained a Re foil furnace. After reaching the starting pressure the samples were heated to 1500 or 1573 K and statically annealed for at least one hour before starting the deformation. The experiments were deformed in pure shear at medium ( $10^{-5} \text{ s}^{-1}$ ) to very low ( $10^{-7} \text{ s}^{-1}$ ) strain rates to investigate the role of differential stress, which led to experimental durations of up to two weeks. The assembly of one experiment (DD 150) has additionally been fired after assemblage for 1 h in a vacuum furnace immediately before starting the experiment to ensure sample and assembly dryness.

The retrieved samples were cut and polished before investigation by SEM orientation contrast (OC) and electron backscatter diffraction (EBSD). Olivine microstructures showed irregular curved grain boundaries, local bending of crystal lattices, and subgrain boundaries indicating a component of dislocation creep (Fig. 3.6-4). The resulting CPOs display a generally strong alignment of [010] parallel to the compression axis and varying alignments of [100] and [001] depending on experimental condition (Fig. 3.6-4). The dry, high-pressure sample SA 150 displays a moderate but clear alignment of [001] in the elongation direction, termed B type texture in contrast to the A type texture commonly found at low pressure that aligns [100] in the elongation direction. The precisely controlled strain rate of about  $2.5 \times 10^{-7} \text{ s}^{-1}$  likely resulted in a much lower flow stress than in previous deformation experiments that were performed at strain rates of at least one order of magnitude faster. Likewise, observations on the heat treated assembly indicate that the B type texture was not initiated by a high water content in the olivine. We therefore interpret this as support for the hypothesis that the glide

system switch is pressure-induced, while acknowledging the fact that the laboratory flow stresses are still significantly above natural conditions.

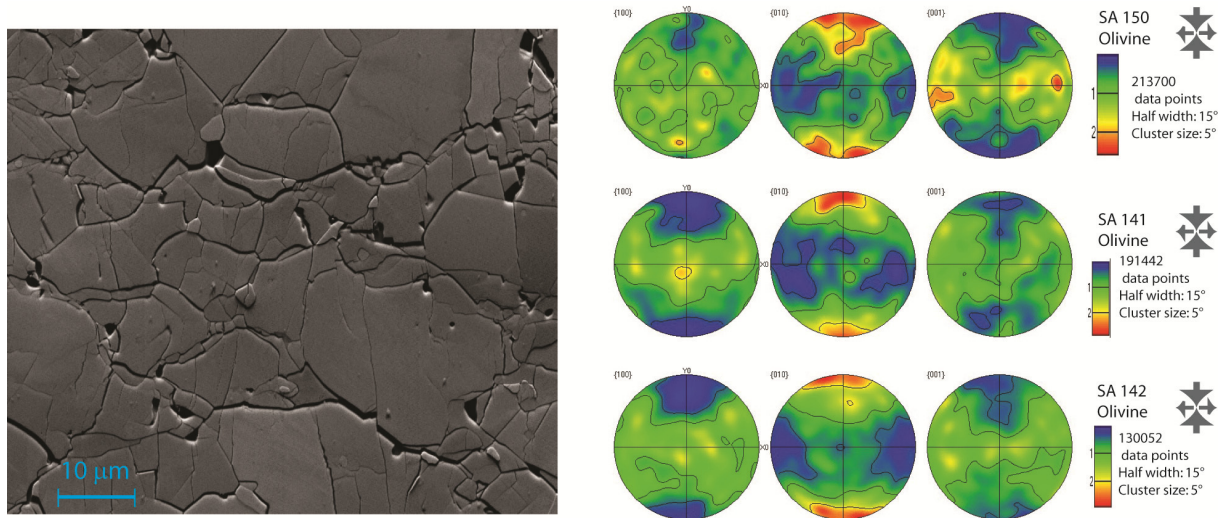


Fig. 3.6-4: (left) SEM orientation contrast image of SA-150, deformed at 13 GPa, 1573 K, and  $\dot{\epsilon} \approx 2 \times 10^{-7} \text{ s}^{-1}$ . Large grains with irregular grain boundaries suggest grain boundary migration recrystallization, an indication for dislocation creep. (right) Pole figures (equal area lower hemisphere projections) of olivine deformation experiments: SA 150 (13 GPa, 1573 K,  $\dot{\epsilon} \approx 2 \times 10^{-7} \text{ s}^{-1}$ ) showing a B type texture, SA 141 (2-12 GPa, 1500 K,  $\dot{\epsilon} \approx 5 \times 10^{-6} \text{ s}^{-1}$ ) and SA 142 (2-12 GPa, 1500 K,  $\dot{\epsilon} \approx 2 \times 10^{-5} \text{ s}^{-1}$ ) showing an AG type texture likely resulting from A type – B type textural interference.

Two experiments were performed to investigate the resulting texture in samples that experienced progressive strain at increasing pressure thereby simulating the transport of material from the shallow towards the deep upper mantle. One experiment was deformed while continuously increasing the pressure from 2 to 12 GPa (SA 141), while another was first deformed at 2 GPa, followed by a static pressure increase to 12 GPa, which was followed by another episode of deformation (SA 142). Despite these differences and a difference in strain rate by a factor of 4, both experiments display similar CPO with a girdle of [100] and [001] in the shear plane and [010] parallel to the compression direction. This so-called AG type texture has been found in natural olivine and causes a very low seismic anisotropy. In our samples this CPO is likely caused by the interplay of a dominantly [100](010) glide system at low pressure followed by an [001](010) glide system at high pressure. Based on annealing experiments, it has previously been suggested that the AG type texture is caused by a near identical mobility of a and c line dislocations under low differential stress conditions (see previous annual reports). Our results suggest that A type – B type texture interference may be an alternative and possibly complementary mechanism to explain the low seismic anisotropy in the deep upper mantle.

c. *Experimental study of pinch-and-swell structures in viscously contrasting materials (R. Farla/Hamburg, F. Heidelbach, M. Urgese, P. Bons/Tübingen, E. Gomez-Rivas/Tübingen and A. Griera/Barcelona)*

A particular deformation structure, called pinch-and-swell or boudinage, is common to layered formations that experienced strain localization. Recent availability of computing power made it possible to numerically model the evolution of these structures. In all cases, the model is a simple layered structure of two materials, with a middle layer of material A sandwiched between outer layers of material B. By varying the material properties and instabilities on the layer interfaces, pinch-and-swell structures in the typically harder middle layer may develop with different amplitude, period and symmetric or asymmetric characteristics. In contrast to previous work, numerical simulations have shown that with additional complexity, such as shear heating, pinch-and-swell structures form during Newtonian creep (with stress exponent  $n = 1$ ) in addition to non-Newtonian creep ( $n > 1$ ).

In spite of large efforts from the modeling community, few if any, such experimental studies of Earth materials have been documented. The main requirement is the need for a specialized apparatus that can perform true triaxial testing while keeping the pressure, temperature and displacement rates on the sample constant. A 6-ram large volume press (LVP) at the Bayerisches Geoinstitut (BGI) is capable of deforming a typically cylindrical sample in a cubic pressure medium by compressing the axial direction of the sample with one pair of rams, whereas another pair of rams retracts permitting the sample to preferentially flow in this direction. Experiments were carried out on two different layered structures according to the aforementioned model. Inside a Pt capsule, pre-sintered olivine discs sandwich a pre-sintered orthopyroxene or alumina disc with half the thickness (Fig. 3.6-5). The samples in a cubic assembly were compressed to a target pressure of 3.0 GPa. Temperature was increased in the range of 900-1200 °C via resistive heating of graphite. Triaxial deformation at various estimated constant strain rates of  $3 \times 10^{-6}$  to  $1 \times 10^{-4}$  /s were carried out to total strains of 40-70 %.

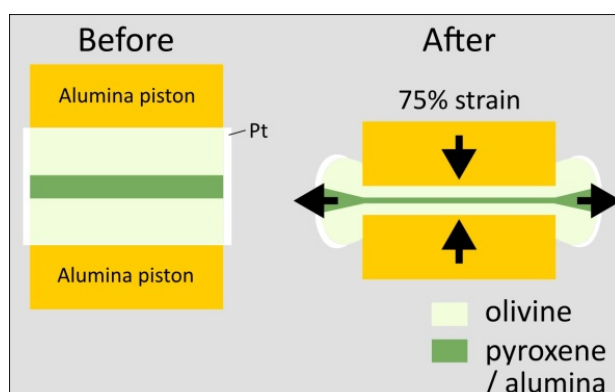


Fig. 3.6-5: High-strain deformation on a layered assembly.

Experimental results show a variety of outcomes, but in particular highlight the challenge of interpreting the middle layer as more viscous or 'boudinaged'. This is particularly true for the

olivine-orthopyroxene experiments in a range of conditions of temperature and strain rates. Attempts were made to seek out deformation conditions for olivine and orthopyroxene, which would lead to exponential creep (with large stress exponent), keeping grain sizes as large as possible to avoid significant grain-size sensitive creep (with small stress exponents), but not too large such that the middle layer has a thickness of a single grain (up to 50  $\mu\text{m}$ ).

Relatively fast ( $2 \times 10^{-5}$  /s), high-temperature ( $> 1200$   $^{\circ}\text{C}$ ) experiments did not produce boudinage. An experiment at a lower temperature (1000  $^{\circ}\text{C}$ ) where exponential creep should operate, resulted in serious grain size reduction ( $< 0.5$   $\mu\text{m}$ ) from high stresses, such that indexing by electron backscatter diffraction (EBSD) was nearly impossible. No boudinage was observed. Slow deformation experiments ( $3 \times 10^{-6}$  /s for 74 hours) at 1000  $^{\circ}\text{C}$  mitigated serious grain size reduction, yet boudinage in the middle orthopyroxene layer is again not observed (Fig. 3.6-6A). The addition of stress concentrators such as alumina grains on the layer interfaces, which may enhance the growth rate of instabilities, also did not appear to

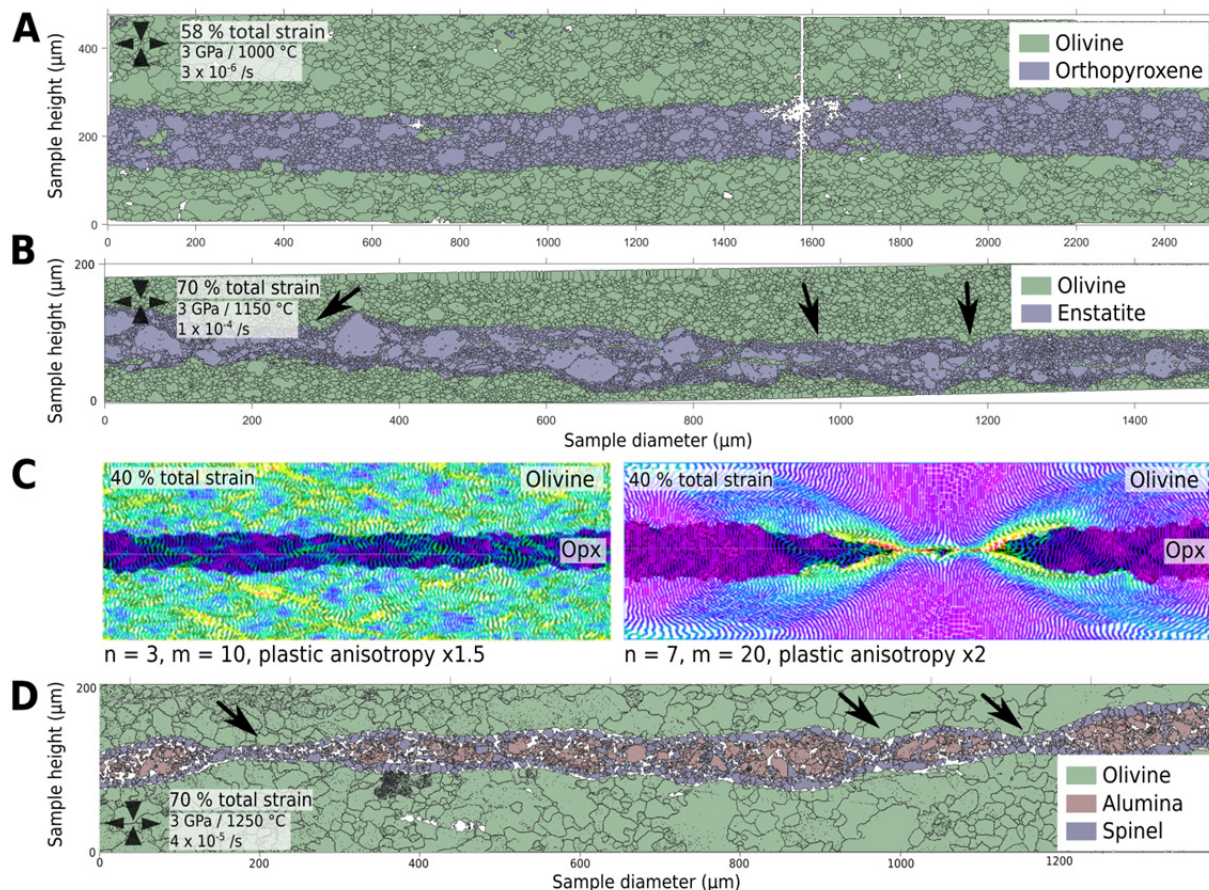


Fig. 3.6-6: Deformed samples (EBSD maps) with arrows showing possible pinch points. **A.** olivine-orthopyroxene layered sample. **B.** olivine-enstatite (Fe-free) layered sample. **C.** numerical modeling results showing layer geometry and finite strain distributions. No strain localization for  $m=10$ . Increase of  $m$ ,  $A$  and CRSS or increase of  $n$  brings development of pinch-and-swell structures. Purple-blue colours indicate low strain values, while orange-red colours indicate high strain or domains with strain localization. **D.** olivine-alumina/spinel layered sample showing pinch-and-swell structures.

promote boudinage. Finally, attempts to use a laboratory pre-cursor enstatite (Fe-free orthopyroxene), which was coarse-grained before deformation, appears to present some pinch-and-swell structure (Fig. 3.6-6B). This set of experiments has shown that a reported viscosity contrast of a factor 2 between olivine (softer) and orthopyroxene (harder) may not be sufficient for significant boudinage development. This was confirmed by numerical modeling incorporating grain size distributions and slip systems. Only in the most extreme case of a large stress exponent (7), viscosity contrast ( $m = 20$ ), and plastic anisotropy (neglecting dynamic recrystallization), can boudinage develop (Fig. 3.6-6C).

Assuming the viscosity contrast is the major variable; we replaced orthopyroxene with alumina as the middle layer and carried out another experiment to large strain. The results potentially show the first experimental evidence of boudinage under extreme conditions, despite nucleation of spinel grains in the alumina layer (Fig. 3.6-6D).

**d. Experimental deformation of natural magnetite at high pressure and temperature (D. Silva-Souza/Ouro Preto, C. Bollinger and F. Heidelbach)**

Iron oxides such as magnetite ( $\text{Fe}_3\text{O}_4$ ) and hematite ( $\text{Fe}_2\text{O}_3$ ) are important mineral constituents of Banded Iron Formations, and a common accessory mineral on many igneous as well as sedimentary rocks. They are the main phases of deformed iron deposits found in the southeast of Brazil in the Iron Quadrangle region, where deformation and weathering play an important role on the economical viability of the deposits. The understanding of the effects of deformation of magnetite grains, its transformation to hematite and the textural aspects involved are very important to the understanding of the formation these rocks. We investigated the influence of plastic deformation on the magnetite-hematite transformation experimentally using the Mavo 6-anvil press.

The starting material was taken from the BGI's mineral collection, consisting largely (> 95 %) of coarse grained magnetite (> 200  $\mu$ , Fig. 3.6-7a) and small amounts of hematite and quartz,. The deformation experiments were performed in pure shear at a range of temperatures 900 °C - 1100 °C, strain rates of  $5 \times 10^{-5} \text{ s}^{-1}$  and  $8.3 \times 10^{-5} \text{ s}^{-1}$  and a confining pressure of 3 GPa and 100 minutes of duration. Since the conditions in the sample chamber during the experiment are rather oxidizing magnetite tends to transform into hematite. We aim to investigate the influence of strain/strain rate (strain rate being proportional to stress) and temperature on the transformation and the related textures developed by the different phases. Deformed samples were sectioned and polished in the plane containing the compression and extension directions for microstructural analysis with SEM-EBSD allowing to determine the phase proportions and fabrics of the different phases. Comparison with the starting material and samples transformed without deviatoric stress and plastic deformation allowed to quantify the influence of deformation on the progress of the magnetite hematite transformation.

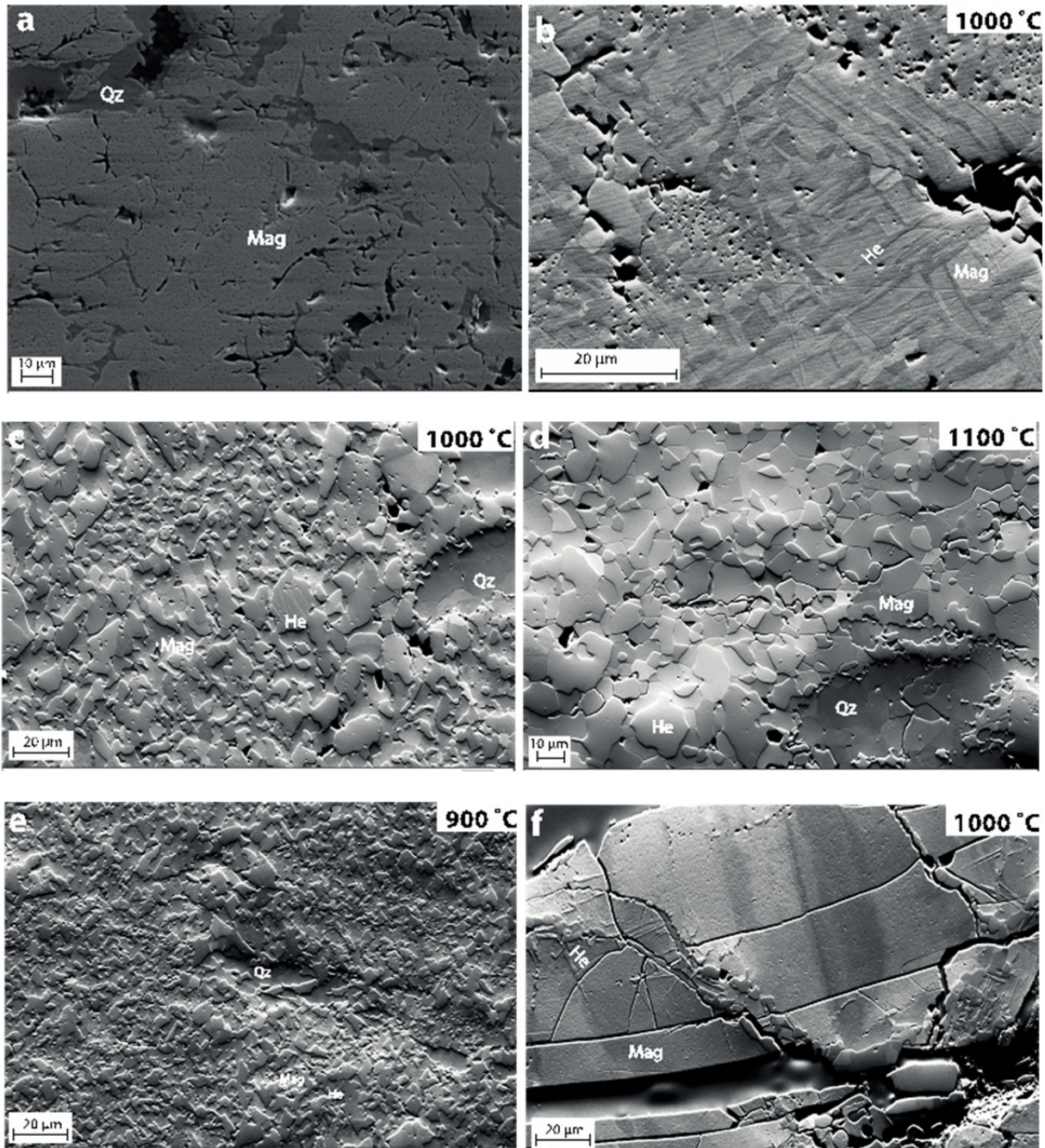


Fig. 3.6-7: SEM orientation contrast images of experimental samples, compression/extension axis is vertical/horizontal for deformed samples: a) starting material; b) M599, 30 % strain; c) M601, 50 % strain; d) M607, 50 % strain; e) M608, 50 % strain; f) M609, 0 % strain.

Results show that the amount of magnetite transformed to hematite is positively correlated with plastic strain increasing from 24 % (no strain, Fig. 3.6-7f), to 34 % (30 % strain, Fig. 3.6-7b) and 49 % (50 % strain, Fig. 3.6-7c) at 1000 °C. For samples deformed to 50 % strain the hematite content increases with decreasing temperature, reaching a maximum percentage of 55 % at 900 °C (Fig. 3.6-7e). This temperature dependence is surprising as higher

temperatures cause a more oxidizing sample environment. However, at lower temperature the stresses needed for deformation are higher, apparently offsetting the oxygen fugacity effect.

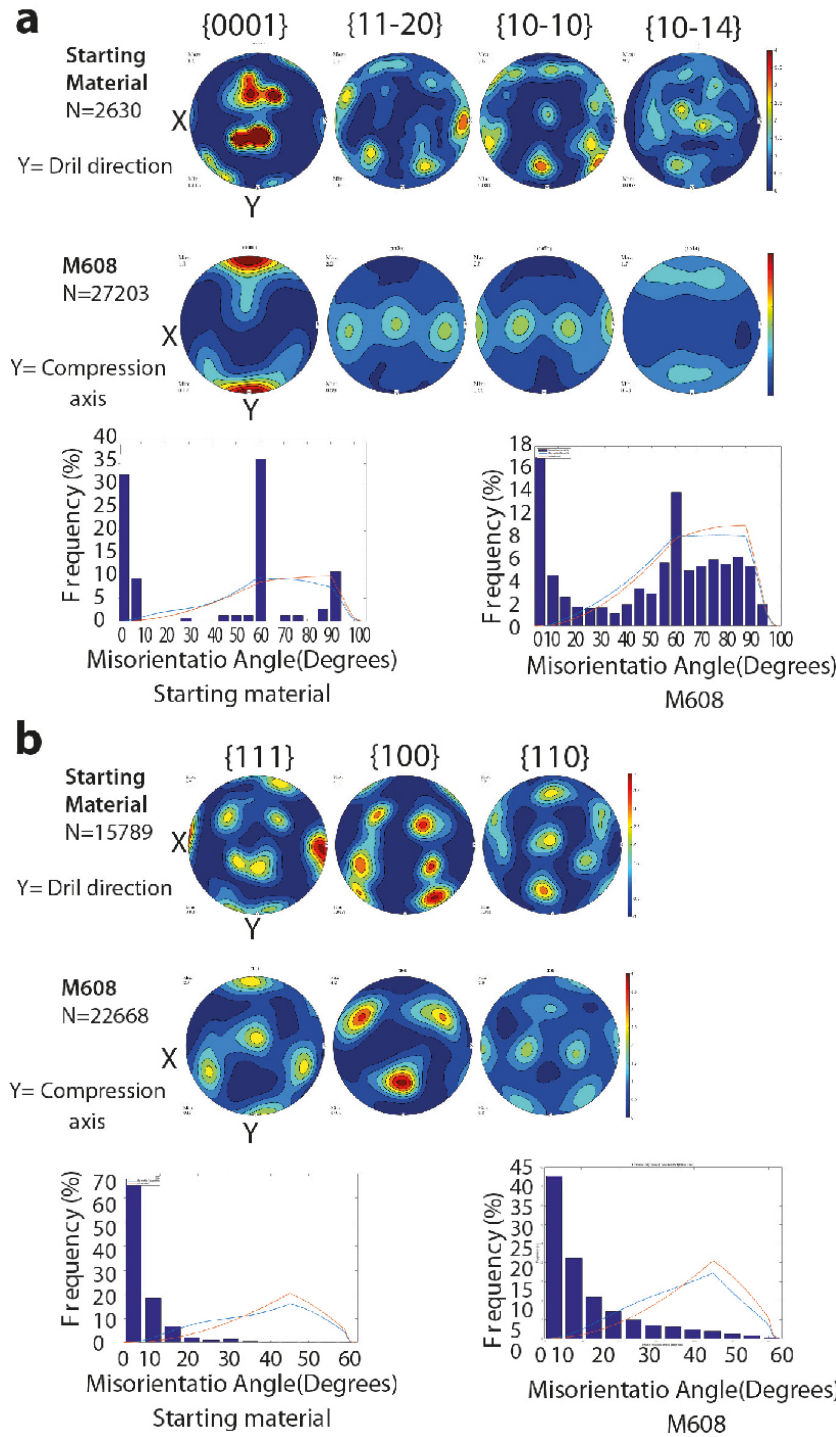


Fig. 3.6-8: Pole figures and misorientation histograms for the starting material and sample M608, deformed to 50 % strain at 900 °C; a) hematite, b) magnetite.

The topotaxy of crystallographic lattices which is typical for the magnetite-hematite transition is overprinted by deformation-induced CPOs in both phases. Both minerals apparently deform plastically by dislocation creep as indicated by the increased lattice distortion inside grains

(Fig. 3.6-8 a,b), with hematite developing a  $\langle c \rangle$  axis fiber texture parallel to the compression direction in agreement with dislocation glide on the basal slip plane  $(0001)\langle 11\bar{2}0 \rangle$ . Magnetite shows a CPO with poles of  $\{111\}$  poles near parallel to the compression direction on most of the experiments and  $\{110\}$  aligning in the extension direction, being roughly consistent with slip on  $\{111\}\langle 110 \rangle$ , a typical slip system for spinel structures. Due to the CPOs in the two phases a statistical orientation relationship between the two phases is formed which is however much weaker than the one formed due to transformation alone.

In conclusion it can be said that the formation of hematite from magnetite is enhanced by the deviatoric stresses imposed during plastic deformation, but their topotaxial relationship from transformation are largely obliterated by the deformation. The stress effect in enhancing the transformation rate may partially overcome the effect of lower oxygen fugacity. This also indicates that hematite is the plastically weaker phase under the experimental conditions accommodating larger strains as documented by the stronger CPO.

*e. High-temperature/-pressure deformation experiments of (Mg,Fe)O indicate  $\{100\}\langle 011 \rangle$  slip in Earth's lower mantle (J. Immoor, H. Marquardt, H.-P. Liermann/Hamburg, L. Miyagi/Salt Lake City, F. Lin/Salt Lake City, S. Speziale/Potsdam, S. Merkel/Lille, J. Buchen and A. Kurnosov)*

Seismic anisotropy in Earth's lowermost mantle, resulting from Crystallographic Preferred orientation (CPO) of elastically anisotropic minerals, is among the most promising observables to map mantle flow patterns. Ferropericlasite, the second most abundant mineral in the lower mantle, is characterized by pronounced elastic anisotropy that steadily increases with depth. In the Earth's lowermost mantle, the elastic anisotropy of ferropericlasite is significantly larger as compared to bridgmanite or post-perovskite. This makes ferropericlasite a strong candidate phase to generate seismic anisotropy in the lower mantle. The extent, however, to which the intrinsic anisotropy of ferropericlasite contributes to seismic anisotropy observed in the lowermost mantle, depend on the CPO of ferropericlasite that develops in the flow field of the mantle. CPO development is controlled by the relative activities of various available slip systems. Previous work has shown that dislocation creep in (Mg,Fe)O takes place by slip along  $\langle 110 \rangle$  directions on either the  $\{100\}$  or the  $\{110\}$  planes, *i.e.*, the slip systems  $\{100\}\langle 011 \rangle$  and  $\{110\}\langle 1\bar{1}0 \rangle$ . The effects of lower mantle pressure and temperature conditions on the relative contribution of these two slip systems is experimentally unconstrained, hampering any reliable modeling of the contribution of ferropericlasite to lower mantle seismic anisotropy. In particular, it was suggested that only slip on  $\{100\}$  is consistent with the seismic record in the D" layer in the lowermost mantle, but room-pressure diamond anvil cell work by synchrotron radial X-ray diffraction (rXRD) on polycrystalline MgO and (Mg,Fe)O concluded that slip on  $\{110\}$  is dominant to pressures of almost 100 GPa. In this contribution, we measured the high-pressure/-temperature deformation behaviour of (Mg,Fe)O ferropericlasite (FP).

*In situ* deformation experiments on powders of  $(\text{Mg}_{0.8}\text{Fe}_{0.2})\text{O}$  ferropericlase have been conducted in a graphite heated diamond anvil cell (DAC) using angle dispersive synchrotron X-ray diffraction (XRD). Different runs at temperatures of 300 K, 800 K, 1150 K and 1400 K and pressures up to 74 GPa were performed. The experimental data were fit with the program MAUD (Materials Analysing Using Diffraction) to extract texture, strain and inverse pole figures (IPF). Additionally, slip system activities were quantified by modelling the experimental results with the EVPSC (Elasto-Viscoplastic Self Consistent) code (see also contribution by Lin *et al.* in annual report 2016).

Our data reveal a significant contribution of slip on  $\{100\}$  to ferropericlase CPO at high-pressure/-temperature conditions. Texture development represented by IPF of the compression direction as derived from this work and our previous experiments at 300 K is summarized in Fig. 3.6-9. Experimental runs at 300 K, 800 K, and 1150 K are characterized by the development of a strong 100 maximum upon initial pressure increase. At experimental temperatures of 300 K and 800 K, texture strength increases when pressure is increased, but the appearance of the IPF is generally unchanged. We observe a tendency for the maximum to develop a shoulder towards 110 in the IPF at 800 K. Deformation at higher temperature shows a different behaviour. At pressures of about 30-40 GPa at 1150 K, a secondary texture maximum clearly develops at 110. At 1400 K, this maximum is present throughout the entire high-temperature compression in the experiment and gradually strengthens with pressure. According to recent theoretical work and modeling based on experiments (Fig. 3.6-10), the secondary maximum at 110 in the IPF is a clear indication for increased activity of  $\{100\}\langle 011\rangle$  slip.

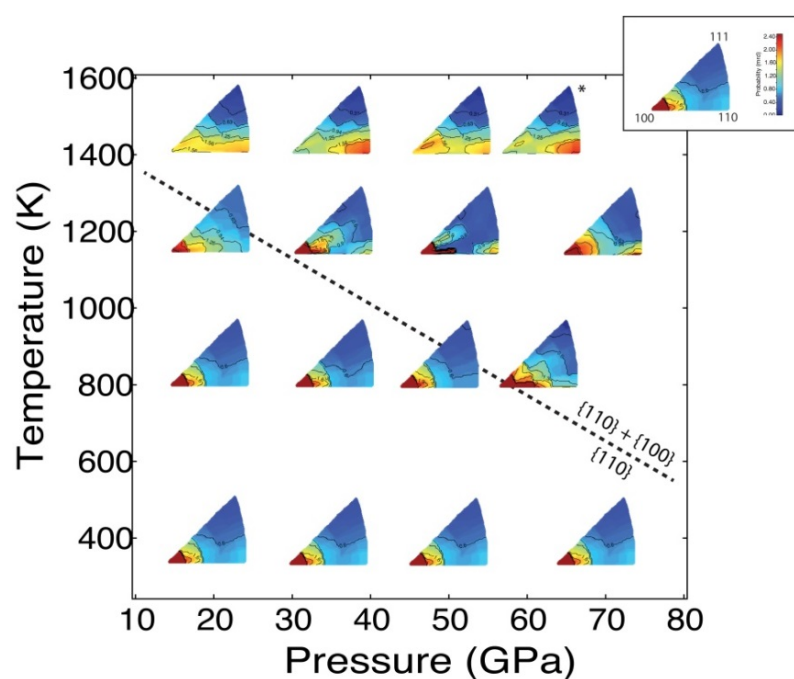


Fig. 3.6-9: Ferropericlase texture evolution observed in our experiments. The lower right corners of the IPFs are placed at the corresponding P/T-conditions. The dashed line is intended for illustration only and highlights the transition from dominant slip on  $\{110\}$  to a regime where slip on  $\{110\}$  and  $\{100\}$  are equally important as judged from the IPF appearances. The inset shows the axes and colour scale of the IPF.

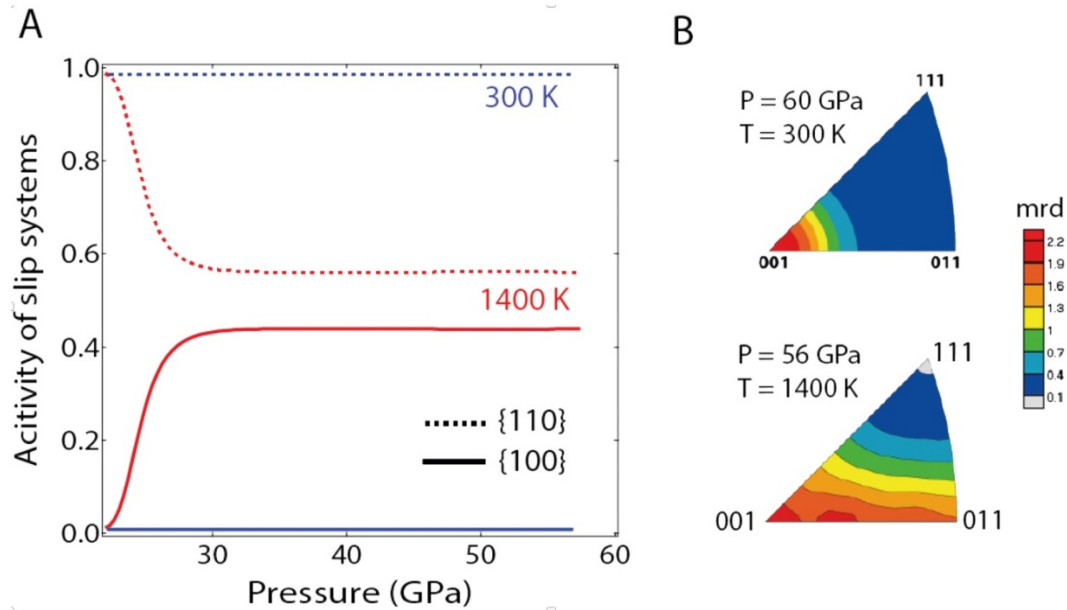


Fig. 3.6-10: Results of EVPSC modelling of the experimental data. (A) Pressure-/temperature-dependence of slip system activities inferred from modelling the experiments at 1400 K (red) and 300 K (blue). (B) Modelled IPFs at high-P/T. Activity of  $\{100\}\langle 011\rangle$  slip leads to a shift of intensity maximum to 110 in the IPF. Mrd: multiples of random distribution.

**f. Rheology of forsterite: Crystal slip plasticity vs. grain boundary sliding (C. Bollinger, K. Marquardt, F. Ferreira, M. Thielmann and P. Knödler/Bayreuth)**

Large-scale convective motions drive plate tectonics in the upper mantle, where olivine is the dominant phase. Olivine has a strong elastic anisotropy, which may be responsible for seismic anisotropy in the upper mantle down to 410-km depth. It is usually considered that dislocation creep of olivine grains produces Crystal Preferred Orientation (CPO) and thus the seismic anisotropy. Contributions of grain-boundary networks to rock deformation are generally neglected. Some experiments suggest that not only intracrystalline creep (crystal slip plasticity, CSP) but also relative displacement between adjacent grains account for deformation of olivine aggregates (grain boundary sliding, GBS). Hence, the GBS would be an important deformation mechanism in addition to diffusion and dislocation creeps. We developed the following experimental technique to detect and to quantify the contribution of both mechanisms.

Cylindrical samples for investigation at the conditions of the upper mantle were cored from synthetic forsterite aggregates with an initial grain size of 20 to 100  $\mu\text{m}$ . The cores were cut along the long axis of the cylinders. One diameter and one face was polished for EBSD mapping before and after the deformation experiments. As a strain-marker a grid was milled at this surface using the *focused ion beam (FIB)*. Both halves-cylinder were put together again to perform the deformation experiments using a 6-axis multianvil apparatus in simple shear (pressure 4-6 GPa, temperature 1000  $^{\circ}\text{C}$  - 1200  $^{\circ}\text{C}$ , strain rate  $2 \times 10^{-5} \text{ sec}^{-1}$ ).

After deformation experiments, distortions of grid markers in recovered samples were observed using SEM to measure relative *in-plane* displacement between adjacent grains as a response to applied stresses. We also detected the *out-of-plane* displacement of the grains (Fig. 3.6-11), which remains so far the best evidence of GBS at these experimental conditions. EBSD examination was conducted to determine the change in interfacial relations associated with deformation and using the following post-treatments of orientation maps: the *Kernel Average Misorientation* (KAM), which highlights the local strain gradients from pixel to pixel misorientations, like subgrain boundaries or dislocations density accumulations; while the *Grain Reference Orientation Deviation* (GROD) highlights misorientation changes with respect to an average orientation of a grain.

Comparing these samples before and after the experiments shows that the development of strain mostly localized at triple points and grain boundaries, and to a lesser extent subgrain boundaries. The KAM is rather heterogeneous. The *KAM distribution* shows the deformation effect regardless of the experimental conditions. This distribution is closely followed by the exposed surface of the sample, where the surface is free and the grains are free to move in the *out-of-plane* direction, and for the bulk (*i.e.*, inside the sample), attesting that the mechanisms accommodating the deformation at the surface are comparable and also happen in the bulk. The comparison of the KAM distribution for all the samples deformed in the same conditions but at different temperatures shows a shift of the distribution to the right (Fig. 3.6-12). At a temperature higher than 1100 °C, a mechanism (and in that case, GBS is strongly assumed) becomes more active to ensure a more homogenous deformation of the sample with less contribution of the intracrystalline defects.

This study is the best experimental evidence of GBS occurring in the dislocation creep regime. Because of the resolution of the grid, we are not able to detect the migration of the grains. Hence, it is still not possible to quantify the exact contribution of each mechanism, which would be mandatory to well constrain the rheological law of olivine required and model the visco-plasticity of the upper mantle.

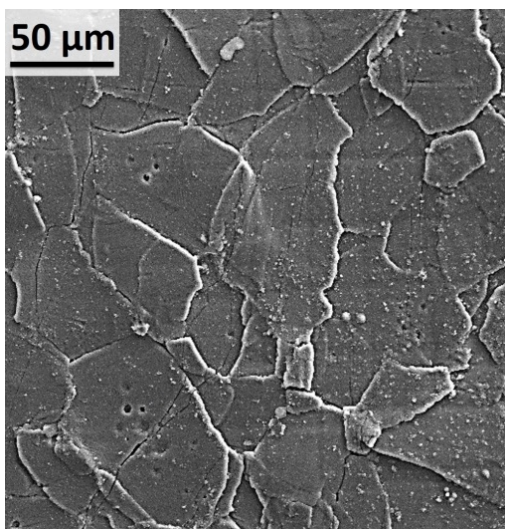


Fig. 3.6-11: SE picture of sample M640 (40 %-1000 °C, 5 GPa, strain rate  $2 \times 10^{-5} \text{ s}^{-1}$ ) showing out-of-plane displacement of the grains during the deformation.

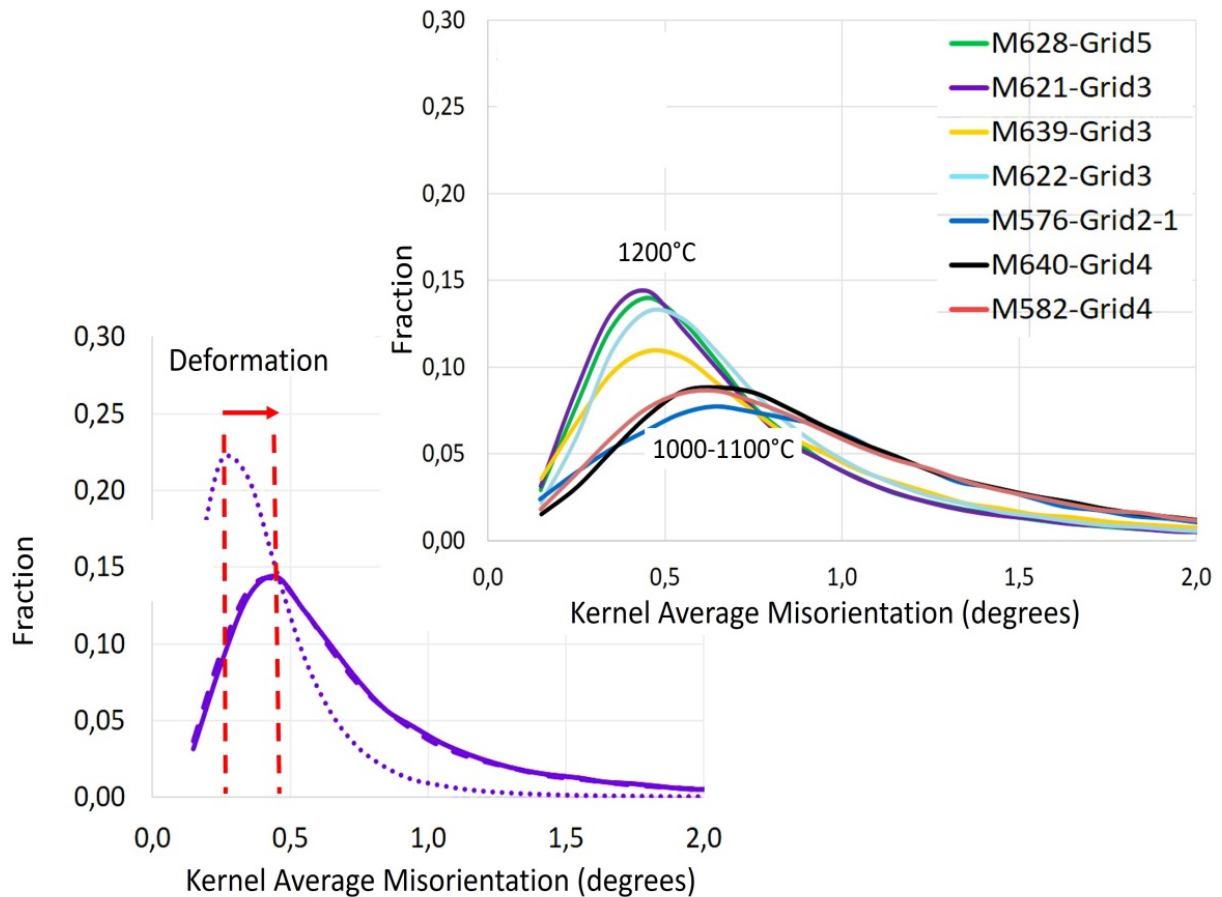


Fig. 3.6-12: (bottom) KAM distribution sample M621 (violet) deformed at 1200 °C. The initial KAM distribution (dotted lines) is shifted to the right due to the strain, for the bulk (dashed lines) and the surface (full lines). (Top) Deforming at higher temperature leads to less strain heterogeneities due to activation of GBS.

**g. Transmission of dislocations across olivine grain boundaries (F. Ferreira and K. Marquardt)**

Much of our understanding of the mechanical properties of the Earth's upper mantle relies on coupling large scale geophysical observations to the physical properties of minerals. Since olivine, the most abundant and weakest phase in the upper mantle, is elastically anisotropic, the development of crystal preferred orientations (CPO) by mantle flow leads to large scale seismic anisotropy. In the uppermost part of the upper mantle ( $\lesssim 200$  km of depth), olivine is believed to deform mainly by dislocation creep. In polycrystalline materials, plastic deformation progresses through the transfer of dislocations across individual grain boundaries (slip transmission). Grain boundaries may influence slip transmission through different ways:

- a) Slip transfer occurs through the grain boundary in a (near) direct transmission of dislocations;

b) Slip progress to the next grain with only partial continuity, leaving residual boundary dislocations;

c) Grain boundary is impenetrable and additional slip systems are required to maintain boundary continuity.

Slip transfer requires that geometric compatibility exists between neighbouring grains, *i.e.*, the angle between the slip plane normal,  $\psi$ , and the angle between the slip direction,  $\kappa$ , of the incoming and outgoing slip systems should be as small as possible. This relation is given by the  $m'$  factor (Eq. (1)), which ranges from 0 (impenetrable boundary) to 1 (transparent boundary).

$$m' = (\mathbf{n}_{in} \cdot \mathbf{n}_{out}) (\mathbf{b}_{in} \cdot \mathbf{b}_{out}) = \cos(\psi) \cdot \cos(\kappa) \quad (1)$$

Here we analyse slip transmission and the distribution of grain boundaries in olivine (Fo<sub>50</sub>) torsion – deformed in a Paterson triaxial apparatus. Conditions of deformation are:  $\sigma$  (shear stress) = 168 MPa, T (temperature) = 1200 °C,  $\dot{\gamma}$  (shear strain rate) =  $5 \times 10^{-4} \text{ s}^{-1}$ . Olivine deformation is mainly accommodated by dislocation creep. Slip transmission, obtained through the  $m'$  factor, becomes easier as strain increases (Fig. 13, 14a). Boundaries that share a misorientation axis parallel to [010] are the ones where slip transfer occurs more easily (Fig. 14b). At the highly deformed area, (010) grain boundary planes are the most frequent boundaries (Fig. 14c). This shows that crystal alignment and slip transfer are intrinsically correlated. As deformation progresses, more grains are oriented in such a way that active dislocations, in the respective conditions, can easily glide, here with the (010) planes parallel to the shear plane. This also means that slip systems of adjoining grains are closer to coincidence, thus a feedback process is formed. Further understanding on how grain boundaries affect plastic deformation of olivine should include experimental observations of slip transmission.

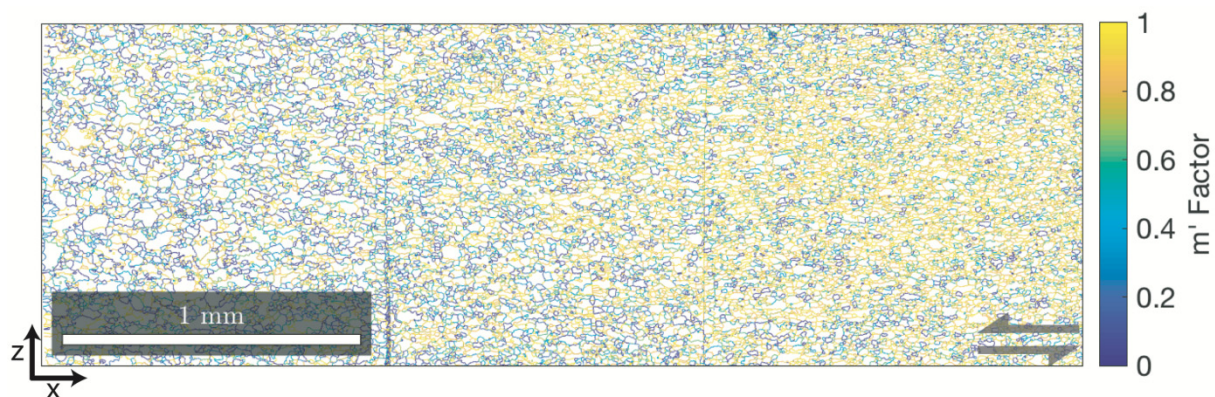


Fig. 3.6-13: Grain boundaries of XZ surface of the torsion deformed sample, coloured by the  $m'$  factor. Strain increases from  $\gamma = 0$  to  $\gamma = 10.9$  towards east. The  $m'$  factor spans from 0 (Impenetrable boundary) to 1 (Transparent boundary).

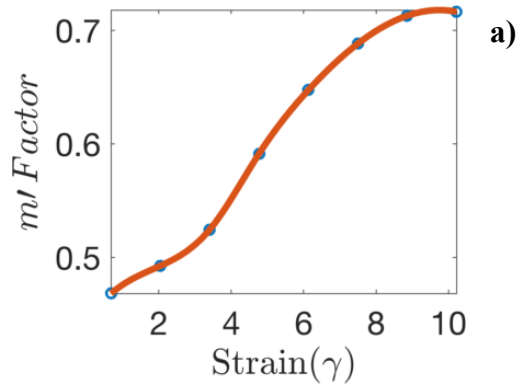
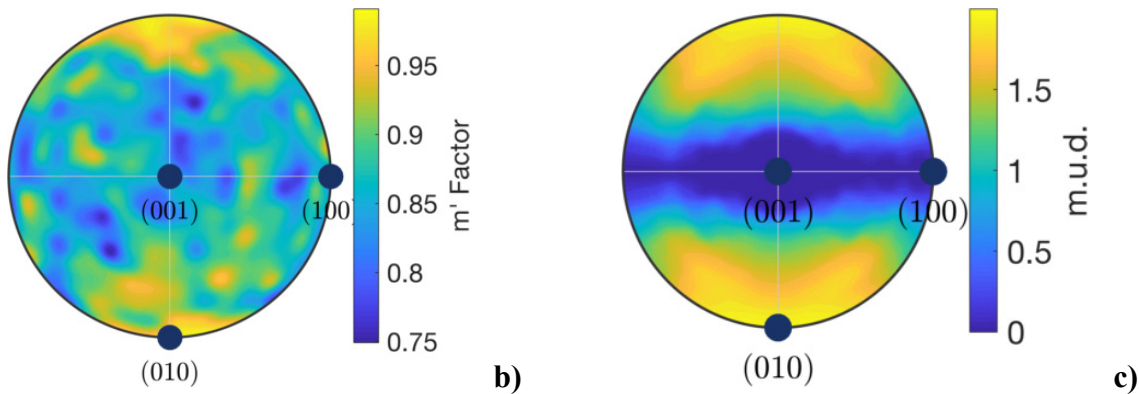


Fig. 3.6-14: **a)** Mean  $m'$  factor as a function of the total strain ( $\gamma$ ). **b)** Misorientation axes distribution contoured for the  $m'$  factor. **c)** Grain Boundary Plane Distribution obtained from Electron Backscattered Diffraction (EBSD) data averaged over three mutually orthogonal surfaces.



**h.** *Chemical signature of migrating grain boundaries in polycrystalline olivine (Y. Boneh/ Providence and K. Marquardt)*

Olivine is the most abundant phase of the upper mantle and influences its physical and chemical properties. The structure and chemistry of olivine grain-boundaries is speculated to be a reservoir for incompatible elements and impact geophysical observables due to their contribution to the mantle's viscosity, electrical conductivity, grain-size, partial melt distribution, and processes coupled with diffusion along grain boundaries. Here we investigate the chemical characteristics of grain boundaries in an olivine-dominated aggregate. The sample is synthesized from San Carlos olivine where fayalite has been added to obtain  $FO_{50}$  olivine composition with minor amounts of enstatite. The sample went through two evolutionary stages. At the first stage, the sample was deformed in torsion to shear strains up to  $\sim 10$  at a constant twist-rate under conditions of 1200 °C and 300 MPa confining pressure. At the second stage, the sample was annealed under hydrostatic conditions of 1250 °C and 1 GPa to investigate the microstructural evolution during post-deformation recovery and grain-growth.

The initial microstructure of the deformed sample consists of a mean grain-size of  $\sim 10$  microns and a narrow, unimodal grain-size distribution. During annealing a transient microstructure develops where some grains experience abnormal and faceted grain-growth (*i.e.*, porphyroblasts, 'p') while highly strained grains experience no significant recrystallization or growth (*i.e.*, matrix, 'm'). This transient microstructure is characterized by a bimodal grain-size distribution (*e.g.*, map in Fig. 3.6-15).

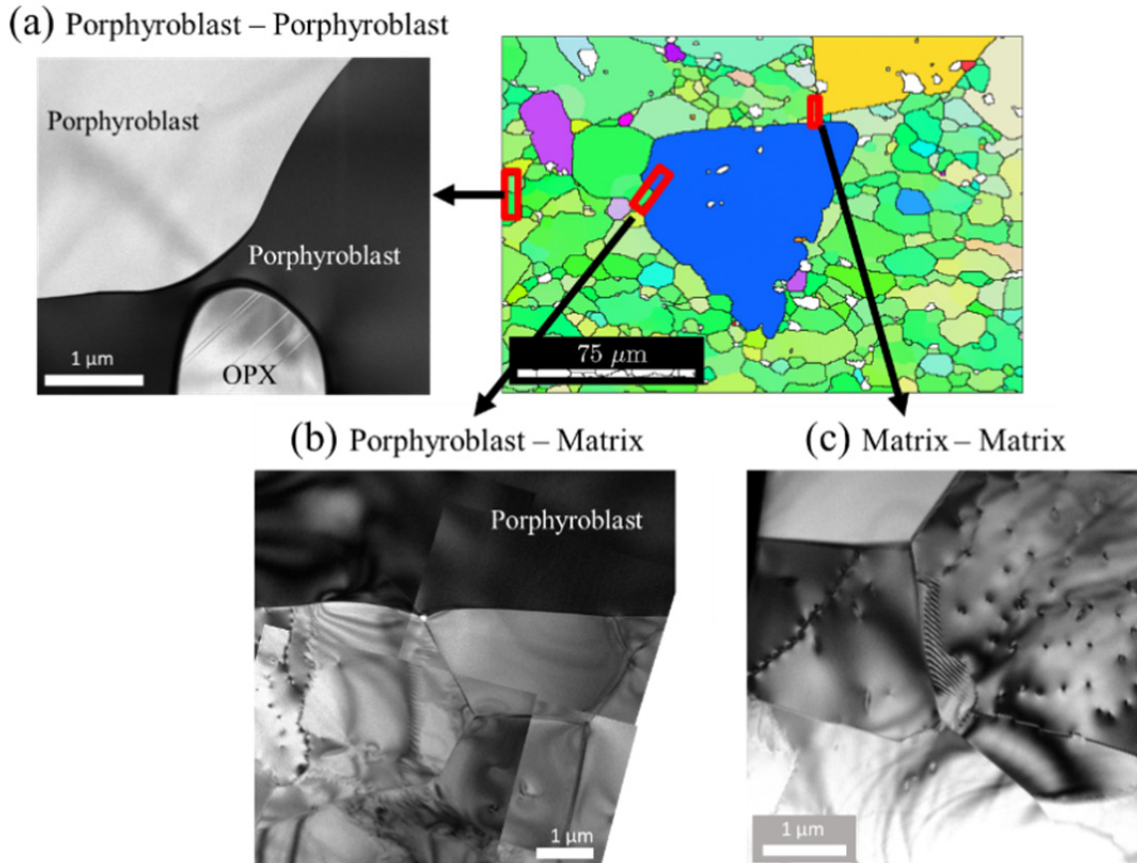


Fig. 3.6-15: Bright field TEM micrographs of three different interfaces that dominate the microstructure at a transient annealing stage. The main interfaces are: a) p-p-grain boundaries, b) p-m-grain boundaries and c) m-m-grain boundaries.

Using transmission electron microscopy (TEM) in conventional mode, high-resolution and analytical mode, *e.g.*, energy dispersive X-ray spectroscopy, we characterized the three main categories of grain boundaries between pairs of porphyroblasts (p-p), pairs of matrix grains (m-m), and grain boundaries between porphyroblast and matrix grains (p-m).

It was found that the p-p-grain-boundaries are enriched in Al and Ca and depleted in Mg, in comparison to grain interiors (Fig. 3.6-16). However, m-m-grain boundaries show less to no chemical segregation of these elements (Fig. 3.6-16).

The process that generates the observed abnormal and faceted grain growth can be interpreted as indicated in Fig. 3.6-17.

The relatively high level of chemical segregation to porphyroblast grain boundaries suggest that during grain boundary migration incompatible elements are swept by the migrating grain boundary and thus enriched. Grain boundary enrichment can be explained by a few processes: (1) The specific grain boundaries of the abnormally grown grain provide a larger density of energetically favourable storage sites for incompatible elements. (2) The segregated elements at the grain boundaries of the abnormally grown grain form distinct phases that enhance the

mobility of these grain boundaries, similar to complexions in ceramics. (3) The low angle grain boundaries are formed by dislocation cores and can thus store only very little amount of impurities (*i.e.*, Cottrell atmosphere). Additionally, diffusion along low angle grain boundaries is too slow to allow for fast chemical equilibration and efficient grain growth.

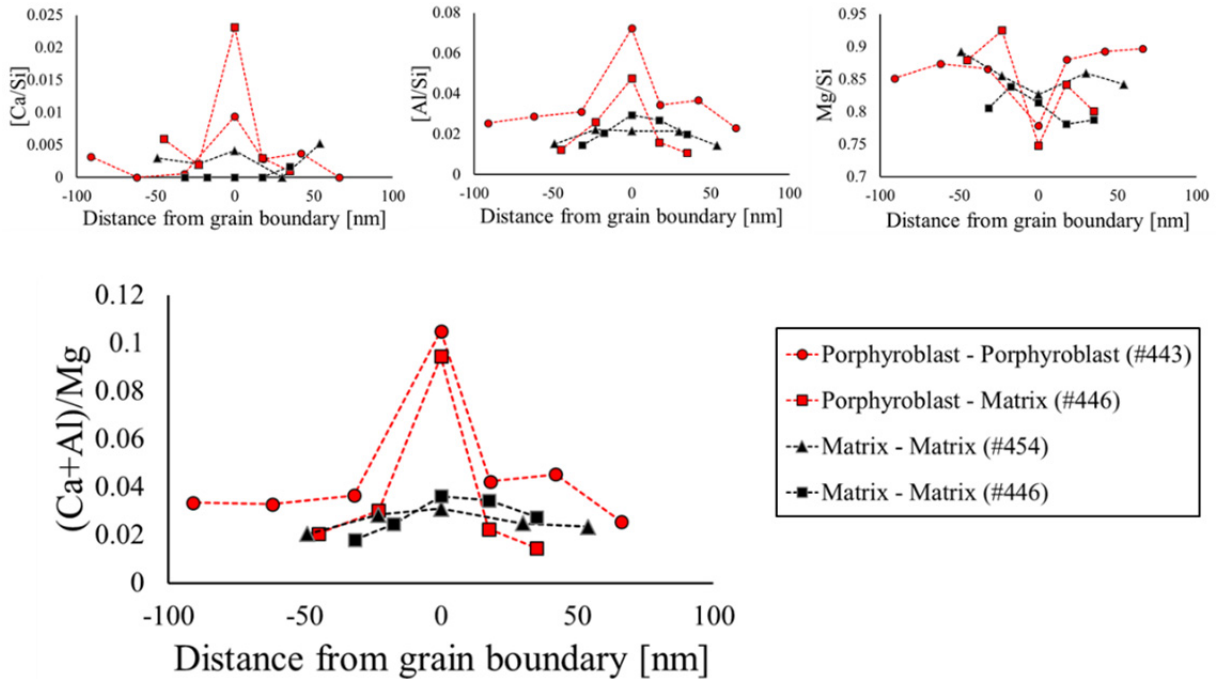


Fig. 3.6-16: Counts of Ca, Al, and Mg normalized by counts of Si (Si is constant along the boundary) across grain boundaries for pairs of grains (see legend). Grain-boundaries associate with porphyroblasts show enrichment of Ca and Al with depletion of Mg.

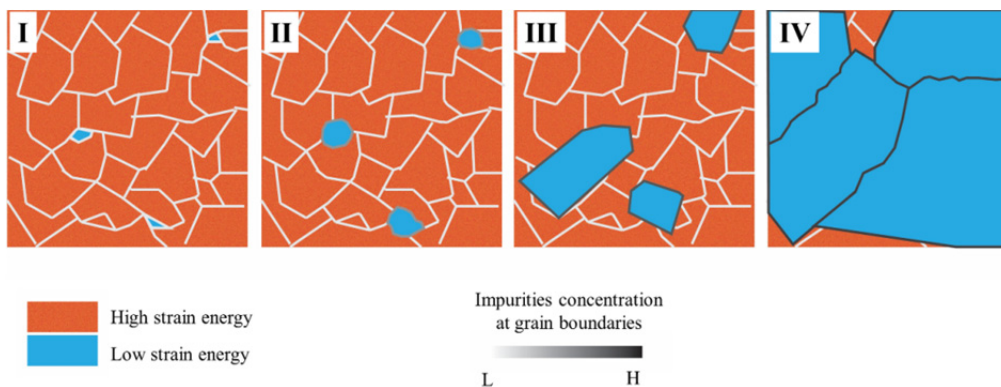


Fig. 3.6-17: (I) The initial, deformed sample with steady-state microstructure includes a small number of grains with low dislocation-density and low strain energy. (II) The gradient in strain energy provides the driving force for initial grain growth. During growth impurities accumulate at their grain boundaries. The accumulated impurities at grain boundaries changes the grain boundary structure and energy (eventually the grain-boundary complexion). (III) The change in GB structure and energy results in abnormal grains with well-developed facets that are independent of the orientation of other grain boundaries (*e.g.*, Fig. 3.6-15). (IV) The sample is fully annealed when the porphyroblasts dominate the microstructure.

**i. Small water dependence of the dislocation mobility in the olivine [001](100) slip system (L. Wang, T. Kawazoe, N. Miyajima and T. Katsura)**

Deformation experiments on olivine suggest that water enhances olivine creep rate to a great extent, with an exponent of 1.2 on the water content. Besides, olivine fabric changes from A-type to E-type to C-type with increasing water content. However, the results from deformation experiments may be biased by the large stress and the existence of free water on the grain boundaries, which is not the case in the asthenosphere. In order to enhance our understanding on the water effect on the rheology of mantle minerals, we employed the dislocation recovery method to study the water effect on dislocation mobility in natural olivine single crystals. Since the C-type fabric is dominant at high water content, we focus on the [001](100) slip system in this study.

Olivine single crystals were first annealed at dry/wet conditions to make starting olivines with water contents ranging from 7 to 100 ppm water. These olivines were then deformed in simple shear in the [001] direction on the (100) plane to activate the target slip system at 5 GPa, 1473 K at dry/wet conditions. The deformed olivines were annealed at the same conditions with the time ranging from 6 to 16 hours to recover the dislocations. In all annealed experiments, the olivine was enclosed by graphite powder acting as a soft material. To make the dry/wet environment during annealing, different amounts of a mixture of talc + brucite + FeO were added. Since dislocation character changes from screw to edge with increasing water content (Fig 3.6-18), dislocation density before and after recovery were measured on the (001) and (010) planes for dry and wet samples by the oxidation-decoration technique using SEM. The dislocation annihilation rate constant ( $k$ ) was obtained from the following equation,  $k = (1/\rho_f - 1/\rho_i)/t$ , where  $\rho_f$  and  $\rho_i$  are the dislocation densities after and before annealing respectively, and  $t$  is the annealing time.

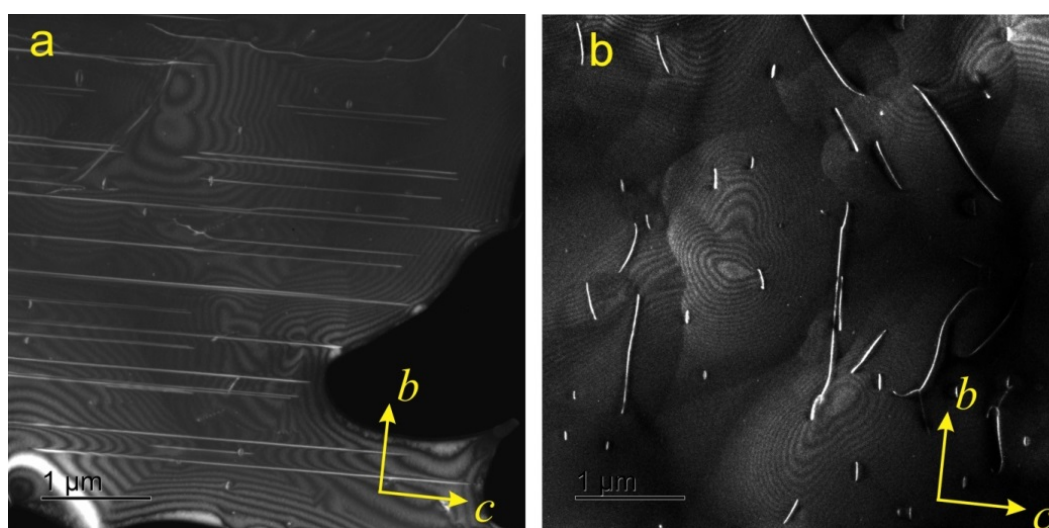


Fig. 3.6-18: TEM images showing [001] dislocation character changes with increasing water content. (a) 7 wt. ppm water. (b) 75 wt. ppm water. Screw and edge dislocations elongate in [001] and [010] direction, respectively.

Examples of a change in density of [001](100) dislocations are shown in Fig. 3.6-19. TEM images showing dislocation character changes are in Fig. 3.6-18 The dislocation annihilation rate constants are plotted against water content in Fig. 3.6-20. By fitting the data to a power law, the water content exponent of annihilation rate constant is  $r = 0.2(2)$ . The water dependence of the rate constant is assumed to be the same as that of dislocation creep. Therefore, water has a small effect on dislocation creep caused by [001](100) dislocations. In addition, comparing our results with those from Blaha and Katsura, both [001](100) and [100](010) slip have the same water dependence. Thus, the fabric transition in olivine should not be caused by the incorporation of water.

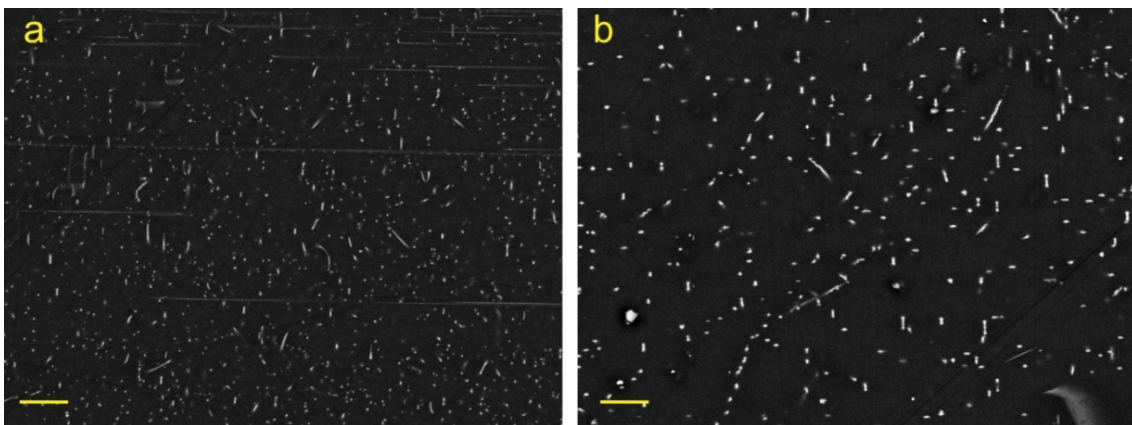


Fig. 3.6-19: Backscattered electron images of the oxidation-decorated olivine. The bright spots indicate presence of dislocations. The scale bars denote 2  $\mu\text{m}$ . (a) Dislocation structure before annealing. (b) Dislocation structure after annealing. The water content before and after annealing is 75 ppm. Annealing time is 16 hours.

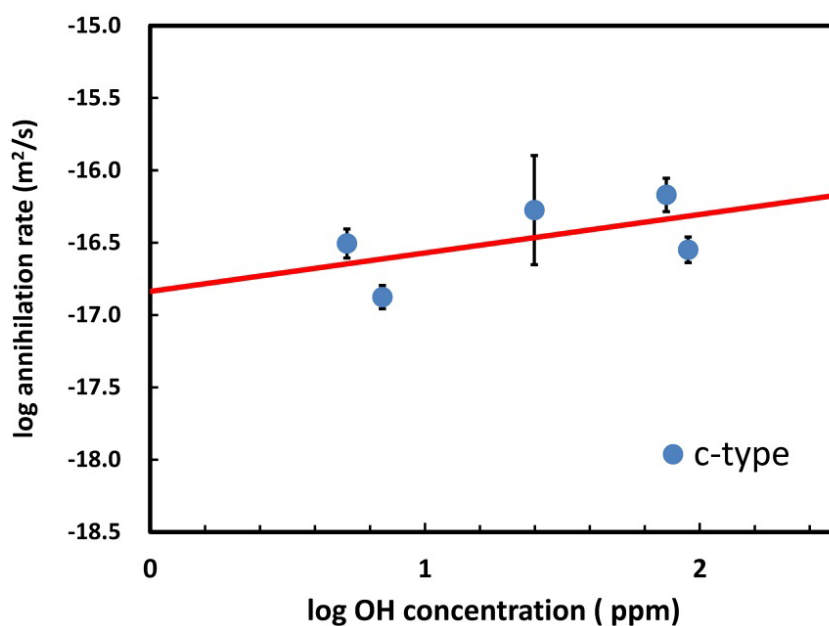


Fig. 3.6-20: Dislocation annihilation rate constants ( $k$ ) in the [001](100) slip systems against water content

**j.** *Activation of the [100](001) slip system by water incorporation in olivine (L. Wang, T. Kawazoe, N. Miyajima and T. Katsura)*

Olivine fabrics are essential to interpret the seismic anisotropy of the upper mantle. Deformation experiments suggest that olivine fabrics change from A-type to E-type to C-type with increasing water content. A-type and C-type are well documented both in natural and laboratory deformed samples and the responsible slip system for these two fabrics are well studied. However, there are not so many reports on the occurrence of E-type fabric in natural sample and the responsible slip system, *i.e.*, [100](001) is not yet reported by TEM observation. In this studies, we check whether [100](001) slip system exists or not.

The olivine single crystals were first annealed at dry/wet condition to make the starting olivines with water content range from 3 to 50 ppm water. Then, these olivine were simple sheared in the [001] direction on (001) plane, in an attempt to activate the target slip system at 2 ~ 5 GPa, 1473 ~ 1600 K at dry/wet conditions. Thin sections of the (001) plane of deformed olivines were prepared and then argon milled for TEM observation. All the images were taken perpendicular to the (001) plane.

TEM images of dislocations generated at dry conditions are in Fig. 3.6-21. After deformation the sample contained less than < 5 wt. ppm water. No dislocation lines are observed on the (001) plane, indicating (001) is not a slip plane at dry conditions. Only [001] direction elongated [100] dislocations were observed. SEM image shows that dislocations aligns in the [010] direction, indicating (010) as a slip plane. Therefore, no [100](001) slip system is activated at dry conditions.

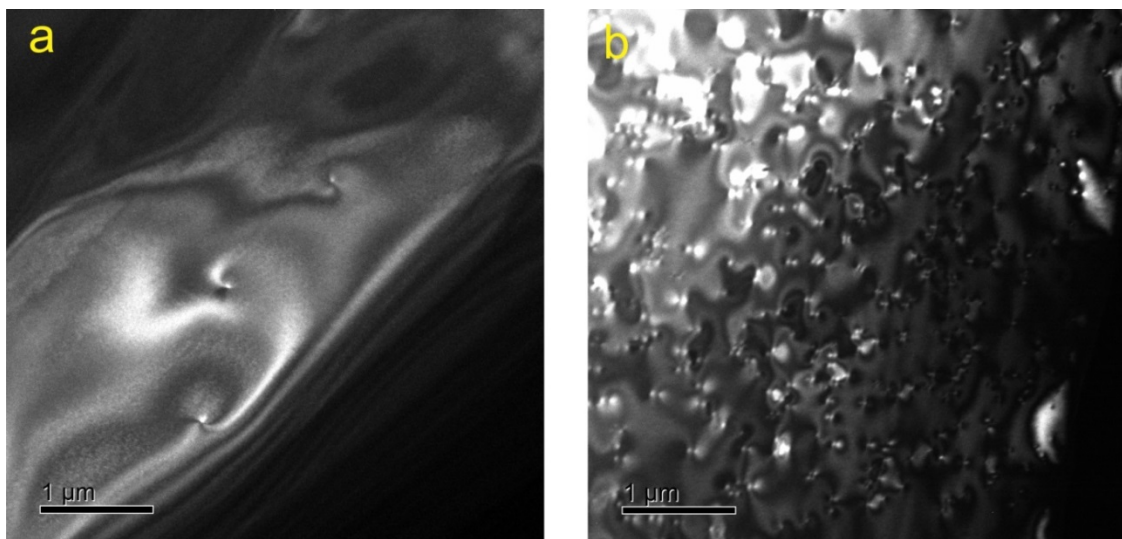


Fig. 3.6-21: TEM images showing dislocation character of sample deformed at dry conditions. a) Sample deformed at 2 GPa, 1473 K with water content 4 wt .ppm. b) Sample deformed at 3 GPa, 1573 K with water content 7 wt .ppm. Images were taken under  $g = 400$  on (001) plane. Only [001] elongated dislocations were observed.

Dislocations generated at hydrous conditions are shown in Fig. 3.6-22. The dominant dislocations are  $[100](001)$  edge dislocations. In addition,  $[001]$  elongated dislocations which are dominant at dry conditions also exist.  $[100](001)$  dislocation are generally curved and kinks on dislocation lines are visible. The curved dislocation line indicates the Peierls stress is reduced by incorporation of water inside olivine and therefore dislocation glide velocity is enhances. The present results suggest that E-type fabric is preferred to occur at hydrous conditions, which is consistent with deformation experiments.

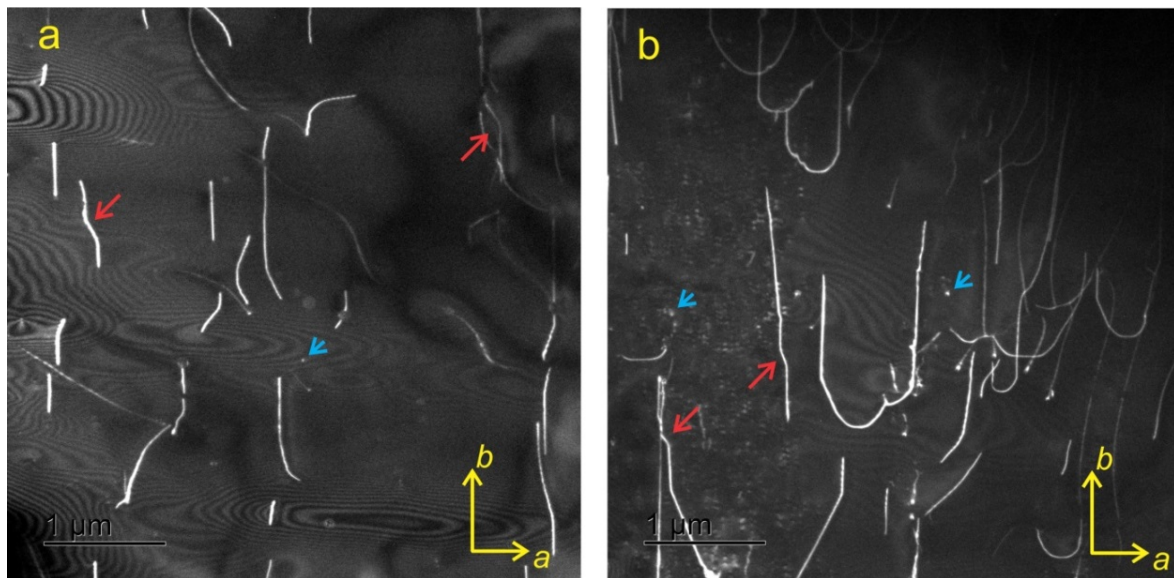


Fig 3.6-22: TEM images showing dislocation character of sample deformed at wet conditions. a) Sample deformed at 2 GPa, 1473 K with 30 wt .ppm water content. b) Sample deformed at 5 GPa, 1473 K with 49 wt .ppm water content. Images were taken under  $g = 400$ .  $[100](001)$  dislocations are generally curved and kinks are shown by red arrows.  $[001]$  elongated  $[100]$  dislocations are indicated by blue arrows.

**k.** *Diffusion controlled motion of  $[001](010)$  screw dislocation in natural olivine (L. Wang and T. Katsura)*

Constitutive equations for olivine dislocation creep at high temperature have been studied intensively. All these equations are based on a climb controlled model, *i.e.*, dislocation motion is rate-limited by diffusion-controlled climb of edge dislocation segments. However, both motion of screw and edge segments are needed for a dislocation loop to produce macroscopic strain. If the rate-limiting process of screw dislocation motion is different from that of edge motion, the rheology of olivine should be reconsidered.

Cross slip of screw dislocations was proposed as a rate limiting process by Poirier et al (1976) based on the fact that cross slip of dissociated dislocations needs additional energy to recombine these partial dislocations. However, whether cross slip can be a rate limiting process for olivine high temperature creep has not been tested by experiments. Therefore we test this hypothesis using the dislocation recovery technique for olivine  $[001](010)$  slip.

Olivine single crystals were first simple sheared in the [001] direction on the (010) plane to activate the target slip system at 3 GPa, 1600 K. The deformed olivines were annealed at room pressure and Ni-NiO oxygen partial pressure conditions from 1473 to 1773 K to determine the activation energy of motion of [001](010) edge dislocation. Dislocation densities before and after recovery were measured on the (100) plane by the oxidation-decoration technique using an SEM. The dislocation annihilation rate constant ( $k$ ) was obtained from the following equation,  $k = (1/\rho_f - 1/\rho_i)/t$ , where  $\rho_f$  and  $\rho_i$  are the dislocation densities after and before annealing respectively, and  $t$  is the annealing time. The obtained activation energy was compared with that of [001](010) screw dislocation from previous studies.

Dislocation structures of [001](010) dislocations before and after annealing are shown in Fig. 3.6-23. Jogs on screw dislocations are visible. The dislocation annihilation rate constants of both [001](010) screw and edge dislocations are shown against reciprocal temperature in Fig. 3.6-24. The activation energy for both dislocations are identical, *i.e.*, 400 kJ/mol, which is identical to that of Si self-diffusion. These indicate that the rate limiting processes in the motion of edge and screw dislocation are identical, *i.e.*, diffusion process. Therefore, the conventional recovery controlled model for olivine creep does not need to be modified by the influence of screw dislocation.

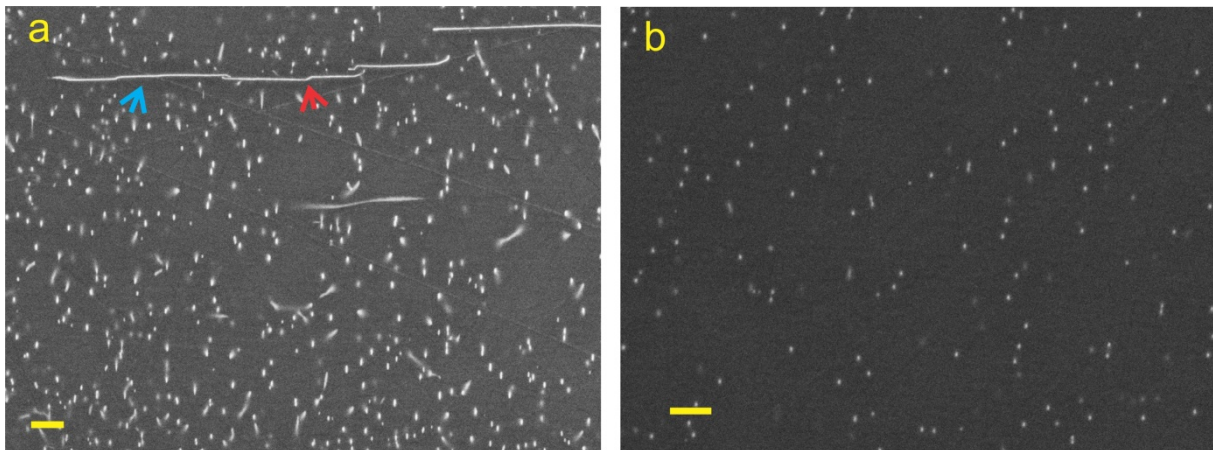


Fig. 3.6-23: BEIs showing the dislocation density (a) before and (b) after annealing at 1763 K for 35 minutes. The images were taken on the (100) plane. Screw and edge dislocations are lines and dots due to the geometry of their dislocation line. The blue arrow indicates a screw dislocation and the red arrow indicates a jog on screw dislocation. The scale bar shown represents 2  $\mu\text{m}$ .

A diffusion controlled motion of screw dislocations is proposed (Fig. 3.6-25). The screw dislocation can form a jog by cross slip to overcome obstacles it meets during glide (Fig. 3.6-23 and 3.6-25). Jog has the same Burgers vector ( $\mathbf{b}$ ) as its parental dislocation but its dislocation line ( $\mathbf{J}$ ) is perpendicular to the direction of  $\mathbf{b}$ . This is different from its parental screw dislocation, whose line direction ( $\mathbf{L}$ ) is parallel to the direction of  $\mathbf{b}$ . Therefore, a jog on

a screw dislocation is of edge character. The slip plane of the jog is defined by a dislocation line of itself and a Burger's vector. Screw dislocations glide perpendicular to their dislocation line and therefore, a jog on the dislocation needs to climb to move along with its parental dislocation. Thus, climb can serve as a rate-limiting process of screw dislocation movement.

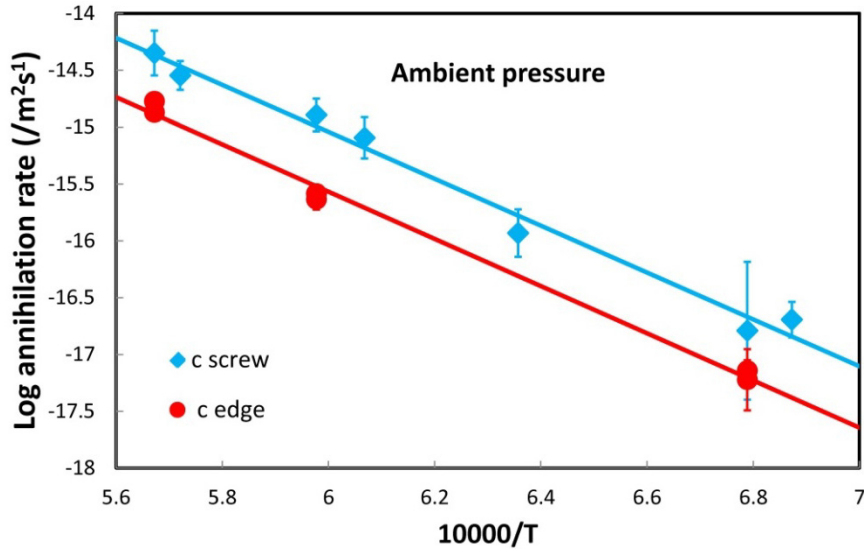


Fig. 3.6-24: Logarithmic dislocation annihilation rate constants of *c*-edge dislocation versus the pressure. Together plotted are the annihilation rate constants of *c*-screw dislocation from previous studies. The activation energy for both dislocation are identical, *i.e.*, 400 kJ/mol.

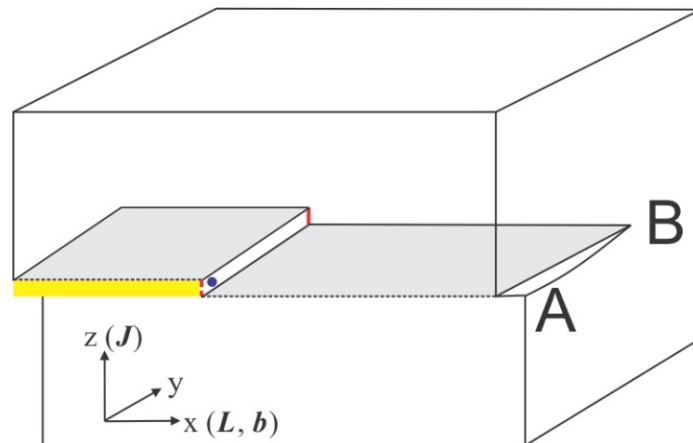


Fig. 3.6-25: Schematic diagram shows the motion of a screw dislocation is controlled by climb of a jog plotted in Cartesian coordinates. The blue spot represents an obstacle which the dislocation meets during glide. Screw dislocations with a jog (red) glide from position A to B along *Y* axis. Line direction of parental screw dislocation (*L*) and direction of Burger's vector (*b*) are parallel to the *X* axis. Line direction of jog (*J*) is parallel to the *Z* axis. The yellow area indicates the glide plane of the jog, which is defined by *J* and *b*. The shaded area indicates the glide plane of parental screw dislocation.

*1. Measurement of the silicon self-diffusion coefficient in single-crystal wadsleyite (D. Druzhbin, H. Fei, R. Dohmen/Bochum, Y. Lin/Beijing, C. Zhang/Beijing, M. Wiedenbeck/Potsdam and T. Katsura)*

Diffusive properties of atoms in mantle minerals at high pressure and high temperature have an important implication for mantle flow studies. Convection of the Earth's mantle is accomplished by plastic deformation of rocks, which is mainly controlled by three mechanisms: diffusion creep, dislocation creep, and grain-boundary sliding. Both the diffusion creep and dislocation creep at high temperatures are believed to be controlled by atomic diffusion. Silicon is the slowest diffusing species in the majority of mantle minerals, and therefore considered as the rate-limiting element for mineral deformation at high temperatures.

Wadsleyite, a high-pressure polymorph of olivine, is one of the most abundant minerals in the upper part of the mantle transition zone (410-520 km). Deformation experiments suggested that water incorporation in wadsleyite significantly enhances the creep rate. However, such experiments were conducted under several orders of magnitude higher stress conditions than those in the Earth's interior, which may cause misinterpretation. Diffusion experiments can bypass this problem because they are performed under hydrostatic conditions. The purpose of this work is to obtain the silicon self-diffusion coefficient ( $D_{Si}$ ) of wadsleyite, as a function of water concentration ( $C_{H_2O}$ ).

In order to avoid grain-boundary diffusion, measurements are conducted using single crystals. As reported in previous annual reports, single crystals of Fe-free wadsleyite were already successfully synthesized. The crystals were oriented and polished on a face parallel to (100), (010) or (001) plane using  $\frac{1}{4}$   $\mu\text{m}$  diamond powder and alkali colloidal silica. The crystals were examined by etching using hydrofluoric acid diluted by acetic acid after alkali colloidal silica polishing to confirm that the whole mechanically damaged layer by diamond powder was removed. Thin films with thickness of 500-600 nm and the  $^{18}\text{O}$  and  $^{29}\text{Si}$  enriched  $\text{Mg}_2\text{SiO}_4$  composition were deposited on the polished faces of Fe-free wadsleyite crystals by a pulsed laser deposition facility at the Institute of Geology, Mineralogy and Geophysics at Ruhr-Universität in Bochum.

Trial runs of diffusion annealing conducted using the multianvil apparatus showed that both dense CsCl pellets and gold as a mechanical buffer helps to prevent the crystal from mechanical breakage at high pressures. Usage of gold prevents wadsleyite crystals from dehydration keeping initial water content around 500 wt. ppm. It was established that the crystals must be placed on a polished hard plane (diamond disk used in this study) to avoid increasing surface roughness during the diffusion annealing. However, the thin film partially sticks to the diamond surface.

The isotopic depth profiles were obtained by NanoSIMS (secondary ion mass spectrometry) with the sputtered crater's dimensions of 10 x 10  $\mu\text{m}$ . Cameca NanoSIMS 50L instrument at

the Institute of Geology and Geophysics, Chinese Academy of Sciences in Beijing was used. Profiles from samples annealed for 10 hours and more showed that silicon completely diffused, only those samples from zero time runs and with one-hour annealing time (Fig. 3.6-26) produced profiles that enabled for further analysis. The depth of the craters was determined using a 3D-Nanofocus confocal microscope. The diffusion coefficient  $D_{Si}$  was obtained by fitting to the solution of Fick's second law:

$$\frac{{}^{29}\text{Si}}{{}^{28}\text{Si}} = \frac{(C_0 - C_i)}{2} \cdot \operatorname{erf}\left(\frac{x - h}{\sqrt{4D_{Si}t + L}}\right) + \frac{(C_0 + C_i)}{2}$$

where  $C_1$  is the initial ratio of isotopic concentrations  ${}^{29}\text{Si}/{}^{28}\text{Si}$  in the isotopic film,  $C_0$  is the initial ratio of isotopic concentration  ${}^{29}\text{Si}/{}^{28}\text{Si}$  in the natural ratio,  $x$  is the distance from the surface (depth),  $h$  is the diffusion interface position (boundary between isotopically enriched film and the crystal),  $L$  is the nominal diffusion length in zero-time diffusion runs, related to surface roughness. The resulting  $D_{Si}$  for dry wadsleyite (< 30 wt. ppm  $\text{H}_2\text{O}$ ), at 1600 °C is  $2 \times 10^{-18} \text{ m}^2/\text{s}$ . This value is more than one order of magnitude faster than the one measured in wet wadsleyite and reported in the literature.

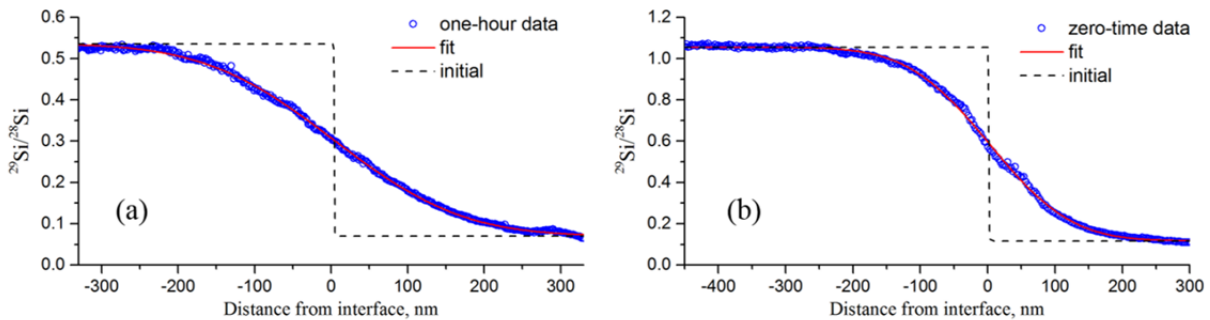


Fig. 3.6-26: (a) Diffusion profile of sample Z1514 (1600 °C, one-hour annealing); (b) diffusion profile of sample Z1702 (1600 °C, zero-time run).

**m. Interplay between shear heating and grain size evolution in ductile shear zones (M. Thielmann and T. Duretz/Rennes)**

Ductile strain localization in the lithosphere might result in lithospheric-scale shear zones that are a prerequisite for subduction initiation. Furthermore, if this process happens on short timescales, it is also capable of generating seismic events, thus providing a mechanism for intermediate-depth earthquakes.

In this project, we are investigating the interplay between two mechanisms that have been shown to result in ductile strain localization: grain size reduction and shear heating. Previous studies have shown that the interplay between those two mechanisms does indeed result in

catastrophic events that resemble earthquakes. We investigate this feedback loop using 2D numerical models and assess the parameter range where it is a feasible nucleation mechanisms for intermediate-depth earthquake generation. To do this, we have overcome a number of numerical challenges concerning numerical stability and convergence of the nonlinear solver. First results show deverse behaviour in deformation styles from stable deformation without catastrophic events to grain size assisted thermal runaway where the initial shear zone splits in two conjugate shear zones (Fig. 3.6-27).

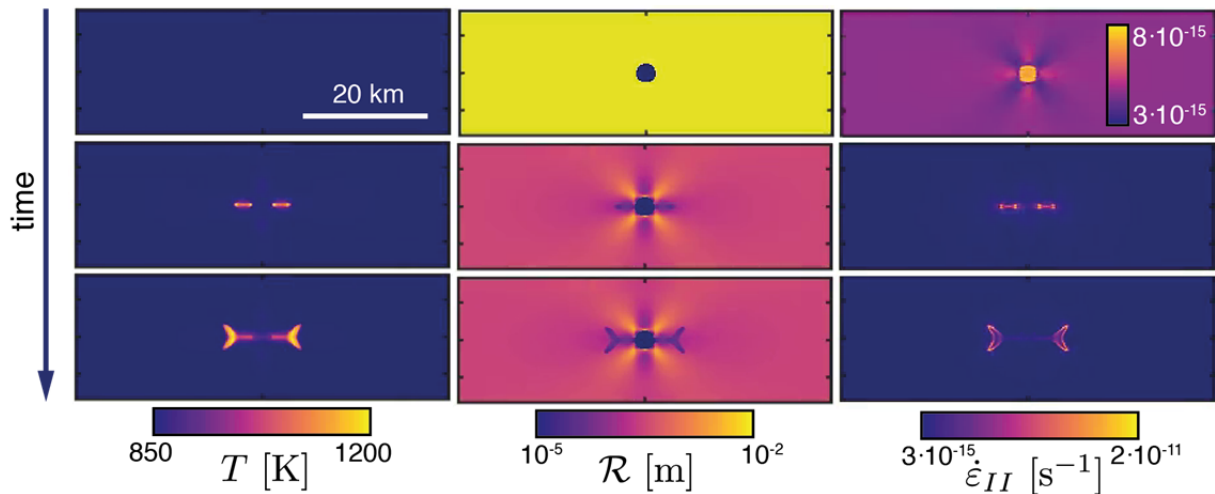


Fig. 3.6-27: Evolution of temperature (left), grain size (middle) and strain rate (right) shown in three snapshots (top to bottom). The model is deformed in simple shear with a strain rate of  $3 \cdot 10^{-15}$  1/s. One can see a shear zone initiating from the initial perturbation (in grain size) and then splitting in two conjugate shear zones. The color scale in the first strain rate plot (top right) has been adjusted for better visibility.

### 3.7 Materials Science

Applications of high pressure research in physics, chemistry and material sciences have always played an important role in research performed at the Bayerisches Geoinstitut, although to a smaller extent than questions in Earth and planetary sciences. Often, they are interlinked and an observation of a planetary material raises questions that are then further investigated with model materials in which the observed phenomena can be better characterized in isolation, rather than in the complex matter that constitutes the Earth or other planets. Prominent examples are transitions from insulating or semiconducting to metallic behavior or crystal structures that occur in both mineralogy and material sciences, such as perovskites.

At the Bayerisches Geoinstitut, a unique combination of expertise, *in-situ* high-pressure technology, and analytical characterisation is available that make sophisticated and challenging research on the physics and chemistry of materials possible. In this annual report, we present results for various classes of solids: elements, binary and complex oxides, nitrides, and carbides. Half of the contributions in this section of the annual report address the characterization of materials by high-pressure *in-situ* single crystal X-ray diffraction, a field in which the Bayerisches Geoinstitut is a pioneer.

Structures of all known boron allotropes ( $\alpha$ -B through  $\epsilon$ -B) are based on various arrangements of B<sub>12</sub> icosahedra, and a predicted non-icosahedral boron allotrope with a  $\alpha$ -Ga type structure has remained elusive for three decades. With *in-situ* single crystal X-ray diffraction at 115 GPa, it was finally possible to confirm the occurrence of this new polymorph ( $\zeta$ -B). At the same time, this study is the first to perform single crystal X-ray diffraction on light elements beyond 1 Mbar. Two more studies use *in-situ* single-crystal X-ray diffraction to characterize new phases in Fe-based binary systems: one for Fe-N, the other for Fe-O. In both, new phases were discovered and characterized. For the Fe-N system, a series of compounds were discovered with Fe<sub>3</sub>N<sub>2</sub>, FeN, FeN<sub>2</sub> and FeN<sub>4</sub> stoichiometry. FeN<sub>4</sub> observed at 135 GPa is of particular interest, as Fe is octahedrally coordinated, and N-N bonds occur both as single and double bonds. For the Fe-O system, the third contribution in this section resolves the structure of FeO<sub>2</sub> with the unusual Fe<sup>4+</sup> oxidation state.

Metal carbides represent an important class of ceramics that exhibit high mechanical strength and extreme thermal stability. Their high-pressure high-temperature stability and behavior, however, remain largely unexplored. One contribution to the annual report characterizes the pressure-volume-temperature of a prototypical carbide, TaC, by *in-situ* X-ray diffraction and confirms its high stability by determining a high bulk modulus.

Using a combination of methods, including *in-situ* X-ray diffraction and Raman spectroscopy, the following two contributions look at germanium and perovskite-structured CaCo<sub>3</sub>V<sub>4</sub>O<sub>12</sub>. The work on Ge shows a transition of the semi-conductor from *n*- to *p*-type conduction with applied pressure (both bulk compression and indentation) that does not revert under

decompression. The work demonstrates tuning of the traditional semiconductor material, like printing of p-type zones on the n-type bulk of a Ge crystal and may inspire new applications in industry. The study on  $\text{CaCo}_3\text{V}_4\text{O}_{12}$  reveals an interesting phenomenon of fundamental interest in perovskite-structured materials. The perovskite structure is formed with  $\text{V}^{4+}$  on the B-site (octahedrally coordinated) and  $\text{Ca}^{2+}$  on the A-site, and  $\text{Co}^{2+}$  occupies large voids in the structure and is coordinated by four  $\text{O}^{2-}$  in planar geometry at low pressure. With compression, the voids become more restricted and  $\text{Co}^{2+}$  is pushed out of these planes, which should lead to a polarization of the crystal that could be tuned by applying an external field.

In a series of experiments in the piston-cylinder and multi-anvil press, the exchange between  $\text{Zn}^{2+}$  and  $\text{Mg}^{2+}$  in the willemite-olivine solid solution is explored, with the goal to better characterize it as a geobarometer. In the pressure range of 0-4 GPa, the solubility of  $\text{Mg}^{2+}$  in  $\text{Zn}_2\text{SiO}_4$  decreases and that of  $\text{Zn}^{2+}$  in  $\text{Mg}_2\text{SiO}_4$  increases which suggest that it can reliably be used as a pressure calibrant over this pressure-range. Near 4 GPa, willemite undergoes a phase transition, and the solubility trend reverses, before melting of willemite near 5 GPa renders its useless as a pressure marker.

The final contribution of the section does not deal with pressure; rather it characterizes the diffusion of incompatible trace elements on grain boundaries of yttrium aluminum garnet (YAG), a common laser crystal. Such processes influence, e.g., the lifetime of laser ceramics. The study demonstrated that grain boundary diffusion of elements with low solubility, in particular La, diffuse with extreme efficiency along grain boundaries, potentially decreasing the stability of the YAG crystal.

**a. Boron allotrope with  $\alpha$ -Ga structure synthesized at high pressure and high temperature (I. Chuvashova, E. Bykova/Hamburg, M. Bykov, L.S. Dubrovinsky, N.A. Dubrovinskaia/Bayreuth, V. Prakapenka/Chicago, M. Mezouar/Grenoble and K. Glazyrin/Hamburg)**

Structures of all hitherto known boron allotropes ( $\alpha$ -B,  $\beta$ -B,  $\gamma$ -B,  $\delta$ -B, and  $\epsilon$ -B) are based on various arrangements of  $\text{B}_{12}$  icosahedra, since three valence electrons of boron are insufficient to form a simple covalent structure. However, theoretical calculations suggest a possibility of the existence of a non-icosahedral boron allotrope with the  $\alpha$ -Ga type structure. Here we report data on the first non-icosahedral boron allotrope, which we denote as  $\zeta$ -B, with the orthorhombic  $\alpha$ -Ga-type structure (space group  $Cmce$ ) synthesized in a diamond anvil cell (DAC) at extreme high-pressure high-temperature conditions (115 GPa and 2100 K). A series of experiments were conducted in DACs using synchrotron *in situ* single-crystal X-ray diffraction. We compressed single crystals of  $\beta$ -B DAC to 38(1) GPa, 50(1) GPa and 102(2) GPa and heated to  $\sim 2000$  K using double-side lasers. After heating the pressure in the DAC increased to 42(1) GPa, 58(1) GPa and 115(2) GPa, respectively. For the two lowest pressure experiments, diffraction spots of  $\gamma$ -B were observed at room temperature, in good agreement with theoretical predictions.

At 115(2) GPa the picture changed dramatically: the color of the sample became black (non-reflecting) and the X-ray diffraction data had to be treated like a powder. Apart from reflections of Re (gasket material) and Ne (used as a pressure-transmitting medium and pressure calibrant), several new reflections were observed, but were relatively weak. The crystal structure was solved as orthorhombic (space group  $Cmce$  with 8 atoms per unit cell) with lattice parameters  $a = 2.7039(10)$  Å,  $b = 4.8703(32)$  Å,  $c = 2.9697(6)$  Å, in good agreement with the predictions (Fig. 3.7-1). This new high-pressure boron allotrope was denoted as  $\zeta$ -B, the sixth boron allotrope. The structure can be described as stacking distorted and corrugated hexagonal nets with the  $3^6$  topology along the (010) direction. Within each net, B atoms connect to six neighbors and one, much shorter, bond between the nets. Nevertheless, interatomic distances do not allow for an interpreting of the  $\zeta$ -B structure as layered, contrary to an earlier proposal.

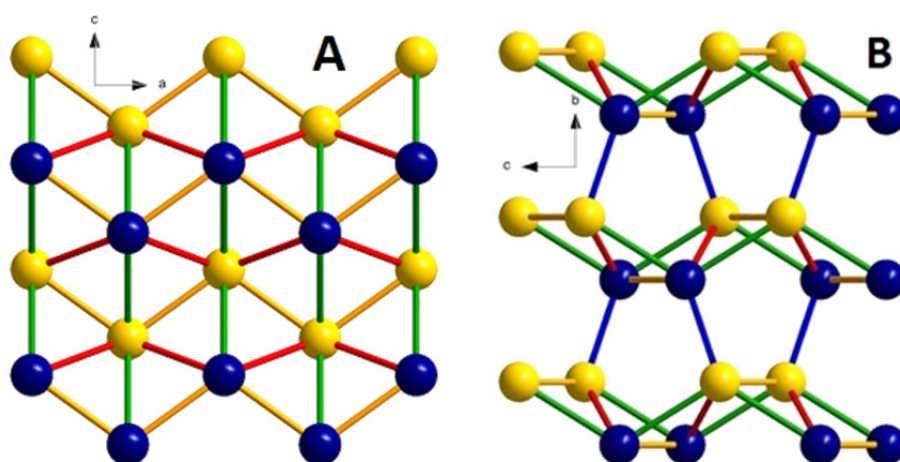


Fig. 3.7-1: Structure of  $\zeta$ -B. (A) The projection of a fragment of one distorted and corrugated hexagonal net on the  $ac$  plane. Such nets are stacked along the (010) direction. Blue and yellow lie in different planes (blue atoms are lower and yellow ones are further up if seen along the (010) direction). Bonds with different lengths are shown in different colors: 1.66(1) Å (orange), 1.72(1) Å (red), and 1.75(1) Å (green). (B) The projection of three nets on the  $bc$  plain. The lengths of bonds connecting the layers (blue) all are 1.59(1) Å.

**b. Novel compounds in the iron-nitrogen system synthesized in laser-heated diamond anvil cells** (M. Bykov, E. Bykova/Hamburg, G. Aprilis, K. Glazyrin/Hamburg, E. Koemets, I. Chuvashova, M. Mezouar/Grenoble, V. Prakapenka/Chicago, H.-P. Liermann/Hamburg, F. Tasnádi/Linköping, A.V. Ponomareva/Moscow, I.A. Abrikosov/Linköping, N.A. Dubrovinskaia/Bayreuth and L.S. Dubrovinsky)

Poly-nitrogen compounds have been considered as potential high energy density materials for a long time. Their energy density grows with the number of catenated nitrogen atoms. High nitrogen content and stability are mutually exclusive, making their synthesis challenging. One way of stabilizing such compounds is the application of pressure. In the present work, through a direct reaction between Fe and  $N_2$  in a laser-heated diamond anvil cell, we synthesized four

novel iron-nitrogen compounds  $\text{Fe}_3\text{N}_2$ ,  $\text{FeN}$ ,  $\text{FeN}_2$  and  $\text{FeN}_4$ . All compounds were characterized by synchrotron-based single-crystal X-ray diffraction.

Laser heating of an Fe foil in nitrogen medium at 50 GPa and 1900(100) K led to the formation of  $\text{Fe}_3\text{N}_2$  and  $\text{FeN}$  (Fig. 3.7-2). Iron nitride  $\text{Fe}_3\text{N}_2$  ( $Pnma$ ,  $Z = 4$ ,  $a = 5.4227(6)$ ,  $b = 2.6153(3)$ ,  $c = 10.590(11)$  Å at 50 GPa) is isostructural to  $\text{Cr}_3\text{C}_2$ . The structure is built of quadrilateral face-capped trigonal prisms  $\text{NFe}_7$ , which are interconnected by sharing trigonal faces and edges.  $\text{FeN}$  has a NiAs structure type ( $P6_3/mmc$ ,  $Z = 2$ ,  $a = 2.6299(11)$ ,  $c = 4.819(7)$  Å at 50 GPa)

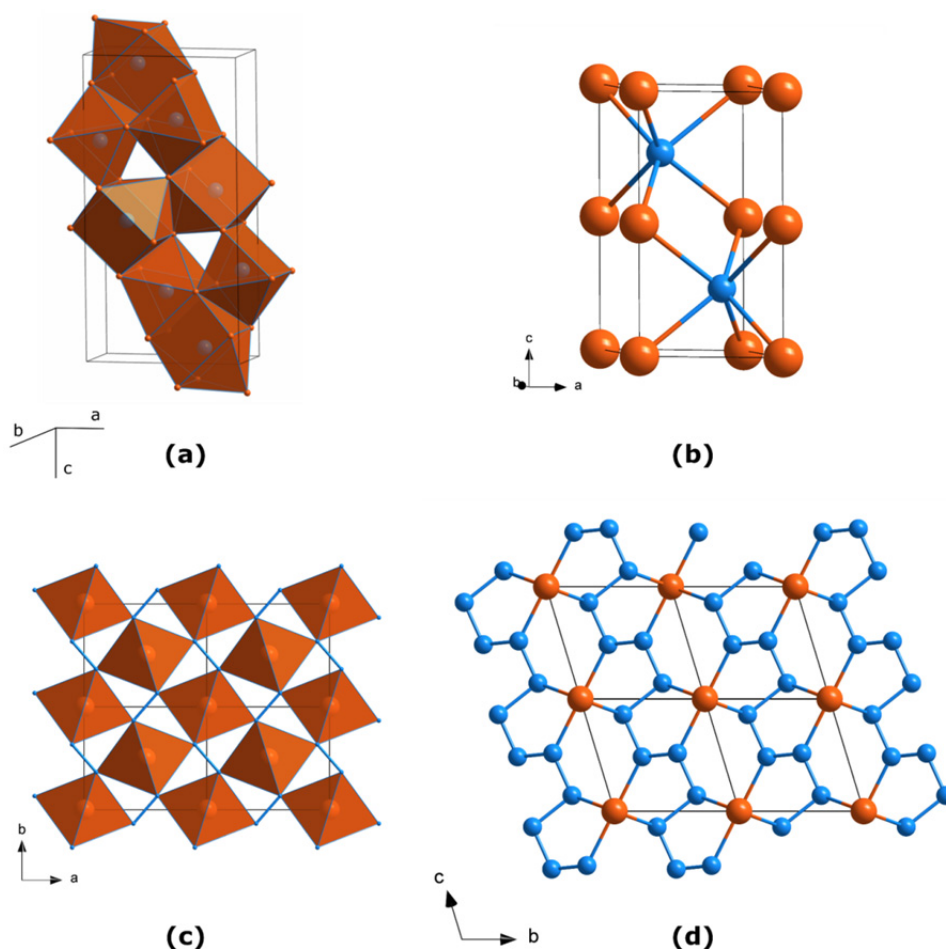


Fig. 3.7-2: Crystal structures of iron-nitrogen compounds. Orange and blue balls show the positions of Fe and N atoms, respectively. (a)  $\text{Fe}_3\text{N}_2$  at 50 GPa; (b)  $\text{FeN}$  at 50 GPa with NiAs structure type; (c)  $\text{FeN}_2$  at 58 GPa; and (d)  $\text{FeN}_4$  at 135 GPa.

The  $\text{FeN}_2$  phase was first observed after heating of Fe in a N medium at 58 GPa to above 2000 K.  $\text{FeN}_2$  has marcasite-type structure ( $Pnmm$ ,  $Z = 2$ ,  $a = 4.4308(19)$ ,  $b = 3.7218(11)$ ,  $c = 2.4213(18)$  Å at 58.5 GPa) that can be described as consisting of chains of edge-sharing  $\text{FeN}_6$  octahedra aligned along the  $c$ -axis. These chains are interconnected through common vertices. Additional linkage between  $\text{FeN}_6$  octahedra is provided via N-N bonds (Fig. 3.7-2).

The synthesis of FeN<sub>4</sub> was first performed at 106 GPa by laser-heating in nitrogen medium of the mixture of FeN and FeN<sub>2</sub>, both synthesized in the reaction between Fe and N<sub>2</sub> at 60 GPa. Indexing the diffraction pattern shows a triclinic unit cell with the parameters  $a = 2.5079(5)$ ,  $b = 3.5270(14)$ ,  $c = 3.5402(6)$  Å,  $\alpha=105.08(2)$ ,  $\beta=110.231(16)$ ,  $\gamma=92.05(2)^\circ$ . In the FeN<sub>4</sub> structure, six nitrogen atoms coordinate each iron atom in a highly distorted octahedron: each Fe atom is a member of two non-planar five-member Fe[N<sub>4</sub>] metallacycles, which are almost parallel to the (1-10) lattice plane (Fig. 3.7-2). Two more nitrogens complete the octahedron. The most intriguing feature of the crystal structure is that nitrogen atoms form infinite zigzag chains, running along the  $c$ -direction.

The geometry of the polymeric nitrogen chains provides insight into the electron localization in the compound. Half of the nitrogen atoms (N1) have three neighboring atoms in planar triangular geometry, whereas the other nitrogen atoms (N2) have tetrahedral coordination. This suggests a  $sp^2$  hybridization of the N1 atoms and a  $sp^3$  hybridization of the N2 atoms. Additionally, at 135 GPa there is a significant difference in N1-N1, N1-N2 and N2-N2 bond distances, which are ~1.22, 1.33, and 1.43 Å, respectively. Comparing these values with the average N=N double bond length (1.238 Å at ambient conditions) and the single bond in polymeric cg-N (1.346 Å at 115 GPa), one can classify N1-N1 as N=N double bonds, and N1-N2 and N2-N2 as the single bonds. Therefore, the nitrogen chains in FeN<sub>4</sub> can be considered as catena-poly[tetraz-1-ene-1,4-diyl] anions. The FeN<sub>4</sub> phase synthesized at 106 GPa was preserved under decompression to 23 GPa.

*c. Investigation of chemical reactions between Fe and oxygen at pressures up to 70 GPa and high temperature (E. Koemets, E. Bykova/Hamburg, M. Bykov, G. Aprilis, S. Chariton; J. Haines, S. Clement and J. Rouquette/Montpellier; V. Prakapenka/Chicago, M. Hanfland/Grenoble and L.S. Dubrovinsky)*

During the last few years, many novel iron oxides with unusual stoichiometry were synthesized by high-pressure high-temperature techniques (Fe<sub>4</sub>O<sub>5</sub>, Fe<sub>5</sub>O<sub>6</sub>, Fe<sub>5</sub>O<sub>7</sub>, Fe<sub>7</sub>O<sub>9</sub>, Fe<sub>25</sub>O<sub>32</sub>, FeO<sub>2</sub>, etc). All this novel iron oxides, especially FeO<sub>2</sub>, have attracted great scientific interest. Finding novel iron oxides and uncovering their properties have drastic effects on our understanding of chemistry in the Fe-O system at high pressure, chemical processes in Earth's mantle and at the core-mantle boundary, oxygen fugacity in its deep interior, the nature of the oxygen and hydrogen cycles, and even on our understanding of the origin of life and its evolution. Although FeO<sub>2</sub> has been proposed to be an important chemical component of the Earth's mantle, details of its crystal structure and high-pressure behaviour remains poorly understood.

Here we report results from a series of experiments investigating direct reactions between iron and oxygen at high-pressure high-temperature conditions using the laser-heated diamond anvil cell (DAC) technique. We assembled a series of DACs equipped with 250 μm cullet size

diamonds and pure rhenium (oil-free) gaskets. Gaskets were pre-indented to a thickness of  $\sim 15 \mu\text{m}$  for each cell and drilled in order to create a sample chamber.  $^{57}\text{Fe}$  iron chips were placed inside the chambers and cells were loaded cryogenically with oxygen at BGI and ESRF.

In one of the experiments we compressed iron and oxygen to 55 GPa and heated the sample to temperatures between 1800 K and 2300 K. After temperature quenching, pressure had increased to 58 GPa and we observed the formation of a cubic phase with lattice parameter  $a=4.386(4) \text{ \AA}$  (Fig. 3.7-3). Furthermore, the sample formed several single crystal domains, which allowed us to perform single-crystal XRD diffraction. For one of the domains we collected 257 reflections which were indexed with spacegroup Pa-3. Relying on this data we performed a structure solution and refinement from which we established the phase to be  $\text{FeO}_2$  with the HP-PdF<sub>2</sub> structure (shortest O-O distance  $\sim 2.1 \text{ \AA}$ ).

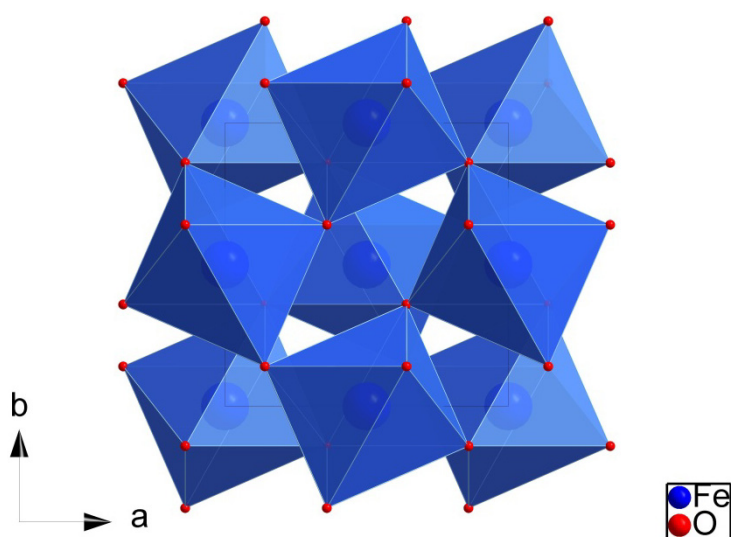


Fig. 3.7-3: Structure of cubic iron (IV) dioxide ( $\text{FeO}_2$ ) as determined by single crystal X-ray diffraction at 55 GPa.

**d.** Equation of state of TaC to 39 GPa and 1073 K (S. Speziale/Potsdam, J. Immoor, H.-P. Liermann/Hamburg, S. Merkel/Lille and H. Marquardt)

Tantalum carbide  $\text{TaC}_x$  ( $0.6 < x < 1$ ) is a B1-structured (space group  $Fm\bar{3}m$ ) ultra-high temperature ceramic (UHTC). UHTC materials have high potentials for technological applications because of their combined high mechanical strength and extreme thermal stability. Tantalum carbide has extremely high melting temperature, low electrical conductivity and unusual mechanical behaviour with respect to other B1-structured monocarbides of group IV and V transition metals. The elastic properties of TaC have been the subject of many experimental and computational studies exploring the effect of pressure or temperature and non-stoichiometry on the elastic properties of single crystals or polycrystals. While computations provide models for the isothermal compression behaviour of TaC, only two experimental studies investigate its compression behaviour to the multi-GPa stress range using the diamond anvil cell (DAC), but at ambient temperature.

In this project, we performed static compression experiments on TaC in a resistively heated DAC combined with *in situ* synchrotron X-ray diffraction at beamline P02.2, PETRA III, DESY. We performed measurements up to 38.8 GPa and up to 1073 K, and place quantitative constraints on its pressure-volume-temperature equation of state. While 300 K experiments were performed in axial scattering geometry, in the high-temperature experiments the axis of the diamond anvils is perpendicular to the incident X-ray beam, passing through an X-ray transparent sample chamber, made of a mixture of amorphous boron and epoxy. Pressure in the DAC is controlled remotely by a gas membrane system. Temperature is measured by two type-R thermocouples placed in contact with the diamond at short distance from the culets. The DAC is placed in a customized vacuum vessel to protect it from oxidation, and an Au chip was placed above the sample center as a position marker and pressure calibrant.

The unit cell volumes of TaC<sub>0.99</sub> measured in the experiments at 300 K performed in axial geometry were utilized to perform the fit of a third order Birch-Murnaghan equation of state. In the fit, we fixed the unit cell volume at zero pressure  $V_0$  to 88.478 Å<sup>3</sup>, based on previous measurements. The fit to our data (Fig. 3.7-4) yields  $K_{0T}=305\pm 5$  GPa and  $(\partial K_T/\partial P)_{T0}=6.1\pm 0.5$ , where  $K_{0T}$  is the initial bulk modulus and  $(\partial K_T/\partial P)_{T0}$  is its initial pressure derivative. The high-temperature dataset (Fig. 3.7-4) combined with the parameters of the ambient temperature isotherm were used to fit the thermal coefficients of a Birch-Murnaghan-Debye equation of state. In the fit we fixed the value of  $\theta_0$  to 570±10 K averaged between the available literature data, from which we obtained a initial value of the Grüneisen parameter of  $\gamma_0=1.2\pm 0.1$ .

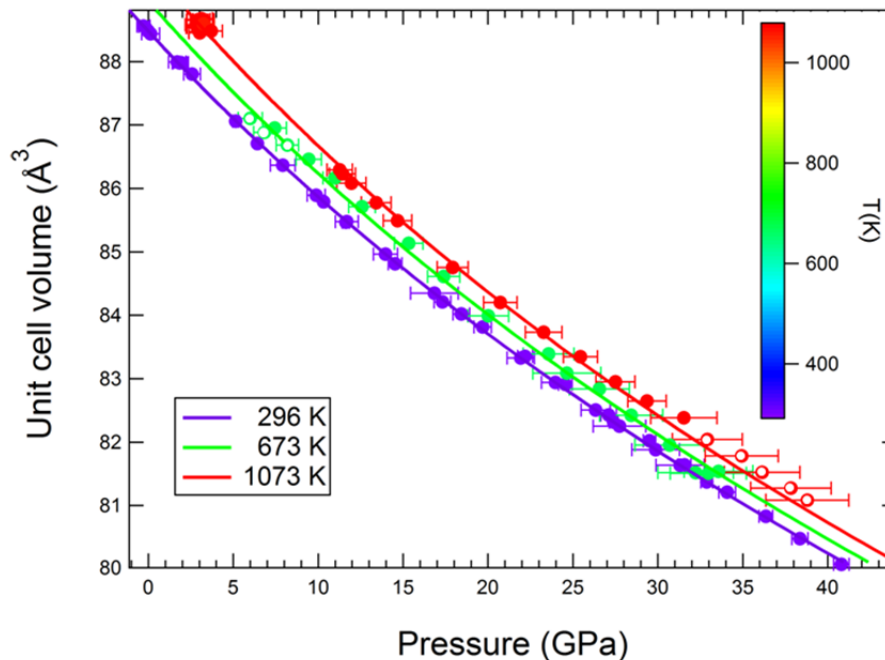


Fig. 3.7-4:  $P$ - $V$ - $T$  compression behaviour of TaC<sub>0.99</sub>. The curves present the best-fit model for  $P$ - $V$  isotherms at the temperatures of the datasets (296 K, 673 K, 1073 K). The five highest pressure points at 1073 K (open symbols) were not used for fitting.

e. *Inversion of conduction type of germanium under pressure (S.V. Ovsyannikov, in collaboration with N.V. Morozova and I.V. Korobeinikov/Yekaterinburg)*

The control of electrical conduction in semiconducting materials, including a possibility of switching between different conduction types ( $p$ -,  $n$ -), is important for various industrial applications. The germanium samples were characterized by an indirect band gap of about 0.65 eV and a minimal direct band gap of 0.8 eV (Fig. 3.7-5). Electrical conduction of germanium was measured by means of thermoelectric power (Seebeck coefficient), and we found that the  $n$ -type conduction of Ge converted to  $p$ -type under an applied pressure of a few GPa; upon decompression to ambient conditions it remained as such (Fig. 3.7-5).

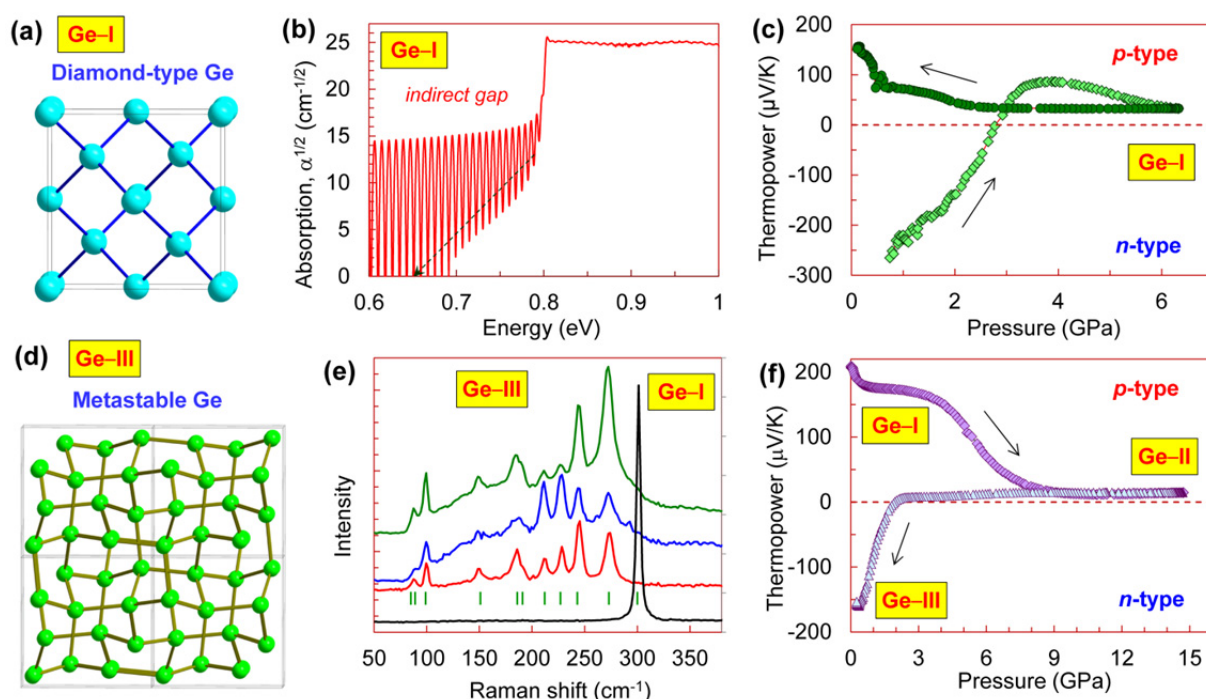


Fig. 3.7-5: Crystal structure of cubic-diamond-type Ge-I (a) and metastable tetragonal Ge-III (d) polymorphs of germanium. (b) Near infrared absorption of Ge-I showing its indirect band gap of ~ 0.65 eV and a direct one of ~ 0.8 eV. Pressure dependence of the thermopower for the Ge-I phase (c) and across the Ge-I → Ge-II → Ge-III transitions (f). (e) Comparative Raman spectra of Ge-I and Ge-III phases; the ticks show wave numbers of Raman peaks reported for Ge-III in the literature.

As established in earlier work, both the indirect and direct band gaps in the cubic-diamond-structured phase of germanium (Ge-I) weakly widen with pressure, and hence, this  $p$ - $n$  inversion is related to enhancement of the hole contribution. As known from the literature, the top of the valence band of germanium at the  $\Gamma$  point of the Brillouin zone consists of two overlapping hole bands of so-called "light" and "heavy" holes. The possibility of pressure-stimulated splitting of these two hole bands and a following charge transfer of hole carriers from the "heavy" hole band to the "light" one was already mentioned in the literature. The

mobility values of carriers of the "light" hole band should be essentially higher than those of carriers of the "heavy" hole band, and therefore, upon this charge transfer, the hole contribution to the electrical conduction should be significantly enhanced. The irreversibility of the shift to the *p*-type conduction under pressure release might be related to the conservation of residual strains.

Compression of the *p*-type samples of germanium above the semiconductor-metal (Ge-I → Ge-II) phase transition around 10 GPa, followed by a decompression to ambient pressure, led to a *p-n* conversion below 2 GPa (Fig. 3.7-5). It is known that decompression of the metal phase of Ge does not lead to a reversal of the Ge-II → Ge-I phase transition, but to the formation of a metastable polymorph. Thermopower measurements showed that this polymorph is semiconducting with *n*-type electrical conduction. The recovered samples were examined by Raman spectroscopy and X-ray diffraction. The Raman spectra collected from different points at its surface exhibited peaks at 88, 99, 149, 185, 191, 212, 228, 244, 273, and 300 cm<sup>-1</sup> (Fig. 3.7-5). Intensities of these Raman peaks vary strongly (Fig. 3.7-5), indicating that spectra are highly sensitive to the orientation of crystal grains. The Raman spectra agree well with those observed in previous work for a metastable polymorph of germanium, prepared either in diamond anvil cells, or by surface nanoindentation. In the literature, spectra were assigned to a simple tetragonal lattice with 12 atoms per unit cell, also known as Ge-III (*st12*, space group #96 – *P4<sub>3</sub>2<sub>1</sub>2*) (Fig. 3.7-5). X-ray diffraction confirmed the tetragonal structure and found unit cell parameters of  $a = 5.927(2) \text{ \AA}$ ,  $c = 6.969(6) \text{ \AA}$ ,  $V = 244.8(5) \text{ \AA}^3$ , and  $Z = 12$ .

The conversions in the conduction type of single-crystal Ge under pressure can inspire novel applications of this material. Among those, we can anticipate different micro- and nanoscale junctions with stress-controlled properties (*n-p* switches), embedded in various integrated circuits (Fig. 3.7-6). Potentially, one can "print" circuits and zones of different conduction

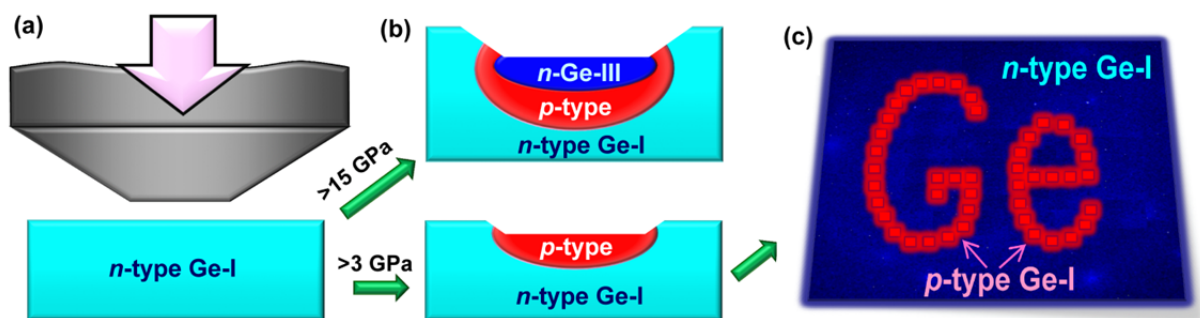


Fig. 3.7-6: (a) A schematic view of a hard tip for "printing" either *p*- or *n*-type zones on a surface of Ge-I. (b) Schematic side view of profile depths of "printed" zones, depending on applied stress. A stress distribution inside the material can lead to formation of multilayered structures with alteration of different conduction types (e.g., *n-p-n*). (c) A schematic top view of *p*-type zone "printed" on a surface of *n*-type germanium.

types on the surface of a Ge crystal. The simplest examples are: (i) "writing" of a thin  $p$ -type layer on a surface of  $n$ -type germanium, *i.e.*, *in situ* fabrication of  $p$ - $n$  diodes (Fig. 3.7-6), or (ii) "writing" of a thin  $n$ -type layer of the metastable Ge-III polymorph on a surface of conventional cubic-diamond-structured germanium. In the latter case, if the germanium wafer has  $n$ -type conduction, stress distribution in the material should lead to the fabrication of an additional intermediate  $p$ -type layer of the cubic-diamond-type germanium between the  $n$ -type germanium wafer and the  $n$ -type Ge-III surface layer, as shown in Fig. 3.7-6. Thus,  $n$ - $p$ - $n$  transistor transition in germanium may be fabricated by applying stress.

**f.** *Unusual phase transition in  $\text{CaCo}_3\text{V}_4\text{O}_{12}$  perovskite under high pressure (S.V. Ovsyannikov; E. Bykova and A. Pakhomova/Hamburg; D.P. Kozlenko/Dubna, M. Bykov, S.E. Kichanov/Dubna; N.V. Morozova and I.V. Korobeinikov/Yekaterinburg; F. Wilhelm and A. Rogalev/Grenoble; A.A. Tsirlin/Augsburg, A. Kurnosov; Y.G. Zainulin, N.I. Kadyrova and A.P. Tyutyunnik/Yekaterinburg and L.S. Dubrovinsky)*

Recently, a novel and unique perovskite material,  $\text{CaCo}_3\text{V}_4\text{O}_{12}$  with the  $\text{Co}^{2+}$  ions occupying the crystallographic sites with the square-planar oxygen coordination and simultaneously adopting the high-spin (HS) state, was synthesized as high quality single crystals (Fig. 3.7-7), and in the current work, we examined the evolution of its structural and vibrational properties up to 60 GPa. Near 30 GPa we found anomalous behaviour in the Co-O bond length in the square-planar oxygen planes, reflected by an abnormally high compressibility, which we relate to a pressure-driven extrusion of the large HS- $\text{Co}^{2+}$  ions from the oxygen planes (Fig. 3.7-7).

We investigated the high-pressure behaviour of  $\text{CaCo}_3\text{V}_4\text{O}_{12}$  at room temperature by means of single-crystal X-ray diffraction, establishing that the cubic crystal structure of this perovskite is preserved up to at least 55 GPa. We analyzed the pressure evolution of the oxidation states of all cations by means of the conventional bond valence sum method and found that they change weakly with pressure and essentially stay at values of  $\text{Ca}^{2+}$ ,  $\text{Co}^{2+}$ , and  $\text{V}^{4+}$ . The pressure evolution of the unit cell volume of  $\text{CaCo}_3\text{V}_4\text{O}_{12}$  did not exhibit any distinct discontinuities (Fig. 3.7-7), and by fitting the whole data set to a third-order Birch-Murnaghan equation of state we estimated the zero pressure bulk modulus value as of  $B_0 = 198.1(5)$  GPa and its pressure derivative as  $B'_0 = 3.9(1)$ . We have analyzed pressure evolution of the basic structural parameters of  $\text{CaCo}_3\text{V}_4\text{O}_{12}$ , which included the shortest cation-oxygen distances, atomic displacements, and others.

As found earlier, the  $\text{Co}^{2+}$  ions in the  $\text{CaCo}_3\text{V}_4\text{O}_{12}$  perovskite are in the HS state, and under compression the HS ions can turn either to the low-spin (LS) state or to an intermediate-spin (IS) state with a concurrent reduction in the ionic radius. Hence, one would expect that under strong compression the HS- $\text{Co}^{2+}$  ions in  $\text{CaCo}_3\text{V}_4\text{O}_{12}$  could undergo a transition to the LS state, which should be characterized by a smaller ionic radius. A HS $\rightarrow$ LS transition should be accompanied by noticeable volume collapse because of the sizable difference in the ionic radii

of HS-Co<sup>2+</sup> and LS-Co<sup>2+</sup> ions (88.5 pm vs. 79 pm for six-coordinated ions). Given the difference in ionic radii of HS-Co<sup>2+</sup> and LS-Co<sup>2+</sup>, one would anticipate about 1 % volume drop at the HS→LS transition. However, our data does not show a volume collapse (Fig. 3.7-7), but the abnormal enhancement in the compressibility of the Co-O bond above 30 GPa (Fig. 3.7-7) might potentially be related to a very sluggish pressure-driven HS→LS transition. However, other observations, *e.g.*, an abrupt enhancement of the anisotropic displacements of the Co<sup>2+</sup> ions above 30 GPa do not support this hypothesis.

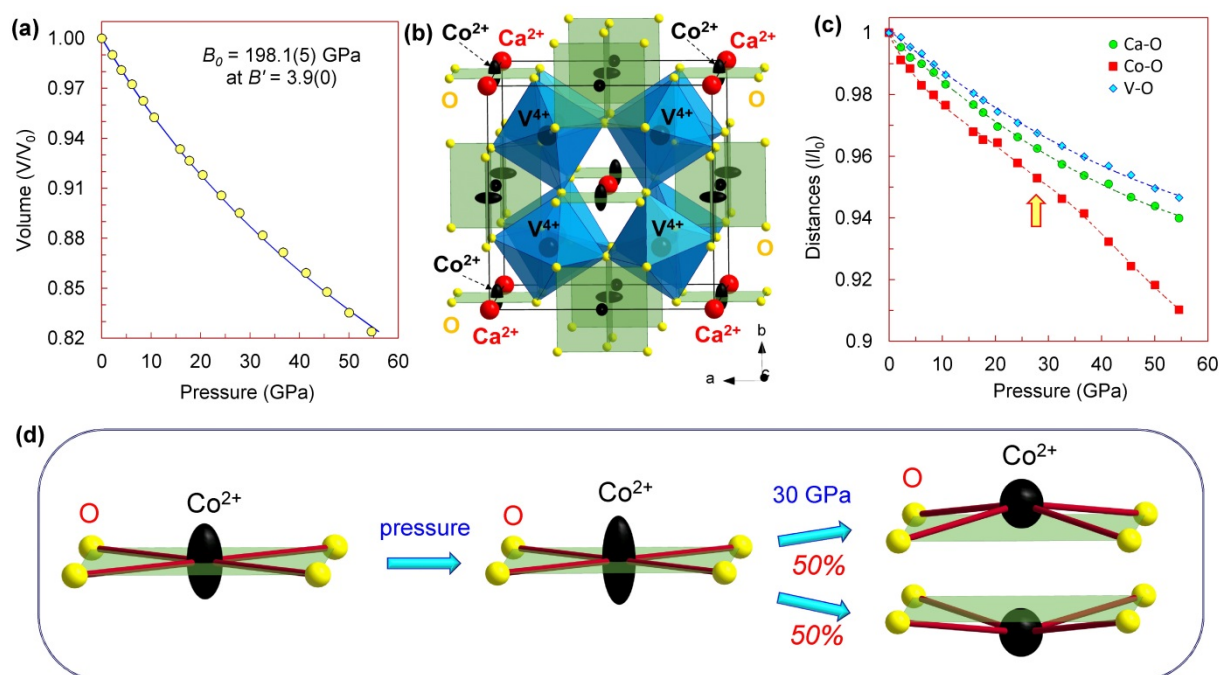


Fig. 3.7-7: Cubic crystal structure of CaCo<sub>3</sub>V<sub>4</sub>O<sub>12</sub> double perovskite (b) and pressure evolution of its volume (a) and of the shortest cation-oxygen distances (c). (d) A schematic representation of the pressure effect on the Co<sup>2+</sup> ions in the square-planar oxygen coordination. Applied pressure strongly compresses the large HS-Co<sup>2+</sup> ions initially, and above 30 GPa pushes them out of the planes.

Upon compression, the environment around the HS-Co<sup>2+</sup> ions becomes more densely packed, and, above a threshold pressure, cations are pushed out of the oxygen planes, but continue to vibrate near them. In CaCo<sub>3</sub>V<sub>4</sub>O<sub>12</sub> perovskite, the Co<sup>2+</sup> ions and oxygen atoms constituting the square-planar coordination are constrained by the symmetry to be coplanar. Thus, it seems plausible that above 30 GPa, the Co<sup>2+</sup> ions can occupy some unstable positions above and below the oxygen planes (Fig. 3.7-7). Hence, the anomalous compression of the Co-O bond length above 30 GPa (Fig. 3.7-7) may be explained by the fact that above 30 GPa, the "crystallographic" bond length, calculated for the Co (0, 1/2, 1/2) position located in the center of the oxygen planes starts to differ from the "true" Co-O bond length. The departure of the Co<sup>2+</sup> ions from the oxygen planes above 30 GPa leads to a strong contraction of the oxygen planes.

At ambient conditions, the non-polarized Raman spectra of  $\text{CaCo}_3\text{V}_4\text{O}_{12}$  crystals exhibit two rather broad peaks at  $396$  and  $475\text{ cm}^{-1}$  (Fig. 3.7-8) that shift to higher frequencies under pressure (Fig. 3.7-8). This behaviour is typically linked to pressure-driven contraction in the chemical bonds. Above  $10\text{ GPa}$ , we noticed the appearance of a new broad peak in the vicinity of  $550\text{ cm}^{-1}$ , with intensity increased upon further compression (Fig. 3.7-8). The first two peaks were assigned to the  $A_g$  modes linked to rotation-like vibrations of the  $\text{VO}_6$  octahedra, the third one we assign to the  $F_g$  mode linked to O–V–O antistretching. Above  $25\text{ GPa}$ , we noted a smooth crossover in the spectra, at which the pressure dependencies of the wave numbers exhibited noticeable changes in their slopes; for example, this is well seen for the  $475\text{ cm}^{-1}$  mode (Fig. 3.7-8). Above  $25\text{ GPa}$ , all the peaks demonstrate a progressive decrease in their intensity and a pronounced broadening (Fig. 3.7-8). This crossover corresponds to the structural modification observed by single crystal X-ray diffraction and may indicate structural destabilization. In visual examinations, we observed no changes in the color of the single-crystal of  $\text{CaCo}_3\text{V}_4\text{O}_{12}$  up to  $60\text{ GPa}$  (Fig. 3.7-8). This observation suggests that  $\text{CaCo}_3\text{V}_4\text{O}_{12}$  is not metallic up to  $60\text{ GPa}$ .

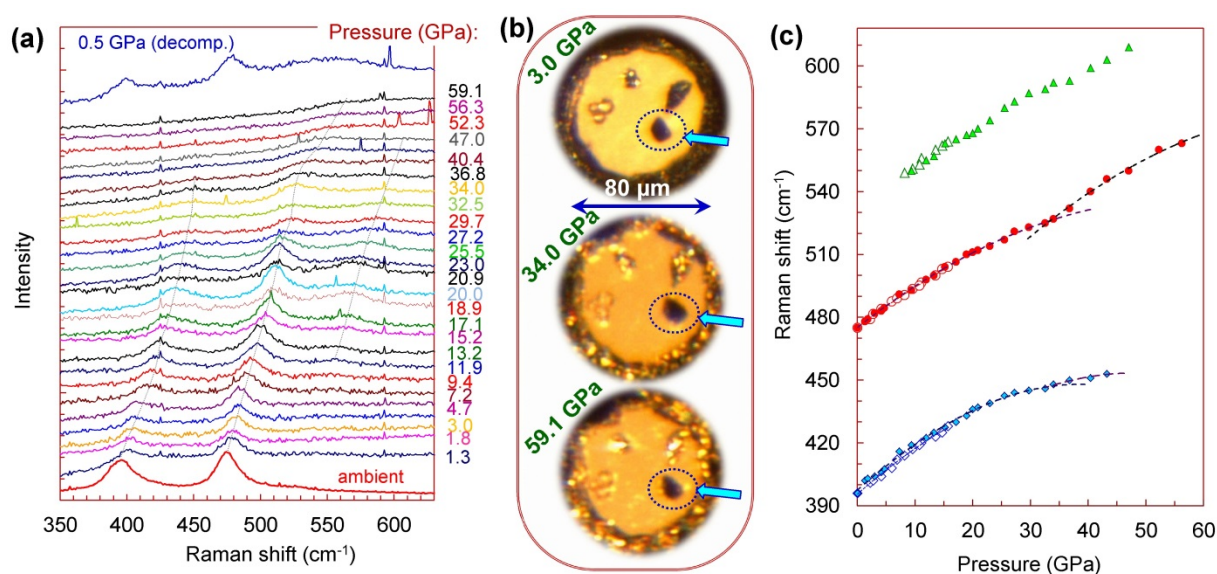


Fig. 3.7-8: Pressure evolution of (a) the Raman spectra and (c) wave numbers of single crystal of  $\text{CaCo}_3\text{V}_4\text{O}_{12}$  at  $295\text{ K}$  and (b) photographs inside a diamond anvil cell (sample pointed out by arrow).

**g.** *Phase relations and activity-composition relations in the system  $\text{ZnO-MgO-SiO}_2$  (N. Farmer/Acton, in collaboration with P. Condamine and D.J. Frost)*

$\text{Zn}^{2+}$  and  $\text{Mg}^{2+}$  are divalent cations of similar size, with distinctly dissimilar electronic configuration; as a result, the coordination of cations in Zn- and Mg-oxide and silicate phases at ambient pressure varies, with  $\text{Zn}^{2+}$  typically found in tetrahedral coordination, as in

phenakite-structured willemite ( $\text{Zn}_2\text{SiO}_4$ ) or wurtzite-structured zincite ( $\text{ZnO}$ ), while  $\text{Mg}^{2+}$  favors octahedral coordination as in olivine or rocksalt-structured periclase. Piston-cylinder experiments have established that the partitioning of Zn and Mg between coexisting willemite and forsterite solid solutions, which are separated by a miscibility gap over a wide compositional range, is strongly pressure dependent (Fig. 3.7-9).

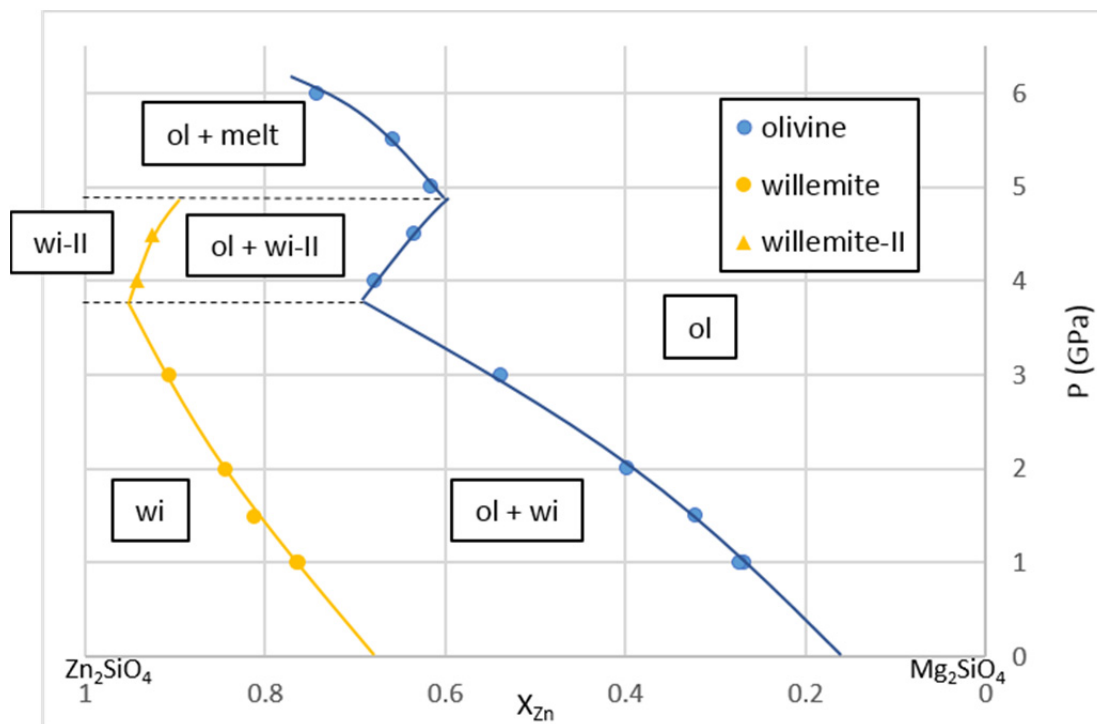


Fig. 3.7-9: Experimentally determined pressure-composition relations in the system  $\text{Mg}_2\text{SiO}_4\text{-Zn}_2\text{SiO}_4$  at 1100 °C. Dashed lines indicate approximate positions of phase transitions in willemite, the first is the transition of willemite to a high-pressure polymorph willemite-II, and the second represents melting of willemite-II. Solid lines indicate the trend in solubility limits.

This manifests itself as a shift in composition of each phase toward the Zn end-member with increasing pressure in the range 0-4 GPa. Because of this, and the insensitivity of these compositions and phase relations to capsule material, oxygen fugacity, small amounts of volatiles, or small changes in bulk composition, the olivine-willemite system is an ideal pressure standard for solid media experiments. The change of composition (expressed as  $X_{\text{Zn}}$ , molar  $\text{Zn}/[\text{Zn}+\text{Mg}]$ ) in olivine and willemite is  $\sim 0.5$  and  $\sim 0.3$  respectively from 0-4 GPa, which, combined with analytical precision better than 0.003 achievable by electron microprobe analysis (EMPA), allows pressure to be estimated with a precision of greater than 0.05 GPa. As the sample volumes required for EMPA analysis are miniscule, this can be easily run *in situ* in an auxiliary capsule as a pressure calibrant in piston-cylinder or multianvil experiments.

Multianvil experiments were conducted at BGI from 4.5-7 GPa, 800-1100 °C, using compositions on the  $Zn_2SiO_4$ - $Mg_2SiO_4$  binary, to extend the range of conditions for pressure-composition relations. The experiments revealed an unexpected reversal in the trend of  $X_{Zn}$  with pressure in the willemite-II and olivine stability fields (Fig. 3.7-9), with the immiscibility region shifting to lower  $X_{Zn}$ . In addition, the decline in the melting point of willemite with increasing pressure was steeper than expected, from ~ 1450 °C at 1 atm. pressure to below 1050 °C at 6 GPa. A disproportionation of the high-pressure willemite-II polymorph to  $ZnSiO_3$ -pyroxene and ZnO above ~ 5 GPa was also observed at 1000 °C in the experiments.

**h.** *Grain boundary diffusion and grain boundary segregation of multiple elements in Yttrium Aluminium Garnet (YAG) – experimentally determined using the bicrystal setup (J. Polednia, K. Marquardt and R. Dohmen/Bochum)*

Grain boundary (GB) diffusion and segregation are of fundamental interest as they significantly influence many processes in engineering or geologically relevant materials. GB diffusion and segregation govern element exchange reactions and chemical fractionation between non-touching grains, as elements are transported along grain boundaries. Thus, GB diffusion and segregation have an impact on geothermometry, geospeedometry, and geochronology. On the other hand, GB diffusion and segregation of elements influences applicability, purity, and life-time of engineering materials, such as laser ceramics.

Grain boundaries are frequently enriched in elements that have low solubility in the crystal lattice. This is caused by the less ordered structure of GBs, where typical atomic distances are larger than in the crystal lattice. This causes such elements to segregate to the GB and thus change their chemical composition compared to the interior of crystals or grains. Furthermore, segregated trace elements can change the GB structure by influencing atomic bonds and/or vacancy concentrations. Thus, physical and rheological material properties, such as cohesion, mobility, microhardness, and interface energy are affected by trace elements and cause variations in GB diffusion, sliding, fracture, migration and grain growth. In an aggregate, trace elements at GBs can influence polycrystalline (=bulk) material properties, such as creep behaviour of polycrystalline material.

Grain boundary diffusion of La, Fe, Mg, and Ti has been studied on a geometrically well-defined grain boundary in pure yttrium aluminium garnet (YAG) (Fig. 3.7-10). We studied the effect of ionic size and charge variation and how these elements influence their respective transport properties. We synthesized bicrystals using the wafer bonding method and used pulsed laser deposition to produce a  $La_{3.60}Al_{4.40}O_{12}$  thin-film, co-doped with these elements. The film is deposited perpendicular to the grain boundary to form the diffusion couple with the bicrystal. Diffusion experiments have been conducted at 1000 °C and 1450 °C.

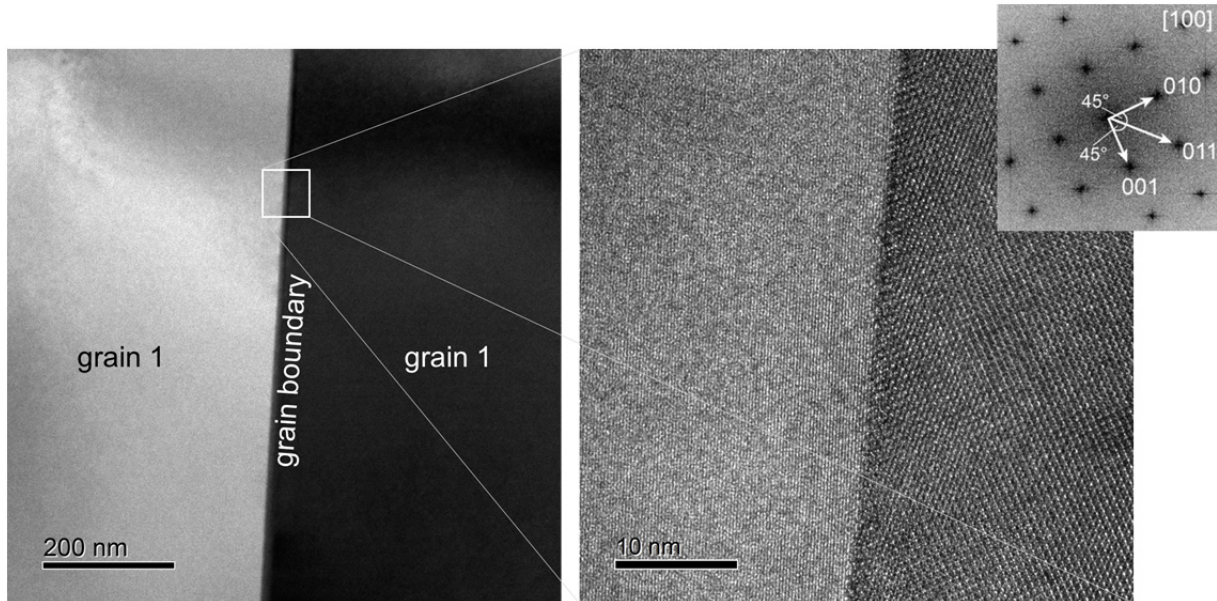


Fig. 3.7-10: Transmission Electron Microscopy (TEM) images of the YAG grain boundary. Left: bright field image, right: High resolution TEM image. The right grain is oriented along the [100] zone axis. The structural GB width is in the range of 1 nm.

The volume and grain boundary diffusion coefficients are determined by fitting a numerical diffusion model to experimental elemental maps obtained by transmission electron microscopy. The grain boundary diffusion coefficients of the elements are at least 8 orders of magnitude faster than volume diffusion, with a minimum diffusivity of  $9 \times 10^{-11} \text{ m}^2/\text{s}$  at 1450 °C. The product of the segregation factor times the effective GB width at 1450 °C is higher for La than for Fe and Mg. This difference is likely caused by the low solubility of La, compared to moderate solubility of Fe and Mg in YAG. Furthermore, La grain boundary diffusion is reduced in the presence of Ti. We conclude that elements of low solubility in the crystal lattice can diffuse highly efficiently along grain boundaries and that they can influence their mutual incorporation and thereby the material's properties.

### 3.8 Methodological Developments

An important goal in experimental studies relevant to Earth, planetary and material sciences is to develop new techniques as well as improving current ones. Such developments include the extension of the maximum achievable pressure-temperature ( $P$ - $T$ ) conditions of experiments, improvements in the control and characterisation of the sample environment in such high- $P$  experiments and new methods for analysing the chemical compositions of mineral and fluid phases that are produced experimentally. The eleven contributions in this section cover many of important aspects of such methodological developments.

The first nine contributions in this methodological section are concerned with laser-heated diamond anvil cell (DAC) experiments. The laser-heated DAC is the main experimental apparatus for studying materials at pressures greater than those achievable with the multianvil apparatus. It is used to perform experiments up to megabar pressures and temperatures up to around 5000 K and is the main experimental tool for understanding the Earth's deep mantle and metallic core as well as early processes of planetary differentiation. Due to the transparency of the diamond anvils a wide range of *in situ* measurements are possible on samples at high pressures and temperatures. The first contribution describes a new anvil design for the DAC that has a number of important advantages. In particular, the design greatly facilitates and improves *in situ* single-crystal X-ray diffraction experiments at high pressures. The second contribution describes developments of single crystal X-ray diffraction experiments up to unprecedentedly high pressures of more than 200 GPa. To achieve such high pressures, this study used a recently-developed double-stage DAC with an extremely small sample size of only 1  $\mu\text{m}$ . Mössbauer spectroscopy is a technique of major importance for characterizing the oxidation state and the structural, dynamic and magnetic properties of materials. This technique has now been developed to measure samples at simultaneous high pressures and temperatures in the laser-heated DAC using double-sided pulsed laser heating to achieve high temperatures in samples where continuous laser heating is not possible. This development will enable properties such as thermal conductivity under extreme conditions to be investigated in the future. Nuclear magnetic resonance (NMR) is a versatile major technique that has been used to characterize the atomic structures of materials (*e.g.*, silicate glasses previously quenched at high pressure) under ambient conditions. The fourth contribution below describes challenging developments that will enable *in situ* NMR measurements on samples at high pressure in diamond anvil cells to be made. This is followed by a description of the development of a portable CO<sub>2</sub> laser-heating system for the DAC. The use of CO<sub>2</sub> lasers for heating samples in DAC experiments has been limited in the past because of a range of technical difficulties but a major advantage is that optically-transparent samples can be heated to high temperatures. The success of the current developments is demonstrated by the measurement of sound wave velocities in single crystal MgO at temperatures up to 2300 K using Brillouin spectroscopy. The sixth contribution describes developments that enable changes in optical transparency of samples at high pressure to be measured, that result from pressure-induced structural changes. This is followed by a description of the use of metal capsules to contain samples in laser-heated DAC experiments.

This is challenging because of very small sample volumes but has advantages, especially for petrological experiments, such as avoiding chemical contamination and greatly reducing the normally-high thermal gradients across the sample. The final two laser-heated DAC contributions are concerned with the use of this apparatus to study the partitioning of elements between liquid silicate and metal in order to understand the geochemistry of planetary core formation. The first of these investigates the problems of analysing extremely-small, thin DAC samples with the electron microprobe and quantifies the errors and limitations using carefully prepared synthetic samples as well as theoretical modelling. The final DAC contribution describes the microstructure and chemistry of quenched liquid iron using atom probe tomography with nanometre scale resolution.

The final two contributions in this section describe methodological developments in the areas of spectroscopy and mineral solubility in fluids, respectively. First, the use of EELS and ELNES spectroscopy in the transmission electron microscope is further developed in order to study the oxidation state of iron in high-pressure mineral assemblages, relevant to Earth's lower mantle, that are synthesized in the multianvil apparatus. Finally a new single-crystal diamond trap method is described for investigating the compositions of trapped fluids that have been equilibrated chemically with minerals.

**a. Diamond anvils with a round table (DART-anvils) designed for high-pressure experiments in DAC** (L.S. Dubrovinsky, N.A. Dubrovinskaia/Bayreuth, E. Koemets, M. Bykov, G. Aprilis/Bayreuth; E. Bykova, A. Pakhomova and K. Glazyrin/Hamburg; V. Prakapenka and E. Greenberg/Argonne)

Most of the novel and quickly developing methods of *in situ* investigations of pressurised materials (single-crystal X-ray diffraction, inelastic X-ray scattering, Brillouin spectroscopy, etc.) require moving diamond anvil cells (DACs) with respect to the beam of electromagnetic radiation (*e.g.*, X-ray and laser), which is used for heating, exciting, or probing material properties at extreme pressure and variable temperature conditions. Conventional anvils have "flat plate" geometries, and rotation of a cell at any angle with respect to the stationary beam leads to strong refraction, as diamond displays a high refractive index ( $n = 2.425$  at 532 nm). This destroys the sample alignment with respect to the optical beam. Certain types of experiments involving DAC rotations cannot be performed while keeping lasers or optical components stationary. For example, immobile laser heating of a sample in a DAC with conventional (flat-table) anvils during single-crystal X-ray diffraction data collection is impossible, as the sample gets out of the focus of the laser beam upon cell rotation.

We propose a new design of diamond anvils, the Diamond Anvil with a Round Table (DART), which eliminates a number of problems associated with the use of conventional anvils in DACs. The major feature of the new DART-anvil design is a spherical shape of both the crown and table of a diamond with the centre of the culet located exactly in the centre of the sphere (Fig. 3.8-1).

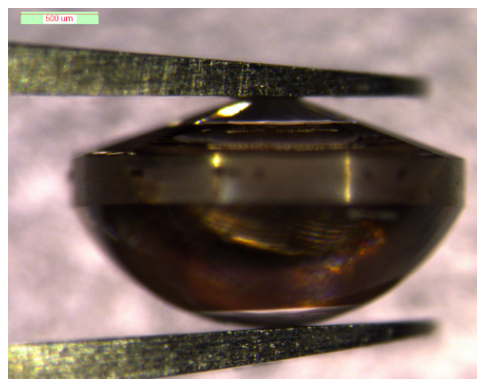
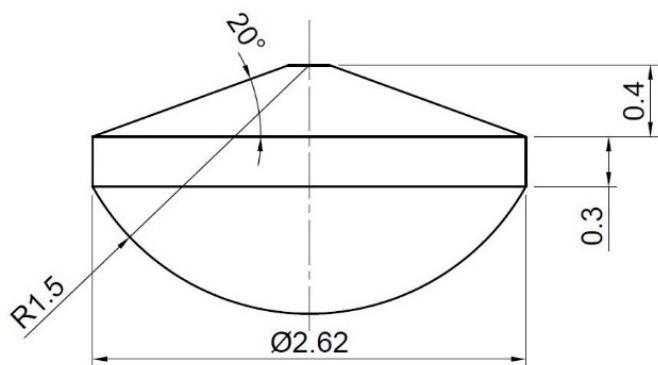


Fig. 3.8-1: A schematic (left) and a microscope image (right) of the DART-anvil (Diamond Anvil with a Round Table). (Dimensions may be scaled/adjusted in accordance with experimental needs.)

DART-anvils provide a number of advantages, which are unavailable with any of hitherto known types of anvils. First, they enable  $\sim 2.4$  times enlargement of the sample image in a DAC. They also enhance the physical resolution of the imaging, which is proportional to the numerical aperture,  $NA = n \sin(\omega)$ , of the observation channel being essentially increased due to high refractive index of the lens material (diamond). Imaging from the center of a spherical lens is also characterised by a remarkable feature from the point of view of aberrations; for the practically-used NA, the image is free not only from spherical aberrations but also coma and astigmatism in a zone around the surface centre. This drastically simplifies the alignment procedure and provides high quality imaging, even in case of misalignments or de-focusing. Diamond anvils of known design have two parallel optical surfaces and thus the object image observed through the anvils does not coincide with the object's physical position along the optical axis, while the DART is free of that problem. As a result, the optical and X-ray alignment of the DACs equipped with DART-anvils (*e.g.*, with respect to the goniometer axes) becomes much more simple and accurate; no refraction correction is needed once the sample is aligned to the optical focal point, thus simplifying the procedure of aligning to the X-ray focus.

**b.** *Single crystal X-ray diffraction experiments above 200 GPa (S. Khandarkhaeva, L.S. Dubrovinsky, N.A. Dubrovinskaia/Bayreuth; P. Sedmak and J. Wright/Grenoble)*

High-pressure, high-temperature studies are crucial for understanding the mineralogy, petrology, dynamics, and chemistry of materials inside the Earth, celestial bodies, and extrasolar planets. Solid-state matter under extreme conditions is able to not only undergo phase transitions but also exhibit unexpected chemical stoichiometry or reactions that are unknown under ambient conditions. *In situ* high-pressure single crystal X-ray diffraction studies in diamond anvil cells (DACs) enable phase analysis, structural characterisation, and compositional refinement of material under extreme conditions. At multi-megabar pressures, sample dimensions are typically about  $1 \mu\text{m}$ . To investigate physical and chemical properties

*in situ* under high pressures, powerful penetrating nano-sampling probes must be used to reach the samples through the wall of the pressure chamber and to separate the weak sample signal from the background signal of the massive surrounding materials.

We report here a diffraction experiment conducted at the nanoprobe beamline ID11 at the European Synchrotron Radiation Facility, Grenoble, France (Frelon4M detector, wavelength  $\lambda = 0.3099 \text{ \AA}$ , and spot size  $\sim 450 \times 450 \text{ nm}^2$  at FWHM). A double-stage (ds) Re-gasketed DAC was loaded with NiO powder and compressed to 420(10) GPa (Fig. 3.8-2a). A typical absorption profile through the inner part of the dsDAC is shown in Fig. 3.8-2b. After pulsed-laser heating at  $\sim 3000 \text{ K}$ , the pressure decreased to about 245(5) GPa. Pressure was estimated according to the equation of state of Re.

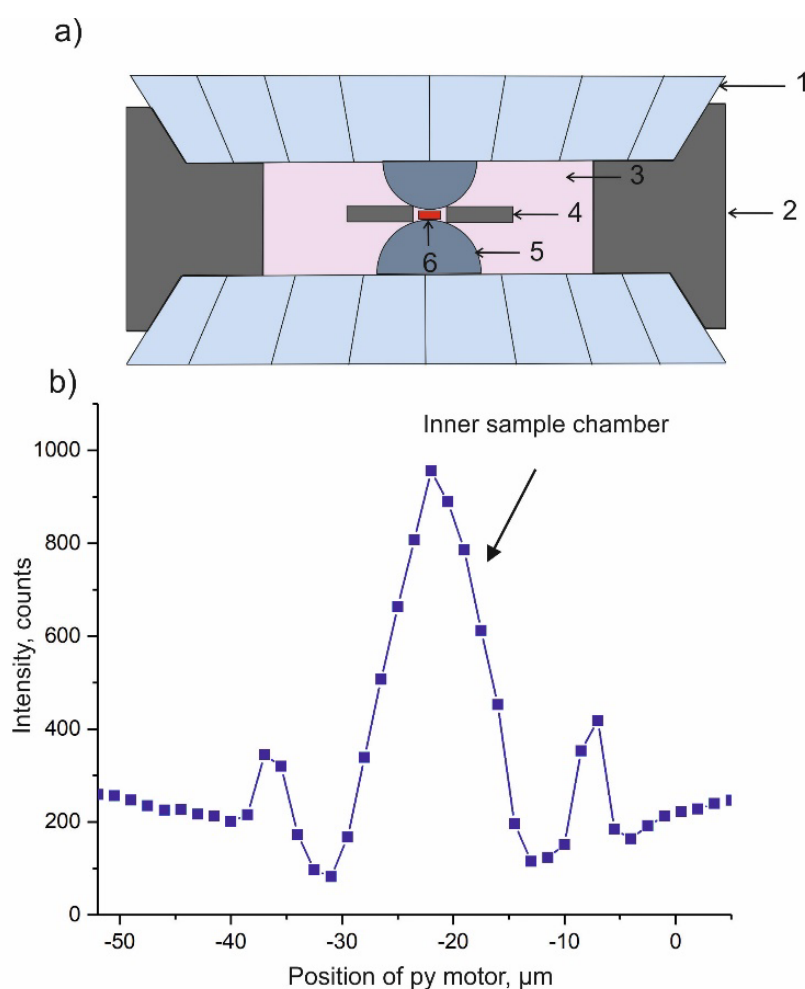


Fig. 3.8-2: Details of the experiment in a dsDAC. (a) A schematic of a dsDAC (1 – external (first stage) diamond anvil, 2 – indented external gasket, 3 – pressure medium, 4 – internal gasket, 5 – nano-diamond half-sphere (secondary anvil), 6 – sample). (b) Typical absorption profile recorded by the Pin-diode upon horizontal sample scanning.

Diffraction patterns were first collected by mapping a sample area of  $20\mu\text{m} \times 20\mu\text{m}$ , centred on the sample, with a step of  $0.5 \mu\text{m}$  and acquisition time of 20 s. As seen in Fig. 3.8-3, the diffraction images show spots characteristic for crystalline domains. The volume of the studied single-crystal domain was estimated, based on the maps, to be  $\sim 1 \mu\text{m}^3$ . Despite such a small sample size and very high pressure, we were able to collect a single-crystal data set in

step-scans when the DAC was rotated around the  $\omega$ -axis from  $-38^\circ$  to  $+38^\circ$  using an angular step of  $0.5^\circ$  and acquisition time of 10 s/step. The reflections were indexed and the single-crystal data analysis revealed the crystal structure of rhenium carbide  $\text{Re}_2\text{C}$ , (refined to  $R_1=6.6\%$ ), which likely formed as a result of a chemical reaction of carbon from the diamond anvil and Re of the internal gasket.

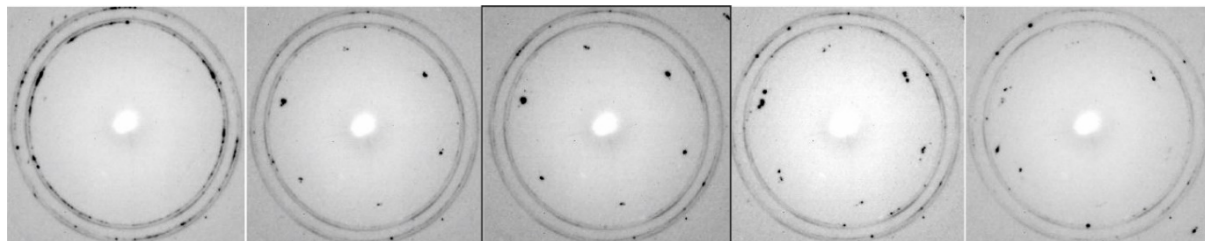


Fig. 3.8-3: Selected diffraction patterns taken in the course of mapping a sample area of  $20\mu\text{m} \times 20\mu\text{m}$  with a step of  $0.5\mu\text{m}$  and acquisition time of 20s. The patterns correspond to five points of the central array of the map; only a part of the patterns up to d-spacings of  $2\text{ \AA}$  is shown. The irradiated area at each point is about  $0.45\mu\text{m} \times 0.45\mu\text{m}$ , as enabled by the X-ray spot size. The linear size of the sample is about  $1\mu\text{m}$ : peaks in the middle pattern are relatively sharp and strong, but at a distance of  $1\mu\text{m}$  (second step from the middle), the intensities of the single-crystal spots decrease or disappear.

c. *Fully time resolved synchrotron Mössbauer spectroscopy for pulsed laser heating experiments in diamond anvil cells* (C. Strohm/Hamburg, G. Aprilis/Bayreuth, I. Kupenko/Münster and D. Vasiukov/Bayreuth; V. Cerantola, A.I. Chumakov and R. Rüffer/Grenoble; C.A. McCammon and L.S. Dubrovinsky)

Laser-heated diamond anvil cells provide an ideal sample environment to investigate Earth and planetary materials under relevant pressure and temperature conditions. Mössbauer spectroscopy is particularly suited for the study of structural, dynamic, and magnetic properties of geomaterials. The combination of both methods for *in situ* experiments became possible through synchrotron Mössbauer spectroscopy, which meets the requirement to approximately match optical and X-ray focal spot sizes. Recently, pulsed laser heating has made it possible to reach high temperatures in samples where prolonged continuous heating is not possible.

We have developed an event-based detection scheme to apply double-sided pulsed laser heating with synchrotron Mössbauer spectroscopy. After completion, the data can be explored and binned into the three dimensions of laser intensity, Mössbauer drive velocity and acquisition time.

The experiments were carried out using the Synchrotron Mössbauer Source (SMS) at the nuclear resonance beamline ID18 at the European Synchrotron Radiation Facility (ESRF). A data acquisition system based on a TDC (Time to Digital Converter), coupled with the SMS

set up, gives the possibility to acquire time-resolved Mössbauer absorption spectra correlated to the period of a laser pulse, with the aim of probing the state of the sample over a range of temperatures. Every incident  $\gamma$ -photon detected, is annotated with an energy and timestamp value, combining information from the Mössbauer Drive as well as the laser triggering. Time resolution is limited mainly by the necessary quality of statistics and could in principle be as short as the half-life of the Mössbauer effect transition, *i.e.*, on the order of 100 ns. At the same time, the thermal radiation is observed from both sides of the sample and the surface temperature is estimated with spectroradiometry. Using a fast-gated intensified CCD detector (iCCD), the temperature information is also time-resolved with respect to the laser pulse.

As a result, it is possible to "follow" the response of the heated sample on the microsecond scale through the variations in temperature and Mössbauer spectra. As seen in Fig. 3.8-4, the collapse of the magnetic field in a  $\text{Fe}_{25}\text{O}_{32}$  sample at 77 GPa can be observed when heating above its critical temperature. Owing to the extreme sensitivity of Mössbauer spectroscopy to even tiny Doppler velocities, we were able to reveal minute displacements of the sample during the heating cycle that are most likely to be attributed to thermal expansion of the sample inside the pressure chamber of the diamond anvil cell (Fig. 3.8-5). Critical temperatures of magnetically ordered geomaterials, thermal conductivity and thermal expansion coefficients of iron bearing compounds under high pressure are some of the important properties that can be investigated in the future.

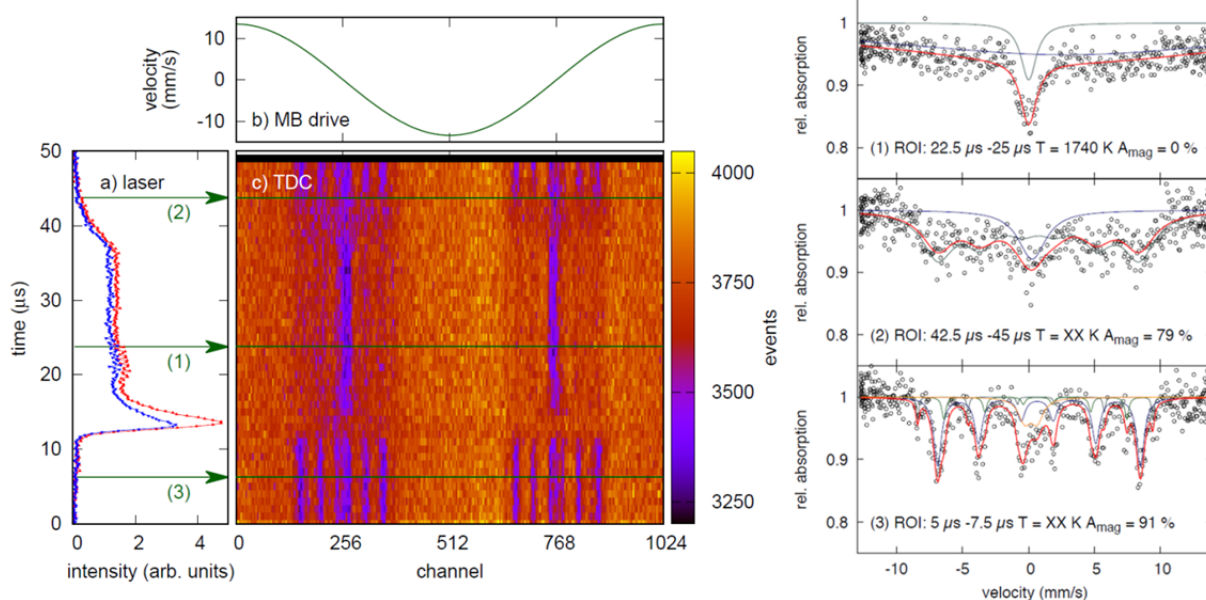


Fig. 3.8-4: Double-sided heating of a  $\text{Fe}_{25}\text{O}_{32}$  sample in Ar pressurised at 77 GPa. Left: (a) Laser intensities, (b) the Mössbauer drive velocity and (c) raw Mössbauer spectra over the laser pulse period. Right: Characteristic spectra, corresponding to the green lines on the left, from different time windows along the heating cycle. The collapse of magnetism is evident during heating;  $A_{\text{mag}}$  is the ratio of the magnetic over the non-magnetic component.

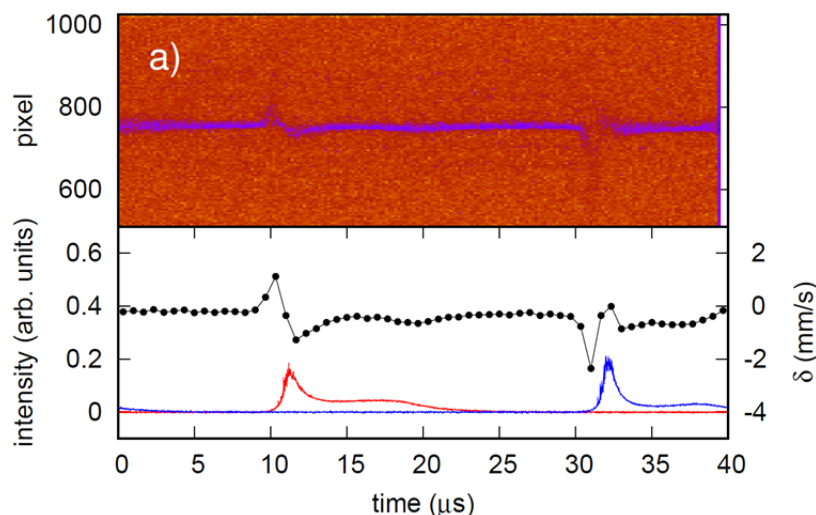


Fig. 3.8-5: Laser-heated Fe in Ar at 36 GPa using asynchronous laser pulses. Top: Color-coded Mössbauer spectra of the sample. Bottom: Blue and red are the laser intensities from each heating side, and black is the Mössbauer absorption central shift as a function of time. The reverse direction of the central shift, depending on the heating side, is evidence of the iron sample's velocity inside the argon environment, induced by heating.

**d.** *Development of novel techniques for high-pressure NMR in diamond anvil cells (T. Meier, S. Petitgirard and L.S. Dubrovinsky)*

Nuclear magnetic resonance (NMR) experiments in a diamond anvil cell operating at pressures close to a megabar are considered one of the most challenging projects for this very versatile and wide-spread spectroscopic method. In recent decades, even application at pressures close to 5 GPa was thought to be impossible due to inherently low sensitivities of the magnetically polarised nuclear spins, and the problem of placing a radio-frequency (r.f.) antenna close enough to the sample in order to pick up to the very small NMR signal of the precessing nuclear spins.

Over the course of the last year, we have been able to implement so-called Lenz lenses as an r.f. transmitter and receiver in a diamond anvil cell (Fig. 3.8-6). This set-up was found to allow for significantly increased sensitivities by several orders of magnitude compared with former approaches, while operating at pressures up to 72 GPa. Figure 3.8-7 summarises and compares NMR sensitivities for all known high-pressure set-ups and Fig. 3.8-8 shows the first test measurements used for sensitivity estimations.

Two-dimensional nutation experiments on long chained alkanes,  $C_nH_{2n+2}$  ( $n=16-24$ ), as well as homonuclear correlation spectroscopy on thymine,  $C_5H_6N_2O_2$ , were employed to demonstrate the feasibility of this approach for higher dimensional NMR experiments, with a spectral resolution of at least 2 ppm. This approach opens up the field of ultra-high pressure sciences for one of the most versatile spectroscopic methods available in a pressure range that has been previously unprecedented.

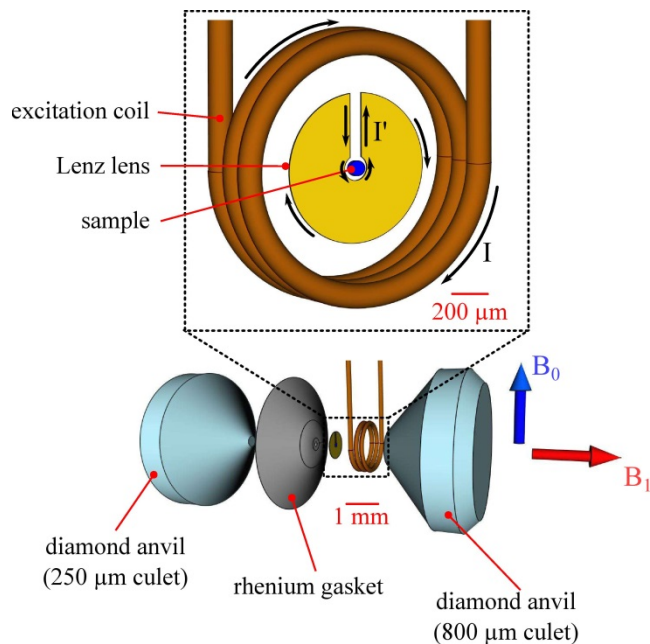


Fig. 3.8-6: Schematic explosion diagram of the resonator set-up and anvil/gasket arrangement.

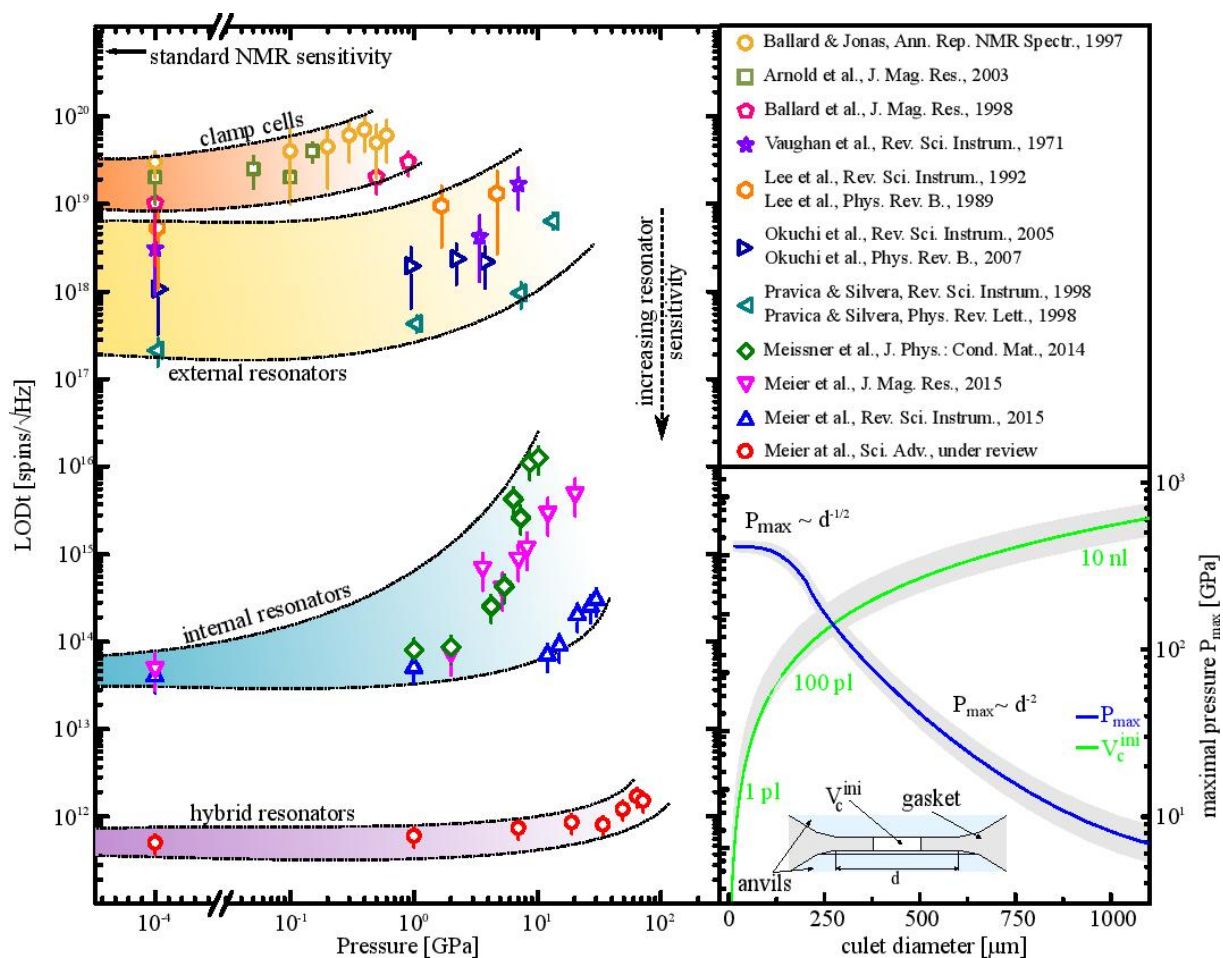


Fig. 3.8-7: Comparison of NMR sensitivities of several high-pressure NMR set-ups.

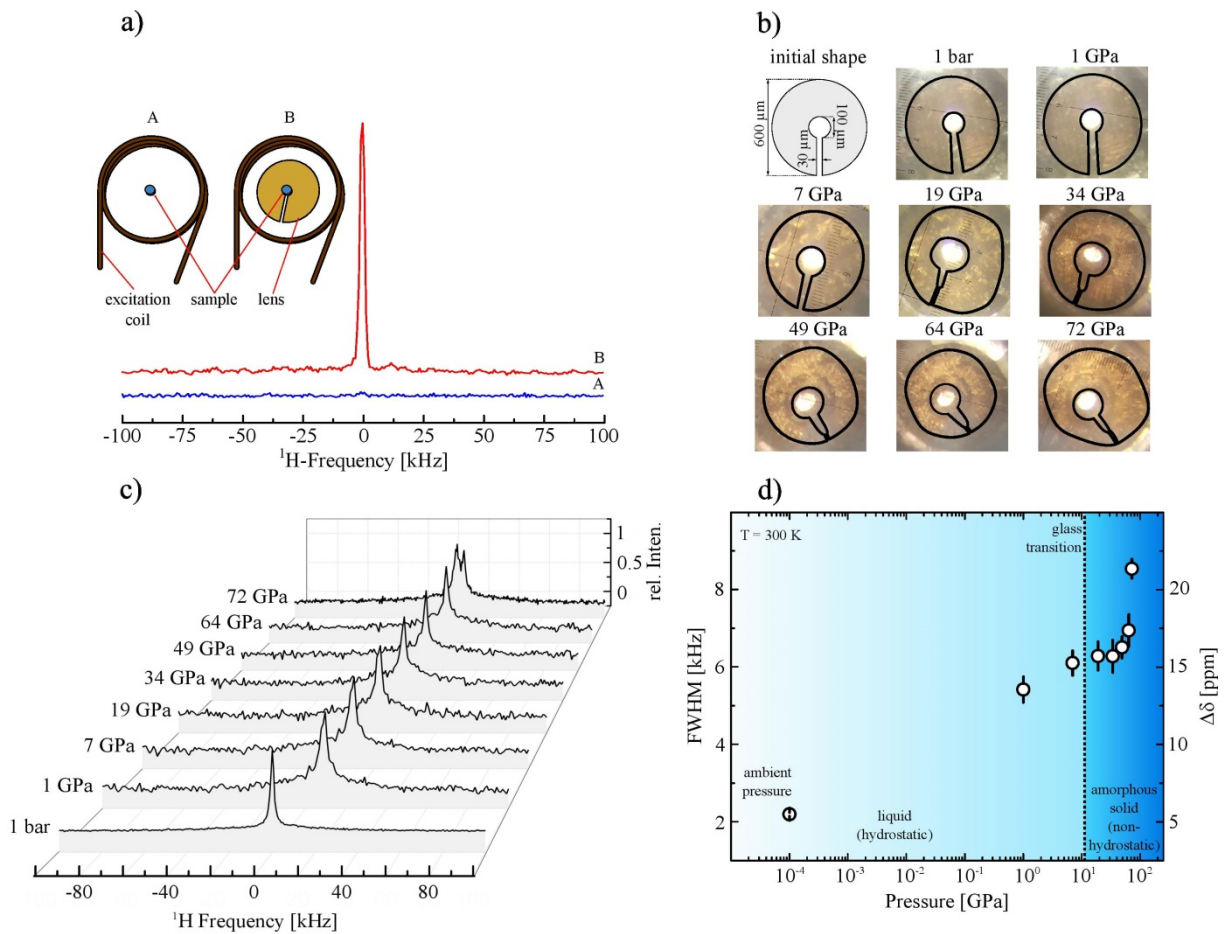


Fig. 3.8-8: a) Proton spectra of paraffin at ambient pressure with and without the use of a Lenz lens. b) Photographs of different deformation states of the lens under pressure. c) Recorded  $^1\text{H}$  NMR spectra. d) Pressure dependence of the FWHM line widths.

**e. Development and calibration of a waveguide-based flexible  $\text{CO}_2$  laser heating system: High-temperature Brillouin spectroscopy measurement of single crystal MgO (A. Kurnosov, H. Marquardt and L.S. Dubrovinsky)**

The laser-heated diamond anvil cell (DAC) allows the complete range of P/T-conditions of Earth's mantle to be simulated. Over the last few years, the increasing availability of compact high-power fiber lasers emitting radiation with a wavelength of about  $1\ \mu\text{m}$  has triggered the development of portable systems based on typically-used near infrared lasers of 1064-nm wavelength. However, many (mantle) minerals are optically transparent and only weakly absorb laser radiation of this wavelength. In addition, inhomogeneous distribution of iron (clustering), that is mostly causing laser absorption, may lead to substantial spatial variations in sample temperature. These limitations can be overcome by using  $\text{CO}_2$  laser heating with a significantly longer ( $10.6\ \mu\text{m}$ ) wavelength. The obvious advantages of using  $\text{CO}_2$  lasers are associated with significant technical challenges, such as the necessity of using special materials for all optical elements (lenses, mirrors, laser guides, etc.), dealing with different optical properties, which makes the use of visible light for optical alignment impossible, and

the danger of reflecting invisible high power radiation by operating a non-encapsulated laser beam. For these reasons, only limited publications employing CO<sub>2</sub> laser heating in a DAC have appeared in the literature until present. The recent availability of 10- $\mu$ m wavelength transmitting waveguides opens the possibility to design flexible CO<sub>2</sub> laser heating systems that can be conveniently used in combination with a variety of experimental samples. The portable laser-heating setup drastically simplifies the application of laser heating to DACs and opens the perspective for new types of experiments, including single-crystal X-ray diffraction (XRD) and Brillouin spectroscopy in the laser-heated DAC.

Here we present results of Brillouin scattering measurements of a laser-heated single crystal of MgO at ambient pressure (Fig. 3.8-9) using a fan-cooled CO<sub>2</sub> laser coupled to a commercially available Hollow Silica Core Waveguide and cage system that contains ZnSe optics to focus the laser radiation onto the sample. The system was installed on the combined Brillouin/XRD system at BGI, and the temperature during heating was measured through the Brillouin collecting optics. Due to extremely low emissivity (in the visible range) of optically transparent samples (especially well polished single crystals), we were able to perform Brillouin scattering to temperatures of about 2300(200) K. On the other hand, due to low thermal emissivity, we were only able to estimate the sample temperature above 1900 K. Lower temperatures in this test were estimated by interpolation of temperatures between 300 K and 2300 K assuming that they are proportional to the output laser power. The collection of Brillouin spectra at temperatures higher than 2300 K was no longer possible because the intensity of the thermal emission rapidly increases, which makes Brillouin peaks indistinguishable from the thermal background (Fig. 3.8-10).

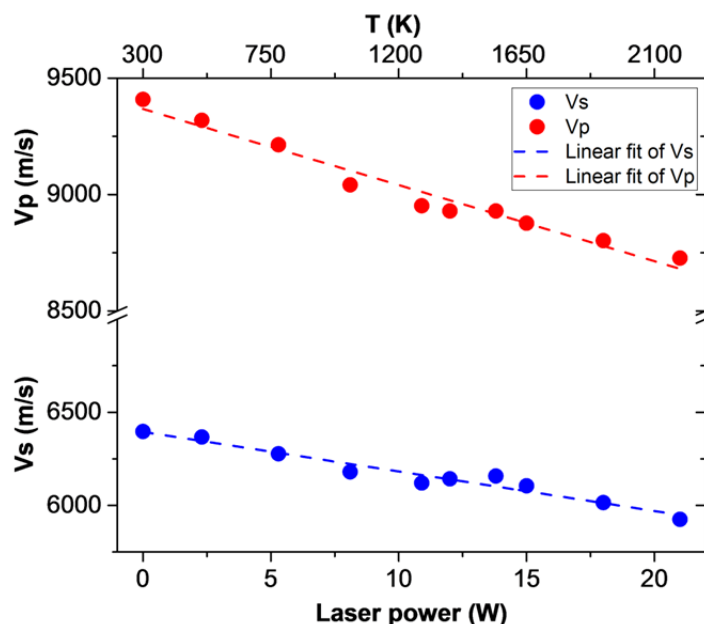


Fig. 3.8-9: Sound wave velocities measured from single crystal MgO as a function of laser power/temperature. Red: compressional wave velocities; blue: shear wave velocities.

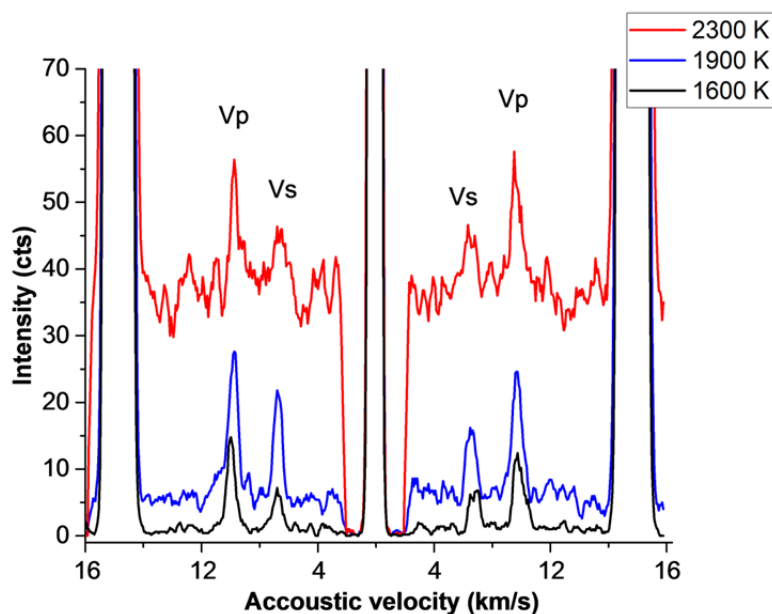


Fig. 3.8-10: Brillouin spectra of single crystal MgO with CO<sub>2</sub> laser heating at 1600 K (black), 1900 K (blue) and 2300 K (red).

**f.** *A portable system for the measurement of optical losses of visible light in DACs (T. Fedotenko/Bayreuth, S. Khandarkhaeva, E. Koemets, N.A. Dubrovinskaia/Bayreuth and L.S. Dubrovinsky)*

It is well known that pressure can cause significant changes in the optical transparency of matter. Changes in oxygen transparency are a striking example of such a phenomenon. During compression, initially transparent oxygen experiences a phase transition at 6 GPa and becomes solid. Subsequent compression to 54 GPa does not lead to a further phase transition although the transparency of oxygen, related to the change of its electronic properties, decreases significantly (Fig. 3.8-11). The transparency of hydrogen was recently reported to slowly decrease above 335 GPa, and that hydrogen becomes metallic at 495 GPa. As X-ray diffraction does not allow for detection of structural changes in such light elements, optical observations remain the only reliable analytical tool.

In order to study the optical properties of materials at ultra-high pressure, we designed and built a portable system, as shown schematically in Fig. 3.8-12. The image of the sample placed into a Re gasket is provided due to the propagation of light through the sample chamber. The beam of light goes through a zoom objective and is then split into two by a beam splitter. One beam goes to a CCD camera for observations and the other beam through an optical fiber to the spectrometer (Ocean Optics QE65000) for transmitted light intensity measurement. We focus illumination light using Nikon CFI Plan Apochromat DM Lambda 40XC objective to increase the flux of light going through the sample chamber. As a zoom lens, we are using a 50x Mitutoyo Plan Apo SL Infinity Corrected Objective with correction of chromatic aberration for red, blue, and yellow colours, which minimises the distortion in

measuring visible spectra. With a 10- $\mu\text{m}$  hole in the Re gasket, we obtain an image size at the focus plane of about 300  $\mu\text{m}$ , which is projected onto the entrance of an optical fibre with a core diameter of 400  $\mu\text{m}$ . The image can be seen in reflected light using the second beam splitter with an illumination front light source.

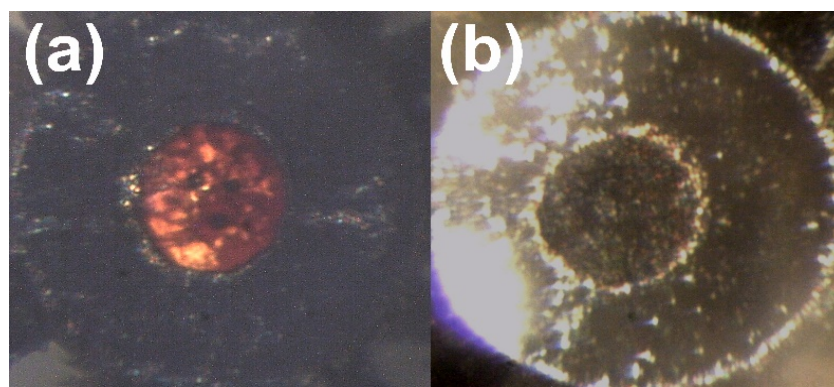


Fig. 3.8-11: Transparency of oxygen in a DAC at (a) 22 GPa and (b) 54 GPa, both at ambient temperature.

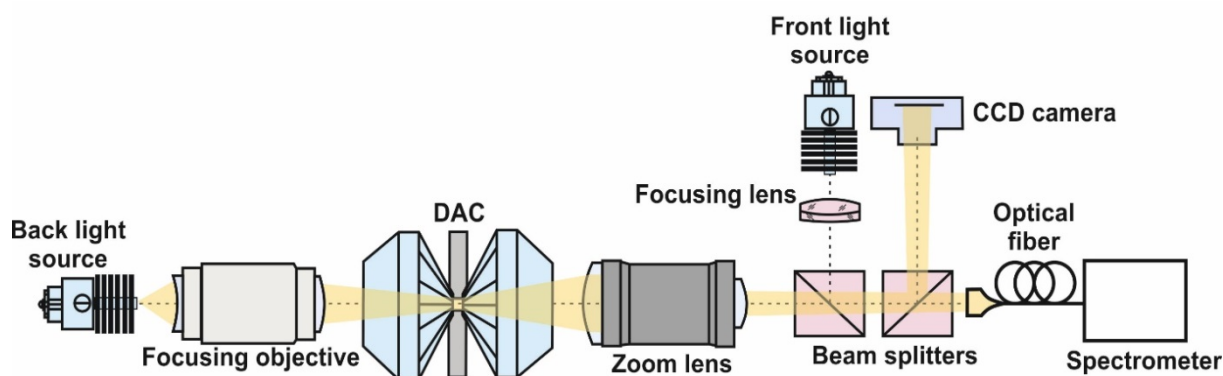


Fig. 3.8-12: Schematic illustration of the designed system.

**g.** *LH-DAC experiments with metal-encapsulated samples: Preliminary results and numerical modelling (M.A. Baron/Paris, O.T. Lord/Bristol, M.J. Walter/Bristol, M. Thielmann, N. Miyajima; S. Petitgirard and R.G. Trønnes/Oslo)*

In order to overcome significant temperature gradients in conventional laser-heated diamond anvil cell (LH-DAC) experiments and therefore be able to perform more equilibrated experiments at well-defined P-T conditions relevant for studying planetary interiors, we have developed an innovative experimental setup with metal-encapsulated samples. Here we present a brief summary of the encapsulated sample preparation, preliminary experimental results, in addition to numerical simulations of the temperature distribution in the new experimental setup.

The primary advantage of metal-encapsulation is the dual function of the metal-capsule, which acts as a micro-heater (YAG laser absorber) and provides a mechanical barrier between the sample and pressure medium. The setup results in uniform and stable heating and prevents chemical contamination. We have conducted LH-DAC experiments using metal-encapsulated samples up to 80 GPa and 4000 K in order to determine the subsolidus and melting phase relations of a natural basalt (BIR-1) and basaltic analogue composition in the  $\text{MgSiO}_3\text{-SiO}_2$  (MS) system.

Micro-manufacturing of the encapsulated samples involves several steps including metal filament preparation, laser-drilling of various parts of the filament, resistive heating, melting of the starting material and further laser-fabrication. The resulting glassy silicate samples are held in an annulus of molybdenum metal of 7-10  $\mu\text{m}$  thickness and 30-80  $\mu\text{m}$  diameter, with a centrally located sample chamber of  $\sim 10\text{-}15$   $\mu\text{m}$  in diameter. The samples and the surrounding Mo ring are almost completely released from the filaments by laser cutting before being coated on both sides with a  $\sim 3\text{-}4$   $\mu\text{m}$  layer of molybdenum using a magnetron sputtering system. For the LH-DAC experiments, the capsules are loaded between two layers of an insulating pressure medium ( $\sim 15$   $\mu\text{m}$  thick) and pressurised in a DAC using ruby fluorescence measurements. Figure 3.8-13 shows the details of the experimental assembly. High temperatures are achieved by double-sided laser-heating with spot sizes of  $\sim 10\text{-}20$   $\mu\text{m}$ , somewhat larger than the sample diameter. A limited number of recovered samples were subsequently selected and prepared for further transmission electron microscopy (TEM) analyses using a focused ion beam (FIB) system at BGI. An example of the encapsulated silicate sample cut by FIB is shown in Fig. 3.8-13c.

Experiments held under subsolidus conditions for an extended period of time (15-60 min) were homogeneous in composition and contained the phases expected in basaltic lithologies, *i.e.*, bridgmanite, Ca-perovskite, stishovite and a calcium-ferrite structured Al-rich phase. The model basaltic MS composition resulted in a bridgmanite-stishovite assemblage. TEM imaging indicated that short experiments at higher temperatures, at which melting is expected, did not produce any quenched melt pockets. We therefore performed numerical modelling of the temperature regime in the new LH-DAC assembly in order to understand the thermal distribution and potentially find ways to improve it.

The numerical models of the temperature distribution inside the LH-DAC assembly indicate that the temperature gradients inside the encapsulated samples might have been substantial (up to 700 K at 40 GPa, Fig. 3.8-14a). In order to find ways to improve the pressure cell, we performed a parametric study of the numerical model in which we tested the importance of different capsule dimensions using various laser setups. A reduction of the encapsulated sample thickness and most importantly a reduction of the Mo-capsule and sample radius (Fig. 3.8-14b), combined with a 'doughnut shaped' laser beam (Fig. 3.8-14c), can decrease the temperature gradient significantly. Thus, further development of the metal-encapsulated setup has great potential to achieve more isothermal LH-DAC experiments. Ongoing experimental work is underway.

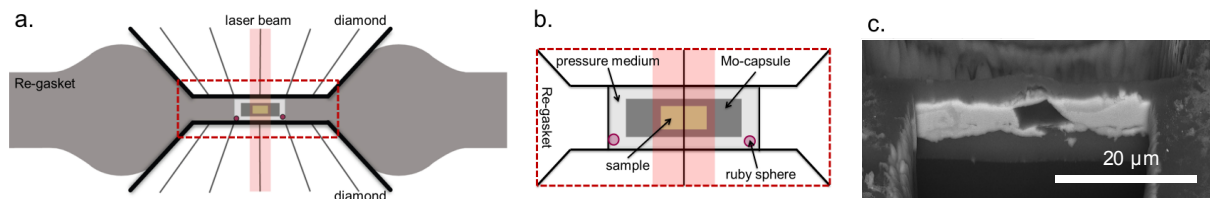


Fig. 3.8-13: (a) Schematic cross-section of the experimental setup with an encapsulated sample loaded together with a few ruby spheres for pressure estimation and surrounded by KCl pressure medium inside the pre-indented Re-gasket. (b) Magnified view of the experimental configuration of the loaded encapsulated sample and laser heating area (red shading) (c) Backscattered electron image of the recovered silicate sample fully encapsulated in the Mo-container surrounded by KCl pressure medium after being pressurised to 45 GPa and heated to 2500K. The sample was cut from both sides using a FIB system and subsequently prepared for TEM observations at BGI.

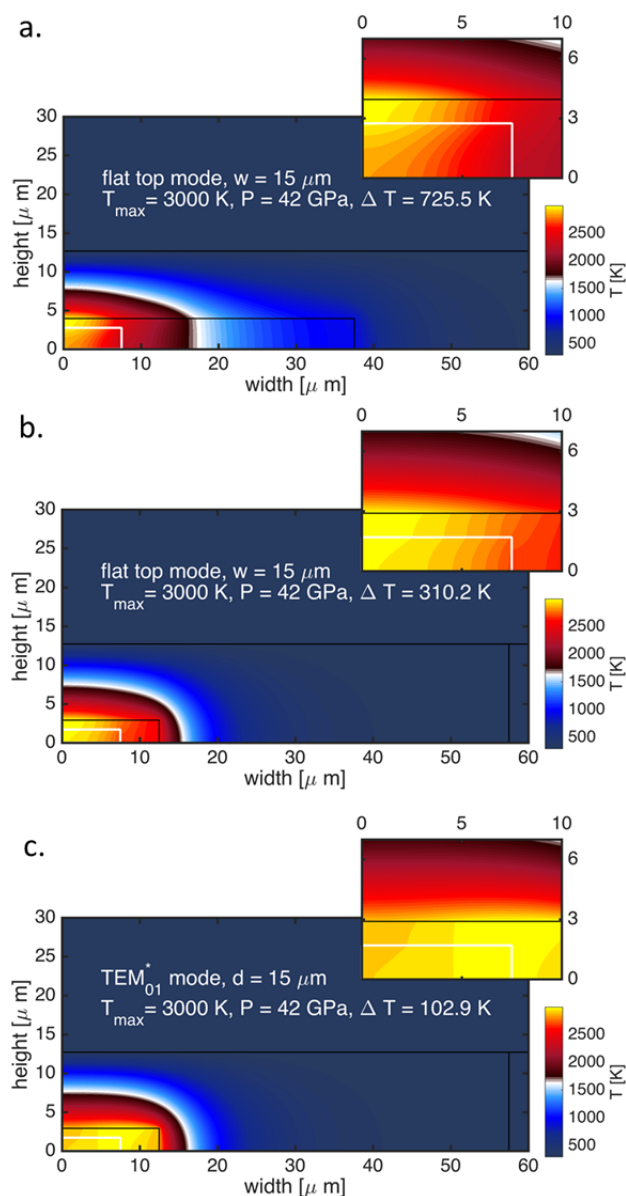


Fig. 3.8-14: Numerically computed temperature distribution in the upper right-hand quadrant of the LH-DAC assembly at 42 GPa and 3000 K with (a) 'flat top' laser distribution and primary capsule dimensions, (b) 'flat top' laser distribution and smaller capsule size, and (c) 'doughnut-shape' laser distribution and smaller capsule size. Black lines illustrate the diamond culet (upper line) and Mo capsule surface, respectively. Samples are outlined in white. The upper right-hand insets show magnified views of the samples with their immediate surroundings.

**h.** *Diamond anvil cell partitioning experiments for core formation studies: Testing the limitations of electron microprobe analysis (E.S. Jennings, V. Laurenz, J. Wade/Oxford, S. Petitgirard and D.C. Rubie)*

Core formation occurred during planetary accretion as a result of metal segregation from one or more magma oceans. Metal-silicate equilibration may have occurred at significant pressures and temperatures at the base of magma oceans, and in order to understand the distribution of elements between the core and mantle without extrapolating from lower pressure experiments, partitioning experiments are now commonly being performed at very high  $P$ - $T$  conditions in a laser-heated diamond anvil cell (DAC).

Samples from DAC partitioning experiments are commonly prepared as thick lamellae by FIB and analysed by electron probe (EPMA). DAC experimental sample volumes are orders of magnitude smaller than those from even the highest pressure multianvil experiments. The cut samples are necessarily thin (1-4  $\mu\text{m}$ ) and quenched silicate glass tends to form a rim around an immiscible metal blob that may be no thicker than 5  $\mu\text{m}$  (typical sample dimensions are illustrated in Fig. 3.8-15) and may contain entrained and quenched metal. Such thin materials with measurement spots so close to phase boundaries do not allow routine EPMA measurements: special consideration must be given to potential analytical artefacts that can usually be ignored. Although the primary interaction volume of a 15-kV focussed electron beam is around 1  $\mu\text{m}$ , fluoresced secondary X-rays can be generated from distances of > 20  $\mu\text{m}$ . A significant overestimate can result when measuring trace element concentrations close to an interface with a material in which that element is more abundant. This is particularly problematic when measuring siderophile element concentrations in the silicate phase of DAC partitioning experiments, where the metal (the major siderophile host) is in close proximity.

We have performed measurements and simulations on synthetic samples in order to quantify the limitations of EPMA analyses of DAC experiments, and to provide guidelines of what can and cannot be measured without significant analytical artefacts. Measurements were performed at 15 kV using the BGI JEOL JXA 8200 EPMA on interfaces and wedge-shaped samples prepared by FIB. Monte Carlo simulations were performed using the PENEPMA software, which uses the PENELOPE algorithm to calculate particle transport and secondary particle generation in irradiated materials, and predictions of X-ray spectra from realistic EPMA and sample geometries were generated. CalcZAF was used to convert relative intensities to compositions.

Our results indicate that X-ray intensities started to noticeably drop off in basaltic glass that was thinner than  $\sim 2 \mu\text{m}$  (Fig. 3.8-15), whereas the intensity in the metal phase was not significantly affected until the thickness was less than 500 nm (not shown). However, metal totals tended to reach only 99 % even in much thicker samples due to the loss of deep fluoresced secondary X-rays from iron when calibrated using thick standards. A greater thickness of basaltic glass is required for analysis relative to metal because the lower density and average atomic number of the glass means that it stops electrons less efficiently, and has a larger excitation volume and secondary fluoresced signal.

Secondary fluorescence from the silicate when measuring the metal was found to be below typical microprobe uncertainty, *i.e.*, negligible (not shown), although this may not be true of energy lines higher than Si  $K\alpha_1$ . However, fluorescence from the adjacent metal phase in measurements and simulations of pure forsterite was significant, which implies that trace siderophile elements in glass would be overestimated. We can define a partition coefficient ( $D = X_{\text{metal}}/X_{\text{silicate}}$ ) "detection limit": this is the maximum siderophility (*i.e.*, the maximum  $\log D$ ) that is detectable by EPMA in a DAC experiment (Fig. 3.8-15). For many elements, around 0.5 % of the metal concentration will be measured in the silicate within around 4  $\mu\text{m}$  of the interface. High-energy X-ray line measurements suffer the worst fluorescence, which explains why Fe, Cr, Co, Ni ( $K\alpha_1$ ) and W ( $L\alpha_1$ ) fluoresce to much larger extent than the low-energy Mo ( $L\alpha_1$ ) line (Fig. 3.8-15). If appropriate, fluorescence problems can be mitigated to some extent by choosing low energy X-ray lines.

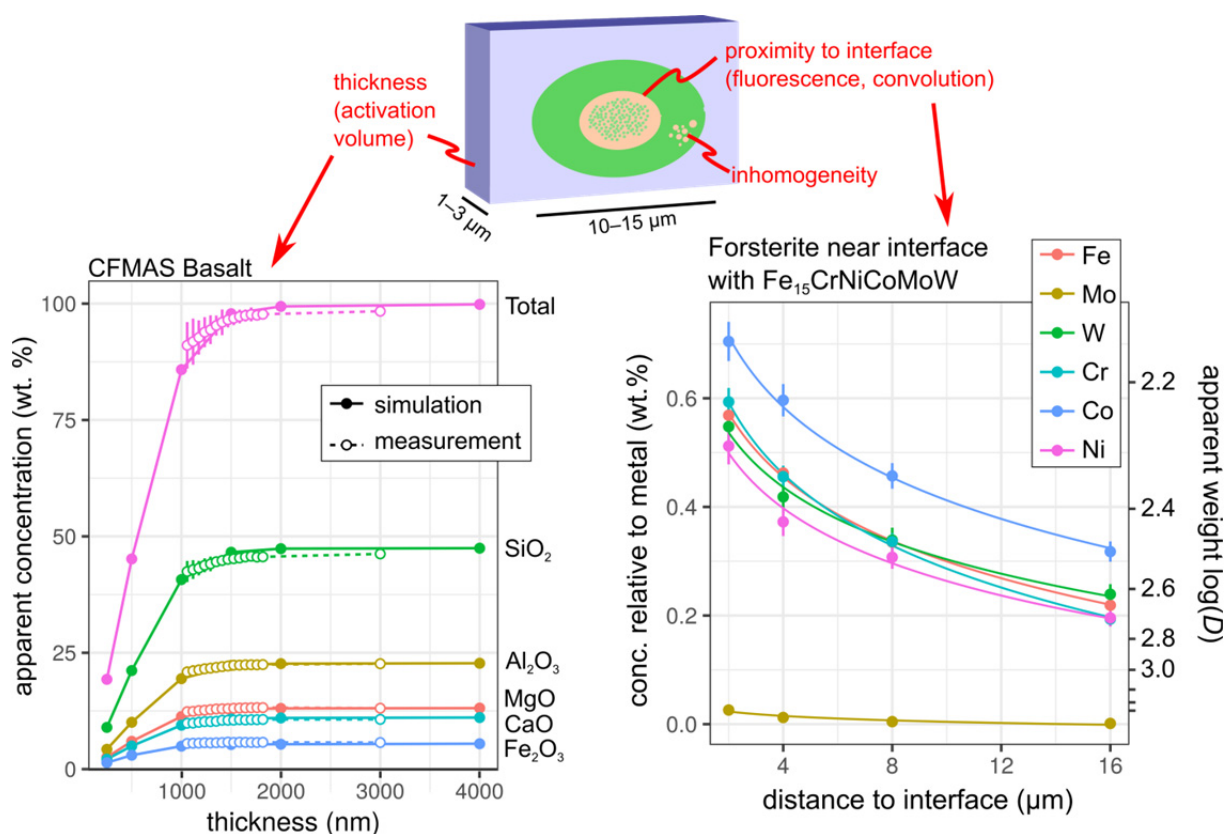


Fig. 3.8-15: Top: Typical dimensions of samples from DAC experiments prepared for EPMA analysis, highlighting some potential analytical difficulties. Orange: metal; green: silicate; purple: unreacted starting material. Left: Simulated and measured compositions of a wedge of basaltic glass, plotted as a function of glass thickness. Right: Apparent concentrations of various siderophile elements in simulations of forsterite close to a metal ( $\text{Fe}_{15}\text{CrNiCoMoW}$ ) interface. Concentrations are shown as a percentage of the actual metal concentrations, plotted as a function of distance from the interface. The apparent  $\log D$  is shown on the right.

We summarise by noting that consistent results were obtained when simulations and measurements were used to study the same synthetic sample, which suggests that PENEPMA simulation is an appropriate and useful tool for checking the validity of microprobe measurements. In most published studies, samples are cut to at least 2  $\mu\text{m}$  thick, so thickness will not cause a significant loss of signal. Fluorescence of lithophile elements in metal analyses is not a problem, although fluorescence of siderophile elements in silicate analyses may present a major problem when there is a strong concentration difference. This may have resulted in underestimates of the partition coefficient  $D$  in literature data, making some elements appear more lithophile at extreme  $P$ - $T$  conditions.

*i. An Atom Probe Tomography (ATP) investigation of exsolution textures in quenched metal from DAC partitioning experiments (E.S. Jennings, J. Wade and J. Douglas/Oxford and D.C. Rubie)*

In order to understand the distribution of various elements between the core and mantle at realistic deep magma ocean conditions, liquid-liquid metal-silicate partitioning experiments are increasingly being performed at a minute scale in diamond anvil cells (DAC). The product is always a quenched metal ball suspended in a silicate glass (Fig. 3.8-16), and each phase is measured by EPMA or TEM. In detail, the metal phase always contains tiny spheres ( $\sim 100$  nm diameter) of material with a lower atomic number than the iron matrix. These presumably oxide spheres are problematic, as they interfere with the EPMA measurement of the metal by violating the assumptions of the  $\Phi(\rho z)$  correction, resulting in consistently low totals in the measurements. The different elements will not necessarily retain their correct relative proportions when the element total is low. Determining the compositions of these nm-sized spheres should help to determine the validity of EPMA measurements, and allow the data to be corrected. In addition, understanding the composition of the balls and matrix and the nature of the interface between them can guide our interpretation of their origin: if they quenched on exsolution, they should be considered soluble in iron during the experiment, whereas if they formed through some other mechanism, they should be considered not as a part of the iron, but as another phase. This has significant implications for the applicability of partition coefficients obtained from such experiments.

We prepared the metallic portion of the sample from a DAC partitioning experiment as fine needles with  $< 40$  nm tips by FIB at BGI, and analysed two of these needles by atom probe tomography (APT) at the University of Oxford. APT is the only technique that can provide 3-dimensional compositional information at the tiny spatial scales required. Fig. 3.8-16 provides images of the experimental sample and the ATP needles and data; Fig. 3.8-17 shows a proxigram of compositions across the matrix-inclusion boundary. The spheres are almost pure  $\text{SiO}_2$ , the matrix is iron with 10 at. % C (despite the experiments being nominally carbon-free), and a rim region exists at the interface that is enriched in C, Mg, Al, and other trace impurities. Interpretation is in progress.

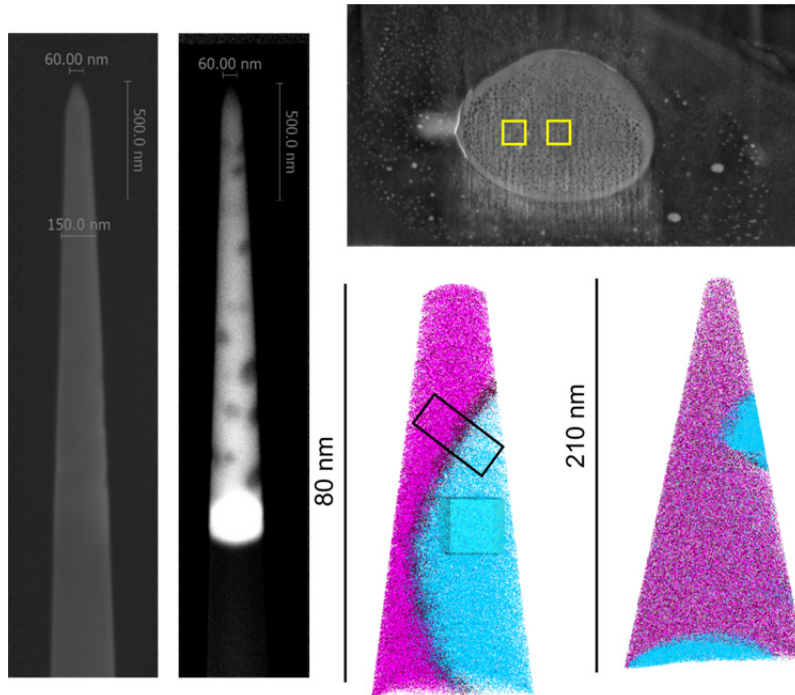


Fig. 3.8-16: Top right: Experimental DAC partitioning sample from which two needles are cut (field of view 15  $\mu\text{m}$ ; yellow boxes show needle locations). Two images at left: SE and BSE images of a finished needle that was prepared by FIB (oxide spheres and Pt weld visible on BSE image). Lower right: results of APT measurements showing locations of iron (pink), carbon (maroon) and oxygen (light blue) atoms in the two needles. The black rectangle shows the location of a cylindrical volume that was integrated across to produce the results shown in Fig. 3.8-17.

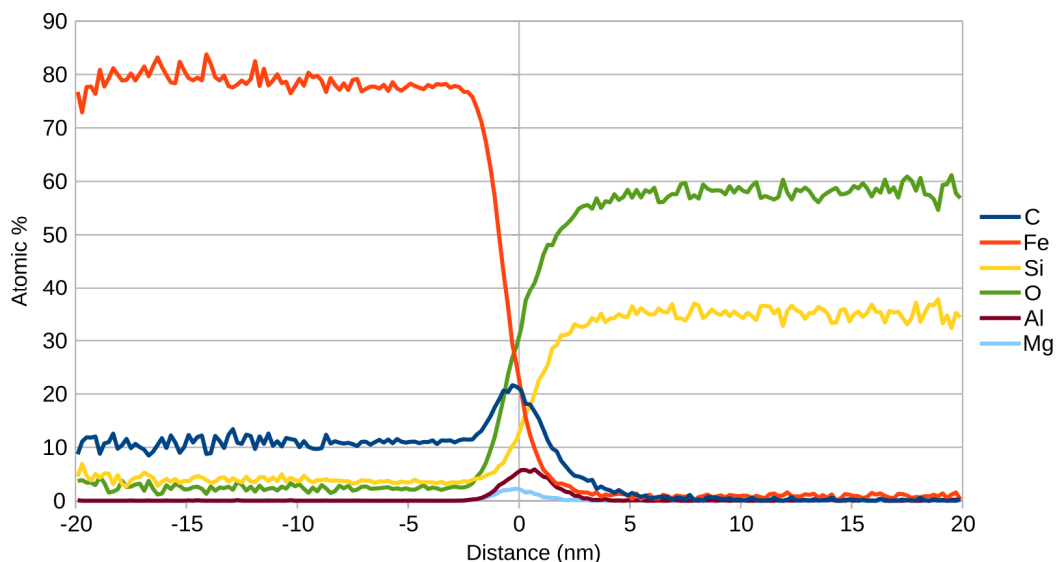


Fig. 3.8-17: Proxigram of compositions, where distances are from an isosurface of Si concentration. On the left is the iron matrix, containing 10 atomic % C. On the right is near-stoichiometric  $\text{SiO}_2$ , representing the spheres. The rim region (around distance = 0) is enriched in C and trace elements.

**j.** *Quantitative determination of iron oxidation states in minerals using Fe  $L_{2,3}$ -edge electron energy-loss near-edge structure spectroscopy: A geochemical application of EELS revisited (N. Miyajima, R. Huang, F. Sorbadere/Issoire, T. Boffa Ballaran, C.A. McCammon and D.J. Frost)*

Ferric iron in bridgmanite has been under the spotlight since reasonable probes, such as Mössbauer spectroscopy, X-ray absorption spectroscopy, and electron energy loss spectroscopy (EELS), have been acquired for its evaluation. The crystal chemistry of bridgmanite can be largely controlled by the behaviour of trivalent cations of aluminium and ferric iron in the  $ABO_3$  orthorhombic perovskite structure. The nature of the charge balance determines the influence on physical and chemical properties of bridgmanite. Fe- $L_{2,3}$  edge ELNES is a powerful tool to determine ferric / ferrous iron ratios in iron-bearing minerals coexisting at the submicron scale. The pioneering studies of Fe- $L_{2,3}$  edge ELNES were performed mainly using dedicated scanning transmission electron microscopy (STEM) and conventional transmission electron microscopy (TEM) with a parallel EELS system. In the previous system, a core-loss spectrum and corresponding low-loss spectrum from the same area are acquired at separate times on a single array photodiode detector (1-dimensional detector). On the contrary, in our new system they can be acquired simultaneously with independent exposure times onto different domains of a 2-dimensional CCD detector. This incurs a negligible increase in the exposure time per spectrum. The new system can provide new capabilities such as better precision in energy scale of the Fe- $L_{2,3}$  edge ELNES. In this work we revisit a quantitative determination of iron oxidation states in minerals by using a new EELS system with a dual spectra mode, "DualEELS".

We first performed Fe- $L_{2,3}$  edge ELNES on an orthopyroxene containing ferric iron (0.06  $Fe^{3+}/\Sigma Fe$  in 2 at. % Fe) in STEM-EELS mode (Fig. 3.8-18). The energy resolution of averaged zero-loss peaks is 0.71(1) eV at full width at half maximum (FWHM) in the total measuring time of 50-150 sec. The measured energy values of the Fe- $L_{2,3}$  edge peaks are fit to those of high-spin six-coordinated iron in the literature. The differences are within the value of selected energy dispersion, 0.05 eV per channel. The ferric iron content from EELS is 0.09(3)  $Fe^{3+}/\Sigma Fe$ , which was evaluated from intensity ratios of Gaussian peaks fitted to the  $L_3$  peak [van Aken and Liebscher, 2002, PCM, 29: 188].

Currently, we are measuring Fe- $L_{2,3}$  edge ELNES of high-pressure mineral assemblages recovered from multianvil experiments under the Earth's lower mantle conditions. A typical example of TEM-EELS analysis of coexisting ferropericlase (17 at. % Fe) and bridgmanite (1.8 at. % Fe) synthesized under reduced conditions is shown in Fig. 3.8-19. The bright field TEM image displays the existence of submicrometer-sized grains of metallic iron in the vicinity of the crystalline bridgmanite phase, which implies the charge disproportionation reaction:  $3Fe^{2+} = 2Fe^{3+} + Fe^0$ . The Fe- $L_{2,3}$  edge ELNES of ferropericlase demonstrates almost no ferric iron based on the energy value of  $L_3$  peak maximum and intensity ratio of the Gaussian fitted peaks. On the other hand, the bridgmanite is likely to contain some amounts of ferric iron, based on the existence of a small right shoulder in the  $L_3$  peak. This is consistent with the existence of submicrometer-sized metallic iron grains. In conclusion, we can determine a dominant valence state of iron in Fe-bearing minerals containing less than 2

at. % Fe, based on the absolute energy value of the peak maximum of Fe  $L_{3}$ -edge peaks (at around 708 eV for ferrous iron) in the new EELS system. Quantitative EELS evaluation of ferric / ferrous iron ratios in high-pressure minerals, such as bridgmanite, is a challenging task and requires careful sample preparation and control of irradiation damages with microscope conditions.

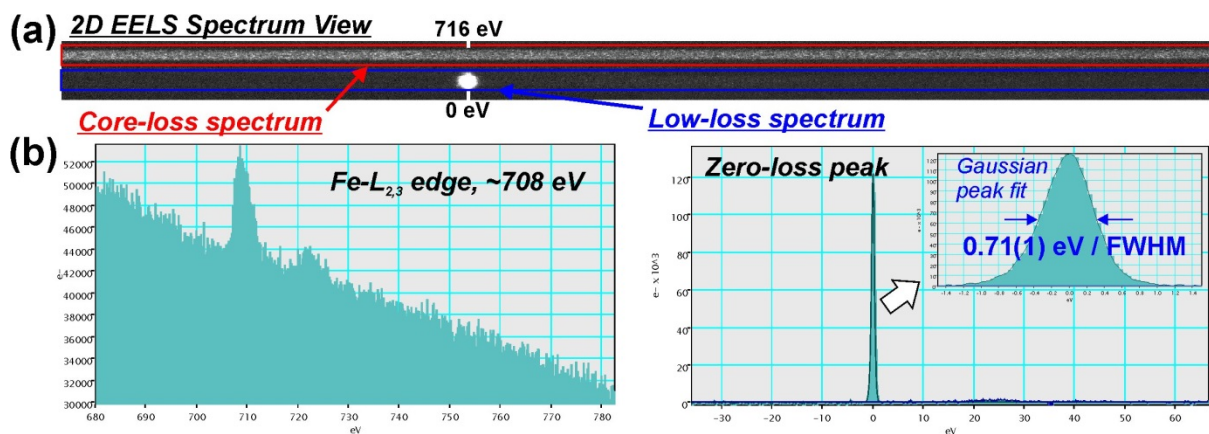


Fig. 3.8-18: Typical low-loss and core-loss spectra of an orthopyroxene as projected on opposite sides of the CCD camera in the DualEELS mode of operation. (a) The upper half of the CCD containing the core loss data is shifted to the amplifiers on the top of the CCD while the lower half of the CCD containing the low-loss data is shifted to the amplifiers on the bottom of the CCD, preventing the two spectra from interacting during read-out. The short lines on the left of the CCD (2D EELS Spectrum View) indicate 0 eV and 716 eV for the lower and upper spectrum, respectively. (b) The total energy range for both core- and low-loss spectra is 102.4 eV.

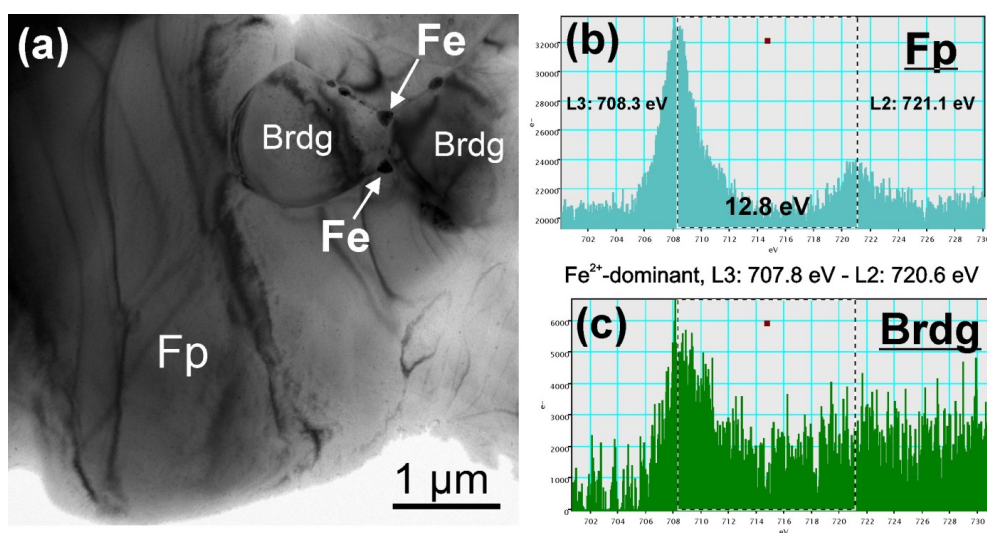


Fig. 3.8-19: (a) Typical bright field TEM image and (b&c)  $Fe-L_{2,3}$  ELNES of coexisting ferropericlaste (Fp) and bridgmanite (Brdg) under reducing conditions with metallic iron (Fe). The measured energy values of 708.3 eV and 721.1 eV in Fp (b) were calibrated as 707.8 eV and 720.6 eV, respectively, for the quantitative evaluation of  $Fe^{3+}/\Sigma Fe$  of Brdg (c).

**k. The single-crystal diamond trap (SCDT) method: A new way to determine mineral solubilities in fluids at high pressure and high temperature (S. Abeykoon and A. Audétat)**

The presence of aqueous fluids has important effects on processes within the Earth's mantle such as melting and rock deformation. Experimental approaches to determine the composition of high-pressure, high-temperature fluids in equilibrium with minerals/rocks is important for understanding fluid transport in the mantle and how it affects melting and other processes. Several experimental techniques for investigating fluid-mineral interactions at high P-T have been developed in the past decades.

The classical diamond trap method (Ryabchikov *et al.*, 1989) involves a layer of fine diamond powder in the capsule, such that experimentally-generated fluids/melts infiltrate into the pore space of the diamond layer and precipitate their solute content during quenching. To optimise diamond trap analysis via LA-ICP-MS, Kessel *et al.* (2004) introduced a freezing method in which the entire capsule is kept frozen during opening and analysis in order to prevent re-distribution and loss of water-soluble components. An important assumption made for all such experiments is that all components analysed in the diamond trap were dissolved in the fluid at the time of quenching. However, this is not necessarily a valid assumption. For example, if the experiments contain glassy starting material, then the fluid will initially attain a high solute content but further heating leads to precipitation of crystalline phases within the diamond trap (Keppler 2007). Furthermore, material can be continuously dissolved in some parts of the capsule and re-precipitated within the diamond trap.

In order to address these problems and obtain larger crystals suitable for trace element analysis, we developed a single-crystal diamond trap (SCDT). The SCDT contains two square-shaped, polished, single-crystal synthetic diamonds (about 3 mm max. dimension), one of which has 12-16 holes (~ 90 µm diameter; ~ 90 µm deep) drilled using a high-power laser beam. The SCDT is assembled by aligning the two diamonds face-to-face and then sealing them into a platinum tube, which is subsequently partly reopened with a razor blade to allow fluid access. A sketch of the SCDT and capsule setup is shown in Fig. 3.8-20. Following experimentation, the SCDT was retrieved from the capsule and opened by sliding away the upper diamond crystal. Once the fluid in the holes evaporated, the holes were filled with hot glue and analysed individually by LA-ICP-MS.

We initially performed a control experiment at ambient conditions using 9.7 wt. % Na<sub>2</sub>SiO<sub>3</sub> solution doped with Rb and Cs, which returned reproducible and accurate results. We then performed several tests on model systems at high *P-T* to compare our results with literature data. Results obtained for quartz solubility, albite solubility, and the enstatite + olivine system show considerable scatter, but the lowest values agree well with the reference values. The latter analyses also tend to return the most accurate results with regard to the secondary internal standard, which provides an independent means to select the most reliable analyses. Large mineral solubility values obtained in some analyses appear to be caused by loss of the

internal standard elements rather than by precipitation of minerals in the laser ablation holes. As a final step, we tested the method using a natural eclogite starting material and compared the results with those obtained from an identical run performed using the classical diamond trap method. Even though both runs developed a leak during quenching, element ratios normalised to Si suggest that the SCDT approach provides more accurate results than the classical DT method with regard to Zr, Y, and potentially many other trace elements. Another major advantage of the SCDT method is that high fluid/rock-ratios can be used, which facilitates the growth of large crystals and determination of fluid/mineral partition coefficients. In conclusion, our experimental results show that the SCDT technique is promising improvement to the classical DT method.

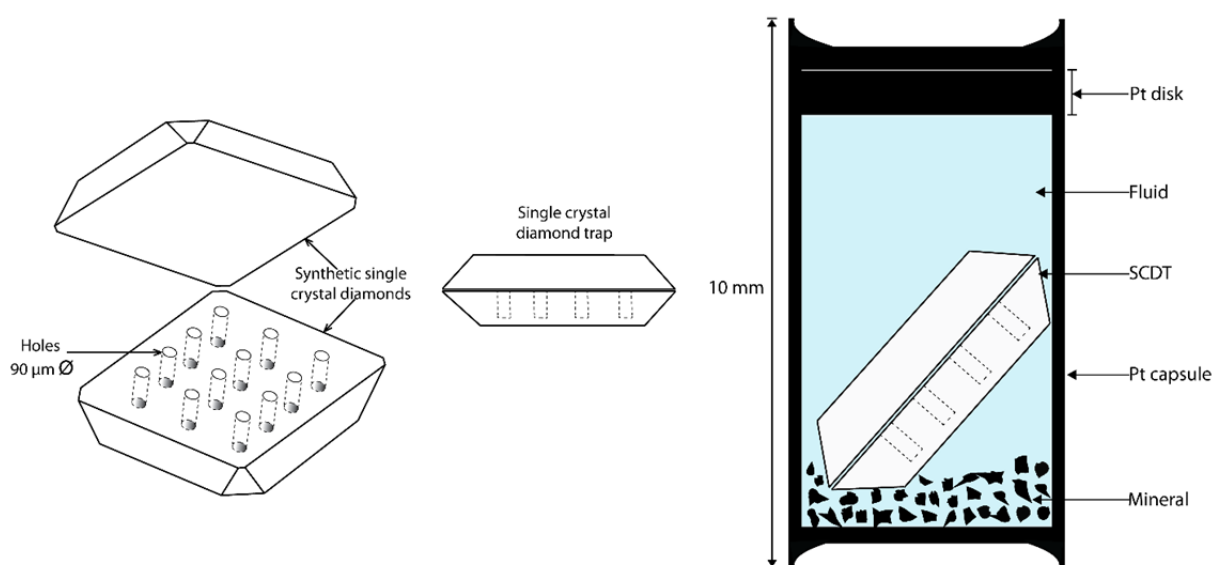


Fig. 3.8-20: Sketches of (a) the single crystal diamond trap, and (b) capsule cross-section used in experiments designed to measure solubility.



#### 4. International Research and Training Group – "Deep Earth Volatile Cycles" (DFG GRK 2156/1)

The International Research and Training Group (IRTG) "Deep Earth Volatile Cycles" is funded by the *Deutsche Forschungsgemeinschaft* (DFG). This graduate school for doctoral studies started in April 2016 for a period of 4.5 years. It is a cooperation between the Bayerisches Geoinstitut (BGI) and the Department of Earth Sciences at Tohoku University, Sendai/Japan. The IRTG is chaired by Dan Frost/Bayreuth and Michihiko Nakamura/Sendai.

The objective of this collaborative research effort is to study the cycling of volatile elements through the deep interior of the Earth. Using mainly experimental and computational methods the group's goal is to quantify how volatile elements such as carbon, hydrogen and nitrogen are transported, stored and expelled from the interior as a result of plate tectonic processes. Doctoral researchers receive training in modern experimental and modelling techniques employed in solid Earth geosciences in a structured learning programme. At the same time they pursue independent research into geochemical and geophysical aspects of the internal volatile cycle. Doctoral researchers from the BGI spend between 6 to 12 months at Tohoku University as part of a complementary research exchange that sees scientists from Tohoku University spending time at the BGI.

In 2017 the following PhD students were enrolled in the IRTG at BGI:

<i>Marija Putak-Juriczek</i> (M.Sc. 2016, Zagreb) since March	<i>Behavior of water in the upper mantle.</i> <u>Supervisor:</u> Prof. H. Keppler
<i>Lisa Eberhard</i> (M.Sc. 2017, Bern) since July	<i>The effect of water on the speciation of carbon in subduction zones.</i> <u>Supervisor:</u> Prof. D. Frost
<i>Niccoló Satta</i> (M.Sc. 2016, Potsdam) since July	<i>High pressure elasticity of antigorite and phase E single crystals.</i> <u>Supervisor:</u> Dr. H. Marquardt
<i>Enrico Marzotto</i> (M.Sc. 2017, Padua) since October	<i>Global-scale geodynamical models of volatile mixing in the Earth's mantle.</i> <u>Supervisor:</u> Prof. G. Golabek
<i>Caterina Melai</i> (MSc. 2017, Bayreuth) since November	<i>Fractionation processes affecting volatile-bearing fluids and melts in the deep mantle.</i> <u>Supervisor:</u> Prof. D. Frost
<i>Dmitry Bondar</i> (MSc. 2017, Moscow) since December	<i>Water partitioning between upper mantle minerals and melts.</i> <u>Supervisor:</u> Prof. T. Katsura

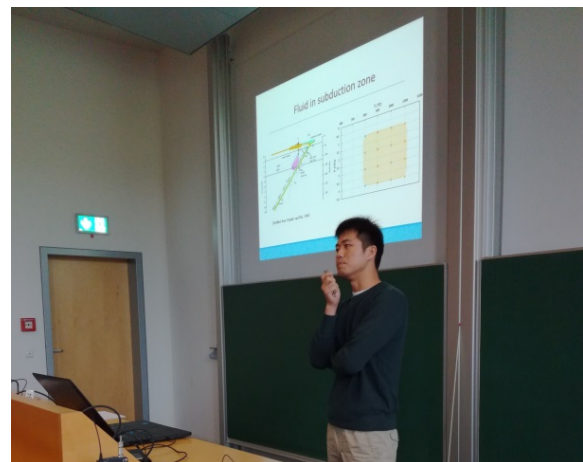
## IRTG Activities in 2017:

*Earth, Sea and Sky II: International Joint Graduate Program Workshop in Earth and Environmental Sciences co-hosted by the Tohoku University GP-EES and JSPS-DFG Japanese-German Graduate Externship, 28-30<sup>th</sup> May*

The three-day workshop was held at Tohoku University and comprised seminars and posters by the PhD students, plenary lectures by invited speakers and a field trip to Zao volcano led by Professor Michihiko Nakamura. Professor Tomoo Katsura and Dr. Catherine McCammon from BGI held two of the plenary lectures presenting new results about electrical conductivity of the asthenosphere and the state of iron in the deep Earth respectively.

*Joint doctoral seminar, BGI, Bayreuth University, 14-15<sup>th</sup> September*

The second IRTG meeting was held on September 14-15 at Bayreuth, where all the students involved in the program presented their PhD projects. Seven of those presentations were given by students from Tohoku University. The meeting was rounded up by a plenary lecture by Pierre Cartigny from Institut de Physique du Globe de Paris about the deep carbon cycle in the Earth and a geological field trip to the Oberpfalz.



Posterpresentation (left) and guest student Yongsheng Huang (Universität Tohoku, right) during his talk at the IRTG work shop.

## *Softskill-course*

Within the framework of the IRTG graduate school a softskill course 'Project management' was offered on September 11-12 at BGI through the consulting company Kempkes.Gebhardt from Cologne. The course was supported with equal opportunity funds and fully booked with 14 participants (3 Postdocs, 10 PhD students, 1 Master student) offering a practical introduction into effective planning and realization of scientific projects.



Participants of the softskill course 'Project management' at BGI.

In 2017 several staff members and students of the two participating institutes made visits to the collaborating institutions for discussion of projects, presentations, experiments and internships:

Tohoku colleagues visiting BGI in 2017:

Name	Period	Name	Period
Matsuoka, Moe	09.01.-06.02.	Nakajima, Ayano	20.08.-02.09.
Maeda, Fumiya	09.02.-28.02.	Ohira, Itaru	28.08.-02.09.
Nakatani, Takayuki	19.02.-15.03.	Maeda, Fumiya	28.08.-02.09.
Huang, Yongsheng	19.02.-15.03.	Liang, Yuan	29.08.-16.10.
Tsujimori, Tatsuki	20.02.-01.03.	Huang, Yongsheng	30.08.-26.11.
Hirano, Naoto	14.03.-18.03.	Sakoda, Yozora	01.09.-30.09.
Sato, Yuki	14.03.-18.03.	Ohira, Itaru	09.09.-24.09.
Okumura, Satoshi	23.03.-04.04.	Maeda, Fumiya	09.09.-12.10.
Nakamura, Michihiko, Prof.	23.03.-29.03.	Fujita, Wakana	10.09.-18.09.
Okumura, Satoshi	05.06.-10.06.	Araka, Naoki	11.09.-30.09.
Nakamura, Michihiko, Prof.	05.06.-10.06.	Nakamura, Michihiko, Prof.	13.09.-20.09.
Araya, Naoki	05.06.-10.06.	Maeda, Fumiya	29.09.-12.10.
Nakamura, Michihiko, Prof.	17.06.-23.06.	Fujita, Wakana	13.10.-12.02.18
Araya, Naoki	17.06.-23.06.	Suzuki, Akio	20.12.-08.01.18
Matsuoka, Moe	19.06.-25.07.	Goto, Ken-ichi	20.12.-08.01.18
Suzuki, Akio	20.08.-02.09.		

BGI colleagues visiting Tohoku in 2017:

<b>Name</b>	<b>Period</b>	<b>Name</b>	<b>Period</b>
Katsura, Tomoo, Prof.	08.01.-14.01.	Eichheimer, Philipp	25.05.-01.06.
McCammon, Catherine	18.05.-01.06.	Yoshioka, Takahiro	28.08.-13.09.
Katsura, Tomoo, Prof.	28.05.-01.06.		

## 5. Publications, Conference Presentations, Seminars

### 5.1 Publications (published)

Supplement to **2016** (papers published at the end of 2016):

- MIYAHARA, M.; OHTANI, E.; EL GORESY, A.; OZAWA, S.; GILLET, P. (2016): Phase transition processes of olivine in the shocked Martian meteorite Tissint: Clues to origin of ringwoodite-, bridgmanite- and magnesiowüstite-bearing assemblages. *Physics of the Earth and Planetary Interiors* 259, 18-28
- OVSYANNIKOV, S.V.; MOROZOVA, N.V.; KOROBENNIKOV, I.V.; HABORETS, V.; YEVIYCH, R.; VYSOCHANSKII, Y.; SHCHENNIKOV, V.V. (2016): Tuning the electronic and vibrational properties of  $\text{Sn}_2\text{P}_2\text{Se}_6$  and  $\text{Pb}_2\text{P}_2\text{S}_6$  crystals and their metallization under high pressure. *Dalton Transactions* 46, 4245-4258
- PALOT, M.; JACOBSEN, S.D.; TOWNSEND, J.P.; NESTOLA, F.; MARQUARDT, K.; MIYAJIMA, N.; HARRIS, J.W.; STACHEL, T.; MCCAMMON, C.A.; PEARSON, D.G. (2016): Evidence for  $\text{H}_2\text{O}$ -bearing fluids in the lower mantle from diamond inclusion. *Lithos* 265, 237-243

## 2017

### a) Refereed international journals

- AKAOGI, M.; ABE, K.; YUSA, H.; ISHII, T.; TAJIMA, T.; KOJITANI, H.; MORI, D.; INAGUMA, Y. (2017): High-pressure high-temperature phase relations in  $\text{FeTiO}_3$  up to 35 GPa and 1600 °C. *Physics and Chemistry of Minerals* 44, 63-73
- APRILIS, G.; STROHM, C.; KUPENKO, I.; LINHARDT, S.; LASKIN, A.; VASIUKOV, D.M.; CERANTOLA, V.; KOEMETS, E.G.; MCCAMMON, C.; KURNOSOV, A.; DUBROVINSKY, L. (2017): Portable double-sided pulsed laser heating system for time-resolved geoscience and materials science applications. *Review of Scientific Instruments* 88, 084501
- ARAKCHEEVA, A.; BYKOV, M.; BYKOVA, E.; DUBROVINSKY, L.; PATTISON, P.; DMITRIEV, V.; CHAPUIS, G. (2017): Incommensurate atomic density waves in the high-pressure IVb phase of barium. *IUCrJ* 4, 152-157
- ARATÓ, R.; AUDÉTAT, A. (2017):  $\text{FeTiMM}$  – a new oxybarometer for mafic to felsic magmas. *Geochemical Perspectives Letters* 5, 19-23
- ARATÓ, R.; AUDÉTAT, A. (2017): Vanadium magnetite–melt oxybarometry of natural, silicic magmas: a comparison of various oxybarometers and thermometers. *Contrib Mineral Petrol* 172, 52
- ARATÓ, R.; AUDÉTAT, A. (2017): Experimental calibration of a new oxybarometer for silicic magmas based on vanadium partitioning between magnetite and silicate melt. *Geochimica et Cosmochimica Acta* 209, 284-295

- ASSCHER, Y.; DAL SASSO, G.; NODARI, L.; ANGELINI, I.; BOFFA BALLARAN, T.; ARTIOLI, G. (2017): Differentiating between long and short range disorder in infra-red spectra: on the meaning of "crystallinity" in silica. *Physical Chemistry Chemical Physics* 19, 21783-21790
- AUDÉTAT, A.; LI, W. (2017): The genesis of Climax-type porphyry Mo deposits: Insights from fluid inclusions and melt inclusions. *Ore Geology Reviews* 88, 436-460
- BEYER, C.; FROST, D.J. (2017): The depth of sub-lithospheric diamond formation and the redistribution of carbon in the deep mantle. *Earth and Planetary Science Letters* 461, 30-39
- BLANCHARD, I.; SIEBERT, J.; BORENSZTAJN, S.; BADRO, J. (2017): The solubility of heat-producing elements in Earth's core. *Geochemical Perspectives Letters* 5, 1-5
- CERANTOLA, V.; BYKOVA, E.; KUPENKO, I.; MERLINI, M.; ISMAILOVA, L.; MCCAMMON, C.; BYKOV, M.; CHUMAKOV, A.I.; PETITGIRARD, S.; KANTOR, I. (2017): Stability of iron-bearing carbonates in the deep Earth's interior. *Nature Communications*, 8, 15960, doi: 10.1038/ncomms15960
- ČERNOK, A.; MARQUARDT, K.; CARACAS, R.; BYKOVA, E.; HABLER, G.; LIERMANN, H.-P.; HANFLAND, M.; MEZOUAR, M.; BOBOCIOIU, E.; DUBROVINSKY, L. (2017): Compressional pathways of  $\alpha$ -cristobalite, structure of cristobalite X-I, and towards the understanding of seifertite formation. *Nature Communications* 8, 15647
- CHARITON, S.; CERANTOLA, V.; ISMAILOVA, L.; BYKOVA, E.; BYKOV, M.; KUPENKO, I.; MCCAMMON, C.; DUBROVINSKY, L. (2017): The high-pressure behavior of spherocobaltite ( $\text{CoCO}_3$ ): a single crystal Raman spectroscopy and XRD study. *Phys Chem Minerals*, doi: 10.1007/s00269-017-0902-5
- CHUVASHOVA, I.; BYKOVA, E.; BYKOV, M.; PRAKAPENKA, V.; GLAZYRIN, K.; MEZOUAR, M.; DUBROVINSKY, L.; DUBROVINSKAIA, N.A. (2017): Nonicosahedral boron allotrope synthesized at high pressure and high temperature. *Physical Review B* 95, 180102
- CHUVASHOVA, I.; BYKOVA, E.; BYKOV, M.; SVITLYK, V.; GASHAROVA, B.; MATHIS, Y.-L.; CARACAS, R.; DUBROVINSKY, L.; DUBROVINSKAIA, N. (2017): High-pressure behavior of  $\alpha$ -boron studied on single crystals by X-ray diffraction, Raman and IR spectroscopy. *Journal of Solid State Chemistry* 245, 50-60
- CLARK, W.P.; STEINBERG, S.; DRONSKOWSKI, R.; MCCAMMON, C.; KUPENKO, I.; BYKOV, M.; DUBROVINSKY, L.; AKSELRUD, L.G.; SCHWARZ, U.; NIEWA, R. (2017): High-pressure NiAs-type modification of FeN. *Angewandte Chemie International Edition* 56, 7302-7306
- DEMOUCHY, S.; SHCHEKA, S.; DENIS, C.M.M.; THORAVAL, C. (2017): Subsolvus hydrogen partitioning between nominally anhydrous minerals in garnet-bearing peridotite. *American Mineralogist* 102, 1822-1831
- DUBROVINSKY, L.; KOEMETS, E.; BYKOV, M.; BYKOVA, E.; APRILIS, G.; PAKHOMOVA, A.; GLAZYRIN, K.; LASKIN, A.; PRAKAPENKA, V.B.; GREENBERG, E. (2017): Diamond anvils with a round table designed for high pressure experiments in DAC. *High Pressure Research* 37, 475-485

- DUCHOSLAV, M.; MARKS, M.A.W.; DROST, K.; MCCAMMON, C.; MARSCHALL, H.R.; WENZEL, T.; MARKL, G. (2017): Changes in tourmaline composition during magmatic and hydrothermal processes leading to tin-ore deposition: The Cornubian Batholith, SW England. *Ore Geology Reviews* 83, 215-234
- FARLA, R.J.M.; ROSENTHAL, A.; BOLLINGER, C.; PETITGIRARD, S.; GUIGNARD, J.; MIYAJIMA, N.; KAWAZOE, T.; CRICHTON, W.A.; FROST, D.J. (2017): High-pressure, high-temperature deformation of dunite, eclogite, clinopyroxenite and garnetite using *in situ* X-ray diffraction. *Earth and Planetary Science Letters* 473, 291-302
- FEI, H.; YAMAZAKI, D.; SAKURAI, M.; MIYAJIMA, N.; OHFUJI, H.; KATSURA, T.; YAMAMOTO, T. (2017): A nearly water-saturated mantle transition zone inferred from mineral viscosity. *Science Advances* 3, e1603024, doi: 10.1126/sciadv.1603024
- FEI, H.; HUANG, R.; YANG, X. (2017): CaSiO<sub>3</sub>-perovskite may cause electrical conductivity jump in the topmost lower mantle. *Geophysical Research Letters* 44, 10226-10232
- FENG, L.; MIYAHARA, M.; NAGASE, T.; OHTANI, E.; HU, S.; EL GORESY, A.; LIN, Y. (2017): Shock-induced P-T conditions and formation mechanism of akimotoite-pyroxene glass assemblages in the Grove Mountains (GRV) 052082 (L6) meteorite. *American Mineralogist* 102 (6), 1254-1262
- FUKUI, H.; BARON, A.; ISHIKAWA, D.; UCHIYAMA, H.; OHISHI, Y.; TSUCHIYA, T.; KOBAYASHI, H.; MATSUZAKI, T.; YOSHINO, T.; KATSURA, T. (2017): Pressure dependence of transverse acoustic phonon energy in ferropericlase across the spin transition. *Journal of Physics: Condensed Matter* 29, 245401
- GLAZYRIN, K.; SINMYO, R.; BYKOVA, E.; BYKOV, M.; CERANTOLA, V.; LONGO, M.; MCCAMMON, C.; PRAKAPENKA, V.B.; DUBROVINSKY, L. (2017): Critical behavior of Mg<sub>1-x</sub>Fe<sub>x</sub>O at the pressure-induced iron spin-state crossover. *Physical Review B* 95, 214412
- GOLOSOVA, N.O.; KOZLENKO, D.P.; DUBROVINSKY, L.S.; CERANTOLA, V.; BYKOV, M.; BYKOVA, E.; KICHANOV, S.E.; LUKIN, E.V.; SAVENKO, B.N.; PONOMAREVA, A.V.; ABRIKOSOV, I.A. (2017): Magnetic and structural properties of FeCO<sub>3</sub> at high pressures. *Physical Review B* 96, 134405
- GREENBERG, E.; XU, W.M.; NIKOLAEVSKY, M.; BYKOVA, E.; GARBARINO, G.; GLAZYRIN, K.; MERKEL, D.G.; DUBROVINSKY, L.; PASTERNAK, M.P.; ROZENBERG, G.K. (2017): High-pressure magnetic, electronic, and structural properties of MFe<sub>2</sub>O<sub>4</sub> (M=Mg,Zn,Fe) ferric spinels. *Physical Review B* 95, 195150
- GRUENINGER, H.; ARMSTRONG, K.; GREIM, D.; BOFFA BALLARAN, T.; FROST, D.J.; SENKER, J. (2017): Hidden Oceans? Unravelling the structure of hydrous defects in the Earth's deep interior. *Journal of the American Chemical Society* 139, 10499-10505
- GUO, H.; AUDÉTAT, A. (2017): Transfer of volatiles and metals from mafic to felsic magmas in composite magma chambers: An experimental study. *Geochimica et Cosmochimica Acta* 198, 360-378
- GUO, H. (2017): *In situ* infrared spectra of OH in rutile up to 1000 °C. *Physics and Chemistry of Minerals* 44(8), 547-552

- GUO, H.; XIAO, Y.; XU, L.; SUN, H.; HUANG, J.; HOU, Z. (2017): Origin of allanite in gneiss and granite in the Dabie orogenic belt, Central East China. *Journal of Asian Earth Sciences* 135, 243-256
- ISHII, T.; YAMAZAKI, D.; TSUJINO, N.; XU, F.; LIU, Z.; KAWAZOE, T.; YAMAMOTO, T.; DRUZHBIN, D.; WANG, L.; HIGO, Y.; TANGE, Y.; YOSHINO, T.; KATSURA, T. (2017): Pressure generation to 65 GPa in Kawai-type multi-anvil apparatus with tungsten carbide anvils. *High Pressure Research* 37, 507-515
- ISHII, T.; SINMYO, R.; KOMABAYASHI, T.; BOFFA BALLARAN, T.; KAWAZOE, T.; MIYAJIMA, N.; HIROSE, K.; KATSURA, T. (2017): Synthesis and crystal structure of  $\text{LiNbO}_3$ -type  $\text{Mg}_3\text{Al}_2\text{Si}_3\text{O}_{12}$ . A possible indicator of shock conditions of meteorites. *American Mineralogist* 102, 1947-1952
- ISHII, T.; FUJINO, K.; KOJITANI, H.; ARII, H.; TSUJINO, N.; MIYAJIMA, N.; KUNIMOTO, T.; AKAOGI, M. (2017): A shallow origin of so-called ultrahigh-pressure chromitites, based on single-crystal X-ray structure analysis of the high-pressure  $\text{Mg}_2\text{Cr}_2\text{O}_5$  phase, with modified ludwigite-type structure. *American Mineralogist* 102, 2113-2118
- ISMAILOVA, L.; BYKOV, M.; BYKOVA, E.; BOBROV, A.; KUPENKO, I.; CERANTOLA, V.; VASIUKOV, D.; DUBROVINSKAIA, N.; MCCAMMON, C.; HANFLAND, M.; GLAZYRIN, K.; LIERMANN, H.-P.; CHUMAKOV, A.; DUBROVINSKY, L. (2017): Effect of composition on compressibility of skiaigite-Fe-majorite garnet. *American Mineralogist* 102, 184-191
- JACOBSON, S.A.; HERNLUND, J.; RUBIE, D.C.; MORBIDELLI, A. (2017): Formation, stratification, and mixing of Earth's core. *Earth and Planetary Science Letters* 474, 375-386
- KATSURA, T.; BABA, K.; YOSHINO, T.; KOGISO, T. (2017): Electrical conductivity of the oceanic asthenosphere and its interpretation based on laboratory measurements. *Tectonophysics* 717, 162-181
- KATSURA, T. (2017): Experimental geophysics – measurement of physical and chemical properties of major mantle minerals at high pressures and temperatures (in Japanese). *Jap. Mag. Mineral. Petrol. Sci.* 46, 1-14
- KAWAZOE, T.; OHIRA, I.; ISHII, T.; BOFFA BALLARAN, T.; MCCAMMON, C.; SUZUKI, A.; OHTANI, E. (2017): Single crystal synthesis of  $\delta$ -(Al,Fe)OOH. *American Mineralogist* 102, 1953-1956
- KEPPLER, H. (2017): Fluids and trace element transport in subduction zones. *American Mineralogist* 102, 5-20
- KEPPLER, H.; ZAREI, A. (2017): Comment on "Experimentally-determined carbon isotope fractionation in and between methane-bearing melt and fluid to upper mantle temperatures and pressures" by Mysen. *Earth and Planetary Science Letters* 479, 387-388
- KLUMBACH, S.; SCHILLING, F.R. (2017): Anisotropic viscoelastic properties of quartz and quartzite in the vicinity of the alpha-beta phase transition. *Phys Chem Minerals* 44, 627, doi: 10.1007/s00269-017-0888-z
- KOROBENIKOV, I.V.; MOROZOVA, N.V.; SHCHENNIKOV, V.V.; OVSYANNIKOV, S.V. (2017): Dramatic changes in thermoelectric power of germanium under pressure: Printing *n-p* junctions by applied stress. *Scientific Reports* 7, 44220

- KURNOSOV, A.; MARQUARDT, H.; FROST, D.J.; BOFFA BALLARAN, T.; ZIBERNA, L. (2017): Evidence for a Fe<sup>3+</sup>-rich pyrolytic lower mantle from (Al,Fe)-bearing bridgmanite elasticity data. *Nature* 543, 543-546
- LAUMONIER, M.; FARLA, R.J.M.; FROST, D.J.; KATSURA, T.; MARQUARDT, K.; BOUVIER, A.; BAUMGARTNER, L. (2017): Experimental determination of melt interconnectivity and electrical conductivity in the upper mantle. *Earth and Planetary Science Letters* 463, 286-297
- LIAO, J.; GERYA, T.V.; THIELMANN, M.; WEBB, A.A.G.; KUFNER, S.-K.; YIN, A. (2017): 3D geodynamic models for the development of opposing continental subduction zones: The Hindu Kush–Pamir example. *Earth and Planetary Science Letters* 480, 133-146, doi: 10.1016/j.epsl.2017.10.005
- LIN, F.; HILAIRET, N.; RATERRON, P.; ADDAD, A.; IMMOOR, J.; MARQUARDT, H.; TOMÉ, C.N.; MIYAGI, L.; MERKEL, S. (2017): Elasto-viscoplastic self consistent modeling of the ambient temperature plastic behavior of periclase deformed up to 5.4 GPa. *Journal of Applied Physics* 122, 205902
- LIU, Z.; NISHI, M.; ISHII, T.; FEI, H.; MIYAJIMA, N.; BOFFA BALLARAN, T.; OHFUJI, H.; SAKAI, T.; WANG, L.; SHCHEKA, S.; ARIMOTO, T.; TANGE, Y.; HIGO, Y.; IRIFUNE, T.; KATSURA, T. (2017): Phase relations in the system MgSiO<sub>3</sub>-Al<sub>2</sub>O<sub>3</sub> up to 2300 K at lower-mantle pressures. *Journal of Geophysical Research: Solid Earth* 122, 7775-7788
- LIU, Z.; ISHII, T.; KATSURA, T. (2017): Rapid decrease in oxygen-vacancy substitution in aluminous bridgmanite with pressure. *Geochemical Perspectives Letters* 5, 12-18
- MAEDA, F.; KAMADA, S.; OHTANI, E.; HIRAO, N.; MITSUI, T.; MASUDA, R.; MIYAHARA, M.; MCCAMMON, C. (2017): Spin state and electronic environment of iron in basaltic glass in the lower mantle. *American Mineralogist* 102, 2106-2112
- MARQUARDT, K.; DE GRAEF, M.; SINGH, S.; MARQUARDT, H.; ROSENTHAL, A.; HIRAGA, T.; KOIZUMI, S. (2017): Quantitative electron backscatter diffraction data (EBSD) analyses using the dictionary indexing (DI) approach: Overcoming indexing difficulties on geological materials. *American Mineralogist* 102, 1843-1855
- MASOTTA, M.; KEPPLER, H. (2017): A new hydrothermal moissanite cell apparatus for optical *in situ* observations at high pressure and high temperature, with applications to bubble nucleation in silicate melts. *American Mineralogist* 102, 2022-2031
- MEIER, T.; WANG, N.; MAGER, D.; PETITGIRARD, S.; DUBROVINSKY, L. (2017): Magnetic flux tailoring through lenz lenses for ultra-small samples: A new pathway to high pressure nuclear magnetic resonance. *Science Advances* 3, no. 12, eaao5242, doi: 10.1126/sciadv.aao5242
- MILANI, S.; ANGEL, R.J.; SCANDOLO, L.; MAZZUCHELLI, M.L.; BOFFA BALLARAN, T.; KLEMME, S.; DOMENEGHETTI, M.C.; MILETICH, R.; SCHEIDL, K.S.; DERZSI, M.; TOKAR, K.; PRENCIPE, M.; ALVARO, M.; NESTOLA, F. (2017): Thermo-elastic behavior of grossular garnet at high pressures and temperatures. *American Mineralogist* 102, 851-859

- MOLDWIN, M.B.; FLORINDO, F.; OKIN, G.; ROBOCK, A.; ROHLING, E.J.; CARDENAS, B.; CARLTON, A.; CHEN, K.H.; CRUCIFIX, M.; GETTELMAN, A.; HUBBARD, A.; KATSURA, T.; PAINTER, T.H. (2017): Why and how to write a high-impact review paper: Lessons from eight years of editorial board service to *Reviews of Geophysics*. *Reviews of Geophysics* 55, doi: 10.1002/2017RG000587
- MYHILL, R.; FROST, D.J.; NOVELLA, D. (2017): Hydrous melting and partitioning in and above the mantle transition zone: Insights from water-rich MgO-SiO<sub>2</sub>-H<sub>2</sub>O experiments. *Geochimica et Cosmochimica Acta* 200, 408-421
- NISHIYAMA, N.; ISHIKAWA, R.; OHFUJI, H.; MARQUARDT, H.; KURNOSOV, A.; TANIGUCHI, T.; KIM, B.-N.; YOSHIDA, H.; MASUNO, A.; BEDNARCIK, J.; KULIK, E.; IKUHARA, Y.; WAKAI, F.; IRIFUNE, T. (2017): Transparent polycrystalline cubic silicon nitride. *Scientific Reports* 7, 44755
- NOVELLA, D.; DOLEJŠ, D.; MYHILL, R.; PAMATO, M.G.; MANTHILAKE, G.; FROST, D.J. (2017): Melting phase relations in the systems Mg<sub>2</sub>SiO<sub>4</sub>-H<sub>2</sub>O and MgSiO<sub>3</sub>-H<sub>2</sub>O and the formation of hydrous melts in the upper mantle. *Geochimica et Cosmochimica Acta* 204, 68-82
- OVSYANNIKOV, S.V.; BYKOVA, E.; PAKHOMOVA, A.; KOZLENKO, D.P.; BYKOV, M.; KICHANOV, S.E.; MOROZOVA, N.V.; KOROBENNIKOV, I.V.; WILHELM, F.; ROGALEV, A.; TSIRLIN, A.A.; KURNOSOV, A.V.; ZAINULIN, Y.G.; KADYROVA, N.I.; TYUTYUNNIK, A.P.; DUBROVINSKY, L. (2017): Structural and magnetic transitions in CaCo<sub>3</sub>V<sub>4</sub>O<sub>12</sub> perovskite at extreme conditions. *Inorganic Chemistry* 56, 6251-6263
- PAKHOMOVA, A.; BYKOVA, E.; BYKOV, M.; GLAZYRIN, K.; GASHAROVA, B.; LIERMANN, H.-P.; MEZOUAR, M.; GORELOVA, L.; KRIVOVICHEV, S.; DUBROVINSKY, L. (2017): A closer look into close packing: Pentacoordinated silicon in a high-pressure polymorph of danburite. *IUCrJ* 4, 671-677
- PAKHOMOVA, A.; ISMAILOVA, L.; BYKOVA, E.; BYKOV, M.; BOFFA BALLARAN, T.; DUBROVINSKY, L. (2017): A new high-pressure phase transition in clinoferrosilite: *In situ* single-crystal X-ray diffraction study. *American Mineralogist* 102, 666-673
- PETITGIRARD, S.; MALFAIT, W.J.; JOURNAUX, B.; COLLINGS, I.E.; JENNINGS, E.; BLANCHARD, I.; KANTOR, I.; KURNOSOV, A.; COTTE, M.; DANE, T.; BURGHAMMER, M.; RUBIE, D.C. (2017): SiO<sub>2</sub> glass density to lower-mantle pressures. *Physical Review Letters* 119, 215701
- PISTONE, M.; MÜNTENER, O.; ZIBERNA, L.; HETÈNY, G.; ZANETTI, A. (2017): Report on ICDP workshop DIVE (Drilling the Ivrea-Verbano zone). *Scientific Drilling* 23, 47-56
- POLISHOOK, D.; JACOBSON, S.A.; AHARONSON, O.; MORBIDELLI, A. (2017): A Martian origin for the Mars Trojan asteroids. *Nature Astronomy* 1, 179, 1-6
- POSNER, E.S.; RUBIE, D.C.; FROST, D.J.; VLČEK, V.; STEINLE-NEUMANN, G. (2017): High *P-T* experiments and first principles calculations of the diffusion of Si and Cr in liquid iron. *Geochimica et Cosmochimica Acta* 203, 323-342
- POSNER, E.S.; RUBIE, D.C.; FROST, D.J.; STEINLE-NEUMANN, G. (2017): Experimental determination of oxygen diffusion in liquid iron at high pressure. *Earth and Planetary Science Letters* 464, 116-123

- POSNER E.S.; STEINLE-NEUMANN G.; VLČEK V.; RUBIE D.C. (2017): Structural changes and anomalous self-diffusion of oxygen in liquid iron at high pressure. *Geophysical Research Letters* 44, 3526-3534
- ROUT, S.; HECK, P.R.; ZALUZEC, N.; ISHII, T.; WEN, J.; MILLER, D.; SCHMITZ, B. (2017): Shocked chromites in fossil L chondrites: A Raman spectroscopy and transmission electron microscopy study. *Meteoritics and Planetary Science* 52, 1776-1796
- ROZEL, A.B.; GOLABEK, G.J.; JAIN, C.; TACKLEY, P.J.; GERYA, T.V. (2017): Continental crust formation on early Earth controlled by intrusive magmatism. *Nature* 545, 332-335
- SCHULZE, K.; BUCHEN, J.; MARQUARDT, K.; MARQUARDT, H. (2017): Multi-sample loading technique for physical property measurements in the diamond-anvil cell. *High Pressure Research* 37, 159-169
- SHCHIPALKINA, N.; CHUKANOV, N.; PEKOV, I.; AKSENOV, S.; MCCAMMON, C.; BELAKOVSKY, D.; BRITVIN, S.; KOSHLyakOVA, N.; SCHÄFER, C.; SCHOLZ, R.; RASTSVETAeva, R. (2017): Ferrorhodonite,  $\text{CaMn}_3\text{Fe}[\text{Si}_5\text{O}_{15}]$ , a new mineral species from Broken Hill, New South Wales, Australia. *Physics and Chemistry of Minerals* 44, 323-334
- SIRSCH, N.C.; BOFFA BALLARAN, T.; UENVER-THIELE, L.; WOODLAND, A.B. (2017): Compressibility and high-pressure structural behavior of  $\text{Mg}_2\text{Fe}_2\text{O}_5$ . *American Mineralogist* 102, 845-850
- SINMYO, R.; KEPLER, H. (2017): Electrical conductivity of NaCl-bearing aqueous fluids to 600 °C and 1 GPa. *Contrib Mineral Petrol* 172, 4
- SINMYO, R.; MCCAMMON, C.; DUBROVINSKY, L. (2017): The spin state of  $\text{Fe}^{3+}$  in lower mantle bridgmanite. *American Mineralogist* 102, 1263-1269
- STEKIEL, M.; NGUYEN-THANH, T.; CHARITON, S.; MCCAMMON, C.; BOSAK, A.; MORGENROTH, W.; MILMAN, V.; REFSON, K.; WINKLER, B. (2017): High pressure elasticity of  $\text{FeCO}_3$ - $\text{MgCO}_3$  carbonates. *Physics of the Earth and Planetary Interiors* 271, 57-63
- THOMSON, M.D.; RABIA, K.; MENG, F.; BYKOV, M.; VAN SMAALEN, S.; ROSKOS, H.G. (2017): Phase-channel dynamics reveal the role of impurities and screening in a quasi-one-dimensional charge-density wave system. *Scientific Reports* 7, 2039
- UENVER-THIELE, L.; WOODLAND, A.B.; BOFFA BALLARAN, T.; MIYAJIMA, N.; FROST, D.J. (2017): Phase relations of  $\text{MgFe}_2\text{O}_4$  at conditions of the deep upper mantle and transition zone. *American Mineralogist* 102, 632-642
- UENVER-THIELE, L.; WOODLAND, A.B.; BOFFA BALLARAN, T.; MIYAJIMA, N.; FROST, D.J. (2017): Phase relations of Fe-Mg spinels including new high-pressure post-spinel phases and implications for natural samples. *American Mineralogist* 102, 2054-2064
- VALKOVSKIY, G.A.; YASHINA, E.G.; DYADKIN, V.A.; TSVYASHCHENKO, A.V.; FOMICHEVA, L.N.; BYKOV, M.; BYKOVA, E.; DUBROVINSKY, L.; CHERNYSHOV, D.Yu.; GRIGORIEV, S.V. (2017): High-pressure single-crystal synchrotron diffraction study of MnGe and related compounds. *Journal of Physics: Condensed Matter* 29, 85401

- VASIUKOV, D.M.; ISMAILOVA, L.; KUPENKO, I.; CERANTOLA, V.; SINMYO, R.; GLAZYRIN, K.; MCCAMMON, C.; CHUMAKOV, A.I.; DUBROVINSKY, L.; DUBROVINSKAIA, N. (2017): Sound velocities of skiagite–iron–majorite solid solution to 56 GPa probed by nuclear inelastic scattering. *Phys Chem Minerals*, 1-8, doi: 10.1007/s00269-017-0928-8
- WANG, L.; BLAHA, S.; KAWAZOE, T.; MIYAJIMA, N.; KATSURA, T. (2017): Identical activation volumes of dislocation mobility in the [100](010) and [001](010) slip systems in natural olivine. *Geophysical Research Letters* 44, 2687-2692
- WU, Y.; QIN, F.; WU, X.; HUANG, H.; MCCAMMON, C.A.; YOSHINO, T.; ZHAI, S.; XIAO, Y.; PRAKAPENKA, V.B. (2017): Spin transition of ferric iron in the calcium-ferrite type aluminous phase. *Journal of Geophysical Research: Solid Earth* 122, 5935-5
- YAXLEY, G.M.; BERRY, A.J.; ROSENTHAL, A.; WOODLAND, A.B.; PATERSON, D. (2017): Redox preconditioning deep cratonic lithosphere for kimberlite genesis – evidence from the central Slave Craton. *Scientific Reports* 7, 30, doi: 10.1038/s41598-017-00049-3
- YOSHINO, T.; ZHANG, B.; ZHAO, C.; FEI, H. (2017): Pressure dependence of electrical conductivity in forsterite. *Journal of Geophysical Research: Solid Earth* 122, 158-171
- YUSENKO, K.V.; BYKOVA, E.; BYKOV, M.; RIVA, S.; CRICHTON, W.A.; YUSENKO, M.V.; SUKHIKH, A.S.; ARNABOLDI, S.; HANFLAND, M.; DUBROVINSKY, L.S. (2017): Ir–Re binary alloys under extreme conditions and their electrocatalytic activity in methanol oxidation. *Acta Materialia* 139, 236-243
- YUSENKO, K.V.; BYKOVA, E.; BYKOV, M.; GROMILOV, S.A.; KURNOSOV, A.V.; PRESCHER, C.; PRAKAPENKA, V.B.; CRICHTON, W.A.; HANFLAND, M.; MARGADONNA, S.; DUBROVINSKY, L.S. (2017): High-pressure high-temperature stability of hcp-IrxOs1-x (x = 0.50 and 0.55) alloys. *Journal of Alloys and Compounds* 700, 198
- XU, F.; YAMAZAKI, D.; SAKAMOTO, N.; SUN, W.; FEI, H.; YURIMOTO, H. (2017): Silicon and oxygen self-diffusion in stishovite: implications for stability of SiO<sub>2</sub>-rich seismic reflectors in the mid-mantle. *Earth and Planetary Science Letters* 459, 332-339
- ZHANG, D.; AUDÉTAT, A. (2017): Chemistry, mineralogy and crystallization conditions of porphyry Mo-forming magmas at Urad–Henderson and Silver Creek, Colorado, USA. *Journal of Petrology* 58, 277-296
- ZHANG, D.; AUDÉTAT, A. (2017): What caused the formation of the giant Bingham Canyon porphyry Cu-Mo-Au deposit? Insights from melt inclusions and magmatic sulfides. *Economic Geology* 112, 221-244
- ZIBERNA, L.; GREEN, E.C.R.; BLUNDY, J.D. (2017): Multiple-reaction geobarometry for olivine-bearing igneous rocks. *American Mineralogist* 102 (12), 2349-2366

*b) Popular scientific magazines*

- MÜNKLER, L.; MARQUARDT, H. (2017): Vom Spezial- zum Interdiskurs: Zur Problematik der Aufarbeitung wissenschaftlicher Erkenntnisse für die Öffentlichkeit. *Akademie Aktuell* 02/2017, 21-26

## 5.2 Publications (submitted, in press)

- AKAOGI, M.; KAWAHARA, A.; KOJITANI, H.; YOSHIDA, K.; ANEGAWA, Y.; ISHII, T.: High-pressure phase transitions in  $\text{MgCr}_2\text{O}_4\text{-Mg}_2\text{SiO}_4$  composition: Reactions between olivine and chromite with implications for ultrahigh-pressure chromitites. *American Mineralogist* (in press)
- ARAKCHEEVA, A.; BYKOV, M.; BYKOVA, E.; DUBROVINSKY, L.; PATTISON, P.; DMITRIEV, V.: Incommensurate density waves in the high-pressure IV-B phase of barium. *IUCRJ* (submitted)
- BEYER, C.; ROSENTHAL, A.; MYHILL, R.; CRICHTON, W.A.; YU, T.; WANG, Y.; FROST, D.J.: Internally consistent pressure calibration of geobarometers applicable to the Earth's upper mantle using *in situ* XRD. *Geochimica et Cosmochimica Acta* (accepted)
- BIANCHI, F.; THIELMANN, M.; HERRMANN, H.J.: Critical bursts in filtration. *Physical Review Letters* (in press)
- BIANCHI, F.; WITTEL, F.; THIELMANN, M.; TRTIK, P.; HERRMANN, H.J.: Tomographic study of internal erosion of particle flows in porous media. *Transport in Porous Media* (submitted)
- BINDER, B.; WENZEL, T.; KEPPLER, H.: The partitioning of sulfur between multicomponent aqueous fluids and felsic melts. *Contrib Mineral Petrol* (submitted)
- BORCHARDT, S.; EBERT, T.; KONRAD-SCHMOLKE, M.; MCCAMMON, C.; NEVERMANN, H.; TRAUTH, M.H.: Correlating hyperspectral reflectance data with weathering induced chemico-mineralogical changes in a phonolite from the Suguta Valley, Kenya. *Journal of Geophysical Research: Solid Earth* (submitted)
- BUCHEN, J.; MARQUARDT, H.; BOFFA BALLARAN, T.; KAWAZOE, T.; MCCAMMON, C.: The equation of state of wadsleyite solid solutions: Constraining the effects of anisotropy and crystal chemistry. *American Mineralogist* (in press)
- BUCHEN, J.; MARQUARDT, H.; SPEZIALE, S.; KAWAZOE, T.; BOFFA BALLARAN, T.; KURNOSOV, A.: Experiments reveal unexpected low sensitivity of seismic velocities to water in the shallow transition zone. *Nature Communications* (submitted)
- BYKOVA, E.; BYKOV, M.; ČERNOK, A.; TIDHOLM, J.; SIMAK, S.I.; HELLMAN, O.; BELOV, M.; ABRIKOSOV, I.A.; LIERMANN, H.-P.; HANFLAND, M.; PRAKAPENKA, V.B.; PRESCHER, C.; DUBROVINSKAIA, N.; DUBROVINSKY, L.: Squeezed silica with pentacoordinate silicon and face-sharing octahedra. *Science* (submitted)
- CHARITON, S.; CERANTOLA, V.; ISMAILOVA, L.; BYKOVA, E.; BYKOV, M.; KUPENKO, I.; MCCAMMON, C.; DUBROVINSKY, L.: The high-pressure behavior of spherocobaltite ( $\text{CoCO}_3$ ): A single crystal Raman spectroscopy and XRD study. *Physics and Chemistry of Minerals* (in press)
- CHUST, T.C.; STEINLE-NEUMANN, G.; DOLEJŠ, D.; SCHUBERTH, B.S.A.; BUNGE, H.-P.: MMA-EoS: A computational framework for mineralogical thermodynamics. *Journal of Geophysical Research – Solid Earth*, doi: 10.1002/2017JB014501 (in press)

- DANG, N.T.; ZAKHVALINSKII, V.S.; KOZLENKO, D.P.; PHAN, T.-L.; NEKRASOVA, YU.S.; TRANG, T.T.; KICHANOV, S.E.; SAVENKO, B.N.; THANH, T.D.; TARAN, S.V.; JABAROV, S.G.; OVSYANNIKOV, S.V.; KHIEM, L.H.: Influence of Fe doping on the structural, magnetic and electrical transport properties of  $\text{La}_{0.7}\text{Ca}_{0.3}\text{Mn}_{0.5}\text{Fe}_{0.5}\text{O}_3$ . *Journal of Electronic Materials* (submitted)
- FEI, H.; WIEDENBECK, M.; SAKAMOTO, N.; YURIMOTO, H.; YOSHINO, T.; YAMAZAKI, D.; KATSURA, T.: Negative activation volume of oxygen self-diffusion in forsterite. *Physics of the Earth and Planetary Interiors* (submitted)
- FEI, H.; KOIZUMI, S.; SAKAMOTO, N.; HASHIGUCHI, M.; YURIMOTO, H.; MARQUARDT, K.; MIYAJIMA, N.; KATSURA, T.: Mg lattice diffusion in iron-free olivine and implications to conductivity anomaly in the oceanic asthenosphere. *Earth and Planetary Science Letters* (submitted)
- GOLABEK, G.J.; EMSENHUBER, A.; JUTZI, M.; ASPHAUG, E.I.; GERYA, T.V.: Coupling SPH and thermochemical models of planets: Methodology and example of a Mars-sized body. *Icarus* (in press)
- GUO, H.; AUDÉTAT, A.: Solubility of gold in oxidized, sulfur-bearing fluids at 500-850 °C and 200-230 MPa: A synthetic fluid inclusion study. *Geochimica et Cosmochimica Acta* (in press)
- GUO, H.; AUDÉTAT, A.: Gold diffusion into and out of quartz-hosted fluid inclusions during re-equilibration experiments at 600-800 °C and 2 kbar. *Chemical Geology* (in press)
- HAKIM, K.; RIVOLDINI, A.; VAN HOOLST, T.; COTTENIER, S.; JAEKEN, J.; CHUST, T.; STEINLE-NEUMANN, G.: A new *ab initio* equation of state of hcp-Fe and its implication on the interior structure and mass-radius relations of rocky super-Earths. *Icarus* (submitted)
- HUNT, A.C.; COOK, D.L.; LICHTENBERG, T.; REGER, P.M.; EK, M.; GOLABEK, G.J.; SCHÖNBÄCHLER, M.: Late metal-silicate separation on the IAB parent asteroid: Constraints from combined W and Pt isotopes and thermal modelling. *Earth and Planetary Science Letters* (accepted)
- IMMOOR, J.; MARQUARDT, H.; MIYAGI, L.; LIN, F.; SPEZIALE, S.; MERKEL, S.; BUCHEN, J.; KURNOSOV, A.; LIERMANN, H.-P.: Evidence for  $\{100\}\langle 011\rangle$  slip in ferropericlase in Earth's lower mantle from high-pressure/high-temperature experiments. *Earth and Planetary Science Letters* (submitted)
- IMMOOR, J.; MARQUARDT, H.; MIYAGI, L.; LIN, F.; SPEZIALE, S.; MERKEL, S.; BUCHEN, J.; KURNOSOV, A.; LIERMANN, H.-P.: Experimental deformation of  $(\text{Mg,Fe})\text{O}$  at temperature/pressure-conditions of Earth's lower mantle. *Nature Geoscience* (submitted)
- ISHII, T.; HUANG, R.; FEI, H.; KOEMETS, I.; LIU, Z.; MAEDA, F.; YUAN, L.; WANG, L.; DRUZHBIN, D.; YAMAMOTO, T.; BHAT, S.; FARLA, R.; KAWAZOE, T.; NORIYOSHI, T.; KULIK, E.; HIGO, Y.; TANGE, Y.; KATSURA, T.: Complete agreement of the post-spinel transition in  $\text{Mg}_2\text{SiO}_4$  with the 660-km discontinuity. *Nature Geoscience* (submitted)

- ISHII, T.; KOJITANI, H.; AKAOGI, M.: Phase relations and mineral chemistry in pyrolitic mantle at 1600-2200 °C under pressures up to the uppermost lower mantle: Phase transitions around the 660-km discontinuity and dynamics of upwelling hot plumes. *Physics of the Earth and Planetary Interiors* (in press)
- JACOBSON, S.A.: Asteroid geophysics from applying tidal theory to binary asteroids. *Astronomy and Astrophysics* (submitted)
- KISEEVA, E.S.; VASIUKOV, D.M.; WOOD, B.J.; MCCAMMON, C.; STACHEL, T.; BYKOV, M.; BYKOVA, E.; CHUMAKOV, A.; CERANTOLA, V.; HARRIS, J.W.; DUBROVINSKY, L.: Oxidised iron in garnets from the mantle transition zone. *Nature Geoscience* (submitted)
- KOROBENIKOV, I.V.; MOROZOVA, N.V.; LUKYANOVA, L.N.; USOV, O.A.; KULBACHINSKII, V.A.; SHCHENNIKOV, V.V.; OVSYANNIKOV, S.V.: Stress-controlled thermoelectric module for energy harvesting and its application for significant enhancement of power factor of Bi<sub>2</sub>Te<sub>3</sub>-based thermoelectrics. *Journal of Physics D: Applied Physics* (in press)
- KRESSALL, R.D.; FEDORTCHOUK, Y.; MCCAMMON, C.; ELLIOT, B.: Stability of chromite and ilmenite in a silicate melt at various  $fO_2$  at 0.1 MPa: New insights into use of oxides as diamond indicator minerals in kimberlites. *Journal of Petrology* (submitted)
- LICHTENBERG, T.; GOLABEK, G.J.; DULLEMOND, C.P.; SCHÖNBÄCHLER, M.; GERYA, T.V.; MEYER, M.R.: Impact splash chondrule formation during planetesimal recycling. *Icarus* (accepted)
- LIN, F.; MERKEL, S.; HILAIRET, N.; MARQUARDT, H.; IMMOOR, J.; TOMÉ, C.; MIYAGI, L.: Elasto-visco-plastic self-consistent (EVPSC) modeling of periclase deformation at high pressure. *Journal of Applied Physics* (in press)
- MALLIK, A.; LI, Y.; WIEDENBECK, M.: Nitrogen evolution within the Earth's atmosphere-mantle system assessed by recycling in subduction zones. *Earth and Planetary Science Letters* (in press)
- MAHAN, B.; SIEBERT, J.; BLANCHARD, I.; BADRO, J.; MOYNIER, F.: Pebbles or Bamm-Bamm?: Insights into Earth's source material, accretion and differentiation from HP-HT Zn metal-silicate partitioning. *Geochimica et Cosmochimica Acta* (submitted)
- MCGOWAN, N.; GRIFFIN, W.L.; O'REILLY, S.Y.; CLARK, S.M.; ROQUE-ROSELL, J.; MARCUS, M.A.; MCCAMMON, C.A.; PEARSON, N.J.: The oxidation state of Fe in chromite by  $\mu$ -XRD and K-edge  $\mu$ -XANES: A record of deep Earth processes? *Geochimica et Cosmochimica Acta* (submitted)
- MEIER, T.: At its Extremes: NMR at Giga-Pascal Pressures. *Annual Reports on NMR Spectroscopy* (in press), doi: 10.1016/bs.arnmr.2017.08.004
- MIYAJIMA, N.; LI, Y.; ABEYKOON, S.; HEIDELBACH, F.: Electron channelling contrast imaging of individual dislocations in geological materials using a field emission scanning electron microscope equipped with an EBSD system. *European Journal of Mineralogy* (in press)
- MONTEUX, J.; GOLABEK, G.J.; RUBIE, D.C.; TOBIE, G.; YOUNG, E.D.: Water and the interior structure of terrestrial planets and icy bodies. *Space Science Reviews* (in press)

- MORBIDELLI, A.; NESVORNY, D.; MARCHI, S.; RUBIE, D.; ELKINS-TANTON, L.; JACOBSON, S.A.; LAURENZ, V.: The lunar late heavy bombardment as the tail-end of accretion. *Icarus* (accepted)
- MORBIDELLI, A.; NESVORNY, D.; LAURENZ, V.; MARCHI, S.; RUBIE, D.C.; ELKINS-TANTON, L.; WIECZOREK, M.; JACOBSON, S.: The timeline of the Lunar bombardment – revisited. *Icarus* (in press)
- O'BRIEN, D.P.; RAYMOND, S.N.; RUBIE, D.C.; JACOBSON, S.A.; IZIDORO, A.: The delivery of water during terrestrial planet formation. – In: BLANC, M.; MORBIDELLI, A. (Eds.): The delivery of water to proto-planets, planets and satellites. Space Science Series of ISSI 64 (submitted)
- PATRICK, M.; INDARES, A.; MCCAMMON, C.: The influence of ferric iron on phase stability in midpressure anatectic aluminous gneisses. *Canadian Mineralogist* (submitted)
- POMMIER, A.; KOHLSTEDT, D.L.; HANSEN, L.N.; MACKWELL, S.J.; TASAKA, M.; HEIDELBACH, F.; LEINENWEBER, K.: Experimental investigation of the effect of shear on the electrical properties of polycrystalline olivine. *Contributions to Mineralogy and Petrology* (submitted)
- POMMIER A.; LAURENZ, V.; DAVIES, C.J.; FROST, D.J.: Melting phase relations in the Fe-S and Fe-S-O systems at core conditions in small terrestrial bodies. *Icarus* (submitted)
- ROSENTHAL, A.; YAXLEY, G.M.; GREEN, D.H.; CRICHTON, W.A.; KOVACS, I.; SPANDLER, C.; HERMANN, J.; SANDORNE, J.K.: Phase relations and melting of nominally 'dry' residual eclogites with variable CaO/Na<sub>2</sub>O from 3 to 5 GPa and 1250 to 1500 °C; implications for refertilisation of upwelling heterogeneous mantle. *Lithos* (submitted)
- SCHULZE, K.; MARQUARDT, H.; KAWAZOE, T.; BOFFA BALLARAN, T.; MCCAMMON, C.; KOCH-MÜLLER, M.; KURNOSOV, A.; MARQUARDT, K.: Seismically invisible water in Earth's transition zone? *Earth and Planetary Science Letters* (submitted)
- SHEKHAR, S.; FROST, D.J.; WALTE, N.; HEIDELBACH, F.; MIYAJIMA, N.: Deformation experiments on polycrystalline olivine up to 12 GPa and implications for upper mantle seismic anisotropy. *Earth and Planetary Science Letters* (submitted)
- SIEBERT, J.; SOSSI, P.; BLANCHARD, I.; MAHAN, B.; BADRO, J.; MOYNIER, F.: Chondritic Mn/Na ratio and limited post-nebular volatile loss of the Earth. *Earth and Planetary Science Letters* (submitted)
- SOLFERINO, G.F.D.; GOLABEK, G.J.: Olivine grain growth in partially molten Fe-S: A proxy for the genesis of pallasite meteorites. *Earth and Planetary Science Letters* (submitted)
- SORBADÉRE F.; LAURENZ, V.; FROST, D.; WENZ, M.; ROSENTHAL, A.; RIVARD, C.; MCCAMMON, C.: The behavior of ferric iron during partial melting of peridotite. *Geochimica et Cosmochimica Acta* (submitted)
- THIELMANN, M.: Grain size assisted thermal runaway as a nucleation mechanism for continental mantle earthquakes: Impact of complex rheologies. *Tectonophysics* (in press), doi: 10.1016/j.tecto.2017.08.038

- UENVER-THIELE, L.; WOODLAND, A.B.; MIYAJIMA, N.; BOFFA BALLARAN, T.; FROST, D.J.: Behavior of  $\text{Fe}_4\text{O}_5$ – $\text{Mg}_2\text{Fe}_2\text{O}_5$  solid solutions and their relation to coexisting Mg-Fe silicates and oxide phases. *Contributions to Mineralogy and Petrology* (submitted)
- VASIUKOV, D.; ISMAILOVA, L.; DUBROVINSKY, L.; KUPENKO, I.; CERANTOLA, V.; MCCAMMON, C.; CHUMAKOV, A.I.; DUBROVINSKAIA, N.: Sound velocities of skiaigite-iron-majorite solid solution to 56 GPa probed by Nuclear Inelastic Scattering. *Physics and Chemistry of Minerals* (in press)
- VASIUKOV, D.M.; DUBROVINSKY, L.; KUPENKO, I.; CERANTOLA, V.; APRILIS, G.; ISMAILOVA, L.; BYKOVA, E.; MCCAMMON, C.; PRESCHER, C.; CHUMAKOV, A.I.; DUBROVINSKAIA, N.: Pressure-induced spin pairing transition of  $\text{Fe}^{3+}$  in oxygen octahedra. *Physical Review B* (submitted)
- VOGEL, A.K.; JENNINGS E.S.; LAURENZ, V.; RUBIE, D.C.; FROST, D.J.: The dependence of metal-silicate partitioning of moderately volatile elements on oxygen fugacity and Si contents of Fe metal: Implications for their valence states in silicate liquid. *Geochimica et Cosmochimica Acta* (submitted)
- WAGLE, F.; STEINLE-NEUMANN, G.: Electrical resistivity discontinuity of iron along the melting curve. *Geophysical Journal International*, doi: 10.1093/gji/ggx526 (in press)
- WANG, L.; KATSURA, T.: Diffusion controlled motion of [001](010) screw dislocation in natural olivine. *Earth and Planetary Science Letters* (submitted)
- WEI, Q.; MCCAMMON, C.; GILDER, S.A.: High-pressure phase transition of iron: A combined magnetic remanence and Mössbauer study. *Geochemistry, Geophysics, Geosystems* (submitted)
- YOSHIOKA, T.; WIEDENBECK, M.; SHCHEKA, S.; KEPPLER, H.: Nitrogen solubility in the deep mantle and the origin of Earth's primordial nitrogen budget. *Earth and Planetary Science Letters* (submitted)
- ZAREI, A.; LI, Y.; FEI, H.; KATSURA, T.: A nearly zero temperature gradient furnace system for high pressure multi-anvil experiments. *High Pressure Research* (submitted)

### *5.3 Presentations at scientific institutions and at congresses*

- ABEYKOON, S.; LAURENZ, V.; FROST, D.J.; RUBIE, D.C.; VOGEL, A.K.: 13.-18.08.2017, Goldschmidt 2017, Paris, France: "Sulfide-silicate partitioning of moderately siderophile elements at high P-T", *Goldschmidt Abstracts*, 2017, 9
- ADAMS, A.; THIELMANN, M.; GOLABEK, G.: 23.-28.04.2017, European Geosciences Union General Assembly 2017, Vienna, Austria: "Viability of Archean subduction initiation from gravitational spreading", *Geophysical Research Abstracts* 19, EGU2017-679, 2017
- APPEL, K.; KONOPKOVA, Z.; DUBROVINSKY, L.; LIERMANN, H.-P.; MARQUARDT, H.; TSCHENTSCHER, Th.: 21.-28.08.2017, 24<sup>th</sup> Congress and General Assembly of the International Union of Crystallography (IUCr), Hyderabad, India: "Novel platform for high-pressure static and dynamic X-ray diffraction experiments"

- ARMSTRONG, K.; FROST, D.J.; RUBIE, D.C.; MCCAMMON, C.M.; BOFFA BALLARAN, T.: 29.05.-03.06.2017, Interdisciplinary Workshop on 'Accretion and Early Differentiation of the Terrestrial Planets', Nice, France: "Iron speciation in silicate melts as a function of pressure: implications for magma ocean and early atmosphere evolution"
- ARMSTRONG, K.; FROST, D.J.; MCCAMMON, C.A.; RUBIE, D.C.; BOFFA BALLARAN, T.: 24.-29.09.2017, GeoBremen 2017, Joint Meeting of DGGV and DMG, Bremen, Germany: "The effect of pressure on the oxidation state of iron in silicate melts at a fixed oxygen fugacity", Abstract A-468, 2017
- ARMSTRONG, K.; FROST, D.J.; MCCAMMON, C.A.; RUBIE, D.C.; BOFFA BALLARAN, T.: 11.-15.12.2017, AGU Fall Meeting, New Orleans, USA <sup>\*B</sup> (*invited*): "The effect of pressure on iron speciation in silicate melts at a fixed oxygen fugacity: The possibility of a redox profile through a terrestrial magma ocean", Abstract MR54A-04, 2017
- AUDÉTAT, A.: 02.02.2017, TUM München, Germany: "The use of melt inclusions in studying the formation of magmatic-hydrothermal ore deposits"
- AUDÉTAT, A.: 28.08.2017, CUG Wuhan, China: "The use of fluid inclusions and melt inclusions in ore deposits research"
- AUDÉTAT, A.: 28.08.2017, CUG Wuhan, China: "Magmatic controls on porphyry Cu ( $\pm$ Au, Mo) formation"
- AUDÉTAT, A.: 20.11.2017, GeoZentrum Nordbayern, Erlangen, Germany: "Die Genese porphyrischer Cu- und Mo-Lagerstätten: herkömmliche Modelle und neue Erkenntnisse"
- BARON, M.; LORD, O.; MYHILL, R.; THIELMANN, M.; THOMSON, A.; WANG, W.; TRØNNES, R.; WALTER, M.: 24.-28.09.2017, HPMP-9, Saint Malo, France <sup>\*A</sup>: "Eutectic melting in the MgO-SiO<sub>2</sub> system and its implication to Earth's lower mantle evolution"
- BLANCHARD, I.; SIEBERT, J.; BADRO, J.: 24.-28.09.2017, HPMP-9, Saint Malo, France <sup>\*A</sup>: "Budget of radioactive elements (K, U) in Bulk Earth"
- BLANCHARD, I.; SIEBERT, J.; BADRO, J.: 29.05.-03.06.2017, Interdisciplinary Workshop on 'Accretion and Early Differentiation of the Terrestrial Planets', Nice, France: "How much potassium is in the core?"
- BLUNDY, J.D.; MIUR, D.; ZIBERNA, L.; BROOKER, R.: 14.-18.08.2017, IAVCEI 2017 Scientific Assembly, Portland, USA: "Dacite petrogenesis at Cerro Uturuncu Volcano, Bolivia"
- BOFFA BALLARAN, T.; HUANG, R.; KURNOSOV, A.; FROST, D.: 24.-28.09.2017, HPMP-9, Saint Malo, France <sup>\*A</sup>: "Structure-elastic behaviour relationship in minerals at high-pressure"
- BONEH, Y.; MARQUARDT, K.; SKEMER, P.A.: 11.-15.12.2017, AGU Fall Meeting, New Orleans, USA <sup>\*B</sup>: "Chemical signature of a migrating grain boundaries in polycrystalline olivine", Abstract V11B-0345, 2017
- BUCHEN, J.; MARQUARDT, H.; SPEZIALE, S.; KAWAZOE, T.; BOFFA BALLARAN, T.; KURNOSOV, A.: 14.-15.09.2017, IRTG Doctoral Seminar, Bayreuth, Germany: "Single-crystal elasticity of wadsleyite at high pressures and high temperatures: Seismic signals of water in the shallow transition zone"

- BUCHEN, J.; MARQUARDT, H.; SPEZIALE, S.; KAWAZOE, T.; BOFFA BALLARAN, T.; KURNOSOV, A.: 24.-28.09.2017, HPMP-9, Saint Malo, France <sup>\*A</sup>: "High-pressure high-temperature single-crystal elasticity of iron-bearing wadsleyite: Reappraising the water sensitivity of seismic observables"
- BUCHEN, J.; MARQUARDT, H.; BOFFA BALLARAN, T.; KAWAZOE, T.; SPEZIALE, S.; KURNOSOV, A.: 11.-15.12.2017, AGU Fall Meeting, New Orleans, USA <sup>\*B</sup>: "How the 410-km discontinuity reflects mantle water content: Constraints from high-pressure experiments on wadsleyite single-crystal elasticity", Abstract D11B-02, 2017
- BYKOV, M.; BYKOVA, E.; APRILIS, G.; GLAZYRIN, K.; CHUVASHOVA, I.; KOEMETS, E.; MEZOUAR, M.; PRAKAPENKA, V.; DUBROVINSKY, L.: 27.-30.03.2017, 25<sup>th</sup> Annual Conference of the German Crystallographic Society, Karlsruhe, Germany: "Novel nitrogen-rich iron nitrides synthesized at high-pressure high-temperature conditions"
- BYKOV, M.; BYKOVA, E.; APRILIS, G.; GLAZYRIN, K.; KOEMETS, E.; CHUVASHOVA, I.; MEZOUAR, M.; PRAKAPENKA, V.; LIERMANN, H.-P.; DUBROVINSKAIA, N.; DUBROVINSKY, L.: 19.-24.08.2017, 26<sup>th</sup> AIRAPT International Conference on High Pressure Science and Technology, Beijing, China: "Novel iron nitrides synthesized in laser-heated diamond anvil cells"
- BYKOV, M.; BYKOVA, E.; APRILIS, G.; KOEMETS, E.; CHUVASHOVA, I.; GLAZYRIN, K.; MEZOUAR, M.; PRAKAPENKA, V.; LIERMANN, H.-P.; DUBROVINSKY, L.: 21.-28.08.2017, 24<sup>th</sup> Congress and General Assembly of the International Union of Crystallography, Hyderabad, India: "Novel nitrogen-rich iron nitrides synthesized at high-pressure high-temperature conditions"
- BYKOVA, E.; BYKOV, M.; LIERMANN, H.-P.; HANFLAND, M.; PRAKAPENKA, V.; DUBROVINSKY, L.: 13.-18.08.2017, Goldschmidt 2017, Paris, France (*invited*): "Crystal chemistry of compounds in Fe-O system at conditions of Earth's lower mantle", Goldschmidt Abstracts, 2017, 521
- CERANTOLA, V.; NESTOLA, F.; MILANI, S.; ANZOLINI, C.; MCCAMMON, C.; NOVELLA, D.; KUPENKO, I.; CHUMAKOV, A.; RUEFFER, R.; HARRIS, J.W.: 03.-08.09.2017, International Conference on the Applications of the Mössbauer Effect, St. Petersburg, Russia: "Synchrotron Mössbauer Source technique for *in situ* measurement of iron-bearing inclusions in natural diamonds"
- CHARITON, S.; MCCAMMON, C.; VASIUKOV, D.; CERANTOLA, V.; APRILIS, G.; CHUMAKOV, A.; DUBROVINSKY, L.: 13.-18.08.2017, Goldschmidt 2017, Paris, France: "Elastic wave velocities of Fe-bearing carbonates: A nuclear inelastic scattering study for deep carbon", Goldschmidt Abstracts, 2017, 611
- CHARITON, S.; BYKOVA, E.; BYKOV, M.; CERANTOLA, V.; VASIUKOV, D.; STEKIEL, M.; APRILIS, G.; KUPENKO, I.; ISMAILOVA, L.; CHUMAKOV, A.I.; WINKLER, B.; MCCAMMON, C.A.; DUBROVINSKY, L.S.: 11.-15.12.2017, AGU Fall Meeting, New Orleans, USA <sup>\*B</sup>: "Looking for carbonates in the deep Earth: an experimental approach at extreme conditions", Abstract MR43A-0447, 2017
- CONDAMINE, P.: 14.11.2017, Centre de Recherches Pétrographiques et Géochimiques, Nancy, France: "The role of volatile elements on K-rich magma genesis"

- DEMOUCHY, S.; SHCHEKA, S.; DENIS, C.M.M.; THORAVAL, C.: 11.-15.12.2017, AGU Fall Meeting, New Orleans, USA<sup>\*B</sup>: "H partitioning between NAMs in garnet-bearing peridotite at subsolidus conditions", Abstract V33F-0567, 2017
- DUBROVINSKY, L.S.; DUBROVINSKAIA, N.A.; CHARITON, S. (*invited*): 11.-15.12.2017, AGU Fall Meeting, New Orleans, USA<sup>\*B</sup>: "Structural mineral physics at extreme conditions", Abstract MR33E-02, 2017
- EICHHEIMER, P.; THIELMANN, M.; GOLABEK, G.: 23.-28.04.2017, European Geosciences Union General Assembly 2017, Vienna, Austria: "Numerical modelling of volatiles in the deep mantle", Geophysical Research Abstracts 19, EGU2017-4677, 2017
- EICHHEIMER, P.; THIELMANN, M.; GOLABEK, G.: 28.-30.05.2017, Earth, Sea and Sky II: International Joint Graduate Program Workshop in Earth and Environmental Sciences, Sendai, Japan: "3D numerical permeability determination"
- EICHHEIMER, P.; THIELMANN, M.; GOLABEK, G.: 27.-31.08.2017, 15<sup>th</sup> International Workshop on Modelling of Mantle and Lithosphere Dynamics, Putten, The Netherlands: "Numerical modelling of volatiles in Earth's mantle"
- EICHHEIMER, P.; THIELMANN, M.; GOLABEK, G.: 14.-15.09.2017, IRTG Doctoral Meeting, Bayreuth, Germany: "Numerical modelling of volatiles in Earth's mantle", Abstract T33B-0702, 2017
- EICHHEIMER, P.; THIELMANN, M.; GOLABEK, G.: 09.-13.10.2017, 4. Central European Geomorphology Conference, Bayreuth, Germany: "Numerical modelling of volatiles in Earth's mantle"
- EICHHEIMER, P.; THIELMANN, M.; GOLABEK, G.: 11.-15.12.2017, AGU Fall Meeting, New Orleans, USA<sup>\*B</sup>: "Towards modelling of water inflow into the mantle",
- FAUL, U.; FARLA, R.; CLINE, C.; BERRY, A.; LE LOSQ, C.: 11.-15.12.2017, AGU Fall Meeting, New Orleans, USA<sup>\*B</sup>: "Water incorporation in olivine at upper mantle pressures and water-undersaturated conditions", Abstract V11B-0344, 2017
- FEI, H.: 18.01.2017, Nanjing University, School of Earth Sciences and Engineering, Nanjing, P.R. China: "Conductivity anomaly in the oceanic asthenosphere due to water enhanced Mg diffusion"
- FEI, H.: 22.05.2017, Zhejiang University, School of Earth Sciences, Hangzhou, P.R. China: "An introduction to high-pressure and high-temperature experiments"
- FROST, D.J.: 26.04.2017, (public lecture in the series) Vortragsreihe 'Vulkanismus – Wenn die Erde überkocht', GEO-Zentrum an der KTB, Windischeschenbach, Germany: "Der Erdmantel als Quelle des Vulkanismus"
- FROST, D.; HUANG, R.; ARMSTRONG, K.; BOFFA BALLARAN, T.: 13.-18.08.2017, Goldschmidt 2017, Paris, France (*invited*): "Thermodynamic constraints on the mineralogy of the lower mantle", Goldschmidt Abstracts, 2017, 1224
- FROST, D.J.: 09.-13.10.2017, 4. Central European Geomorphology Conference, Bayreuth, Germany: "The formation of diamonds and their journey to the surface"
- GOLABEK, G.J.; BOURDON, B.; ROZEL, A.B.; GERYA, T.V.: 23.-28.04.2017, European Geosciences Union General Assembly 2017, Vienna, Austria: "Post-magma ocean mixing in the angrite parent body", Geophysical Research Abstracts 19, EGU2017-2851, 2017

- GOLABEK, G.J.; EMSENHUBER, A.; JUTZI, M.; ASPHAUG, E.I.; GERYA, T.V.: 29.05.-03.06.2017, Interdisciplinary Workshop on 'Accretion and Early Differentiation of the Terrestrial Planets', Nice, France: "Coupling giant impacts and longer-term evolution models"
- GOLABEK, G.J.; LICHTENBERG, T.; MEYER, M.R.; GERYA, T.V.; KELLER, T.; KATZ, R.F.: 18.-23.06.2017, Gordon Research Conference, Mount Holyoke, USA: "Magma dynamics and devolatilization of planetesimals during planet formation"
- GOLABEK, G.J.; ROZEL, A.B.; GERYA, T.V.; BOURDON, B.: 27.-31.08.2017, 15<sup>th</sup> International Workshop on Modelling of Mantle and Lithosphere Dynamics, Putten, The Netherlands: "Post-magma ocean mixing in the angrite parent body"
- GOLABEK, G.J.; ROZEL, A.B.; JAIN, C.; TACKLEY, P.J.; GERYA, T.V.: 02.10.2017, Northwestern University, Evanston, USA: "Formation of the first continental crust"
- GOLABEK, G.J.; SOLFERINO, G.F.D.; NIMMO, F.; SCHMIDT, M.W.: 03.10.2017, University of Chicago, Department of the Geophysical Sciences, Chicago, USA: "Laboratory and numerical experiments on pallasite formation"
- GOLABEK, G.J.; ROZEL, A.B.; JAIN, C.; TACKLEY, P.J.; GERYA, T.V.; EMSENHUBER, A.; JUTZI, M.; ASPHAUG, E.I.: 05.10.2017, Carnegie Institution for Science, Washington DC, USA: "Modelling crust formation on Archean Earth and terrestrial planets"
- GOLABEK, G.J.; SOLFERINO, G.F.D.; NIMMO, F.; SCHMIDT, M.W.: 06.10.2017, Carnegie Institution for Science, Washington DC, USA: "Laboratory and numerical experiments on pallasite formation"
- GOLABEK, G.J.; ROZEL, A.B.; JAIN, C.; TACKLEY, P.J.; GERYA, T.V.: 09.10.2017, University of California, Davis, USA "Modelling crust formation on Archean Earth"
- GOLABEK, G.J.; ROZEL, A.B.; JAIN, C.; TACKLEY, P.J.; GERYA, T.V.: 13.10.2017, Stanford University, USA: "Modelling crust formation on Archean Earth"
- GOLABEK, G.J.; LICHTENBERG, T.; MEYER, M.R.; GERYA, T.V.; KELLER, T.; KATZ, R.F.; ALIBERT, Y.: 17.10.2017, University of Michigan, Michigan Institute for Research in Astrophysics, 'The Origins of Volatiles in Habitable Planets: The Solar System and Beyond', Ann Arbor, USA: "Magma dynamics and devolatilization of planetesimals during planet formation"
- GOLABEK, G.J.; SOLFERINO, G.F.D.: 11.-15.12.2017, AGU Fall Meeting, New Orleans, USA<sup>\*B</sup>: "The origin of pallasites. A combined experimental and numerical approach", Abstract V33E-0566, 2017
- HAKIM, K.; RIVOLDINI, A.; VAN HOOLST, T.; COTTENIER, S.; JAEKEN, J.; CHUST, T.; STEINLE-NEUMANN, G.: 11.-15.12.2017, AGU Fall Meeting, New Orleans, USA<sup>\*B</sup>: "A new *ab initio* equation of state of hcp-Fe and its implication on the interior structure and mass-radius relations of rocky super-Earths", Abstract DI21A-0399, 2017
- HUANG, Y.; NAKATANI, T.; NAKAMURA, M.; MCCAMMON, C.: 28.-30.05.2017, Earth, Sea and Sky II: International Joint Graduate Program Workshop in Earth and Environmental Sciences, Sendai, Japan: "Experimental constraints on the dihedral angle between olivine and multicomponent aqueous fluids in the upper mantle conditions"

- HUNT, A.C.; COOK, D.L.; LICHTENBERG, T.; REGER, P.M.; EK, M.; GOLABEK, G.J.; SCHÖNBÄCHLER, M.: 13.-18.08.2017, Goldschmidt 2017, Paris, France: "Combining W and Pt isotopes with thermal modelling to determine the evolution of the IAB parent asteroid", Goldschmidt Abstracts, 2017, 1746
- ISMAILOVA, L.; BYKOV, M.; BYKOVA, E.; BOBROV, A.; DUBROVINSKAIA, N.; MCCAMMON, C.; DUBROVINSKY, L.: 13.-18.08.2017, Goldschmidt 2017, Paris, France: "Effect of composition on compressibility of skiaigite-Fe-majorite garnet", Goldschmidt Abstracts, 2017, 1791
- IMMOOR, J.; MARQUARDT, H.; SPEZIALE, S.; MIYAGI, L.; LIERMANN, H.-P.; MERKEL, S.; KURNOSOV, A.; SCHULZE, K.; BUCHEN, J.: 26.-27.01.2017, DESY Photon Science Users' Meeting, 'Research with Synchrotron Radiation and FELs', Hamburg, Germany: "Radial diffraction experiments at the ECB, P02.2 DESY, Hamburg"
- IMMOOR, J.; MARQUARDT, H.; MIYAGI, L.; LIN, F.; SPEZIALE, S.; MERKEL, S.; LIERMANN, H.-P.; KURNOSOV, A.; BUCHEN, J.: 14.-15.09.2017, IRTG Doctoral Seminar, Bayreuth, Germany: "Experimental deformation of (Mg,Fe)O ferropericlasite at pressure and temperature conditions of the lower mantle"
- IMMOOR, J.; MARQUARDT, H.; MIYAGI, L.; LIN, F.; SPEZIALE, S.; MERKEL, S.; LIERMANN, H.-P.; KURNOSOV, A.; BUCHEN, J.: 20.11.2017, Workshop BAdW 'Mantle Dynamics and Deep Earth Material Cycles', München, Germany: "Experimental deformation of (Mg,Fe)O at lower mantle P/T-conditions"
- IMMOOR, J.; MARQUARDT, H.; MIYAGI, L.; LIN, F.; SPEZIALE, S.; MERKEL, S.; BUCHEN, J.; KURNOSOV, A.; LIERMANN, H.-P.: 11.-15.12.2017, AGU Fall Meeting, New Orleans, USA<sup>\*B</sup>: "Experimental deformation of (Mg,Fe)O ferropericlasite in a resistive-heated DAC at conditions of the Earth's lower mantle", Abstract DI41A-0327, 2017
- ISHII, T.; FEI, H.; LIU, Z.; KAWAZOE, T.; TSUJINO, N.; TAKAFUMI, T.; WANG, L.; DRUZHBIN, D.; KULIK, E.; MAEDA, F.; HIGO, Y.; TANGE, Y.; KATSURA, T.: 19.-24.08.2017, 26<sup>th</sup> AIRAPT International Conference on High Pressure Science and Technology, Beijing, China: "Precise determination of post-spinel transition in MgO-FeO-SiO<sub>2</sub> system"
- ISHII, T.; HUANG, R.; FEI, H.; KOEMETS, I.; LIU, Z.; MAEDA, F.; YUAN, L.; WANG, L.; DRUZHBIN, D.; YAMAMOTO, T.; BHAT, S.; FARLA, R.J.; KAWAZOE, T.; TSUJINO, N.; KULIK, E.; HIGO, Y.; TANGE, Y.; KATSURA, T.: 11.-15.12.2017, AGU Fall Meeting, New Orleans, USA<sup>\*B</sup>: "New results of the post-spinel transition pressure in Mg<sub>2</sub>SiO<sub>4</sub> by means of *in situ* X-ray diffraction in a multi-anvil press: Complete agreement with the 660-km discontinuity depth", Abstract DI11B-06, 2017
- JACOBSON, S.A.: 23.01.2017, Northwestern University, Department of Earth and Planetary Sciences, Evanston, Illinois, USA: "A combined astronomic-geologic approach to understanding planet formation"
- JACOBSON, S.A.: 06.02.2017, APS colloquia, University of Colorado, Astrophysical and Planetary Sciences, Boulder, USA: "A combined astronomic-geologic approach to understanding planet formation"

- JACOBSON, S.A.: 27.02.2017, Planetary Lunch Seminar, Cornell University, Department of Astronomy, Ithaca, USA: "Activated asteroids, missing family members, and pieces of planets"
- JACOBSON, S.A.: 28.02.2017, Department colloquia, Cornell University, Department of Astronomy, Ithaca, USA: "A combined astronomic-geologic approach to understanding planet formation"
- JACOBSON, S.A.: 03.03.2017, York University, Centre for Research in Earth and Space Science, Toronto, Canada: "A combined astronomic-geologic approach to understanding planet formation"
- JACOBSON, S.A.: 10.-14.04.2017, 13<sup>th</sup> ACM Conference, Montevideo, Uruguay: "A Martian origin for the Mars Trojans and the A-type Hungarias"
- JACOBSON, S.A.: 29.05.-03.06.2017, Interdisciplinary Workshop on 'Accretion and Early Differentiation of the Terrestrial Planets', Nice, France: "Mantle composition constraints on planet formation scenarios"
- JACOBSON, S.A.: 12.-15.06.2017, 48<sup>th</sup> DDA, London, U.K.: "A Martian origin for the Mars Trojans and the A-type Hungarias"
- JACOBSON, S.; RUBIE, D.; MORBIDELLI, A.; IZIDORO, A.; RAYMOND, S.: 13.-18.08.2017, Goldschmidt 2017, Paris, France: "Mantle composition constraints on different planet formation scenarios", Goldschmidt Abstracts, 2017, 1805
- JACOBSON, S.A.: 27.10.2017, University of Chicago, Department of Geophysical Sciences, Chicago, USA: "Pieces of planets in the Solar System: origin of some achondrites and 'differentiated' asteroids"
- JACOBSON, S.A.: 14.11.2017, University of Copenhagen, Centre for Star and Planet Formation, Copenhagen, Denmark: "Pieces of planets in the Solar System: origin of some achondrites and 'differentiated' asteroids"
- JACOBSON, S.A.: 15.11.2017, University of Lund, Lund Observatory, Lund, Sweden: "Pieces of planets in the Solar System: origin of some achondrites and 'differentiated' asteroids"
- JENNINGS, E.; RUBIE, D.; JACOBSON, S.; MORBIDELLI, A.; ARMSTRONG, K.; FROST, D.: 13.-18.08.2017, Goldschmidt 2017, Paris, France: "Sequestration of tungsten into the core during Earth's accretion", Goldschmidt Abstracts, 2017, 1831
- JENNINGS, E.S.; WADE, J.; LAURENZ, V.; KEARNS, S.; BUSE, B.; RUBIE, D.C.: 11.-15.12.2017, AGU Fall Meeting, New Orleans, USA <sup>\*B</sup>: "Measuring DAC metal-silicate partitioning experiments by electron microprobe: Thickness, fluorescence, and oxide spheres", Abstract P51A-2567, 2017
- JENNINGS, E.S.; GIBSON, S.A.; MACLENNAN, J.; HEINONEN, J.S.: 11.-15.12.2017, AGU Fall Meeting, New Orleans, USA <sup>\*B</sup> (*invited*): "Olivine-hosted melt inclusions record efficient mixing of mantle melts in continental flood basalt provinces", Abstract V51G-02, 2017
- JOURNAUX, B.; BROWN, J.M.; ABRAMSON, E.; PETITGIRARD, S.; PAKHOMOVA, A.; BOFFA BALLARAN, T.; COLLINGS, I.: 11.-15.12.2017, AGU Fall Meeting, New Orleans, USA <sup>\*B</sup>: "High pressure study of water-salt systems, phase equilibria, partitioning, thermodynamic properties and implication for large icy worlds hydrospheres", Abstract MR43C-0473, 2017

- KARKIN, A.E.; VORONIN, V.I.; MOROZOVA, N.V.; OVSYANNIKOV, S.V.; TAKARABE, K.; MORI, Y.; NAKAMURA, S.; SHCHENNIKOV, V.V.: 19.-24.08.2017, 26<sup>th</sup> AIRAPT International Conference on High Pressure Science and Technology, Beijing, P.R. China: "Unconventional electronic properties of Mg<sub>2</sub>Si thermoelectrics revealed by fast-neutron-irradiation doping", Abstract p. 559
- KATSURA, T.: 12.01.2017, Lecture, Aobayama Campus of Tohoku University, Graduate School of Natural Science, Sendai, Japan: "Enhancement of ionic conductivity of olivine by water incorporation based on Mg diffusivity"
- KATSURA, T.: 13.01.2017, Lecture, Aobayama Campus of Tohoku University, Graduate School of Natural Science, Sendai, Japan: "Physics and Chemistry of the Earth's Interior – Geochemical thermodynamics and phase relation studies by means of *in situ* X-ray diffraction"
- KATSURA, T.; NISHIYAMA, N.; SONNTAG, S.; KULIK, E.; GAIDA, N.; DRUBE, W.; HOLZHEID, A.: 26.-27.01.2017, DESY Photon Science Users' Meeting, 'Research with Synchrotron Radiation and FELs', Hamburg, Germany: "Current status and plans of the LVP beam line in P61.2"
- KATSURA, T.; LIU, Z.; ISHII, T.: 01.-09.04.2017, 9<sup>th</sup> Meeting of the Study of Matter at Extreme Conditions (SMEC2017), Cruise Ship Freedom of the Seas, Miami – Eastern Caribbean (*invited*): "Development of ultrahigh-pressure multi-anvil press and phase relations in the system MgO-SiO<sub>2</sub>-Al<sub>2</sub>O<sub>3</sub> to 50 GPa"
- KATSURA, T.: 01.-09.04.2017, 9<sup>th</sup> Meeting of the Study of Matter at Extreme Conditions (SMEC2017), Cruise Ship Freedom of the Seas, Miami – Eastern Caribbean: "Introduction of an experimental station for high-pressure and high-temperature *in situ* X-ray observation with a large-volume press in a damping Wiggler beam line in PETRA-III Extension, DESY"
- KATSURA, T.; FEI, H.; KOIZUMI, S.; WIEDENBECK, M.; SAKAMOTO, N.; YURIMOTO, H.: 01.-09.04.2017, 9<sup>th</sup> Meeting of the Study of Matter at Extreme Conditions (SMEC2017), Cruise Ship Freedom of the Seas, Miami – Eastern Caribbean (*invited*): "Measurement of element self-diffusion coefficient at high pressures and high temperatures"
- KATSURA, T.: 07.-12.05.2017, DIMAT 2017 – International Conference on Diffusion in Materials, Haifa, Israel (*invited*): "Silicon, oxygen and magnesium self-diffusion of forsterite as a function of water content"
- KATSURA, T.; BABA, K.; YOSHINO, T.; KOGISO, T.: 28.-30.05.2017, Earth, Sea and Sky II: International Joint Graduate Program Workshop in Earth and Environmental Sciences, Sendai, Japan (*invited*): "Electrical conductivity of the oceanic asthenosphere and its interpretation based on laboratory measurements"
- KATSURA, T.: 16.08.2017, Center for High Pressure Science & Technology Advanced Research (HPSTAR), Shanghai, P.R. China: "Development of ultrahigh-pressure generation using Kawai-type multi-anvil presses with carbide anvils, and its applications to mantle mineralogy"
- KATSURA, T.: 19.-24.08.2017, 26<sup>th</sup> AIRAPT International Conference on High Pressure Science and Technology, Beijing, P.R. China (*invited*): "Generation of ultrahigh pressures by Kawai-type multi-anvil presses with carbide anvils and its application to geosciences"

- KATSURA, T.: 24.08.2017: Chinese Academy of Science, Institute for Geology and Geophysics, Beijing, P.R. China: "Binary phase relations of the postspinel transition in the system  $(\text{Mg,Fe})_2\text{SiO}_4$ : interpretation of the extremely thin 660-km seismic discontinuity"
- KATSURA, T.: 05.-10.09.2017, 2017 Deep Volatiles Programme Fall Meeting, Tenerife, Spain (*invited*): "Temperature, pressure and water-content dependence of dislocation mobilities in olivine"
- KATSURA, T.; LIU, Z.; ISHII, T.: 24.-29.09.2017, GeoBremen 2017, Joint Meeting of DGGV and DMG, Bremen, Germany: "Rapid decrease in the oxygen-vacancy substitution in aluminous bridgmanite with pressure"
- KATSURA, T.: 16.-17.10.2017, PETRA IV Workshop, 'Extreme Conditions Research at the Ultra-Low Emittance Storage Ring PETRA IV', DESY, Hamburg, Germany (*invited*): "Precise determination of phase relations of mantle minerals by means of *in situ* X-ray diffraction in a large-volume press"
- KATSURA, T.; ISHII, T.; HUANG, R.; MAEDA, F.; YUAN, L.; BHAT, S.; FARLA, R.; KAWAZOE, T.; NORIYOSHI, T.; LIU, Z.; FEI, H.; WANG, L.; DRUZHBIN, D.; YAMAMOTO, T.; KULIK, E.; KOEMETS, I.; HIGO, Y.; TANGE, Y.: 11.-15.12.2017, AGU Fall Meeting, New Orleans, USA<sup>\*B</sup>: "Geometry and width of the ringwoodite – bridgmanite+ferropericlase binary loop in the system  $(\text{Mg,Fe})_2\text{SiO}_4$ : Interpretation of the sharpness of the 660-km discontinuity", Abstract D111B-07, 2017
- KEPPLER, H.: 09.-13.10.2017, 4. Central European Geomorphology Conference, Bayreuth, Germany: "Volcano atmosphere interactions"
- KISEEVA, K.; VASIUKOV, D.; WOOD, B.; MCCAMMON, C.; STACHEL, T.; CHUMAKOV, A.; DUBROVINSKY, L.: 13.-18.08.2017, Goldschmidt 2017, Paris, France: "Oxidation state of majoritic garnet inclusions in diamond", Goldschmidt Abstracts, 2017, 2038
- KISEEVA, K.; VASIUKOV, D.; WOOD, B.; STACHEL, T.; MCCAMMON, C.; CHUMAKOV, A.; HARRIS, J.; DUBROVINSKY, L.: 18.-22.09.2017, 11<sup>th</sup> International Kimberlite Conference, Gaborone, Botswana: "Oxidation state of majoritic garnet inclusions in diamond"
- KLUMBACH, S.: 10.04.2017, LBEG Meeting, Karlsruhe, Germany (*invited*): "COBRA-Projekt – Speicher richtig verschließen"
- KLUMBACH, S.: 24.-29.09.2017, GeoBremen 2017, Joint Meeting of DGGV and DMG, Bremen, Germany: "Viscoelastic properties of quartz at the alpha-beta phase transition: What we know, what we don't know, and what we could do to broaden our knowledge", Abstract A-763, 2017
- KLUMBACH, S.; Keppler, H.: 24.-29.09.2017, GeoBremen 2017, Joint Meeting of DGGV and DMG, Bremen, Germany: "Electrical conductivity of aqueous HCl solutions at elevated temperature and pressure from impedance measurements in HDAC experiments", Abstract A-313, 2017
- KOROBENNIKOV, I.V.; MOROZOVA, N.V.; SHCHENNIKOV, V.V.; OVSYANNIKOV, S.V.: 19.-24.08.2017, 26<sup>th</sup> AIRAPT International Conference on High Pressure Science and Technology, Beijing, China: "Pressure-driven inversions of the thermopower in germanium", Abstract p. 554

- KUPENKO, I.; SANCHEZ-VALLE, C.; APRILIS, G.; VASIUKOV, D.; BYKOVA, E.; CHARITON, S.; CERANTOLA, V.; BYKOV, M.; MUKHINA, E.; MCCAMMON, C.; CHUMAKOV, A.; DUBROVINSKY, L.: 24.-28.09.2017, HPMPS-9, Saint Malo, France<sup>\*A</sup>: "Electronic configuration and magnetism in FeO at extreme pressure and temperature"
- KURNOSOV, A.; MARQUARDT, H.; FROST, D.; BOFFA BALLARAN, T.; ZIBERNA, L.: 23.-28.04.2017, European Geosciences Union General Assembly 2017, Vienna, Austria: "High-pressure single-crystal elasticity measurements of Al-Fe-bridgmanite", Geophysical Research Abstracts 19, EGU2017-11310-1, 2017
- KURNOSOV, A.; MARQUARDT, H.; BOFFA BALLARAN, T.; FROST, D.J.: 09.11.2017, Universität Münster, Institut für Mineralogie, Münster, Germany: "High-pressure single-crystal elasticity measurements of Al-Fe-bridgmanite support a Fe<sup>3+</sup>-rich pyrolitic lower mantle"
- LAURENZ, V.; ABEYKOON, S.; VOGEL, A.K.; RUBIE, D.C.; FROST, D.J.: 29.05.-03.06.2017, Interdisciplinary Workshop on 'Accretion and Early Differentiation of the Terrestrial Planets', Nice, France: "The effect of sulfur on the behaviour of moderately siderophile elements during core formation"
- LAURENZ, V.; RUBIE, D.C.; FROST, D.J.: 13.-18.08.2017, Goldschmidt 2017, Paris, France (*invited*): "The behavior of Re and Os during sulfide segregation to the Earth's core", Goldschmidt Abstracts, 2017, 2218
- LAURENZ, V.; ABEYKOON, S.; VOGEL, A.K.; RUBIE, D.C.; FROST, D.J.: 24.-29.09.2017, GeoBremen 2017, Joint Meeting of DGGV and DMG, Bremen, Germany: "The effect of sulfur on the partitioning behaviour of moderately siderophile elements"
- LEE, K.; GU, T.; CREAMY, N.; LI, M.; MCCAMMON, C.: 13.-18.08.2017, Goldschmidt 2017, Paris, France (*invited*): "Facilitating atmosphere oxidation through mantle convection", Goldschmidt Abstracts, 2017, 2239
- LEE, K.K.M.; GU, T.; CREAMY, N.; LI, M.; MCCAMMON, C.A.; GIRARD, J.: 11.-15.12.2017, AGU Fall Meeting, New Orleans, USA<sup>\*B</sup>: "Facilitating atmosphere oxidation through mantle convection", Abstract V24C-04, 2017
- LIERMANN, H.-P.; JENEI, Z.; EVANS, W.; KONOPKOVA, Z.; PAKHOMOVA, A.; MARQUARDT, H. (2017): 13.-15.02.2017, PETRA IV Workshop 'Research with High Energy X-Rays at Ultra-Low Emittance Sources', DESY Hamburg, Germany: "Fast compression experiments at ultra-low emittance light sources: Opportunities and limitations"
- LIERMANN, H.-P.; JENEI, Z.; PAKHOMOVA, A.; SAN JOSÉ, A.; KONOPKOVA, Z.; MARQUARDT, H.; WENDT, M.; WENZ, S.; PENNICARD, D.; ROTHKIRCH, A.; MORGENROTH, W.; EVANS, W. (2017): 19.-24.08.2017, 26<sup>th</sup> AIRAPT International Conference on High Pressure Science and Technology, Beijing, China: "Fast diffraction in the dynamic driven diamond anvil cell employing pink beam and fast GaAs lambda detectors at the Extreme Conditions Beamline, PETRA III, DESY", Abstract P191
- LIU, Z.: 03.01.2017, Physics Frontier Seminar, Jilin University, Changchun, P.R. China: "High-pressure advances in a large-volume Kawai-type multi-anvil press and its application in geophysics"

- LIU, Z.: 13.01.2017, Center for High Pressure Science & Technology Advanced Research (HPSTAR), Beijing, P.R. China: "High-pressure advances in a large-volume Kawai-type multi-anvil press and its application in geophysics"
- LV, M.; DORFMAN, S.; LIU, J.; FARMER, A.B.; POTAPKIN, V.; CHUMAKOV, A.I.; MCCAMMON, C.A.; GREENBERG, E.; PRAKAPENKA, V.B.; POPOV, D.: 11.-15.12.2017, AGU Fall Meeting, New Orleans, USA<sup>\*B</sup>: "Experimental insights into spin state and hyperfine parameters of Fe<sup>3+</sup> in bridgmanite and silicate glass up to 91 GPa", Abstract MR54A-02, 2017
- MAEDA, F.; KAMADA, S.; SAKAMAKI, T.; MIYAJIMA, N.; HIRAO, N.; OHISHI, Y.; SUZUKI, A.: 03.-08.09.2017, 55<sup>th</sup> EHPRG Meeting, Poznan, Poland: "Phase relation of MgCO<sub>3</sub> high-pressure carbonate under the deep lower mantle conditions"
- MALLIK, A.: 06.03.2017, Cornell University, Department of Earth and Atmospheric Studies, Ithaca, USA: "Crust-mantle interaction and melting of the Earth's heterogeneous upper mantle"
- MALLIK, A.: 07.03.2017, Cornell University, Department of Earth and Atmospheric Studies, Ithaca, USA: "Nitrogen carrying capacity of slab-derived melts: Implications for deep nitrogen cycling"
- MALLIK, A.: 13.03.2017, University of Toronto, Department of Earth Sciences, Toronto, Canada: "Crust-mantle interaction and melting of the Earth's heterogeneous upper mantle"
- MALLIK, A.: 16.03.2017, University at Buffalo, Department of Earth Sciences, Buffalo, USA: "Crust-mantle interaction and melting of the Earth's heterogeneous upper mantle"
- MALLIK, A.: 04.10.2017, ETH Zurich, Institute of Fluid Dynamics, Zurich, Switzerland: "Evolution of nitrogen in Earth's mantle and atmosphere constrained by recycling in subduction zones"
- MALLIK, A.; EJAZ, T.; SHCHEKA, S.; GARAPIC, G.; PETITGIRARD, S.; BLANCHARD, I.: 11.-15.12.2017, AGU Fall Meeting, New Orleans, USA<sup>\*B</sup>: "The effect of Fe-Ti-rich cumulate overturn on evolution of the Lunar interior", Abstract DI21A-0394, 2017
- MARQUARDT, H.: 17.01.2017, LMU München, Department für Geo- und Umweltwissenschaften, München, Germany: "Experimental exploration of Earth's mantle"
- MARQUARDT, H.: 06.02.2017, University of Oxford, Department of Earth Sciences, Oxford, U.K.: "Experimental exploration of Earth's deep mantle"
- MARQUARDT, H.; SCHULZE, K.; KURNOSOV, A.; BUCHEN, J.; FROST, D.; BOFFA BALLARAN, T.; MARQUARDT, K.; KAWAZOE, T. (2017): 23.-28.04.2017, European Geosciences Union General Assembly 2017, Vienna, Austria (*invited*): "Understanding the Earth's mantle through advanced elasticity measurements", Geophysical Research Abstracts 19, EGU2017-12224, 2017
- MARQUARDT, H.; SCHULZE, K.; KURNOSOV, A.; BOFFA BALLARAN, T.; KAWAZOE, T.; KOCH-MÜLLER, M.: 13.-18.08.2017, Goldschmidt 2017, Paris, France (*invited*): "Comparative Brillouin Spectroscopy Measurements suggest that water may be seismically invisible in Earth's transition zone", Goldschmidt Abstracts, 2017, 2581

- MARQUARDT, H.; KURNOSOV, A.; FROST, D.; BOFFA BALLARAN, T.; ZIBERNA, L.: 24.-28.09.2017, HPMPS-9, Saint Malo, France<sup>\*A</sup> (*invited*): "High-pressure single-crystal elasticity measurements of Al-Fe-bridgmanite up to lower mantle pressures"
- MARQUARDT, H.; KURNOSOV, A.; DUBROVSINKY, L. POTAPKIN, V.: 24.-28.09.2017, HPMPS-9, Saint Malo, France<sup>\*A</sup>: "A waveguide-based exible CO<sub>2</sub> laser heating system"
- MARQUARDT, H.: 04.10.2017, Deutsches Elektronen-Synchrotron DESY, Hamburg, Germany: "Exploring deep Earth properties and processes at the extreme conditions beamline"
- MARQUARDT, K.; DE GRAEF, M.; POLEDNIA, J.; FERREIRA, F.; FAUL, U.; SING, S.; DOHMEN, R.: 13.-18.08.2017, Goldschmidt 2017, Paris, France (*keynote lecture*): "Nm-scale composition determination, quantitative EBSD measurements: Implications of interfaces for bulk rock properties", Goldschmidt Abstracts, 2017, 2582
- MARQUARDT, K.; MARKL, G.: 11.-15.12.2017, AGU Fall Meeting, New Orleans, USA<sup>\*B</sup>: "Inclusions in minerals: The importance of host mineral composition, pressure and temperature for potential inclusion alteration", Abstract V51G-05, 2017
- MARQUARDT, H.; KURNOSOV, A.; FROST, D.; BOFFA BALLARAN, T.; ZIBERNA, L.: 11.-15.12.2017, AGU Fall Meeting, New Orleans, USA<sup>\*B</sup>: "High-pressure single-crystal elasticity measurements of Al-Fe-bridgmanite support a Fe<sup>3+</sup>-rich pyrolitic lower mantle", Abstract MR31A-0428, 2017
- MASOTTA, M.; KEPPLER, H.: 03.-04.09.2017, Geosciences 2017: 'A tool in a changing world', Pisa, Italy: "A new hydrothermal moissanite cell apparatus for optical *in situ* observations at high pressure and high temperature, with applications to bubble nucleation in silicate melts"
- MATSUOKA, M.; NAKAMURA, T.; MIYAJIMA, N.; IMAE, N.; YAMAGUCHI, A.; KOJIMA, H.: 20.-24.03.2017, 48<sup>th</sup> Lunar and Planetary Science Conference, The Woodlands, Houston, USA: "Vis-IR reflectance spectroscopy of hydrous carbonaceous chondrites with variable heating and dehydration degrees"
- MATSUOKA, M.; NAKAMURA, T.; MIYAJIMA, N.; IMAE, N.; YAMAGUCHI, A.; KOJIMA, H.: 04.-08.12.2017, The Eighth Symposium on Polar Science, The National Institute of Polar Research (NIPR), Tokyo, Japan: "Spectral and mineralogical properties of dehydrated carbonaceous chondrite"
- MCCAMMON, C.: 30.01.2017, Tutorial on Nuclear Resonance Techniques, Grenoble, France: "Mössbauer spectroscopy under pressure"
- MCCAMMON, C.: 13.-15.03.2017, MAX IV User Meeting 2017, Lund, Sweden: "A synchrotron journey inside the Earth"
- MCCAMMON, C.; CARACAS, R.: 20.-25.05.2017, JpGU-AGU Joint Meeting, Makuhari, Japan: "What can mineral physics tell us about the origin of ULVZs?"
- MCCAMMON, C.: 28.-30.05.2017, Earth, Sea and Sky II: International Joint Graduate Program Workshop in Earth and Environmental Sciences, Sendai, Japan: "Iron matters and how it affects the Earth's interior"
- MCCAMMON, C.: 03.-08.09.2017, International Conference on the Applications of the Mössbauer Effect, St. Petersburg, Russia: "Small, smaller, smallest"

MCCAMMON, C.; WAN, M.; PEIFFER, S.: 03.-08.09.2017, International Conference on the Applications of the Mössbauer Effect, St. Petersburg, Russia: "Slow mackinawite reaction in aqueous solutions"

MCCAMMON, C.; CARACAS, R.: 24.-29.09.2017, GeoBremen 2017, Joint Meeting of DGGV and DMG, Bremen, Germany: "What is the origin of ULVZs?"

MCCAMMON, C.; WAN, M.; PEIFFER, S.: 24.-29.09.2017, GeoBremen 2017, Joint Meeting of DGGV and DMG, Bremen, Germany: "Slow mackinawite reaction in aqueous solutions: A Mössbauer study"

MCCAMMON, C.: 27.11.2017, Geophysical Laboratory, Washington DC, USA: "Seeking carbon in the deep Earth"

MCCAMMON, C.: 11.-15.12.2017, AGU Fall Meeting, New Orleans, USA<sup>\*B</sup>: "Tiny tiny things with an amazing power", Abstract ED13F-03, 2017

MCCAMMON, C.; CERANTOLA, V.; BYKOVA, E.; KUPENKO, I.; BYKOV, M.; CHUMAKOV, A.; RÜFFER, R.; DUBROVINSKY, L.: 11.-15.12.2017, AGU Fall Meeting, New Orleans, USA<sup>\*B</sup>: "Tracing iron-carbon redox from surface to core", Abstract V24C-05, 2017

MCCAMMON, C.; WINKLER, B.: 23.-25.03.2017, 3<sup>rd</sup> Deep Carbon Observatory International Science Meeting, St. Andrews, U.K.: "Spotlight on carbonates under pressure"

MEIER, T.: 02.02.2017, Universität Ulm, Institut für Mikroelektronik, Ulm, Germany: "High pressure NMR in diamond anvil cells"

MEIER, T.: 13.04.2017, Karlsruhe Institute of Technology, Institute of Microstructure Technology, Karlsruhe, Germany: "New pathways to high pressure NMR in diamond anvil cells"

MEIER, T.; WANG, N.; MAGER, D.; PETITGIRARD, S.; DUBROVINSKY, L.: 02.-06.07.2017, EUROMAR 2017, Warsaw, Poland: "New horizons in high pressure NMR"

MEIER, T.; WANG, N.; MAGER, D.; PETITGIRARD, S.; DUBROVINSKY, L.: 03.-08.09.2017, 55<sup>th</sup> EHPRG Meeting, Poznan, Poland: "New horizons in high pressure NMR"

MEIER, T.; WANG, N.; MAGER, D.; PETITGIRARD, S.; DUBROVINSKY, L.: 30.09.2017, GdCh Fachgruppentreffen FGMR 2017, Bayreuth, Germany: "Journey to the centre of the Earth: Jules Vernes dream in the laboratory/New horizons in high pressure magnetic resonance"

MEIER, T.: 25.10.2017, Universität Bayreuth, Anorganische Chemie III, Bayreuth, Germany: "New frontiers: NMR at GPa pressures in diamond anvil cells"

MEIER, T.: 09.11.2017, Universität Ulm, Institut für Quantenoptik, Ulm, Germany: "New Frontiers: NMR at GPa Pressures in diamond anvil cells"

MIYAJIMA, N.; LI, Y.; SUMITH A.; HEIDELBACH, F.: 24.-29.09.2017, GeoBremen 2017, Joint Meeting of DGGV and DMG, Bremen, Germany: "Imaging dislocations in a natural olivine by electron channeling contrast in a field emission SEM"

MIYAJIMA, N.; LI, Y.; ABEYKOON, S.; HEIDELBACH, F.: 24.-28.09.2017, HPMPS-9, Saint Malo, France<sup>\*A</sup>: "Electron channeling contrast imaging of individual dislocations in geological materials using a field emission scanning electron microscope"

- MORBIDELLI, A.; NESVORNY, D.; LAURENZ, V.; MARCHI, S.; RUBIE, D.C.; ELKINS-TANTON, L.; JACOBSON, S.: 20.-24.03.2017, 48<sup>th</sup> Lunar and Planetary Science Conference, The Woodlands, Houston, USA: "The lunar late heavy bombardment as a tail-end of planet accretion", Abstract 2298
- MORBIDELLI, A.; NESVORNY, D.; LAURENZ, V.; MARCHI, S.; RUBIE, D.C.; ELKINS-TANTON, L.; JACOBSON, S.: 29.05.-03.06.2017, Interdisciplinary Workshop on 'Accretion and Early Differentiation of the Terrestrial Planets', Nice, France: "The lunar late heavy bombardment as a tail end of planet accretion"
- MORBIDELLI, A.; NESVORNY, D.; LAURENZ, V.; MARCHI, S.; RUBIE, D.; ELKINS-TANTON, L.; JACOBSON, S.: 13.-18.08.2017, Goldschmidt 2017, Paris, France: "HSE removal from the Lunar mantle and the timeline of the Lunar bombardment", Goldschmidt Abstracts, 2017, 2793
- MURAKAMI, M.; MASHINO, I.; MIYAJIMA, N.; PETITGIRARD, S.; FROST, D.: 13.-18.08.2017, Goldschmidt 2017, Paris, France (*keynote lecture*): "Mineralogy of the lower mantle: Constraints from elasticity", Goldschmidt Abstracts, 2017, 2844
- NESTOLA, F.; CERANTOLA, V.; MILANI, S.; ANZOLINI, C.; MCCAMMON, C.; NOVELLA, D.; KUPENKO, I.; CHUMAKOV, A.; RUEFFER, R.; HARRIS, J.W.: 23.-28.04.2017, European Geosciences Union General Assembly 2017, Vienna, Austria: "Synchrotron Mössbauer Source technique for *in situ* measurement of iron-bearing inclusions in natural diamonds", Geophysical Research Abstracts 19, EGU2017-16340, 2017
- OHIRA, I.; KAWAZOE, T.; ISHII, T.; BOFFA BALLARAN, T.; MCCAMMON, C.; SUZUKI, A.; OHTANI, E.: 20.-25.05.2017, JpGU-AGU Joint Meeting, Makuhari, Japan: "Single crystal synthesis of  $\delta$ -(Al,Fe)OOH using multi-anvil apparatus"
- OVSYANNIKOV, S.V.; BYKOV, M.; BYKOVA, E.; KOZLENKO, D.P.; TSIRLIN, A.A.; KARKIN, A.E.; SHCHENNIKOV, V.V.; KICHANOV, S.E.; GOU, H.; ABAKUMOV, A.M.; EGOAVIL, R.; VERBEECK, J.; MCCAMMON, C.; DYADKIN, V.; CHERNYSHOV, D.; VAN SMAALEN, S.; DUBROVINSKY, L.S.: 19.-24.08.2017, 26<sup>th</sup> AIRAPT International Conference on High Pressure Science and Technology, Beijing, China: "Charge ordering in Fe<sub>4</sub>O<sub>5</sub>", Abstract p. 443
- OVSYANNIKOV, S.V.; BYKOVA, E.; PAKHOMOVA, A.; KOZLENKO, D.P.; BYKOV, M.; KICHANOV, S.E.; MORZOVA, N.V.; KOROBENIKOV, I.V.; WILHELM, F.; ROGALEV, A.; TSIRLIN, A.A.; KURNOSOV, A.V.; ZAINULIN, Y.G.; KADYROVA, N.I.; TYUTYUNNIK, A.P.; DUBROVINSKY, L.S.: 19.-24.08.2017, 26<sup>th</sup> AIRAPT International Conference on High Pressure Science and Technology, Beijing, China: "Structural and magnetic transitions in CaCo<sub>3</sub>V<sub>4</sub>O<sub>12</sub> double perovskite", Abstract p. 583
- OVSYANNIKOV, S.V.; BYKOV, M.; BYKOVA, E.; KOZLENKO, D.P.; TSIRLIN, A.A.; KARKIN, A.E.; SHCHENNIKOV, V.V.; KICHANOV, S.E.; GOU, H.; ABAKUMOV, A.M.; EGOAVIL, R.; VERBEECK, J.; MCCAMMON, C.; DYADKIN, V.; CHERNYSHOV, D.; VAN SMAALEN, S.; DUBROVINSKY, L.S.: 03.-08.09.2017, 55<sup>th</sup> EHPRG Meeting, Poznan, Poland (*invited*): "Charge ordering in Fe<sub>4</sub>O<sub>5</sub>", Abstract p. 120

- OVSYANNIKOV, S.V.; BYKOVA, E.; PAKHOMOVA, A.; KOZLENKO, D.P.; BYKOV, M.; KICHANOV, S.E.; MOROZOVA, N.V.; KOROBENIKOV, I.V.; WILHELM, F.; ROGALEV, A.; TSIRLIN, A.A.; KURNOSOV, A.V.; ZAINULIN, Y.G.; KADYROVA, N.I.; TYUTYUNNIK, A.P.; DUBROVINSKY, L.S.: 03.-08.09.2017, 55<sup>th</sup> EHPRG Meeting, Poznan, Poland: "Unusual structural transition in CaCo<sub>3</sub>V<sub>4</sub>O<sub>12</sub> double perovskite under high pressure" Abstract, p. 186
- PANOVSKA, S.; FUQUA-HAVILAND, H.; MALLIK, A.; BREMNER, P.M.; MCDONOUGH, W.F.; CIDER2014 LUNAR GROUP: 11.-15.12.2017, AGU Fall Meeting, New Orleans, USA<sup>\*B</sup>: "Thermal profile of the Lunar interior constrained by revised estimates of concentrations of heat producing elements", Abstract DI21A-0393, 2017
- PETITGIRARD, S.; MALFAIT, W.; KUPENKO, I.; SAHLE, C.; SPIEKERMANN, G.; WEIS, C.; STERNEMANN, C.; SINMYO, R.; HENNET, L.; WILKE, M.; RUBIE, D.: 13.-18.08.2017, Goldschmidt 2017, Paris, France: "Density and structure of amorphous silicate at high pressure conditions", Goldschmidt Abstracts, 2017, 3138
- PETITGIRARD, S.; MALFAIT, W.; KUPENKO, I.; SAHLE, C.; COLLINGS, I.; WEIS, C.; SPIEKERMANN, G.; SINMYO, R.; JENNINGS, E.; BLANCHARD, I.; STERNEMANN, C.; WILKE, M.; RUBIE, D.: 24.-28.09.2017, HPMP5-9, Saint Malo, France<sup>\*A</sup>: "Density and structure of amorphous silicates at high pressure conditions"
- POLEDNIA, J.; MARQUARDT, K.; DOHMEN, R.: 13.-18.08.2017, Goldschmidt 2017, Paris, France: "Grain boundary diffusion and its relation to grain boundary segregation of multiple elements in garnet", Goldschmidt Abstracts, 2017, 3188
- POSNER, E.; RUBIE, D.C.; STEINLE-NEUMANN, G.; FROST, D.J.: 11.-15.12.2017, AGU Fall Meeting, New Orleans, USA<sup>\*B</sup> (*invited*): "Diffusive transport and structural properties of liquid iron alloys at high pressure", Abstract MR24A-02, 2017
- RAI, N.; PERRILLAT, J.-P.; MEZOUAR, M.; COLIN, A.; PETITGIRARD, S.; VAN WESTRENNEN, W.: 13.-18.08.2017, Goldschmidt 2017, Paris, France: "*In situ* viscometry of primitive Lunar magmas at high pressure and high temperature", Goldschmidt Abstracts, 2017, 3264
- ROZEL, A.; GOLABEK, G.; GERYA, T.; JAIN, C.; TACKLEY, P.: 13.-18.08.2017, Goldschmidt 2017, Paris, France: "Generation of Archean TTG rocks: Numerical simulations of thermo-compositional mantle convection", Goldschmidt Abstracts, 2017, 3427
- RUBIE, D.C.; JENNINGS, E.S.; JACOBSON, S.A.; MORBIDELLI, A.; ARMSTRONG, K.; FROST, D.J.: 29.05.-03.06.2017, Interdisciplinary Workshop on 'Accretion and Early Differentiation of the Terrestrial Planets', Nice, France: "The sequestration of tungsten into Earth's core during planetary accretion"
- SCHULZE, K.; MARQUARDT, H.; KAWAZOE, T.; KOCH-MÜLLER, M.; KURNOSOV, A.; BOFFA BALLARAN, T.: 14.-15.09.2017, IRTG Doctoral Seminar, Bayreuth, Germany: "Elastic properties of ringwoodite and the effect of hydration at transition zone pressures"
- SCHULZE, K.; MARQUARDT, H.; KURNOSOV, A.; KAWAZOE, T.; BOFFA BALLARAN, T.: 24.-28.09.2017, HPMP5-9, Saint Malo, France<sup>\*A</sup>: "The effect of hydration on the elastic properties of ringwoodite at transition zone pressures"

- SCHULZE, K.; MARQUARDT, H.; BOFFA BALLARAN, T.; KURNOSOV, A.; KAWAZOE, T.; KOCH-MÜLLER, M.: 11.-15.12.2017, AGU Fall Meeting, New Orleans, USA<sup>\*B</sup>: "Small effect of hydration on elastic wave velocities of ringwoodite in Earth's transition zone", Abstract MR43A-0459, 2017
- SIERSCH, N.; BOFFA BALLARAN, T.; LIU, Z.; ISHII, T.; YU, T.; WANG, Y.; FROST, D.: 24.-28.09.2017, HPMP5-9, Saint Malo, France<sup>\*A</sup>: "Elastic wave velocities of Fe- and Al-bearing akimotoite by means of ultrasonic measurements"
- SINMYO, R.; NAKAJIMA, Y.; MCCAMMON, C.; MIYAJIMA, N.; PETITGIRARD, S.; MYHILL, R.; FROST, D.: 13.-18.08.2017, Goldschmidt 2017, Paris, France: "Effect of Fe<sup>3+</sup> on the subsolidus and melting phase relations under lower mantle conditions", Goldschmidt Abstracts, 2017, 3664
- SMYTH, J.; KAWAZOE, T.; ZHANG, L.: 13.-18.08.2017, Goldschmidt 2017, Paris, France: "Elusive fourth polymorph of olivine", Goldschmidt Abstracts, 2017, 3697
- SPIVAK, A.; LITVIN, Y.; DUBROVINSKY, L.: 13.-18.08.2017, Goldschmidt 2017, Paris, France: "Evolution of the lower mantle magma and diamond-forming melts (experiment at 24-26 GPa)", Goldschmidt Abstracts, 2017, 3738
- STAGNO, V.; MCCAMMON, C.A.; CERANTOLA, V.; ANDREOZZI, G.B.; CARUSO, M.; ARIMOTO, T.; IRIFUNE, T. (*invited*): 13.-18.08.2017, Goldschmidt 2017, Paris, France: "Do Fe-bearing minerals control the deep carbon cycle in the interior of the Earth?", Goldschmidt Abstracts, 2017, 3750
- STEINLE-NEUMANN, G.; POSNER, E.; RUBIE, D.; FROST, D.; VLCEK, V.: 24.-28.09.2017, HPMP5-9, Saint Malo, France<sup>\*A</sup>: "Light element diffusion in liquid Fe for P-T conditions of the Earth's interior"
- STEINLE-NEUMANN, G.; POSNER, E.; RUBIE, D.; FROST, D.; VLČEK, V.: 04.-06.10.2017, 6<sup>th</sup> Joint Workshop on High Pressure, Planetary and Plasma Physics, Göttingen, Germany: "Light element diffusion in liquid Fe for P-T conditions of the Earth's interior"
- STEKIEL, M.; NGUYEN-THANH, T.; CHARITON, S.; MCCAMMON, C.; BOSAK, A.; LUCHITSKAIA, R.; REFSON, K.; MILMAN, V.; WINKLER, B.: 27.-30.03.2017, 25<sup>th</sup> Annual Conference of the German Crystallographic Society, Karlsruhe, Germany: "High pressure elastic properties of FeCO<sub>3</sub> and MgCO<sub>3</sub>"
- STEKIEL, M.; NGUYEN-THANH, T.; CHARITON, S.; MCCAMMON, C.; BOSAK, A.; MORGENROTH, W.; LUCHITSKAIA, R.; MILMAN, V.; REFSON, K.; WINKLER, B.: 19.-24.08.2017, 26<sup>th</sup> AIRAPT International Conference on High Pressure Science and Technology, Beijing, China: "High pressure elasticity of FeCO<sub>3</sub>-MgCO<sub>3</sub> carbonates"
- STEKIEL, M.; NGUYEN-THANH, T.; CHARITON, S.; MCCAMMON, C.; BOSAK, A.; MORGENROTH, W.; LUCHITSKAIA, R.; MILMAN, V.; REFSON, K.; WINKLER, B.: 03.-08.09.2017, 55<sup>th</sup> EHPRG Meeting, Poznan, Poland: "Pressure elasticity of FeCO<sub>3</sub>-MgCO<sub>3</sub> carbonates"
- THIELMANN, M.; ROZEL, A.; KAUS, B.; RICARD, Y.: 27.-30.03.2017, 77. Jahrestagung der Deutschen Geophysikalischen Gesellschaft, Potsdam, Germany "Grain size assisted thermal runaway: A mechanism to generate intermediate-depth earthquakes and ductile shear zones"

- THIELMANN, M.: 23.-28.04.2017, European Geosciences Union General Assembly 2017, Vienna, Austria: "Impact of different weakening parameterizations on crust and lithosphere deformation", Geophysical Research Abstracts 19, EGU2017-18329, 2017
- THIELMANN, M.; ROZEL, A.; KAUS, B.; RICARD, Y.: 23.-28.04.2017, European Geosciences Union General Assembly 2017, Vienna, Austria: "Grain size assisted thermal runaway: a mechanism to generate intermediate-depth earthquakes and ductile shear zones", Geophysical Research Abstracts 19, EGU2017-14219, 2017
- THIELMANN, M.; DABROWSKI, M.: 27.-31.08.2017, 15<sup>th</sup> International Workshop on Modelling of Mantle and Lithosphere Dynamics, Putten, The Netherlands: "Towards modeling of magma mixing and mingling due to particle/bubble segregation"
- THIELMANN, M.: 09.-13.10.2017, 4. Central European Geomorphology Conference, Bayreuth, Germany: "Latest developments in Earth dynamics models and their impact on surface processes"
- THIELMANN, M.; DURETZ, T.: 11.-15.12.2017, AGU Fall Meeting, New Orleans, USA<sup>\*B</sup>: "Earthquakes below the brittle-ductile transition: The role of grain size assisted thermal runaway", Abstract T11E-01, 2017
- UENVER-THIELE, L.; WOODLAND, A.; BOFFA BALLARAN, T.; MIYAJIMA, N.; FROST, D.J.: 24.-29.09.2017, GeoBremen 2017, Joint Meeting of DGGV and DMG, Bremen, Germany: "New hp-phases of Fe-Mg spinels: Implications for the formation and uplift history of inclusions in diamonds"
- VELICOGNA, M.; DE MIN, A.; ZIBERNA, L.; MARZOLI, A.; CHIARADIA, M.; ALBERTI, A.: 03.-06.09.2017, 'Geosciences – A tool in a changing world', Pisa, Italy: "Triassic magmatism in eastern Alps"
- WAGLE, F.; STEINLE-NEUMANN, G.: 24.-28.09.2017, HPMP-9, Saint Malo, France<sup>\*A</sup>: "Electrical resistivity of liquid iron with high concentration of light element impurities"
- WAGLE, F.; STEINLE-NEUMANN, G.: 04.-06.10.2017, 6<sup>th</sup> Joint Workshop on High Pressure, Planetary and Plasma Physics, Göttingen, Germany: "Electrical resistivity of liquid iron with high concentration of light element impurities"
- WAGLE, F.; STEINLE-NEUMANN, G.: 11.-15.12.2017, AGU Fall Meeting, New Orleans, USA<sup>\*B</sup>: "Electrical resistivity of liquid iron with high concentration of light element impurities", Abstract MR31A-0437, 2017
- WEI, Q.; GILDER, S.A.; MCCAMMON, C.: 23.-28.04.2017, European Geosciences Union General Assembly 2017, Vienna, Austria: "Magnetism of Fe under pressure from SQUID magnetometer and Mössbauer spectrometer measurements", Geophysical Research Abstracts 19, EGU2017-2105-2, 2017
- YAO, J.; STEINLE-NEUMANN, G.: 29.-31.03.2017, Second General Meeting DFG SPP 1833 'Building a Habitable Earth', Jena, Germany: "Liquid and glass structure of Mg<sub>2</sub>SiO<sub>4</sub> and MgSiO<sub>3</sub> at high pressure"
- ZHANG, S.; RUDNICK, R.; MCCAMMON, C.: 18.-22.09.2017, 11<sup>th</sup> International Kimberlite Conference, Gaborone, Botswana: "Oxidation of lithospheric mantle beneath Tanzania by melt reaction"
- ZIBERNA, L.; GREEN, E.C.; BLUNDY, J.D.: 13.-18.08.2017, Goldschmidt 2017, Paris, France: "Geobarometers for igneous rocks with ±1.0 kbar uncertainty?", Goldschmidt Abstracts, 2017, 4536

ZIBERNA, L.; BLUNDY, J.D.: 03.-06.09.2017, 'Geosciences – A tool in a changing world', Pisa, Italy (*keynote lecture*): "The depth of igneous cumulates in the Lesser Antilles island arc"

\*A **High-Pressure Mineral Physics Seminar (HPMPS-9), 24.-28.09.2017, Saint Malo, France**

\*B **AGU: American Geophysical Union Fall Meeting, 11.-15.12.2017, New Orleans, USA**

#### *5.4 Lectures and seminars at Bayerisches Geoinstitut*

ADAMS, Andrea, Bayerisches Geoinstitut, Bayreuth, Germany: "Viability of Archean subduction initiation from continental spreading and plume-continent interactions", 07.03.2017

ARATÓ, Robert, Bayerisches Geoinstitut, Bayreuth, Germany: "New ways to reconstruct magmatic oxygen fugacity", 20.07.2017

AUDÉTAT, Andreas, Bayerisches Geoinstitut, Bayreuth, Germany: "Development of new oxybarometers for mafic to felsic magmas", *Academy Commission Business Meeting*, 04.05.2017

BOLLINGER, Caroline, Bayerisches Geoinstitut, Bayreuth, Germany: "Rheology of forsterite: Crystal slip plasticity vs. grain boundary sliding", 26.10.2017

BONEH, Yuval, Washington University in St. Louis, Earth and Planetary Sciences, St. Louis, USA: "Evolution of olivine crystallographic preferred orientation and anisotropy in the upper mantle", 30.05.2017

BOWER, Dan, Universität Bern, Center for Space and Habitability (CSH), Bern, Switzerland: "Evolution of terrestrial planets from molten to solid", 09.11.2017

BYRNE, James, Universität Tübingen, Angewandte Geowissenschaften, Tübingen, Germany: "Iron biomineralization by bacteria: Insights into the past and uses for the future", 02.03.2017

CHANYCHEV, Artem, Sobolev Institute of Geology and Mineralogy, Novosibirsk, Russia: "High-pressure study of carbon-rich volatiles: from deep fluids to meteorites", 07.11.2017

CORDIER, Patrick, Université Lille 1, UMET - Unité Matériaux et Transformation, CNRS, Villeneuve d'Ascq, France: "Rheology of the deep mantle: new insights from numerical modeling", 27.04.2017

CRAMERI, Fabio, University of Oslo, Department of Geosciences, Oslo, Norway: "The interplay between subducting plates, surface topography, and ... rainbows", 08.06.2017

D'SOUZA, Rameses, University of Victoria, School of Earth and Ocean Sciences, Victoria, Australia: "Enriching arcs: moving S and chalcophile elements in fluids and alkalic melts", 22.08.2017

DURETZ, Thibault, Université de Rennes, Géosciences, Rennes, France: "Modeling the deformation of heterogeneous lithosphere: insights into rifting dynamics", 02.11.2017

FÖRSTER, Michael, Macquarie University, Department of Earth and Planetary Sciences, Sydney, Australia: "The behaviour of nitrogen during subduction-zone metamorphism", 24.08.2017

- GALVEZ, Matthieu, ETH Zurich, Institute of Geochemistry and Petrology, Zurich, Switzerland: "Top-down geochemistry: Carbon and hot fluids in subduction zones", 22.06.2017
- GREEN, Eleanor, ETH Zurich, Institute of Geochemistry and Petrology, Zurich, Switzerland: "Thermodynamic modelling of silicate liquids and more exotic fluids", 05.10.2017
- GUO, Haihao, Bayerisches Geoinstitut, Bayreuth, Germany: "An experimental study on volatiles and metals in fluids of magma chambers and porphyry ore deposits", 13.07.2017
- JACKSON, Ian, The Australian National University, Research School of Earth Sciences, Canberra, Australia: "A laboratory-based framework for the interpretation of seismological models", 02.05.2017
- JUTZI, Martin, Universität Bern, Space Research & Planetary Sciences, Bern, Switzerland: "The shapes and structures of cometary nuclei as probes of the conditions in the early solar system", 23.03.2017
- KATZ, Richard, University of Oxford, Department of Earth Sciences, Oxford, U.K.: "Squeezing water (and carbon) from a stone: Volatile-enriched magmatism at mid-ocean ridges", 18.05.2017
- KLUMBACH, Steffen, Bayerisches Geoinstitut, Bayreuth, Germany: "Viscoelastic properties of quartz: A high temperature study crossing the alpha-beta phase transition", 19.10.2017
- KUTZSCHBACH, Martin, Technische Universität Berlin, Institut für Angewandte Geowissenschaften, Berlin, Germany: "Tetrahedral boron in tourmaline: Improving tourmaline as a petrogenetic indicator", 21.12.2017
- LIU, Zhaodong, Bayerisches Geoinstitut, Bayreuth, Germany: "Phase relations in the system MgO–SiO<sub>2</sub>–Al<sub>2</sub>O<sub>3</sub> up to 50 GPa and Al substitution in bridgmanite", 20.03.2017
- MARQUARDT, Hauke, Bayerisches Geoinstitut, Bayreuth, Germany: "Insights into the nature of Earth's mantle from elasticity and rheology measurements", 06.03.2017
- MARQUARDT, Katharina, Bayerisches Geoinstitut, Bayreuth, Germany: "nm-scale properties & the grain boundary character distribution of olivine", 29.03.2017
- MELAI, Caterina, Bayerisches Geoinstitut, Bayreuth, Germany: "High pressure behaviour of magnetite-magnesioferrite solid solution", 03.08.2017
- POSNER, Esther, Bayerisches Geoinstitut, Bayreuth, Germany: "Mass transport and structural properties of liquid iron alloys at high pressure", 12.01.2017
- ROTTIER, Bertrand, University of Geneva, Section of Earth and Environmental Sciences, Geneva, Switzerland: "How magmatic-hydrothermal system control the metal budget of porphyry-epithermal ore deposits", 16.02.2017
- SAKI, Morvarid, Westfälische Wilhelms-Universität Münster, Institut für Geophysik, Münster, Germany: "Detailed investigation of upper mantle seismic discontinuities beneath the Northern Atlantic", 31.08.2017
- SHIMOYAMA, Yuta, Osaka University, Department of Earth and Space Science, Osaka, Japan: "Thermoelastic properties of iron-carbide and carbonate melts under high pressure: Implication for carbon in the Earth's and lunar interiors", 28.03.2017
- THIELMANN, Marcel, Bayerisches Geoinstitut, Bayreuth, Germany: "Numerical modelling of the temperature distribution in encapsulated DAC experiments", 19.01.2017

- TOSI, Nicola, Technische Universität Berlin, Zentrum für Astronomie und Astrophysik, Berlin, Germany: "Solid-state convection during magma ocean solidification", 23.11.2017
- WANG, Lin, Bayerisches Geoinstitut, Bayreuth, Germany: "Soft asthenosphere indicated by glide controlled deformation mechanism in olivine", 16.11.2017
- XIE, Longjian, Okayama University, Institute for Planetary Materials, Misasa, Japan: "Viscosity measurement of silicate melt up to the lower mantle conditions by *in situ* falling sphere method", 06.12.2017
- XU, Fang, Okayama University, Department of Experimental Planetary Physics, Tottori, Japan: "Deformation of deep mantle minerals", 28.03.2017
- YONEDA, Akira, Okayama University, Institute for Planetary Materials, Misasa, Japan: "Single crystal elasticity of gold, platinum, and bridgmanite under high pressure by inelastic X-ray scattering", 07.12.2017
- YOSHIOKA, Takahiro, Bayerisches Geoinstitut, Bayreuth, Germany: "Nitrogen solubility in transition zone and lower mantle minerals", *Academy Commission Business Meeting*, 04.05.2017
- ZAREI, Alireza, Bayerisches Geoinstitut, Bayreuth, Germany: "On the feasibility of measuring hydrogen isotope fractionation by *in situ* Raman spectroscopy", 20.09.2017

### 5.5 Conference organization

- 01.-05.05.2017, International Continental Drilling Program (ICDP) workshop "Drilling the continental crust to the Moho transition zone (Ivrea-Verbano zone, Italy)", Baveno, Italy (L. ZIBERNA, M. PISTONE, A. ZANETTI, O. MÜNTENER)
- 20.-25.05.2017, Japan Geoscience Union-American Geophysical Union Joint Meeting 2017, Makuhari, Japan: Session S-IT26: Fluid-mediated processes and properties near convergent plate boundaries (B. MYSEN, E. OHTANI, H. IWAMORI, C. MCCAMMON)
- 29.05.-03.06.2017, Interdisciplinary Workshop on "Accretion and Early Differentiation of the Terrestrial Planets", Nice, France (D.C. RUBIE, A. MORBIDELLI)
- 17.-22.09.2017, European Planetary Science Congress 2017, 'General planetary dynamics', Riga, Latvia (G. GOLABEK)
- 18.-22.09.2017, PhD short course "Mineralogy, mineral physics and seismology of Earth's mantle", Bayreuth, Germany (H. MARQUARDT)
- 24.-29.09.2017, GeoBremen 2017, Joint Meeting of DGGV and DMG, Bremen, Germany: Session 2.4: "Compositional evolution, dynamics and physical properties of Earth's mantle" (S. SPEZIALE, A. STRACKE, H. MARQUARDT, D. FROST)
- 20.11.2017, Workshop "Mantle Dynamics and Deep Earth Material Cycles", BAfW, München, Germany (H. MARQUARDT)
- 11.-15.12.2017, American Geophysical Union Fall Meeting, New Orleans, USA: Session DI51A: "Interdisciplinary perspectives on mantle melting and volcanism" (J. DANNBERG, Z. EILON, J. LIU, A. MALLIK)
- 11.-15.12.2017, American Geophysical Union Fall Meeting, New Orleans, USA: Session MR24A: "Elastic and Transport Properties of Core and Mantle Materials" (J. LIU, H. MARQUARDT, S. STACKHOUSE, M. MOOKHERJEE)

## 6. Visiting scientists

### *6.1 Visiting scientists funded by the Bayerisches Geoinstitut*

- BONATI, Irene, ETH Zurich, Switzerland: 03.-04.07.2017
- BONEH, Yuval, Washington University in St. Louis, Earth and Planetary Sciences, St. Louis, USA: 23.05.-01.06.2017
- BOWER, Dan, Universität Bern, Center for Space and Habitability (CSH), Bern, Switzerland: 08.-10.11.2017
- BYRNE, James, Universität Tübingen, Angewandte Geowissenschaften, Tübingen, Germany: 02.-03.03.2017
- CHEN, Qi, University of Science and Technology of China, School of Earth and Space Sciences, Hefei, P.R. China: 19.-24.03.2017
- CIALDELLA, Laura, Università degli Studi di Padova, Dipartimento di Geoscienze, Padova, Italy: 26.06.-31.08.2017
- CRAMERI, Fabio, University of Oslo, Department of Geosciences, Oslo, Norway: 07.-09.06.2017
- DOLEJŠ, David, Universität Freiberg, Institut für Geo- und Umweltwissenschaften, Freiberg, Germany: 20.-24.02.2017, 05.-06.04.2017
- DURETZ, Thibault, Université de Rennes, Géosciences, Rennes, France: 30.10.-03.11.2017
- FEDOTENKO, Timofey, Novosibirsk State University, Novosibirsk, Russia: 06.-10.02.2017
- JACKSON, Ian, The Australian National University, Research School of Earth Sciences, Canberra, Australia: 01.-03.05.2017
- JUTZI, Martin, Universität Bern, Space Research & Planetary Sciences, Bern, Switzerland: 22.-24.03.2017
- KATZ, Richard, University of Oxford, Department of Earth Sciences, Oxford, U.K.: 17.-19.05.2017
- KHANDARKHAEVA, Saiana, Novosibirsk State University, Novosibirsk, Russia: 06.-10.02.2017
- KUTZSCHBACH, Martin, Technische Universität Berlin, Institut für Angewandte Geowissenschaften, Berlin, Germany: 20.-22.12.2017
- MASOTTA, Matteo, Università di Pisa, Dipartimento di Scienze della Terra, Pisa, Italy: 18.-26.02.2017
- ROTTIER, Bertrand, University of Geneva, Section of Earth and Environmental Sciences, Geneva, Switzerland: 15.-17.02.2017
- SCHWARZ, Marcus, TU Bergakademie Freiberg, Institut für Anorganische Chemie, Freiberg, Germany: 20.-25.02.2017
- SHIMOYAMA, Yuta, Osaka University, Department of Earth and Space Science, Osaka, Japan: 27.-29.03.2017
- SILVA SOUZA, Danielle, Universidade Federal de Ouro Preto, Brazil: 19.01.-17.03.2017
- THOMAS, Christine, Westfälische Wilhelms-Universität Münster, Institut für Geophysik, Münster, Germany: 05.-06.03.2017
- TOSI, Nicola, Technische Universität Berlin, Zentrum für Astronomie und Astrophysik, Berlin, Germany: 22.-24.11.2017

WU, Lei, Chinese Academy of Sciences, Institute of Geochemistry, Guiyang, P.R. China: 30.05.-03.06.2017  
XIE, Longjian, Okayama University, Institute for Planetary Materials, Misasa, Japan: 05.-08.12.2017  
XU, Fang, Okayama University, Department of Experimental Planetary Physics, Tottori, Japan: 27.-29.03.2017  
YONEDA, Akira, Okayama University, Institute for Planetary Materials, Misasa, Japan: 05.-08.12.2017

### *6.2 Visiting scientists supported by other externally funded BGI projects*

BARTENSTEIN, Alexander, Johann Wolfgang Goethe-Universität, Frankfurt/Main, Germany: 22.-23.01.2017 (IRTG<sup>\*C</sup>)  
BONDAR, Dmitry, Moscow State University, Department of Igneous Petrology, Moscow, Russia: 17.-20.09.2017 (IRTG<sup>\*C</sup>)  
CARTIGNY, Pierre, Institut de Physique du Globe de Paris, France: 14.-15.09.2017 (IRTG<sup>\*C</sup>)  
CHANY SHEV, Artem, Sobolev Institute of Geology and Mineralogy, Novosibirsk, Russia: 05.-10.11.2017 (IRTG<sup>\*C</sup>)  
COBDEN, Laura, University of Utrecht, Faculty of Geosciences, Utrecht, The Netherlands: 20.-22.09.2017 (DFG<sup>\*B</sup>)  
D'SOUZA, Rameses, University of Victoria, School of Earth and Ocean Sciences, Victoria, Australia: 20.-24.08.2017 (IRTG<sup>\*C</sup>)  
EBERHARD, Lisa, University of Bern, Switzerland: 22.-23.01.2017 (IRTG<sup>\*C</sup>)  
GREEN, Eleanor, ETH Zurich, Institute of Geochemistry and Petrology, Zurich, Switzerland: 02.-06.10.2017 (IRTG<sup>\*C</sup>)  
HECKMANN, Paul, Georg-August-Universität Göttingen, Germany: 21.-22.03.2017 (DFG<sup>\*B</sup>)  
GALVEZ, Matthieu, ETH Zurich, Institute of Geochemistry and Petrology, Zurich, Switzerland: 21.-23.06.2017 (IRTG<sup>\*C</sup>)  
HERNLUND, Christine, Tokyo Institute of Technology, Earth-Life Science Institute, Tokyo, Japan: 07.-22.09.2017 (IRTG<sup>\*C</sup>)  
HERNLUND, John, Tokyo Institute of Technology, Earth-Life Science Institute, Tokyo, Japan: 07.-22.09.2017 (IRTG<sup>\*C</sup>)  
MARZOTTO, Enrico, Università degli Studi di Padova, Dipartimento di Geoscienze, Padova, Italy: 11.-13.09.2017 (IRTG<sup>\*C</sup>)  
PU, Chang, Chinese Academy of Sciences, Institute of Geochemistry, Guiyang, P.R. China: 16.-22.09.2017 (IRTG<sup>\*C</sup>)  
PUTAK JURIČEK, Marija, University of Zagreb, Croatia: 10.-12.01.2017 (IRTG<sup>\*C</sup>)  
SAN JOSÉ MÉNDEZ, Alba, Centro de Astrobiología, Madrid, Spain: 21.-22.03.2017 (DFG<sup>\*B</sup>)  
SAKI, Morvarid, Westfälische Wilhelms-Universität Münster, Institut für Geophysik, Münster, Germany: 29.08.-01.09.2017 (DFG<sup>\*B</sup>)

SATTA, Niccolò, Sapienza – Università di Roma, Dipartimento di Scienze della Terra, Roma, Italy: 27.-29.03.2017 (IRTG<sup>\*C</sup>)

SCHÖLMERICH, Markus, Johann Wolfgang Goethe-Universität, Frankfurt/Main, Germany: 22.03.2017 (DFG<sup>\*B</sup>)

SMYTH, Joseph R., University of Colorado at Boulder, Department of Geological Sciences, Boulder, USA: 17.-30.09.2017 (DFG<sup>\*B</sup>)

THOMAS, Christine, Westfälische Wilhelms-Universität Münster, Institut für Geophysik, Münster, Germany: 17.-20.09.2017 (DFG<sup>\*B</sup>)

WALTE, Nico, TU München, Forschungs-Neutronenquelle Heinz Maier-Leibnitz (FRM II), Garching, Germany: 04.-05.05.2017, 18.-20.10.2017, 25.-26.10.2017, 29.11.-01.12.2017 (BMBF<sup>\*A</sup>)

<sup>\*A</sup>) **BMBF: Bundesministerium für Bildung und Forschung**

<sup>\*B</sup>) **DFG: Deutsche Forschungsgemeinschaft**

<sup>\*C</sup>) **IRTG: International Research Training Group "Deep Earth Volatile Cycles" (DFG)**

### *6.3 Visiting scientists supported by the DFG Core Facility programme*

BEYER, Christopher, Ruhr-Universität Bochum, Institut für Geologie, Mineralogie und Geophysik, Bochum, Germany: 21.-28.04.2017

MATJUSCHKIN, Vladimir, Johann Wolfgang Goethe-Universität, Physikalisch-Chemische Mineralogie, Frankfurt/M., Germany: 21.-28.11.2017

MYHILL, Robert, University of Bristol, School of Earth Sciences, Bristol, U.K.: 21.-28.04.2017

NEAVE, David, Leibniz Universität Hannover, Institut für Mineralogie, Hannover, Germany: 19.-27.07.2017

UENVER-THIELE, Laura, Johann Wolfgang Goethe-Universität, Physikalisch-Chemische Mineralogie, Frankfurt/M., Germany: 21.-25.11.2017

### *6.4 Visitors (externally funded)*

ANDO, Junichi, Hiroshima University, Department of Earth and Planetary Systems Science, Hiroshima, Japan: 06.-09.01.2017

ANZOLINI, Chiara, Università degli Studi di Padova, Dipartimento di Geoscienze, Padova, Italy: 06.-26.11.2017

ARAYA, Naoki, Tohoku University, Graduate School of Science, Department of Earth Science, Sendai, Japan: 05.-10.06.2017, 17.-23.06.2017, 11.-30.09.2017

BEYER, Christopher, Ruhr-Universität Bochum, Institut für Geologie, Mineralogie und Geophysik, Bochum, Germany: 29.05.-02.06.2017

BRAUN, Johannes, Helmholtz-Zentrum Dresden-Rossendorf, Germany: 14.12.2017

BUREAU, H el ene, Institut de min eralogie, de physique des mat eriaux et de cosmochimie (IMPMC), Paris, France: 04.-11.12.2017

CHOBAL, Oleksandr, Uzhhorod National University, Uzhhorod, Ukraine: 01.07.-06.09.2017

CORDIER, Patrick, Universit e Lille 1, UMET - Unit e Mat eriaux et Transformation, CNRS, Villeneuve d'Ascq, France: 25.-28.04.2017

DOBSON, David, University College London, Department of Earth Sciences, London, U.K.: 16.-22.01.2017

DOMINIJANNI, Serena, Sapienza – Universit a di Roma, Dipartimento di Scienze della Terra, Roma, Italy: 17.07.-25.09.2017

DU, Jingguo, China University of Geosciences, Department of Earth Sciences and Resources, Beijing, P.R. China: 10.09.-31.12.2017

DURAND, Stephanie, Westf alische Wilhelms-Universit at M unster, Institut f ur Geophysik, M unster, Germany: 20.-22.09.2017

FARMER, Nicholas, Australian National University, Research School of Earth Sciences, Canberra, Australia: 04.09.-30.10.2017

F ORSTER, Michael, Macquarie University, Department of Earth and Planetary Sciences, Sydney, Australia: 23.-25.08.2017

FUJITA, Wakana, Tohoku University, Division of Earth and Planetary Materials Science, Sendai, Japan: 10.-18.09.2017, 13.10.-31.12.2017

GOTO, Ken-ichi, Tohoku University, Department of Earth Science, Sendai, Japan: 20.-31.12.2017

HIRANO, Naoto, Tohoku University, Center for Northeast Asian Studies, Sendai, Japan: 14.-18.03.2017

HUANG, Yongsheng, Tohoku University, Division of Earth and Planetary Materials Science, Sendai, Japan: 19.02.-15.03.2017, 30.08.-21.11.2017

ISKRINA, Anastasiya, Lomonosov Moscow State University, Moscow, Russia: 17.07.-22.08.2017

KEIM, Max, Eberhard Karls Universit at T ubingen, Petrologie und Mineralische Rohstoffe, T ubingen, Germany: 27.11.-01.12.2017

KUDRYAVTSEV, Daniil, Gubkin Russian State University of Oil and Gas, Moscow, Russia: 02.03.-31.03.2017

LEIBNER, Lisa, TU Bergakademie Freiberg, Institut f ur Anorganische Chemie, Freiberg, Germany: 19.-25.03.2017

LI, Wancai, University of Science and Technology of China, Department of Geophysics and Planetary Sciences, Hefei, P.R. China: 01.08.-28.10.2017

LI, Yuan, Chinese Academy of Sciences, Guangzhou Institute of Geochemistry, Guangzhou, P.R. China: 19.-23.08.2017

LICHTENBERG, Tim, ETH Zurich, Institute of Geophysics, Zurich, Switzerland: 16.-19.05.2017

LIMANOV, Evgeny, Institute of Experimental Mineralogy, Chernogolovka, Moscow region, Russia: 18.02.-04.03.2017

MAEDA, Fumiya, Tohoku University, Division of Earth and Planetary Materials Science, Sendai, Japan: 09.-28.02.2017, 28.08.-02.09.2017, 09.09.-12.10.2017

MATSUOKA, Moe, Tohoku University, Division of Earth and Planetary Materials Science, Sendai, Japan: 09.01.-06.02.2017, 19.06.-25.07.2017

MEUSBURGER, Johannes, Universität Wien, Institut für Mineralogie und Kristallographie, Wien, Austria: 14.06.-21.07.2017

MIYAGI, Lowell, University of Utah, Department of Geology & Geophysics, Salt Lake City, USA: 18.-21.11.2017

NAKAJIMA, Ayano, Tohoku University, Department of Earth Science, Sendai, Japan: 20.08.-02.09.2017

NAKAMURA, Michihiko, Tohoku University, Graduate School of Science, Department of Earth Science, Sendai, Japan: 23.-29.03.2017, 05.-10.06.2017, 17.-23.06.2017, 13.-20.09.2017

NAKATANI, Takayuki, Tohoku University, Division of Earth and Planetary Materials Science, Sendai, Japan: 19.02.-15.03.2017

OHIRA, Itaru, Tohoku University, Division of Earth and Planetary Materials Science, Sendai, Japan: 28.08.-02.09.2017, 09.-24.09.2017

OKUMURA, Satoshi, Tohoku University, Graduate School of Science, Department of Earth Science, Sendai, Japan: 23.03.-04.04.2017, 05.-10.06.2017

PAMATO, Martha, University College London, Department of Earth Sciences, London, U.K.: 16.-22.01.2017

PASHKIN, Oleksiy, Helmholtz-Zentrum Dresden-Rossendorf, Germany: 14.12.2017

PRESCHER, Clemens, Universität zu Köln, Institut für Geologie und Mineralogie, Köln, Germany: 13.-19.02.2017, 27.-28.02.2017

RAEPSAET, Caroline, Institut de minéralogie, de physique des matériaux et de cosmochimie (IMPMC), Paris, France: 04.-08.12.2017

ROSENTHAL, Anja, Laboratoire Magmas et Volcans, Aubière, France: 25.-26.04.2017

ROZEL, Antoine, ETH Zurich, Institute of Geophysics, Zurich, Switzerland: 12.-14.06.2017

SAKODA, Yozora, Hiroshima University, Department of Earth and Planetary Systems Science, Hiroshima, Japan: 06.-09.01.2017, 01.-30.09.2017

SATO, Yuki, Tohoku University, Center for Northeast Asian Studies, Sendai, Japan: 14.-18.03.2017

SCHULZ, Falko, Deutsches Zentrum für Luft- und Raumfahrt e.V. (DLR), Institut für Planetenforschung, Berlin, Germany: 19.-20.12.2017

SMYTH, Joseph R., University of Colorado at Boulder, Department of Geological Sciences, Boulder, USA: 06.-17.02.2017, 04.-19.05.2017

SPIVAK, Anna: Institute of Experimental Mineralogy, Chernogolovka, Moscow region, Russia: 01.-31.07.2017

STAGNO, Vincenzo, Sapienza – Università di Roma, Dipartimento di Scienze della Terra, Roma, Italy: 04.-07.07.2017

SUZUKI, Akio, Tohoku University, Department of Earth Science, Sendai, Japan: 20.08.-02.09.2017, 20.-31.12.2017

TSUJIMORI, Tatsuki, Tohoku University, Center for Northeast Asian Studies, Sendai, Japan: 20.02.-01.03.2017

XU, Yigang, Chinese Academy of Sciences, Guangzhou Institute of Geochemistry,  
Guangzhou, P.R. China: 19.-23.08.2017

YUAN, Liang, Tohoku University, Department of Earth and Planetary Material Sciences,  
Sendai, Japan: 29.08.-16.10.2017

ZAKHARCHENKO, Egor, Institute of Experimental Mineralogy, Chernogolovka, Moscow  
region, Russia: 01.-31.07.2017

## 7. Additional scientific activities

### 7.1 Habilitation/Theses

#### *Habilitation*

MCCAMMON, Catherine: Die Erde zur Zeit des Hadaikums.

#### *Ph.D. theses*

ARATÓ, Robert: Magnetite–melt oxybarometry.

BLAHA, Stephan: Water content dependence of dislocation mobility of olivine in the [100](010) slip system.

CERANTOLA, Valerio: The effect of pressure, temperature and oxygen fugacity on the stability of subducted carbonates and implications for the deep carbon cycle.

CHUST, Thomas: A computational framework for mineralogical thermodynamics of the Earth's mantle.

CHUVASHOVA, Irina: High pressure synthesis and investigations of properties of boron allotropes and boron carbide.

GUO, Haihao: An experimental study on volatiles and metals in fluids of magma chambers and porphyry ore deposits.

POSNER, Esther: Mass transport and structural properties of liquid iron alloys at high pressure.

#### *M.Sc. theses*

ADAMS, Andrea: Viability of Archean subduction initiation by continental spreading and plume-continent interactions.

MELAI, Caterina: High pressure behaviour of magnetite-magnesioferrite solid solution.

ZAREI, Alireza: On the feasibility of measuring hydrogen isotope fractionation by in-situ Raman spectroscopy.

### 7.2 Honours and awards

BUCHEN, Johannes                      Best Poster Award, 9<sup>th</sup> High-Pressure Mineral Physics Seminar, Saint Malo, France, September 2017

DUBROVINSKY, Leonid                (and Natalia DUBROVINSKAIA) received the Gregori Aminoff Prize in Crystallography 2017 by the Royal Swedish Academy of Sciences

JACOBSON, Seth received the 2017 Ronald Greeley Early Career Award in Planetary Science of the American Geophysical Union

MCCAMMON, Catherine received the Science Award of the International Board on the Applications of the Mössbauer Effect

### *7.3 Editorship of scientific journals*

DUBROVINSKY, Leonid Member, Editorial Board of the Journal of High Pressure Research

KATSURA, Tomoo Associate Editor "Reviews of Geophysics"

KEPPLER, Hans Editorial Board "Contributions to Mineralogy and Petrology"  
Editorial Board "ACS Earth and Space Chemistry"

MCCAMMON, Catherine Chief Editor and Managing Editor "Physics and Chemistry of Minerals"

MIYAJIMA, Nobuyoshi Associate Editor "European Journal of Mineralogy"

### *7.4 Membership of scientific advisory bodies*

BOFFA BALLARAN, Member of the Review Panel for allocation of beam-time at the  
Tiziana Advanced Light Source, Berkeley  
Member, Dana Medal Committee, American Mineralogical Society

DUBROVINSKY, Leonid Member, Review Panel for allocation of beam-time at ESRF  
Member, Review Panel of Canadian Light Source  
Chair, Subcommission on Spectroscopy, Diffraction, and new Instrumentations in Mineral Physics of the International Mineralogical Association  
Member, Deep Carbon Observatory Scientific Steering Committee  
Member, Review Panel of PETRA III

FROST, Dan Chair of the Executive Committee for Elements Magazine  
Elected member of the Bavarian Academy of Sciences  
Member of the Selection committee for Alexander von Humboldt Professorships  
Member of the ERC Starting grants review panel

JACOBSON, Seth	Vice Chair, Division on Dynamical Astronomy, American Astronomical Society
KEPPLER, Hans	Member, Abraham Gottlob Werner Medal Committee, German Mineralogical Society (DMG) Member, Commission for Research of Bayreuth University (Präsidentalkommission für Forschung und wissenschaftlichen Nachwuchs) Member, German National Academy of Sciences (Leopoldina) Member, Bavarian Academy of Sciences Member, Deep Carbon Observatory Scientific Steering Committee Member, Alexander von Humboldt Foundation Selection Panel for Humboldt Awardees Member, Committee CE31 "Subatomic physics, sciences of the universe, structure and history of the Earth", Agence Nationale de la Recherche, Paris Member, Advisory Board, Dachverband Geowissenschaften
MARQUARDT, Hauke	Member, Bavarian Academy of Sciences (Young Scholars' Programme)
MCCAMMON, Catherine	Member, Consolidator Grant Shadow Panel PE10, European Research Council Member, Council, International Mineralogical Association Member, Council, Deutsche Mineralogische Gesellschaft Member, Governance Committee of the American Geophysical Union Chair, Bunsen Medal Committee, European Geosciences Union Chair, Sub-committee "Earth's Deep Interior" of the Commission of the Physics of Minerals, International Mineralogical Association Member, IASPEI/IAVCEI/IAGA Commission on Physics and Chemistry of Earth Materials



## 8. Scientific and Technical Personnel

Name		Position	Duration in 2017	Funding source
ABEYKOON, Sumith	B.Sc.	Student. Hilfskraft	to 10.05. from 11.05.	DFG IRTG
ADAMS, Andrea	B.Sc.	Student. Hilfskraft	to 14.04.	DFG
ARATÓ, Robert	M.Sc.	Wiss. Mitarbeiter	to 14.10.	DFG
ARMSTRONG, Katherine	M.Sc.	Wiss. Mitarbeiterin	to 28.02. from 01.03.	DFG IRTG
AUDÉTAT, Andreas	Dr.	Akad. Rat		BGI
BHAT, Shrikant	Dr.	Wiss. Mitarbeiter		BMBF
BLANCHARD, Ingrid	Dr.	Wiss. Mitarbeiterin		DFG
BÖHM, Ulrich		Mechaniker		BGI
BOFFA BALLARAN, Tiziana	Dr.	Akad. Oberrätin		BGI
BOLLINGER, Caroline	Dr.	Forschungsstipendiatin	to 30.09. from 02.10.	AvH UBT <sup>2</sup>
BONDAR, Dmitry	M.Sc.	Wiss. Mitarbeiter	from 15.12.	IRTG
BUCHEN, Johannes	Dipl.-Min.	Wiss. Mitarbeiter	to 30.04. from 01.05.	DFG IRTG
BUCHERT, Petra		Fremdsprachen- sekretärin		BGI
BYKOV, Maxim	Dr.	Wiss. Mitarbeiter		DFG
BYKOVA, Elena	Dr.	Wiss. Mitarbeiterin	to 31.01.	DFG
CHANG, Jia	M.Sc.	Stipendiat		CSC
CHARITON, Stella	M.Sc.	Wiss. Mitarbeiterin		DFG
CHUVASHOVA, Irina	Dipl.-Chem.	Wiss. Mitarbeiterin	to 30.06.	DFG
CONDAMINE, Pierre	Dr.	Wiss. Mitarbeiter		Leibniz
CRINITI, Giacomo	B.Sc.	Student. Hilfskraft	from 01.11.	DFG
DRUZHBIN, Dmitry	M.Sc.	Wiss. Mitarbeiter		DFG
DUBROVINSKY, Leonid	Apl. Prof. Dr.	Akad. Direktor		BGI
EBERHARD, Lisa	M.Sc.	Wiss. Mitarbeiterin	from 01.07.	IRTG
EICHHEIMER, Philipp	M.Sc.	Wiss. Mitarbeiter		IRTG
EL GORESY, Ahmed	Prof. Dr.			BGI/VP <sup>1</sup>
FARLA, Robert	Dr.	Forschungsstipendiat	to 30.04.	AvH
FEI, Hongzhan	Dr.	Wiss. Mitarbeiter		DFG
FERREIRA, Filipe	M.Sc.	Wiss. Mitarbeiter	from 01.02.	IRTG
FISCHER, Heinz		Mechaniker		BGI
FISCHER, Nicole	RAmtfr	Verwalt. Beamtin		BGI
FLANIGAN, Michaela	M.Sc.	Wiss. Mitarbeiterin	from 01.10.	Leibniz
FROST, Daniel	Prof. Dr.	Leiter		BGI

GOLABEK, Gregor	Prof. Dr.	Professor		BGI
GUO, Haihao	M.Sc.	Stipendiat	to 30.09.	CSC
	Dr.	Wiss. Mitarbeiter	from 15.10.	DFG
HEIDELBACH, Florian	Dr.	Wiss. Mitarbeiter	to 30.11.	UBT <sup>2</sup>
			from 01.12.	BGI
HUANG, Rong	M.Sc.	Wiss. Mitarbeiterin		AvH
IMMOOR, Julia	Dipl.-Geol.	Wiss. Mitarbeiterin		DFG
ISHII, Takayuki	Dr.	Stipendiat		JSPS
JACOBSON, Seth	Dr.	Wiss. Mitarbeiter	to 31.08.	EU
JENNINGS, Eleanor	Dr.	Wiss. Mitarbeiterin		EU
KATSURA, Tomoo	Prof. Dr.	Stellvertr. Leiter		BGI
KAWAZOE, Takaaki	Dr.	Akad. Rat	to 30.09.	BGI
KEPPLER, Hans	Prof. Dr.	Professor		BGI
KEYSSNER, Stefan	Dr.	Akad. Oberrat	to 30.09.	BGI
KHANDARKHAEVA, Saiana	M.Sc.	Wiss. Mitarbeiterin	from 01.05.	DFG
KISON-HERZING, Lydia		Sekretärin		BGI
KLASINSKI, Kurt	Dipl.-Ing. (FH)	Techn. Angestellter	to 21.05.	BGI
KLUMBACH, Steffen	Dr.	Wiss. Mitarbeiter		DFG
KOEMETS, Egor	M.Sc.	Wiss. Mitarbeiter		IRTG
KOEMETS, Iuliia	B.Sc.	Student. Hilfskraft	to 18.01.	HiWi u. UBT <sup>3</sup>
			19.01.-27.09.	DFG u. UBT <sup>3</sup>
			28.09.-31.10.	DFG
			from 01.11.	IRTG
KRAUBE, Detlef	Dipl.-Inform. (FH)	Techn. Angestellter		BGI
KRIEGL, Holger		Haustechniker		BGI
KULIK, Eleonora	Dipl.-Physik- ingenieurin	Wiss. Mitarbeiterin	from 03.10.	DFG
KURNOSOV, Alexander	Dr.	Wiss. Mitarbeiter	to 31.03. from 01.04.	Leibniz DFG
LAURENZ-HEUSER, Vera	Dr.	Wiss. Mitarbeiterin		EU
LI, Yang	B.Sc.	Student. Hilfskraft	to 22.01.	DFG
LINHARDT, Sven		Elektrotechniker		BGI
LIU, Zhaodong	Dr.	Wiss. Mitarbeiter		BGI/VP
MAKOWSKA, Malgorzata	Dr.	Wiss. Mitarbeiterin		BMBF
MALLIK, Ananya	Dr.	Stipendiatin		AvH
MANDOLINI, Tommaso	B.Sc.	Student. Hilfskraft		IRTG
MARQUARDT, Hauke	Dr.	Nachwuchs- gruppenleiter		DFG

MARQUARDT, Katharina	Dr.	Akad. Rätin		BGI
MARZOTTO, Enrico	M.Sc.	Wiss. Mitarbeiter	from 15.11.	IRTG
MCCAMMON, Catherine	Privatdozentin	Akad. Direktorin		BGI
	Dr.			
MEIER, Thomas	Dr.	Wiss. Mitarbeiter		BGI/VP
MELAI, Caterina	B.Sc.	Student. Hilfskraft	to 30.06.	GIF
			01.07.-14.10.	IRTG
	M.Sc.	Wiss. Mitarbeiterin	from 15.10.	IRTG
MISRA, Sourav	B.Sc.	Student. Hilfskraft	to 03.05.	DFG
			04.05.-23.06.	HiWi
			from 24.06.	IRTG
MIYAJIMA, Nobuyoshi	Dr.	Akad. Oberrat		BGI
NJUL, Raphael		Präparator		BGI
OVSYANNIKOV, Sergey	Dr.	Wiss. Mitarbeiter		DFG
PETIGIRARD, Sylvain	Dr.	Wiss. Mitarbeiter		DFG
POLEDNIA, Joana	M.Sc.	Wiss. Mitarbeiterin		DFG
POSNER, Esther	M.Sc.	Wiss. Mitarbeiterin	to 30.04.	EU
			20.10.-30.11.	BGI/VP
			from 01.12.	UBT <sup>2</sup>
POTZEL, Anke		Chem.-Techn. Assistentin		BGI
PUTAK JURIČEK, Marija	M.Sc.	Wiss. Mitarbeiterin	from 01.03.	IRTG
RAMMING, Gerd		Elektroniker		BGI
RAUSCH, Oliver		Mechaniker		BGI
REBAZA MORILLO, Anna Mireia	B.Sc.	Student. Hilfskraft	15.04.-05.10.	DFG
			from 06.10.	IRTG
ROTHER, David Alexander		Präparator	from 01.11.	BGI
ROTTIER, Bertrand	Dr.	Stipendiat	from 01.09.	SNF
RUBIE, David C.	Prof. Dr.	Professor		EU
RUSTIONI, Greta	M.Sc.	Wiss. Mitarbeiterin		IRTG
SAN JOSÉ MÉNDEZ, Alba	M.Sc.	Wiss. Mitarbeiterin	from 01.06.	DFG
SATTA, Niccolò	M.Sc.	Wiss. Mitarbeiter	from 01.07.	IRTG
SCHARFENBERG, Romina	B.Sc.	Sekretärin		BGI
SCHULZE, Hubert		Präparator	to 31.07.	BGI
			from 01.08.	GIF
SCHULZE, Kirsten	M.Sc.	Wiss. Mitarbeiterin		DFG
SEROVAISKII, Aleksandr	M.Sc.	Stipendiat	to 28.02.	DAAD
SHCHEKA, Svyatoslav	Dr.	Wiss. Mitarbeiter		DFG
SIERSCH, Nicki	M.Sc.	Wiss. Mitarbeiterin		Leibniz
SIMONOVA, Dariia	M.Sc.	Wiss. Mitarbeiterin		DFG
STEINLE-NEUMANN, Gerd	Dr.	Akad. Oberrat		BGI

THIELMANN, Marcel	Dr.	Wiss. Mitarbeiter		BGI/VP
TRENZ, Ulrike		Biol.-Techn. Assistentin		BGI
TRYBEL, Florian	M.Sc.	Wiss. Mitarbeiter	from 15.08.	IRTG
ÜBELHACK, Stefan		Mechaniker		BGI
URGESE, Matteo	B.Sc.	Student. Hilfskraft		IRTG
WAGLE, Fabian	M.Sc.	Wiss. Mitarbeiter	to 31.03. 01.04.-21.04.	DFG
			from 22.04.	DFG
WANG, Biao	B.Sc.	Student. Hilfskraft	from 01.11.	DFG
WANG, Lin	M.Sc.	Wiss. Mitarbeiter		DFG
WIESNER, Dorothea		Techn. Assistentin		BGI
YAO, Jie	M.Sc.	Wiss. Mitarbeiter		DFG
YOSHIOKA, Takahiro	M.Sc.	Wiss. Mitarbeiter		DFG
ZAREI, Alireza	B.Sc.	Student. Hilfskraft	to 19.10.	IRTG
ZIBERNA, Luca	Dr.	Forschungsstipendiat		AvH

#### Abbreviations/explanations:

AvH	Alexander von Humboldt Foundation
BGI	Staff Position of Bayerisches Geoinstitut
BGI/VP	Visiting Scientists' Program of Bayerisches Geoinstitut
BMBF	Federal Ministry of Education and Research
CSC	Chinese Science Council
DAAD	German Academic Exchange Service
DFG	German Science Foundation
EU	European Union
GIF	German-Israeli Foundation for Scientific Research and Development
HiWi	Hilfskraftmittel BGI
IRTG	International Research Training Group "Deep Earth Volatile Cycles"
JSPS	Japanese Society for the Promotion of Science
Leibniz	Leibniz-Preis der Deutschen Forschungsgemeinschaft Prof. Frost
SNF	Swiss National Foundation
UBT	Universität Bayreuth

<sup>1</sup> partially funded by the Visiting Scientists' Program of Bayerisches Geoinstitut

<sup>2</sup> freie Stellenmittel

<sup>3</sup> Mittel zur Erfüllung des Gleichstellungsauftrages

## Index

Abeykoon, S. ....	42, 206
Abrikosov, I.A. ....	88, 173
Aprilis, G. ....	85, 93, 173, 175, 187, 190
Arató, R. ....	56
Arimoto, T. ....	61
Armstrong, K. ....	52, 136
Asphaug, E.I. ....	26
Audétat, A. ....	56, 63, 69, 72, 74, 206
Baron, M.A. ....	197
Bell, A.S. ....	136
Belov, M. ....	88
Beyer, C. ....	53
Bhat, S. ....	29
Blanchard, I. ....	47
Blundy, J. ....	67
Boffa Ballaran, T. ....	52, 61, 78, 79, 82, 102, 107, 108, 110, 111, 113, 117, 204
Bollinger, C. ....	150, 155
Boneh, Y. ....	159
Bons, P. ....	148
Bremner, P. ....	28
Buchen, J. ....	107, 115, 118, 153
Bulanova, G. ....	55
Bykov, M. ....	85, 88, 90, 93, 95, 172, 173, 175, 180, 187
Bykova, E. ....	85, 88, 90, 93, 95, 172, 173, 175, 180, 187
Cai, N. ....	113
Cerantola, V. ....	55, 85, 93, 190
Černok, A. ....	88
Chang, J. ....	69
Chariton, S. ....	93, 175
Chaudhari, A. ....	118
Chumakov, A.I. ....	85, 190
Chuvashova, I. ....	60, 172, 173
Clement, S. ....	175
Condamine, P. ....	62, 132, 134, 182
Criniti, G. ....	78
Diamond, M.R. ....	28
Dohmen, R. ....	168, 184
Dominijanni, S. ....	61
Douglas, J. ....	202
Druzhbin, D. ....	29, 120, 168

Dubrovinskaia, N.A. ....	60, 85, 88, 172, 173, 187, 188, 196
Dubrovinsky, L.S. ....	58, 60, 84, 85, 88, 90, 93, 95, 112, 172, 173, 175, 180, 187, 188
.....	190, 192, 194, 196
Dullemond, C.P. ....	24
Duretz, T. ....	169
Eberhard, L. ....	65
Eichheimer, P. ....	31, 34
Ejaz, T. ....	27
Elkins-Tanton, L. ....	45
Emsenhuber, A. ....	26
Faccincani, L. ....	55
Farla, R. ....	29, 148
Farmer, N. ....	182
Faul, U. ....	28
Fedotenko, T. ....	196
Fei, H. ....	29, 120, 168
Ferreira, F. ....	155, 157
Francomme, J. ....	134
Frost, D.J. ....	40, 42, 44, 49, 52, 55, 61, 62, 65, 79, 82, 113, 117, 132, 136, 146, 182, 204
Fujita, W. ....	34
Fuqua, H. ....	28
Garapic, G. ....	27
Gasharova, B. ....	90
Gerya, T.V. ....	24, 26
Gilmore, K. ....	87
Glazyrin, K. ....	90, 172, 173, 187
Golabek, G.J. ....	24, 26, 31, 32, 34
Gomez-Rivas, E. ....	148
Gorelova, L. ....	90
Gréaux, S. ....	113
Green, E.C.R. ....	67
Greenberg, E. ....	187
Griera, A. ....	148
Grüninger, H. ....	79
Guo, H. ....	72
Haines, J. ....	175
Hanfland, M. ....	85, 88, 93, 175
Heidelberg, F. ....	143, 146, 148, 150
Hellman, O. ....	88
Hernlund, J. ....	32
Higo, Y. ....	29
Huang, R. ....	29, 79, 82, 204

Immoor, J. ....	153, 176
Irifune, T. ....	61, 113
Ishii, T. ....	29, 78, 117
Jacobson, S.A. ....	39, 40
Jennings, E.S. ....	40, 47, 200, 202
Jutzi, M. ....	26
Kadyrova, N.I. ....	180
Kamada, S. ....	92
Katsura, T. ....	29, 79, 84, 117, 120, 162, 164, 165, 168
Kawazoe, T. ....	29, 85, 95, 107, 108, 110, 162, 164
Keppler, H. ....	63, 127, 128, 130, 140
Khachtryan, G. ....	60
Khandarkhaeva, S. ....	188, 196
Kichanov, S.E. ....	180
Klumbach, S. ....	130, 140
Knödler, P. ....	155
Koch-Müller, M. ....	108
Koemets, E. ....	93, 173, 175, 187, 196
Koemets, I. ....	29, 112
Korobeinikov, I.V. ....	178, 180
Kozlenko, D.P. ....	180
Krivovichev, S. ....	90
Kulik, E. ....	29
Kupenko, I. ....	85, 190
Kurnosov, A. ....	102, 107, 108, 110, 112, 118, 153, 180, 194
Lagos, M. ....	44
Laporte, D. ....	134
Laurenz, V. ....	42, 44, 45, 200
Li, Y. ....	132
Lichtenberg, T. ....	24
Liermann, H.-P. ....	85, 88, 90, 97, 115, 153, 173, 176
Lin, F. ....	153
Lin, Y. ....	168
Litvin, Y. ....	58, 60
Liu, Z. ....	29, 79, 84, 113, 117
Lock, S.J. ....	28
Lognonne, P.H. ....	28
Lord, O.T. ....	197
Maeda, F. ....	29, 92
Malfait, W. ....	27
Mallik, A. ....	27, 28, 132
Mandolini, T. ....	143

Marquardt, H. ....	32, 34, 97, 98, 107, 108, 110, 112, 115, 118, 153, 176, 194
Marquardt, K. ....	53, 108, 155, 157, 159, 184
Masotta, M. ....	128
McCammon, C.A. ....	52, 53, 55, 82, 84, 85, 93, 103, 108, 190, 204
Médard, E. ....	132, 134
Meier, T. ....	192
Melai, C. ....	55, 102
Méndez, A.S.J. ....	97, 98, 115
Merkel, S. ....	153, 176
Meyer, M.R. ....	24
Mezouar, M. ....	90, 172, 173
Miyagi, L. ....	153
Miyajima, N. ....	82, 92, 162, 164, 197, 204
Morbidelli, A. ....	39, 40, 45
Morozova, N.V. ....	178, 180
Myhill, R. ....	53, 85
Nakajima, Y. ....	40
Nakamura, M. ....	34
Nakamura, T. ....	127
Nakashima, D. ....	127
Newville, M. ....	136
Nishikawa, Y. ....	28
Nishiyama, N. ....	118
Okumura, S. ....	34
Ovsyannikov, S.V. ....	178, 180
Pakhomova, A. ....	90, 111, 180, 187
Pamato, M.G. ....	111
Panero, W.R. ....	28
Panovska, S. ....	28
Peiffer, S. ....	103
Perez, H.J. ....	28
Petitgirard, S. ....	27, 47, 87, 192, 197, 200
Polednia, J. ....	184
Ponomareva, A.V. ....	173
Posner, E.S. ....	49
Prakapenka, V. ....	85, 88, 172, 173, 175, 187
Prescher, C. ....	88
Rogalev, A. ....	180
Rose-Weston, L.A. ....	40
Rouquette, J. ....	175
Rubie, D.C. ....	39, 40, 42, 44, 45, 47, 49, 52, 200, 202
Rüffer, R. ....	190

Rustioni, G. ....	63
Sahle, C. ....	87
Sakamaki, T. ....	92
Satta, N. ....	110
Schönbächler, M. ....	24
Schröder, C. ....	103
Schulze, K. ....	108, 111, 118
Sedmak, P. ....	188
Senker, J. ....	79
Shahar, A. ....	28
Shcheka, S. ....	27, 127
Siersch, N.C. ....	78, 113, 117
Silva-Souza, D. ....	150
Simak, S.I. ....	88
Simonova, D. ....	58, 60, 95
Smith, C. ....	55
Sorbadere, F. ....	204
Speziale, S. ....	107, 118, 153, 176
Spiekermann, G. ....	87
Spivak, A. ....	58, 60
Stagno, V. ....	61
Steinle-Neumann, G. ....	49, 99, 122, 138
Strohm, C. ....	190
Suzuki, A. ....	92
Takafumi, T. ....	29
Tange, Y. ....	29
Tasnádi, F. ....	173
Thielmann, M. ....	31, 32, 34, 155, 169, 197
Tidholm, J. ....	88
Trønnes, R.G. ....	197
Trybel, F. ....	99
Tsirlin, A.A. ....	180
Tsujino, N. ....	29
Tyutyunnik, A.P. ....	180
Uenver-Thiele, L. ....	102
Urgese, M. ....	32, 148
van Driel, J. ....	85
Vasiukov, D.M. ....	85, 190
Vlček, V. ....	49
Vogel, A.K. ....	40, 42
Wade, J. ....	200, 202
Wagle, F. ....	122, 138

Walte, N. ....	146
Walter, M.J. ....	197
Wan, M. ....	103
Wang, L. ....	29, 162, 164, 165
Wang, Y. ....	117
Weis, C. ....	87
Wieczorek, M. ....	45
Wiedenbeck, M. ....	132, 168
Wilhelm, F. ....	180
Wilke, M. ....	27, 87
Woodland, A.B. ....	102
Wright, J. ....	188
Yao, J. ....	138
Yoshioka, T. ....	127
Yu, T. ....	117
Yuan, L. ....	29
Zainulin, Y.G. ....	180
Zakharchenko, E. ....	58
Zarei, A. ....	140
Zhang, C. ....	168
Zhang, D. ....	74
Ziberna, L. ....	55, 61, 67



### **Obituary Kurt Klasinski (\* 24.5.1957, † 21.5.2017)**

It is with great sadness that we report the death of Kurt Klasinski, the Bayerisches Geoinstitut's electronics and software engineer, just three days short of his 60<sup>th</sup> birthday. Kurt Klasinski was the longest serving employee at the institute at the time of his death, having worked here almost since the institute's foundation 30 years ago. He was responsible for developing many of the control and data acquisition protocols for laboratory equipment created at the institute and he wrote many software applications for this purpose. Kurt was adept at developing functional user interfaces that turned complex experimental procedures into relatively routine measurements. This was a particular benefit to the many short-term visitors to the institute as it allowed them to quickly master experimental devices. His very professional support and innovative solutions helped many researchers to focus on and realize their scientific goals. He will be remembered for his remarkable problem-solving abilities and for his mischievous sense of humor. To quote from his obituary in the local newspaper,

"The finest thing to leave behind is a smile on the face of those who think of him."

We mourn the loss of an exceptional engineer and colleague and we will honor his memory.

### **Nachruf Kurt Klasinski (\* 24.5.1957, † 21.5.2017)**

Mit großer Trauer geben wir den Tod von Kurt Klasinski, Elektronik- und Software-Ingenieur des Bayerischen Geoinstituts, nur 3 Tage vor seinem 60. Geburtstag, bekannt. Kurt Klasinski war zum Zeitpunkt seines Todes der am längsten am Institut tätige Mitarbeiter, nachdem er fast seit der Gründung des Instituts vor 30 Jahren hier gearbeitet hatte. Er war verantwortlich für die Entwicklung zahlreicher Kontroll- und Datenerfassungsprotokolle für Laborgeräte, die am Institut entwickelt wurden, und er schrieb viele Softwareanwendungen für diesen Zweck. Kurt war geschickt darin, funktionale Benutzerschnittstellen zu entwickeln, die komplexe experimentelle Verfahren in relativ routinemäßige Messungen verwandelten. Dies war ein besonderer Vorteil für die vielen kurzzeitigen Besucher des Instituts, da es ihnen möglich war, experimentelle Geräte schnell zu handhaben. Seine sehr professionelle Unterstützung und seine innovativen Lösungen haben vielen Forschern geholfen, sich auf ihre wissenschaftlichen Ziele zu konzentrieren und diese zu verwirklichen. Er wird für seine bemerkenswerten Fähigkeiten zur Problemlösung und für seinen schelmischen Sinn für Humor in Erinnerung bleiben. Um aus seinem Nachruf in der lokalen Zeitung zu zitieren,

"Das Schönste, was ein Mensch hinterlassen kann, ist ein Lächeln im Gesicht derjenigen, die an ihn denken."

Wir trauern um einen außergewöhnlichen Ingenieur und Kollegen und werden sein Andenken in Ehren halten.

